

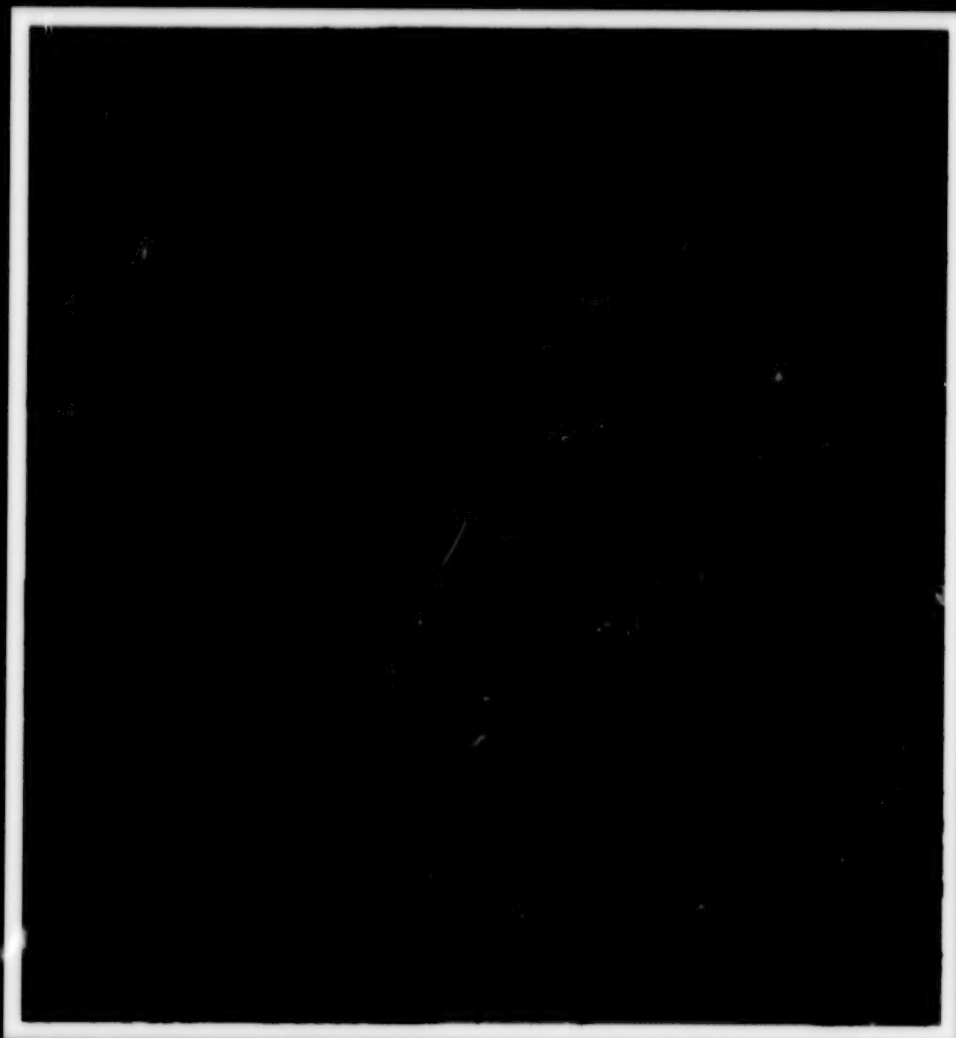
ARCTIC SEA ICE, 1973-1976: SATELLITE PASSIVE-MICROWAVE OBSERVATIONS

(NASA-SP-489) ARCTIC SEA ICE, 1973-1976:
SATELLITE PASSIVE-MICROWAVE OBSERVATIONS
(NASA) 301 p Avail: NTIS MF A01 CSCL 08L

N87-24670

Unclass

H1/48 0082258



ORIGINAL CONTAINS
COLOR ILLUSTRATIONS

**ORIGINAL CONTAINS
COLOR ILLUSTRATIONS**

**ARCTIC SEA ICE, 1973-1976:
SATELLITE PASSIVE-MICROWAVE OBSERVATIONS**

ARCTIC SEA ICE, 1973-1976:
SATELLITE PASSIVE-MICROWAVE OBSERVATIONS

**Claire L. Parkinson, Josefino C. Comiso, H. Jay Zwally,
Donald J. Cavalieri, Per Gloersen**
*Laboratory for Oceans
Goddard Space Flight Center
Greenbelt, Maryland 20771*

William J. Campbell
*U.S. Geological Survey
Ice and Climate Project
University of Puget Sound
Tacoma, Washington 98416*



Scientific and Technical Information Branch 1987
National Aeronautics and Space Administration
Washington, DC

PRECEDING PAGE BLANK NOT FILMED

END INTENTIONALLY BLANK

Library of Congress Cataloging-in-Publication Data

Arctic sea ice, 1973-1976.

(NASA SP: 489)

Bibliography: P.

Includes index.

- I. Sea ice--Arctic regions--Remote sensing.
2. Nimbus (Meteorological satellite) I. Parkinson, Claire L. II. United States. National Aeronautics and Space Administration. Scientific and Technical Information Branch. III. Series

GV2595.A73 1987 551.3'43 86-23876

For sale by the Superintendent of Documents, U.S. Government
Printing Office, Washington, D.C. 20402

FOREWORD

The Arctic region plays a key role in the climate of the Earth. The sea ice cover affects the radiative balance of the Earth and radically changes the fluxes of heat between the atmosphere and the ocean. Both the atmospheric and oceanic circulations at midlatitudes are affected by processes in the polar oceans; seasonal variability as well as interannual changes are reflected in and partially caused by changes in ice cover and ice transport.

The principal contributions of NASA to national and international programs of research on global climate and the dynamics of global change derive from broad applications of space technology to such programs. Satellite data provide time series of synoptic data; little or no such data are available from observations from aircraft, buoys, land stations or ships. As we are now beginning to discover new uses and methods of interpretation of satellite data, it is important to make overviews of data available to the scientific community, so that investigators can determine where further exploration may be possible using the data and other observations.

This publication summarizes the observations of the Arctic made by the Electrically Scanning Microwave Radiometer on board the Nimbus 5 research satellite over the period 1973 through 1976. It is hoped that the information will make this book a useful reference for climatologists and polar oceanographers.

W. Stanley Wilson
Chief, Oceanic Processes Branch
Office of Space Science and Applications, NASA

Erik Mollo-Christensen
Chief, Laboratory for Oceans
Goddard Space Flight Center

PREFACE

Those who are interested in the polar regions and also those who are intrigued by the latest achievements in remote sensing from satellites will certainly welcome this volume. They will probably recognize that it is a sequel to an earlier (1983) atlas by nearly the same group of scientists at the NASA Goddard Space Flight Center and the United States Geological Survey entitled *Antarctic Sea Ice, 1973-1976: Satellite Passive-Microwave Observations*. Now both of the polar regions have been heard from—loudly and clearly.

What, exactly, is this atlas all about? In a nutshell, it summarizes the observations made of the Arctic by the Electrically Scanning Microwave Radiometer (ESMR) onboard the Nimbus 5 polar orbiting meteorological satellite. A major advantage of microwave observations over the more common visible and infrared satellite observations is that the former can penetrate clouds. Furthermore, the microwave data can be collected both day and night. This atlas also explains in some detail how these microwave observations can be interpreted in terms of area of ocean covered by sea ice and the kind of ice (whether first-year or multiyear ice). It even goes into the climatology of the Arctic and the reasons for the seasonally changing distributions and motions of the ice pack under the influence of winds and ocean currents.

To call this volume an "atlas" is actually misleading, since it is obviously much more than that. To be sure, it contains a large number of beautiful maps in many colors depicting various aspects of the state of the Arctic in a 4-year period in the 1970s, but its significance and its message extend far beyond those maps. The oceanic and atmospheric processes that take place in the Arctic are crucial to the weather and climate of the entire Northern Hemisphere, and here we have a moving picture of the Arctic as seen from space with a completeness and clarity never before achieved. Furthermore, this volume contains the information needed to study the details of the changes in the Arctic Ocean that may well ensue if the global warming that many believe is now taking place accelerates in the years ahead. Rarely have climatologists had such a good milestone from which to start.

The text that accompanies and explains the satellite passive-microwave observations is excellent, and indeed the report as a whole is a kind of textbook on the processes involved in the freezing and thawing of sea ice—as well as the remote sensing techniques for observing them. (The same can be said of the preceding volume.) However, the sense of excitement and adventure that has motivated this team of scientists from the start seems to be carefully muted in their own professional accounts.

To appreciate this sense of excitement one should turn back the clock a good many years, to the period when Dr. William Nordberg of the Goddard Space Flight Center and his colleagues (numbering among them some of the present authors) were developing and testing the first of those microwave radiometers from jet aircraft flying high over the frozen Arctic.

The instrument worked well enough, as it turned out, and the next challenge was to demonstrate that its measurements could be interpreted in a useful way in terms of the actual conditions in the ice pack far below the observing platform—as has now been amply illustrated in this volume.

Enter the eager apostles of “ground truth.” These were the men and women who ventured into the ice pack in ships, who flew over it in helicopters and light planes, and who lived for months at a time in observing stations on the shifting sea ice, far from shore. (Again, many of the present authors were involved in this kind of activity. One of them, demonstrating an audacity that belied his very considerable intelligence, was the first person to don diving gear and explore the ice pack from underneath.)

The pictures in Chapter 1 convey a small idea of the environment that they faced—but I note that these photographs seem to have always been taken in *good* weather. Perhaps the most ambitious of these ventures onto the Arctic ice was the Arctic Ice Dynamics Joint Experiment (AIDJEX), largely sponsored by the National Science Foundation and the Office of Naval Research, with the cooperation of NASA and the Canadian Polar Continental Shelf Project. Some readers might not know that the drifting triangle shown in Figure 3-7 marks where men and women were living in the AIDJEX tents and huts. They lived there in four stations until, one day in October 1975, the ice split apart with a loud crackling sound and a lead of open water suddenly threaded its way through the base station, dividing it in two and leaving the mess hall hanging out over the water. (In spite of this, the AIDJEX carried on to the scheduled end of its mission in April 1976.)

So the days of Arctic exploration and adventure in the pursuit of science are far from a thing of the past. There are new and compelling reasons for going there, of course, including the oil and other natural resources to be found there, and the probability that the Arctic Ocean has already become an important theater of operations for both U.S. and Soviet submarines. And, as referred to earlier, a progressively warmer Earth would undoubtedly make the Arctic more attractive for a variety of other activities, including a laboratory for the study of climate change in progress.

We must therefore look upon this atlas of the Arctic as but one step in a continuing research effort, an effort in which NASA will, as in the past, join forces with other government agencies, such as the National Oceanic and Atmospheric Administration (NOAA), the National Science Foundation (NSF), the United States Geological Survey (USGS), and the Department of Defense (DOD), and with other countries bordering on the Arctic Ocean.

This volume contains the record obtained by the Nimbus 5 satellite and its ESMR, a single-frequency radiometer that has now been retired from active duty. Now there are (or will shortly be) multichannel microwave radiometers on NASA, NOAA, and DOD satellites. The pioneering work of the Goddard Space Flight Center's Oceans and Ice Branch, together with the USGS, has set the stage admirably for continuing surveys of the Arctic from the vantage point of space.

William W. Kellogg
Senior Scientist
National Center for Atmospheric Research
Boulder, Colorado

ACKNOWLEDGMENTS

We thank the many people who have contributed to the efforts involved in producing this volume. Carrie Brezinski, Scott Bringen, Bob Kostic, and Bob Lutz of Science Applications Research put considerable time and effort into helping with the computer generation of the color images and the line plots and were assisted in this effort with excellent support from GSFC's Atmospheric and Oceanographic Information Processing System, GSFC's Photographic Section, and Bara Photographic, Inc. Reviewers Roger Barry, Seelye Martin, and Frank Carsey each carefully read through the text and offered many valuable comments and suggestions; and the book's scientific content was further strengthened as a result of numerous discussions with Erik Mollo-Christensen, John Walsh, Seelye Martin, Roger Barry, Bob Thomas, Will Kellogg, and Jim Marsh. We also appreciate the support of GSFC's Space and Earth Sciences Directorate. Finally, Stan Wilson, Bob Thomas, and Ken Jezek of NASA's Oceanic Processes Branch encouraged and supported the project and provided the funding that made the work possible.

CONTENTS

<i>Chapter</i>	<i>Page</i>
FOREWORD	v
PREFACE	vii
ACKNOWLEDGMENTS	ix
SUMMARY	xv
1. INTRODUCTION	1
1.1 Overview	1
1.2 Sea Ice as a Component of the Climate System	2
1.3 Sea Ice Formation and Types	2
1.4 Sea Ice Properties	10
1.5 Satellite Imaging of Sea Ice; The ESMR Data	16
1.6 Preview	18
2. OCEANOGRAPHIC AND ATMOSPHERIC CONDITIONS INFLUENCING THE ARCTIC SEA ICE COVER	21

<i>Chapter</i>	<i>Page</i>
2.1 Introduction	21
2.2 Bathymetry	21
2.3 Ocean Circulation	24
2.4 Ocean Temperatures and Salinities	26
2.5 The Arctic and Global Atmospheric Energy Balances	26
2.6 Atmospheric Temperatures, Pressures, and Winds	30
2.7 Synoptic Characteristics of the Arctic Atmosphere	31
3. THEORY OF MICROWAVE EMISSION, THE ESMR BRIGHT- NESS TEMPERATURE DATA, AND THE DERIVATION OF SEA ICE PARAMETERS	41
3.1 Introduction	41
3.2 Microwave Emissivity and Brightness Temperature	42
3.3 Sea Ice Emissivity	43
3.4 Aircraft and Surface Observations	48
3.5 Monthly Brightness Temperature Images	54
3.6 Determination of Ice Concentration and Multiyear Ice Fraction	94
3.7 Error Analysis	101
4. SEASONAL SEA ICE CYCLE AND REGIONAL CHARACTERISTICS	109
4.1 Introduction	109
4.2 Arctic Ocean	124
4.3 Sea of Okhotsk	172
4.4 Bering Sea	176
4.5 Hudson Bay	180
4.6 Baffin Bay/Davis Strait	185

<i>Chapter</i>	<i>Page</i>
4.7 Greenland Sea	190
4.8 Kara and Barents Seas	198
4.9 Canadian Archipelago	203
5. THE ARCTIC SEA ICE COVER AS A WHOLE AND INTERREGIONAL COMPARISONS	211
5.1 Introduction	211
5.2 Oceanographic Influences	211
5.3 Atmospheric Influences and Out-of-Phase Relationships in the Sea Ice Cover	214
5.4 Overall Sea Ice Trends and Interregional Comparisons	215
REFERENCES	231
APPENDIX A. Data Processing, Compilation, and Storage	241
APPENDIX B. Ice Edge Contour Maps	253
APPENDIX C. Areal Distributions of Ice Concentrations	265
APPENDIX D. Acronyms	287
INDEX	289

SUMMARY

Sea ice is an important component in the highly interactive global climate system, reflecting and influencing conditions in both the atmosphere and oceans. Although typically overlying approximately 7 percent of the world's oceans, the sea ice cover experiences considerable seasonal variability in both hemispheres: in the eight regions described in this atlas, encompassing most of the Northern Hemisphere sea ice area, the total extent of sea ice varies from a minimum of about 7.8×10^6 square kilometers in September to a maximum of about 14.8×10^6 square kilometers in March, and in the Southern Hemisphere the extent varies from about 4×10^6 square kilometers in February to about 20×10^6 square kilometers in September. The ice significantly reduces the amount of solar radiation absorbed at the Earth's surface, greatly restricts exchanges of heat, mass, and momentum between ocean and atmosphere, and affects the density structure of the upper ocean through the salt and heat fluxes associated with the freezing and melting processes. The changes in density structure at times lead to deep-water and even bottom-water formation, and the net equatorward advection of sea ice provides a transport of cold, low-salinity water out of the polar regions. In this document, the sea ice cover of the Northern Hemisphere over the 4-year period 1973 through 1976 is described from the passive microwave data of the Electrically Scanning Microwave Radiometer (ESMR) on the Nimbus 5 satellite. The book is a companion volume to *Antarctic Sea Ice, 1973-1976: Satellite Passive-Microwave Observations* (Zwally et al., 1983a), and the two volumes together provide a global picture of sea ice conditions in the mid-1970s.

Data collected by the Nimbus 5 ESMR from its launch in December 1972 through most of the next 4 years provide the earliest all-weather, all-season imagery of global sea ice. For 39 months of the 4-year period, good quality Northern Hemisphere data were transmitted, and these data are the basis of the sea ice maps, plots, and analysis in this volume. The data have been interpolated for spatial and temporal gaps, averaged on a monthly basis into monthly averaged microwave brightness temperatures, and displayed in color-coded polar maps. The large contrast in microwave emissivities between sea ice and open water enables a conversion of the brightness temperatures to sea ice concentrations (percentages of the ocean area covered by sea ice) providing that all sea ice in the field of view has approximately the same emissivity. In many of the seas and bays peripheral to the Arctic Ocean, the ice is predominantly first-year sea ice, with an emissivity near 0.92, so that a straightforward conversion from brightness temperatures to sea ice concentrations is possible. In the Arctic Ocean itself and some of the immediately adjacent waters, multiyear sea ice with an emissivity near 0.84 exists in addition to first-year sea ice, complicating the interpretations. In these areas, sea ice concentrations can be calculated from the brightness temperatures as a function of multiyear ice fraction. The same function is valid for first-year sea ice regions as well, with the multiyear ice fraction set at zero. Color-coded maps of the resulting sea ice concentrations are presented in monthly averaged formats, with associated nomograms relating the color scale, multiyear

ice fraction, and sea ice concentration. Various other color-coded images, including ice concentration yearly averages, 4-year averages for individual months, and differences from month to month, are also presented, as are plots of a variety of variables such as total areal extent of sea ice, area of ice in various ice concentration categories, and area of actual ice coverage. The plots are presented for each of eight regions, covering most of the Northern Hemisphere sea ice area, and for the sum of the eight regions. The eight regions are the Arctic Ocean, the Sea of Okhotsk, the Bering Sea, Hudson Bay, Baffin Bay/Davis Strait, the Greenland Sea, the Kara and Barents Seas, and the Canadian Archipelago.

The ESMR data reveal many of the details of the distribution and dynamics of the Northern Hemisphere sea ice cover, including considerable interannual variability and interregional contrasts. At the time of maximum ice extent in March, the ice cover is nearly complete in the Arctic Ocean, Hudson Bay, the Kara Sea, and the Canadian Archipelago, and is extensive for large portions of the other peripheral seas and bays. The springtime retreat of the ice edge tends to begin first in Davis Strait and the northern North Atlantic and last in the Bering Sea and Hudson Bay. At the time of minimum ice extent in September, the ice pack is mostly confined to the central Arctic Ocean and portions of the Greenland Sea, the Kara Sea, and the Canadian Archipelago. Essentially no ice remains in the Bering Sea, Hudson Bay, the Sea of Okhotsk, or Baffin Bay/Davis Strait. Noticeable autumn ice-edge advance begins first in the Greenland Sea, between August and September, then becomes apparent throughout the remainder of the ice-covered region between September and November.

Certain consistent latitudinal asymmetries in the extent of the ice are readily explained by major ocean currents, whereas many regional interannual contrasts in the ice are explainable by interannual differences in the atmospheric pressure and wind fields. Currents with major impacts include the warm, north-flowing Norwegian, West Greenland, and West Kamchatka Currents, which prevent or delay ice formation in the Barents Sea, immediately southwest of Greenland, and along the west coast of Kamchatka Peninsula, respectively, and the cold, south-flowing East Greenland and Labrador Currents, which transport ice far to the south along the east coasts of Greenland and Canada. Among the phenomena which appear closely connected to atmospheric conditions are the interannual variabilities in the timing of maximum sea ice extent in the Bering and Greenland Seas.

The ESMR data reveal an approximately symmetrical growth/decay cycle of the ice in the Northern Hemisphere and no systematic trend in the overall area of ice coverage over the 4 years 1973 through 1976. This contrasts with the situation revealed for the same 4 years for the Southern Hemisphere, where the seasonal ice decay proceeded far more rapidly than the seasonal ice growth and a marked decreasing trend was apparent in the overall ice area.

INTRODUCTION

1.1 OVERVIEW

Sea ice is an integral part of the climate and life environment of the polar regions. The highly variable ice cover in the Arctic has been the scene of dramatic human adventures, exemplified by historic attempts to find a Northwest Passage or to reach the North Pole. Its practical impacts include hindrance of shipping operations and oil extraction, plus modification of submarine acoustics. The sea ice edge in particular is a region of high biological productivity, with the distribution of sea ice affecting the distributions of marine resources in both polar regions (Alexander, 1980; Botkin et al., 1981). The climatic importance, however, along with its varied facets, is the aspect of most concern for the present volume.

Sea ice is a vital, interactive component of the climate system, affecting and reflecting climate change. The presence of sea ice restricts exchanges of heat, mass, momentum, and chemical constituents between ocean and atmosphere, reduces the amount of solar radiation absorbed at the Earth's surface, and affects oceanic and atmospheric circulation patterns (Barry, 1983; Fletcher, 1969; WMO/ICSU, 1982). The freezing and melting of the ocean surface and the associated fluxes of salt and heat produce major changes in the density structure of the ocean waters and are thus major factors in driving the thermohaline circulation (Warren, 1981). Also, the equatorward advection of sea ice provides a transport of cold, relatively fresh waters out of the polar regions. All of these factors contribute to making the study of sea ice an important part of the study of polar climate (Polar Research Board, 1984).

Data collected by the Nimbus 5 Electrically Scanning Microwave Radiometer (ESMR), launched in December 1972, provided the first all-weather, all-season imagery of global sea ice. Good-quality data were transmitted from the ESMR for much of the next 4 years, creating a sound data base for examining sea ice conditions in the mid-1970s. The Southern Hemisphere sea ice observations from the ESMR are described in *Antarctic Sea Ice, 1973-1976: Satellite Passive-Microwave Observations* (Zwally et al., 1983a), hereafter referred to as *Antarctic Sea Ice, 1973-1976*, whereas the Northern Hemisphere sea ice observations are described in this companion volume. Together, the two volumes provide a global picture of sea ice conditions in the mid-1970s.

As the maps in this volume indicate, at the summer minimum sea ice covers roughly 8×10^6 square kilometers in the central Arctic, reaching to the north coast of Greenland and to many of the northern Canadian islands but not to the coast along much of the Alaskan, Siberian, and European coastlines. During winter the ice cover expands considerably, covering almost the entire Arctic Ocean and portions of many of the peripheral seas and bays, in particular the Sea of Okhotsk, Bering Sea, Hudson Bay, Baffin Bay, Davis Strait, Greenland Sea, Barents Sea, and Kara Sea. At its maximum each year, the areal coverage of Northern Hemisphere sea ice is about 15×10^6 square kilometers, yielding a seasonal range of 8 to 15×10^6 square kilometers in Northern Hemisphere sea ice, far less than the 4 to 20×10^6 square kilometer range of sea ice area in the Southern Hemisphere. The ESMR data described in this volume and in *Antarctic Sea Ice, 1973-1976* show the interannual variations in these basic features over the 4 years 1973 through 1976, as well as details of the seasonal and regional sea ice covers.

1.2 SEA ICE AS A COMPONENT OF THE CLIMATE SYSTEM

The large area of seasonal and perennial ice in the Arctic has a significant climatic impact that varies seasonally and regionally. In winter, the ice serves as an insulator, restricting exchanges between the relatively warm ocean waters and the extremely cold polar atmosphere. The strength of the insulation is such that the flux of heat to the atmosphere from the open water and thin ice in leads and polynyas can exceed by two orders of magnitude the flux of heat conducted through the adjacent thicker ice (Maykut, 1978). In spring and summer, although the ice covers less area and the temperature contrast between ocean and atmosphere is smaller, the ice still plays a significant role, reducing the total solar heating of the Earth's surface by reflecting four to seven times as large a fraction of the incident solar radiation as open water reflects.

As ice forms during fall and winter, salt rejection tends to increase the density of the oceanic mixed layer, often leading to a deepening of that layer. In some regions characterized by a weak or unstable density structure, this can lead to the formation of deep water and bottom water, thereby affecting much of the world's deep-ocean circulation. In fact, it is believed that a large part of the world's bottom water derives initially from polar latitudes, in the region of the sea ice cover (Stommel, 1962; Gordon, 1978; Warren, 1981; Killworth, 1983). Furthermore, as the ice melts in spring and summer, the resulting relatively fresh water layer creates a strong oceanic vertical salinity gradient and thus affects the vertical density gradient and thereby surface water circulations.

The freezing and melting of the ice also affect climate by releasing energy (during the change of state from liquid to solid) in the winter season and absorbing energy (during the change of state from solid to liquid) in the summer, thus reducing seasonal temperature extremes. The same mechanism reduces regional temperature contrasts as well, because of the overall ice dynamics, which produce a net outflow of ice from the Arctic Ocean: the net ice formation in the central Arctic releases heat to the polar oceans and atmosphere while the net ice decay farther equatorward absorbs heat from the subpolar oceans and atmosphere. The result has been termed a "*negative heat transport*" out of the polar regions.

This is complemented by a similar situation regarding salt transport. The salt rejection process increases water salinities in regions of net ice formation and results in sea ice having much lower salinities than sea water. Consequently, in regions of net ice decay the melting of the ice produces decreased upper ocean salinities. The net equatorward transport of ice therefore contributes to increasing water salinities in the polar regions and decreasing water salinities in the subpolar regions. This is sometimes referred to as a "*negative salt transport*" out of the polar regions, analogously to the negative heat transport.

The sea ice cover, in turn, is influenced by both the atmosphere and the oceans, as detailed in Chapter 2. Winds and currents directly affect ice motions, whereas ocean temperatures and salinities are crucial in the timing of ice formation and bottom melt, and atmospheric temperatures and cloud cover directly affect surface melt. Sea ice, hence, is intricately connected to the rest of the climate system, influencing and being influenced by the other major climatic components.

The intricate connection of sea ice to the rest of the climate system adds to the importance of sea ice records, since these records shed light on the more general climate state. For example, observations suggest that sea ice in the North Atlantic extended several degrees farther equatorward during the Little Ice Age of the mid-15th to mid-18th centuries than it does today and extended as far south as 50°N during the last glacial maximum approximately 18,000 years ago. Documentary records of ice conditions, such as those recorded for the coast of Iceland over the past millennium, can be useful as climate indicators, as can much longer term but less explicit evidence of the ice edge position deduced from sea-floor sediments (Lamb, 1972; CLIMAP Project Members, 1976; Imbrie and Imbrie, 1977; Ruddiman and McIntyre, 1977, 1979, 1981). Satellite imagery, and particularly passive microwave imagery, is now providing far more detailed and consistent global sea ice records than any records obtainable in the past.

1.3 SEA ICE FORMATION AND TYPES

Sea ice is a complex material formed by the freezing of sea water and composed of all three phases of matter: a solid phase consisting of ice crystals and salt precipitates, a liquid phase consisting of a brine solution, and a gaseous phase in the form of air

pockets. Physically, sea ice varies from fine ice particles suspended in water to thick blocks of ice hundreds of meters across. On a large scale, sea ice, although often very compact, never completely covers the ocean, because differential motion, fracturing, and melting of the ice that cause the formation of open-water areas. These include narrow, roughly linear "leads" (Figures 1-1 through 1-4), ranging from meters to kilometers in width, and broader "polynyas," ranging in area to thousands of square kilometers. Frequent deformation of the ice pack tends to break uniform expanses of ice into irregular shapes called "floes" (Figures 1-5 through 1-8). Other irregularities in the ice cover include the "ridges" formed when ice is compressed with sufficient force to crumble it into piled rows of broken ice (Figures 1-3, 1-8, and 1-9) and the "rafted floes" formed as one ice floe overrides another (Figures 1-5 and 1-7). Ice floe thicknesses in the central Arctic average 2 to 4 meters (Maykut and Untersteiner, 1971), although ridges and the underlying keels sometimes measure up to 30-meters thick (Weeks, 1976). Some ice floes remain in the Arctic for decades; others remain no more than a few months, being located in regions of extensive summer melting or in regions from which the ice moves into warmer waters.

Sea ice varies significantly in both space and time, being affected, especially during its formation, by air temperature, winds, currents, and water salinity. As a result, many different types of sea ice have been defined. As sea water begins to freeze, individual ice crystals, spicules, and platelets form first, "*frazil ice*" being the term given to fine spicules suspended in water. When sea ice is formed under calm conditions, the ice crystals often coagulate to form a solid sheet; but when the water is agitated by waves or currents, the crystals frequently form a soupy layer on the surface termed "*grease ice*" (Figure 1-10). "*Slush*," by contrast, is a viscous floating mass formed initially from a mixture of snow and water (Figure 1-11). "*Shuga*," often formed from grease ice or slush under agitated conditions, is an accumulation of spongy ice pieces a few centimeters across. "*Nilas*" is a later stage of new ice, after the ice has consolidated into a thin elastic sheet of 0.01 to 0.1 meter in thickness. This sheet is highly flexible, bending easily with waves and swell. Under sufficient pressure, it has a tendency to thrust into a pattern of interlocking "*fingers*" called "*finger rafting*" (Figure 1-12).

At times ocean waves cause grease ice, shuga, slush, or nilas to break and form into predominantly circular pieces of ice from 0.3 to 3 meters in diameter. Such ice, termed "*pancake ice*," can be up to 0.1-meter thick and often has raised rims all along its edge, produced by the striking of ice pieces against each other (Figure 1-13).

As the sea ice surface consolidates, brine is trapped between the ice crystals, accounting for the high salinity of newly consolidated ice. Further ice thickening proceeds through downward growth driven by heat loss to the atmosphere. The resulting ice, termed "*columnar ice*," has a characteristic columnar structure of crystals with vertical basal planes. Ice that has thickened to 0.10 to 0.30 meter is termed "*young ice*," a classification with two subclassifications named according to color but defined according to thickness: "*gray ice*" is young ice that is 0.10- to 0.15-meter thick, and "*gray-white ice*" is young ice that is 0.15- to 0.30-meter thick. Gray ice is less elastic than nilas and tends to raft under pressure. Gray-white ice is still less elastic and tends to ridge under pressure.

When sea ice reaches a thickness of 0.30 meter, it is termed "*first-year ice*" (Figures 1-5 through 1-9, 1-14a, and 1-14b). It remains first-year ice until either disappearing or surviving a summer melt period. Undeformed first-year ice rarely reaches thicknesses greater than 2 meters, although ridged first-year ice can have local thicknesses in excess of 20 meters.

Ice that has survived at least one summer melt period is substantially altered from first-year ice, because water from melt ponds (Figure 1-15) percolates through the ice causing desalination of the surface and underlying layers. Such ice, termed "*multiyear ice*," is distinguished by its low salinity and its rough, rolling, and hummocky surface (Figures 1-16 and 1-17). [World Meteorological Organization (WMO) usage is more restrictive, terming ice that has survived only one melt season "*second-year ice*" and reserving "*multiyear ice*" for ice that has survived two or more melt seasons. To have ice classifications that correspond better with the distinctions observable from passive microwave imagery, in Chapter 3 we not only combine the WMO's "*second-year ice*" and "*multiyear ice*" but also combine frazil ice, grease ice, slush ice, shuga, and nilas into a category called "*new ice*" and include young ice in the first-year ice classification.]

ORIGINAL PAGE
COLOR PHOTOGRAPH



Figure 1-1. Lead in the Beaufort Sea, with gradations of gray ice in the lead indicating different stages of new ice growth, April 1975. The width of the lead is on the order of 200 meters to 1 kilometer. [Photo by H. J. Zwally, taken from the NASA Convair 990 aircraft.]



Figure 1-2. Lead in the Beaufort Sea that has undergone periodic openings and freezings, April 1975. Rectangular patterns in the gray-white ice in the lower part of the lead are caused by finger rafting where alternate sections are thrust over or under the thicker ice. The width of the lead is on the order of 50 to 100 meters. [Photo by H. J. Zwally, taken from the NASA Convair 990 aircraft.]

ORIGINAL PAGE
COLOR PHOTOGRAPH

ORIGINAL PAGE
COLOR PHOTOGRAPH



Figure 1-3. Frozen lead in the Beaufort Sea with shapes indicating the direction of ice divergence (upper left to lower right) and with gradations of gray ice in the lead indicating intermittent stages of divergence. Lead width is about 50 to 200 meters. Extensive ridging in the center of the scene indicates prior ice convergence. The smoother area with rounded ridges in the upper left appears to be multiyear ice, and the smoother area with no ridges in the lower right is young ice. [Photo by H. J. Zwally, taken from the NASA Convair 990 aircraft.]



Figure 1-4. A lead, approximately 20 meters across, partially covered with thin ice in the Beaufort Sea multiyear ice pack, August 1975. The dark blue/black coloring of the lead contrasts with the turquoise blue of the melt ponds. Ponds that have melted through the ice appear darker. Note also the snow cover. [Photo by C. Parkinson, taken from the NASA Convair 990 aircraft.]

ORIGINAL PAGE
COLOR PHOTOGRAPH



Figure 1-5. First-year ice in the Bering Sea, March 1981, framed by portions of the NOAA research vessel *Surveyor*. Small, oval pancake ice floes can be seen in the foreground, along with larger first-year ice floes showing an edge mounding. Two of the three largest foreground floes show rafting as well. [Photo by C. Parkinson, taken from the NOAA ship *Surveyor*.]



Figure 1-6. Close up of first-year ice floes in the Bering Sea, February 1981. Typical diameters of the floes are 5 to 10 meters. [Photo by C. Parkinson, taken from the NOAA ship *Surveyor*.]

ORIGINAL PAGE
COLOR PHOTOGRAPH



Figure 1-7. First-year ice floes in the Bering Sea, February 1981. A prominent crack is forming in the major, triangular-shaped ice floe in the right center of the picture, and a thin veneer of ice can be seen to have formed in the space opened following the earlier cracking and separation of that floe from the floe to the right. The sharp edge of the floes on either side of the earlier crack contrasts with the raised edges, on the order of a few centimeters, seen around floes that have had longer exposure to waves and brushing against other floes. The result of the rafting of one thin ice floe upon another can be seen in the upper rightmost floe. [Photo by C. Parkinson, taken from the NOAA ship *Surveyor*.]

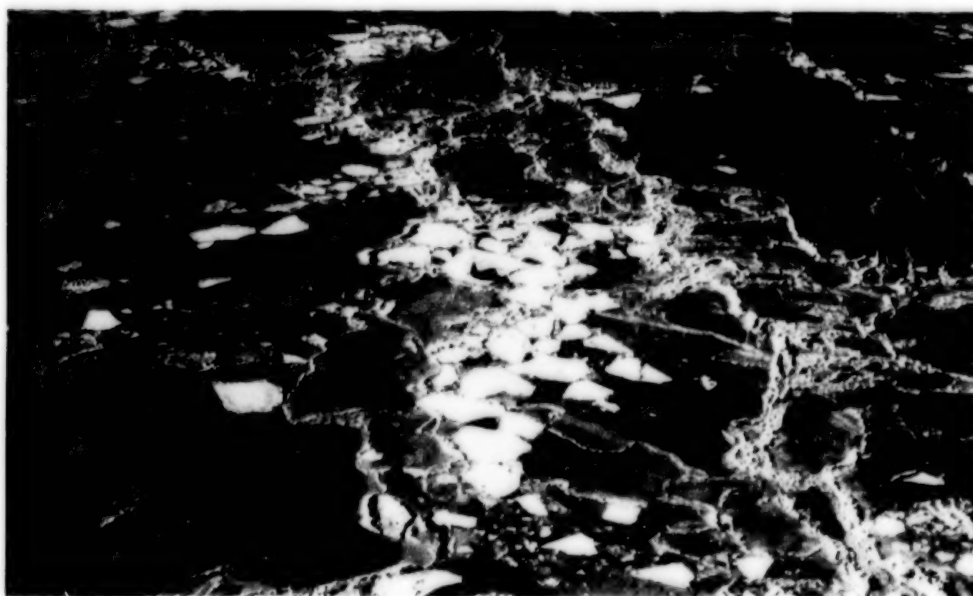


Figure 1-8. White ice floes in an area of predominantly gray ice in the Bering Sea, February 1973. Linear patterns of ridging and rafting separate areas of generally smooth ice. The photograph was taken from a helicopter at an altitude of almost 500 meters. A companion red helicopter is seen on a white ice floe in the center of the image. [Courtesy of R. O. Ramseier, Canadian Atmospheric Environmental Service.]

ORIGINAL PAGE
COLOR PHOTOGRAPH



Figure 1-9. Ridging of thick first-year ice in the Bering Sea, February 1983. [Courtesy of S. Martin, University of Washington.]



Figure 1-10. Grease ice in the Bering Sea, February 1983. The term grease ice comes from the matte appearance of the surface, which results from the damping of the surface capillary waves by the slurry of frazil ice crystals. The floes in the lower center range in diameter from 0.1 to 1 meter. [Courtesy of S. Martin, University of Washington.]

ORIGINAL PAGE
COLOR PHOTOGRAPH



Figure 1-11. Heavy slush ice surrounded by white ice floes in the Bering Sea, February 1973. Scale is apparent from the footprints on the ice. [Courtesy of R. O. Ramseier, Canadian Atmospheric Environmental Service.]

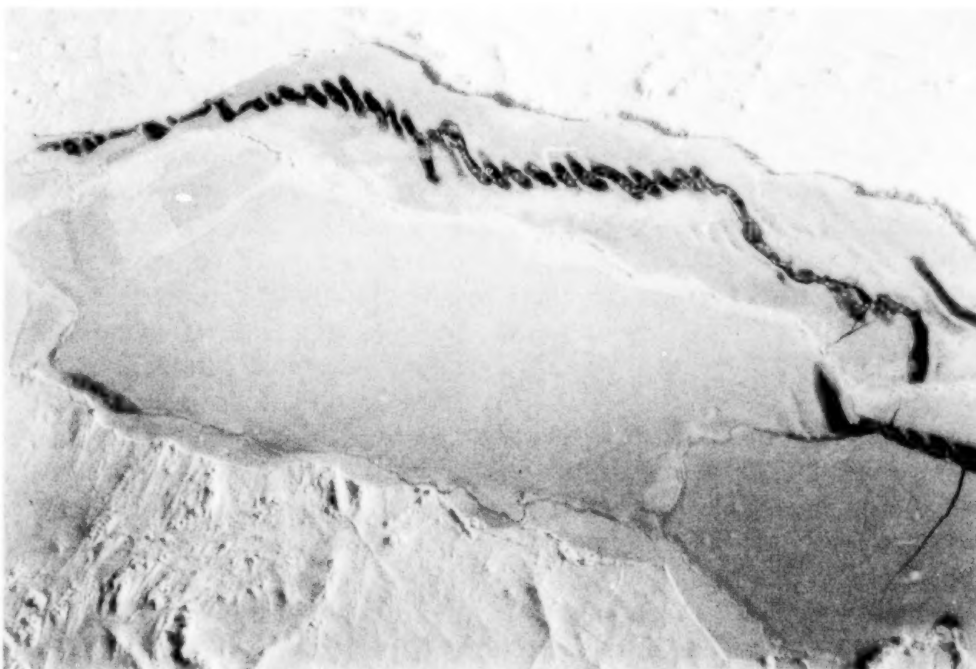


Figure 1-12. Frozen polynya with evidence of recent finger rafting and flooding, Beaufort Sea, April 1975. The characteristic width of the flooded patches is about 3 meters. [Photo by H. J. Zwally, taken from the NASA Convair 990 aircraft.]

ORIGINAL PAGE
COLOR PHOTOGRAPH



Figure 1-13. Pancake ice floes held fast by consolidated grease ice, Bering Sea, February 1983. Floes average approximately 0.3 meters across. [Courtesy of S. Martin, University of Washington.]

Around the rim of the Arctic Ocean, another category of ice, termed "*shorefast ice*," exists through much of the winter. This ice is attached to the shore or to anchoring points in the sea bed. Ice formation is aided in these areas by the shallow depth of the ocean, low salinities, and relatively quiescent surface conditions. Seaward from the shorefast ice there is in many areas a "*shear zone*," where winds drive the polar ice pack against the shorefast ice, causing heavy deformation and extensive pressure ridging.

1.4 SEA ICE PROPERTIES

Among the important properties of sea ice for the analysis of microwave emissions are its salinity, density, snow cover, and thickness, all of which vary at least somewhat among ice types. New ice and first-year ice tend to be characterized by relatively high salinities and smooth surfaces, with the initial salinity strongly influenced by the rate of freezing (Weeks and Ackley, 1982). Figure 1-18 shows a sequence of salinity profiles for such ice from a site in Eclipse Sound near Pond Inlet, Baffin Island. At this site, the salinities in the top 25 millimeters, from which most of the microwave emission occurs, fluctuate

from 7 to 14 parts per thousand. The temporary periods of surface salinity increase within the ice-growth season are believed to be atypical.

Generally, the amount of brine held in the freeboard portion of the ice decreases with time. This is especially true during the summer melt period, when flushing occurs as the surface meltwater percolates through the ice, although much of the salt can be lost by simple drainage before the ice surface becomes permeable (Holt and Digby, 1985). Brine drainage can also be caused by thermal expulsion or by downward movement of the relatively heavy brine due to gravitation (Untersteiner, 1968; Lake and Lewis, 1970). First-year ice with a snow cover and an intervening snow-ice layer formed from the melting and refreezing of the snow typically has its highest salinity in the snow-ice layer and has a temperature profile such that temperature increases with depth (Figure 1-19a). Cores collected from hummocks on multiyear ice generally show a systematic increase of salinity from 0 at the surface to about 4 parts per thousand at the bottom of the ice floe, whereas those from depressions are much more saline and show large salinity fluctuations. A plot of

ORIGINAL PAGE
COLOR PHOTOGRAPH



Figure 1-14a. Downwind side of a band of sea ice in the first-year ice cover of the Bering Sea, March 1981. The well-defined edge and fairly uniform size of the ice floes (1 to 5 meters across) contrasts with the jumbled and more diffuse nature of the ice of the upwind side of the same band, shown in Figure 1-14b. [Photo by C. Parkinson, taken from the NOAA ship *Surveyor*.]



Figure 1-14b. Upwind side of the band of sea ice depicted in Figure 1-14a. [Photo by C. Parkinson, taken from the NOAA ship *Surveyor*.]

ORIGINAL PAGE
COLOR PHOTOGRAPH

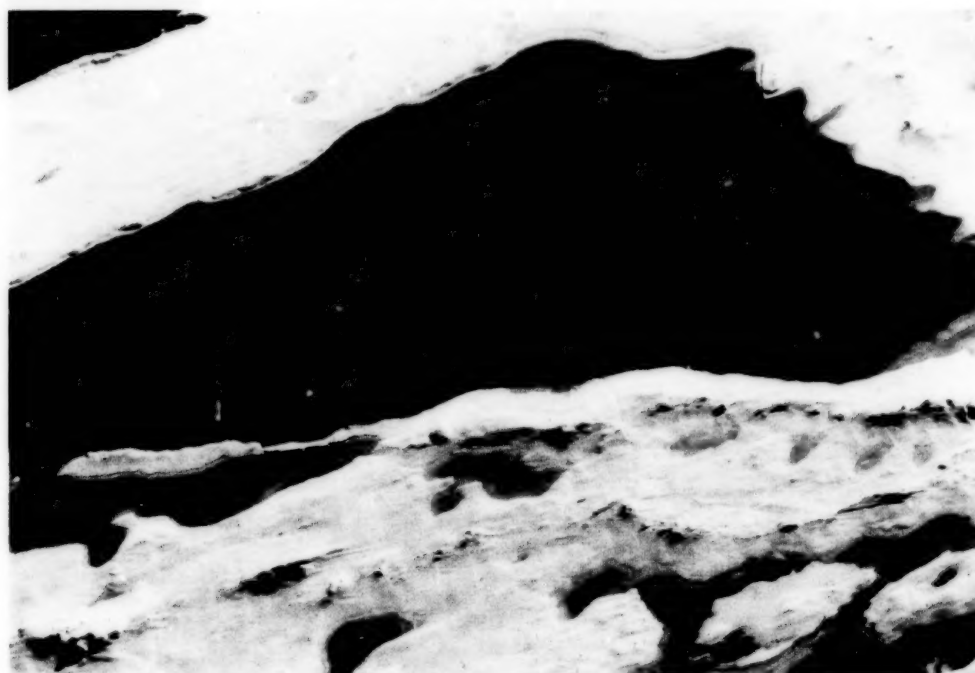


Figure 1-15. Prominent melt pond on multiyear sea ice in the Beaufort Sea, August 1975, with a thin, broken layer apparent at the edges and with the characteristic turquoise blue meltpond coloring. [Photo by C. Parkinson, taken from the NASA Convair 990 aircraft with a 55-millimeter lens from an altitude of about 900 meters.]



Figure 1-16. Multiyear ice in the Beaufort Sea, spring 1984, showing weathered hummocks on the surface. A red hut in the background indicates the scale. [Courtesy of R. Andersen, University of Washington.]



Figure 1-17. Arctic pack ice from 10,000 meters, showing a variety of multiyear and first-year ice floe shapes and sizes in the Beaufort Sea, August 1975. Surface patterns visible on the floes are caused by meltponding. [Photo by C. Parkinson, taken from the NASA Convair 990 aircraft with a 55-millimeter lens.]

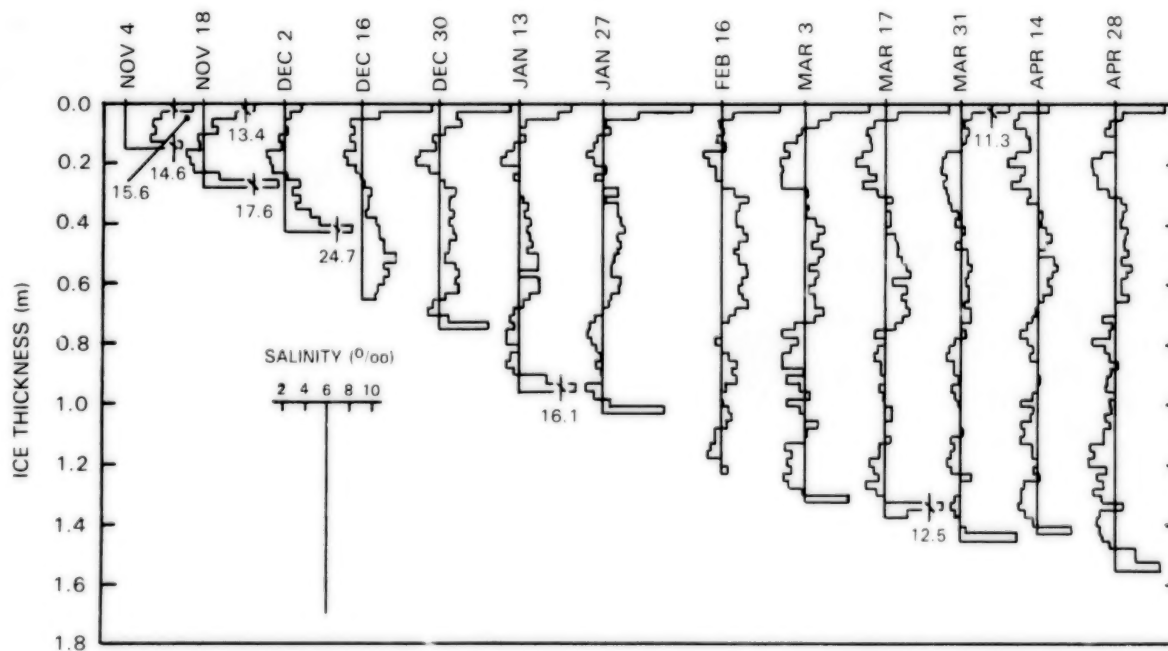


Figure 1-18. Vertical profiles of the salinity structure of the ice in Eclipse Sound at intervals of 2 weeks during the winter of 1977-1978. For each profile, the vertical solid line positions the horizontal axis, with the vertical line marking the salinity value of six parts per thousand for that profile. [From Nakawo and Sinha (1981).]

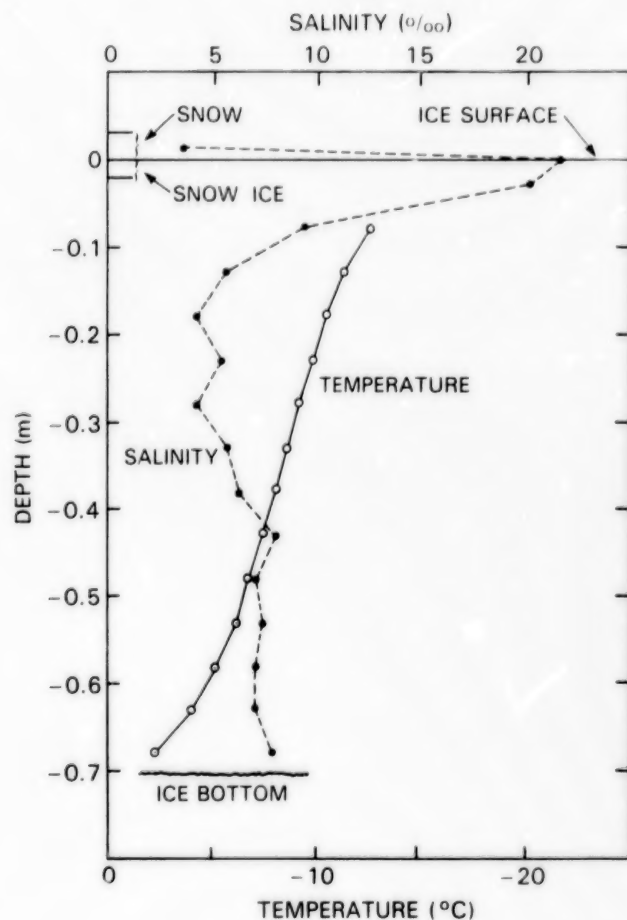


Figure 1-19a. Salinity and temperature profiles measured on a first-year ice floe in the Bering Sea. [Redrawn and modified from Martin (1979).]

the salinity and temperature profiles from a hummocked multiyear ice floe is shown in Figure 1-19b. Both temperature and salinity tend to increase with depth.

The density of sea ice is affected by brine content, air pockets, and other inhomogeneities in the ice. For first-year ice, the density is typically about 900 to 920 kilograms per cubic meter, whereas for multiyear ice, the values are somewhat lower and show greater variation, reflecting, in part, nonuniformity in the brine drainage in the portion of the sea ice above sea level (the freeboard layer). Examples of density profiles for several ice types are shown in Figure 1-20. Surface measurements are not included because of the difficulty of obtaining representative surface samples.

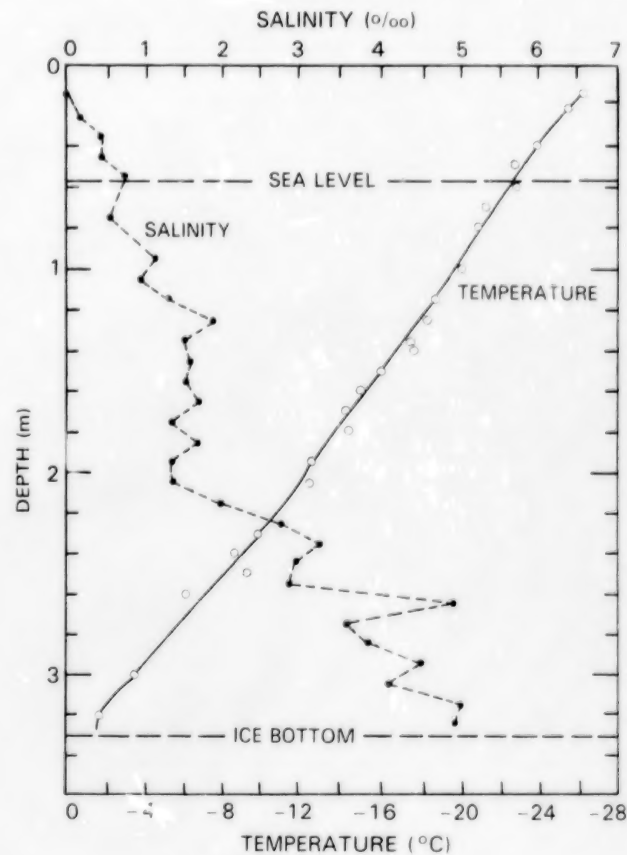


Figure 1-19b. Salinity and temperature profiles of a hummocked multiyear ice floe. [From Cox and Weeks (1974).]

The amount of snowfall in the Arctic region varies spatially and from year to year. Soviet data from several years at several locations in the central Arctic show an average seasonal cycle in snow thickness exhibiting a slow increase from about 0.1 meter in September to a peak of about 0.4 meter in May, followed by a rapid decrease to 0.05 meter in July (Loshchilov, 1964; Barry, 1983). If the snowload is heavy enough to submerge the ice surface, sea water intrudes into the snow/ice interface and freezes with the snow to form a modified surface layer. This refrozen layer is saline and has a crystal structure and composition that differ from those of the rest of the sea ice surface.

The thickness distribution of Arctic ice is not well known, although multiyear ice is on average significantly thicker than first-year ice, and ice in the central pack is generally thicker than that near the ice edge. An equilibrium thickness of approximately 3

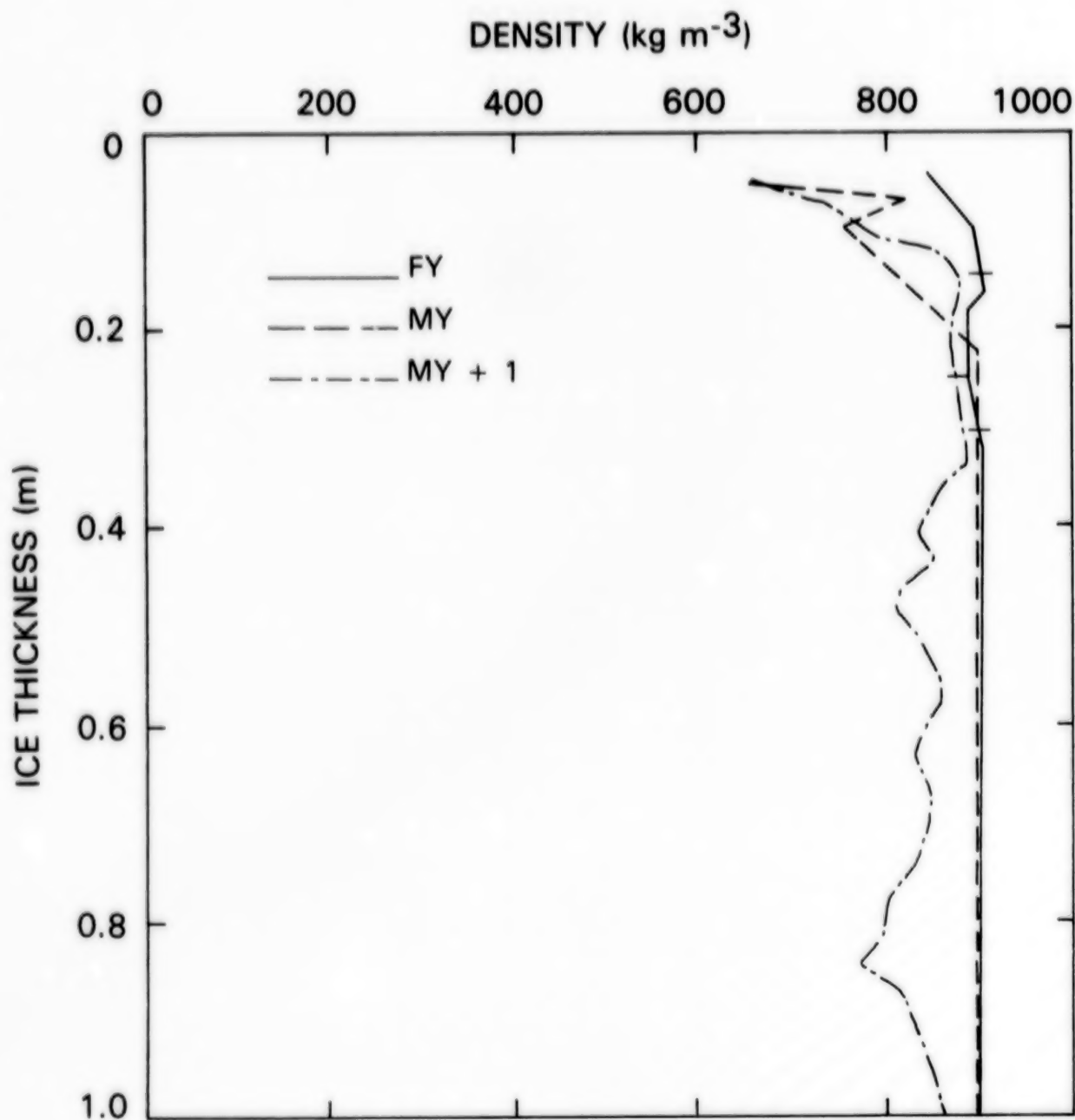


Figure 1-20. Density profiles observed for a first-year ice floe (FY), a multiyear ice floe (MY), and an ice floe measured in fall which had been identified as multiyear ice prior to the previous summer season (MY + 1). [Redrawn from Campbell et al. (1978).]

meters in the central Arctic has been suggested by modeling studies of Maykut and Untersteiner (1971), but thicknesses greater than 6 meters have been observed on undeformed ice (Walker and Wadhams, 1979), and ridges several times higher than that have been reported in the coastal regions north of Greenland and along the Canadian Archipelago (Weeks, 1976). Analysis of submarine data from Fram Strait

has revealed average thicknesses of about 3 meters and 2 meters for multiyear and first-year ice floes, respectively, and analysis of submarine data from the Beaufort Sea region has revealed an average thickness of 3.7 meters (Wadhams and Horne, 1980). The amount of ridging varies significantly both regionally and temporally, with particularly heavy ridging occurring just north of Greenland. Ridging

substantially increases the roughness of an ice surface and therefore dramatically affects the drag coefficient of the ice pack. It also changes the average salinity profile. Each of these factors leads to greater variance in the sea ice microwave signature in regions of heavy ridging.

During the period in which freeze-thaw cycles occur, generally from May through September, additional physical properties of the freeboard layer contribute to determining the microwave signatures. Among the most important of these are the moisture content in the freeboard and overlying snow cover, plus melt ponding. As the melt period begins, the moisture content of the snow increases, with dramatic effects on the microwave emission, as discussed in Chapter 3. This is followed by a total melting of the snow and subsequent creation of melt ponds. Melt ponds generally consist of fresh water, although some contain salt water either because of flooding of the ice or because the pond has melted through to the sea below. In the latter case, what had been a melt pond in essence becomes a miniature polynya. Melt ponds in the Arctic grow rapidly in the early summer, and by mid-July have normally reached their maximum extent. Values of 25 to 30 percent for total melt pond area at the time of maximum melt are believed to be about average, although the available data are limited. Ten summers of Soviet "North Pole" station observations in the vicinity of 80°N revealed an average melt-pond areal percentage of 25 percent for mid-July, with local values for individual ice floes reaching as high as 45 percent (Barry, 1983). The effects on microwave emission of the moisture content in the snow and ice, melt ponding, and other physical properties are discussed in Chapter 3.

1.5 SATELLITE IMAGING OF SEA ICE; THE ESMR DATA

In recent decades, much greater detail on the ice edge and internal ice pack has been obtainable than ever before, from surface, ship, aircraft, and satellite observations (Figures 1-1 through 1-17 and 1-21). Although surface, ship, and aircraft data are invaluable for determining local sea ice conditions, these data are not feasible for routine, continuing measurements over a large area, especially in the face of the harsh polar conditions. For the large scale, satellite imaging is the sole feasible method for obtaining consistent, long-term records.

Some satellite data of sea ice in the visible and infrared wavelengths were available in the late 1960s and early 1970s, but these data could not be obtained during darkness and were often obscured by cloud cover during light, making quantitative estimates of the ice cover difficult. Since the polar regions are either dark or cloud covered for much of the year, these limitations of the visible and infrared wavelengths effectively prevented the generation of consistent, long-term data records. Accordingly, the all-weather, day/night features of the passive microwave data collected by the Nimbus 5 ESMR introduced a major advance in the usefulness of satellite sea ice imaging.

The ESMR operated from its launch in December 1972 through March 1983, although with a significant reduction in data quality after October 1976 because of degeneration of the instrument. For various reasons discussed in Appendix A, notable gaps appear in the data even in the 4-year period 1973 through 1976. During these 4 years, however, a great deal of high-quality data was collected; and the purpose of this volume is to present the resulting data set for the Arctic region in an organized format, supplemented by discussion and analysis of the sea ice cover. The ESMR data have a spatial resolution of approximately 30 kilometers and an irregular temporal resolution, with the satellite orbit typically passing over a given Arctic location approximately four times a day. The combination of global coverage and fine-scale temporal resolution has allowed the satellite passive microwave data to reveal information on the cryosphere that is unattainable by any other available method.

Before the Nimbus 5 satellite ESMR was launched, a prototype aircraft instrument was flown on the NASA aircraft "Galileo I" Convair 990 during several missions to the Arctic in the period 1967 through 1972. Missions in 1967 and 1970 established the existence of a strong contrast between the microwave signature of sea ice and that of open water (Wilheit et al., 1972), a contrast crucial to the use of the ESMR data for examining the sea ice cover and particularly for determining sea ice concentrations, as detailed in Chapters 3 and 4. Missions in 1971 and 1972 over the Beaufort Sea were undertaken in conjunction with ground observations from manned ice stations (Campbell, 1973). Later Convair 990 missions after the launch of the Nimbus 5 ESMR, along with ground observations during three major



Figure 1-21. NOAA 7 AVHRR image of the Bering, Chukchi, and Beaufort Seas. The Bering Sea ice, including easily distinguishable large floes, appears bright against the dark open ocean areas. Features indicative of the dynamic nature of the ice cover include a large shore lead along the northern Alaskan coast, long curved leads extending from the coast into the Beaufort Sea, and the coastal polynyas south of the Bering Sea islands and west of Alaska. [Courtesy NOAA/NESDIS.]

international experiments, allowed verification of the satellite data interpretations. The three experiments were the Arctic Ice Dynamics Joint Experiment (AIDJEX) (Untersteiner, 1980; Campbell et al., 1978) and the Skylab Snow and Ice Experiment (Campbell et al., 1977), both with participation from the United States and Canada, and the Bering Sea Experiment (BESEX) (Kondratyev et al., 1975), with participation from the United States and the Soviet Union. BESEX included a field expedition in the spring of 1973, Skylab included field expeditions in the winters and springs of 1973 and 1974, and AIDJEX included field expeditions throughout the year from spring 1975 through spring 1976.

Analysis of the data collected by the Nimbus 5 ESMR and coincident data from ground and aircraft

expeditions in 1973 through 1976 established several results of fundamental importance for the usefulness of the satellite data in determining sea ice conditions. These include further confirmation of the previously mentioned ability to distinguish sea ice from open water (Gloersen et al., 1975a), the ability to distinguish different sea ice types (Gloersen et al., 1973), and the ability to delineate the variation of ice types from season to season (Campbell et al., 1978), as well as the creation of an algorithm for calculating sea ice concentrations from the Nimbus 5 ESMR data (Gloersen et al., 1974). It is particularly important that even though the 30-kilometer resolution of the Nimbus 5 ESMR is not fine enough to resolve most individual ice floes, leads, or open-water areas within the ice pack, the percent ice coverage within the 30- by 30-kilometer grid squares can be derived

from the microwave measurements, due to the sharp contrast between the microwave emission of sea ice and the microwave emission of open water. Details of this derivation are given in Chapter 3.

Because the data from the Nimbus 5 ESMR provide the first detailed depiction of global sea ice conditions throughout the annual cycle, the compiled Arctic data in this volume and Antarctic data in *Antarctic Sea Ice, 1973-1976* constitute an important climatic base to compare with sea ice conditions in the future. The Southern Hemisphere analysis was done first because the Northern Hemisphere analysis involves additional complications due to the distinctly different microwave signature of multiyear ice in the Arctic. Much of the Arctic summertime ice is subject to the depletion of salt in the upper layer during the summer melt period. This reduces the microwave emissivity of Arctic multiyear ice, giving it a value between the microwave emissivity of open water and that of first-year and younger ice, thus adding an ambiguity in the determination of sea ice concentrations or open-water fractions. The problem is not as severe in the Antarctic because only 20 percent of the winter Antarctic sea ice survives the summer (Zwally et al., 1983a), and much of that 20 percent does not experience significant surface summer melt (Andreas and Ackley, 1982).

The ambiguities caused by the decreased microwave emissivity of Arctic multiyear ice and the various effects of snow cover, moisture, and melt ponding are discussed in more detail in Chapter 3. Because of these ambiguities, and because both multiyear ice and melt ponding cover large portions of the central Arctic, the sea ice concentration maps of Chapter 4 are accompanied by nomograms relating brightness temperature, ice concentration, and multiyear ice fraction. With multifrequency instruments, such as the Scanning Multichannel Microwave Radiometer (SMMR) on the Nimbus 7 satellite, launched in 1978, multifrequency algorithms can be developed to eliminate some of the ambiguity inherent in single-frequency data, such as the data from the ESMR.

The Nimbus 5 ESMR data have been used to produce 3-day-averaged maps of the Northern Hemisphere brightness temperatures for the years 1973 through 1976. For the months within that period with sufficient data available, the 3-day averages have been further averaged over monthly time periods to produce monthly averaged brightness temperature maps, with linear spatial and temporal inter-

polations used to fill in small data gaps. The resulting 39 monthly maps, presented in Chapter 3, cover all months from January 1973 through October 1976 except March, April, May, and August of 1973 and June, July, and August of 1975. Details of the mapping and interpolation procedures appear in Appendix A.

The monthly averaged brightness temperature data have been used in conjunction with climatological atmospheric temperature data to produce monthly averaged sea ice concentration maps. These maps indicate the percent of the ocean area covered by sea ice in each 30- by 30-kilometer map element. The technique for obtaining ice concentrations is based on a linear relationship between an average observed brightness temperature of 138.3 K for open water (including atmospheric effects) and an observationally determined brightness temperature of sea ice that depends on the ice temperature and ice emissivity. Multiyear ice fractions are accounted for by the associated nomograms. Details of the nomogram and the ice concentration determinations are provided in Chapter 3, with the ice concentration maps being presented in Chapter 4. The estimated accuracy of the derived sea ice concentrations is ± 15 percent over regions of predominantly first-year ice and ± 25 percent over regions with an unknown mixture of first-year ice and multiyear ice.

1.6 PREVIEW

In this volume, the Arctic sea ice cover during the 4 years 1973 through 1976 is examined through brightness temperature and ice concentration maps derived from the Nimbus 5 passive microwave data. Chapter 2 provides background material on the general physical characteristics of the Arctic Ocean and peripheral seas, the relevant oceanography and meteorology, and the connection with the sea ice cover. Chapter 3 presents mapped monthly averaged ESMR brightness temperature data, along with discussions of the theoretical basis for the microwave interpretations, aircraft and surface observations, error analyses, the ice concentration algorithm and nomogram, and the effects of such complicating factors as melt ponds and snow cover. The remaining two chapters deal with the sea ice conditions as determined from the ESMR brightness temperatures. In Chapter 4, these conditions are examined region by region for eight regions; and in Chapter 5, they are examined for the broader Northern Hemisphere perspective,

for some comparisons with the Southern Hemisphere, and for interregional comparisons. These two chapters include plots of areal ice coverage for the individual regions and the sum of all eight regions, as well as spatial maps of sea ice concentrations. The division into regions is as follows: the Sea of Okhotsk, Bering Sea, Hudson Bay, Baffin Bay/Davis Strait, Greenland Sea, Kara and Barents Seas, Arctic Ocean, and the Canadian Archipelago. Technical details of the data handling are included in Appendix A, monthly contour maps of the ice edge are included in Appendix B, and selected histograms of sea ice concentrations are included in Appendix C. A list of acronyms used in the book is presented in Appendix D.

Even though the ESMR data presented in this volume extend over only a 4-year period, in view of the

good spatial and temporal resolution the data record reveals a great deal about Arctic sea ice conditions, the seasonal cycle of those conditions, the contrasts and interactions among regions, and the interannual variability. Analysis of the 4-year ESMR data set has revealed previously unidentified complexities in the ice cover in terms of both structure and dynamics. Sizable areas of reduced microwave emission have been found in the central Arctic Ocean pack, the variable and recurring nature of several polynyas has been determined, and a more complicated circulation pattern is indicated than the well known schematic representation of a Beaufort Gyre and a Transpolar Drift Stream. The record of sea ice distributions revealed in this volume should be valuable for studies of climate, the atmosphere and oceans, and marine resources, and for planning operational activities in the Arctic region.

2

OCEANOGRAPHIC AND ATMOSPHERIC CONDITIONS INFLUENCING THE ARCTIC SEA ICE COVER

2.1 INTRODUCTION

Sea ice formation, growth, and decay are all influenced by oceanographic and meteorological factors. Sea ice in turn influences both the atmosphere and the ocean through complex interactive processes in the interconnected ocean/ice/atmosphere system. (See Crane, 1978; Rogers, 1978; Rogers and van Loon, 1979; Walsh and Johnson, 1979b; Crawford and Parkinson, 1981; Walsh and Sater, 1981; Crane et al., 1982; Crane, 1983; Niebauer, 1983; Parkinson and Gratz, 1983; Wadhams and Squire, 1983; Lemke, 1986). This chapter summarizes some of the major oceanographic and atmospheric features affecting the sea ice of the north polar region.

Oceanographic factors play a primary role in determining the timing and amount of sea ice formation. Surface water temperatures, of course, must be at or below the freezing point before ice will form; but the freezing point depends on the salinity, and the formation of ice at the freezing point depends on the existence of condensation nuclei. Condensation nuclei favor ice formation, as do low surface salinities, deriving, for instance, from freshwater river inflows. The salinity effect results from the decrease of the freezing point with increasing salinity. Another factor relevant to sea ice formation is that the density of ocean water (assuming salinities above 24.7 parts per thousand) increases as the temperature decreases to the freezing point. This often causes convection and delays the formation of ice at the surface. The depth over which active convection occurs, termed the "*convective depth*," determines the amount of water that needs to be cooled to or near the freezing point before freezing is likely to begin.

Naturally, all other factors that influence surface water temperatures, such as atmospheric conditions, solar radiation, and heat flux from deeper waters, also influence ice formation. Furthermore, once ice has formed, the continuing influence of oceanographic factors is complemented by direct atmospheric influences, particularly through the contributions of wind stress to ice motion, snowfall to ice insulation, and atmospheric temperatures and radiative fluxes to surface ice melt.

This chapter provides an overview of relevant oceanographic features of the Arctic region, followed by an overview of relevant atmospheric features. The sections on oceanography include a discussion of the ocean bathymetry, which influences the large-scale ocean circulation and in some regions determines the convective depth, a discussion of the ocean circulation patterns, and a discussion of the surface temperature and salinity, the two water properties most relevant to sea ice formation. The sections on meteorology include discussions of the atmospheric temperature, pressure, and wind fields.

2.2 BATHYMETRY

The Arctic Ocean contains approximately 13×10^6 cubic kilometers of water and extends over a horizontal area of about 12×10^6 square kilometers (Herman, 1974). Surrounded by major land masses, this ocean is relatively isolated from the deep waters of the rest of the world ocean, having only one deep passage into it, that being the Fram Strait between Greenland and Spitsbergen. (See Figures 2-1 and 2-2.) The continental shelf around the Arctic is unusually broad and shallow north of Europe and

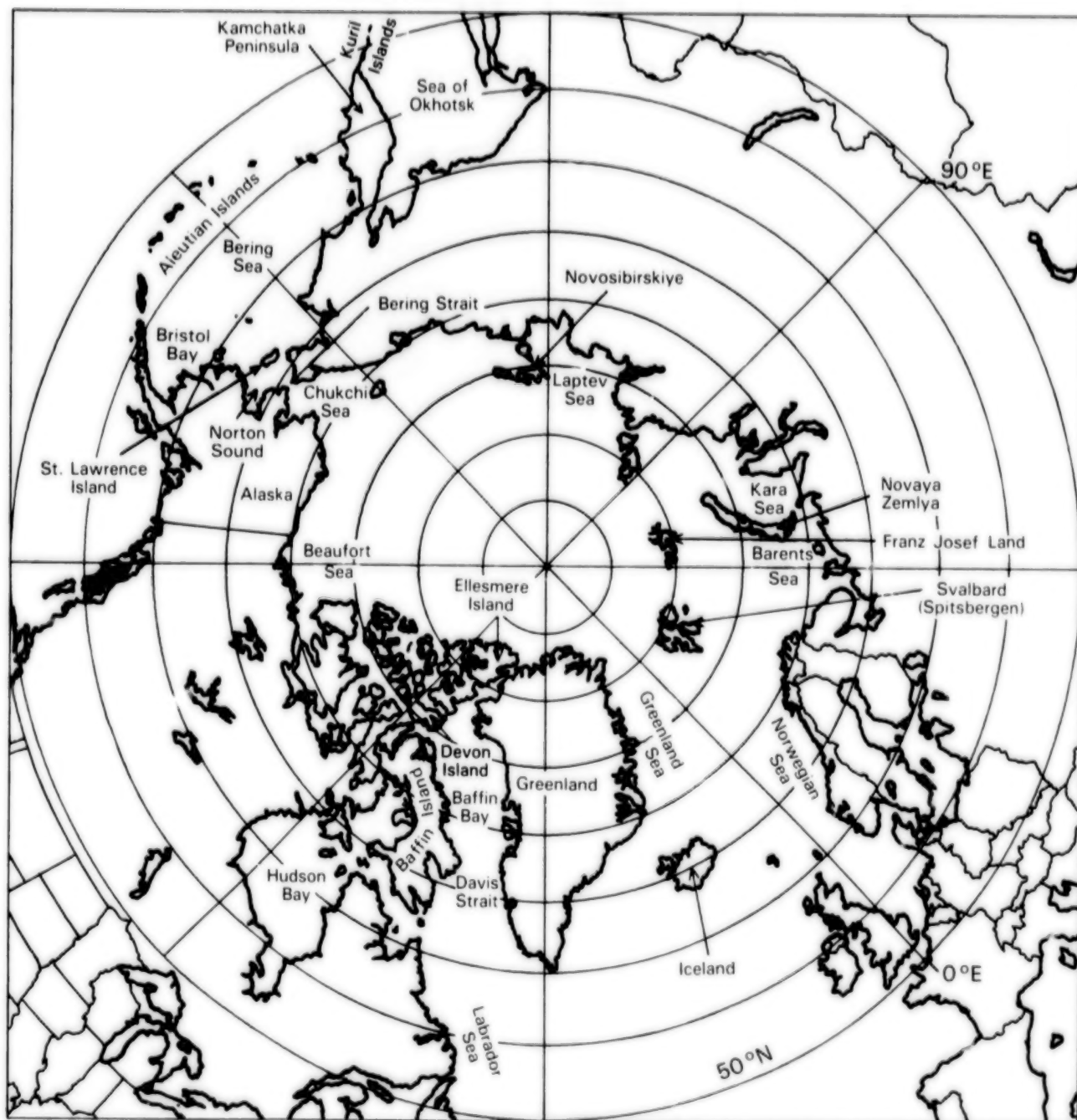


Figure 2-1. Location map for the north polar region.

ORIGINAL PAGE
COLOR PHOTOGRAPH

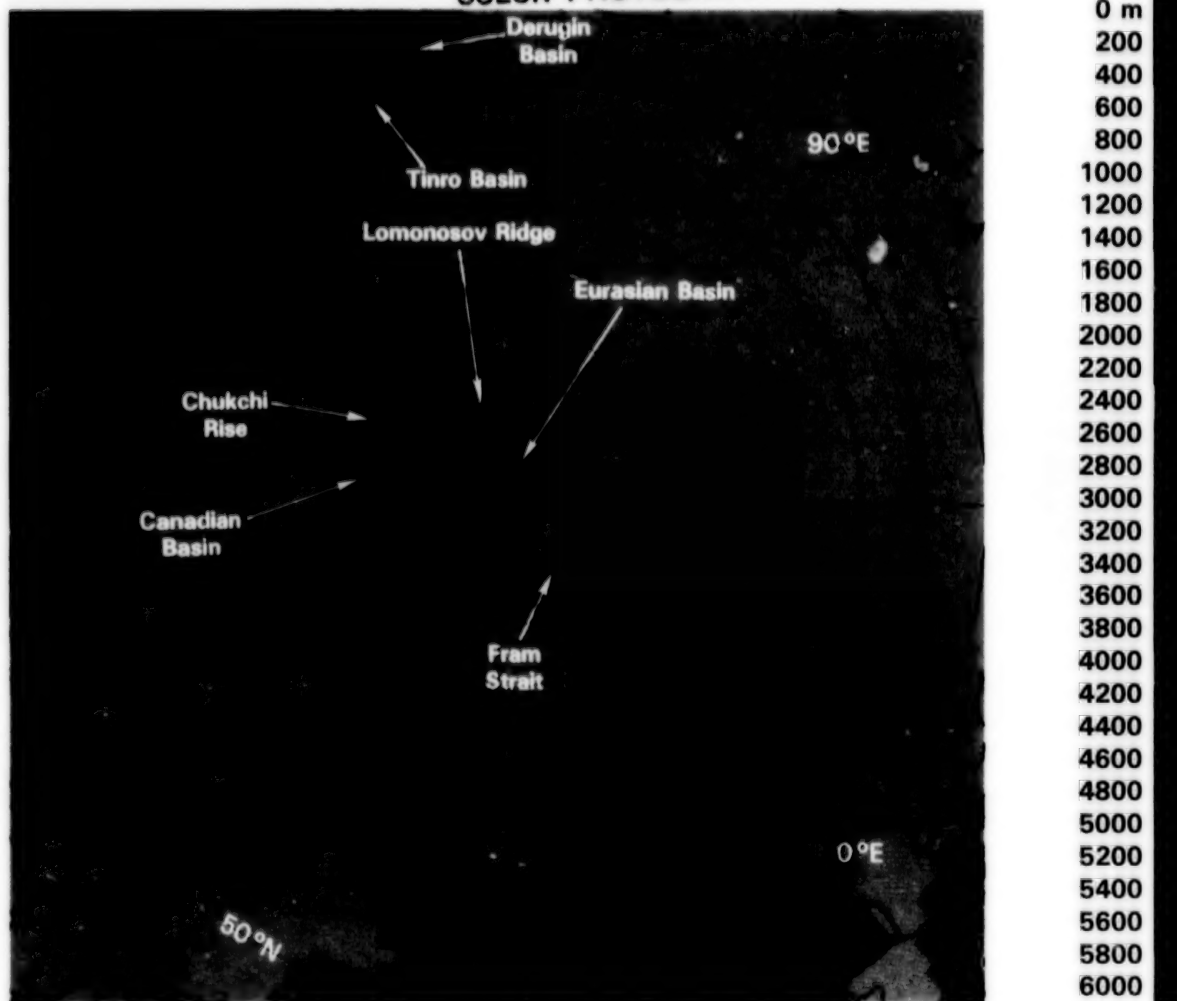


Figure 2-2. Ocean bathymetry, color coded and mapped from digital data obtained from the Defense Mapping Agency Hydrographic/Topographic Center in Washington, D.C. The color break between grays and blues comes at 500 meters, generally occurring along the continental slope.

Asia, where the widths are approximately 1000 kilometers in the Barents Sea and 800 kilometers north of Siberia. By contrast, in the Western Hemisphere, from Greenland to Barrow, Alaska, the shelf extends approximately 100 kilometers from land. A major bathymetric feature of the central Arctic is the Lomonosov Ridge, which forms a boundary between the two major Arctic deep-ocean basins: the Canadian Basin in the Western Hemisphere and the smaller but generally deeper Eurasian Basin in the Eastern Hemisphere. Another prominent feature is the Chukchi Rise, which extends 700 kilometers northward into the Canadian Basin (Figure 2-2).

Surrounding the central Arctic Ocean are several seas that have seasonal sea ice covers. The Kara and Barents Seas lie over the Eurasian continental shelf, and the Norwegian, Greenland, and Labrador Seas lie over deep basins that allow inflow and outflow of Atlantic waters. In this volume, the Laptev, Chukchi, and Beaufort Seas are considered part of the Arctic Ocean.

The Bering Sea is connected to the central Arctic by the narrow (85-kilometers wide), shallow (45-meters deep) Bering Strait and is bounded to the south by the Aleutian Islands and to the east and

west by Alaska and the Kamchatka Peninsula, respectively (Figure 2-1). The continental shelf is unusually wide and flat in the northeast, covering over a third of the sea. The shelf along the Kamchatka coast, by contrast, is extremely narrow, and much of the basin in the southwest Bering Sea has depths greater than 3000 meters (Figure 2-2).

The major bathymetric features of the Sea of Okhotsk include three relatively deep basins and a shallow shelf area that is most extensive in the northern portion of the sea. The basins are the 500-meter-deep Tinro Basin, the 1600-meter-deep Derugin Basin, and the even deeper Kuril Basin to the south of the region mapped in Figure 2-2 (which is identical to the region included in the ESMR brightness temperature maps of Chapter 3 and the derived ice concentration maps of Chapter 4). Since for most of the Sea of Okhotsk the sea floor is effectively the bottom of the convective layer, the depth of water that needs to be cooled before freezing begins is largely determined by the bathymetry (Leonov, 1960). Baffin Bay is deeper, with some depths exceeding 2000 meters, whereas Hudson Bay is much shallower, with no depths exceeding 500 meters (Figure 2-2).

2.3 OCEAN CIRCULATION

Figure 2-3 is a schematic diagram of the general surface water circulations in the Arctic region. The warm North Atlantic Current, extending northeastward from the Gulf Stream, and the Norwegian Current extending northeastward from the North Atlantic Current, contribute to maintaining the Norwegian Sea free of ice. The Atlantic waters enter the central Arctic largely through Fram Strait between Greenland and Spitsbergen, although some also enter through the passage between Spitsbergen and Norway. Much of this inflow of Atlantic waters occurs as a warm, saline undercurrent. The flow of the surface waters between the North Atlantic and the Arctic is generally outward from the Arctic rather than inward, flowing largely in the ice-laden waters of the Transpolar Drift Stream and the East Greenland Current. The surface flow through the Bering Strait, by contrast, is generally into the Arctic, with the northward transport from the Bering Sea averaging over 1×10^6 cubic meters per second for the April through October season for which measurements are available (Coachman, 1980). Major freshwater in-

flows to the Arctic include those from the Mackenzie River on the North American side, the Lena River in Siberia, and, particularly, the Ob and Yenisei Rivers into the Kara Sea. The flows into the Kara Sea account for 40 percent of the 100×10^3 cubic meters per second river inflow to the Arctic (Aagaard, 1980).

Two major features of the Arctic surface water circulation are the anticyclonic, clockwise gyre in the Canadian Basin, often called the Beaufort Gyre or sometimes the Pacific Gyre, and the Transpolar Drift Stream running lengthwise across the Eurasian Basin from off the Siberian coast out through the western Fram Strait. The Transpolar Drift Stream as it flows southward becomes the East Greenland Current, flowing from north to south along the east coast of Greenland (Figure 2-3). The average rate of flow is only 2 to 3 centimeters per second in the Laptev Sea, increasing to 8 to 10 centimeters per second in the Fram Strait. In the Beaufort Gyre, the rates of flow are generally about 2 to 3 centimeters per second (Aagaard, 1980).

Surface Atlantic waters flow into Davis Strait and Baffin Bay along their eastern boundaries in the northward flowing West Greenland Current. These waters circulate through Davis Strait and Baffin Bay in a counterclockwise direction, exiting on the west into the Labrador Sea and proceeding southward along the coast of Newfoundland. The flow in Baffin Bay is affected also by inputs from Smith Sound between Ellesmere Island and Greenland and, to a lesser extent, by the flows from Lady Ann Strait between Ellesmere Island and Devon Island and from Lancaster Sound between Devon Island and Baffin Island.

Pacific waters enter the Bering Sea through multiple channels within the Aleutian Island chain. Waters entering eastward of about 175°E tend to flow toward the east, then north, with some of the waters passing northward through the Bering Strait and others continuing counterclockwise around the cyclonic Bering Gyre. Along the Kamchatka Peninsula, the waters form the East Kamchatka Current, which flows southwestward out of the Bering Sea through the deep passes between Kamchatka and the western Aleutian Islands (Figure 2-3). [These general circulation patterns in the Bering Sea are based on observations from April through October (Coachman, 1980).]

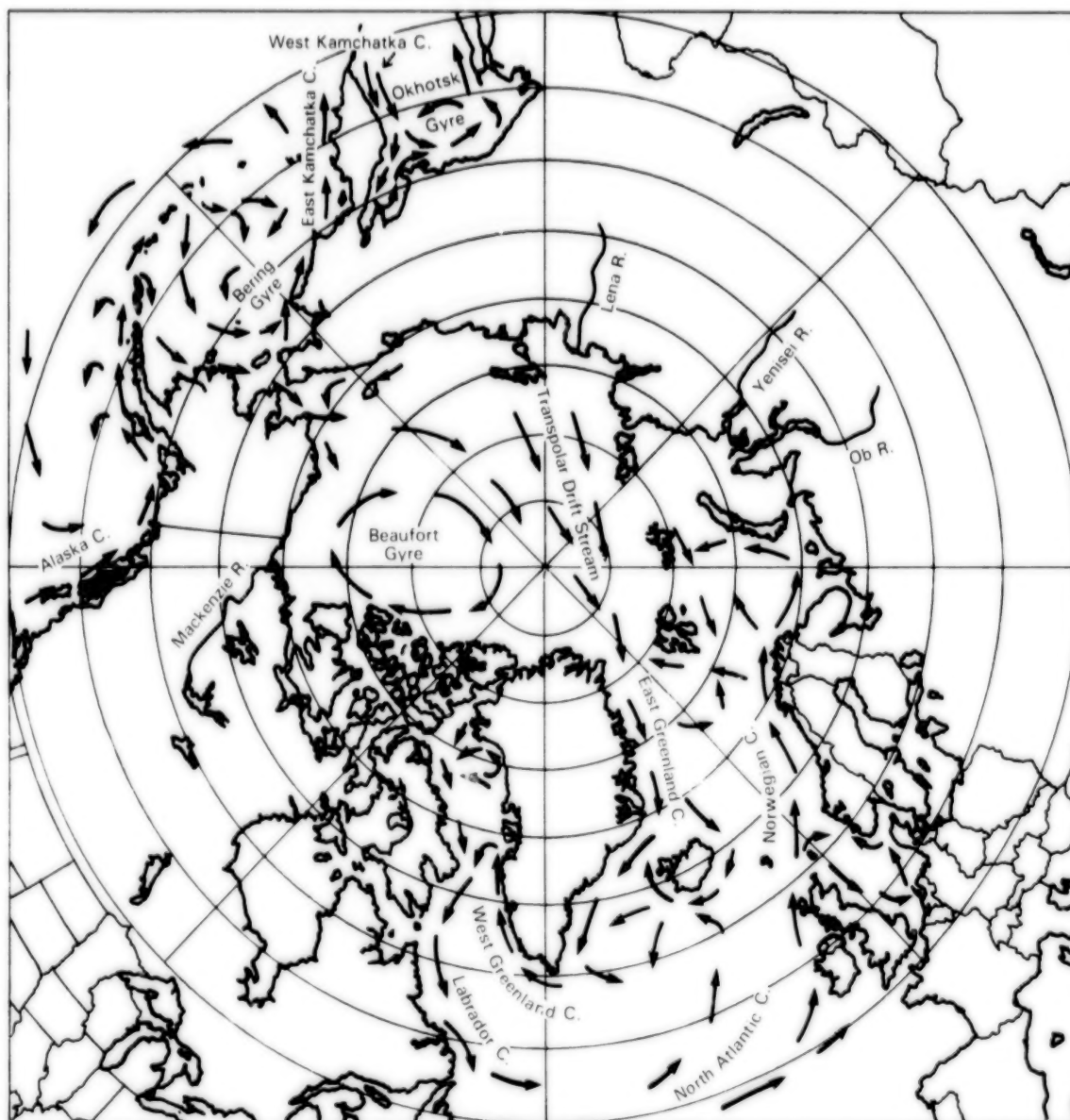


Figure 2-3. Schematic of the large-scale horizontal circulation patterns in the surface waters of the north polar region. The four rivers providing the major river inflows to the Arctic Ocean are also indicated.

In the Sea of Okhotsk, water circulation is dominated by the cyclonic flow in the Okhotsk Gyre. Pacific waters enter the sea through channels in the eastern Kuril chain, flow northward along the Kamchatka Peninsula, and continue approximately parallel to the coastline, finally exiting the sea by moving southward through the western Kurils (Figure 2-3). Flow along the coast is also influenced locally by the many river inflows.

2.4 OCEAN TEMPERATURES AND SALINITIES

Significant horizontal variation in surface water properties exists throughout the Arctic and surrounding ocean regions as a result of counteracting inflows of cold fresh waters from coastal runoff and warm saline waters from the Atlantic and Pacific Oceans. Seasonally averaged surface salinities are presented in Figure 2-4. The salinities are relatively low in the Arctic Ocean, averaging about 30 parts per thousand compared with values of about 33 parts per thousand in the northern North Pacific and about 35 parts per thousand in the northern North Atlantic. Partially as a result of the freshwater river inflows and the relatively high salinities in the Atlantic and the Pacific, the general trend in Arctic surface salinities is from low values of about 27 parts per thousand along the Siberian coast south of Novosibirskiye and along the northern Alaskan coast to high values of about 34 parts per thousand at the North Atlantic boundary of the ocean. The local high of about 32 parts per thousand just northward of the Bering Strait results from the influence of the surface water flow from the Bering Sea. Salinities in the Bering Sea and the Sea of Okhotsk, both affected by significant Pacific inflows, are generally 31 to 33 parts per thousand, with the lower salinities correlating positively with the continental shelf regions and being more prevalent in summer than in winter.

The largely enclosed Hudson Bay has significantly lower salinities than the rest of the region of interest, increasing from below 27 parts per thousand in the south to about 31 parts per thousand in the north, where the passages outward to the wider ocean exist. In Baffin Bay/Davis Strait, salinities are relatively low in the center of the bay and increase southward to the pronounced indentation of higher salinities from the Atlantic waters in the West Greenland Cur-

rent. Salinities are low along the east coasts of Greenland and Newfoundland because of the transport of melting ice by the East Greenland and Labrador Currents.

Ocean surface temperatures show a pronounced seasonal cycle and marked spatial variations (Figure 2-5). The Gulf Stream and North Atlantic Current maintain relatively high temperatures in the northern North Atlantic throughout the year, with the average monthly temperatures being lowest in March and highest in August. Warm North Atlantic waters enter the Davis Strait/Baffin Bay region through the West Greenland Current, whereas warm North Pacific waters enter the Bering Sea and the Sea of Okhotsk through numerous passages in the eastern Aleutian Island and eastern Kuril Island chains. The sharpest seasonal temperature contrasts, in the regions containing sea ice, occur in the Bering Sea and the Sea of Okhotsk, with ocean surface temperatures ranging from freezing to above 283 K. Minimum monthly averaged temperatures occur in February in the Bering Sea and in April in the Sea of Okhotsk, whereas maximum temperatures occur in August in the Bering Sea and in September in the Sea of Okhotsk.

In much of the Arctic Ocean, a relatively uniform upper mixed layer with a depth of 30 to 50 meters overlies a very stable density structure down to a depth of about 200 meters. This stable structure is a result of the strong increase of salinity with depth, especially in the Eurasian Basin, where the salinity is 34.9 to 35.0 parts per thousand at 200 meters. Temperatures are generally less than -1.5°C at depths between 0 and 100 meters and increase to 0°C at about 200 meters (Aagaard, 1980). The density structure is a significant factor for sea ice growth because the stable stratification implies that the convective depth to which cooling occurs before freezing commences at the surface is generally not large, and the heat and salt from the waters underneath the top 200 meters generally do not upwell to the surface. Hence the surface waters, influenced also by the freshwater river inflows, remain relatively fresh and cold.

2.5 THE ARCTIC AND GLOBAL ATMOSPHERIC ENERGY BALANCES

Global atmospheric circulation patterns are driven by differential solar heating of the Earth's surface.

ORIGINAL PAGE
COLOR PHOTOGRAPH

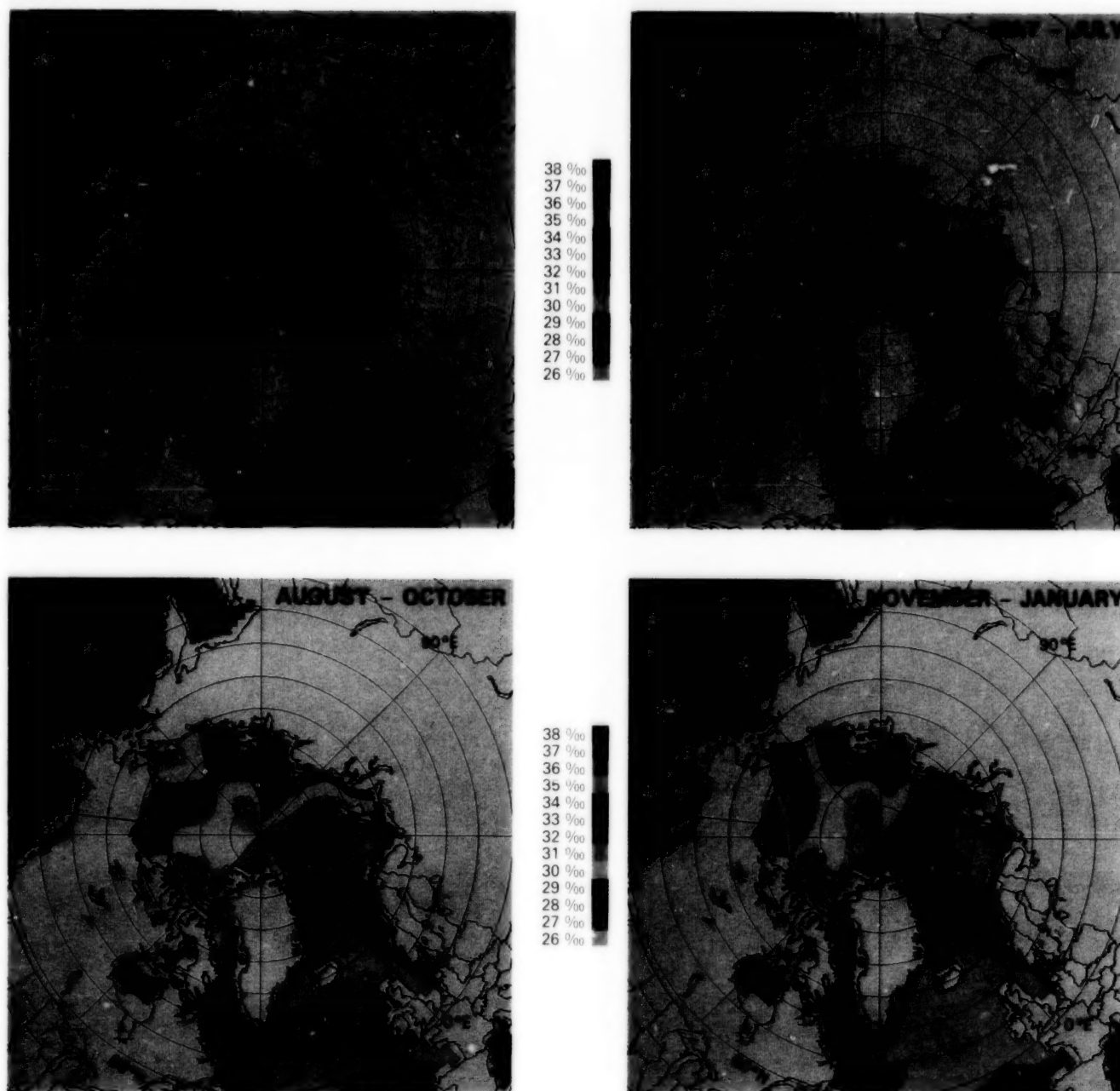


Figure 2-4. Seasonally averaged surface water salinities. These have been color coded and mapped from digital data compiled by S. Levitus and obtained from the National Oceanic and Atmospheric Administration's National Oceanographic Data Center in Washington, D.C.

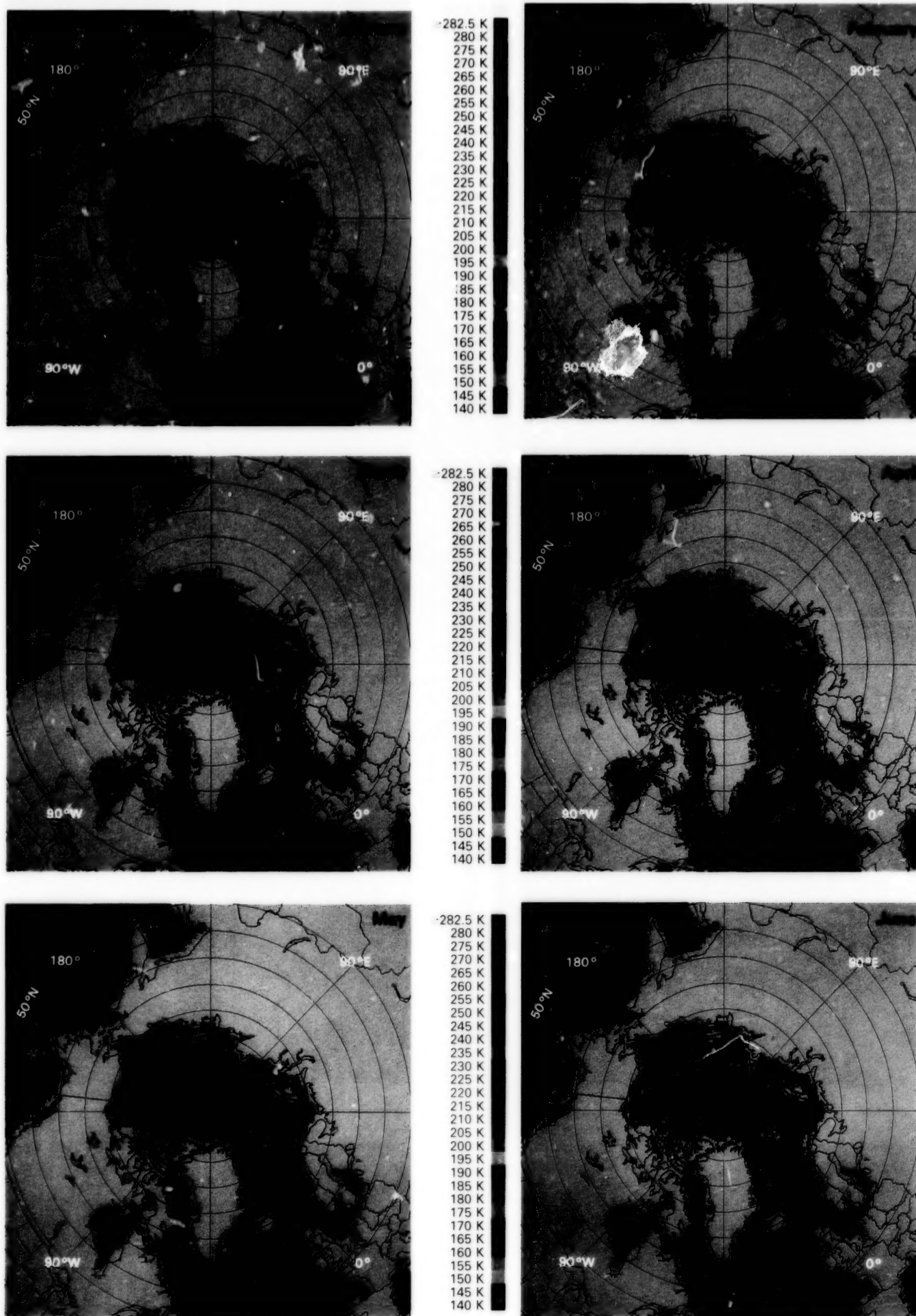


Figure 2-5a. Mean monthly climatological surface water temperatures, January through June. These have been color coded and mapped from digital data compiled by S. Levitus and obtained from the National Oceanic and Atmospheric Administration's National Oceanographic Data Center in Washington, D.C.

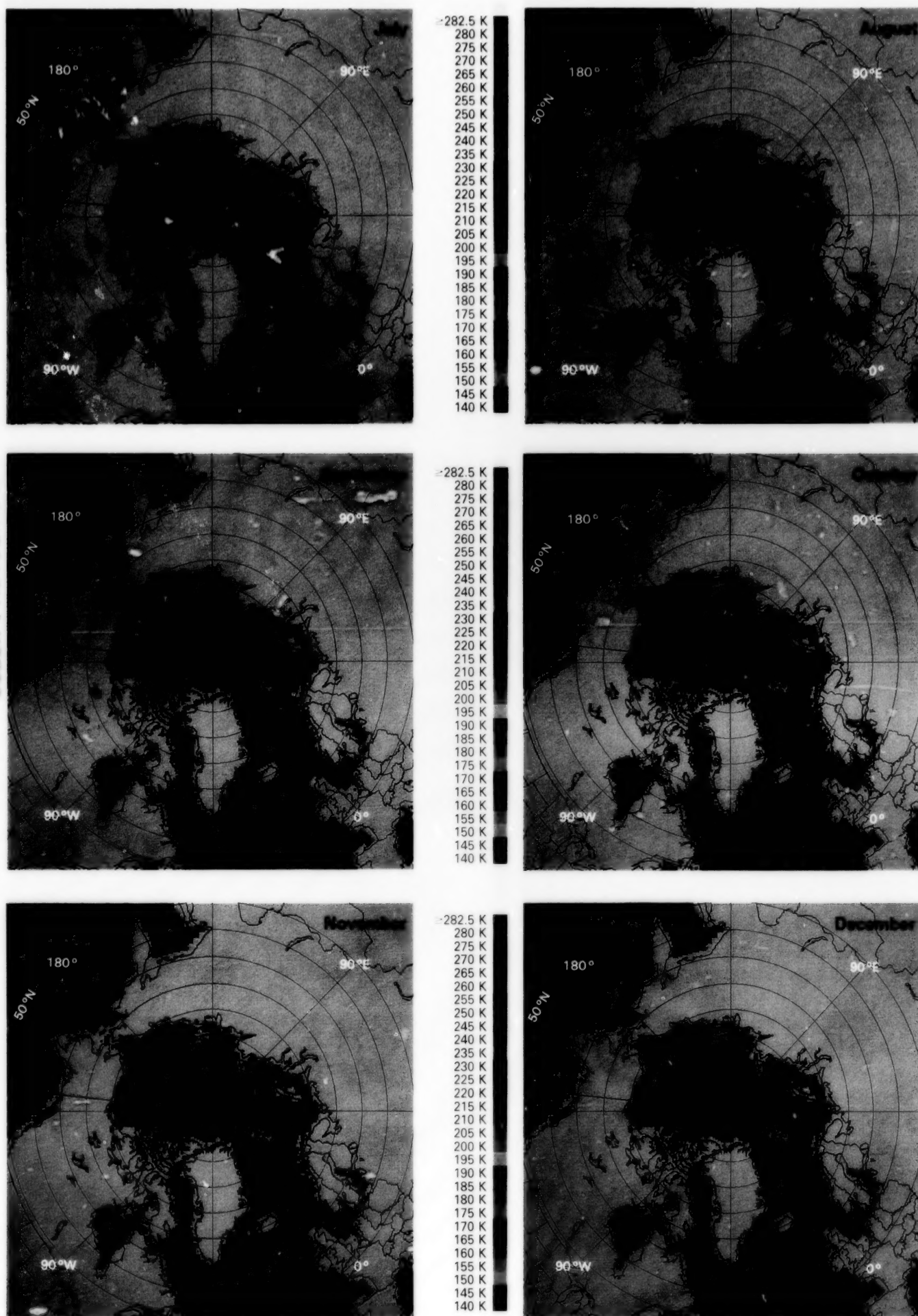


Figure 2-5b. Mean monthly climatological surface water temperatures, July through December. These have been color coded and mapped from digital data compiled by S. Levitus and obtained from the National Oceanic and Atmospheric Administration's National Oceanographic Data Center in Washington, D.C. The Hudson Bay data for October appear inconsistent with the rest of the yearly cycle and may be flawed due to a faulty instrument or other difficulty.

Energy balance studies of the Earth-atmosphere system using satellite observations indicate a net radiative energy gain equatorward of 35-degrees latitude and a net radiative energy loss poleward of this latitude. Although the incoming radiative flux at the top of the atmosphere in the polar regions during summer can be as large as in the tropics, the perennial Arctic ice cover reflects much of the incoming radiation back to space. To maintain regional heat balances, the surplus energy at low latitudes must be transported poleward to regions of radiative energy deficit. About 60 percent of this poleward energy transport occurs within the atmosphere, and the remainder occurs within the oceans. The chief heat-transport mechanisms of the atmosphere include mean meridional circulations, thought to be most important between the Equator and 30-degrees latitude, and horizontal transports resulting from eddies, more effective at mid and high latitudes. The Arctic region is thereby influenced by the energetic subpolar systems transporting heat and momentum into the region, and it in turn influences the general circulation of the atmosphere by being a heat sink for the global weather machine (Vowinckel and Orvig, 1970).

2.6 ATMOSPHERIC TEMPERATURES, PRESSURES, AND WINDS

Monthly climatological fields of atmospheric surface temperatures, sea-level pressures, and geostrophic winds for the region poleward of 50°N, created from the climatological data set of Crutcher and Meserve (1970), are presented in Figures 2-6 through 2-8. The pressure and temperature maps exhibit two distinct seasonal patterns. In winter, a bipolar pattern of pressure and temperature results from the bipolar distribution of land and ocean and the consequent contrast in thermal forcing: pressures are relatively high and temperatures are relatively low over the land versus over the oceans. Smaller-scale factors also influence the pressure and temperature distributions, with, for example, the Gulf Stream and North Atlantic Current influencing the position of the low-pressure region to the southwest of Iceland in October through April (the Icelandic Low). The other major low-pressure system visible in the winter maps is the Aleutian Low in the vicinity of the Aleutian Islands in the northern North Pacific. In summer, the temperature and pressure distributions are more symmetric, reflecting the meridional

temperature difference between the ice-covered central Arctic Ocean and the warm continental land surfaces around the perimeter.

The wintertime asymmetric surface air temperature distribution revealed in Figure 2-6 is determined partly by the radiative properties of the underlying surface. The surface albedo, or fraction of incident solar radiation reflected at the surface, varies strongly with surface type (Grenfell and Maykut, 1977; Robock, 1980; Barry, 1983; Henderson-Sellers and Wilson, 1983). Depending on the season, from 60 to 90 percent of the incoming solar radiation reaching the Arctic surface overall is reflected back (Lamb, 1982). During fall and winter, the albedo increases, to a point, with increasing ice thickness and snow cover. Young sea ice 1-centimeter thick has an albedo of about 0.1, whereas ice 1-meter thick has an albedo of about 0.8. As the ice further thickens from 1 meter to 3 meters, there is only a slight increase in albedo (Grenfell, 1983). Freshly fallen snow has an albedo as high as 98 percent (Vowinckel and Orvig, 1970), although albedos as low as 20 to 30 percent have been recorded over wet, dirty snow (Warren and Wiscombe, 1980). A representative range of albedos for ice-free ocean is 10 to 15 percent (Lamb, 1982). During summer, the overall albedo is greatly reduced over that during winter because of the greater amount of open water and the presence of wet snow and melt ponds on the ice. The albedo of melt ponds varies with the thickness and the underlying ice type but ranges from about 20 to about 60 percent (Grenfell and Maykut, 1977).

Near-surface Arctic atmospheric temperatures are characterized through most of the year by a strong temperature inversion, with air temperatures increasing rather than decreasing with height. This inversion results mainly from the negative surface energy balance. The depth of the inversion depends on the amount of cloud cover, near-surface turbulence, and warm-air advection from lower latitudes and may reach about 2 kilometers into the atmosphere. Changes in these factors will at times destroy the inversion layer, sometimes temporarily increasing the winter surface temperature by as much as 30 K (Vowinckel and Orvig, 1970).

During the midwinter month of February, the temperatures across the ice-covered Arctic Basin

range from 235 K north of the Canadian Archipelago to 250 K in the Chukchi and Kara Seas. As the Sun's elevation increases in the spring, the land masses warm and the temperature distribution becomes more symmetric about the pole, with the exception of the Greenland ice cap. By July, the temperature across the Arctic is fairly uniform at 275 ± 2.5 K, just a few degrees above freezing. In September, cooling initiates the return to the more asymmetric wintertime distribution. The annual spread of the mean latitudinal position of the freezing line (273.15 K isotherm) is approximately 22 degrees, ranging from a mean summer latitude of 78°N to a mean winter latitude of 56°N (Holcombe, 1958).

The January climatological sea-level pressure map shows the dominance of the Icelandic Low in the northern North Atlantic and the eastern Arctic regions (Figure 2-7a). The 1010-millibar contour associated with this system extends westward to eastern Canada and northeastward to Scandinavia and Novaya Zemlya. In the western Arctic, the high-pressure system over Siberia is connected to a smaller high situated over northwestern Canada by a high-pressure bridge that additionally separates the Icelandic Low from the Aleutian Low. The Aleutian Low and Siberian High dominate the circulation over the Bering Sea and the Sea of Okhotsk regions. This pattern of two low-pressure and two high-pressure systems over the north polar region is maintained until May, when the monthly average pressure field becomes more uniform and symmetric. By June the range in mean sea-level pressure across the Arctic is almost a factor of 3 less than in January, and throughout the summer months there are no well-defined systems except the persistent high pressure over the central Arctic Basin. By October a high-pressure ridge begins to form over the Asian land mass, and the low-pressure areas in the vicinity of Iceland and the Aleutian Islands begin to intensify. By December the winter pattern is well established.

Monthly mean geostrophic winds based on the pressure distributions shown in Figure 2-7 are presented in Figure 2-8. In the Northern Hemisphere the geostrophic wind, which results from a balance between the pressure gradient and Coriolis forces (in the absence of friction), is directed counterclockwise around a low-pressure system and clockwise around a high-pressure system, with a speed proportional to the pressure gradient. During the winter months of January and February, the strongest mean

monthly winds are found along the coastal regions of the North Pacific and are associated with the semipermanent low centered over the Aleutian Islands. The so-called "polar easterlies" are not hemispheric in extent but are found poleward of the Icelandic and Aleutian Lows. Over the central Arctic Basin, monthly average winter winds are weaker than over the adjacent seas. As the intensity of the semipermanent pressure systems decreases in the transition months of March, April, and May, the winds weaken on average, but the contrast between the still cold surface of the Arctic pack ice and the warmer continents and open-water areas contributes to creating a frontal zone along the northern shores of Siberia, Alaska, and Canada (Reed, 1960). Intense low-pressure systems move eastward along this zone, termed the Siberian-Canadian Arctic Front, bringing heat and moisture to the Arctic region.

2.7 SYNOPTIC CHARACTERISTICS OF THE ARCTIC ATMOSPHERE

Synoptic weather charts of the Arctic, which show the distribution of cyclones (low-pressure systems) and anticyclones (high-pressure systems) at a given time, can differ considerably from the monthly mean climatological maps presented in Figure 2-7, especially during winter, when the weather patterns are often dominated by intense, rapidly moving low-pressure systems. For instance, the semipermanent Icelandic and Aleutian Lows discussed in Section 2.6 reflect the frequent passage of individual transient systems.

Long-term synoptic observations have provided data for mapping the intensity and frequency of cyclones and anticyclones. Figure 2-9, redrawn from Palmen and Newton (1969), shows the location of the maximum frequency of cyclone and anticyclone tracks, the axis of mean maximum wind, and the mean sea-level pressure in the principal semipermanent high- and low-pressure centers for the winter months. At high latitudes, there are two principal axes of maximum cyclone frequency, one located in the Pacific and the other in the Atlantic. In the North American sector, an axis over eastern Canada converges with a second axis along the east coast of the continent. The point of convergence is in the vicinity of Iceland, defining the Icelandic Low. These cyclones penetrate the Arctic region along a track that follows the ice-free waters of the Norwegian Sea and then progresses into the Barents Sea along the

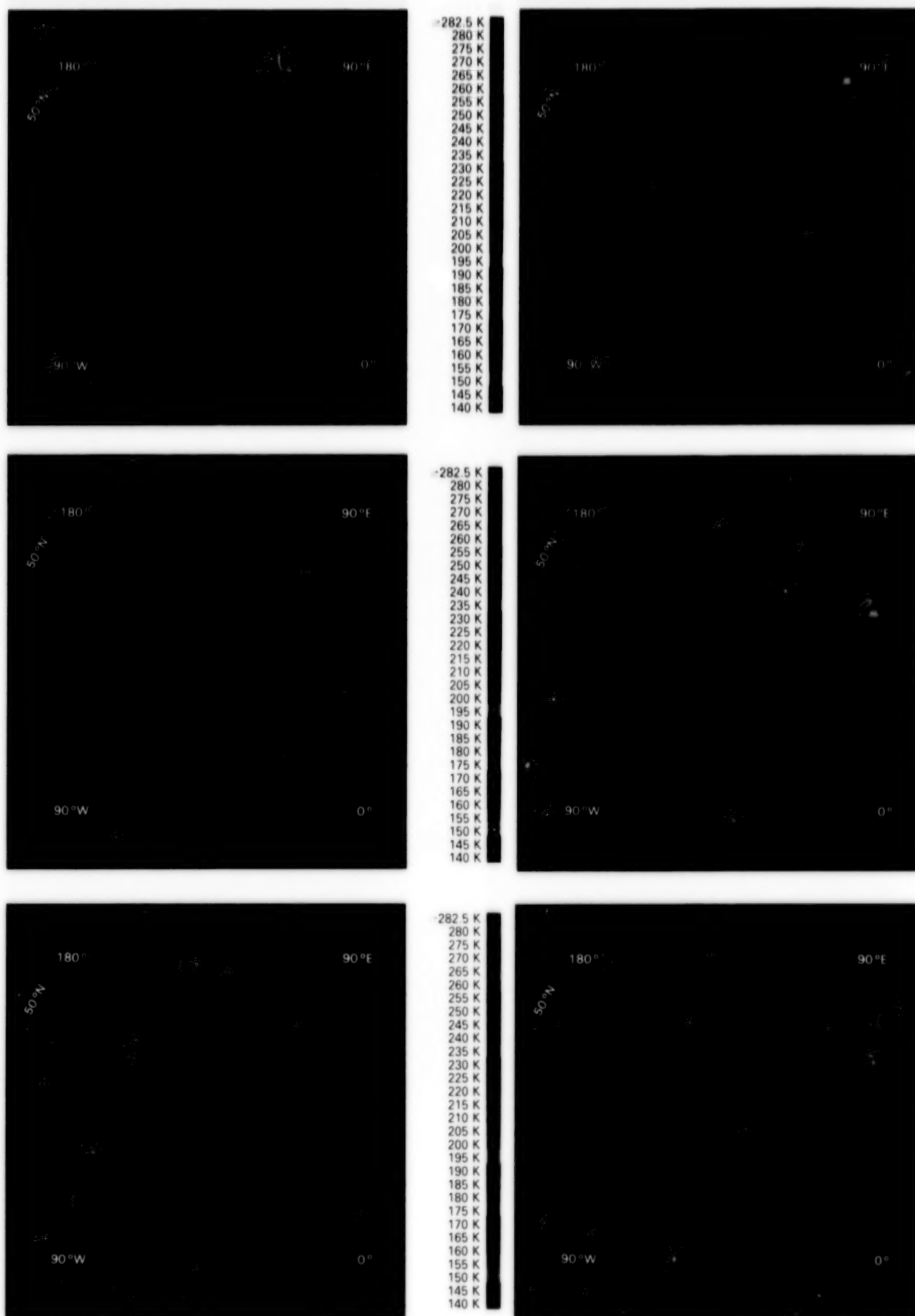


Figure 2-6a. Mean monthly climatological surface air temperatures, January through June. These have been color coded and mapped from digital data compiled by R. Jenne and obtained from the National Center for Atmospheric Research in Boulder, Colorado.

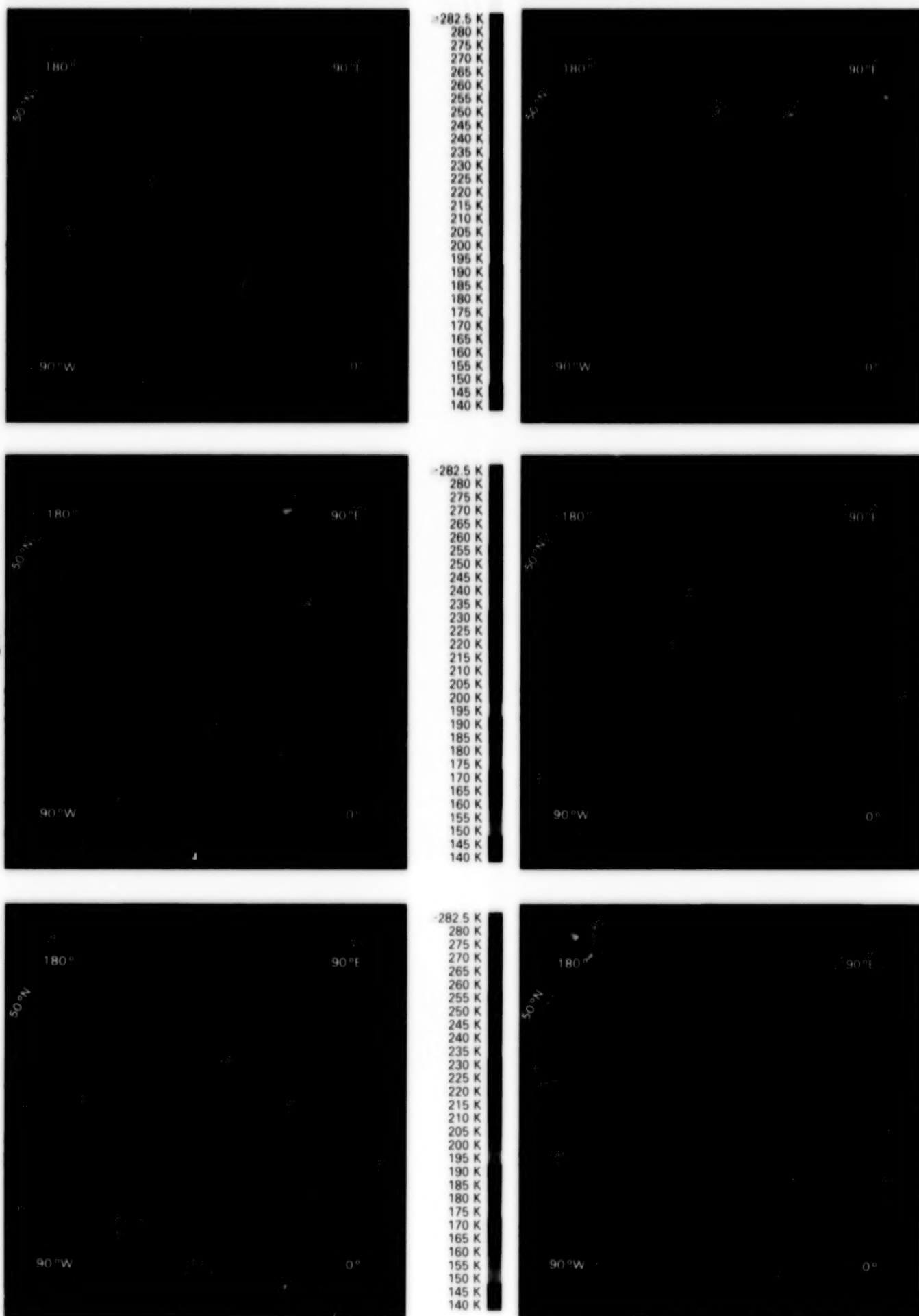
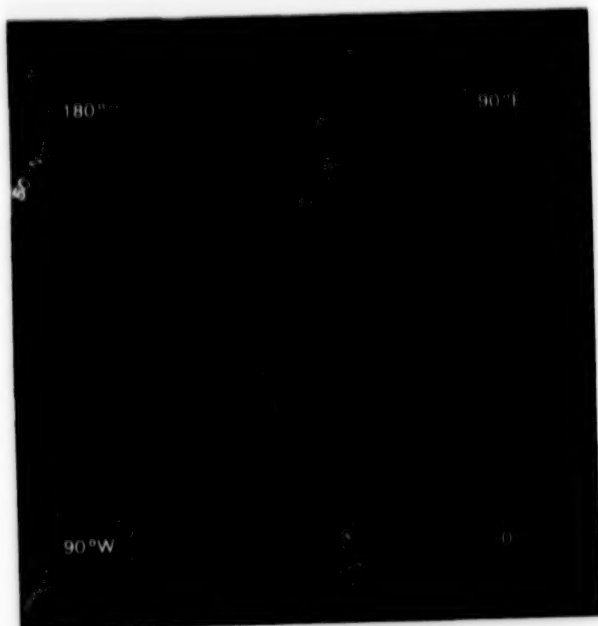
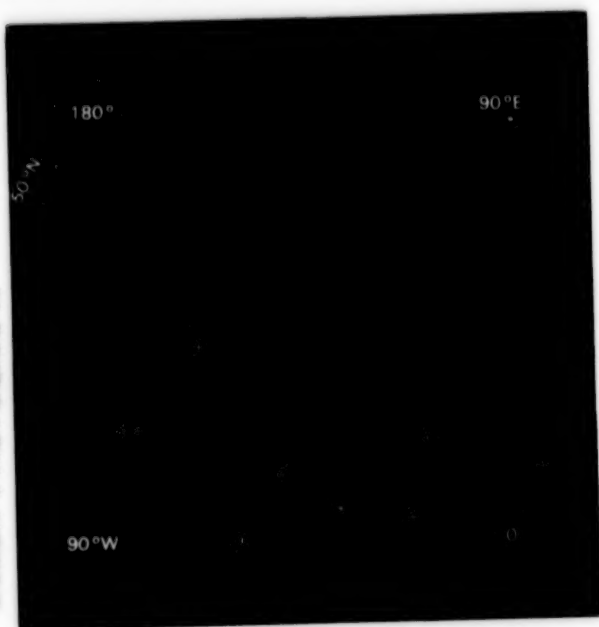
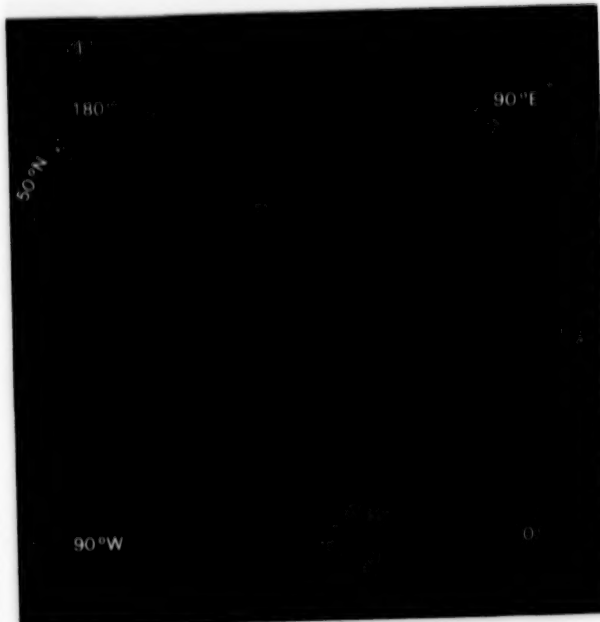


Figure 2-6b. Mean monthly climatological surface air temperatures, July through December. These have been color coded and mapped from digital data compiled by R. Jenne and obtained from the National Center for Atmospheric Research in Boulder, Colorado.

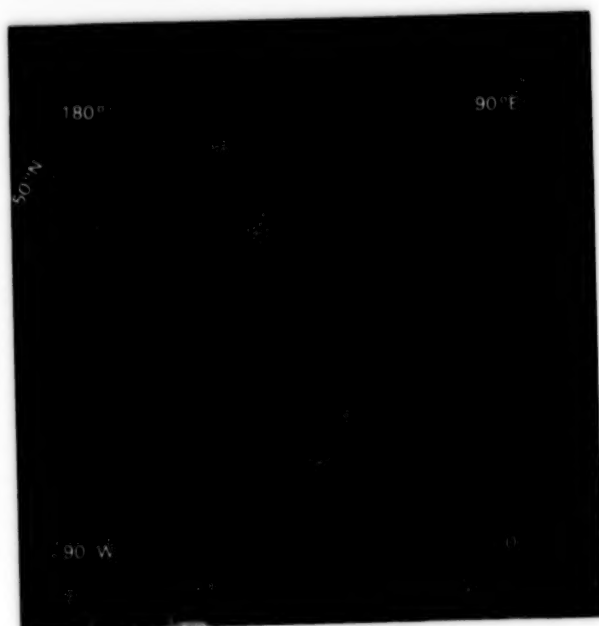
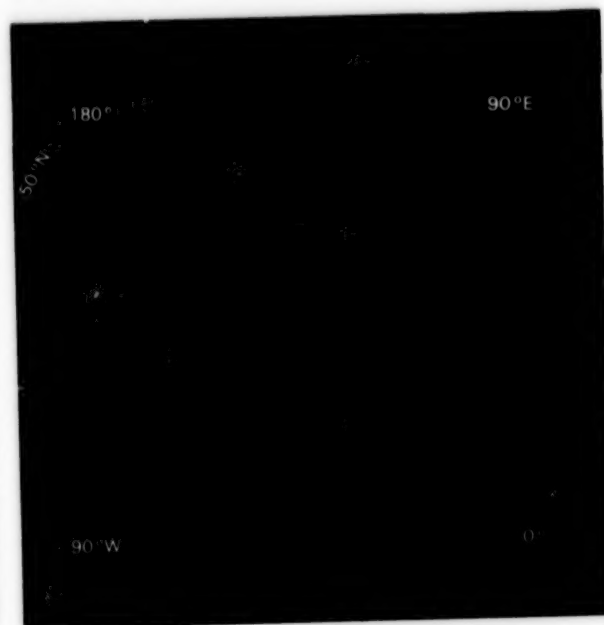
ORIGINAL PAGE
COLOR PHOTOGRAPH



1037 mb
1036 mb
1034 mb
1032 mb
1030 mb
1028 mb
1026 mb
1024 mb
1022 mb
1020 mb
1018 mb
1016 mb
1014 mb
1012 mb
1010 mb
1008 mb
1006 mb
1004 mb
1002 mb
1000 mb
998 mb
996 mb
994 mb
992 mb
990 mb
988 mb
986 mb
984 mb
982 mb
980 mb



1037 mb
1036 mb
1034 mb
1032 mb
1030 mb
1028 mb
1026 mb
1024 mb
1022 mb
1020 mb
1018 mb
1016 mb
1014 mb
1012 mb
1010 mb
1008 mb
1006 mb
1004 mb
1002 mb
1000 mb
998 mb
996 mb
994 mb
992 mb
990 mb
988 mb
986 mb
984 mb
982 mb
980 mb



1037 mb
1036 mb
1034 mb
1032 mb
1030 mb
1028 mb
1026 mb
1024 mb
1022 mb
1020 mb
1018 mb
1016 mb
1014 mb
1012 mb
1010 mb
1008 mb
1006 mb
1004 mb
1002 mb
1000 mb
998 mb
996 mb
994 mb
992 mb
990 mb
988 mb
986 mb
984 mb
982 mb
980 mb

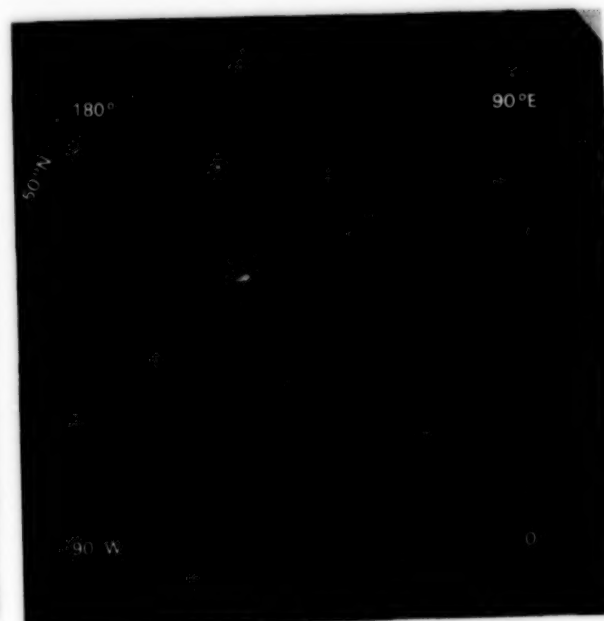
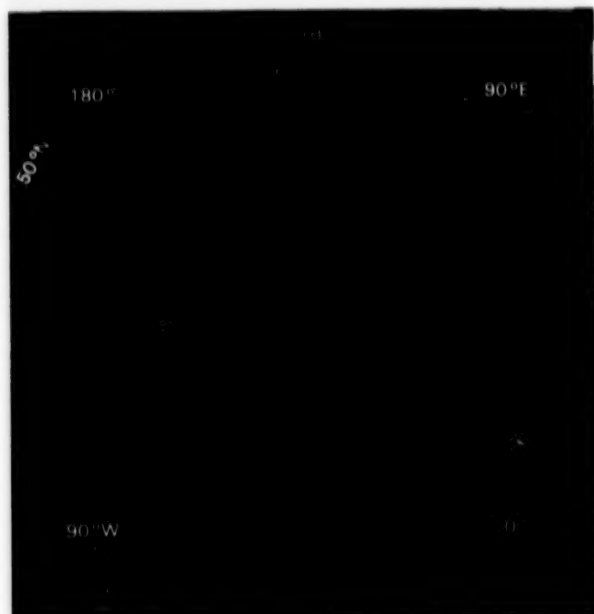
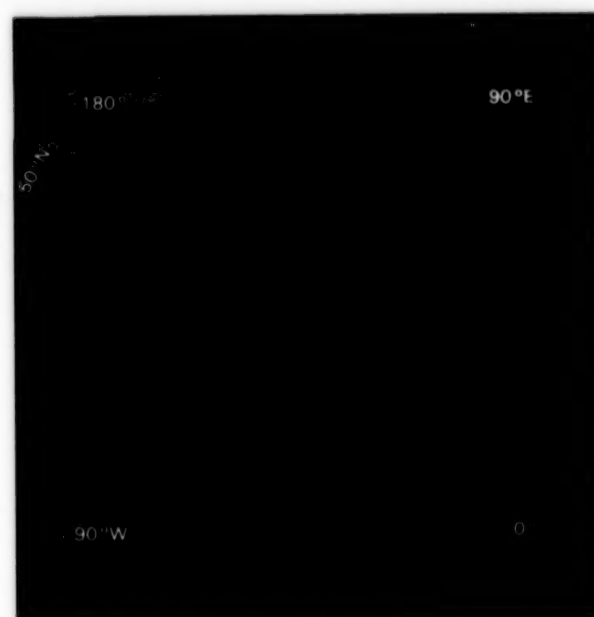
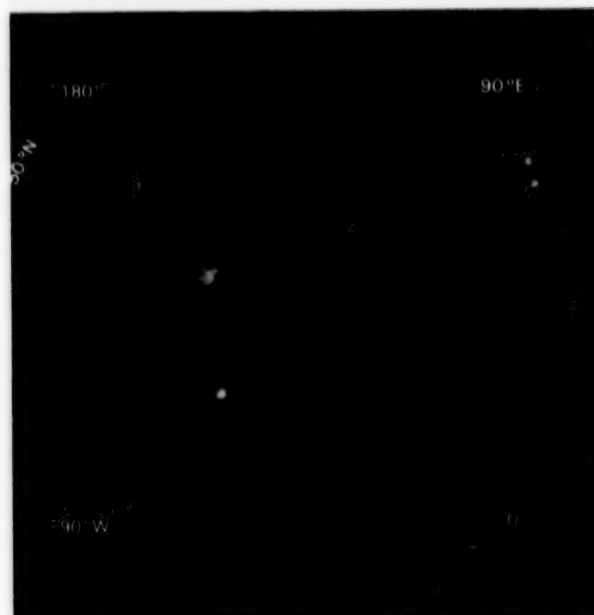


Figure 2-7a. Mean monthly climatological sea-level pressures, January through June. These have been color coded and mapped from digital data compiled by R. Jenne and obtained from the National Center for Atmospheric Research in Boulder, Colorado.

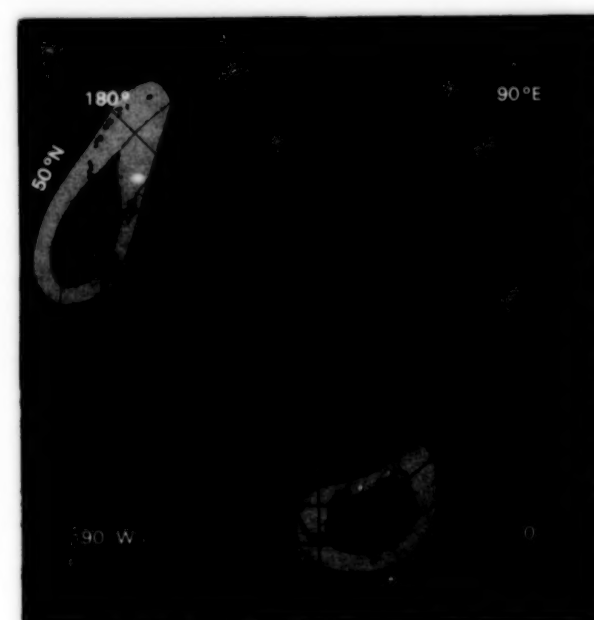
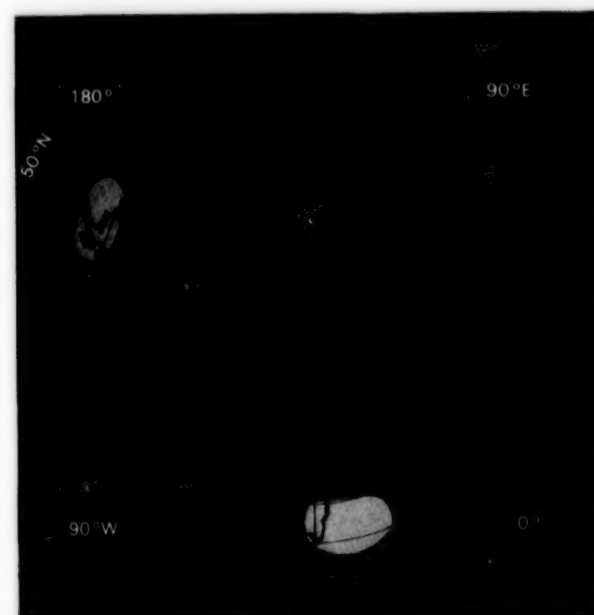
ORIGINAL PAGE



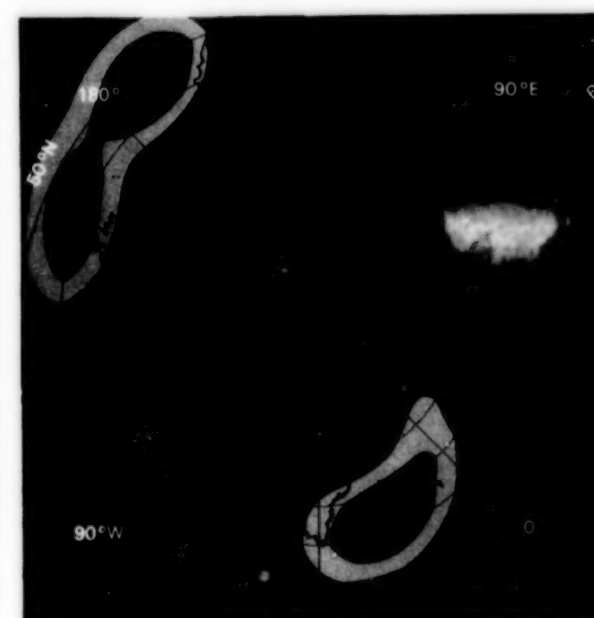
1037 mb
1036 mb
1034 mb
1032 mb
1030 mb
1028 mb
1026 mb
1024 mb
1022 mb
1020 mb
1018 mb
1016 mb
1014 mb
1012 mb
1010 mb
1008 mb
1006 mb
1004 mb
1002 mb
1000 mb
998 mb
996 mb
994 mb
992 mb
990 mb
988 mb
986 mb
984 mb
982 mb
980 mb



1037 mb
1036 mb
1034 mb
1032 mb
1030 mb
1028 mb
1026 mb
1024 mb
1022 mb
1020 mb
1018 mb
1016 mb
1014 mb
1012 mb
1010 mb
1008 mb
1006 mb
1004 mb
1002 mb
1000 mb
998 mb
996 mb
994 mb
992 mb
990 mb
988 mb
986 mb
984 mb
982 mb
980 mb



1037 mb
1036 mb
1034 mb
1032 mb
1030 mb
1028 mb
1026 mb
1024 mb
1022 mb
1020 mb
1018 mb
1016 mb
1014 mb
1012 mb
1010 mb
1008 mb
1006 mb
1004 mb
1002 mb
1000 mb
998 mb
996 mb
994 mb
992 mb
990 mb
988 mb
986 mb
984 mb
982 mb
980 mb



ORIGINAL PAGE
COLOR PHOTOGRAPH

Figure 2-7b. Mean monthly climatological sea-level pressures, July through December. These have been color coded and mapped from digital data compiled by R. Jenne and obtained from the National Center for Atmospheric Research in Boulder, Colorado.

ORIGINAL PAGE IS
OF POOR QUALITY

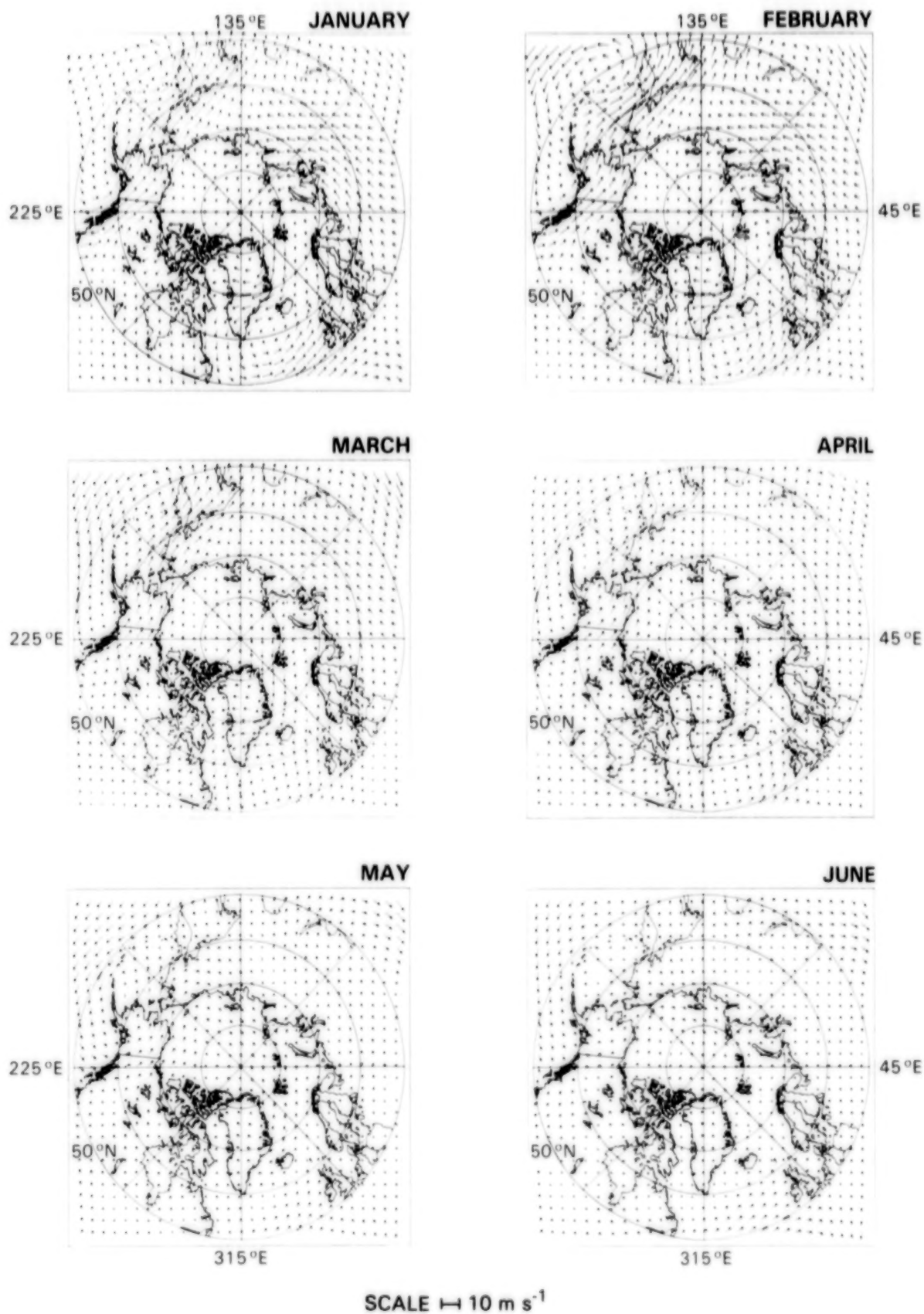


Figure 2-8a. Mean monthly climatological geostrophic winds, January through June. Arrows indicate the directions and magnitudes of the wind vectors, following the scale at the bottom. The data for the images were obtained in digitized form from R. Jenne at the National Center for Atmospheric Research in Boulder, Colorado.

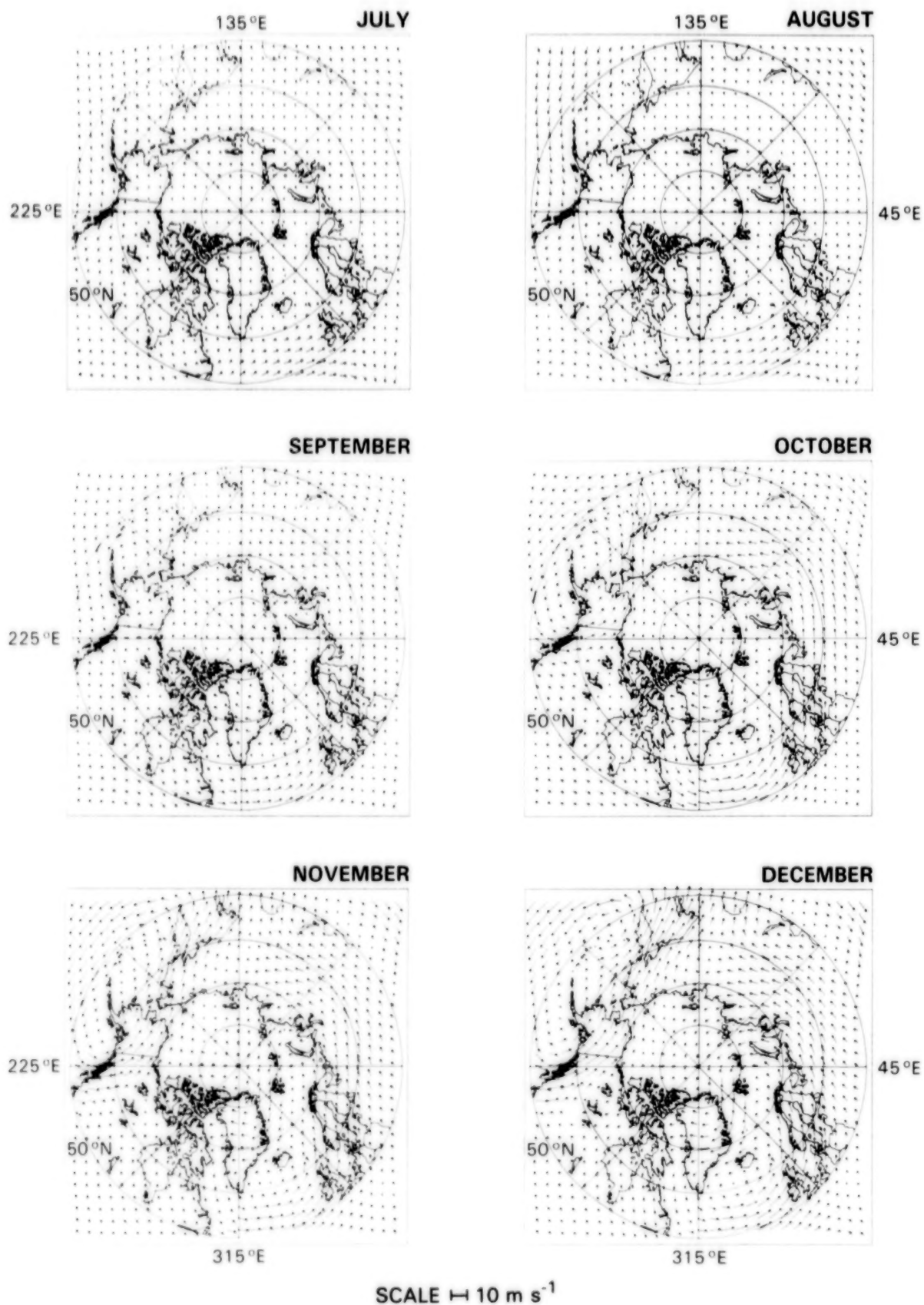


Figure 2-8b. Mean monthly climatological geostrophic winds, July through December. Arrows indicate the directions and magnitudes of the wind vectors, following the scale at the bottom. The data for the images were obtained in digitized form from R. Jenne at the National Center for Atmospheric Research in Boulder, Colorado.

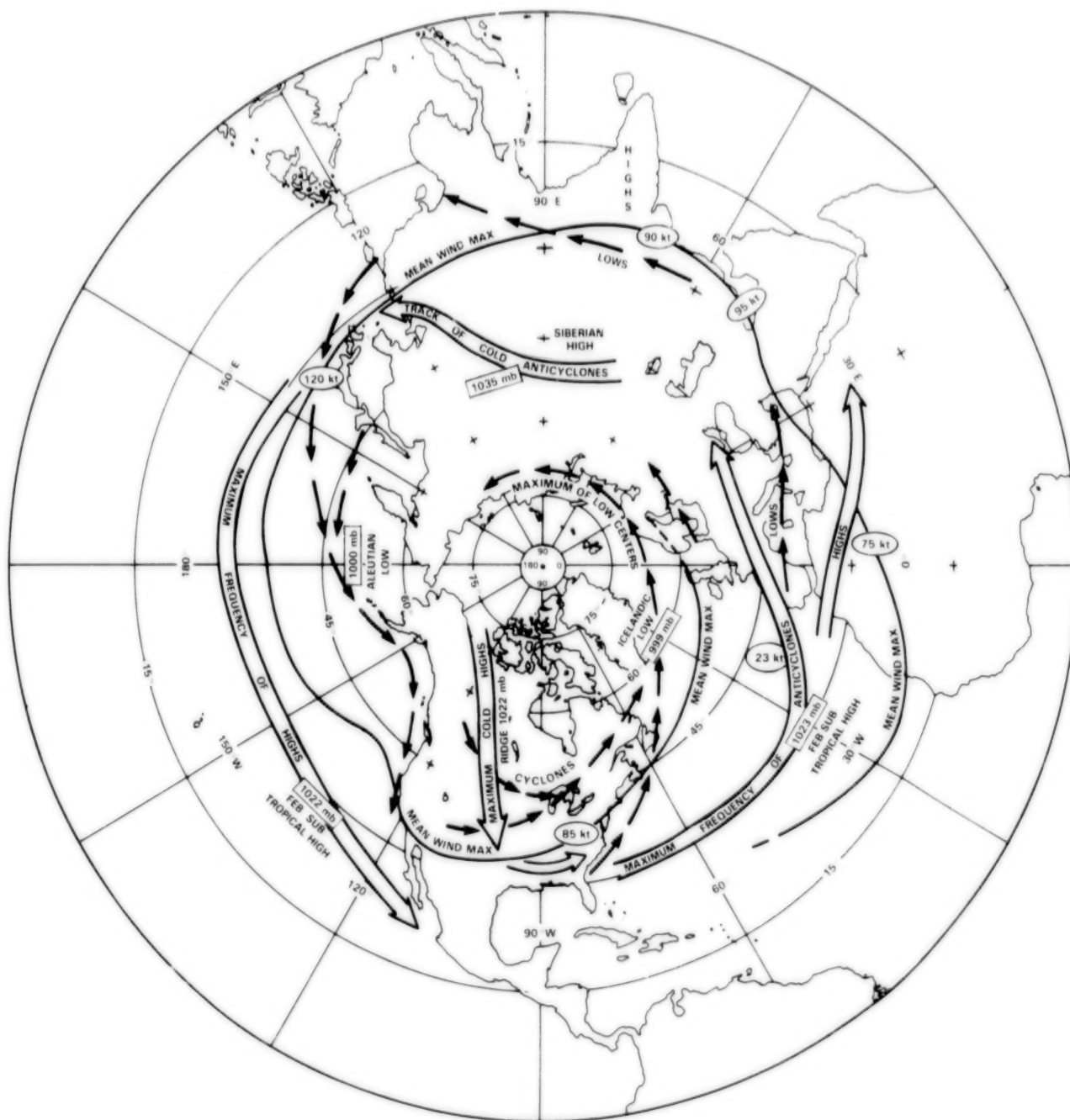


Figure 2-9. Northern Hemisphere winter distribution of the maximum frequency of cyclone and anticyclone tracks, shown as short-solid arrows and double-sided arrows, respectively, and the position of the mean maximum wind, shown as a solid line. The mean sea-level pressures of the principal semipermanent cyclone and anticyclone centers are shown in rectangles, and the maximum upper air wind speeds are shown in ellipses. [Redrawn from Figure 3.17 in Palmen and Newton (1969).]

Eurasian coast. In the Pacific, two axes of maximum frequency track northeastward and converge in the vicinity of the Aleutian Island chain, defining the semipermanent Aleutian Low. The curve of maximum frequency of cyclones then proceeds into the Gulf of Alaska and moves southward along the west coast of North America. The maximum frequency of anticyclones at Arctic latitudes is confined to the North American and Eurasian land masses. These systems are more quiescent than the cyclonic depressions.

During summer, eastward-moving cyclones follow the Siberian, Canadian, and Alaskan coasts, bringing rain and snow. These systems are associated with the Siberian-Canadian Arctic Front, which, as noted earlier, results in part from the contrast between the warm continents and the colder ocean surface and perennial ice cover of the central Arctic (Reed, 1960). Anticyclones form more frequently over the ice in spring and summer and are not simply extensions of the continental areas of divergence as is generally true in winter.

THEORY OF MICROWAVE EMISSION, THE ESMR BRIGHTNESS TEMPERATURE DATA, AND THE DERIVATION OF SEA ICE PARAMETERS

3.1 INTRODUCTION

This chapter describes the theory of microwave emission and the physical basis and mathematical formulae for deriving sea ice concentrations from satellite passive microwave measurements. Some of the material is repeated from the companion volume *Antarctic Sea Ice, 1973-1976* (Zwally et al., 1983a) for the convenience of the reader, with additional information presented as needed to understand the microwave observations in the Arctic regions. The distinctly different microwave properties of Arctic multiyear ice compared with first-year ice complicate the determination of total ice concentration, but the resulting difference in observed microwave emission provides information on the relative distributions of multiyear and first-year sea ice.

The Nimbus 5 ESMR measured primarily the intensity of electromagnetic radiation thermally emitted from the Earth's surface at a wavelength of 1.55 centimeters (corresponding to a frequency of 19.35 GHz). Additional radiative contributions or interference introduced by clouds, other atmospheric effects, and extraterrestrial sources exist but are relatively minor in the polar regions. Although the instrument recorded radiation from 78 scan positions, all observations used were first converted to equivalent nadir observations, as discussed in Appendix A. Unlike the more recent passive microwave conical scan instruments, such as the Scanning Multichannel Microwave Radiometer (SMMR) on the Nimbus 7 satellite and the Special Sensor Microwave Instrument (SSM/I) on the satellites of the Defense Meteorological Satellite Program, the ESMR is a cross-scan instrument.

The microwave signals from the Earth and atmosphere detected by the ESMR are processed and stored in many forms, including digitally format-

ted recordings on magnetic tape and color-coded maps produced from the digital data. For sea ice studies, the microwave radiances are combined with the microwave emissivity of sea ice and estimates of the ice physical temperature to obtain quantitative approximations to sea ice concentrations, according to the procedures described in the following sections. Also discussed in this chapter are some of the extensive aircraft and surface experiments that have been conducted in the Arctic and have contributed to our understanding of the microwave properties of sea ice.

An inherent disadvantage of the satellite passive microwave observations over certain higher resolution satellite observations is that the relatively low resolution of approximately 30 kilometers prevents the identification of individual ice floes. Thus ice floe shapes cannot be determined, nor can individual ice floes be tracked. Determination of the ice edge and other ice features can also be given only to the resolution of the instrument.

An inherent advantage of the satellite passive microwave observations can be understood by describing the measurement method as an integrating technique rather than a resolving technique. Specifically, with passive microwave observations it is not necessary to resolve each open lead or polynya in order to make a quantitative measurement of the total area of open water within some specified area or region. Because the typical size of open water features, often on the order of meters or tens of meters, is even less than the resolution of most high-resolution imagery, determination of open water area by resolving techniques using radar, visible, or infrared imagery is extremely difficult. The integrating method avoids these difficulties by integrating the radiative emission from both open water and ice within the instantaneous field of view

(typically 30 by 30 kilometers) of the satellite sensor, even if the size of the open water area is very small. Furthermore, because the microwave emission from open water is relatively low and the emission from sea ice is relatively high, approximations to the fractional coverages of open water and sea ice are readily deduced by interpolation from the measured total emission within the field of view. The percentage of an ocean area covered by sea ice is termed the "*sea ice concentration*," and the fraction of the sea ice area containing multiyear ice is termed the "*multiyear ice fraction*."

The equations for deriving sea ice concentration and estimating multiyear ice fraction are described in Section 3.6. In Chapter 4, the calculated ice concentrations are mapped and presented with a nomogram relating the ice concentrations to the brightness temperatures and multiyear ice fractions. For regions with only one ice type, the nomogram reduces to a linear scale ranging from 14 to 100 percent total ice concentration.

3.2 MICROWAVE EMISSIVITY AND BRIGHTNESS TEMPERATURE

The intensity of microwave radiation thermally emitted by an object is usually expressed as a brightness temperature, T_B . Units of temperature are appropriate because, as a consequence of the Rayleigh-Jeans approximation to Planck's law of radiative emission, for radiative wavelengths in the microwave range (1 millimeter to 1 meter) the radiation emitted from a perfect emitter is proportional to its physical temperature, T . Most real objects emit only a fraction of the radiation that a perfect emitter would emit at the same temperature, and this fraction is defined as the emissivity, ϵ , of the object. Because of the proportionality between microwave radiation and temperature, ϵ can be calculated as

$$\epsilon = T_B / T \quad (3-1)$$

The usefulness of microwave radiometry as a remote sensing tool derives from the fact that the emissivity of an object depends mainly on its composition and physical structure. Measurements of brightness temperature provide information on the emissivity through equation 3-1, as long as the

physical temperature is independently known or estimated. If the emissivities of the possible media in the field of view are known, then the emissivities calculated from remote sensing can be used to infer information on the physical properties of the radiating media, upon which the emissivity depends. For first-year sea ice, a good estimate of its emissivity can be obtained from Fresnel's law of reflection (Jackson, 1962):

$$r = \left| \frac{1-n}{1+n} \right|^2 \quad (3-2)$$

Here n is the index of refraction and r is the surface reflectance, related to the emissivity ϵ by

$$\epsilon = 1 - r \quad (3-3)$$

The Fresnel equation provides a good approximation in the case of first-year sea ice, because the observed radiation emanates mainly from a thin saline layer at the snow/ice interface. This equation, however, is not applicable for multiyear ice, because the observed radiation for multiyear ice emanates from a considerably thicker layer, as a result of the lower salinity of the surface layer of the multiyear ice. Internal scattering in this thicker emitting layer lowers the emissivity of multiyear ice, as will be discussed later. Although emissivity is generally a function of the wavelength of the radiation, the wavelength-independent equation 3-2 is applicable if the thickness of the layer from which the radiation emanates is small compared to the wavelength, and this proves to be the case with first-year sea ice. Using a refractive index of 1.8 from Vant et al. (1974), the emissivity of first-year sea ice is calculated from equations 3-2 and 3-3 to be 0.92. This value is consistent with emissivities inferred from the ESMR data in regions of known consolidated first-year ice using equation 3-1 with estimated physical temperatures, T , of the radiatively significant portion of the ice.

To understand the features visible on the microwave images, it is important to know the approximate depths from which the radiation emanates. For most emitters, the contribution of any layer to the total emission leaving the radiating source tends to decrease approximately exponentially with the depth of the layer in the source material. The optical depth (based on radiative power attenuation by a factor of $1/e$) is the thickness of the top layer from which

approximately 63 percent of the radiation emanates. At the 1.55-centimeter wavelength, the optical depth is on the order of millimeters for water and first-year sea ice, decimeters for multiyear sea ice, and meters for dry snow. The contrast between the emission depths for first-year and multiyear ice explains the applicability of equation 3-2 to the former and not to the latter. A material is termed optically thin if the optical depth is large and optically thick if the optical depth is small.

Because a surface layer on the order of millimeters in thickness is nearly isothermal, the emissivity of materials with an optical depth on that order is generally well defined. The situation is more complicated if the radiation emanates from a thicker layer that is not isothermal and is further complicated if this thicker layer has internal inhomogeneities that cause internal reflections or scattering of the radiation. In the general case of emission from the bulk of a medium that is not isothermal, equation 3-1 is not immediately applicable, because the physical temperature varies within the emitting medium. A general definition of emissivity for bulk emitting media is given by Zwally (1977), along with a specific application to polar firn. Briefly, the radiative transfer through a medium is affected by the emission, absorption, and scattering of each element of the medium. A radiative transfer function, describing the transfer of radiation from a given point within the medium to the surface, is used as a weighting function to obtain an effective physical temperature, $\langle T \rangle$, which is a weighted average over depth of the physical temperature within the medium. The weighting represents how well the medium transfers emitted radiation from each depth to the surface. The emissivity in this case equals $T_B / \langle T \rangle$, which is analogous to the isothermal case by replacing T by $\langle T \rangle$ in equation 3-1. The bulk emissivity as defined here varies from 0 to 1, but the use of surface temperature in place of $\langle T \rangle$ can at times lead to meaningless values of emissivity exceeding 1.

When radiometric measurements of brightness temperature are made at more than one microwave wavelength and/or polarization, it becomes possible to deduce additional information about the medium. This potential, a consequence of the variation of the emissivity of a medium with the wave-

length and polarization of the radiation, provides the rationale for multifrequency (and dual polarization) brightness temperature measurements and for the development of inversion techniques that calculate the desired physical parameters from the brightness temperatures measured at multiple wavelengths and polarizations (Gloersen and Barath, 1977). This method has been especially useful for determining sea ice concentrations and multiyear ice fractions from the data of the Nimbus 7 SMMR (Svendsen et al., 1983; Cavalieri et al., 1984; Hollinger et al., 1984; Swift et al., 1985; Comiso, 1986). The multichannel SMMR data also provide information on the physical temperature of the emitting ice layer. By contrast, in the case of the single-wavelength, single-polarization ESMR data, an independent estimate or measurement of physical temperature is required.

3.3 SEA ICE EMISSIVITY

The microwave emissivity of sea ice has been the subject of several experimental and theoretical investigations in recent years (Wilheit et al., 1972; Gloersen et al., 1978; Vant et al., 1974; Gloersen and Larabee, 1981; Troy et al., 1981; Carsey, 1982; Grenfell and Lohanick, 1985). Three principal ice types have been identified on the basis of their radiometric signatures: (1) new ice, (2) first-year ice, and (3) multiyear ice. The new-ice category includes the standard (WMO, 1970; Armstrong et al., 1973) newly formed ice types (frazil ice, grease ice, slush ice, and shuga) and nilas. The first-year ice category includes the standard first-year ice (30 centimeters to 2 meters in thickness) as well as young ice (10 to 30 centimeters in thickness). The multiyear ice category defined here includes all ice that has survived at least one summer melt. [As mentioned in Chapter 1, this definition of multiyear ice differs somewhat from WMO terminology, which designates a separate category for second-year ice and defines multiyear ice as ice that has survived two summer melt periods.] A fourth category, referred to as summer ice, includes a mixture of standard ice types with a variety of possible surface features, including wet snow, which increases the emissivity, and extensive meltponding, which decreases the emissivity. Approximate values of the emissivities of sea water and the aforementioned ice types, at the ESMR wavelength of 1.55 centimeters and a nadir viewing angle, are as follows:

<u>Ice Type</u>	<u>ϵ</u>
Open water	0.44
New ice	0.45 to 0.92
First-year ice	0.92
Multiyear ice	0.84
Summer ice	0.45 to 0.95

The basic differences between the various ice types are shown in Figure 3-1. The differences in emissivity are caused primarily by the following: (1) variations in the dielectric properties of the ice, these having been established experimentally to depend largely on salinity, temperature, and surface wetness (Ramseier et al., 1974; Vant et al., 1974, 1978); (2) differences in volume scattering, which depend on the internal ice structure (Gloersen et al., 1974); and (3) for very

thin ice, differences in ice thickness (Gloersen et al., 1975b; Gloersen and Larabee, 1981).

As discussed in Chapter 1, the principal physical property distinguishing new and first-year ice from multiyear ice is the salinity in the freeboard layer (the portion of the ice above sea level). Since salinity has a major impact on the volume fraction of liquid within the ice and on ice density, and these in turn have a major impact on the ice emissivity, understanding the salinity differences among the various ice types is crucial. Generally, new ice has higher salinity near the surface than first-year ice, and first-year ice has higher salinity than multiyear ice (Cox and Weeks, 1974; Campbell et al., 1976). The optical depth for typical saline ice is estimated to be less than one wavelength, so that the relevant microwave emission derives predominantly from the ice which is less than one wavelength below the upper

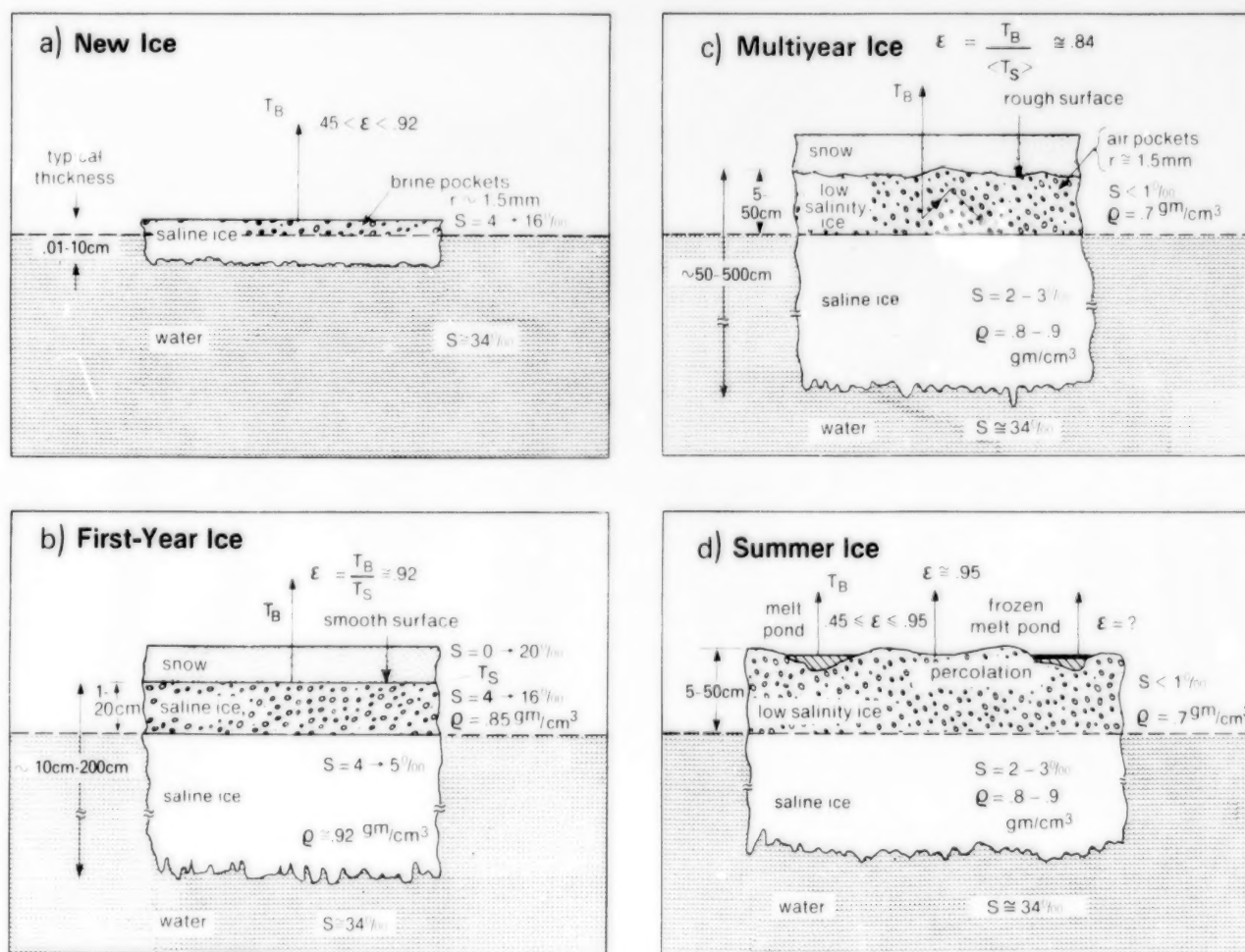


Figure 3-1. Schematic diagrams of the radiometric and physical properties of the principal sea ice types. [Modified from Zwally et al. (1983a).]

ice surface. This remains true even with a snow cover, as long as the snow is dry, fine, nonsaline, and no thicker than about 15 centimeters. Such a snow cover is optically thin and therefore has little effect on the transmission of radiation from the underlying ice. Consequently, even with a thin snow cover, for first-year ice the microwave radiation recorded by the ESMR instrument predominantly emanates from a thin top layer of the ice. Because this layer is approximately isothermal, equation 3-1 can be used to calculate the emissivity. For multiyear ice, with its much lower salinity content in the freeboard layer, the microwave radiation originates from deeper in the ice, where the salinity is higher. Furthermore, for multiyear ice this radiation is modified by scattering in the freeboard layer, and particularly in the air pockets that remain following brine drainage from the earlier brine pockets. As a result, the bulk emissivity of the media is reduced.

New ice generally has somewhat lower emissivities than first-year ice (Gloersen et al., 1975b; Tooma et al., 1975; Ramseier et al., 1975; Ketchum and Lohanick, 1980). For extremely thin ice (on the order of one optical depth), contributions from the water underneath the ice also affect the observed brightness temperature. Radiometer measurements of sea ice grown in a tank confirm the rapid increase of emissivity with thickness, up to a thickness of about 3 centimeters (Grenfell and Comiso, 1986). Another factor affecting the brightness temperature from new ice is the surface temperature, which often exceeds that of first-year ice because of greater heat conduction from the underlying ocean (Vant et al., 1974; see also Maykut (1978, 1982) for estimates of surface temperatures of the ice and for indications of the considerable impact of ice thickness on the conductive heat flux through the ice).

As referred to earlier, because dry, fine snow is relatively transparent at 19.35 GHz, the usual fairly thin, dry snow cover over Arctic sea ice floes in winter has no significant effect on the emissivity of the ice on spatial scales corresponding to low-resolution radiometers (Lohanick and Grenfell, 1986), such as the Nimbus 5 ESMR. However, in the event of a wet snow cover or a snow cover thicker than 40 centimeters, the snow layer can affect the microwave radiation in various ways. For example, the physical temperature of the emitting ice layer,

which for first-year ice is essentially the layer within several wavelengths of the surface, changes with the thickness of the snow cover because of the strong insulating properties of snow. Furthermore, the snow serves as a scatterer and suppresses the amount of emitted radiation, with the amount of suppression increasing with snow thickness and grain size. In spring, when the snow surface acquires a significant liquid content due to melt conditions, the imaginary part of the index of refraction of the snow increases and the snow becomes very emissive. The main source of the microwave radiation reaching the satellite from the snow-covered sea ice is then no longer the ice but the snow, and the effective emissivity of first-year and multiyear ice both increase to about 0.95. (See Grenfell and Lohanick (1985) for results at a frequency of 18 GHz.) Consequently, first-year ice and multiyear ice become indistinguishable in the microwave imagery during periods of snow surface melting.

In spring and summer, repeated diurnal freezing and thawing cause the microwave properties of the ice to fluctuate markedly. During daytime, at locations where the surface temperature is slightly above freezing, the emissivity is high and the radiation emanates basically from the wet snow cover. At night, when the temperature is below freezing, the refrozen melted snow cover becomes so granular that the scattering effect from the snow becomes substantially greater than that of a normal winter snow cover. The scattering suppresses the net emitted radiation and consequently reduces the emissivity. Furthermore, during spring some areas in the central Arctic still have winter conditions at the same time that other areas have melt conditions. This difference results in substantial spatial variability of the emissivity of the ice in spring, with values ranging from approximately 0.84 to approximately 0.95. In summer, melting is more persistent (Barry, 1983), and the open water in the melt ponds, with an emissivity of about 0.44, reduces the average emissivity of the ice floes. The seasonal variation in sea ice emissivity is shown schematically in Figure 3-2 as the ice progresses through its growth and decay stages.

Data averaged over 3-day periods have been used to examine the time variability of the Nimbus 5 ESMR brightness temperatures at two locations: one in a seasonal sea ice region, typifying first-year ice,

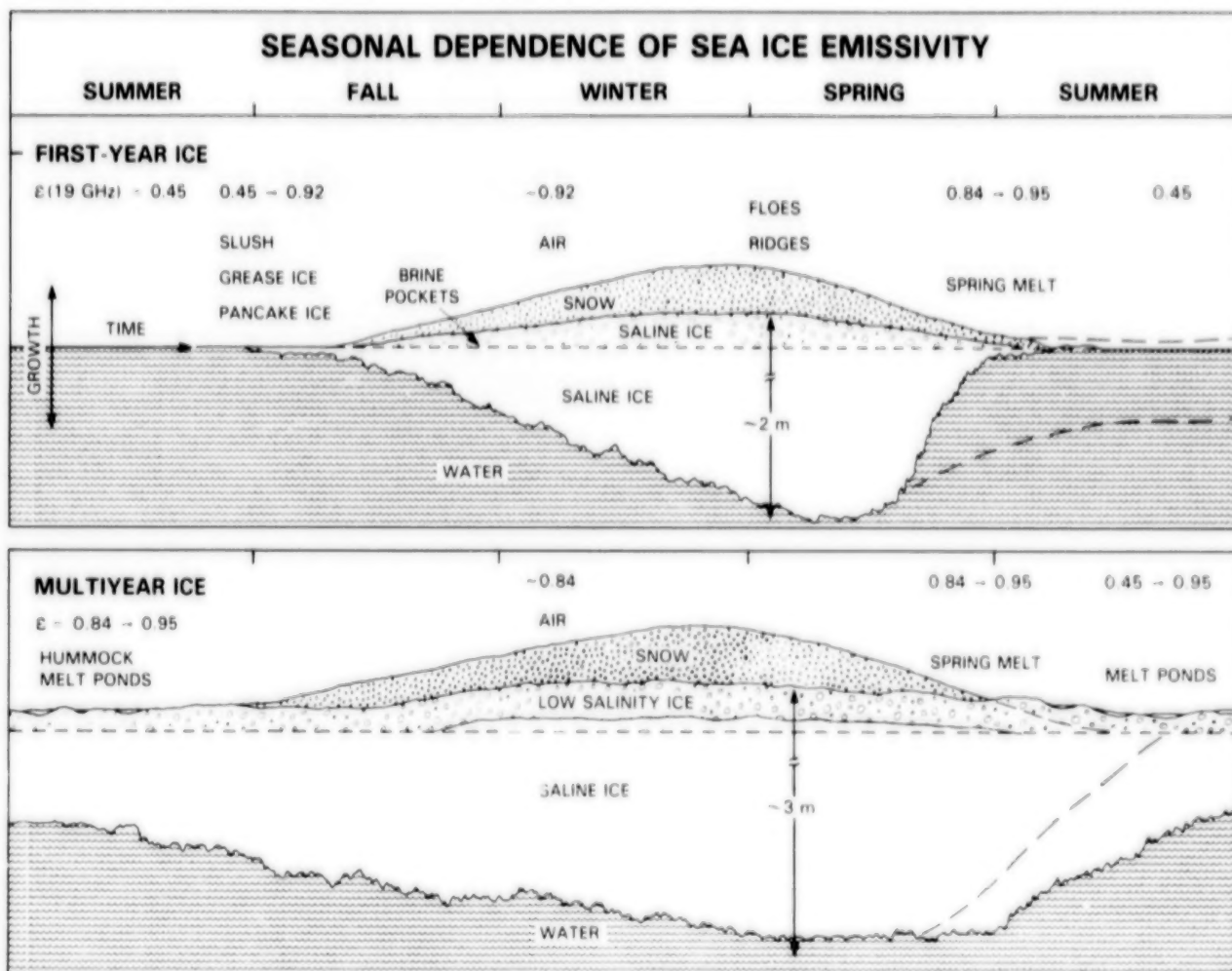


Figure 3-2. Schematic diagram of the seasonal dependence of sea ice emissivity during its first year and subsequent years.

and the other in the central Arctic near Ellesmere Island, typifying multiyear ice. Each location is approximately 300 by 300 kilometers in area, covering 100 ESMR data elements. Figure 3-3a presents for each of the two locations and for each year 1973 through 1976 the time sequences of the maximum brightness temperature, the average brightness temperature, the minimum brightness temperature, and the standard deviation of the brightness temperatures within the 100 data elements. Figure 3-3b presents a subset of these data, showing the maximum brightness temperatures in the first-year ice pack and the minimum brightness temperatures in the multiyear ice pack. In the first-year ice case, the maximum brightness temperatures are assumed to represent consolidated first-year ice (100-percent concentration) for most of the year, with the lower brightness temperatures having an open-water contribution. As

expected, during winter these maximum brightness temperatures for first-year ice are relatively high, being approximately 240 K. In the case of multiyear ice, the minimum brightness temperatures, approximately 200 to 210 K, in winter are assumed to represent consolidated multiyear ice, with the higher brightness temperatures likely having a first-year ice contribution. [The brightness temperatures for second-year ice have been observed to be intermediate to those of first-year ice and older multiyear ice (Tooma et al., 1975; Gray et al., 1982), so that the brightness temperatures above 210 K in the multiyear ice case could also be the result of the inclusion of second-year ice in the multiyear ice pack.]

The overlay of the 4 years of data results in well-defined curves for the first-year ice and multiyear ice regions (Figure 3-3b). Short-term variations may

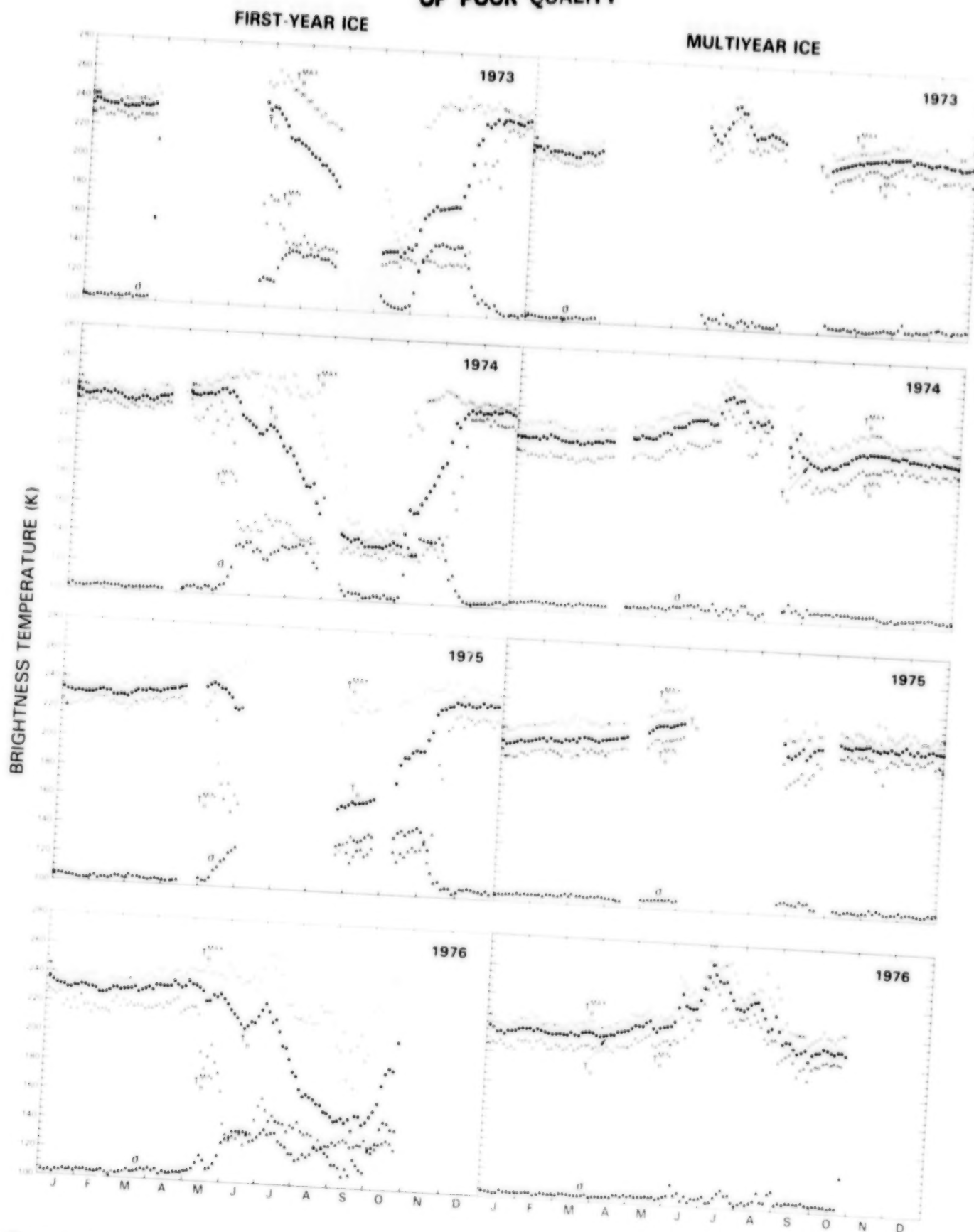


Figure 3-3a. Seasonal variations of microwave radiance of first-year and multiyear sea ice as observed by the Nimbus 5 ESMR, using 3-day-averaged data for 1973, 1974, 1975, and 1976. Maximum, minimum, and average brightness temperatures are plotted, along with the standard deviation.

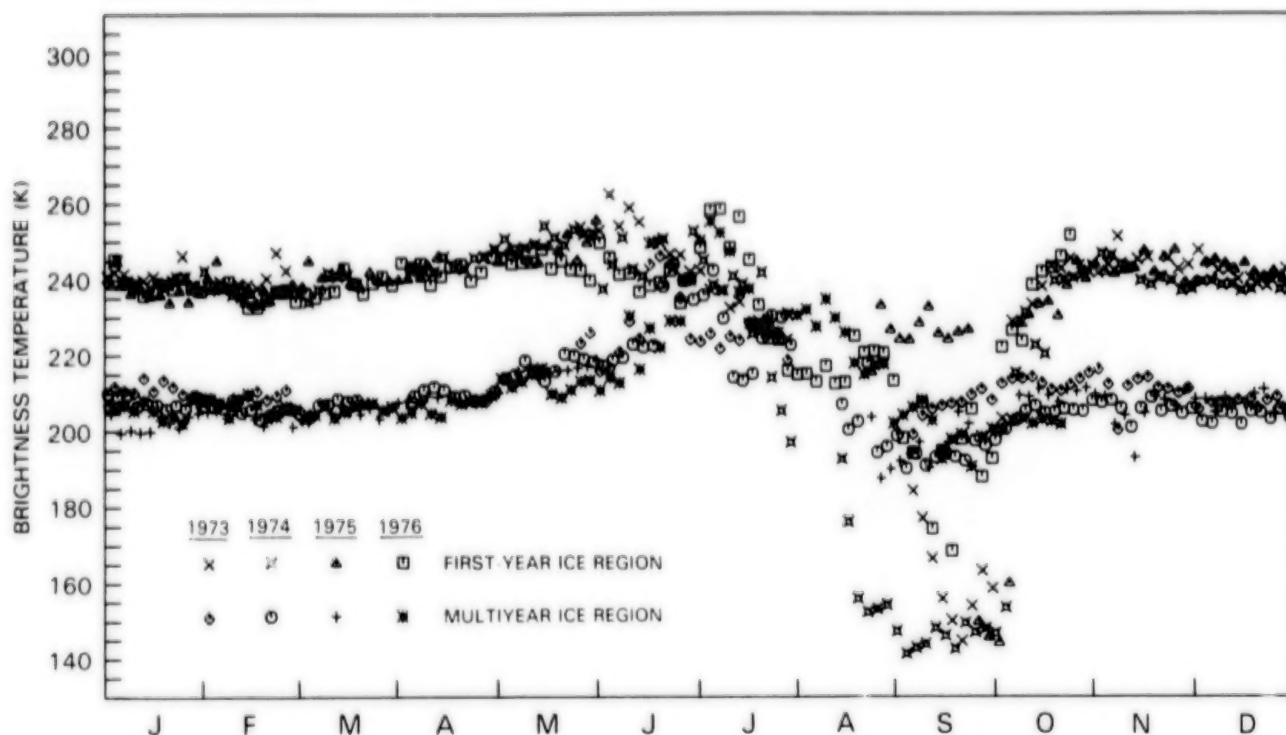


Figure 3-3b. Seasonal variations of microwave radiance for the minimum brightness temperature in a multiyear ice pack in the central Arctic and the maximum brightness temperature in a first-year ice pack in a seasonal sea ice zone, from a subset of the data plotted in Figure 3-3a.

be associated with changes in the physical temperature of the ice or with the opening of leads and polynyas. In spring and early summer, the brightness temperature increases slowly as the physical temperature of the ice increases, then continues to increase due to moisture in the snow cover produced by the onset of snow melt. During late spring, the effect of snow moisture is dominant (Stiles and Ulaby, 1980; Kunzi et al., 1982; Comiso, 1983). In midsummer, decreases in brightness temperature are caused mainly by ice breakup in the seasonal ice region and by meltponding or reduction of ice concentration in the central Arctic, although moisture levels of more than 1 percent in the snow also result in lower radiances (Kunzi et al., 1982). Overall, the observed microwave emissions are consistent with the preceding description of the seasonal radiative characteristics of the ice cover.

3.4 AIRCRAFT AND SURFACE OBSERVATIONS

Surface ice measurements and aircraft observations made during the period of Nimbus 5 ESMR coverage provide information for interpreting the

satellite data. In particular, during the main Arctic Ice Dynamics Joint Experiment (AIDJEX) in the Beaufort Sea in 1975 and 1976, surface and aircraft observations were acquired during all seasons of the year specifically to aid in the interpretation of the ESMR data. Gloersen et al. (1978) compare the spacecraft and aircraft data acquired during this experiment, and Campbell et al. (1978) compare the aircraft and surface data. From aircraft altitudes, in contrast to satellite altitudes, individual areas of open water or uniform ice types are resolvable in the passive microwave imagery, enabling explicit identifications of microwave emission characteristics. The aircraft and surface data can be averaged spatially to compare with spacecraft data.

Figure 3-4 is a color-coded 3-day-averaged satellite ESMR image of the Arctic for April 11-13, 1975, with the paths of two aircraft underflights superimposed in white. The reader is cautioned that in this and the subsequent ESMR images some of the 5 K changes have stronger visual effect than others, even though no particular color change is intrinsically more important than any other. For example, because of the color scale chosen, the changes from

ORIGINAL PAGE
COLOR PHOTOGRAPH

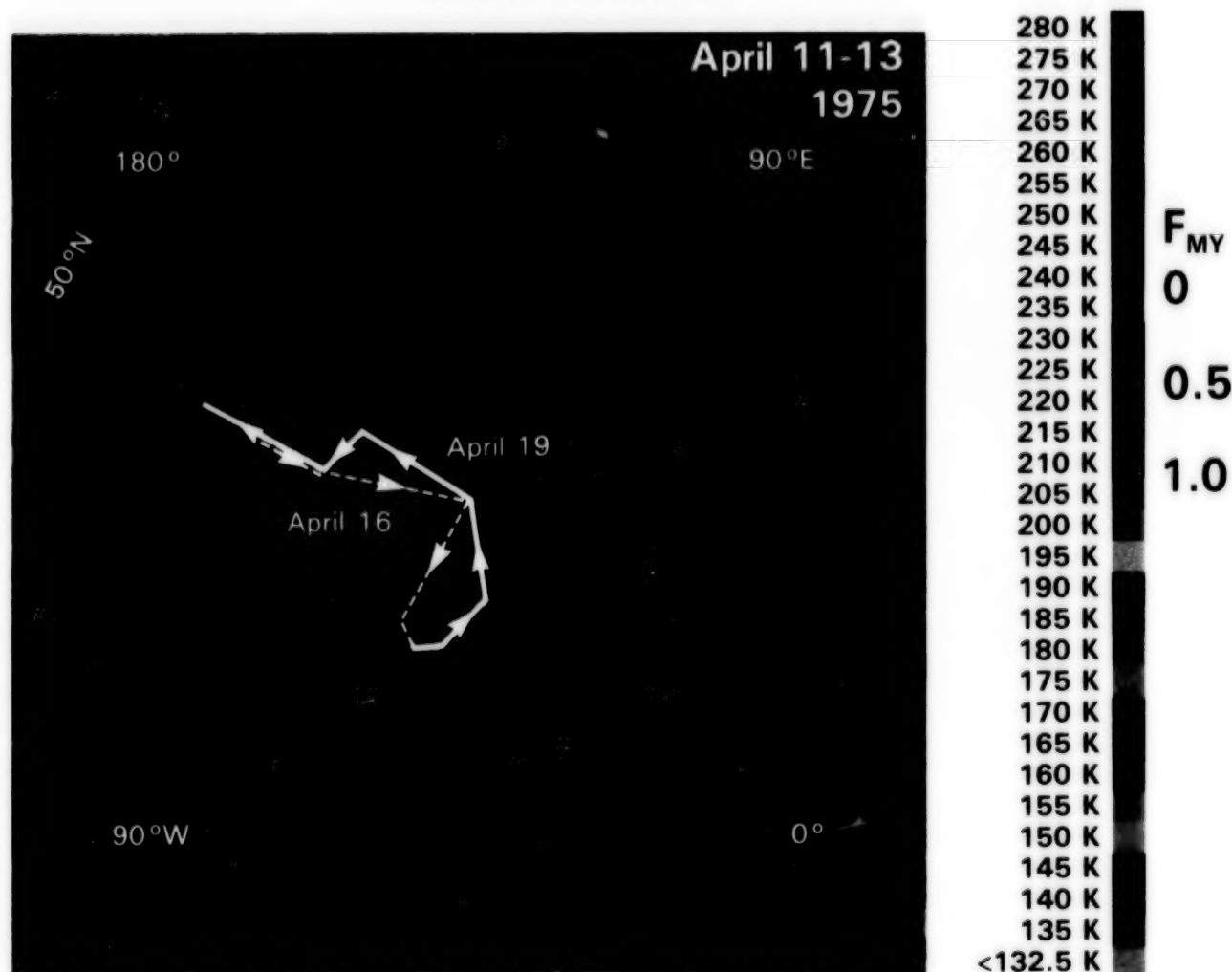


Figure 3-4. Three-day-averaged satellite ESMR image of the Arctic for April 11-13, 1975. The transects on the image indicate the flight paths of the NASA Convair 990 airborne laboratory on April 16 and 19. [Modified from Gloersen et al. (1978).]

190 to 195 K are more obvious than the changes from 185 to 190 K.

The two aircraft flights whose tracks are indicated in Figure 3-4 were carried out with the NASA Convair 990 aircraft on April 16 and 19, within days of the April 11-13 satellite ESMR image, and the ice conditions are assumed to be similar for the full April 11-19 period. [Unfortunately satellite ESMR data are not available for April 14-19, 1975.] Visual observation established the ice to be fully consolidated along the flight tracks. Furthermore, since on both April 16 and 19 the atmospheric conditions were nearly cloud free, surface temperatures could

be determined using a thermal infrared radiometer on board the aircraft. These temperatures were extrapolated to other areas of the pack and used in conjunction with the knowledge of fully consolidated conditions to convert the ESMR brightness temperatures to approximate values of multiyear ice fraction (F_{MY}) by assuming unique brightness temperature signatures of first-year and multiyear ice and linearly interpolating between them. The resulting values of F_{MY} are indicated by the scale on the right-hand side of Figure 3-4. More elaborate scales, or nomograms, indicating the three-way relationship between brightness temperature, ice concentration, and multiyear ice fraction are presented

in subsequent figures in which the ice concentration is not *a priori* believed to be 100 percent in all regions under discussion.

The crosstrack airborne ESMR data collected during the aircraft flights over the paths marked in Figure 3-4 were averaged into the along-track line profiles shown in Figure 3-5. Comparison of Figures 3-4 and 3-5 reveals that, although the absolute calibrations of the aircraft and satellite ESMR in-

struments differ, along the aircraft tracks major features of the relative changes in brightness temperature (and hence the derived first-year/multiyear ice mixture) appear in the data from both instruments. For example, along the flight of April 16 the aircraft data show a decrease in brightness temperature on the order of 10 K from the coast of Alaska to Ellesmere Island. On the ESMR figure the color change corresponds to a 10 K decrease from 220 to 210 K. This 10 K decrease

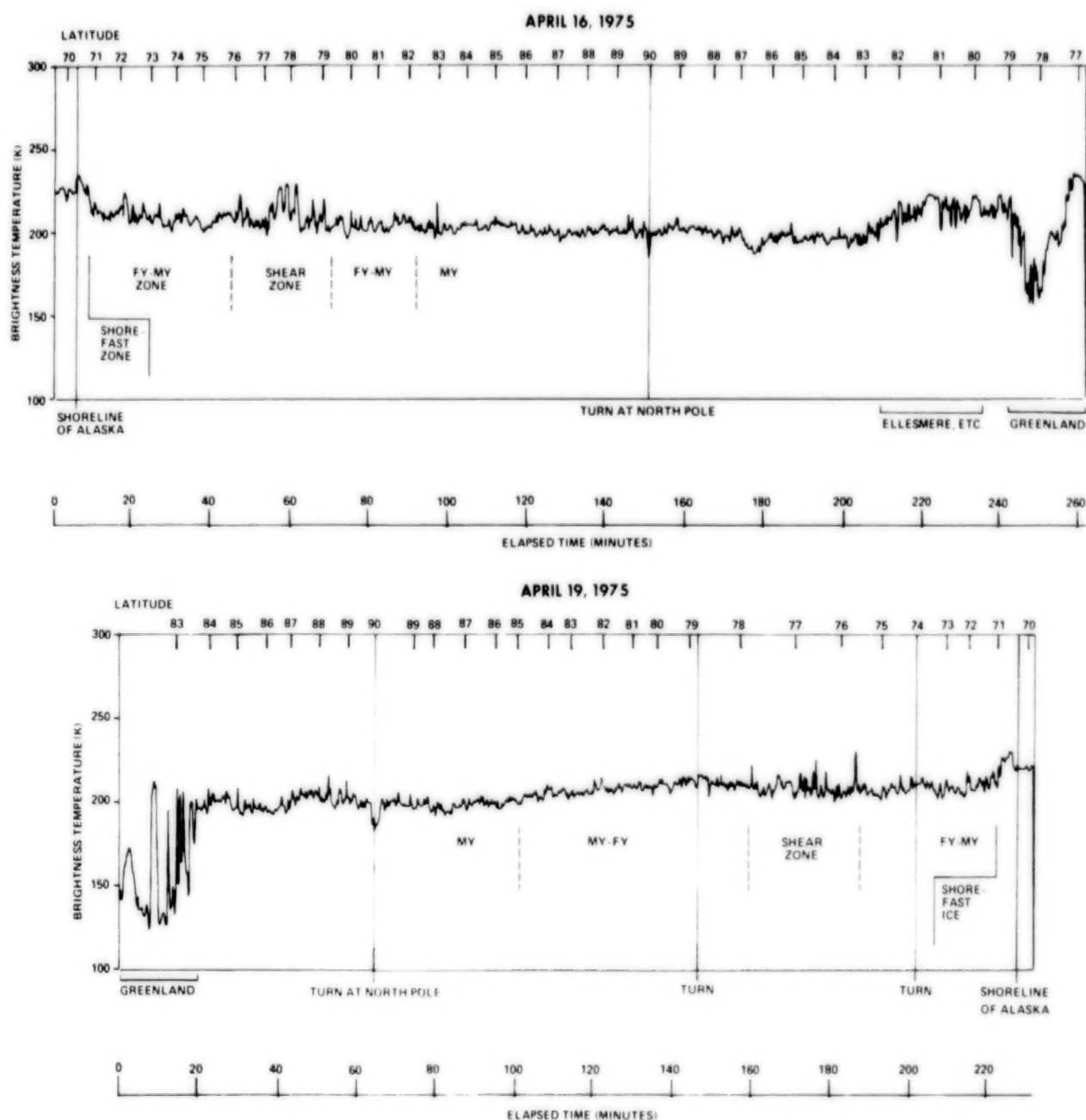


Figure 3-5. Aircraft ESMR brightness temperature profiles along the Convair 990 flight paths shown in Figure 3-4. [Modified from Gloersen et al. (1978).]

is interpreted as being a result of the variability of the sea ice signature from regions of first-year ice and mixed first-year/multiyear ice to a region of highly consolidated multiyear ice.

The transects marked on Figure 3-4 also passed through the main AIDJEX manned drifting station array, allowing comparisons of the data along the aircraft flight paths with surface data and with more detailed aircraft data of the AIDJEX area. The nature of the mixing of multiyear and first-year ice can be seen in a mesoscale airborne microwave image acquired 5 days after the April 19 transect data (Figure 3-6). The image reflects the existence of large multiyear floes (green) separated by areas of first-year ice (brown), with an overall multiyear ice fraction of approximately 0.6. The microwave radiances for first-year and multiyear ice were shown to be consistent with *in-situ* measurements of sea ice physical properties during a pilot AIDJEX program (Gloersen et al., 1973) and during the main AIDJEX (Campbell et al., 1978).

Turning from spring to summer, the most extensive summer surface measurements of sea ice during the 4 primary ESMR years were made as part of AIDJEX in 1975. During August 1975, a series of microwave mapping missions over the AIDJEX manned drifting station array and a series of transects over extensive areas of the Arctic Basin were made from the NASA Convair 990 aircraft. The AIDJEX triangle of drifting stations at the time of these observations was in the southern Beaufort Sea to the north of the Mackenzie Delta (Figure 3-7). The physical conditions of the ice surface at the AIDJEX stations from August 10 to September 4, 1975, are indicated in Figure 3-8 along with 2-meter air temperature readings at each of the camps. The observation periods of the Convair 990 aircraft and the Nimbus 5 ESMR are also noted in the figure. Surface conditions show that during the Convair 990 overflights the melt ponds were ice covered. The conjunction of the biggest seasonal melt increment with a 2°C decrease in air temperatures (Figure 3-8) is consistent with the dominant cause of the melt being back radiation from clouds.

Two of the aircraft ESMR microwave images of the AIDJEX area and three of the Nimbus 5 ESMR images of the Arctic for this period are presented in Figures 3-9 through 3-11. According to the AID-

JEX surface observations, the moisture in the snow surface layer increased steadily during the period of the aircraft flights. The corresponding microwave images (Figures 3-9 and 3-10) show decreasing brightness temperatures of the ice floes, with the average brightness temperature of the floes being approximately 240 K on August 22 and approximately 230 K on August 27, 5 days later. The decrease in microwave brightness temperature is also apparent on the 3-day images of the Nimbus 5 ESMR (Figure 3-11). These results confirm earlier microwave measurements of an alpine snow pack (Edgerton et al., 1971; Stiles and Ulaby, 1980; and Kunzi et al., 1982) and snowpack model computations (Chang and Gloersen, 1975) establishing that the emissivity of snow, after increasing rapidly at the onset of melting, slowly decreases as the free-water content of the snow increases. Because of moisture in the freeboard layer of the ice, the first-year/multiyear ice distinction apparent on the aircraft ESMR images in April (Figure 3-6) is no longer apparent in August (Figures 3-9 and 3-10).

The Nimbus 5 ESMR images of Figures 3-11 reveal several areas of low brightness temperatures ($T_B < 195$ K) in the central Arctic. The two primary surface conditions expected to yield brightness temperatures considerably below 210 K in the central Arctic are significant amounts of open water and extensive areas of ice-free melt ponds. In the absence of surface observations it would be impossible to determine definitively the relative contributions of melt ponds and open water to the low microwave radiances (Crane et al., 1982). Campbell et al. (1984), with the benefit of surface observations, argue that the large areas of low brightness temperature are due primarily to low ice concentrations caused by ice divergence and secondarily to ice-free melt ponds. This interpretation is supported for one of the smaller of these areas (the dark green area on Figure 3-11 adjacent to the northeast, Blue Fox corner of the AIDJEX triangle) by visual and radiometric observations from the aircraft. In particular, the microwave aircraft data for August 22 and August 27 show low radiances in the vicinity of Blue Fox (BF) (Figures 3-9 and 3-10), and visual observations made during an aircraft flight north of the Blue Fox station on August 27 established that the region of relatively low ice concentrations extended to at least 25 kilometers north of the station. These low radiances are also apparent from the Nimbus 5

ORIGINAL ~~BLACK~~
COLOR PHOTOGRAPH

APRIL 24, 1975

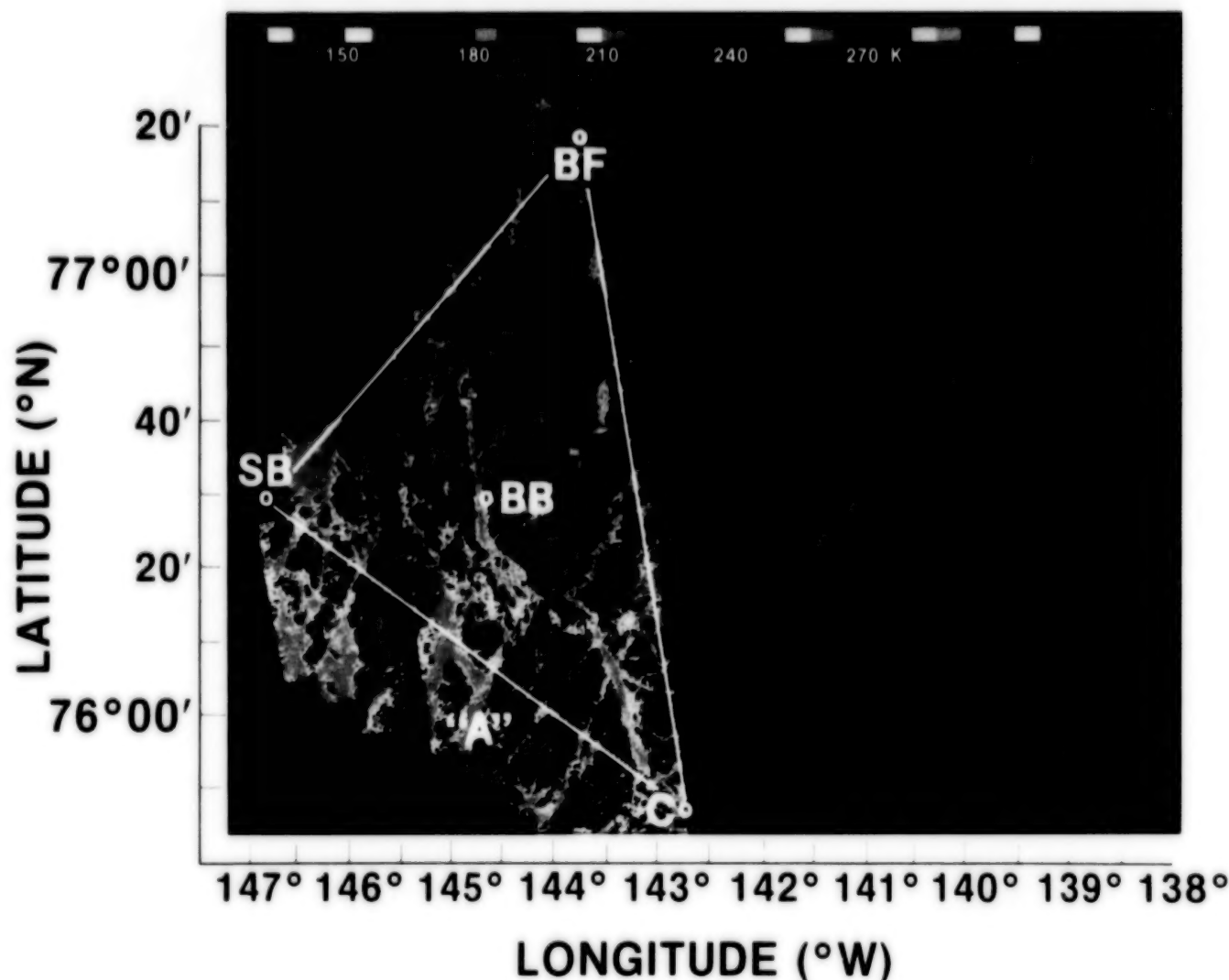


Figure 3-6. Aircraft ESMR image of the AIDJEX area on April 24, 1975. BF, SB, BB, and C denote the AIDJEX camps Blue Fox, Snow Bird, Big Bear, and Caribou, respectively, and "A" identifies an individual floe tracked through Figures 3-6, 3-9, and 3-10. [Modified from Campbell et al. (1978).]

ESMR 3-day-averaged data for August 30 to September 1 (Figure 3-11).

The visual and radiometric observations from aircraft indicate that the average ice concentration from Blue Fox northward for 25 kilometers was approximately 75 percent on August 27. By comparison,

the Nimbus 5 ESMR brightness temperature for this area averaged over August 27 to 29 was 210 K, which converts to an ice concentration of 80 percent, irrespective of multiyear ice fraction, using the nomogram provided at the right of Figure 3-11. The ESMR image for August 30 to September 1 indicates that the ice concentration in the area of Blue Fox

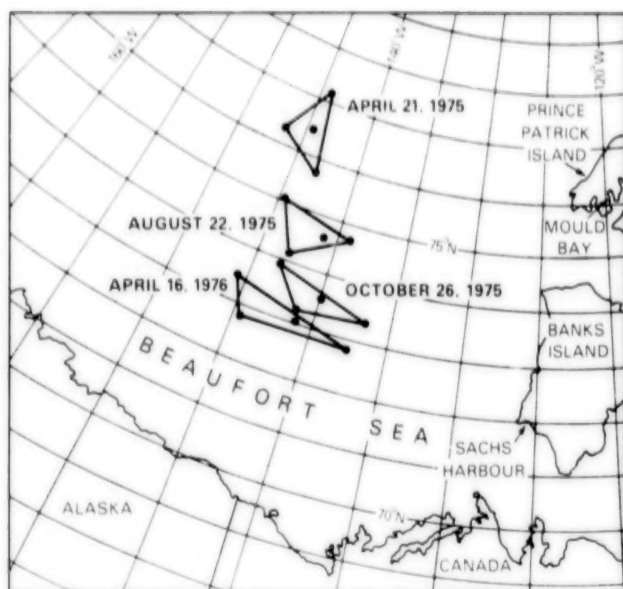


Figure 3-7. Map of the AIDJEX area showing the location of four drifting stations on each of four dates during the period April 21, 1975 to April 16, 1976, including the August 22, 1975 date of one of the NASA aircraft remote sensing flights.

continued to decrease after August 27 (Figure 3-11). The nomogram indicates an ice concentration of 60 percent, consistent with the aircraft observations. A NOAA 4 visible image shows that on August 30 the entire ice pack from the AIDJEX triangle to the pole was covered by a thick stratus cloud layer. Since, according to coincident weather charts, the entire Beaufort Sea had a common surface meteorological environment, with negligible or very low surface wind speeds, it is presumed that all the ice ponds in this larger area were ice covered, as in the AIDJEX area. Therefore, the large low-radiance zones existing as close as 250 kilometers north of the AIDJEX triangle are presumed to have resulted from reduced ice concentrations. These comparisons support the interpretation that the low microwave radiances measured by the ESMR in the AIDJEX area and beyond in August 1975 were due to leads and polynyas.

Further arguments for ascribing to meltponding only a minor role in causing the low microwave radiances observed in the late summer are provided by Campbell et al. (1984). Briefly, if meltponding were the primary factor, this would require unreasonably large areal coverage by ponds in some areas (40 to 60 percent, compared to the 30 percent

or less that have been observed), very restricted locations of ponding on the large-scale, and unusual movements in weather systems. Indeed, an examination of the low-radiance areas at the time of maximum ponding in late summer shows that they occur in patterns associated with ice drift, consistent with the expected patterns of leads and polynyas but not with the expected patterns of melt ponds.

For an indication of the interannual variability in the location of low-brightness areas, Figure 3-12 shows envelopes of the low-radiance areas ($T_B < 197.5$ K) that occurred within the Arctic Basin during August and September in each of the four summers of ESMR, 1973 through 1976. The short-term variation of the low-radiance areas within the 1974 envelope is shown in Figure 3-13. In 1975 the distribution of the low-radiance envelope is quite dissimilar to the distributions in the other 3 years, appearing as a ring at approximately 83°N , whereas the envelopes in the other years lie largely along the Transpolar Drift Stream (Figures 3-12 compared to Figures 2-3 and 4-42). Analysis by Yakovlev (1977) of long-term Soviet drift station and aircraft observations suggests that the circulations in 1973, 1974, and 1976 are similar to the average long-term circulation and furthermore supports the conclusion that the low-radiance zones are primarily due to reduced ice concentrations. Yakovlev shows a long-term "zone of occasional polynyas" that covers a triangularly shaped area with corners at (85°N , 150°E), (72°N , 180°E), and (72°N , 160°W). This polynya zone lies close to the low-radiance zones for 1973, 1974, and 1976 in the Chukchi and East Siberian Seas and extends, as they do, along the beginning of the long-term Transpolar Drift Stream (cf. Figure 4-42).

Finally, winter ESMR data also support the interpretation of the low-radiance areas in summer as being due primarily to reduced ice concentrations. When salt water freezes, even with salinities as low as 2 parts per thousand, it has the signature of first-year ice for thicknesses greater than 1 centimeter (Meeks et al., 1974). Campbell et al. (1978) and Gloersen et al. (1978) confirm that during AIDJEX refrozen melt ponds had microwave signatures of first-year ice. If a large area of ice has sufficient melt-pond coverage to give a combined summertime ice/melt pond signature as low as those in the observed low-radiance areas, say at least 50 percent ponded,

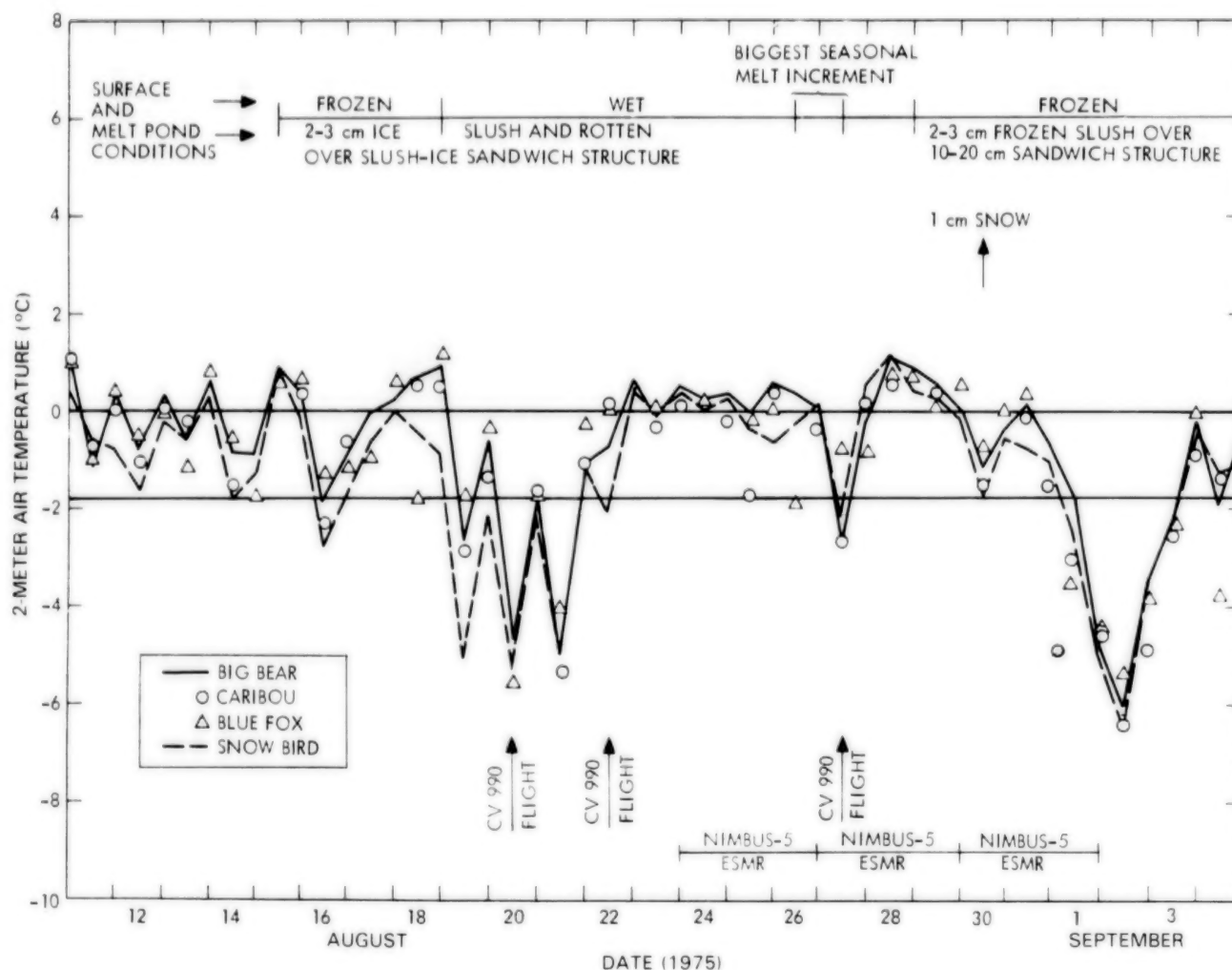


Figure 3-8. Time sequences of 2-meter air temperatures at the four AIDJEX campsites from August 10 through September 4, 1975. Horizontal base lines appear at 0°C and at -1.8°C, the latter being approximately the freezing point of salt water. The physical conditions of the ice at the sites as recorded by Hanson (personal communication) are indicated in the upper portion of the diagram, and the dates of the aircraft flights and satellite passes are indicated in the lower portion of the diagram. [Modified from Campbell et al. (1978).]

then when this area refreezes the ESMR signature should be the signature for ice that is at least 50 percent first-year ice. Figure 3-14 shows ESMR 3-day images for mid-December in 1973, 1974, and 1975. By December, the melt ponds of the previous summer would have completely frozen. The region of the summer low-radiance zone within the Beaufort Gyre in 1975 (Figure 3-12) has a range of brightness temperatures from 200 to 215 K on December 19-21, 1975, corresponding to multiyear ice fractions in the 65 to 100 percent range, assuming a highly compact ice cover (Figure 3-14). Normal ice drift velocities would have advected only a minor part of the ice out of the summer low-radiance envelope in that time. Examination of similar images earlier in December established this time period to be free of

variations in ice concentration in this area, and so interpretation of the low radiances as areas consisting predominantly of multiyear ice is reasonable. Thus, meltponding is excluded as the mechanism for most of the area in question, because melt pond refreezing would have resulted in higher December radiances. A comparison of the 1973 and 1974 low-radiance areas in summer with the December radiances leads to the same conclusions.

3.5 MONTHLY BRIGHTNESS TEMPERATURE IMAGES

In this section monthly averaged Nimbus 5 ESMR brightness temperature images of the north polar

ORIGINAL PAGE
COLOR PHOTOGRAPH

AUGUST 22, 1975

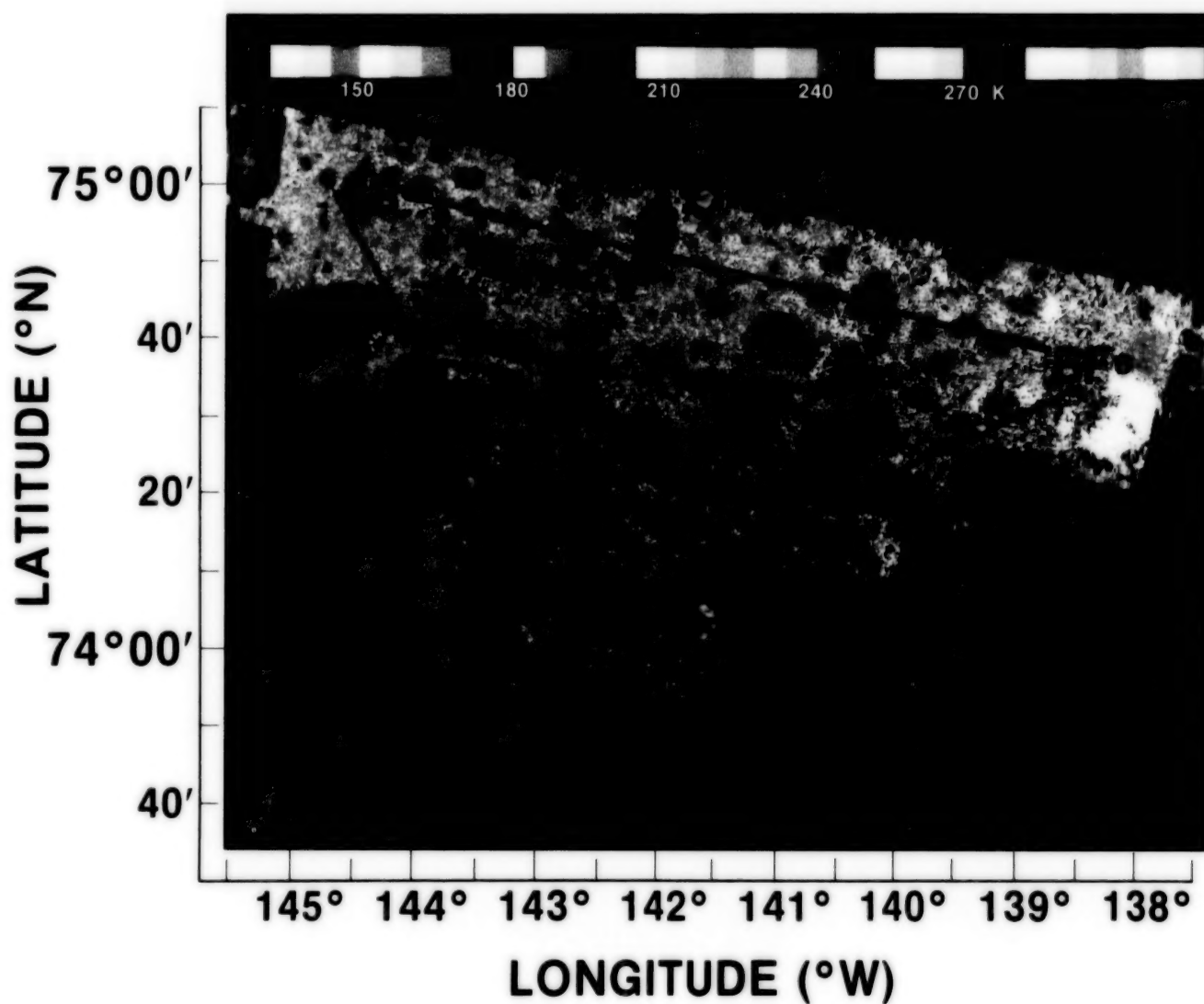


Figure 3-9. Aircraft ESMR image of the AIDJEX area on August 22, 1975. Symbols are explained in the caption for Figure 3-6. [Modified from Campbell et al. (1978).]

region and surroundings are presented for each month with usable ESMR data. This includes all months of the 4-year period 1973 through 1976 except March, April, May, and August of 1973, June, July, and August of 1975, and November and December of 1976. Although the focus of this volume is sea ice, the brightness temperature maps provide

useful information about microwave emission characteristics of other surfaces as well, such as oceans, lakes, and land areas, and hence the data are mapped over the entire region and not just the polar oceans.

The monthly averaged images were generated somewhat differently than the corresponding ones

ORIGINAL PAGE
COLOR PHOTOGRAPH

AUGUST 27, 1975

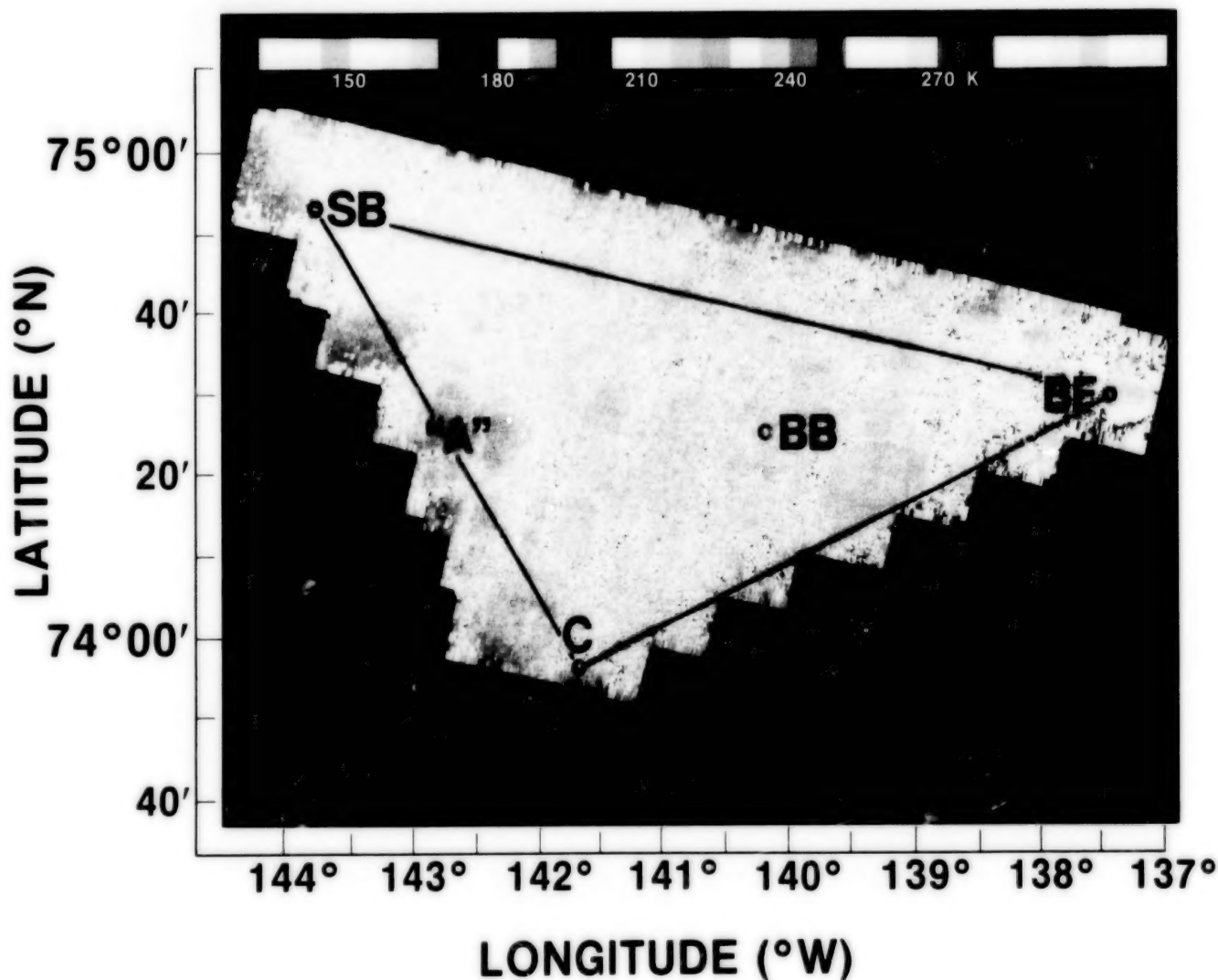
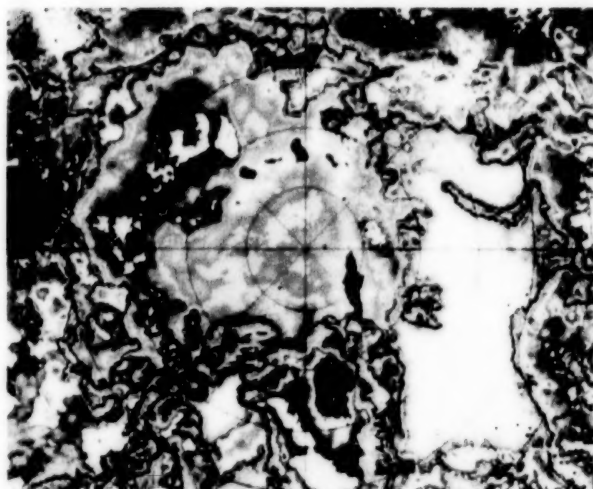


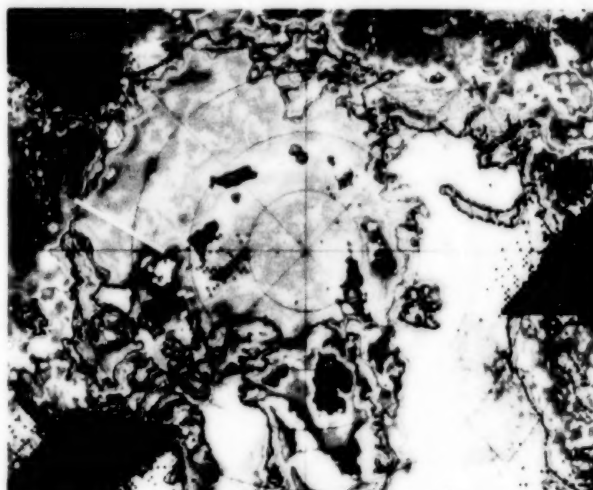
Figure 3-10. Aircraft ESMR image of the AIDJEX area on August 27, 1975. Symbols are explained in the caption for Figure 3-6. [Modified from Campbell et al. (1978).]

for the Antarctic in *Antarctic Sea Ice, 1973-1976*. In particular, because data gaps were more frequent and more extensive in the Arctic, especially near Alaska, temporal and spatial interpolation were used more intensively, as discussed in Appendix A. As a consequence, more areas on the maps have data

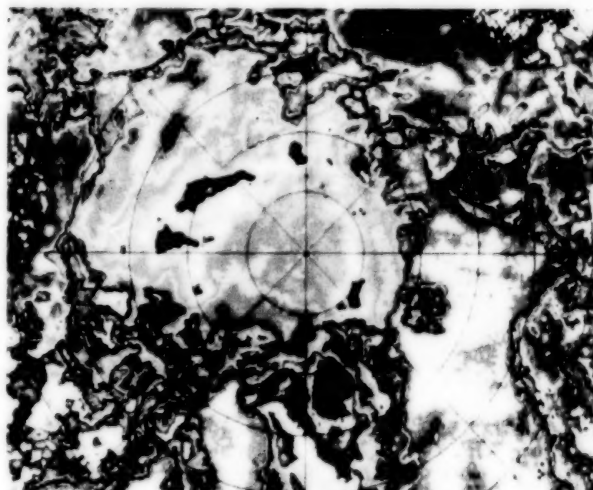
elements that do not represent true monthly averaged data than was the case in the Antarctic volume; however, almost all the problem areas are located either over the ice-free ocean or over land, and the impact of this problem on the analysis of the sea ice conditions is minimal. As in *Antarctic Sea Ice*,



AUGUST 24-26, 1975



AUGUST 27-29, 1975



AUGUST 30-SEPTEMBER 1, 1975

ORIGINAL PAGE
COLOR PHOTOGRAPH

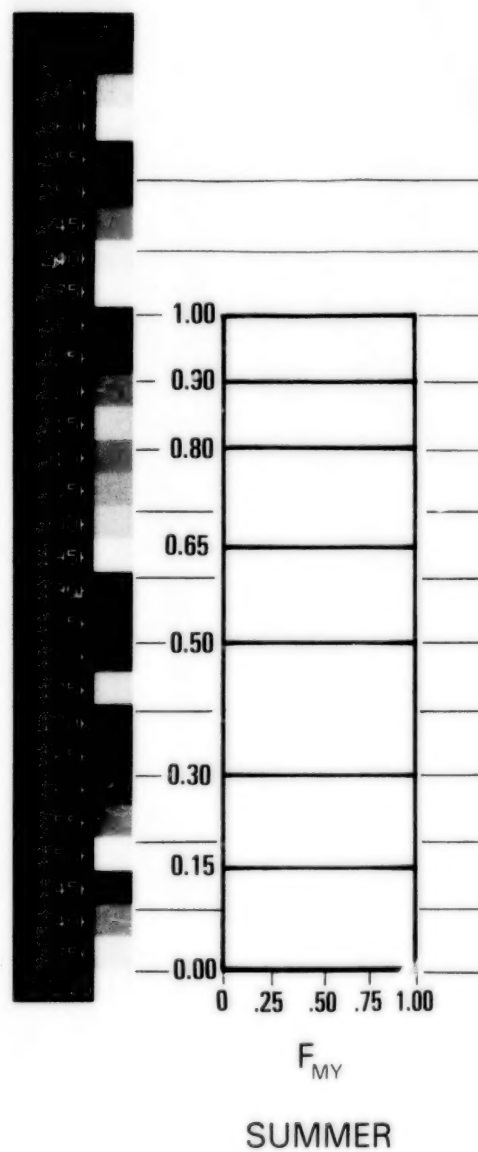


Figure 3-11. Satellite ESMR 3-day-average images for August 24-26, August 27-29, and August 30-September 1, 1975. The position of the AIDJEX triangle is shown in white on the images for August 24-26 and August 30-September 1. [Modified from Gloersen et al. (1978), where the white line on the image for August 27-29 was used to identify a transect for which brightness temperature profiles were created.]

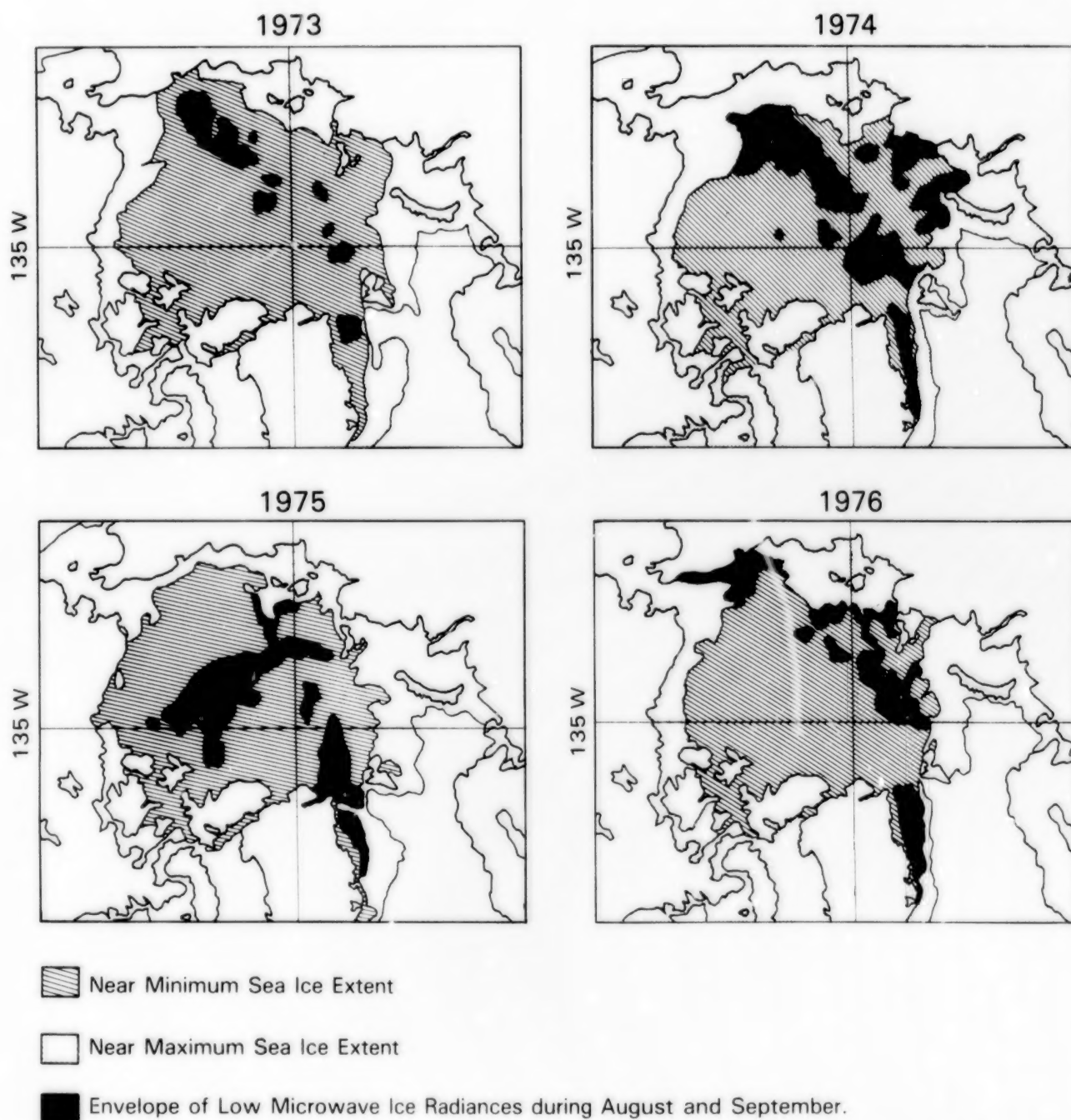


Figure 3-12. Near maximum and near minimum sea ice extents for the Arctic and envelopes of August-September areas of low microwave radiances (less than 197.5 K) derived from satellite ESMR images from each year 1973 through 1976. [Modified from Campbell et al. (1984).]

1973-1976, the data for each month have been normalized to account for biases in instrument calibration, by uniformly adjusting the data over the entire grid to force the average ocean temperature in selected open-ocean regions to equal the 4-year average. In the Northern Hemisphere case this average is 138.3 K, whereas in the Southern

Hemisphere case it was 135.0 K. The 3.3 K difference is attributed to atmospheric and surface effects. The magnitude of the adjustment for each month is tabulated in Appendix A, where a detailed account is given of the data compilation and manipulation. In addition to the interpolations and normalization done for each month throughout the 4-year period,

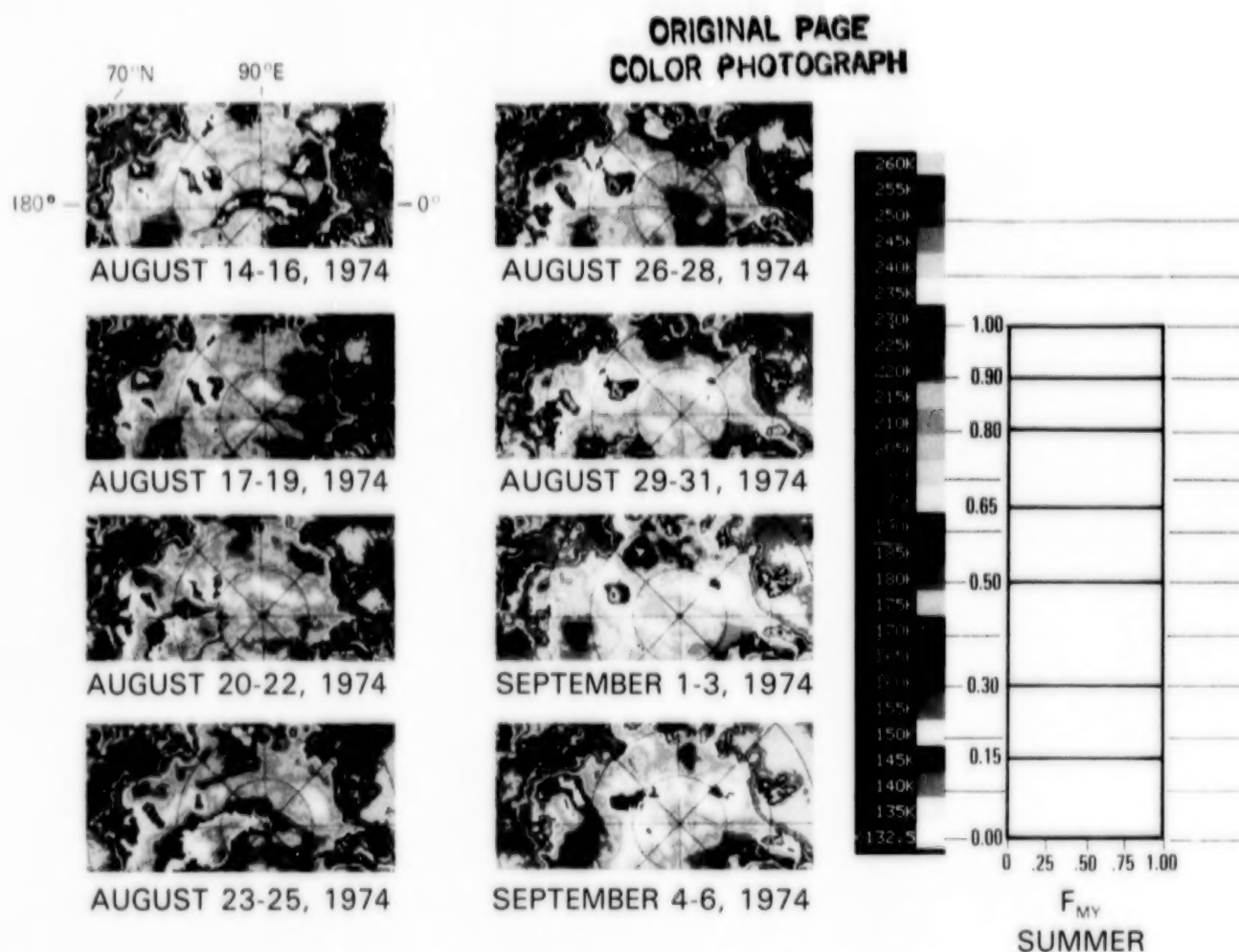


Figure 3-13. Sequential satellite ESMR 3-day-average images of the central Arctic from August 14-16 through September 4-6, 1974. [Modified from Campbell et al. (1984).]

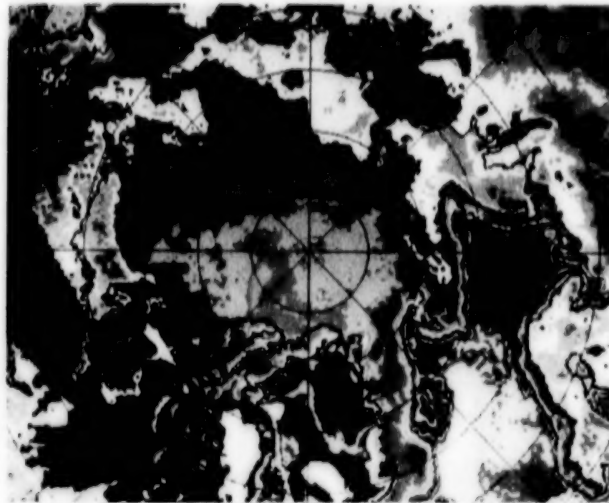
a calibration adjustment is made beginning in May 1976, to account for the apparent degradation of the sensor.

The monthly averaged brightness temperature images are presented in Figures 3-15 through 3-26. The images are arranged by month, so that for each month data from the 4 years are shown together on two adjacent pages, facilitating examination of interannual differences. As in *Antarctic Sea Ice, 1973-1976*, each color-coded image has been enhanced to an 879- by 879-element matrix from the original 293- by 293-element grids. Since the annual cycle of sea ice conditions and their interannual variations are discussed in detail in Chapter 4, with ice-concentration images that do not include land data, this sea ice cycle is not described here from the brightness temperature images. Instead, the discussion in this section centers more broadly on issues

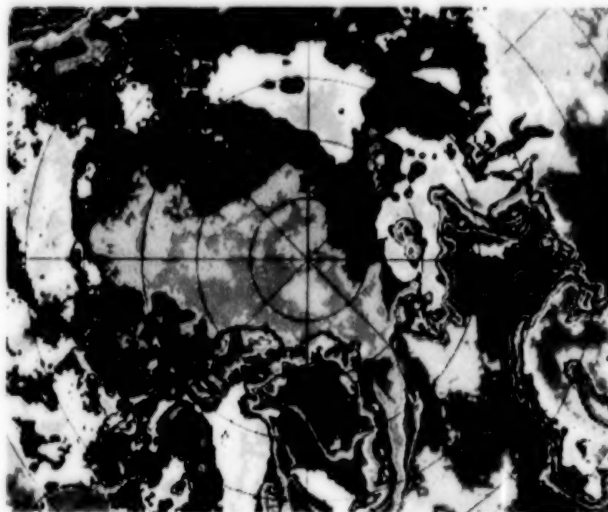
of consistency and the general interpretation of land, ocean, and ice features.

Overall, the monthly averaged brightness temperature images show considerable consistency in the signatures of the various surfaces over the whole mapped region from 1 year to the next, especially over land. Consistency of the signature for a particular surface over several years is a good test of the time stability of the ESMR data. An excellent area to illustrate this is Greenland, which is largely covered by a very thick, slowly varying ice sheet. A comparison of the monthly images, especially for the November to April period when the ice sheet surface is predominantly dry, shows highly consistent brightness temperatures for all 4 years despite spatial and temporal variations in physical temperatures. The consistency of the ice sheet brightness temperatures provides a favorable check on the normalization and

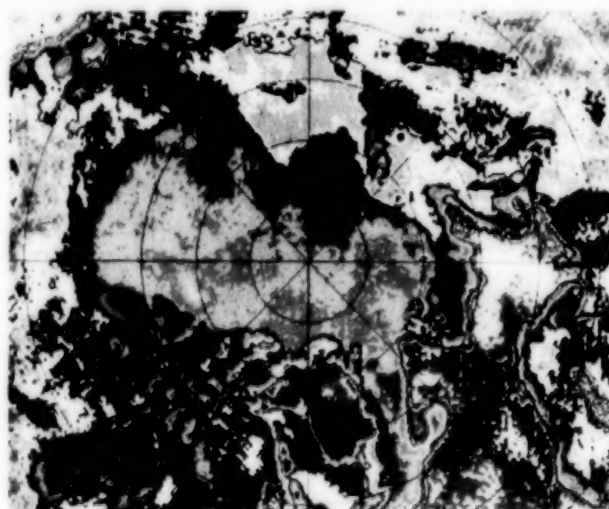
ORIGINAL PAGE
COLOR PHOTOGRAPH



DECEMBER 20-22, 1973



DECEMBER 21-23, 1974



DECEMBER 19-21, 1975

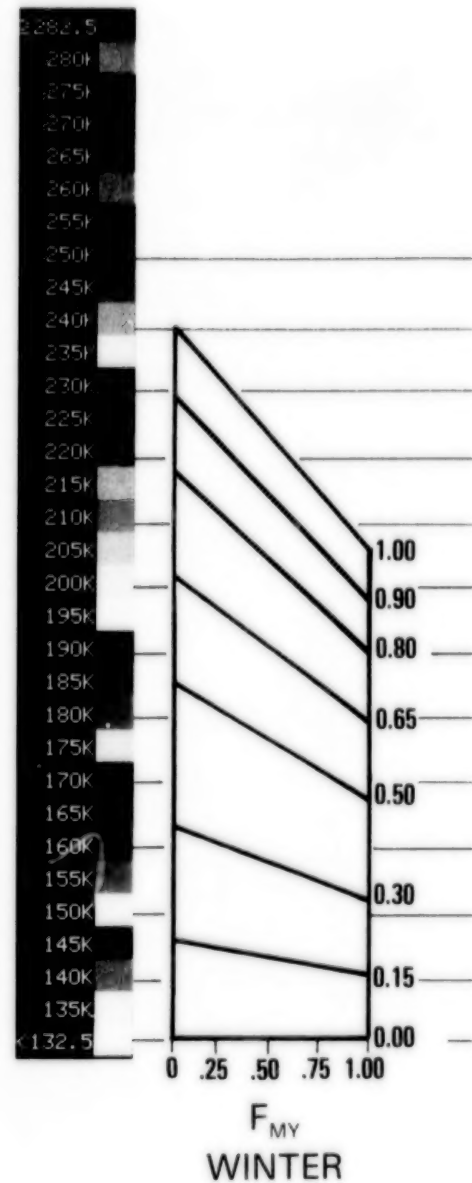


Figure 3-14. Satellite ESMR 3-day-average images of the Arctic for December 20-22, 1973, December 21-23, 1974, and December 19-21, 1975. [Modified from Campbell et al. (1534).]

calibration adjustments made on the data. Furthermore, the resolution of well-defined features like the Great Lakes along the United States/Canada border and Lake Baikal in the Soviet Union (at 53°N, 109°E) is a good indication of the accuracy of the mapping of the orbital data.

Among the large-scale features evident on the monthly averaged maps is the encroachment of relatively high brightness temperatures into higher latitudes during the onset of spring. These high brightness temperatures are first apparent over continental areas and eventually move into the sea ice region. The major causes of these high brightness temperatures are believed to be snow melt and high surface temperatures, in line with the discussion in Section 3.3.

The microwave properties of firn on continental ice sheets and ice shelves differ substantially from the microwave properties of sea ice. Qualitatively, the microwave variations over the ice sheets are mainly attributed to spatial variations in grain size, as the spatial variations in emissivity due to variations in grain size are more significant to the brightness temperatures than the typical spatial variations of surface physical temperature (Zwally and Gloersen, 1977). Because the grain size in the dry firn regions, such as central and northern Greenland, is determined in part by the accumulation rate (larger grains for lower accumulation rates), the observed spatial variations in brightness temperature are related to variations in the accumulation rate over the ice sheet (Zwally, 1977). For example, in Greenland the lowest brightness temperatures (on a large scale) are in the low-accumulation region in the northeast, with increasing brightness temperatures southward toward the higher accumulation central dome (Figures 3-15 through 3-26). In the percolation zone of southern Greenland, very low brightness temperatures are observed during winter due to radiative scattering by large grains formed during periods of summer melt. In early summer, the brightness temperature rises markedly over much of southern Greenland because of surface melting (Figures 3-19 through 3-21).

The onset of spring in snow-covered regions can be determined quite effectively from Figures 3-15 through 3-26 by examining the temporal variability of the brightness temperatures, especially the purple

areas ($T_B > 260$ K) over the continents beginning in April. These areas grow dramatically in May and June of each year, reflecting both increases in emissivity due to melt and higher surface temperatures. In May, increases in brightness temperatures over sea ice are also evident, and by June and July the winter signature of multiyear ice has essentially disappeared, as the effects of snow cover and melt remove the distinction between the microwave signatures of first-year ice and multiyear ice (Section 3.3). Brightness temperatures over sea ice have started to decrease in July, although the land regions still show very high brightness temperatures. These reductions over sea ice are caused by meltponding, reduced ice concentrations, greater granularity in the snow cover, and other changes in surface characteristics (Sections 3.3 and 3.4).

Evidence of multiyear ice signatures, with brightness temperatures of approximately 200 to 210 K, exists in the central Arctic during fall, but there are places where it is difficult to discriminate multiyear ice from first-year ice with lower concentrations. The Arctic ice cover becomes more compact in November, when regions of consolidated first-year ice can be easily identified. There is substantial interannual variability in the position and shape of the ice edge, which is readily identified on these images by the blues and greens marking the sharp gradient between brightness temperatures of approximately 150 K and brightness temperatures of approximately 190 K. In spite of the variability in the edge location, however, the overall areal extent of sea ice in winter is approximately the same for each of the 4 years. Characteristics of the sea ice distributions are discussed in detail in Chapter 4, where ice concentration maps based in large part on the brightness temperature maps of Figures 3-15 through 3-26 are presented.

To indicate the average seasonal cycle over the length of the data record, Figures 3-27 through 3-32 show several-year monthly averages over 4, 3, or 2 years, depending on data availability. Even though the averaging is only over a few years, these maps should better represent long-term averages than the individual monthly maps of Figures 3-15 through 3-26. The several-year-averaged maps show markedly smoother patterns for the ice, especially the multiyear ice in the central Arctic, than do the individual monthly maps. Also included are maps of the yearly averaged conditions in each year (Figure 3-33).

ORIGINAL PAGE
COLOR PHOTOGRAPH



≥ 282.5 K
280 K
275 K
270 K
265 K
260 K
255 K
250 K
245 K
240 K
235 K
230 K
225 K
220 K
215 K
210 K
205 K
200 K
195 K
190 K
185 K
180 K
175 K
170 K
165 K
160 K
155 K
150 K
145 K
140 K
135 K
< 132.5 K

Figure 3-15a. Mean monthly
brightness temperatures for
January 1973 and 1974.

ORIGINAL DATA
COLOR PHOTOGRAPH



≥ 282.5 K

280 K

275 K

270 K

265 K

260 K

255 K

250 K

245 K

240 K

235 K

230 K

225 K

220 K

215 K

210 K

205 K

200 K

195 K

190 K

185 K

180 K

175 K

170 K

165 K

160 K

155 K

150 K

145 K

140 K

135 K

< 132.5 K

Figure 3-15b. Mean monthly
brightness temperatures for
January 1975 and 1976.

ORIGINAL PAGE
COLOR PHOTOGRAPH

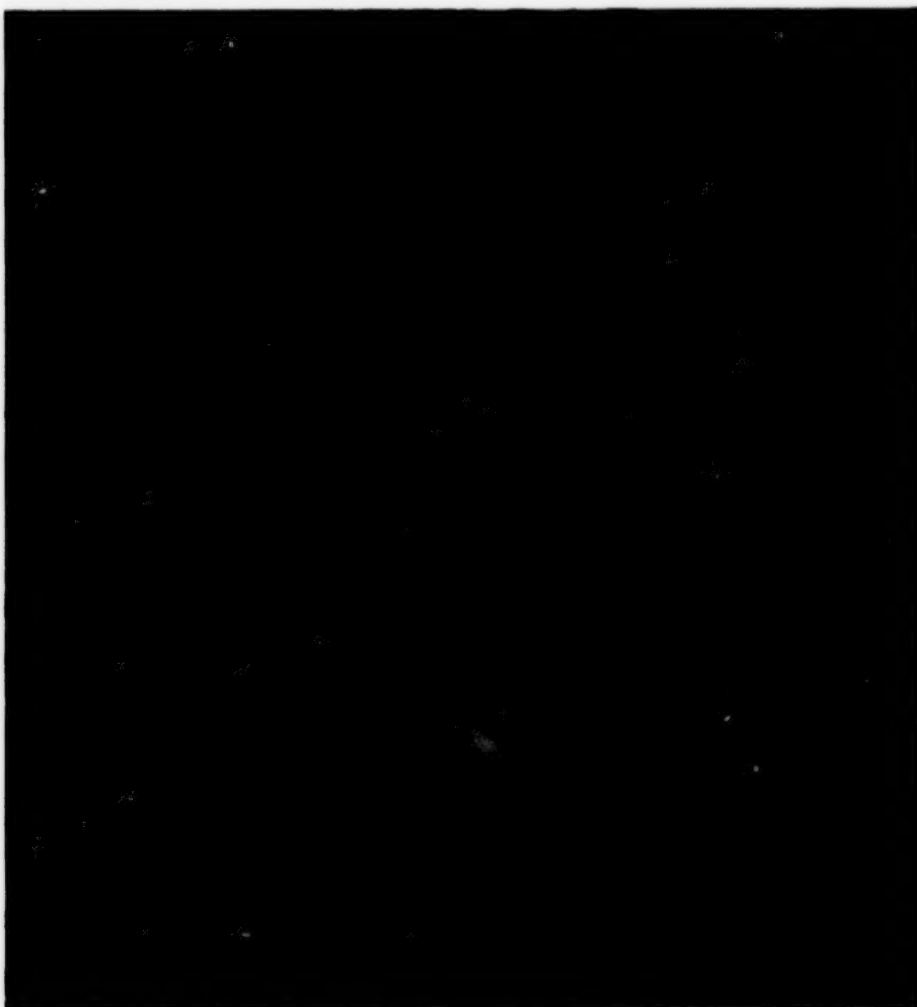


Figure 3-16a. Mean monthly
brightness temperatures for
February 1973 and 1974.

ORIGINAL PAGE
COLOR PHOTOGRAPH

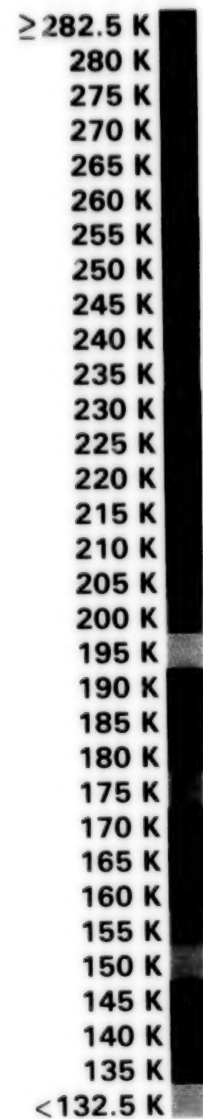
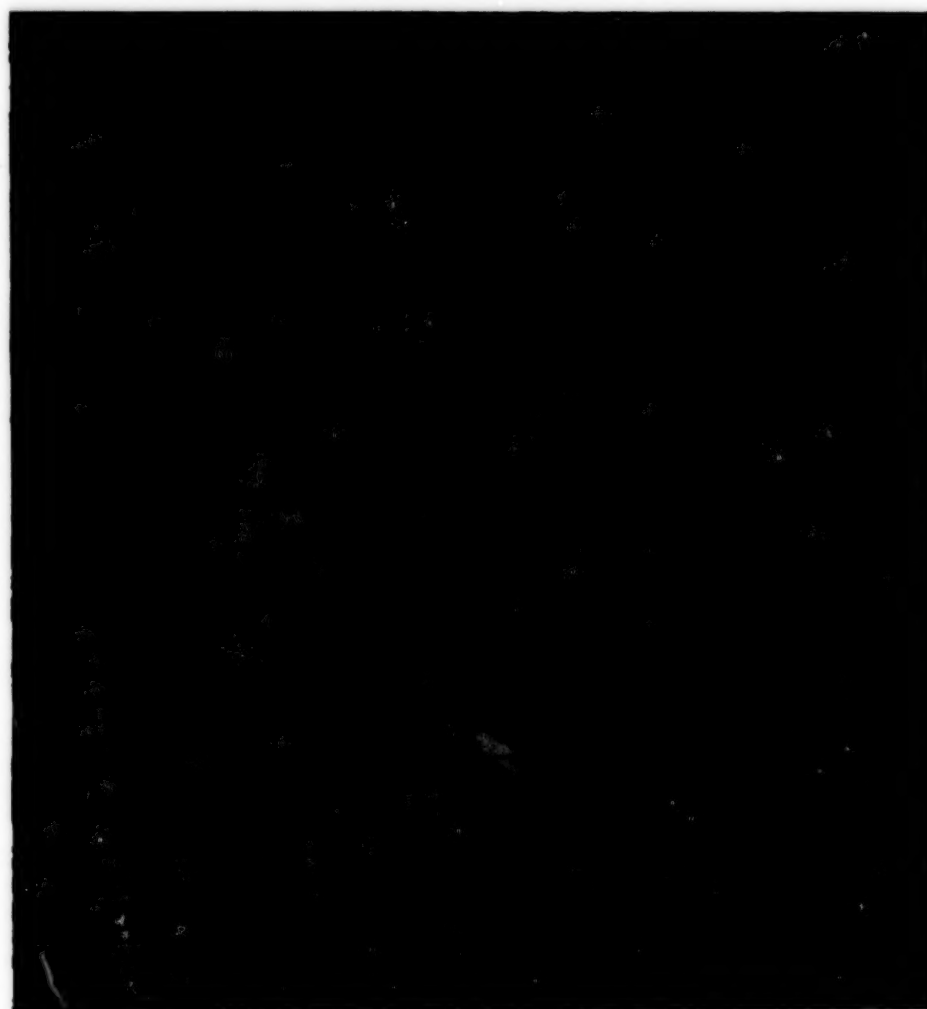
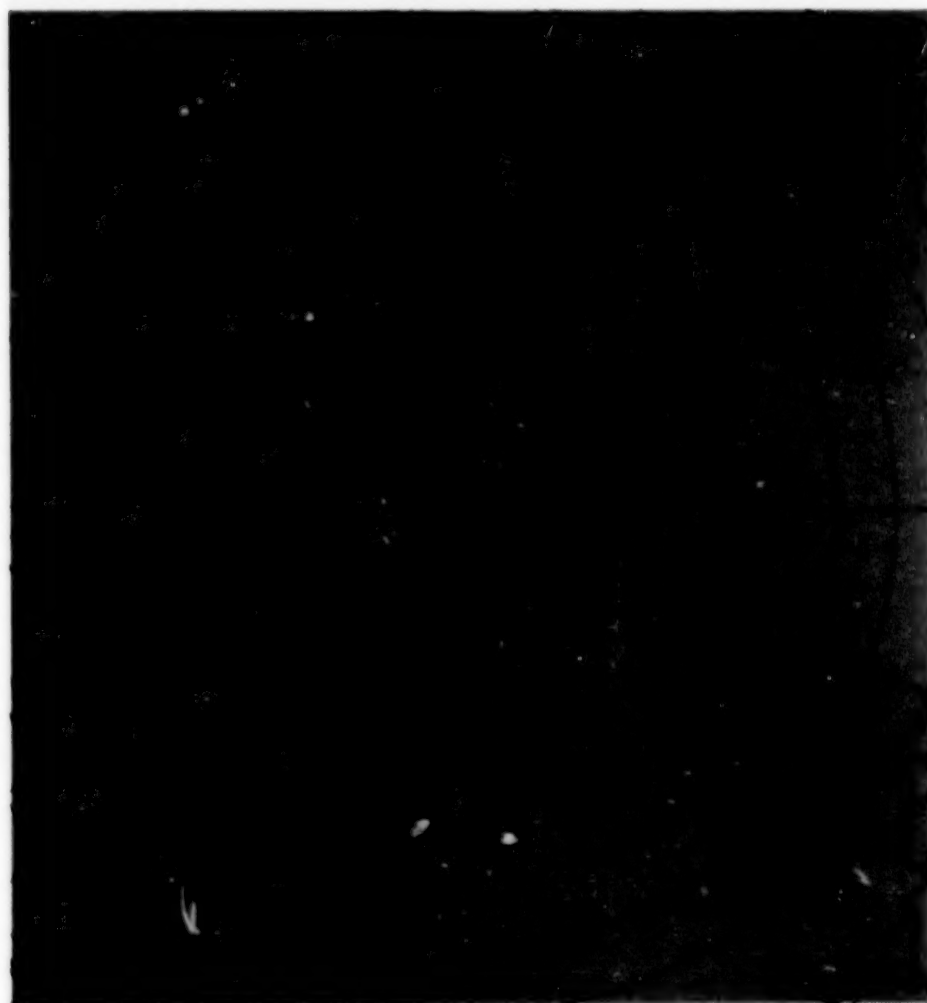


Figure 3-16b. Mean monthly
brightness temperatures for
February 1975 and 1976.

**ORIGINAL PAGE
COLOR PHOTOGRAPH**



≥ 282.5 K
280 K
275 K
270 K
265 K
260 K
255 K
250 K
245 K
240 K
235 K
230 K
225 K
220 K
215 K
210 K
205 K
200 K
195 K
190 K
185 K
180 K
175 K
170 K
165 K
160 K
155 K
150 K
145 K
140 K
135 K
 < 132.5 K

Figure 3-17a. Mean monthly
brightness temperatures for
March 1973 and 1974.

ORIGINAL PAGE
COLOR PHOTOGRAPH

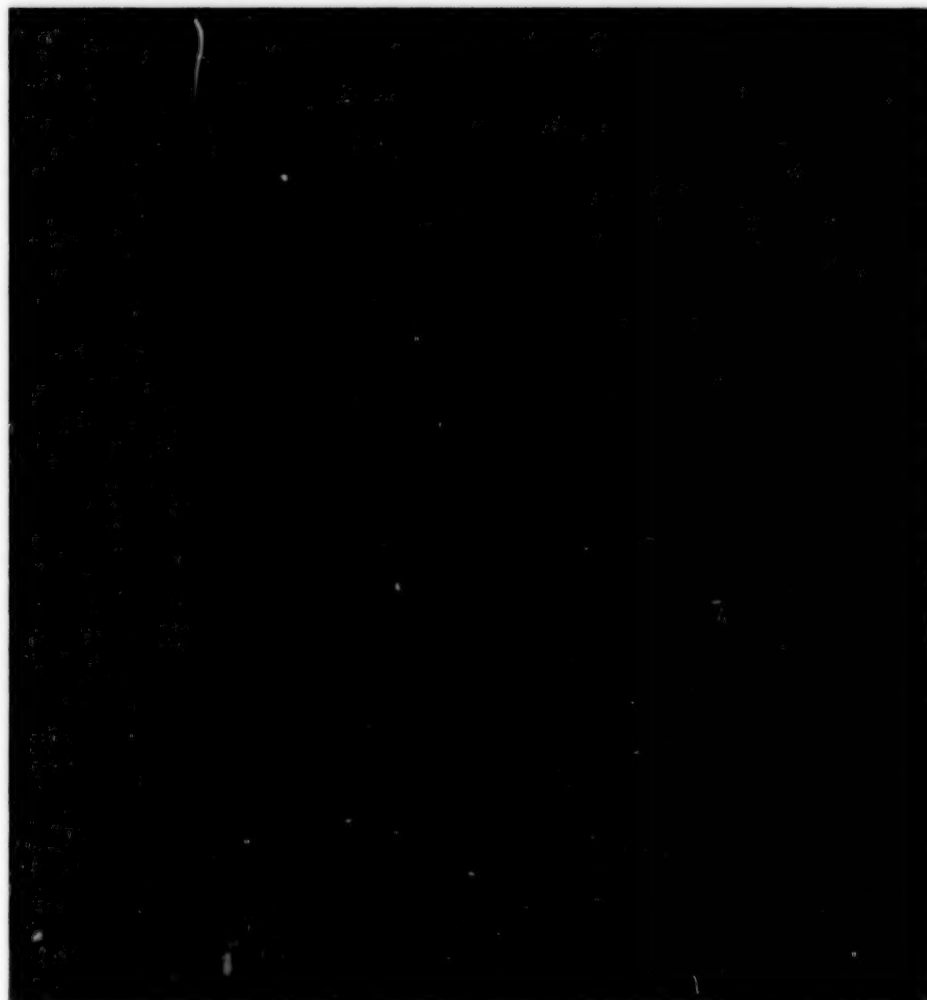
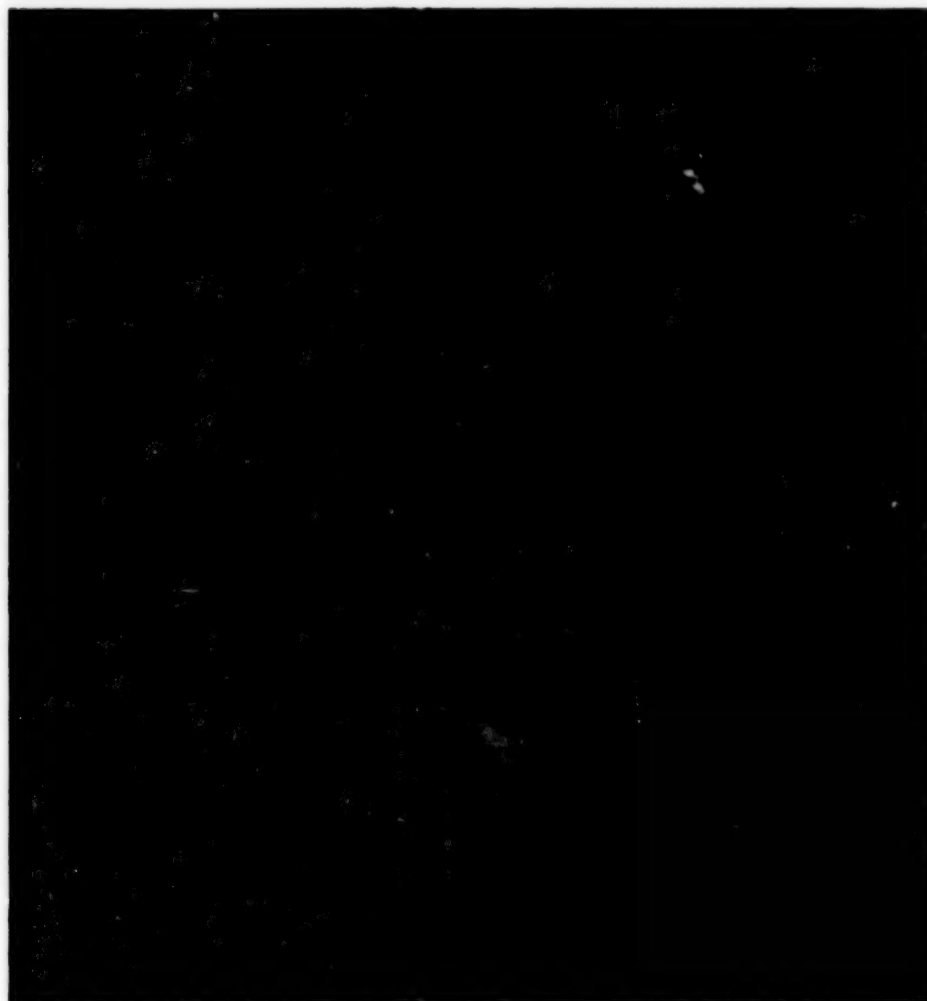
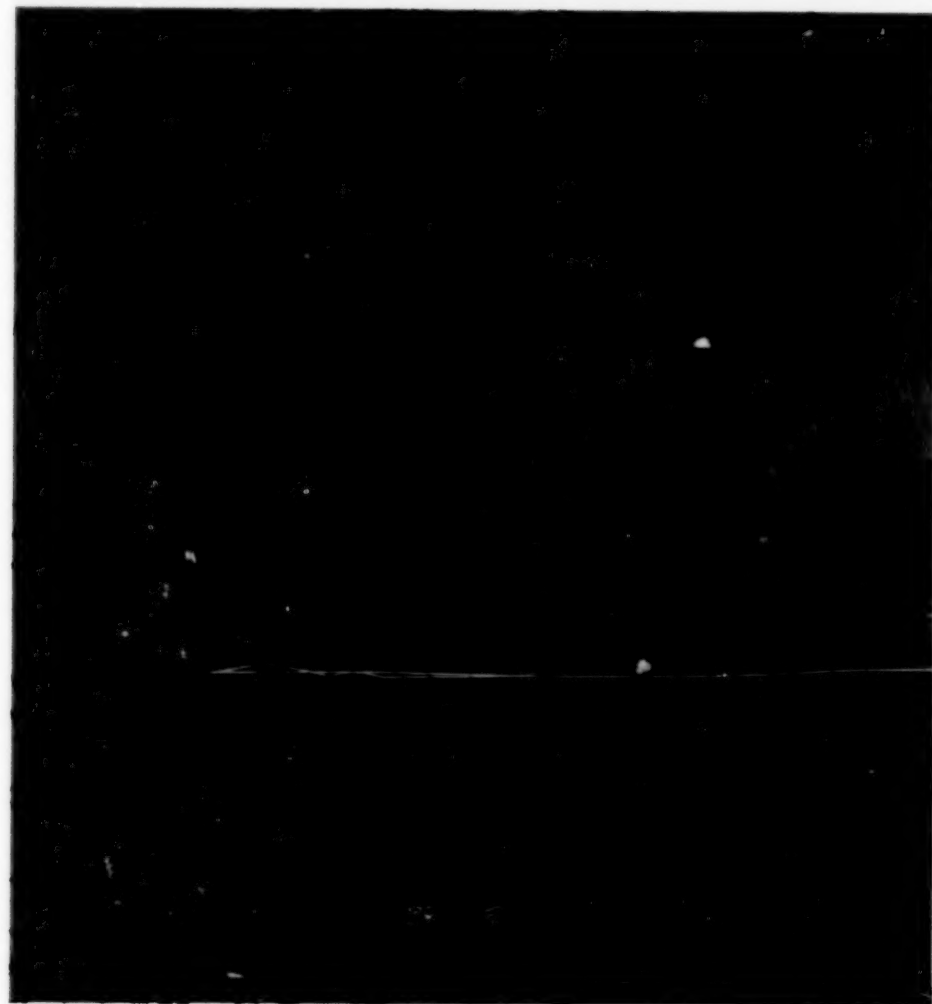


Figure 3-17b. Mean monthly
brightness temperatures for
March 1975 and 1976.

ORIGINAL PAGE
COLOR PHOTOGRAPH



≥ 282.5 K

280 K

275 K

270 K

265 K

260 K

255 K

250 K

245 K

240 K

235 K

230 K

225 K

220 K

215 K

210 K

205 K

200 K

195 K

190 K

185 K

180 K

175 K

170 K

165 K

160 K

155 K

150 K

145 K

140 K

135 K

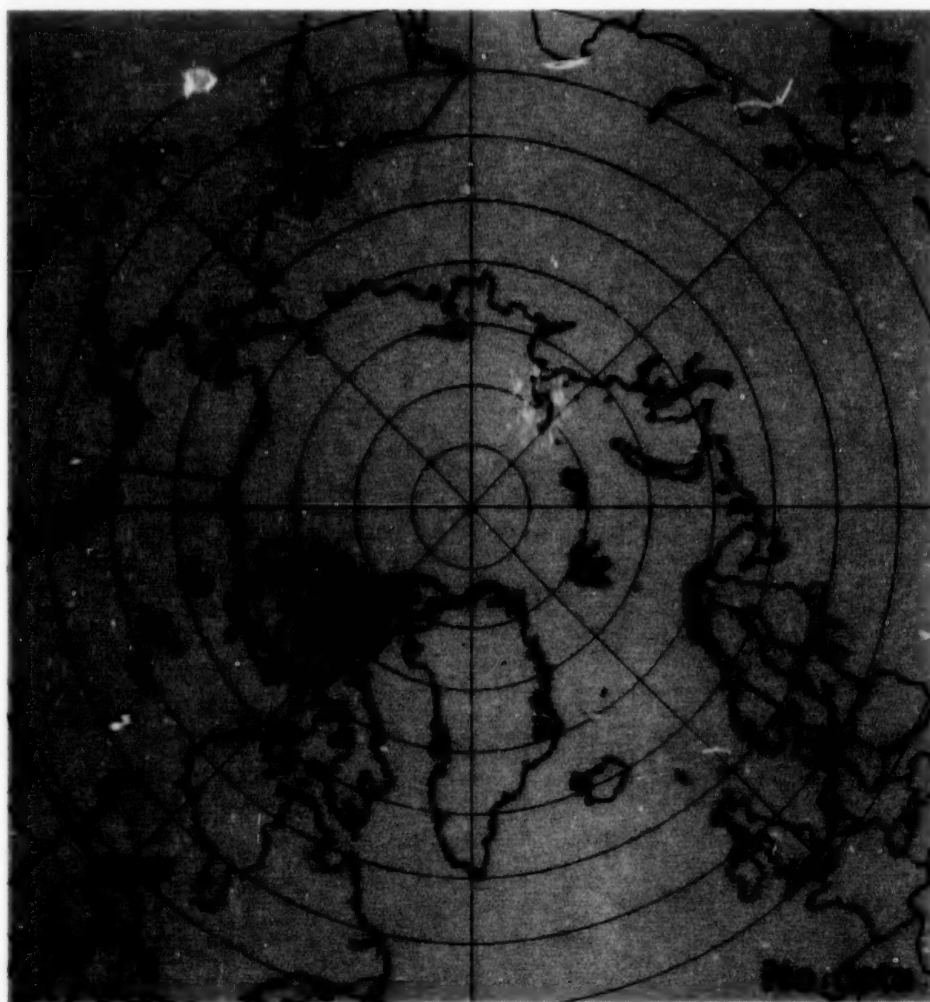
< 132.5 K

Figure 3-18a. Mean monthly
brightness temperatures for April
1973 and 1974.

ORIGINAL PAGE
COLOR PHOTOGRAPH



Figure 3-18b. Mean monthly
brightness temperatures for April
1975 and 1976.



ORIGINAL PAGE
COLOR PHOTOGRAPH

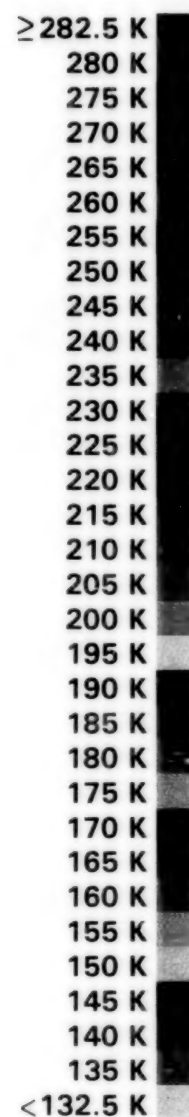


Figure 3-19a. Mean monthly
brightness temperatures for May
1973 and 1974.

ORIGINAL PAGE
COLOR PHOTOGRAPH



Figure 3-19b. Mean monthly
brightness temperatures for May
1975 and 1976.

ORIGINAL PAGE
COLOR PHOTOGRAPH

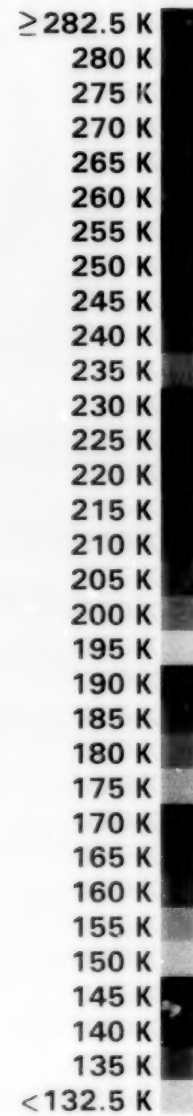
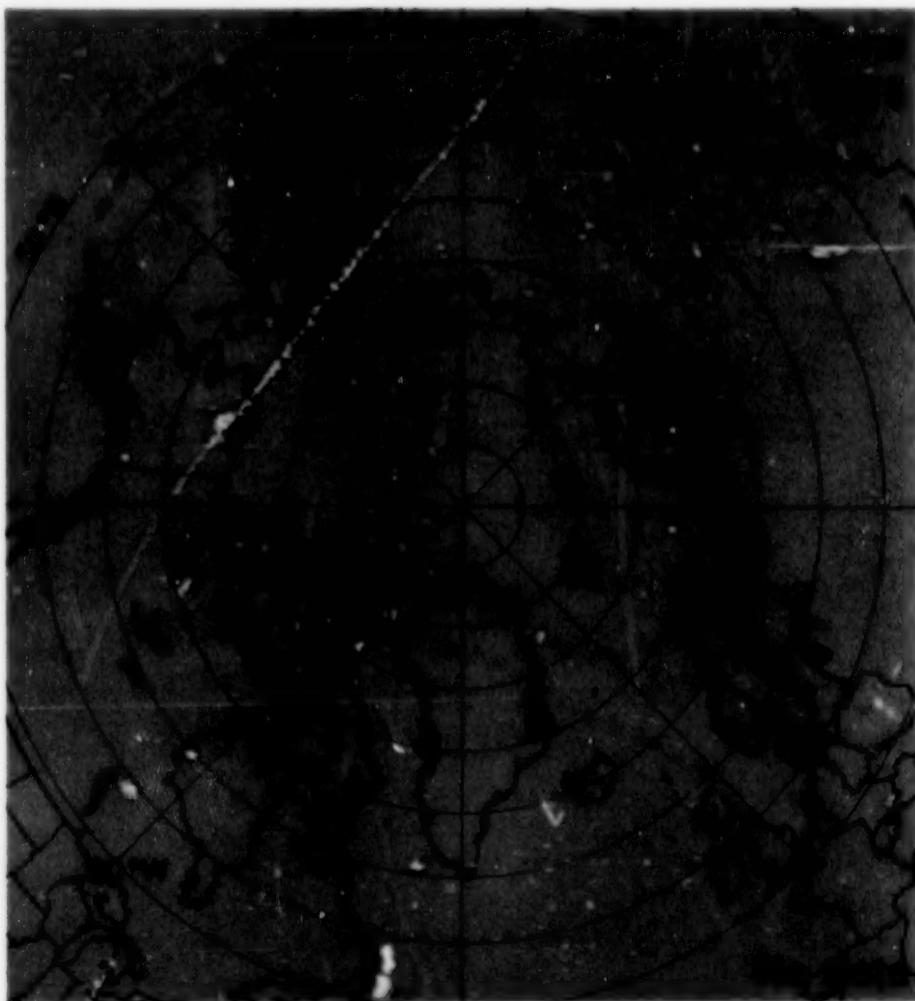


Figure 3-20a. Mean monthly
brightness temperatures for June
1973 and 1974.



ORIGINAL PAGE
COLOR PHOTOGRAPH

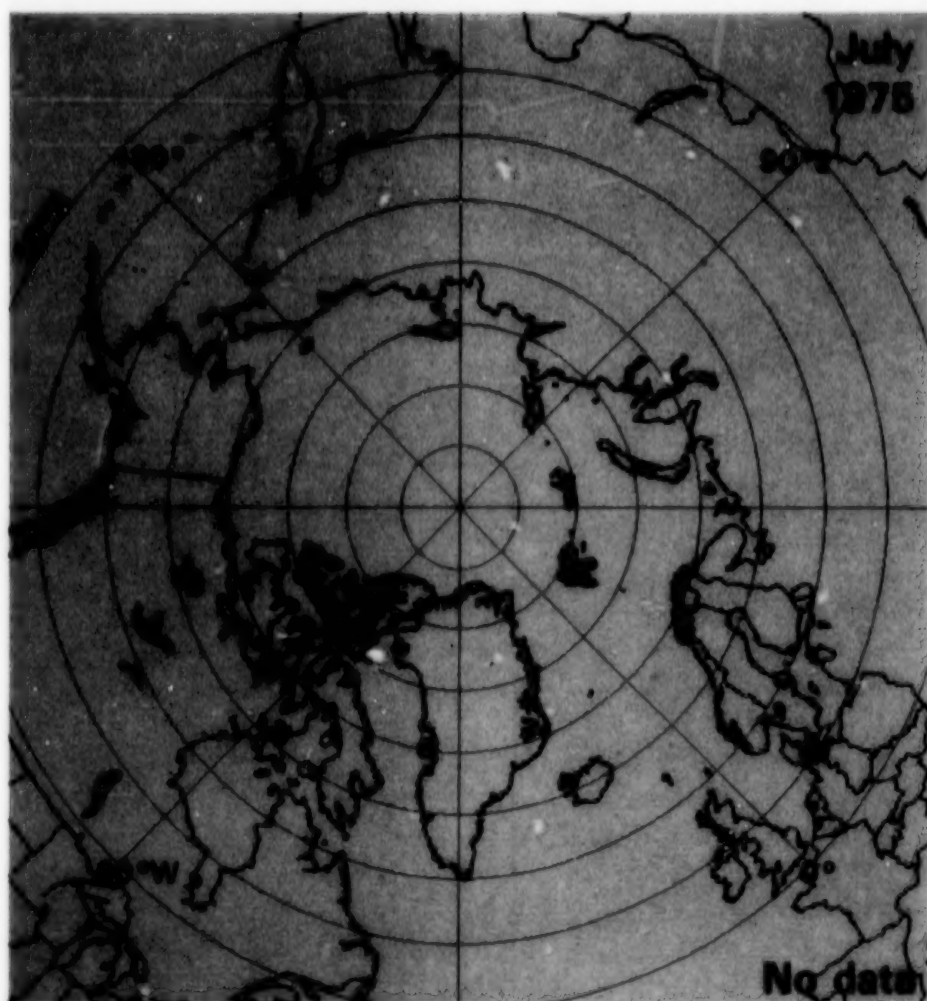


Figure 3-20b. Mean monthly
brightness temperatures for June
1975 and 1976.

ORIGINAL PAGE
COLOR PHOTOGRAPH



Figure 3-21a. Mean monthly
brightness temperatures for July
1973 and 1974.

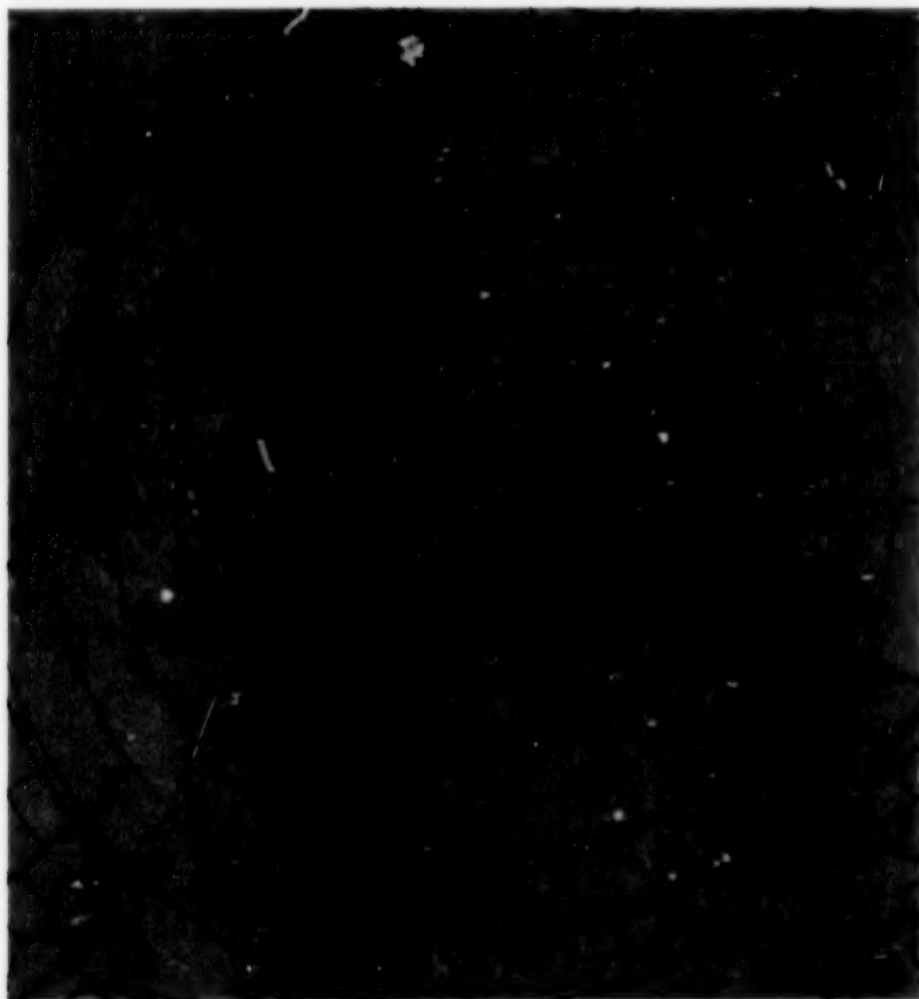


ORIGINAL PAGE
COLOR PHOTOGRAPH

≥ 282.5 K
 280 K
 275 K
 270 K
 265 K
 260 K
 255 K
 250 K
 245 K
 240 K
 235 K
 230 K
 225 K
 220 K
 215 K
 210 K
 205 K
 200 K
 195 K
 190 K
 185 K
 180 K
 175 K
 170 K
 165 K
 160 K
 155 K
 150 K
 145 K
 140 K
 135 K
 < 132.5 K



Figure 3-21b. Mean monthly
brightness temperatures for July
1975 and 1976.



ORIGINAL PAGE
COLOR PHOTOGRAPH

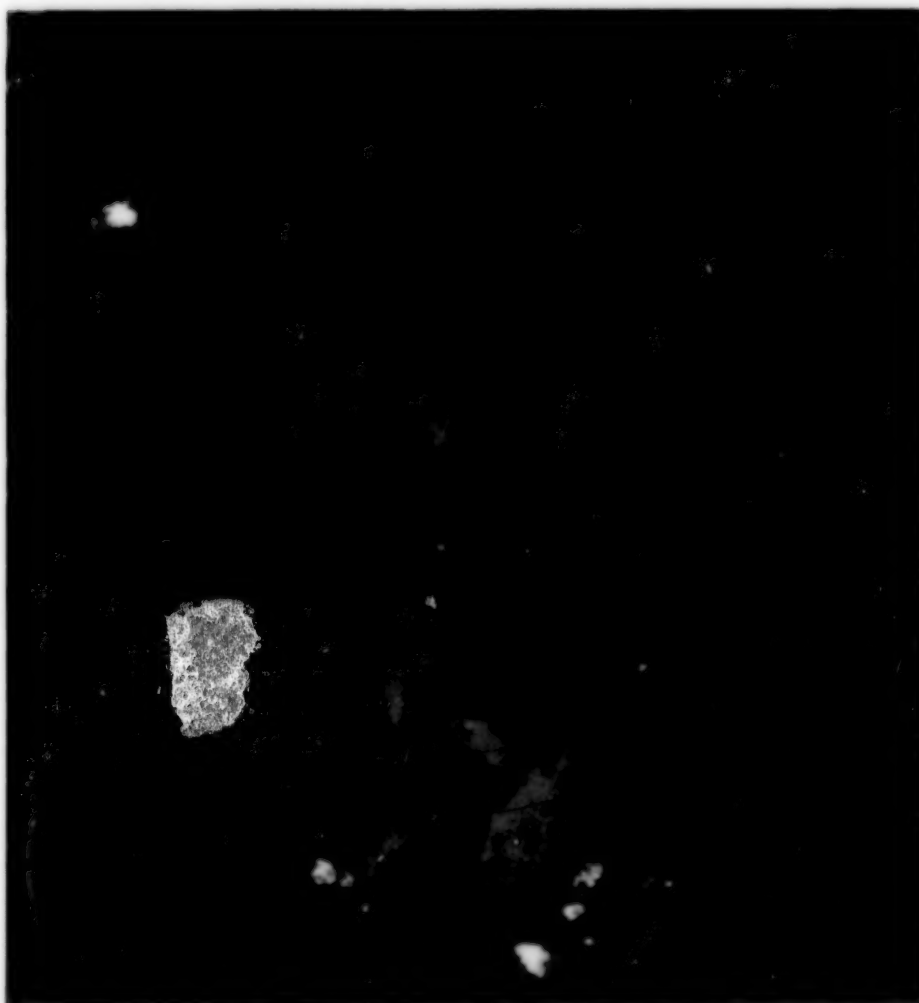


Figure 3-22a. Mean monthly
brightness temperatures for Au-
gust 1973 and 1974.

ORIGINAL PAGE
COLOR PHOTOGRAPH

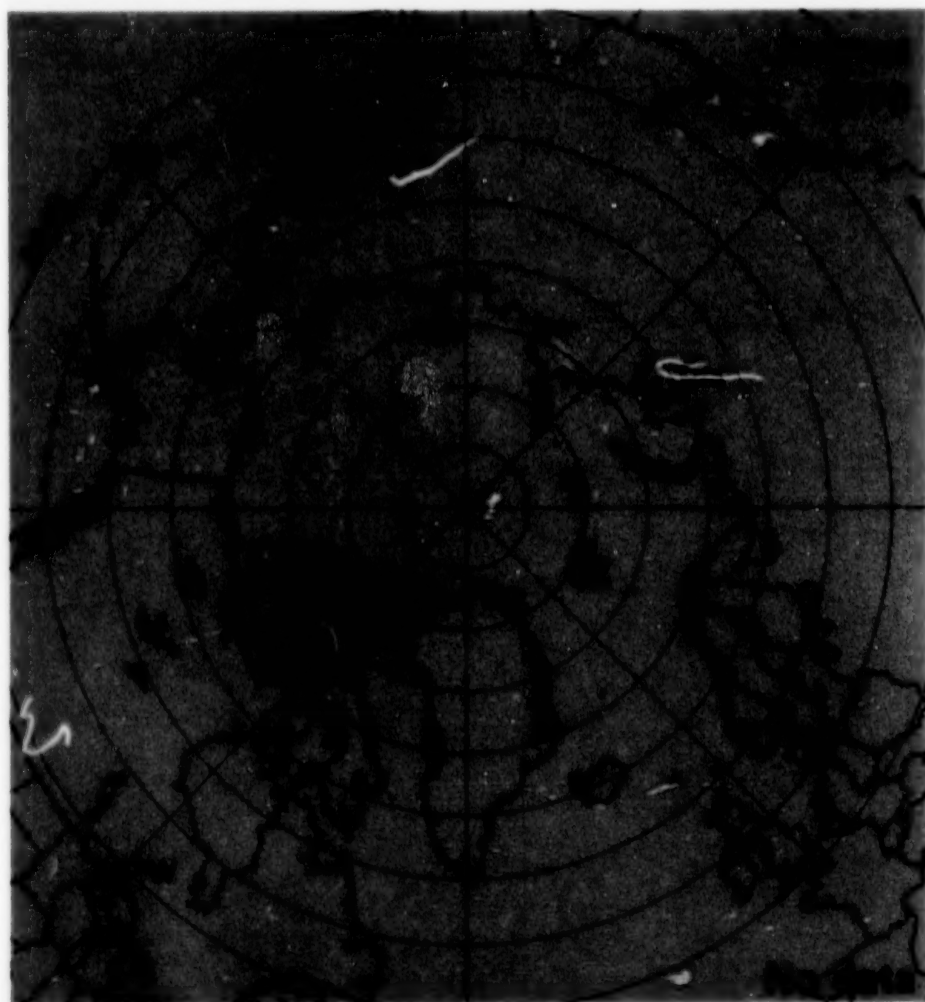
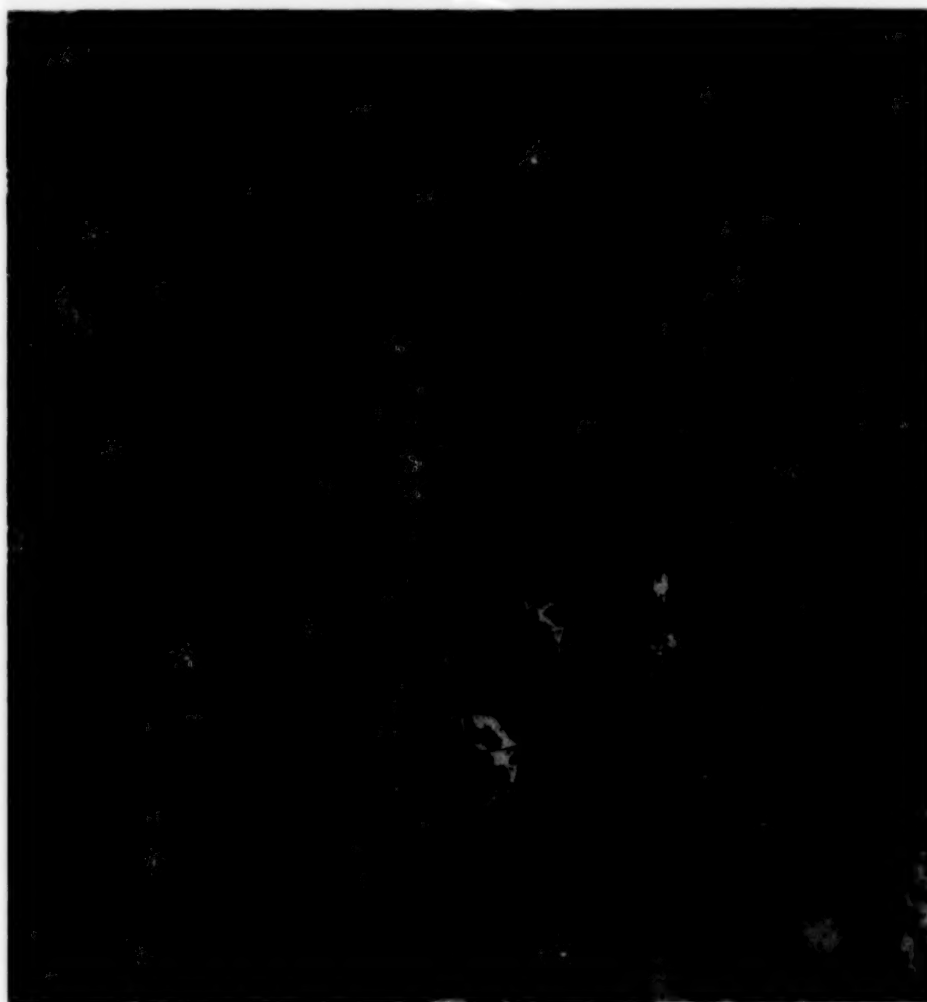


Figure 3-22b. Mean monthly
brightness temperatures for Au-
gust 1975 and 1976.

ORIGINAL PAGE
COLOR PHOTOGRAPH



≥ 282.5 K
 280 K
 275 K
 270 K
 265 K
 260 K
 255 K
 250 K
 245 K
 240 K
 235 K
 230 K
 225 K
 220 K
 215 K
 210 K
 205 K
 200 K
 195 K
 190 K
 185 K
 180 K
 175 K
 170 K
 165 K
 160 K
 155 K
 150 K
 145 K
 140 K
 135 K
 < 132.5 K

Figure 3-23a. Mean monthly brightness temperatures for September 1973 and 1974.

ORIGINAL PAGE
COLOR PHOTOGRAPH



Figure 3-23b. Mean monthly
brightness temperatures for Sep-
tember 1975 and 1976.

ORIGINAL PAGE
COLOR PHOTOGRAPH

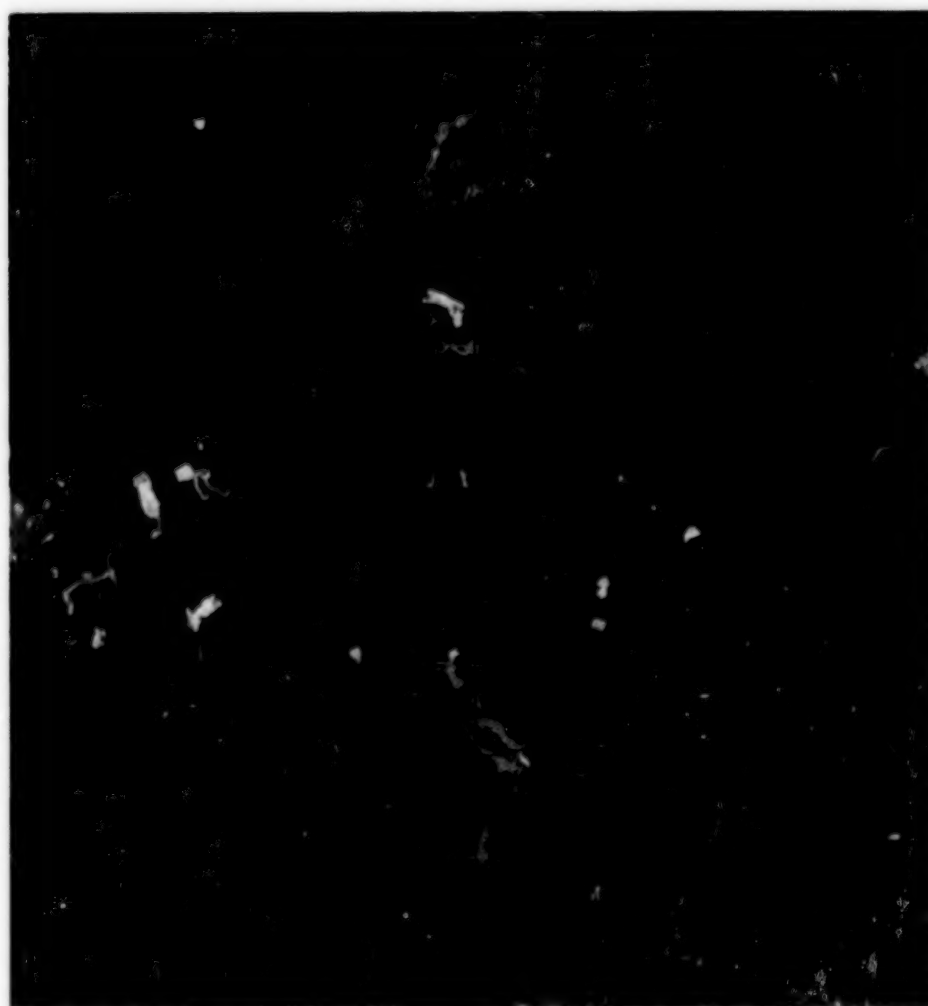


Figure 3-24a. Mean monthly
brightness temperatures for Oc-
tober 1973 and 1974.

ORIGINAL PAGE
COLOR PHOTOGRAPH



≥ 282.5 K

280 K

275 K

270 K

265 K

260 K

255 K

250 K

245 K

240 K

235 K

230 K

225 K

220 K

215 K

210 K

205 K

200 K

195 K

190 K

185 K

180 K

175 K

170 K

165 K

160 K

155 K

150 K

145 K

140 K

135 K

< 132.5 K



Figure 3-24b. Mean monthly
brightness temperatures for Oc-
tober 1975 and 1976.

ORIGINAL PAGE
COLOR PHOTOGRAPH

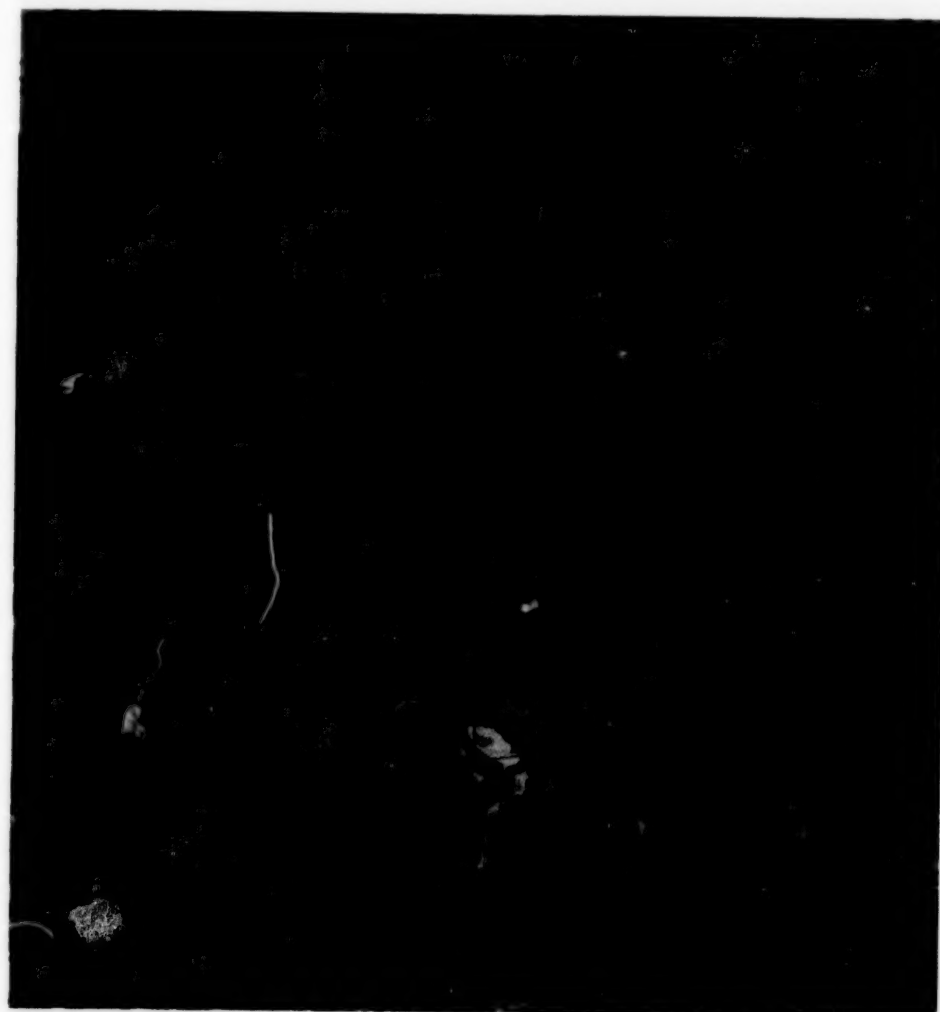


Figure 3-25a. Mean monthly
brightness temperatures for No-
vember 1973 and 1974.

ORIGINAL PAGE
COLOR PHOTOGRAPH

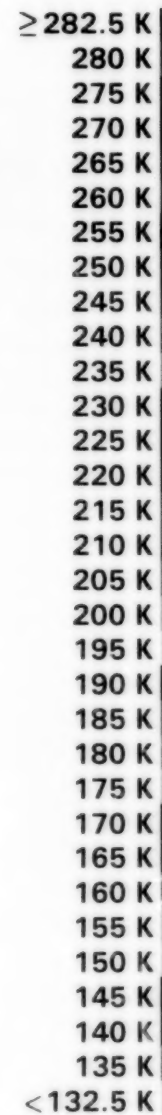
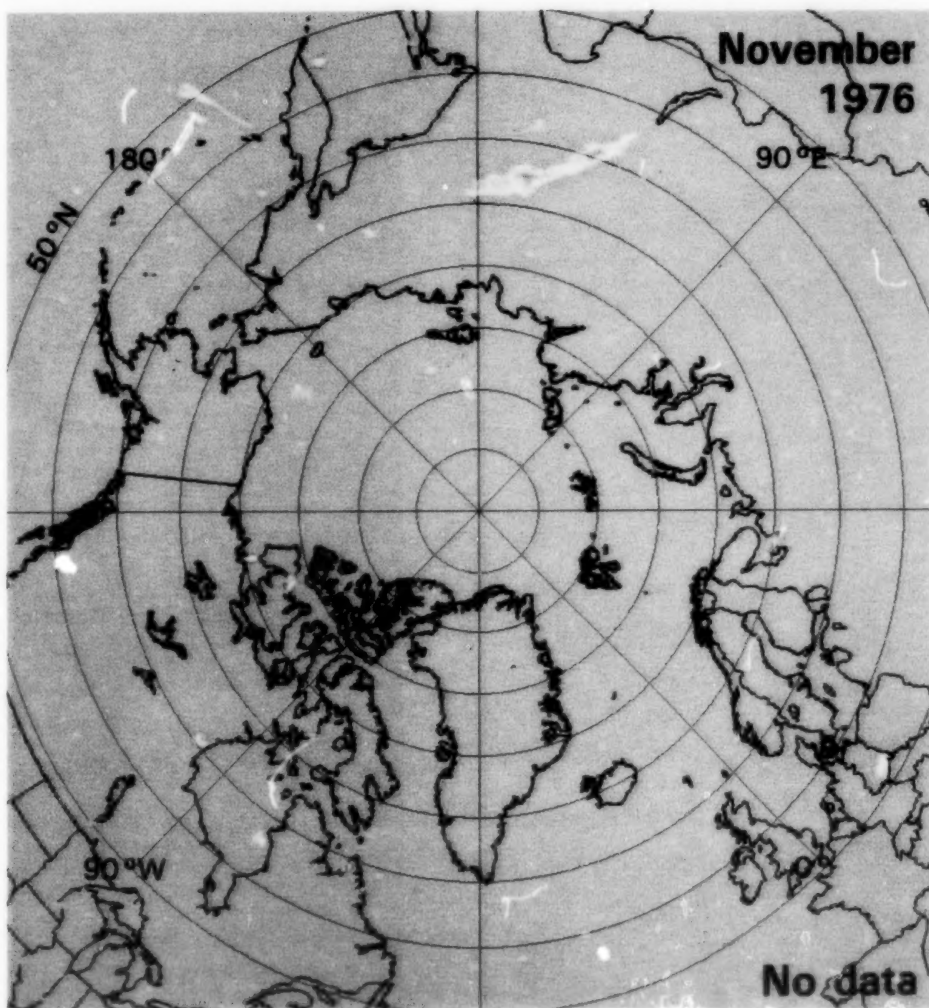
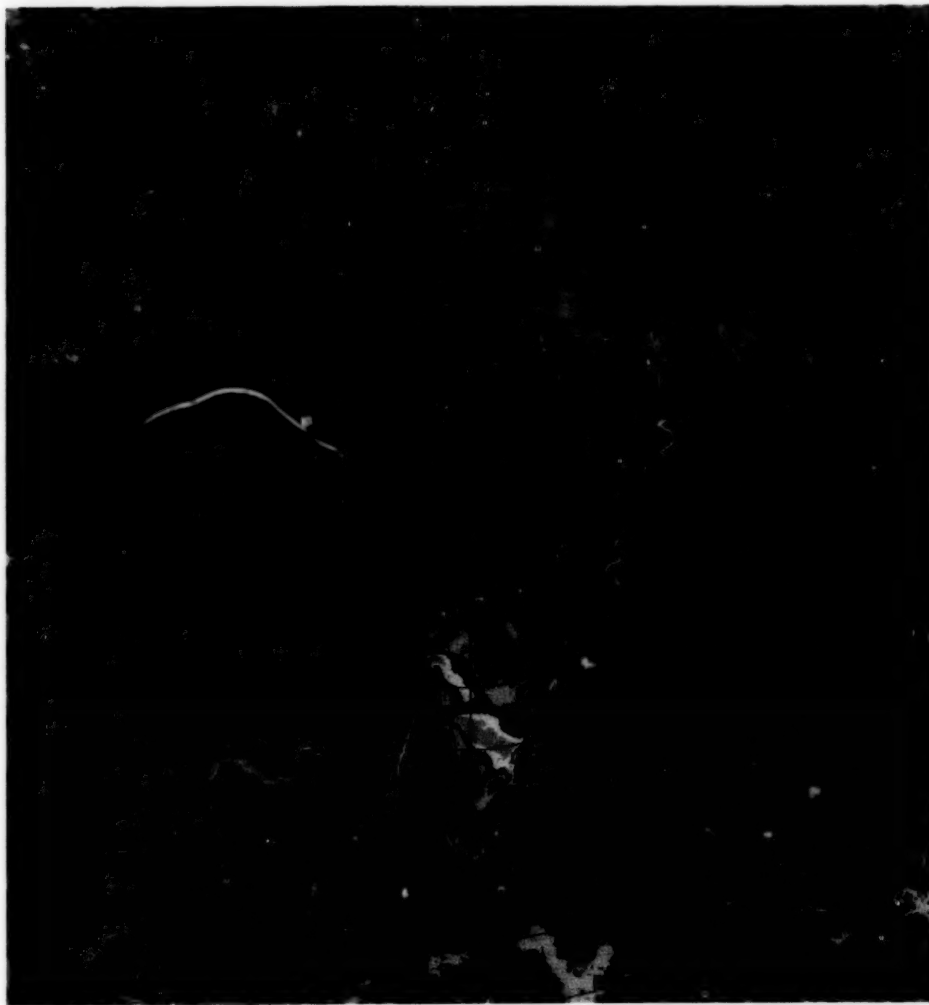


Figure 3-25b. Mean monthly brightness temperatures for November 1975 and 1976.

ORIGINAL PAGE
COLOR PHOTOGRAPH



≥ 282.5 K
280 K
275 K
270 K
265 K
260 K
255 K
250 K
245 K
240 K
235 K
230 K
225 K
220 K
215 K
210 K
205 K
200 K
195 K
190 K
185 K
180 K
175 K
170 K
165 K
160 K
155 K
150 K
145 K
140 K
135 K
< 132.5 K

Figure 3-26a. Mean monthly
brightness temperatures for De-
cember 1973 and 1974.

ORIGINAL PAGE
COLOR PHOTOGRAPH

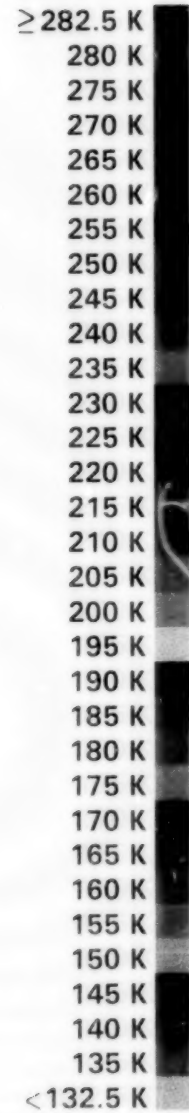
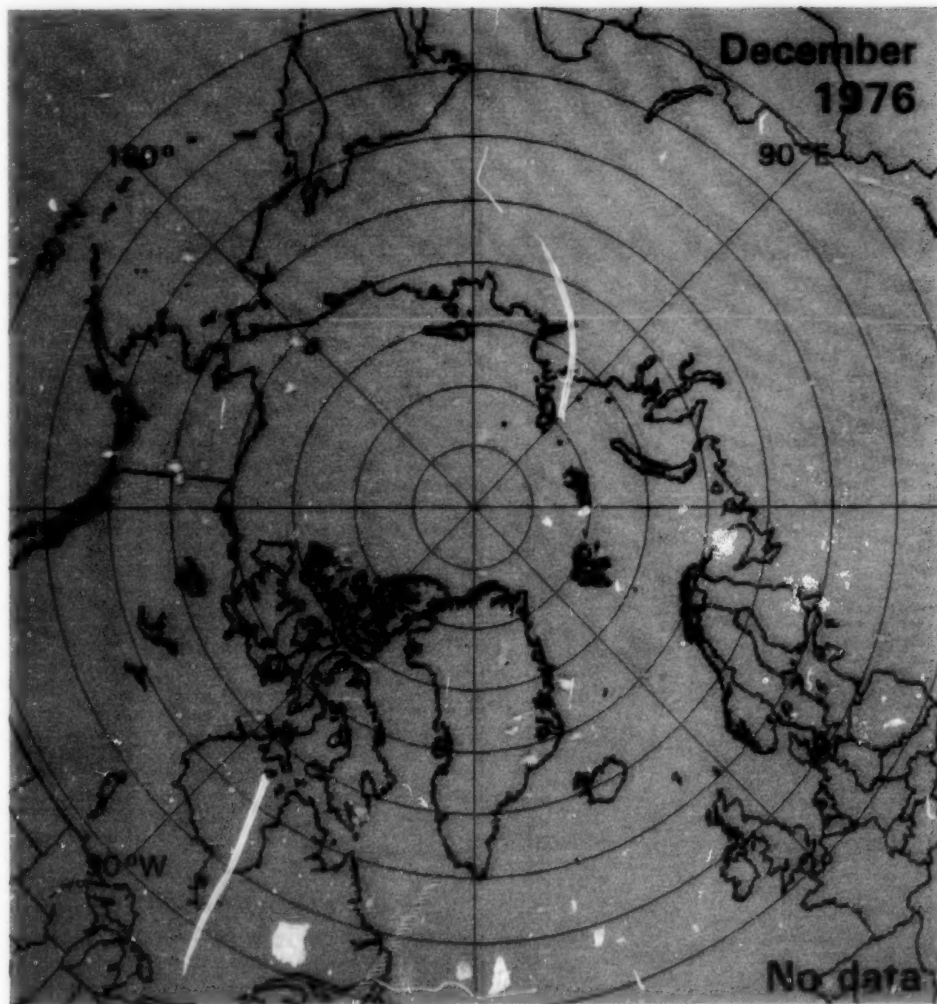
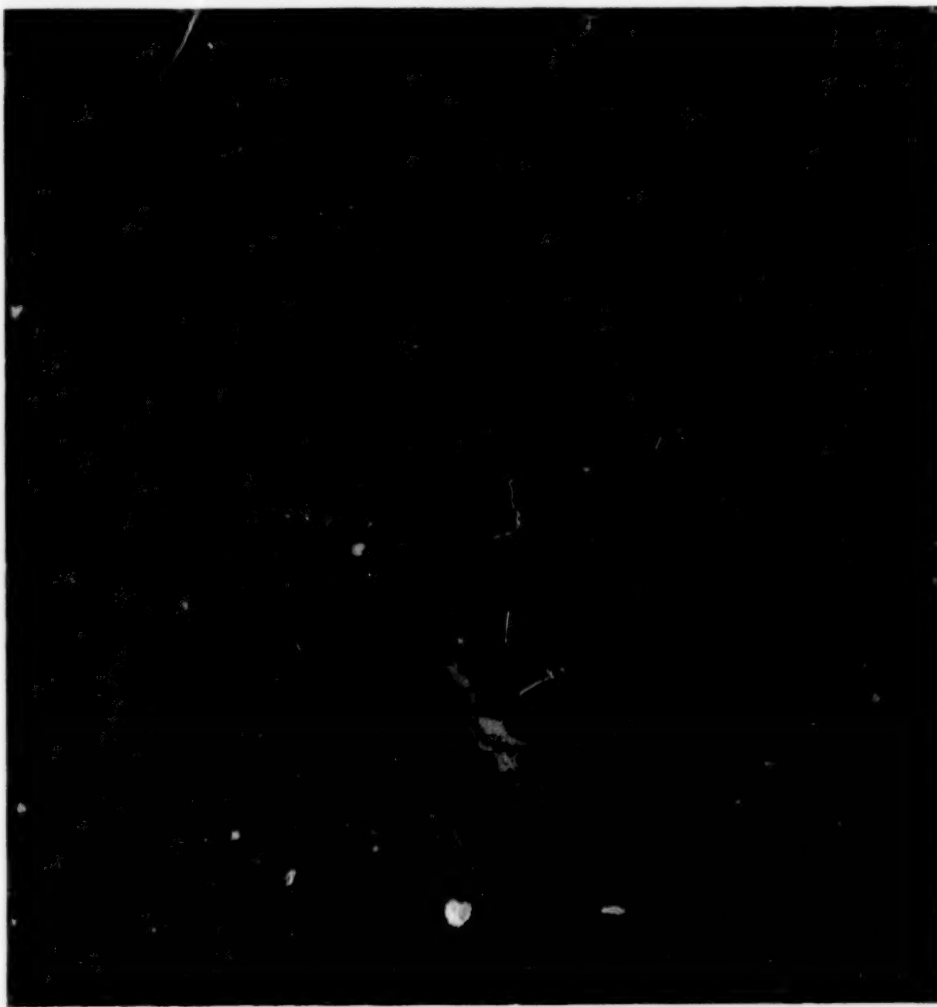


Figure 3-26b. Mean monthly brightness temperatures for December 1975 and 1976.



ORIGINAL PAGE
COLOR PHOTOGRAPH

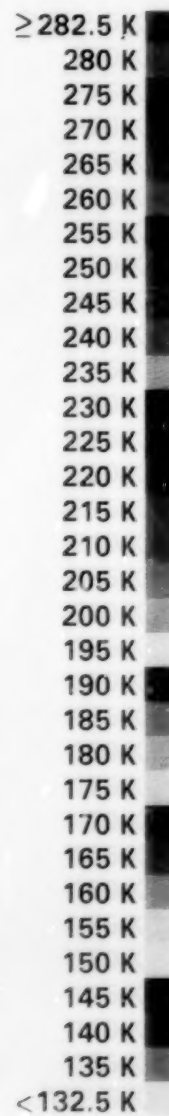


Figure 3-27. Four-year average of mean monthly brightness temperatures for January and February, 1973-1976.

ORIGINAL PAGE
COLOR PHOTOGRAPH



≥ 282.5 K

280 K

275 K

270 K

265 K

260 K

255 K

250 K

245 K

240 K

235 K

230 K

225 K

220 K

215 K

210 K

205 K

200 K

195 K

190 K

185 K

180 K

175 K

170 K

165 K

160 K

155 K

150 K

145 K

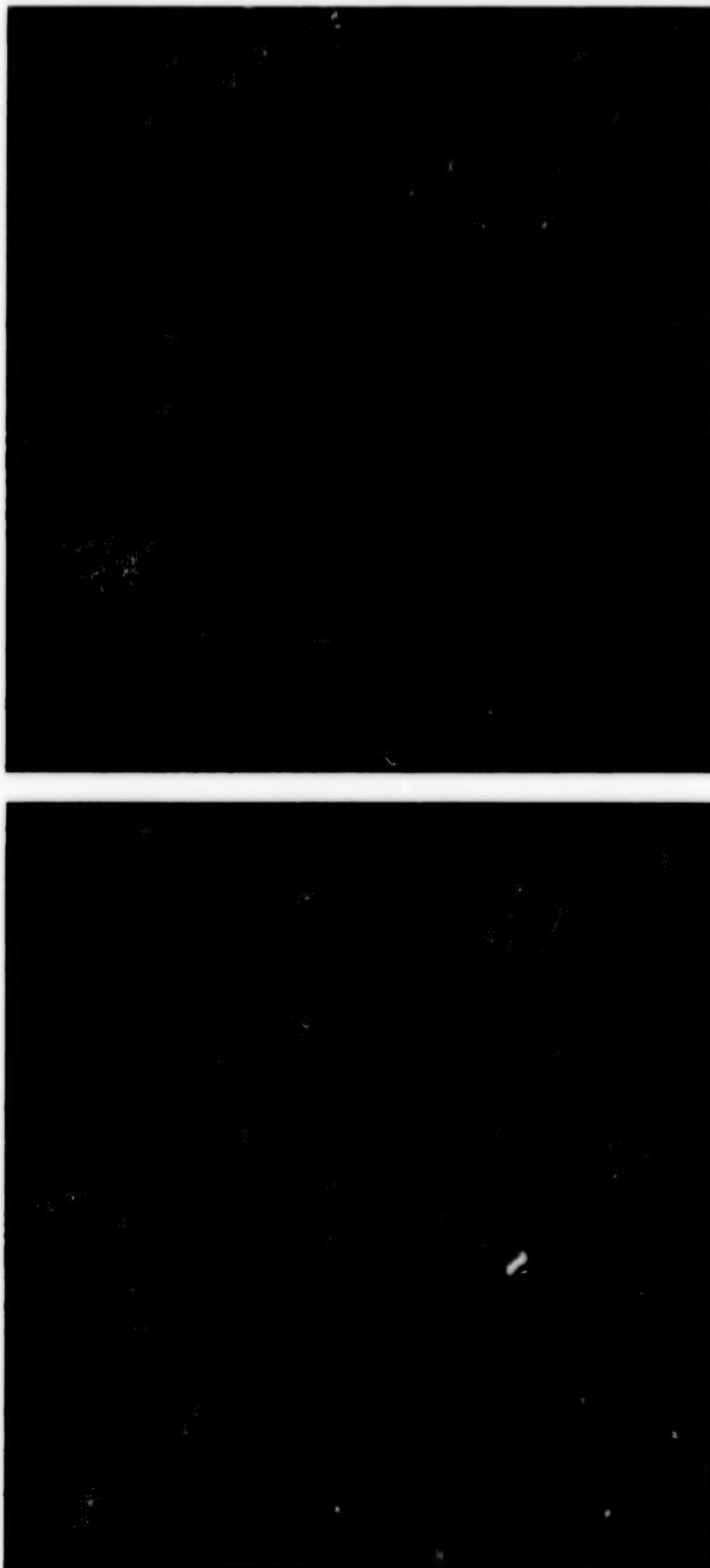
140 K

135 K

< 132.5 K

Figure 3-28. Three-year average of mean monthly brightness temperatures for March and April, 1974-1976.

ORIGINAL PAGE
COLOR PHOTOGRAPH



≥ 282.5 K

280 K

275 K

270 K

265 K

260 K

255 K

250 K

245 K

240 K

235 K

230 K

225 K

220 K

215 K

210 K

205 K

200 K

195 K

190 K

185 K

180 K

175 K

170 K

165 K

160 K

155 K

150 K

145 K

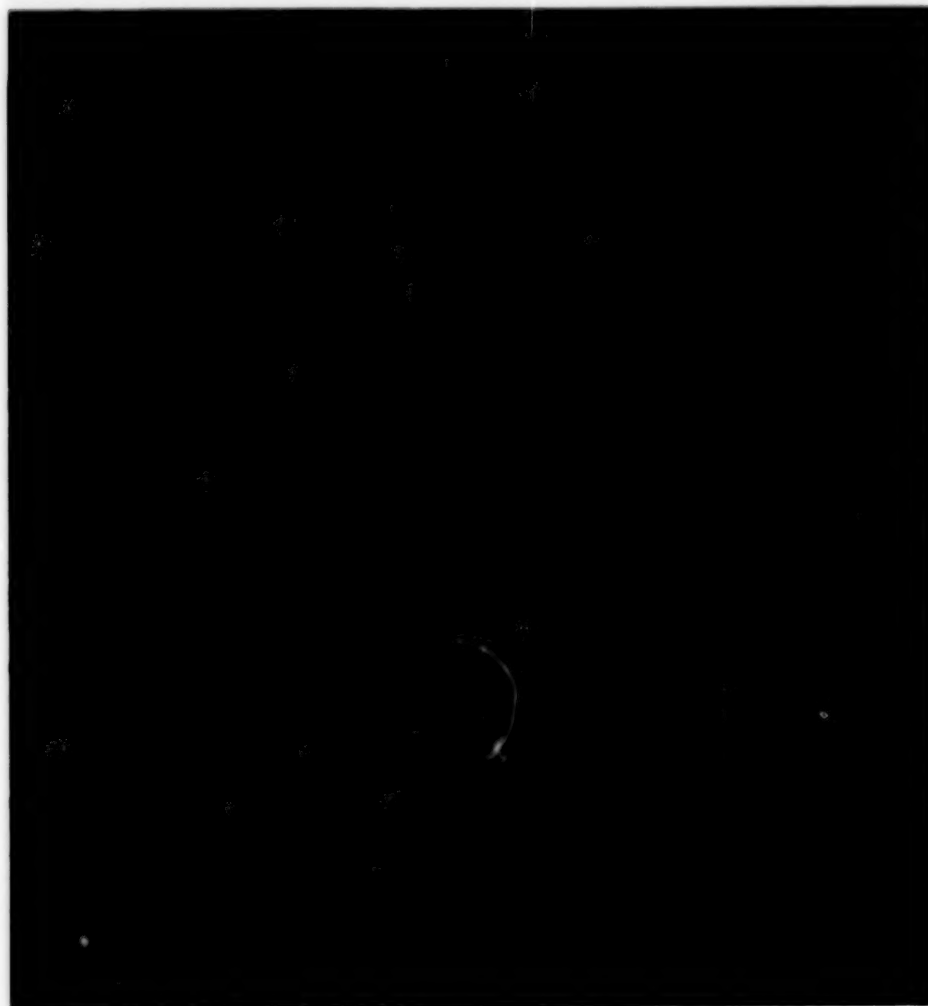
140 K

135 K

< 132.5 K

Figure 3-29. Three-year average of mean monthly brightness temperatures for May 1974-1976 and June 1973, 1974, and 1976.

ORIGINAL PAGE
COLOR PHOTOGRAPH



≥ 282.5 K
 280 K
 275 K
 270 K
 265 K
 260 K
 255 K
 250 K
 245 K
 240 K
 235 K
 230 K
 225 K
 220 K
 215 K
 210 K
 205 K
 200 K
 195 K
 190 K
 185 K
 180 K
 175 K
 170 K
 165 K
 160 K
 155 K
 150 K
 145 K
 140 K
 135 K
 < 132.5 K

Figure 3-30. Three-year average of mean monthly brightness temperatures for July 1973, 1974, and 1976 and 2-year average for August 1974 and 1976.



ORIGINAL PAGE
COLOR PHOTOGRAPH

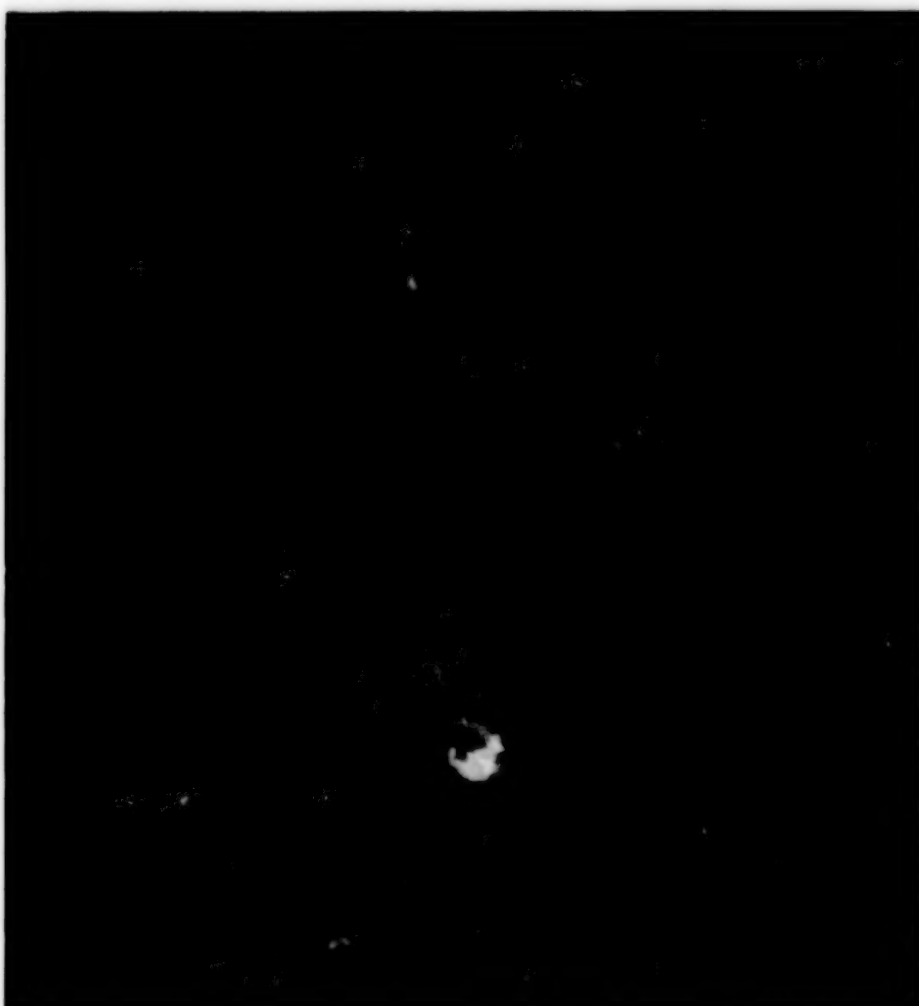
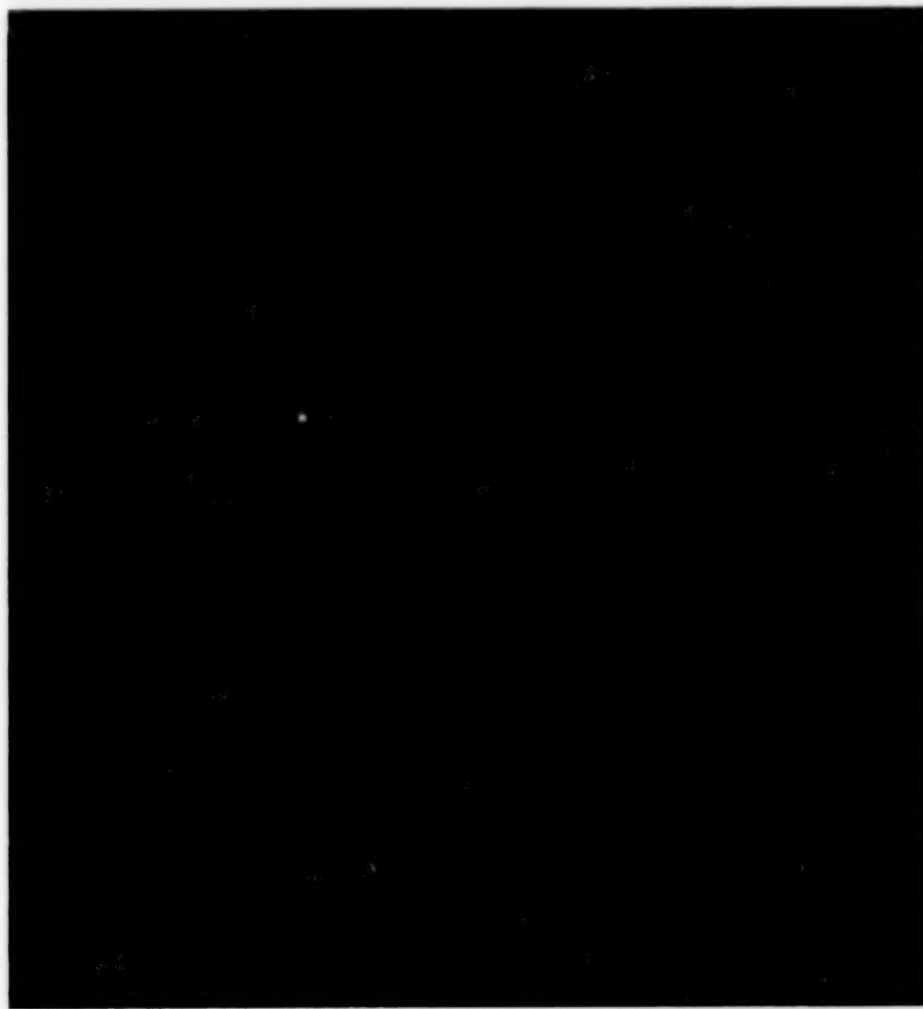


Figure 3-31. Four-year average of mean monthly brightness temperatures for September and October, 1973-1976.

ORIGINAL PAGE
COLOR PHOTOGRAPH



≥ 282.5 K
 280 K
 275 K
 270 K
 265 K
 260 K
 255 K
 250 K
 245 K
 240 K
 235 K
 230 K
 225 K
 220 K
 215 K
 210 K
 205 K
 200 K
 195 K
 190 K
 185 K
 180 K
 175 K
 170 K
 165 K
 160 K
 155 K
 150 K
 145 K
 140 K
 135 K
 < 132.5 K

Figure 3-32. Three-year average of mean monthly brightness temperatures for November and December, 1973-1975.

ORIGINAL PAGE
COLOR PHOTOGRAPH



≥ 282.5 K
 280 K
 275 K
 270 K
 265 K
 260 K
 255 K
 250 K
 245 K
 240 K
 235 K
 230 K
 225 K
 220 K
 215 K
 210 K
 205 K
 200 K
 195 K
 190 K
 185 K
 180 K
 175 K
 170 K
 165 K
 160 K
 155 K
 150 K
 145 K
 140 K
 135 K
 < 132.5 K

Figure 3-33a. Annual mean brightness temperatures for 1973 and 1974. Months without data are accounted for by interpolation.

ORIGINAL PAGE
COLOR PHOTOGRAPH



≥ 282.5 K
280 K
275 K
270 K
265 K
260 K
255 K
250 K
245 K
240 K
235 K
230 K
225 K
220 K
215 K
210 K
205 K
200 K
195 K
190 K
185 K
180 K
175 K
170 K
165 K
160 K
155 K
150 K
145 K
140 K
135 K
< 132.5 K

Figure 3-33b. Annual mean brightness temperatures for 1975 and 1976. Months without data are accounted for by interpolation.

3.6 DETERMINATION OF ICE CONCENTRATION AND MULTIYEAR ICE FRACTION

Variations in the brightness temperature observed over the surface of the Earth are caused by variations in the emissivity of the surface material and variations in physical temperature, according to equation 3-1 ($T_B = \epsilon T$). Generally, the emissivity variations are more significant than the temperature variations. For example, in the case of the polar oceans the physical temperatures of the ice and water can be comparable while the brightness temperatures are markedly different, because the emissivity of sea water at the 1.55-centimeter wavelength of the ESMR instrument is approximately 0.44 whereas the emissivities of first-year and multiyear sea ice are approximately 0.92 and 0.84, respectively.

If the field of view of the sensor includes a mixture of two materials, for example, sea water and sea ice with respective emissivities ϵ_w and ϵ_i and physical temperatures T_w and T_i , then the brightness temperature T_B is approximately a linear combination of the two individual brightness temperatures. Letting C denote the fractional area of the ocean covered by sea ice, termed the "sea ice concentration," then $(1 - C)$ is the fractional area covered by sea water, and the equation for the brightness temperature due to the ice/water combination (ignoring atmospheric effects) becomes:

$$T_B = (1 - C) \epsilon_w T_w + C \epsilon_i T_i \quad (3-4)$$

If the emissivities and physical temperatures are known or estimated, equation 3-4 can be used to calculate sea ice concentration as a function of brightness temperature:

$$C = \frac{T_B - \epsilon_w T_w}{\epsilon_i T_i - \epsilon_w T_w} \quad (3-5)$$

Equation 3-5 is plotted in Figure 3-34 for $\epsilon_w T_w = 138.3$ K, two values of ϵ_i , and three values of T_i . The secondary effects of the atmosphere and various nonlinear radiative terms are accounted for later by reinterpretation of some of the terms in equations 3-4 and 3-5. Large uncertainties in T_i or ϵ_i contribute to uncertainties in the calculated ice concentrations even when all the sea ice is the same type. The problem is compounded when the field of view con-

tains an unknown mixture of first-year ice, multiyear ice, and open water.

If the sea ice pack contains only first-year and multiyear ice, with no open water, then the brightness temperature, ignoring atmospheric effects, is

$$T_B = F_{MY} \epsilon_{IM} T_{IM} + (1 - F_{MY}) \epsilon_{IF} T_{IF} \quad (3-6)$$

where F_{MY} is the fraction of the ice cover that is multiyear ice, ϵ_{IM} and ϵ_{IF} are the emissivities of multiyear ice and first-year ice respectively, and T_{IM} and T_{IF} are the temperatures of multiyear ice and first-year ice. Solving equation 3-6 for F_{MY} yields:

$$F_{MY} = \frac{T_B - \epsilon_{IF} T_{IF}}{\epsilon_{IM} T_{IM} - \epsilon_{IF} T_{IF}} \quad (3-7)$$

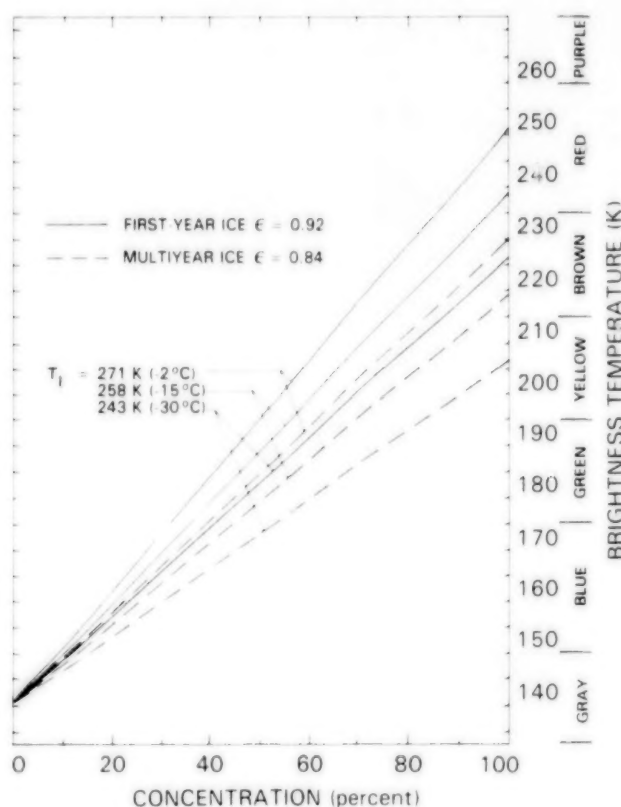


Figure 3-34. Brightness temperature at a wavelength of 1.55 centimeters versus sea ice concentration for three different radiating temperatures T_i , plotted both for first-year and for multiyear sea ice. [This figure is modified from Zwally et al. (1983a) to take account of the difference between the average ocean brightness temperatures in the north and south polar regions.]

If open water is also present, the brightness temperature is

$$T_B = (1-C) \epsilon_w T_w + C [F_{MY} \epsilon_{IM} T_{IM} + (1-F_{MY}) \epsilon_{IF} T_{IF}] \quad (3-8)$$

in which case C cannot be unambiguously determined without an estimate of F_{MY} as well as of the ice temperatures and emissivities. This inherent limitation of the single-channel ESMR instrument is accounted for in Chapter 4 by presenting ice concentration maps with a nomogram representation of equation 3-8, adjusted for atmospheric contributions, in which both C and F_{MY} appear as variables. In *Antarctic Sea Ice, 1973-1976*, a single scale representing equation 3-5, with no multiyear ice dependence, suffices because the ice in the Antarctic is predominantly first-year ice.

The nomogram for the Arctic sea ice concentration maps requires adjustments for atmospheric contributions and appropriate values for sea ice emissivities and temperatures. To describe the approximations involved in determining these values, we present the full radiative transfer equation applicable to nadir passive microwave observations at a given wavelength over a surface with a single surface type:

$$T_B = \epsilon T_S e^{-\tau} + \int_0^{\ell} [T(z) E(z) e^{-\tau - \tau'(z)}] dz + (1-\epsilon) \kappa e^{-\tau} \int_0^{\ell} [T(z) E(z) e^{-\tau'(z)}] dz \quad (3-9)$$

T_B is the observed brightness temperature, ϵ is the emissivity of the surface at the relevant wavelength, T_S is the physical temperature of the surface, $T(z)$ is the temperature at height z in the atmosphere, $\tau'(z)$ and τ are the atmospheric opacities from the surface to height z and from the surface to the satellite height, ℓ , respectively, κ is an estimate of the diffusiveness of the surface reflection, and $E(z)$ is the atmospheric emittance at z . The reflected contribution of free-space radiance, which is a very small additive constant, is neglected. In equation 3-9, the first term on the right-hand side represents the contribution to the observed brightness temperature of the surface as seen through the atmosphere, the second is the upwelling radiation from the atmosphere (directed towards the satellite sensor), and the third is the downwelling atmospheric radiation as observed after reflection at the surface and transmission back through the atmosphere. Using typical atmospheric

conditions over the subpolar oceans, radiative transfer studies have shown that the contribution of the second term is typically 8 K, whereas that of the third term is about 5 K. Over sea ice in polar regions, these contributions are expected to be substantially less because of the lower water vapor content of the atmosphere.

The use of equation 3-9 instead of 3-1 to obtain the equations for ice concentration and multiyear ice fraction can be simplified by defining the atmospheric contributions (the sum of the second and third terms in equation 3-9) to be T_{Aw} over water and T_{Ai} over ice, so that equation 3-9 is reduced to:

$$T_{BIF} = \epsilon_{IF} T_{IF} e^{-\tau} + T_{Ai} \quad (3-10)$$

$$T_{BIM} = \epsilon_{IM} T_{IM} e^{-\tau} + T_{Ai} \quad (3-11)$$

and

$$T_{Bw} = \epsilon_w T_w e^{-\tau} + T_{Aw} \quad (3-12)$$

for the brightness temperatures T_{BIF} , T_{BIM} , T_{Bw} of first-year ice, multiyear ice, and open water respectively, as observed by the satellite, including atmospheric effects. The inclusion of atmospheric terms in equations 3-4 through 3-8 is realized approximately by making the following substitutions:

$$T_I = T_{IF} = T_{IF} e^{-\tau} + T_{Ai}/\epsilon_{IF} \quad (3-13)$$

$$T_{IM} \sim T_{IF} \quad (3-14)$$

$$T_w = T_w e^{-\tau} + T_{Aw}/\epsilon_w \quad (3-15)$$

In this formulation, a linear relationship between ice concentration, multiyear ice fraction, and brightness temperature is maintained, as illustrated in Figure 3-34.

For the calculations of ice concentrations and multiyear ice fractions, the variations of T_{Bw} over time and space are ignored. Within the ice pack, variations in T_{Bw} are small because the physical temperature is approximately uniform at the freezing point and the conditions are relatively calm. The assumed value of T_{Bw} used throughout the ice concentration calculations is obtained from the observed data over ice-free ocean, in different areas of the ocean and different time-averaging periods. The variability of T_{Bw} over ice-free ocean is caused by various effects, including surface roughness, foam,

and atmospheric water vapor content, a combination of which tends to increase the brightness temperature of the ocean by as much as 40 K (Wilheit et al., 1972; Swift, 1980; Wentz, 1983). Figure 3-35 shows plots of brightness temperature distributions during winter over selected areas in both hemispheres where both ice and open ocean appear. For the Northern Hemisphere, the gridded ESMR brightness temperature data in the Bering Sea from 50°N to 65°N are binned at 1 K intervals for monthly, 3-day, and daily averages, and for the Southern Hemisphere, the area in the Weddell Sea from 55°S to 65°S is analyzed similarly. [Plots generated for the North Atlantic show results similar to those for the Bering Sea.] The widths at the half maximum (w_h) of the distributions are 3.0 K, 5.7 K, and 8.0 K in the Northern Hemisphere and 2.0 K, 4.0 K, and 5.5 K in the Southern Hemisphere for the monthly, 3-day, and daily time periods, respectively. The reduction in width from daily to monthly time periods is caused by time averaging of the variable atmospheric and surface conditions. The smaller widths in the Southern Hemisphere than in the Northern Hemisphere suggest that the net atmospheric and surface effects over the ocean are larger in the north than in the south; because it is unlikely that surface roughness is larger in the north, other effects, such as atmospheric water vapor and precipitation, probably predominate. Also interesting is the value of the lowest brightness temperatures in the different plots, being about 130 K for the monthly data and 125 K for both daily and 3-day data. The lowest brightness temperature represents the signature of ice-free ocean least affected by atmospheric and surface effects. The brightness temperature over a motionless ocean without an atmosphere would be about 120 K, which is consistent with these values over the actual ocean observed from space. The difference between the lowest ocean signatures for 3-day data and for monthly data, like the differences in the widths of the ocean distribution, results from the effects of the averaging.

In *Antarctic Sea Ice, 1973-1976*, T_{bw} was taken to be 135 K, the 4-year-average brightness temperature over ice-free regions of the southern ocean. In the north polar region, the corresponding value calculated from the ESMR observations is 138.3 K. The 3.3 K difference is felt to be significant and, as mentioned briefly at the start of Section 3.5, is believed to be caused predominantly by actual dif-

ferences in the average signature of ice-free ocean in the two hemispheres. It could also be caused in part by variations in the sensitivity of the instrument with temperature. The satellite is exposed to solar heating as it approaches the north polar region but is not exposed to solar heating as it approaches the south polar region. Irrespective of the cause of the discrepancy, the T_{bw} used for ice concentration retrieval in the Arctic region is 138.3 K, so that the term $\epsilon_w T_w$ is replaced by 138.3 K at each of its occurrences in equations 3-5 and 3-8. Of the 138.3 K, approximately 120 K derives from the water and the remainder derives from the atmosphere.

Because real-time data for T_i are not available, interpolated monthly climatological air temperature data are used as in *Antarctic Sea Ice, 1973-1976*. The ice temperature, which is usually higher than the air temperature but lower than the water temperature underneath the ice, is estimated from the following empirical formula:

$$T_i = T_{IF} = T_{IM} = T_{air} + f(T_F - T_{air}), \quad (3-16)$$

where T_{air} is the mean monthly climatological air temperature (mapped earlier in Figure 2-6 from data of Crutcher and Meserve, 1970), T_F is the freezing point of sea water (271.2 K), and f is a parameter determined from the observed brightness temperature data by adjusting f until the maximum values of C from equation 3-5 are consistently about 100 percent during winter. A value of $f = 0.25$ was determined for use in *Antarctic Sea Ice, 1973-1976* through examination of the July 1974 data over the southern ocean. Later examination of the Northern Hemisphere data showed that $f = 0.25$ is also appropriate for the Arctic. This value of 0.25 agrees with the overall average of surface measurements made at Pond Inlet in the Canadian Archipelago (Ramseier, personal communication). A comparison of the Pond Inlet results with the formulation used here is shown in Figure 3-36. Over the interval 240 to 270 K, the maximum deviation is 6 K. To summarize, T_i , T_{IF} , and T_{IM} , needed for the calculation of ice concentrations through equations 3-5 and 3-8, are assumed equal and are calculated from equation 3-16 with mean monthly climatological air temperatures used for T_{air} and values of 271.2 K and 0.25 used for T_F and f , respectively.

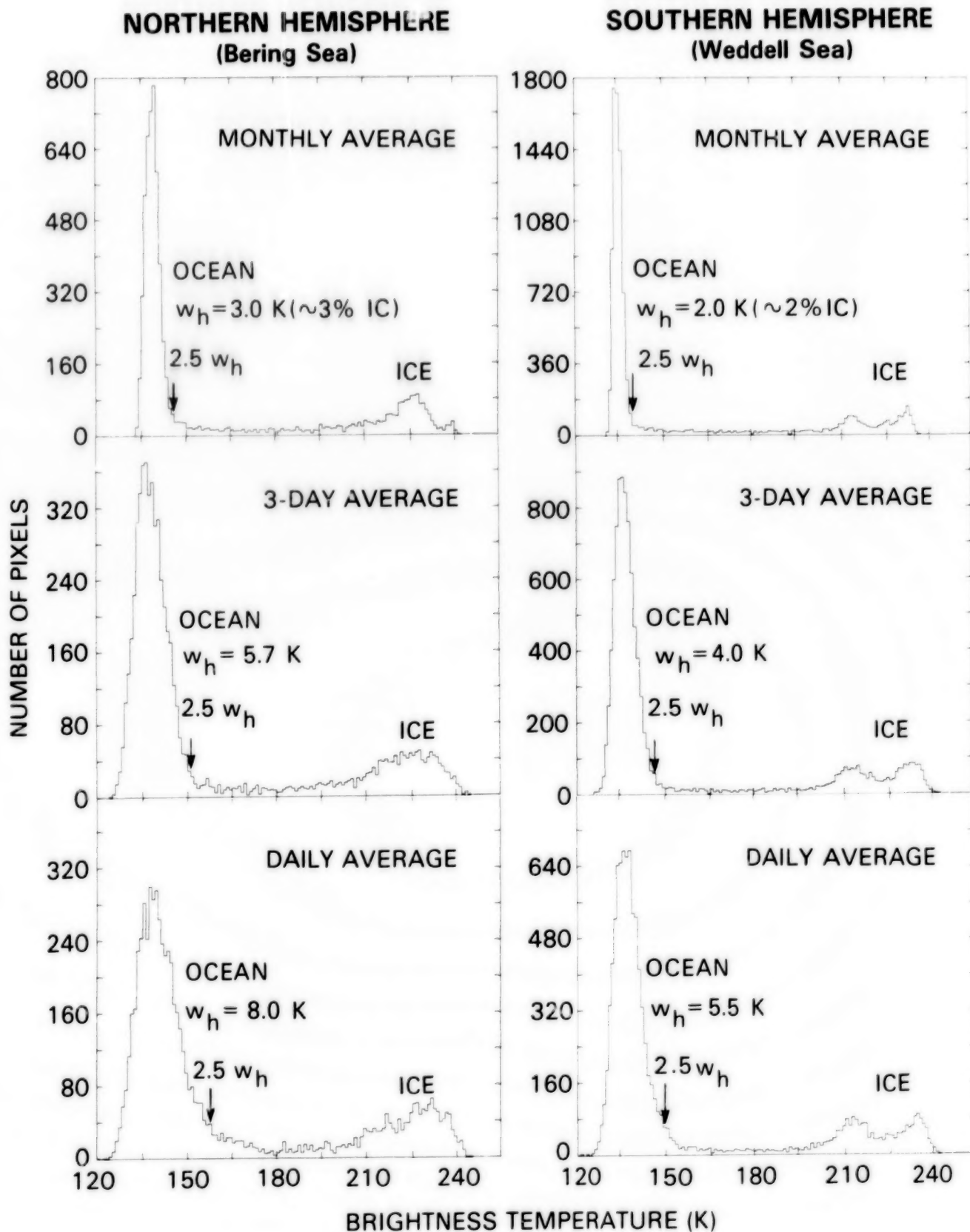


Figure 3-35. Histograms of wintertime distributions of brightness temperatures in the Weddell Sea (for July 1974) and in the Bering Sea (for February 1974), for monthly, 3-day, and daily time periods. IC refers to ice concentration. [Revised from Comiso and Zwally (1984).]

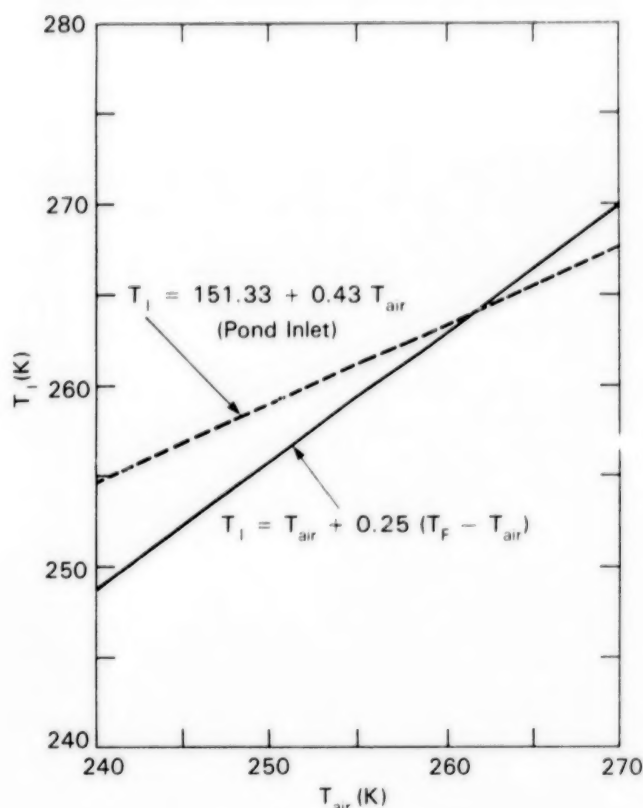


Figure 3-36. Relationship of estimated snow/ice interface physical temperature, T_i , to air temperature, T_{air} , from: (1) the interpolation procedure used in the retrieval of ice concentration, and (2) a least squares fit to measurements at Pond Inlet provided by Ramseier (personal communication, 1982). [Modified from Zwally et al. (1983a).]

To compare the climatological temperatures used for T_{air} in equation 3-16 with other temperature data, Figure 3-37 shows monthly temperatures for February, March, and April of 1979 derived from the Temperature-Humidity Infrared Radiometer (THIR) on board the Nimbus 7 satellite (Comiso, 1986) and the differences of the THIR temperature fields from the climatological data for February, March, and April. Most of the differences over the sea ice region are within ± 5 K. The standard deviation over the central Arctic is 5.5 K in February and 3.5 K in March and April (Figure 3-38). Overall, despite the uncertainties associated with the use of climatological data, it is believed that the use of these temperatures in equation 3-16 increases the accuracy of the retrieval of sea ice concentrations over the use of strict linear interpolation from the ESMR brightness temperatures.

The various elements required for obtaining sea ice concentration maps and associated nomograms have now been described. The ice concentration/multiyear ice fraction maps presented in Chapter 4 are generated from the brightness temperature maps of this chapter by applying equation 3-5 to each map data element, with 138.3 K replacing $\epsilon_w T_w$ and values of T_i determined from equation 3-16 using $f = 0.25$, $T_F = 271.2$ K, and spatially varying mean monthly climatological air temperatures for T_{air} . The emissivity used for first-year sea ice is 0.92, and the maps are generated and color-coded with the color scale used in *Antarctic Sea Ice, 1973-1976*, where only first-year ice is considered. However, as previously emphasized, because the Arctic contains significant amounts of multiyear ice, the first-year-ice scale alone is insufficient for Arctic conditions. Hence the first-year-ice scale is expanded into a nomogram in which both ice concentration, C , and multiyear ice fraction, F_{MY} , are represented as variables (Figure 3-39). The crucial element in the generation of the nomogram is the proper determination of the placement of the concentration values on the right-hand scale, corresponding to exclusively multiyear ice and open water. The right-hand scale on the nomogram was constructed by recognizing that the concentrations C_i calculated with a first-year ice emissivity were determined by

$$C_i = \frac{T_B - T_o}{0.92 T_i - T_o} \quad (3-17)$$

with $T_o = 138.3$ K, whereas for multiyear ice the calculation would have been

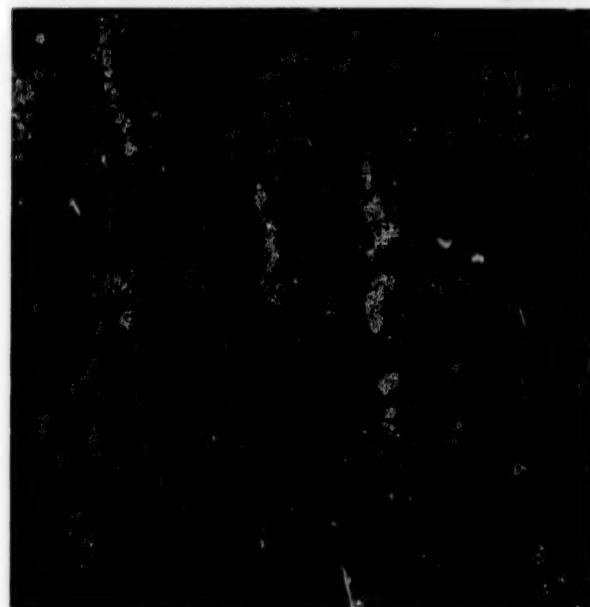
$$\begin{aligned} C_{MY} &= \frac{T_B - T_o}{0.84 T_i - T_o} \\ &= C_i \left(\frac{0.92 T_i - T_o}{0.84 T_i - T_o} \right) \end{aligned} \quad (3-18)$$

Inserting 248 K as an appropriate overall value for T_i , equation 3-18 reduces to $C_{MY} = 1.283 C_i$, which is the conversion used in creating the nomogram. Thus, for instance, the boundary between light pink and deep brown, marking 78 percent concentration for first-year ice, corresponds to 100 percent ($= 1.283 \times 0.78$) concentration for multiyear ice,

THIR (11.5 μm)

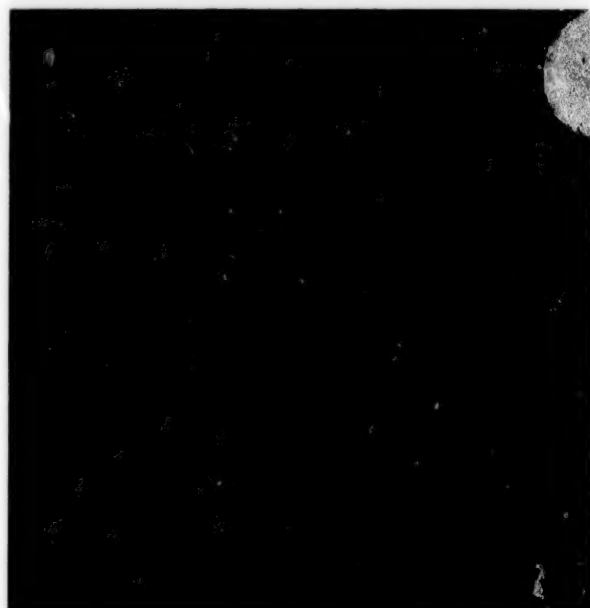
ORIGINAL PAGE
COLOR PHOTOGRAPH

CLIMATOLOGY - THIR



Left
Images

282.5 K
280 K
275 K
270 K
265 K
260 K
255 K
250 K
245 K
240 K
235 K
230 K
225 K
220 K
215 K
210 K
205 K
200 K
195 K
190 K
185 K
180 K
175 K
170 K
165 K
160 K
155 K
150 K
145 K
140 K



Right
Images

57.5 K
55.0 K
50.0 K
45.0 K
40.0 K
35.0 K
30.0 K
25.0 K
20.0 K
15.0 K
10.0 K
5.0 K
0.0 K
-5.0 K
-10.0 K
-15.0 K
-20.0 K
-25.0 K
-30.0 K
-35.0 K
-40.0 K
-45.0 K
-50.0 K
-55.0 K
-57.5 K

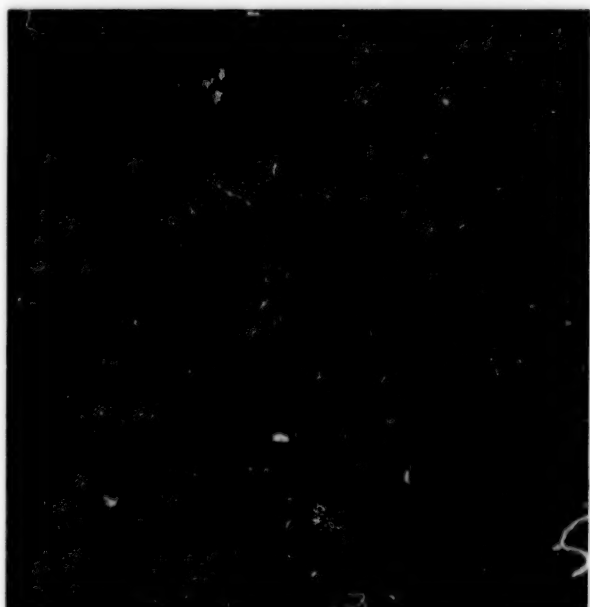
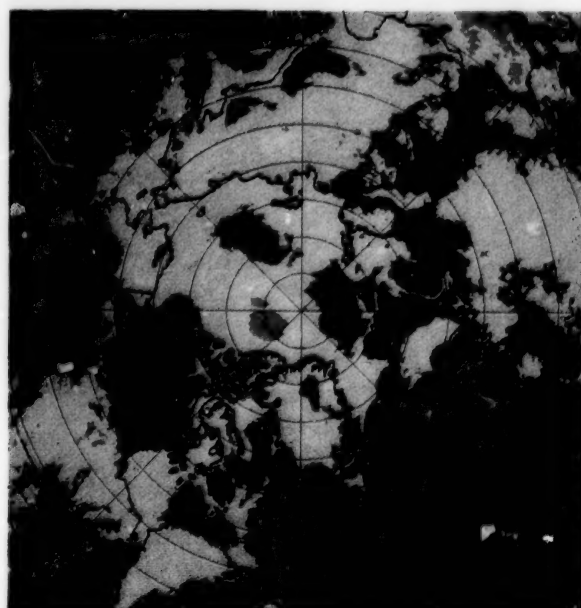


Figure 3-37. February, March, and April physical surface air temperatures inferred from 1979 Nimbus 7 THIR data and the difference between these and the mean monthly climatological data of Figure 2-6a.

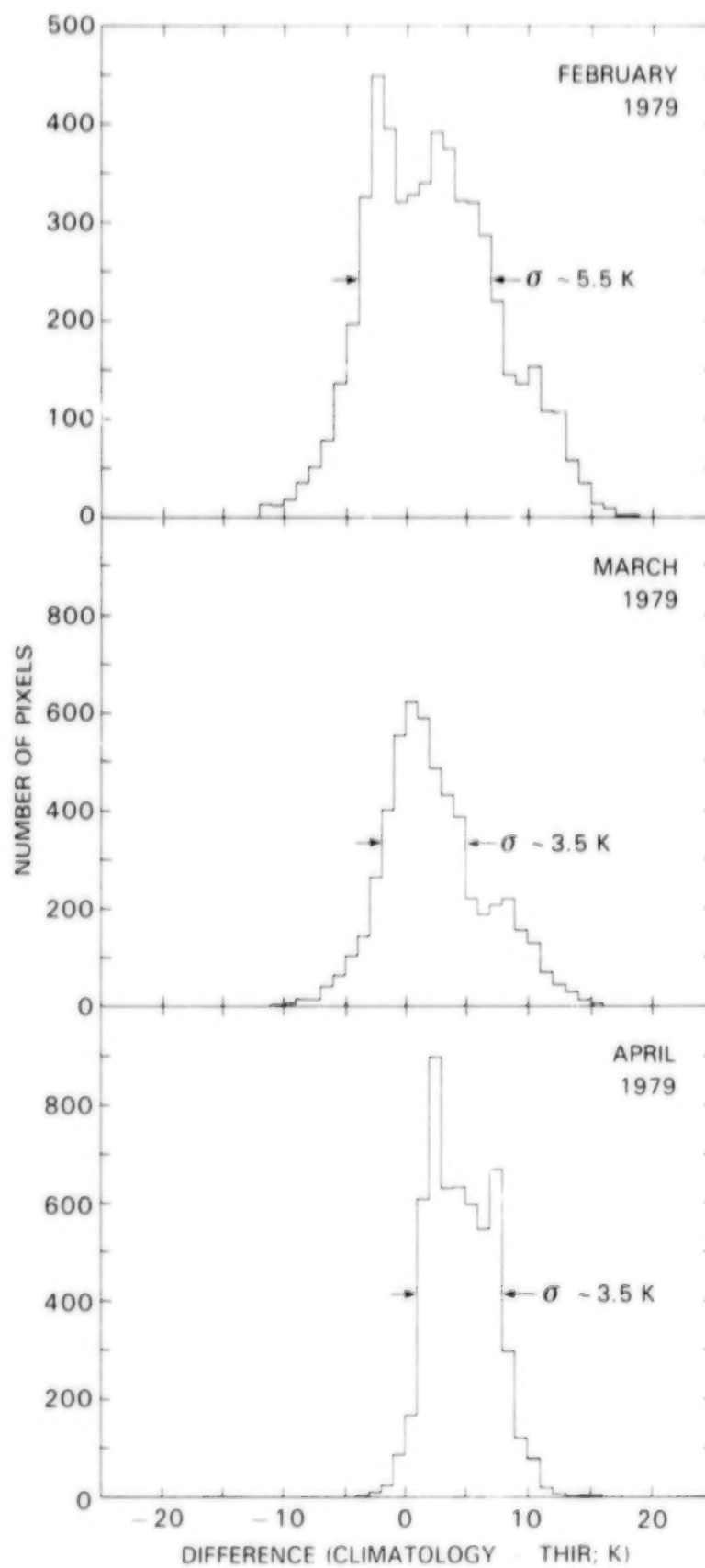


Figure 3-38. Distributions of the difference between mean monthly climatological air temperatures and 1979 surface air temperatures from Nimbus 7 THIR data, over the central Arctic, for February, March, and April.

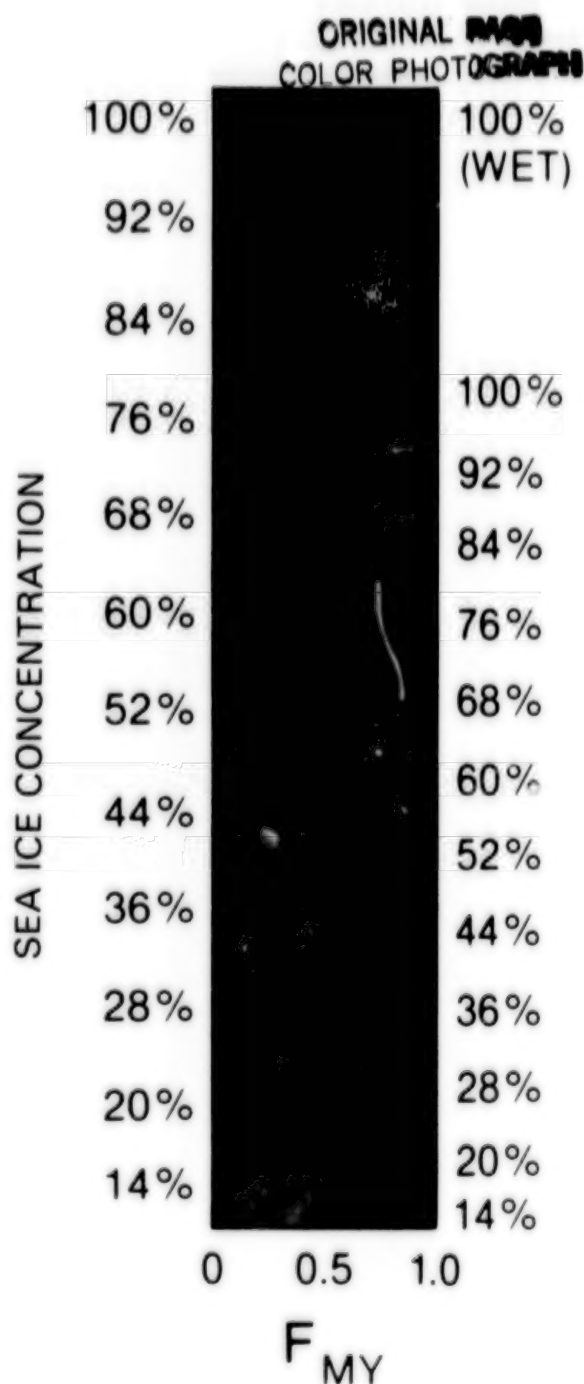


Figure 3-39. Ice concentration/ice type nomogram used for color-coded ice concentration ESMR images in Chapter 4. The horizontal scale refers to the ratio F_{MY} of multiyear ice area to the total ice area.

and the deep green, marking 44 percent concentration for first-year ice, corresponds to 56.5 percent concentration for multiyear ice, as shown in Figure 3-39.

During periods of surface melting, when first-year and multiyear ice are indistinguishable by passive

microwave measurements (Section 3.3), the appropriate scale for both ice types is the scale on the left. Differences between wet and dry first-year ice, which are about 3 percent, are neglected in the nomogram.

In using the nomogram, a given mapped color is associated with a unique ice concentration only if the multiyear ice fraction F_{MY} is known. For instance, in seasonal sea ice regions with only first-year ice, $F_{MY} = 0$ and the appropriate scale is the scale on the left of the nomogram. By contrast, in locations where the observed ice field is believed to be totally multiyear ice ($F_{MY} = 1$) then the appropriate scale is on the right of the nomogram. If no information is known about the multiyear ice fraction, then the nomogram provides a range of ice concentrations for each mapped color. For instance, the second orange level indicates an ice concentration anywhere from 52 percent (if there is no multiyear ice) to 68 percent (if the ice is all multiyear ice). The nomogram can also be used in an inverse manner to determine the multiyear ice fraction, if there is independent knowledge (or an estimate) of the total ice concentration. This will be done in several cases in Chapter 4 for locations where the total ice concentration is believed to be very close to 100 percent.

3.7 ERROR ANALYSIS

Among the sea ice parameters presented in this volume are ice concentration, areal ice extent, and actual ice area. The errors in the calculations of these parameters can be inferred directly from the errors in the following quantities: the observed brightness temperatures, the brightness temperature selected as typical of open water, the physical temperature of the ice estimated from climatology, and the emissivity assumed for consolidated ice. The errors in these quantities can be classified as either random or systematic, the random errors being those associated with statistical fluctuations or uncertainties, some of which can be inferred from the data, and the systematic errors being those associated with undetermined biases.

In order to describe the random errors in the determination of ice concentrations, it is useful to form the differentials of the following modified form of equation 3-5, incorporating atmospheric effects:

$$C = \frac{T_B - T_{Bw}}{\epsilon_i T_i - T_{Bw}}, \quad (3-19)$$

where

T_B is the observed brightness temperature,
 T_{Bw} is the brightness temperature over open water, including atmospheric effects, and
 $T_{Bi} = \epsilon_i T_i$ is the brightness temperature of the ice.

The partial differentials of C with respect to the four variables on the right-hand side of equation 3-19 are:

$$\frac{\partial C}{\partial T_B} = \frac{1}{\epsilon_i T_i - T_{Bw}}, \quad (3-20)$$

$$\frac{\partial C}{\partial T_{Bw}} = \frac{-(1-C)}{\epsilon_i T_i - T_{Bw}}, \quad (3-21)$$

$$\frac{\partial C}{\partial \epsilon_i} = -\frac{C(T_i)}{\epsilon_i T_i - T_{Bw}}, \quad (3-22)$$

and

$$\frac{\partial C}{\partial T_i} = -\frac{C \epsilon_i}{\epsilon_i T_i - T_{Bw}}. \quad (3-23)$$

Because the four variables T_B , T_{Bw} , ϵ_i , and T_i are assumed independent, their total contribution to the error in calculating C may be obtained from the root mean square of their individual fluctuations multiplied by the above partials, namely,

$$dC = \left[\left\{ \frac{\partial C}{\partial T_B} (dT_B) \right\}^2 + \left\{ \frac{\partial C}{\partial T_{Bw}} (dT_{Bw}) \right\}^2 + \left\{ \frac{\partial C}{\partial \epsilon_i} (d\epsilon_i) \right\}^2 + \left\{ \frac{\partial C}{\partial T_i} (dT_i) \right\}^2 \right]^{1/2}, \quad (3-24)$$

where dC , dT_B , dT_{Bw} , $d\epsilon_i$, and dT_i are the errors in C , T_B , T_{Bw} , ϵ_i , and T_i , respectively.

Equation 3-24 is used for generating curves of the uncertainty in ice concentration as a function of ice

concentration based on the uncertainties in the four variables T_{Bw} , T_B , T_i , and ϵ_i . Three such curves are shown in Figure 3-40. For curve A, the errors selected for each of the four variables were the estimated standard deviations (σ). For curve B they were twice the estimated σ 's, and for curve C they were three times the estimated σ 's, with the exception of dT_{Bw} , for which a value of 9 K was used rather than 12 K ($= 3\sigma$) because T_{Bw} is not observed during the 4-year period 1973 through 1976 to vary from its mean by more than 9 K. The estimation of the standard deviations was as follows:

(1) For $d\epsilon_i$, a Gaussian curve was fitted to the consolidated-ice portion of the monthly average histogram of the brightness temperatures for the Bering Sea region in Figure 3-35. This yielded a value of 8 K for the standard deviation of the brightness temperature of consolidated ice, T_{Bi} , which translates to a standard deviation of about 0.03 for ϵ_i , assuming a mean physical temperature of 250 K. [Coincidentally, the 3σ value of 0.09 for $d\epsilon_i$ used in curve C is approximately the difference in emissivities of first-year and multiyear sea ice.]

(2) For dT_{Bw} , a Gaussian curve was fitted to the open-ocean portion of the monthly average histogram of brightness temperatures (Figure 3-35), yielding $\sigma \approx 3$ K.

(3) For dT_i , a comparison was made between temperatures derived from THIR data in various seasons and climatic means for the same area. The comparison revealed that the difference between the THIR data and climatology is as large as 15 K (a combination of temporal and spatial fluctuations), but the standard deviation of the difference is only about 5 K. Hence for dT_i , a value of 5 K was selected for σ .

(4) For dT_B , which reflects variations caused by instrument noise, the root-mean-square noise is estimated to be 3 K for a single image field of view for the ESMR. Taking into account the ESMR duty cycle, overlap between scans, and average swath overlap in the polar region, approximately 62 observations are used in each pixel of the monthly average images shown here. Hence the root-mean-square noise is reduced to about 0.38 K.

Finally, before determining values of the differentials in equations 3-20 through 3-23 for the calculations for equation 3-24, a value of 100 K was used to approximate the denominator $\epsilon_i T_i - T_{Bw}$.

It can be seen from Figure 3-40 that the maximum errors in calculating sea ice concentrations occur for high concentrations, due primarily to the uncertainties in T_i and ϵ_i , which include the complications arising from the use of climatological temperatures rather than actual temperatures and the uncertainties in ice type. Instrument noise is a minor contributor to the errors for all values of C , and fluctuations in the weather, which increase the uncertainty in T_{Bw} , are the major contributors near the ice edge and over the open oceans.

Turning from random to systematic errors, when the first-year ice emissivity of 0.92 is used, a large systematic error in ϵ_i is introduced in areas with considerable multiyear ice, which has an emissivity of approximately 0.84. Within these areas, particularly in the central Arctic Ocean and much of the Canadian Archipelago, the value of 0.03 given earlier as the general overall sigma for the emissivity is appropriate. However, in areas where first-year ice is known to predominate, such as the Bering, Okhotsk, and Barents Seas, a sigma of 0.01 would be more appropriate in the winter months. The reader is referred to Wilheit et al. (1972) and Carsey (1982) for further evaluations of first-year and multiyear ice emissivities in the Arctic.

The use of climatological surface air temperatures in calculating T_i introduces a possible systematic error in T_i due to interannual variability in the surface air temperature. There is also the error introduced by the uncertainty in the appropriateness of the linear relationship (equation 3-16) used between air temperature and the radiating temperature of the ice, as discussed in the previous section.

If the random errors generated for the winter months are used in the summer months, a systematic error arises as a result of changes in the electrical properties of the ice such as those discussed in Sections 3.2 and 3.3. The details of these changes are sufficiently varied to prevent a precise error analysis, but the results suggest an emissivity of 0.92 ± 0.04 for both first-year and multiyear ice types during summer. Measurements made by Grenfell and

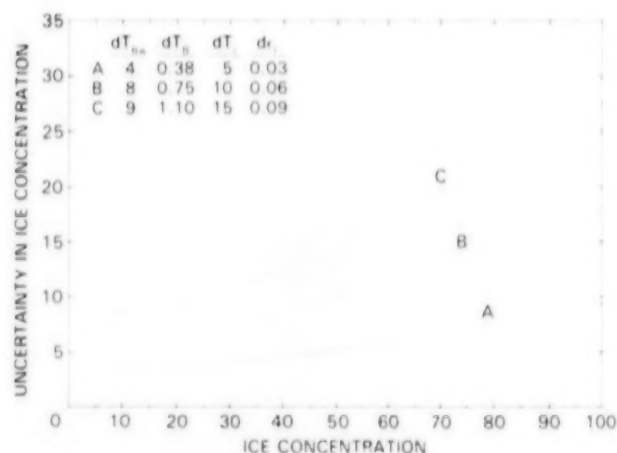


Figure 3-40. Uncertainty in calculated ice concentration as a function of ice concentration, presented for three combinations of errors in the brightness temperature of the water, T_{Bw} , the overall brightness temperature, T_B , the ice interface temperature, T_i , and the ice emissivity, ϵ_i .

Lohanick (1985) in the Canadian Arctic are consistent with this range.

Another systematic error is known to occur in the summer melt period as a result of the formation of unresolved melt ponds and the interpretation of them as open water. This interpretation is appropriate for some purposes, such as climatological and boundary-layer calculations, but not for other purposes, such as ship routing and heat balance studies.

A principal consideration for the analysis of ice coverage is the effect of the uncertainties in the determination of ice concentration on the calculation of the areal extents of ice. Plots of ice extent, actual ice area, and area of ice in various concentration classes are presented in Chapter 4 for the north polar region as a whole and for eight subregions. The areas are determined by using the derived ice concentration as a basis for binning the gridded data. To evaluate the sensitivity of these distributions to the previously discussed errors in ice concentration, a set of three curves was generated for each of five ice concentration categories, presenting the seasonal cycle of the area of ocean containing ice in that category. The middle curve in each set is based on concentrations calculated from equation 3-5 with T_B set at the observed brightness temperature, ϵ_i set at 0.92, T_i determined from equation 3-16, and $\epsilon_w T_w$ replaced

by T_{bw} and set at 138.3 K. The other two curves are based on concentrations calculated similarly, although with T_b , ϵ_i , T_i , and T_{bw} altered according to the uncertainties associated with curve A in Figure 3-40. These sample curves are presented in Figure 3-41 for the entire north polar region and in Figures 3-42 and 3-43 for eight subregions. In each of the plots, the most sensitive distribution is for the highest ice concentrations (the > 85 -percent curve), with the maximum error occurring in the middle of winter. Part of the reason for this sensitivity is the smearing out of the signature of consolidated ice by the presence of both first-year and multiyear ice, with their contrasting microwave emissivities. The cutoff in the > 85 -percent distribution could be near the middle of the multiyear ice spectrum. At the > 65 -percent distribution, the sensitivity is less because most of the consolidated winter ice, whether first-year or multiyear, is included. The sensitivity also lessens as more data are included, so that the ice extent curve (defined as ice of concentration greater than 15 percent) is the least sensitive of any of the curves.

For the curves of Chapter 4, the areal ice coverages are calculated using an ice emissivity of 0.92, appropriate for first-year ice. In regions with multiyear ice as well as first-year ice, the vertical axes of these curves are labeled "pseudo sea ice area" rather than "sea ice area" because of the considerable error introduced by using the first-year ice emissivity. Tables 3-1 and 3-2 show the effect on the sea ice area calculations, for regions with multiyear ice, of changing from an emissivity of 0.92 to the multiyear ice emissivity of 0.84. In Table 3-1 late-summer results are shown for 1974 and 1975, and in Table 3-2 midwinter results are shown for the subsequent Januarys. The percent deviations in September in the individual regions and in the full north polar region are similar in the 2 years, with values of 26 percent in the Arctic Ocean and 27 percent overall for both years. The Kara and Barents Seas show a greater percent deviation in 1975, but that is largely accounted for by the small ice cover in that region in that year.

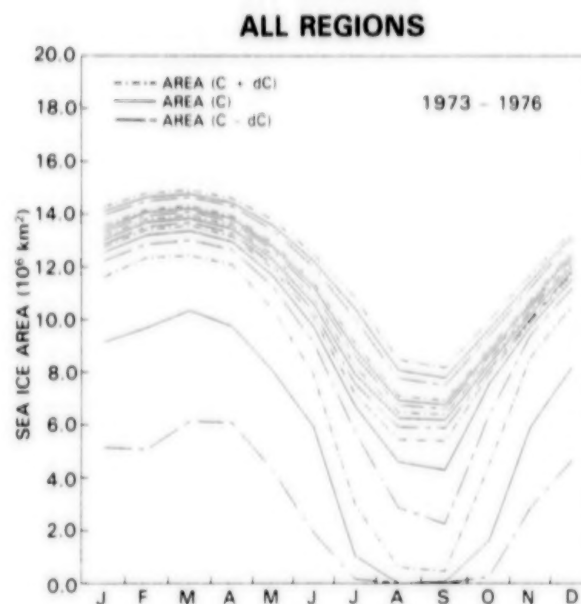


Figure 3-41. Sensitivity of sea ice area determinations to the magnitude of uncertainties in T_{bw} , T_b , T_i , and ϵ_i indicated under category A in Figure 3-40. The areas are calculated for most of the sea ice covered region in the Northern Hemisphere, explicitly for the sum of the eight regions identified in Figure 4-2. The solid curve in each group of three curves represents, for pseudo ice concentrations calculated with an emissivity of 0.92, the area covered by sea ice with pseudo concentrations equal to or greater than 15, 35, 50, 65, and 85 percent, respectively (top to bottom).

In addition to the pseudo ice area calculated with an emissivity of 0.92, Table 3-2 includes both a corrected ice area incorporating the results of Table 3-1 and an estimated multiyear ice percentage determined by dividing the ice area for the preceding September by the corrected January value. The percent errors in January, equal to the difference between the corrected and pseudo ice areas divided by the pseudo ice area, range from 2 to 17 percent.

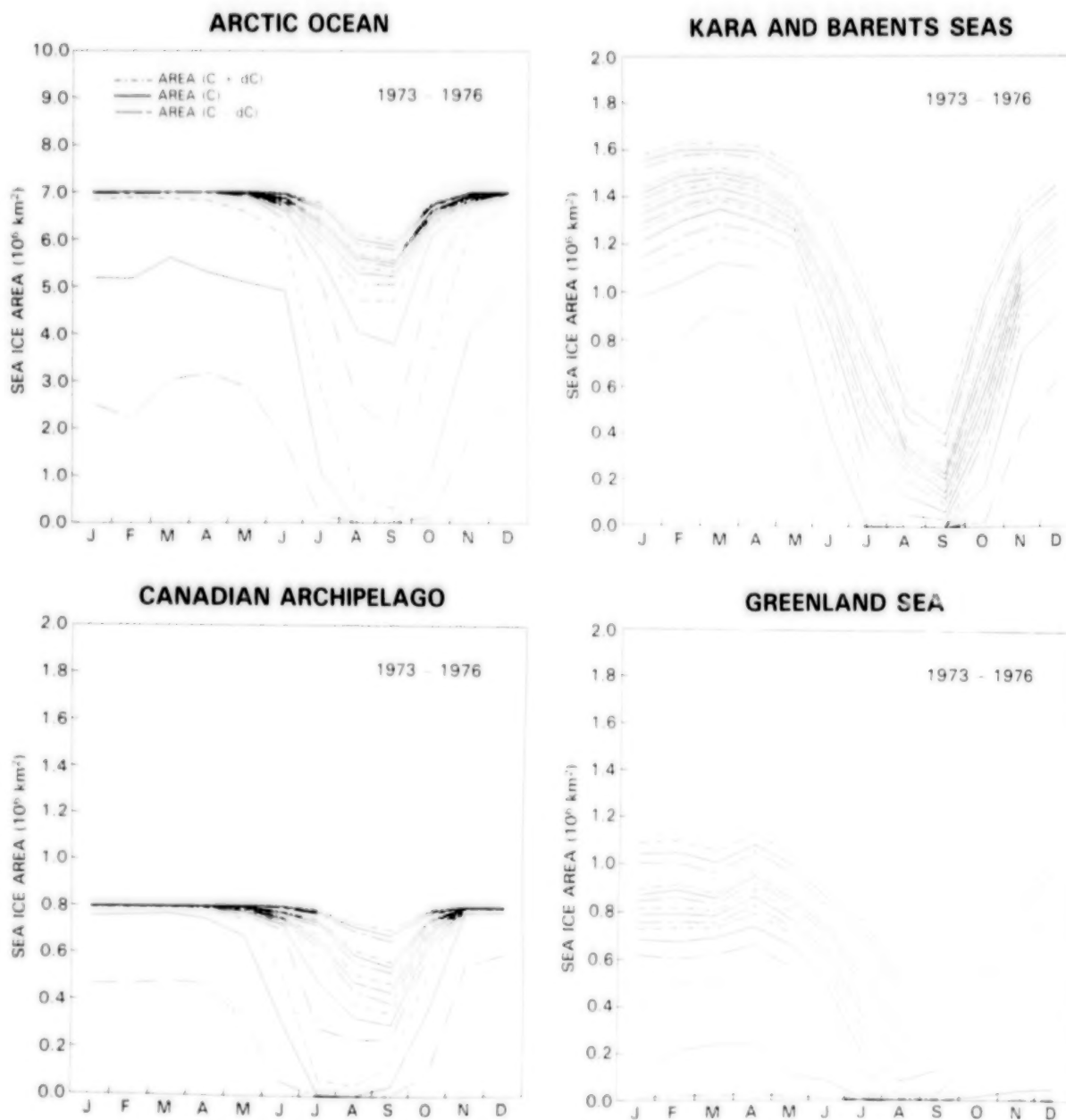


Figure 3-42. Sensitivity of sea ice area determinations to the magnitude of uncertainties in T_{Bw} , T_B , T_i , and ϵ_i indicated under category A in Figure 3-40 for the following regions: Arctic Ocean, Kara and Barents Seas, Canadian Archipelago, and Greenland Sea. The boundaries of these regions are identified in Figure 4-2, and the solid curve for each group of three curves is determined as in Figure 3-41.

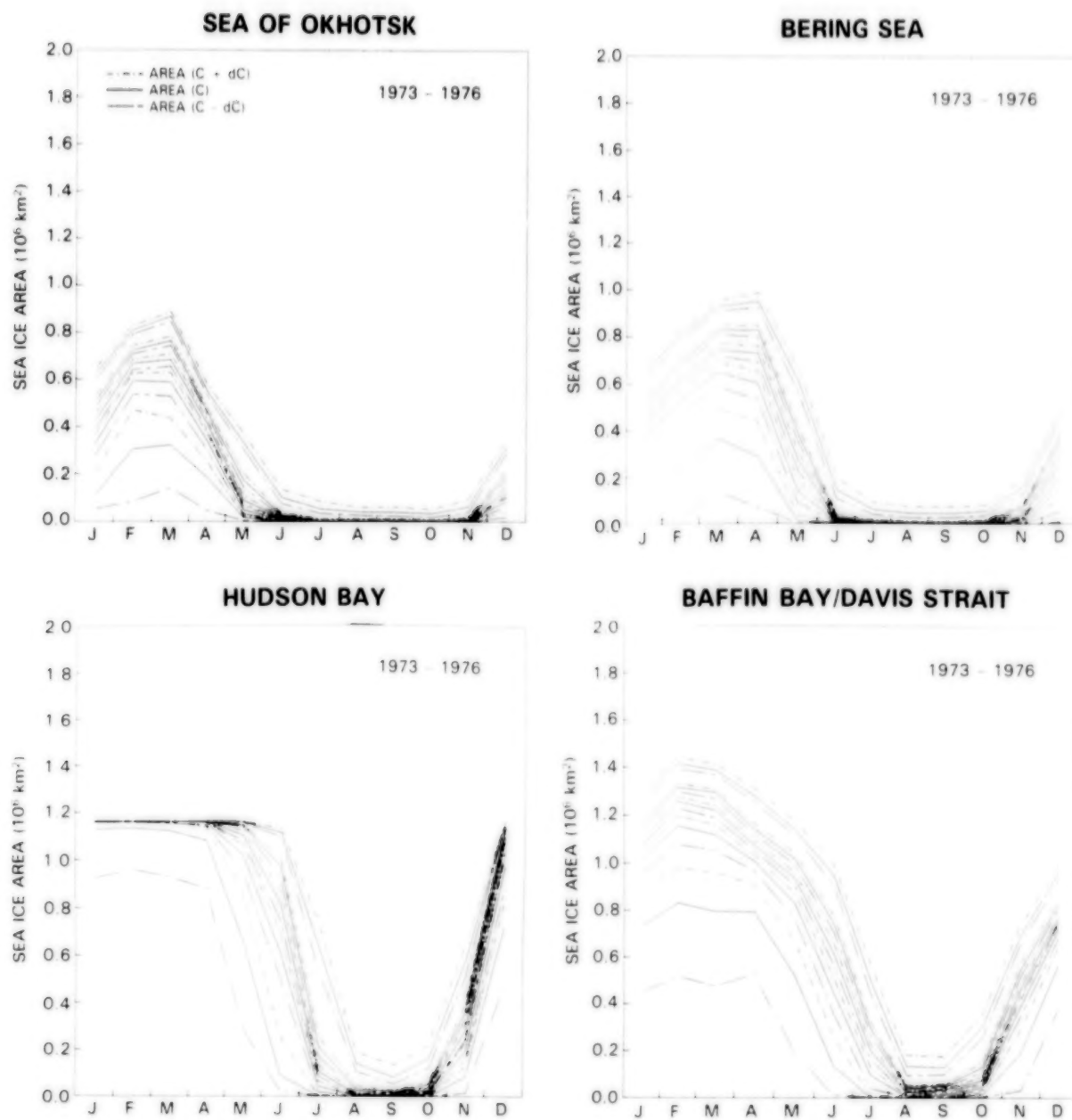


Figure 3-43. Sensitivity of sea ice area determinations to the magnitude of uncertainties in T_{Bw} , T_B , T_I , and ϵ_I indicated under category A in Figure 3-40 for the following regions: Sea of Okhotsk, Bering Sea, Hudson Bay, and Baffin Bay/Davis Strait. The boundaries of these regions are identified in Figure 4-2, and the solid curve for each group of three curves is determined as in Figure 3-41.

Table 3-1
September Ice Cover Determinations (10^6 km^2) and Percent Deviations (%)

Region	1974				1975			
	Using $\epsilon = 0.84$	Using $\epsilon = 0.92$	ΔA	% Δ	Using $\epsilon = 0.84$	Using $\epsilon = 0.92$	ΔA	% Δ
Arctic Ocean	4.327	3.433	0.894	26	5.210	4.141	1.069	26
Greenland Sea	0.301	0.237	0.064	27	0.367	0.286	0.081	28
Kara and Barents Seas	0.365	0.278	0.087	31	0.073	0.046	0.027	59
Canadian Archipelago	0.488	0.392	0.096	24	0.482	0.385	0.097	25
Full North Polar Region	5.603	4.406	1.197	27	6.272	4.938	1.334	27

Table 3-2
January Ice Cover Determinations (10^6 km^2) and Percent Deviations (%)

Region	1975				1976			
	Using $\epsilon = 0.92$	Corrected*	% MY**	% Error	Using $\epsilon = 0.92$	Corrected*	% MY**	% Error
Arctic Ocean	6.292	7.186	60.2	14.2	6.301	7.370	70.7	17.0
Greenland Sea	0.644	0.708	42.5	9.9	0.681	0.762	48.2	11.9
Kara and Barents Seas	1.183	1.270	28.7	7.4	1.334	1.361	5.4	2.0
Canadian Archipelago	0.753	0.849	57.5	12.7	0.756	0.853	56.5	12.8
Full North Polar Region	11.943	13.140	42.6	10.0	11.896	13.230	47.4	11.2

* "Corrected" is the sum of the pseudo ice area calculated with $\epsilon = 0.92$ and the deviation ΔA in the previous September.

** "% MY" is the quotient of the ice area in the previous September (using $\epsilon = 0.84$) and the corrected ice area in the current January.

SEASONAL SEA ICE CYCLE AND REGIONAL CHARACTERISTICS

4.1 INTRODUCTION

A primary feature of the Arctic Ocean and surrounding seas is the seasonal growth/decay cycle of sea ice, which is described in this chapter in detail for the 4 years, 1973 through 1976, of satellite ESMR coverage. The sea ice growth/decay cycle is driven both directly and indirectly by the annual cycle of solar insolation and the resultant cycles of air and ocean temperatures. Due to the thermal inertia of the ice and the importance of indirect processes involving the ocean and the atmosphere, on average maximum sea ice coverage follows minimum solar insolation by almost 3 months, and minimum sea ice coverage follows maximum solar insolation by almost 3 months. The seasonal sea ice cycle, however, varies significantly from one region to another and from year to year, as the plots and discussion of this chapter amply illustrate.

The characteristics of the sea ice growth/decay cycle (Figure 4-1) and its relationship to other atmospheric and oceanic variables provide information on interactive physical processes such as the relative influence on ice extent of ocean heat fluxes, ocean currents, direct solar radiation, winds, and air temperatures. Numerical models of sea ice have successfully simulated certain aspects of the growth/decay cycle by incorporating into the calculations various thermodynamic and dynamic processes affecting the sea ice cover (Campbell, 1965; Parkinson and Washington, 1979; Hibler, 1979; Hibler and Walsh, 1982). Often the failures as well as the successes of the models in reproducing the observed sea ice distributions help to explain elements of the nature of the interactions of the atmosphere, ocean, and sea ice. For instance, models ignoring the warm Norwegian Current consistently fail to produce the observed wintertime open water distributions in the Barents

Sea, confirming the importance of the Norwegian Current in maintaining local ice-free conditions.

This chapter describes the general characteristics of the growth/decay cycle of the Northern Hemisphere sea ice cover on a region-by-region basis. For the purpose of the analysis, eight regions have been defined (Figure 4-2) based on their geographic and sea ice characteristics. The Arctic Ocean is the largest region and contains the largest area and mass of perennial sea ice. The Sea of Okhotsk, Bering Sea, Hudson Bay, and Baffin Bay/Davis Strait regions all have distinct geographic boundaries around much of their borders and become essentially free of ice during the summer season. The Kara and Barents Seas are separated from the Arctic Ocean by a series of islands on their northern borders. The Greenland Sea provides the only deep-water connection to the Arctic Basin and receives a large amount of ice, on the order of 100,000 cubic meters per second (Aagaard, 1980), from the Arctic Ocean. The sea ice regime of the Greenland Sea, however, is quite distinct from that of the Arctic, because of the lower latitudes and the impact of the warm North Atlantic waters. Finally, the Canadian Archipelago region is unusual because its waters consist of channels and straits amongst numerous islands rather than forming a more coherent, relatively unbroken sea, bay, or ocean. The areas of the eight regions are as follows:

Region	Area (km ²)
Arctic Ocean	6,999,617
Sea of Okhotsk	1,206,649
Bering Sea	2,243,490
Hudson Bay	1,160,819

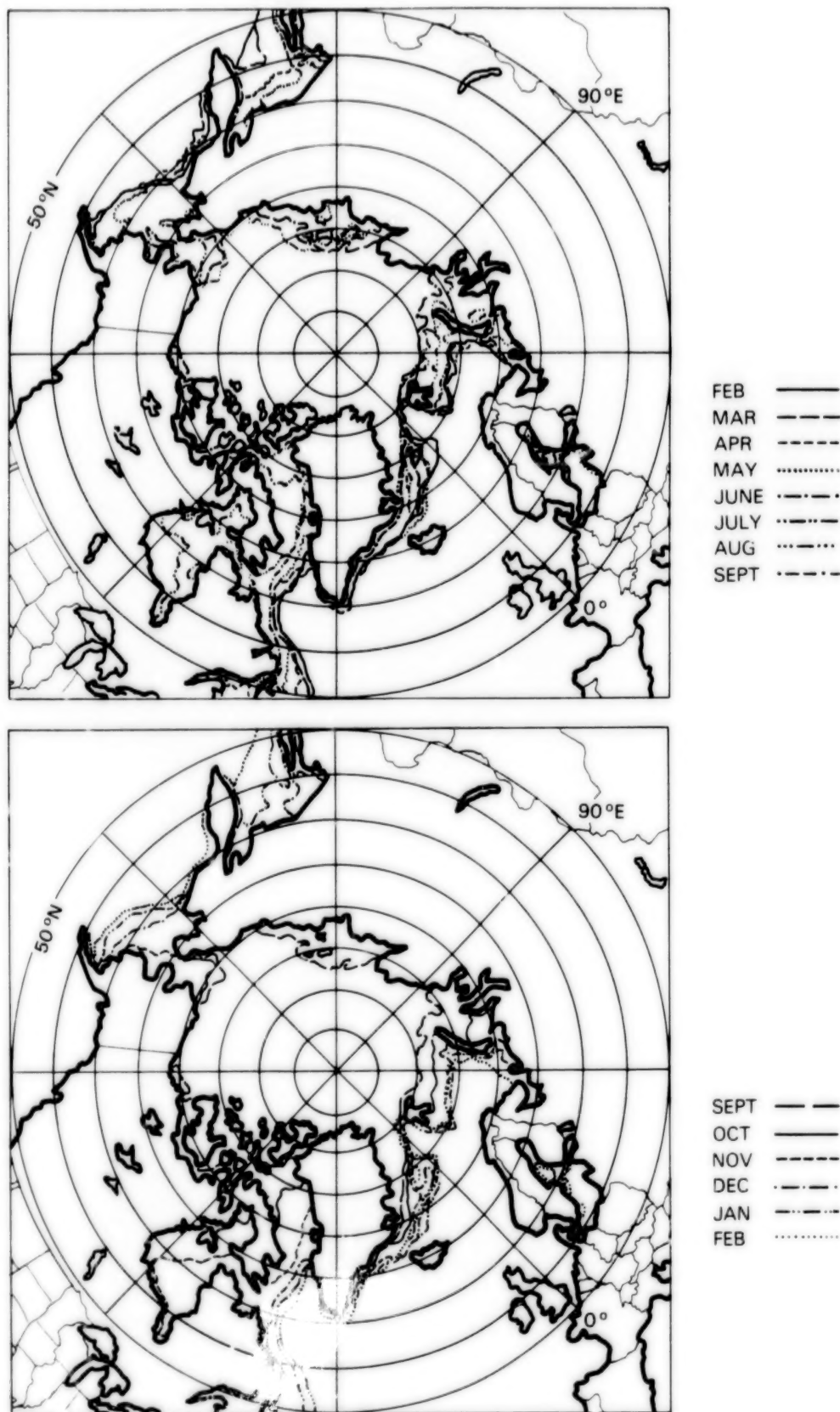


Figure 4-1. Monthly sea ice extents (concentration exceeding 15 percent) averaged for 1973-1976 during the growth and decay seasons. These extents are obtained from the ice concentration data mapped in Figures 4-3 through 4-8.

ORIGINAL PAGE
COLOR PHOTOGRAPH



- Sea of Okhotsk
- Bering Sea
- Hudson Bay
- Baffin Bay/Davis Strait
- Greenland Sea
- Kara and Barents Seas
- Arctic Ocean
- Canadian Archipelago

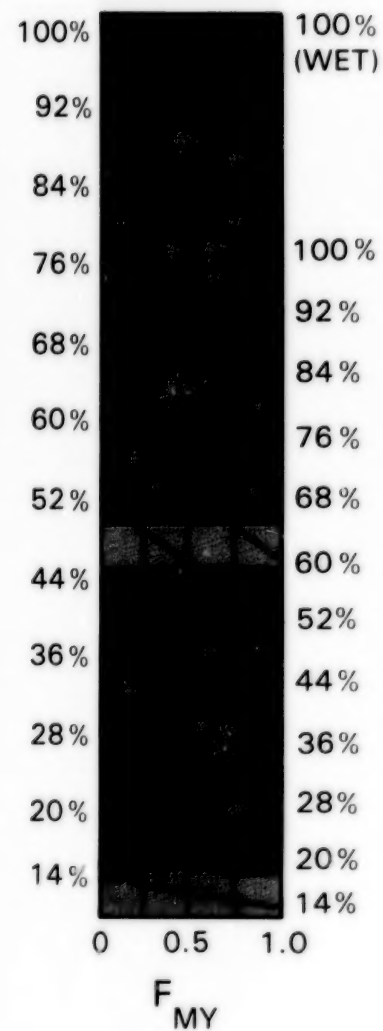
Figure 4-2. Regions used for analysis of observed sea ice cover.

Baffin Bay/Davis Strait	2,267,014
Greenland Sea	2,885,424
Kara and Barents Seas	2,346,032
Canadian Archipelago	799,068
Total	19,908,113

Sections 4.2 through 4.9 deal in turn with each of the regions, with each section including a description of the basic sea ice cycle as reflected in ESMR data averages over the 4 years 1973 through 1976, followed by a highlighting of various interannual differences amongst the 4 years.

The sea ice concentrations presented in the maps and plots are calculated from the ESMR microwave brightness temperatures and climatological surface air temperatures as described in Section 3.6. The nomograms displayed with each of the ice concentration images (and earlier in Figure 3-39) take into account the marked contrast in emissivities between first-year and multiyear ice. Detailed descriptions of the basis of the ice concentration calculations and the meaning and use of the nomograms are presented in Section 3.6.

The monthly average sea ice concentrations for the individual years 1973 through 1976 are combined to produce 4-year monthly averages (Figures 4-3 through 4-8). For months when usable data were not obtained for all 4 years, the maps depict either 2- or 3-year averages, as identified in each case in the map heading. Images of month-to-month differences



ORIGINAL PAGE
COLOR PHOTOGRAPH

Figure 4-3. Four-year-average mean monthly sea ice concentrations for January and February, 1973-1976.

ORIGINAL PAGE
COLOR PHOTOGRAPH

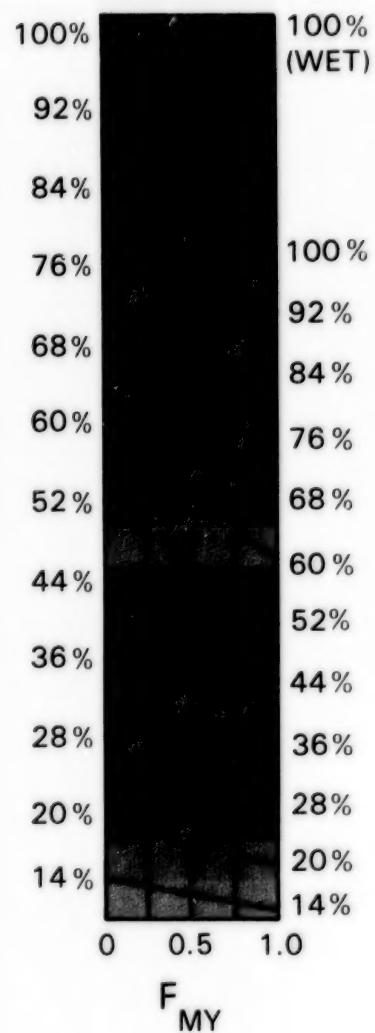


Figure 4-4. Three-year-average mean monthly sea ice concentrations for March and April, 1974-1976.



ORIGINAL PAGE
COLOR PHOTOGRAPH

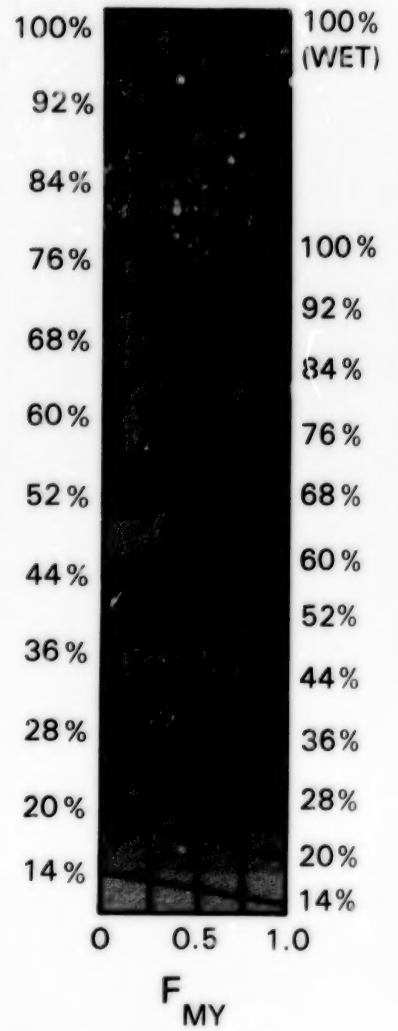


Figure 4-5. Three-year-average mean monthly sea ice concentrations for May 1974-1976 and June 1973, 1974, and 1976.

ORIGINAL PAGE
COLOR PHOTOGRAPH

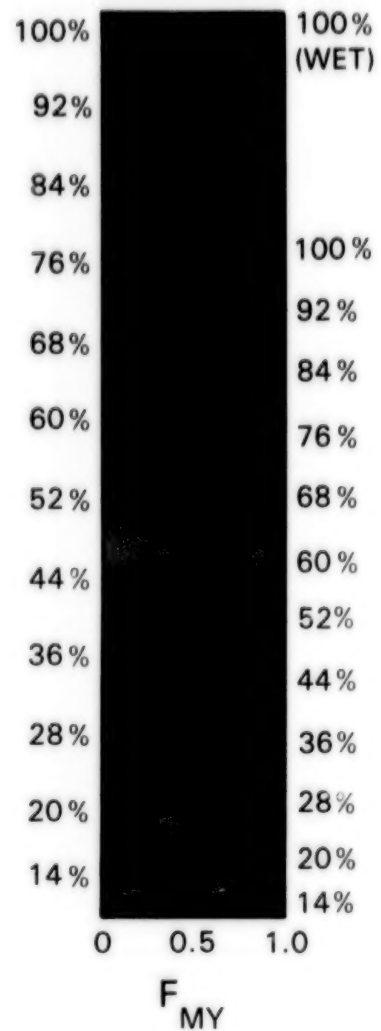
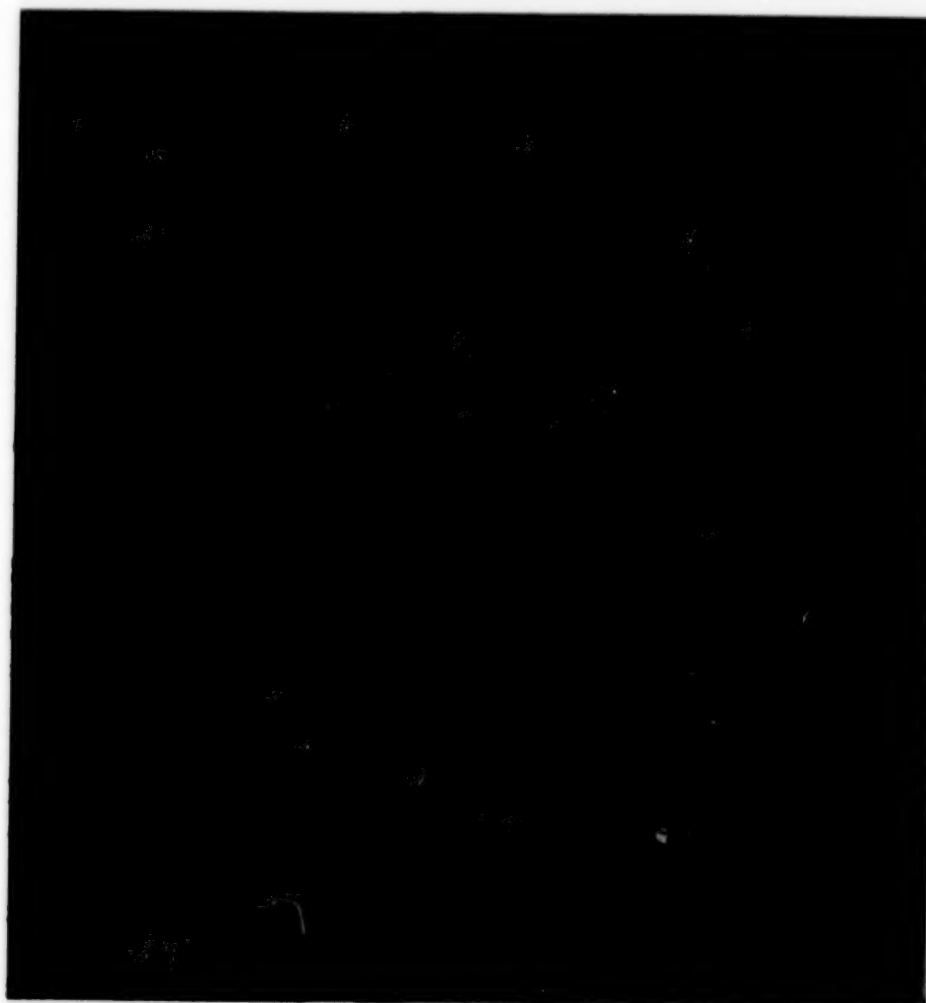


Figure 4-6. Three-year-average mean monthly sea ice concentrations for July 1973, 1974, and 1976 and 2-year-average concentrations for August 1974 and 1976.



**ORIGINAL PAGE
COLOR PHOTOGRAPH**

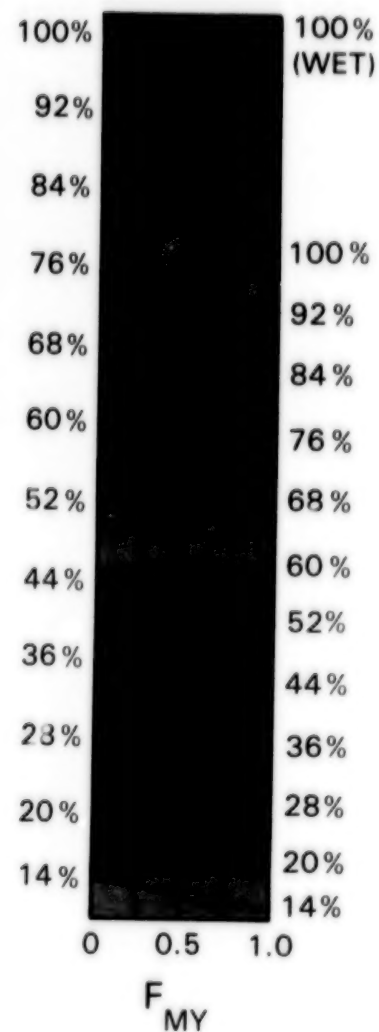


Figure 4-7. Four-year-average mean monthly sea ice concentrations for September and October, 1973-1976.

ORIGINAL PAGE
COLOR PHOTOGRAPH

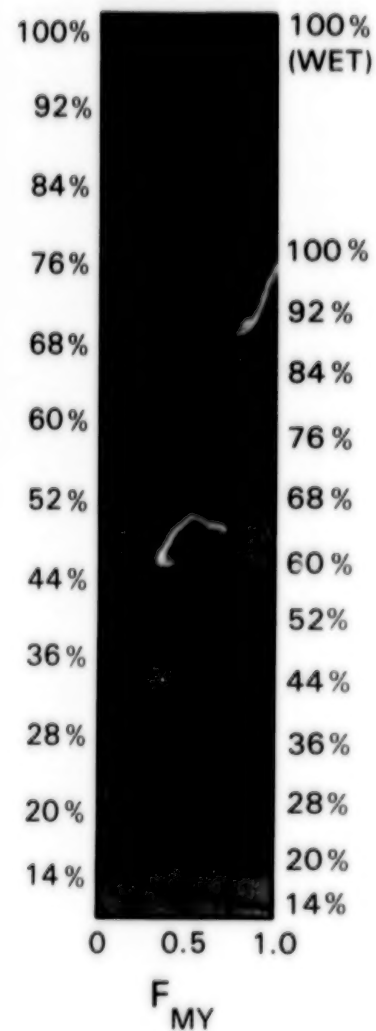
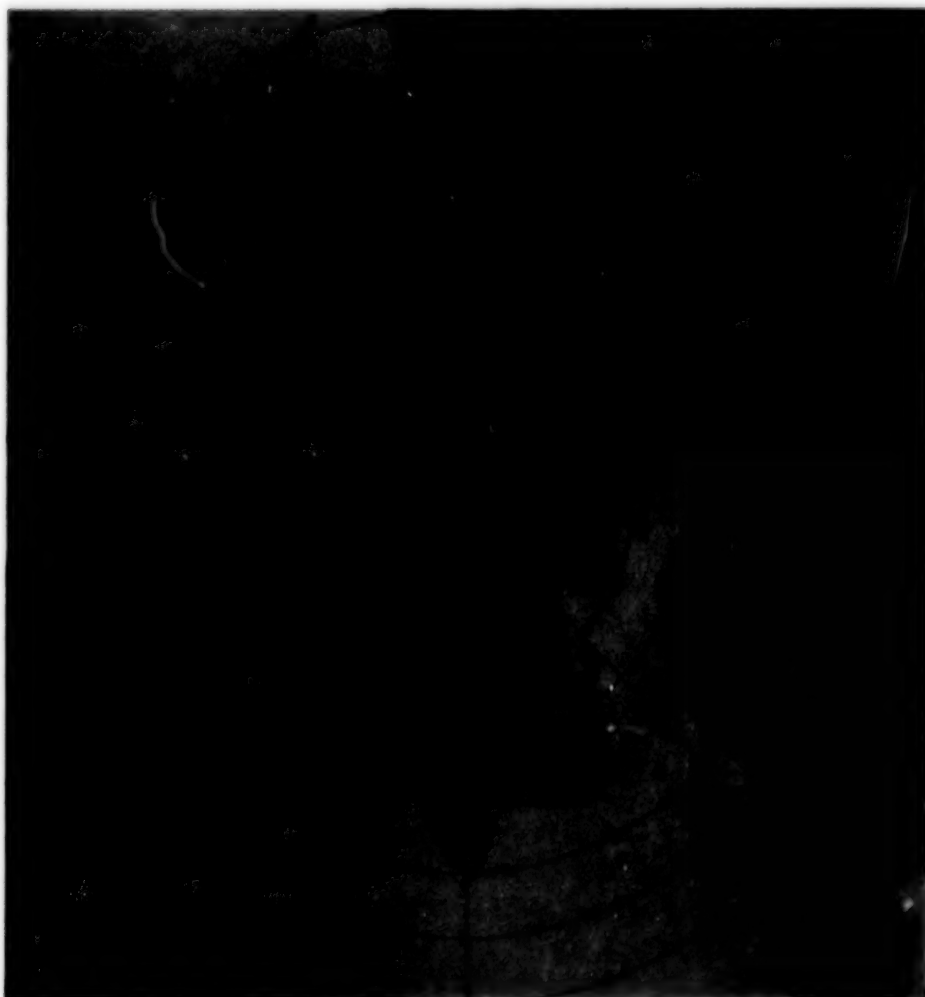


Figure 4-8. Three-year-average mean monthly sea ice concentrations for November and December, 1973-1975.

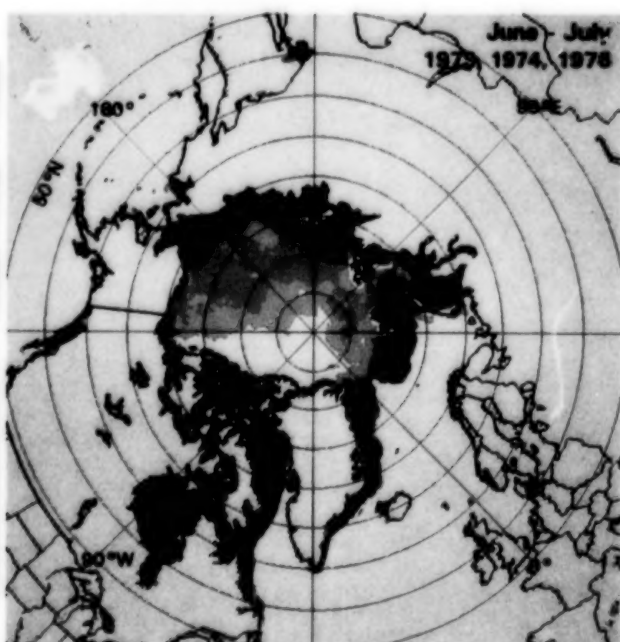
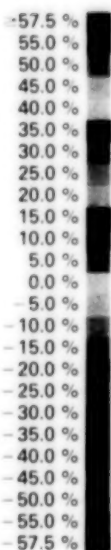
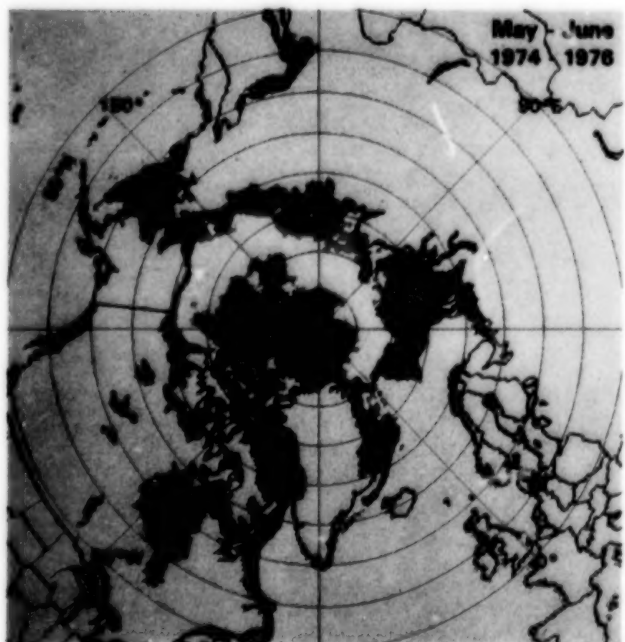
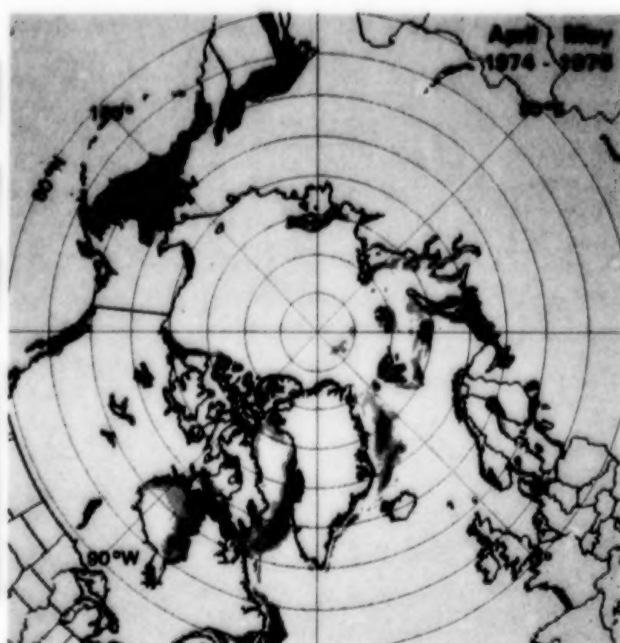
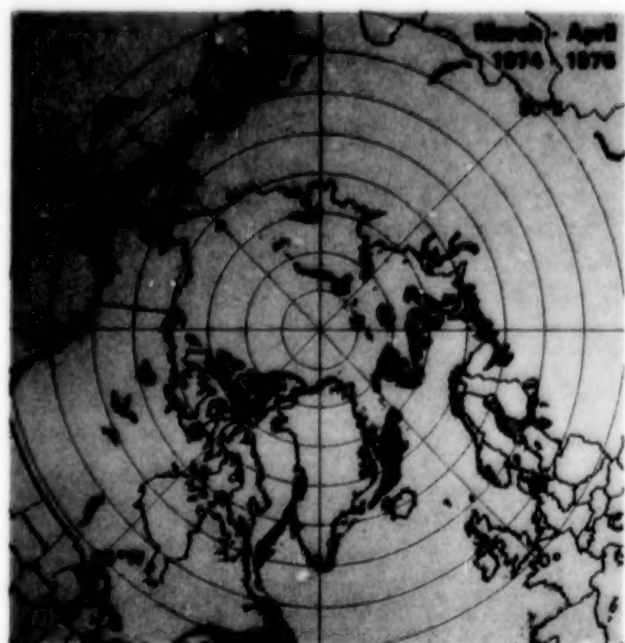
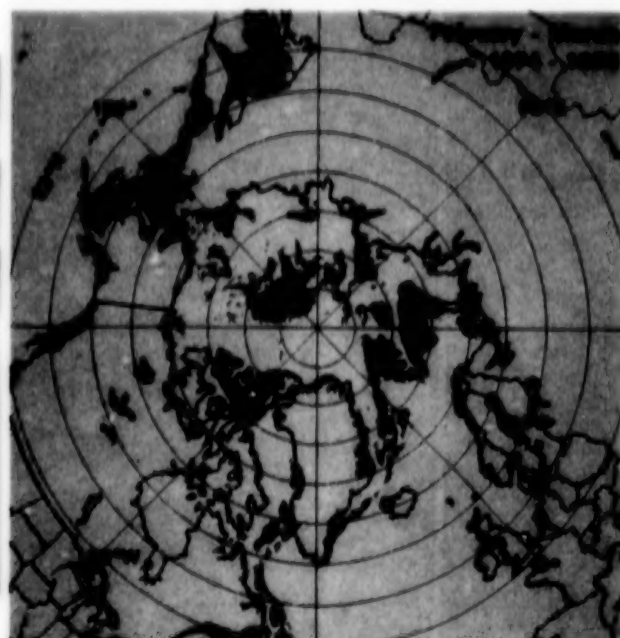
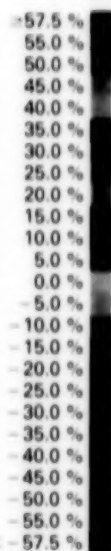
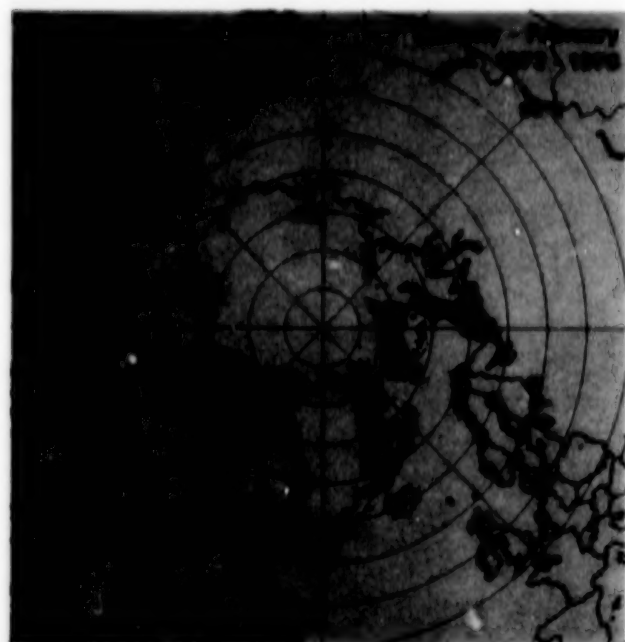
that have been color coded to clearly indicate the growth/decay on a monthly basis are shown in Figure 4-9. Reds, purples, and oranges, signifying a reduction of ice cover, predominate from the April-May map through the July-August map, whereas blues, greens, and grays, signifying an increase of ice cover, predominate from the September-October map through the January-February map, with the December-January and January-February maps both showing some regional decay in the midst of the more general growth patterns. The transition periods, represented by the August-September map and the February-March and March-April maps, show a mixture of growth and decay regions.

To quantify the spatial distribution of the ice cover and its seasonal cycle, the data represented in the ice concentration maps are spatially integrated to determine the area of ice cover as a function of time, resulting in the graphs shown in Figures 4-10 through 4-12. The areas of coverage are determined for the total ice extent, various ice concentration categories, and the actual ice area over the sum of the eight regions of Figure 4-2 and over each region individually. For each month, the area of ice-covered ocean (i.e., the total ice extent) is calculated by summing the areas of all map elements having at least 15-percent ice coverage. Likewise, for the regions with no or almost no multiyear ice, the areas of ocean covered by ice of at least 35-, 50-, 65-, and 85-percent concentration are determined by summing the areas of all map elements having at least those respective percentages of sea ice coverage. For the regions with a mixture of first-year and multiyear ice and for the sum of all regions, the same calculations are made, with an emissivity of 0.92 as for the first-year ice regions, but the results are labeled "pseudo sea ice area" rather than "sea ice area" and the curves are labeled " $\geq P35$ ", " $\geq P50$ ", " $\geq P65$ ", and " $\geq P85$ " rather than " $\geq 35\%$ ", " $\geq 50\%$ ", " $\geq 65\%$ ", and " $\geq 85\%$ ". Because of the sharpness of the ice edge and its weak sensitivity to the ice emissivity (Figures 3-41 through 3-43), it was not felt necessary to attach the adjective "pseudo" in the case of the 15-percent curves. The plots of Figures 4-10 through 4-12 also include the areas obtained by summing the products of the pseudo ice concentration (determined by using $\epsilon = 0.92$) and the geographic area of each map element. These are termed "actual ice areas" for regions with predominantly first-year ice and "pseudo actual ice areas" for regions where multiyear ice is a complicating fac-

tor. Details of the calculations can be found in Appendix A. Although the usefulness of the curves is reduced in regions with multiyear ice, because the multiyear ice emissivity of 0.84 has not been used in the calculations, the curves still indicate the basic seasonal cycle and some of the interannual variations.

To show more clearly the areal coverage of ice in each of the various concentration intervals, the data are plotted in Figures 4-13 through 4-15 for the intervals 15 to 35, 35 to 50, 50 to 65, 65 to 85, and 85 to 100 percent for regions with no or almost no multiyear ice and for the intervals 15 percent to P35, P35 to P50, P50 to P65, P65 to P85, and P85 to P100 for regions with the multiyear ice complication. In each case the calculations proceed by subtracting the appropriate curves from Figures 4-10 through 4-12. Also complementing Figures 4-10 through 4-12 and derived from them are plots of the average monthly change in total ice extent and the average percentage monthly change in total ice extent (Figure 4-16), plus plots of the average monthly change in pseudo actual ice area and the average percentage monthly change in pseudo actual ice area (Figure 4-17).

The same set of curves as plotted in Figures 4-10 through 4-15 for the 4-year averages have been created for each of the individual years and are presented in the following sections grouped according to region. Because of characteristics of the time averaging and spatial summation procedures, the areas derived from the 4-year averages differ slightly from the averages of the respective areas for the individual years, as explained further in Appendix A. For example, in winter the 4-year average ice extent is about 4 percent greater than the average of the 4 individual years, and in summer it is about 5.5 percent greater than the average in the individual years. For the actual ice area, the difference is smaller and in the opposite direction, with the 4-year average being about 0.6 percent less in winter and about 2.5 percent less in summer. These differences are caused by reversing the order of the time averaging and spatial summations and are about the same magnitude as the interannual variations. Consequently, the best absolute values are given by the data of the individual years. Nevertheless, the 4-year averages show the typical ice distributions and seasonal cycles. These plots, together with the 4-year monthly average images of sea ice concentrations (Figures 4-3



ORIGINAL PAGE
COLOR PHOTOGRAPH

ORIGINAL PAGE
COLOR PHOTOGRAPH

Figure 4-9a. Several-year-average sea ice concentration monthly change maps for January-February through June-July. Years included in the calculations, indicated in the upper right of each map, are those containing data for both months of the pair.

ORIGINAL PAGE
COLOR PHOTOGRAPH

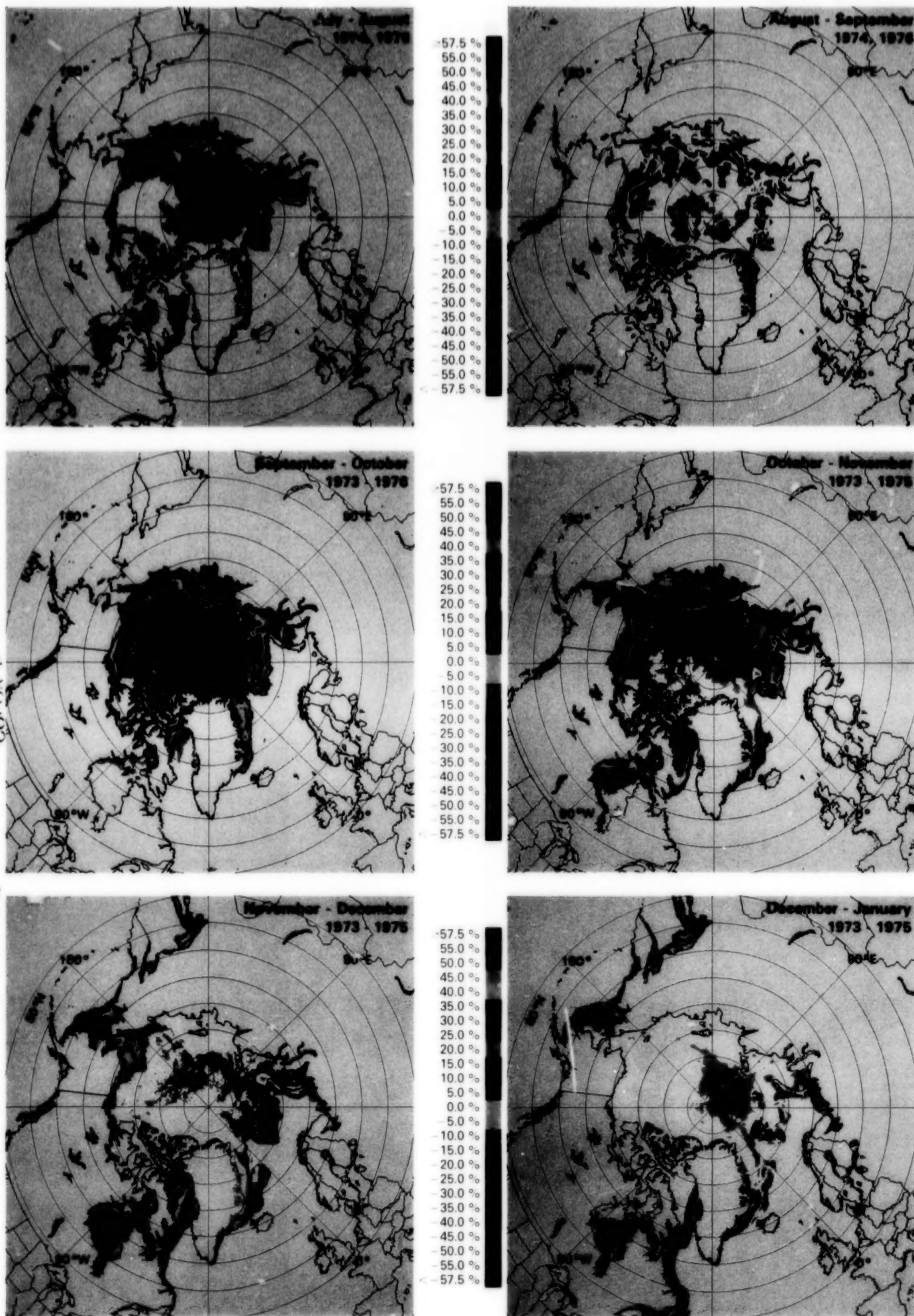


Figure 4-9b. Several-year-average sea ice concentration monthly change maps for July-August through December-January. Years included in the calculations, indicated in the upper right of each map, are those containing data for both months of the pair.

through 4-8), describe the seasonal cycle in detail and are referred to often in the following analyses of the ice covers of the individual regions.

During the seasonal growth/decay cycle, the Northern Hemisphere sea ice extent nearly doubles in area from summer to winter (Figure 4-10), compared to a five-fold variation in the southern ocean. [This hemispheric contrast should not be overinterpreted, as the magnitude of the summer/winter difference in the Northern Hemisphere increases when one considers the snow cover on land as well as the sea ice.] The extent reaches a minimum of 7.8×10^6 square kilometers during September, expands equatorward at a rate of 1.8×10^6 square kilometers per month from September to December, and continues expanding slowly to its maximum extent of 14.8×10^6 square kilometers in March (Figures 4-10 and 4-16). The ice edge retreats slightly from March to May, after which an increasingly rapid retreat occurs from May to August, with the retreat rate peaking at 2.3×10^6 square kilometers per month from July to August. A slight further retreat from August to September brings the ice to its September minimum (Figures 4-10 and 4-16).

An interesting characteristic of the overall growth/decay cycle is its nearly symmetrical pattern (Figure 4-10). This symmetry contrasts with the marked asymmetry in the southern ocean, where, at least over the years 1973 through 1976, the spring/summer melt is significantly faster than the fall/winter growth (*Antarctic Sea Ice, 1973-1976*). Walsh and Johnson (1979a), in an analysis of Arctic ice conditions over the much longer period 1953 through 1977, find an asymmetry in the average Arctic growth/decay cycle which is in the opposite direction to that in the Antarctic, with the Arctic ice growth period proceeding more rapidly than the decay period. Over the 4 years of the ESMR data, this and other aspects of the seasonal cycle differ from region to region, as will be seen in the more detailed discussions that follow.

Spatially, during the period of minimum ice extent in September (Figures 4-1 and 4-7), the ice pack is mostly confined to the central Arctic Ocean, with only a small amount of ice coverage in the Greenland Sea, the Kara and Barents Seas, and the Canadian Archipelago. Essentially no ice remains in the Bering Sea, Hudson Bay, the Sea of Okhotsk, and Baffin Bay/Davis Strait. At the maximum ice extent in

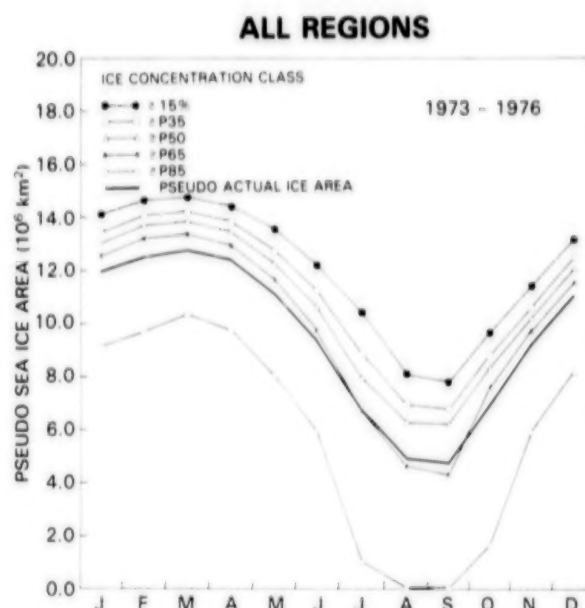


Figure 4-10. Four-year-average yearly cycle of the ocean area covered by sea ice with concentration exceeding 15 percent (ice extent), and 4-year-average yearly cycles of the P35, P50, P65, and P85 curves (for pseudo 35, 50, 65, and 85 percent, respectively) and the pseudo actual ice area, for the sum of the eight regions in Figure 4-2. The P35, P50, P65, and P85 curves are calculated as the ocean area covered with ice of concentration equal to or greater than 35, 50, 65, and 85 percent, respectively. The pseudo actual ice area is the integrated ocean surface area covered by sea ice, excluding leads and polynyas within the ice pack. The term pseudo is used for regions containing multiyear ice because the ice emissivity in the concentration calculations is the 0.92 value appropriate for first-year ice.

March, the ice covers the Arctic Ocean, Hudson Bay, the Kara Sea, the Canadian Archipelago, and large portions of the other peripheral seas and bays (Figure 4-4).

In visual interpretation of the map images, the effects of time averaging on the ice edge should be kept in mind. For instance, although the September image (Figure 4-7) provides a good indication of minimum ice coverage, the absolute minimum ice extent is somewhat less than the monthly average. In addition, the indicated low ice concentrations in the region of the ice boundary should not be interpreted as typical; in fact, at any time the transition from open water to highly concentrated ice is much sharper than shown. Because the ice edge moves over

the span of 1 month, the averaging process combines times of zero ice cover with times of positive ice cover beyond the typical ice boundary, reducing the sharpness of the calculated edge. Finally, because of 4-year arithmetic averaging, the position of the ice edge on the 4-year-average maps will be biased toward the position of the edge in the year with the greatest ice extent.

Figures 4-18 through 4-29 present the individual monthly average ice concentration images, grouped

by month to allow ready identification of interannual differences. These images are followed by a set of ice concentration difference maps for the individual years (Figures 4-30 through 4-37). Both sets of maps reveal that in general each of the 4 years has the same basic seasonal sea ice cycle as previously described for the 4-year-average maps (Figures 4-3 through 4-9) but that each year also has noticeable differences, many of which are identified in Sections 4.2 through 4.9.

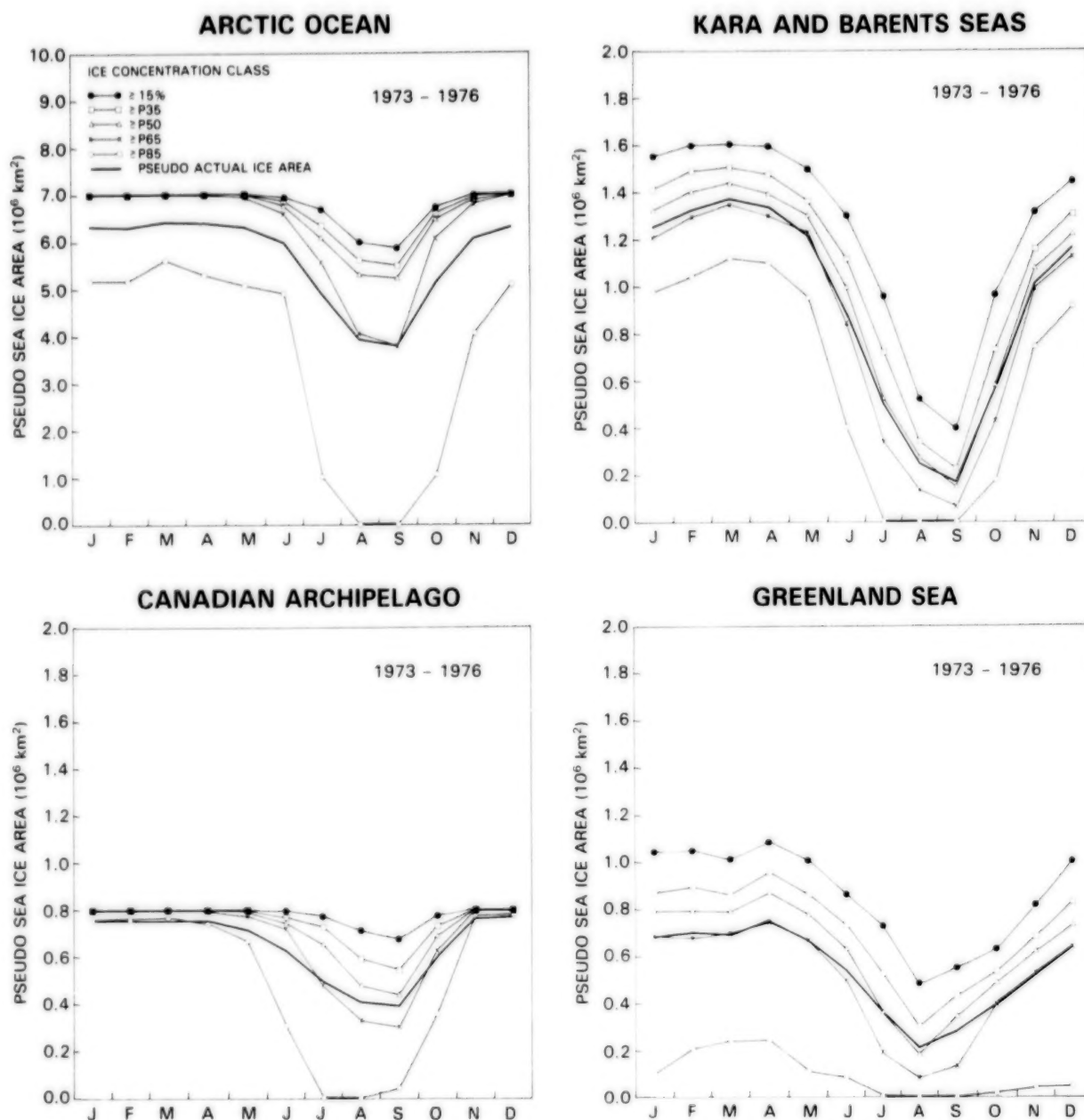


Figure 4-11. Four-year-average yearly cycle of the ocean area covered by sea ice with concentration exceeding 15 percent (ice extent), and 4-year-average yearly cycles of the P35, P50, P65, and P85 curves and the pseudo actual ice area, for the following regions: Arctic Ocean, Kara and Barents Seas, Canadian Archipelago, and Greenland Sea. The curves are determined as in Figure 4-10.

The following sections provide a detailed discussion of the sea ice cover on a regional basis. The discussion in each of the sections utilizes the monthly averaged and 4-year monthly averaged images in Figures 4-3 through 4-9 and 4-18 through 4-37 and the 4-year monthly averaged seasonal cycles plotted in Figures 4-10 through 4-15. Each section also includes a location map and a set of plots for the individual region. These latter plots are: the seasonal cycle of the areas of ice in the various ice concentration

classes (or pseudo ice concentration classes in the cases of regions with a multiyear ice component) for each year; the seasonal cycle of the areas of ice in the various ice concentration intervals (or pseudo ice concentration intervals) for each year; the year-to-year changes in sea ice extent, plotted by month; the year-to-year changes in actual ice area (or pseudo actual ice area), plotted by month; the year-to-year changes in open water area (or pseudo open water area), plotted by month; and the year-to-year

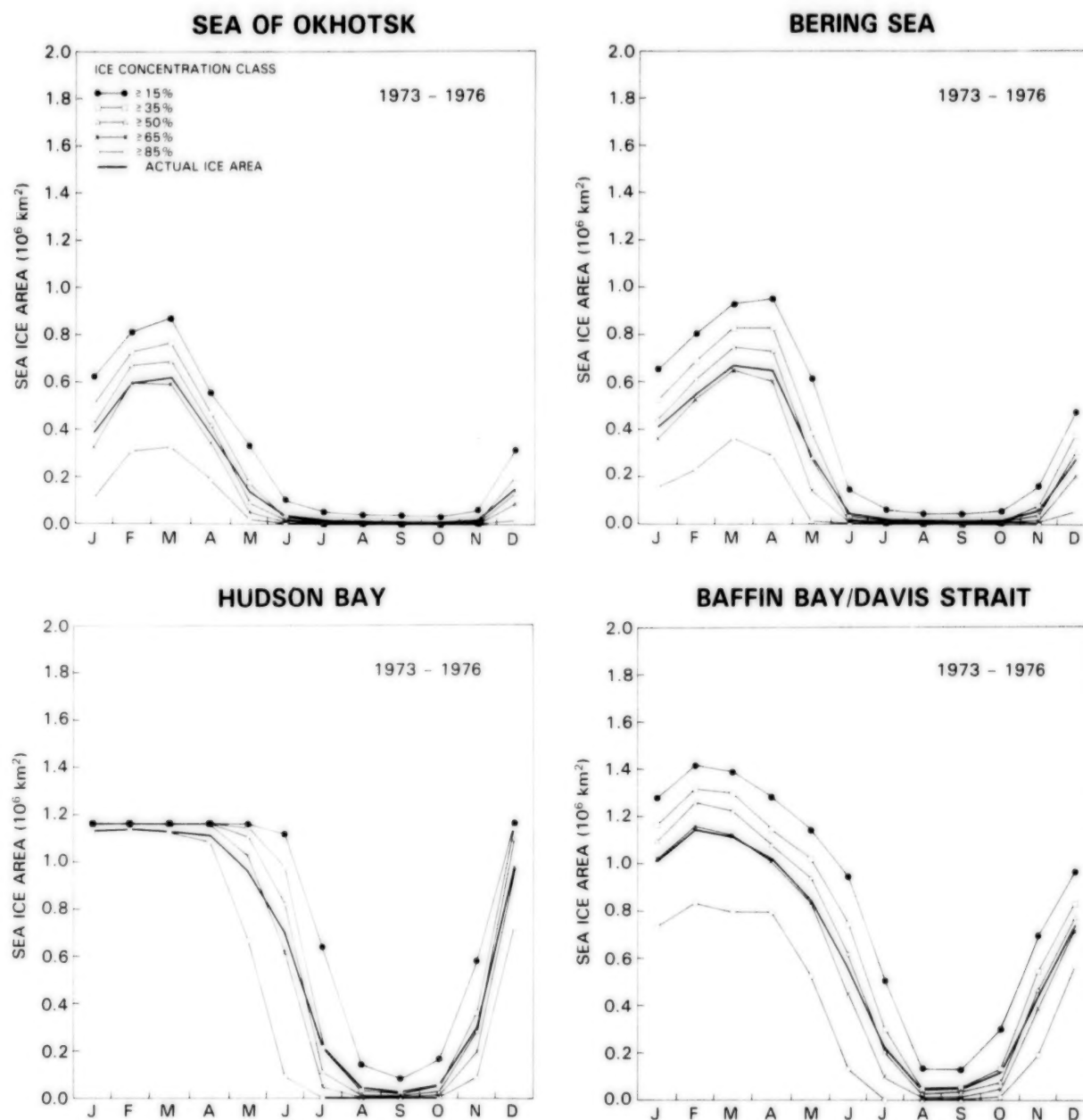


Figure 4-12. Four-year-average yearly cycle of the ocean area covered by sea ice with concentration exceeding 15 (ice extent), 35, 50, 65, and 85 percent, and 4-year-average yearly cycle of the actual ice area for the following regions: Sea of Okhotsk, Bering Sea, Hudson Bay, and Baffin Bay/Davis Strait. The actual ice area is the integrated ocean surface area covered by sea ice, excluding leads and polynyas within the ice pack.

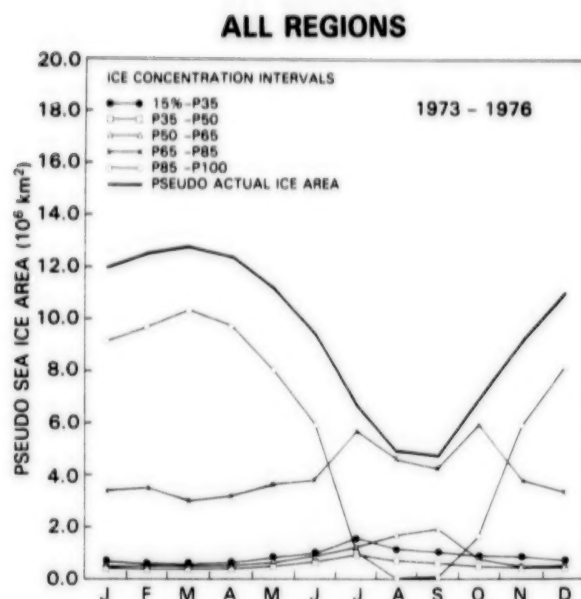


Figure 4-13. Four-year-average yearly cycle of the ocean area covered by sea ice within the intervals 15 percent to P35, P35 to P50, P50 to P65, P65 to P85, and P85 to P100, and 4-year-average yearly cycle of the pseudo actual ice area, for the sum of the eight regions in Figure 4-2. The interval curves are calculated by subtracting the respective curves of Figure 4-10.

changes in mean ice concentration (or pseudo mean ice concentration), plotted by month. The corresponding set of plots is presented for the sum of all eight regions in Figures 4-38 through 4-40. Note that the values in these plots are for the sum of the eight regions and not for the total Northern Hemisphere ice cover. Regions south of the image area, in particular the Sea of Japan and much of the coast of Newfoundland, are excluded. One region within the image area which is not included in the region-by-region analysis or in the area calculations for Figures 4-38 through 4-40, although is included in the color images, is the Baltic Sea and surroundings. The reader is referred to SMHI (1982) for an atlas of ice conditions in this area during the period 1963 through 1979.

4.2 ARCTIC OCEAN

Human perceptions of the high north polar region (Figure 4-41) have had a varied and colorful history. The ancient people of the Arctic called it "Ginun-

gagap," a giant precipice in the darkness from which no traveler returned. The sagas of the Norsemen said it was a dark hell of ice. From medieval times until well into the 19th century many people believed from a map published by Gerardus Mercator in 1578 that a vast continent circled the pole at about 78°N containing at its center, from about 86°N to 90°N, an ice-free ocean. From this ocean flowed four giant ice-free rivers streaming in the directions of the four cardinal points. The map of Mercator, and others derived from it, had a powerful and sometimes tragic influence on Arctic exploration for hundreds of years. In 1611, the Dutch East India Company sent out an expedition with orders to proceed straight north to the pole and across to Asia. Among their tasks was to test a theory that the maximum cold and ice occurred at the Arctic Circle, with temperatures increasing somewhat and the ice cover decreasing somewhat to the north. Although the expedition failed, in the ensuing years the Dutch and others made many more attempts to cross the Arctic. As late as 1818 the British Admiralty sent out two ships with orders to sail via Svalbard directly across the North Pole to Siberia (Mirsky, 1948).

During the 19th century it became apparent that the Arctic is an ice-covered ocean, with a few random islands and virtually surrounded by the northern boundaries of the North American and Eurasian continents (Figure 4-41). Fridtjof Nansen, during his 1893-1896 drift across the Arctic in the *Fram*, established that the high Arctic is a deep ocean, in contrast to then-current speculations that the Arctic is a shallow basin with depths of about 150 meters. Nansen found ocean depths greater than 3,700 meters and suggested that even greater depths exist in other, unexplored areas of the Arctic. As we now know, he was right, and depths greater than 4,300 meters have been found (Figure 2-2).

The Eurasian continental shelf extends well out into the Arctic Ocean, with very shallow depths in the Laptev, East Siberian, and Chukchi Seas. The depths in these seas are generally less than 50 meters and indeed the 50-meter isobath extends as far as 600 kilometers from the shore. The deep part of the ocean is not a single deep depression, as had been thought by many in the early 1900s, but consists of two deep basins separated by a submarine mountain ridge almost 2,000-kilometers long. The basins are the Canadian Basin and the Eurasian Basin, and the ridge is the Lomonosov Ridge, named after the 18th

century Russian scientist Mikhail Lomonosov (Figure 2-2).

The structure and movement of the sea ice cover in the Arctic Basin is complex. During each year, the whole gamut of sea ice types is found, ranging from nilas and frazil to various stages of first-year ice to thick multiyear ice. The pseudo actual ice area for the Arctic Ocean at the summer minimum is about 3.8×10^6 square kilometers, and it increases to about 6.3×10^6 square kilometers at its winter

maximum (Figure 4-11). This large seasonal area oscillation, coupled with the intermittent convergence and divergence of the ice pack, produces within the Arctic Basin an ice pack composed of mixtures of first-year and multiyear ice floes of varying sizes, with a distribution within the basin that varies seasonally, annually, and interannually. The average thickness of the ice pack is approximately 3 to 4 meters, although the actual thickness varies markedly from one point to another. For details on the Arctic ice thickness distribution, the reader is referred

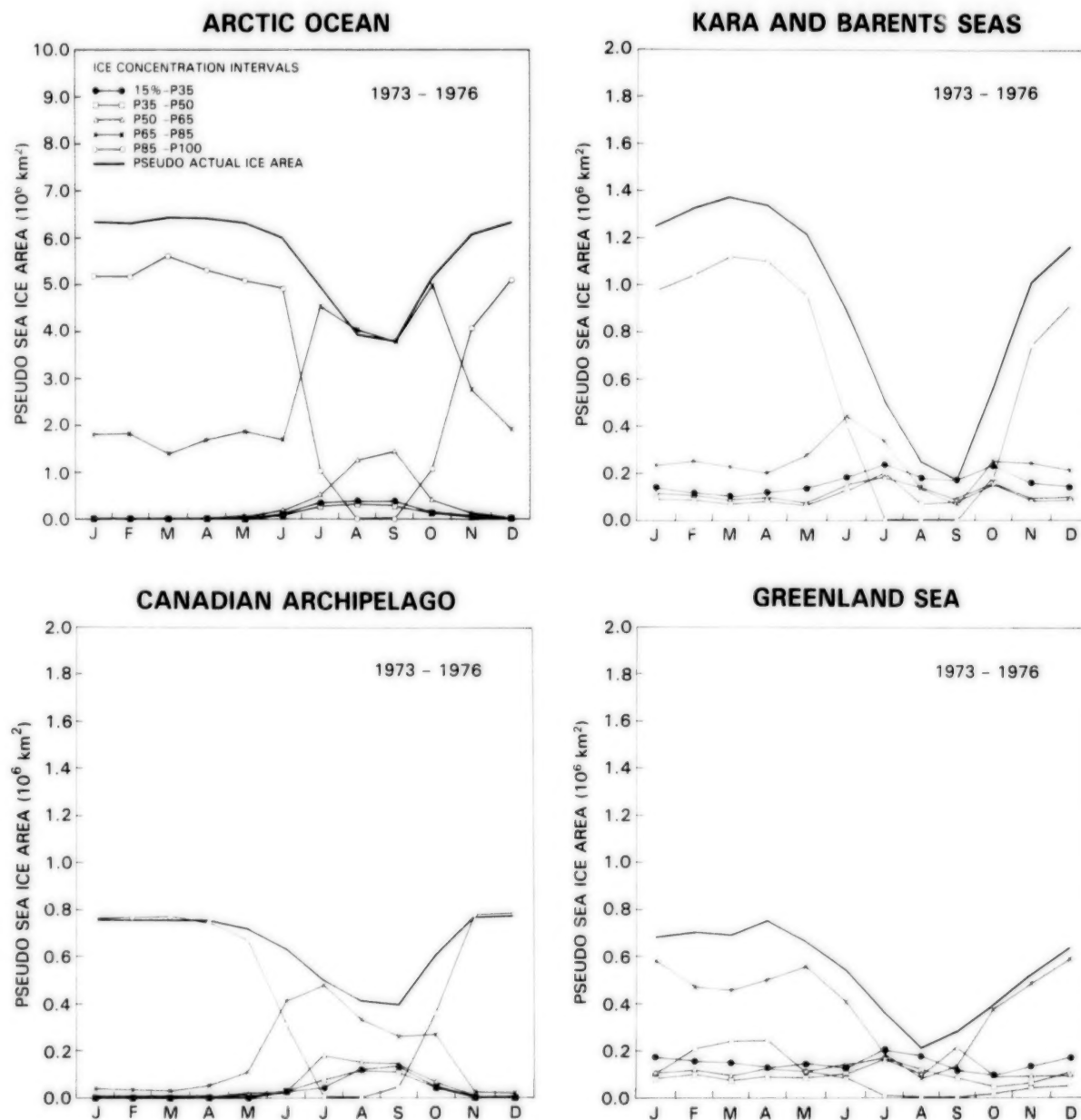


Figure 4-14. Four-year-average yearly cycle of the ocean area covered by sea ice within the intervals 15 percent to P35, P35 to P50, P50 to P65, P65 to P85, and P85 to P100, and 4-year-average yearly cycle of the pseudo actual ice area, for the following regions: Arctic Ocean, Kara and Barents Seas, Canadian Archipelago, and Greenland Sea. The interval curves are calculated by subtracting the respective curves of Figure 4-11.

to the observations of Hibler et al. (1972) and Swithinbank (1972) and to the modeling of the thickness distribution by Thorndike et al. (1975).

The Arctic ice pack floats on an ocean of variable currents having variable fluxes of heat and momentum. The dynamics of the ice are influenced by mass and heat exchanges with the ocean and atmosphere as well as the internal forces within the ice. The first notable data set on the complex ice motion within the basin came from the navigational observations

made during the 1893-1896 voyage of the *Fram*. Between the end of this voyage in 1896 and 1937, several ships were beset in the ice and their drifts extended the data set on Arctic ice dynamics. In 1937, the Soviet Union began its North Pole series of manned drifting research stations. These stations and their western counterparts over the succeeding decades have provided sufficient data to define the general pattern of ice motion. Figure 4-42 shows the drifts of 33 ships and ice stations from the *Fram* through North Pole 20, plus the route of the British

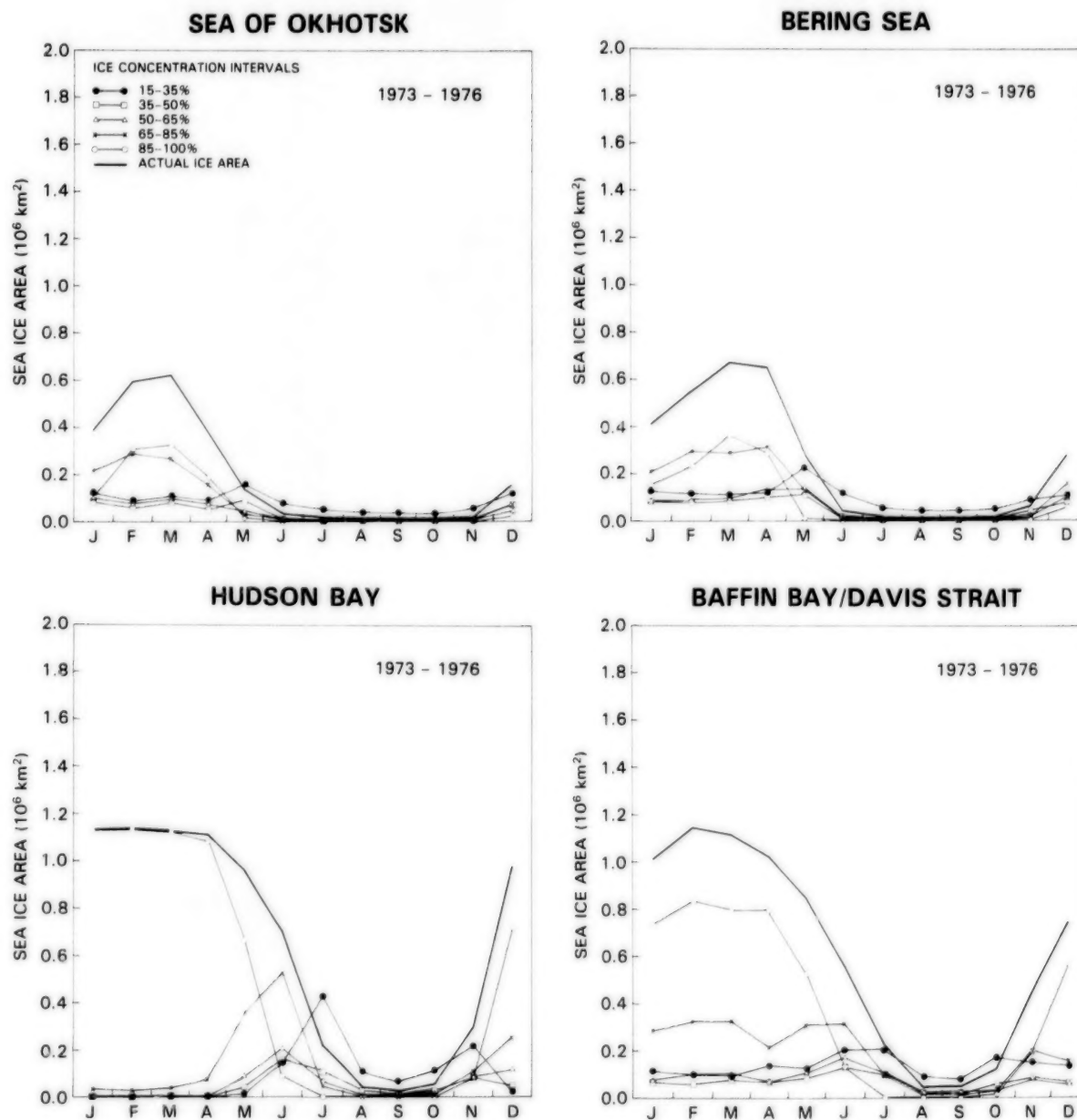


Figure 4-15. Four-year-average yearly cycle of the ocean area covered by sea ice within ice concentration intervals 15 to 35, 35 to 50, 50 to 65, 65 to 85, and 85 to 100 percent, and 4-year-average yearly cycle of the actual ice area, for the following regions: Sea of Okhotsk, Bering Sea, Hudson Bay, and Baffin Bay/Davis Strait.

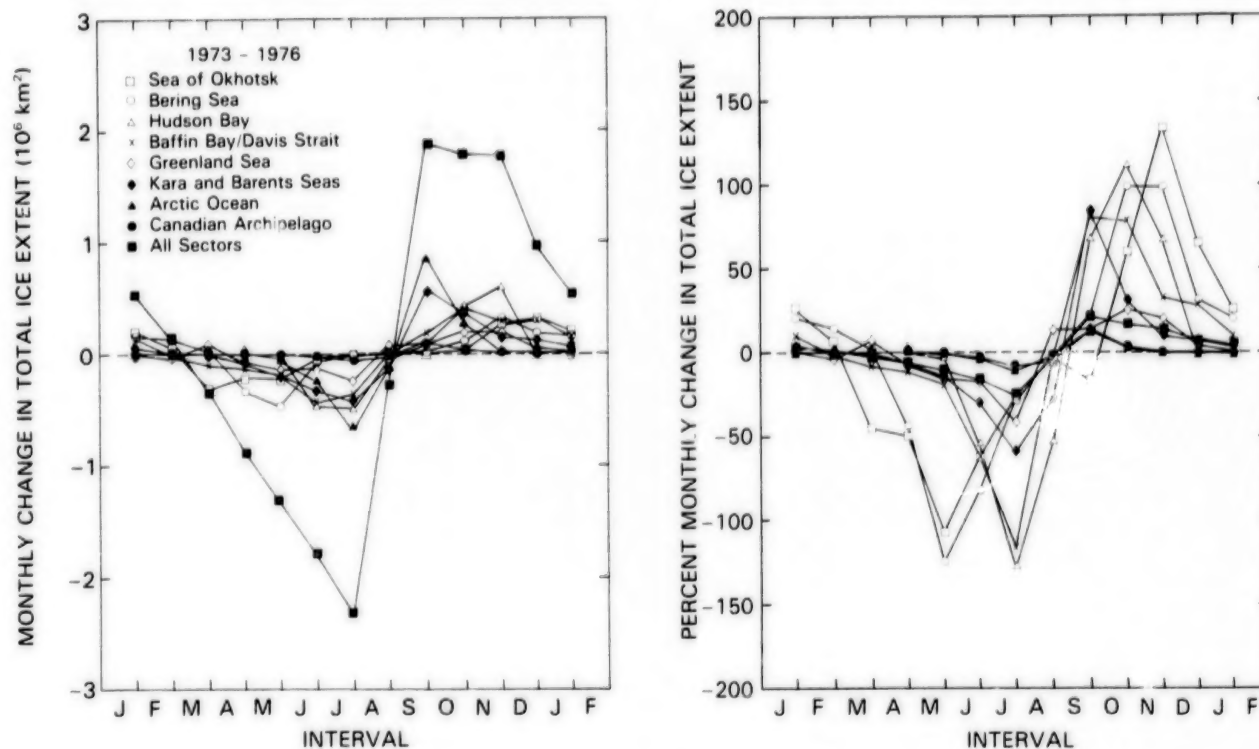


Figure 4-16. Growth/decay rates of total ice extent (concentration exceeding 15 percent) shown as: (a) monthly change in area, and (b) percentage monthly change in area, calculated with respect to the average area in the 2 months.

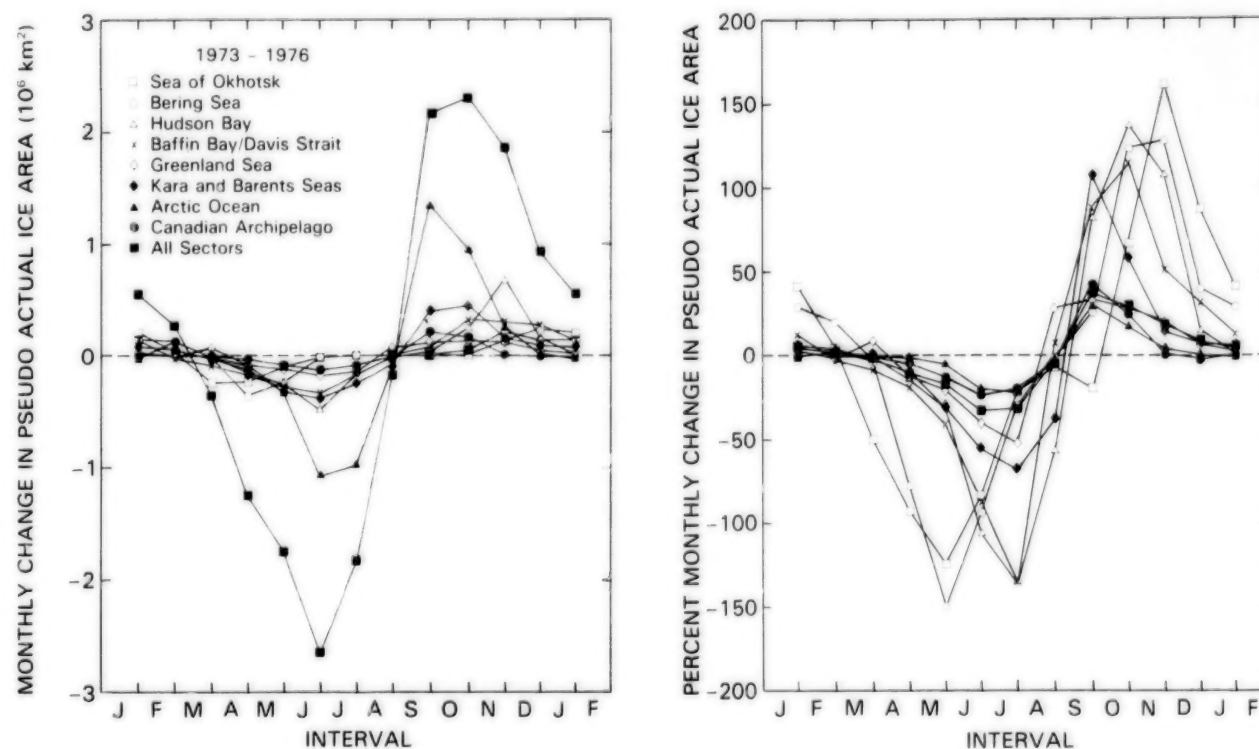


Figure 4-17. Growth/decay rates of pseudo actual ice area (or actual ice area for regions without multiyear ice) shown as: (a) monthly change in area, and (b) percentage monthly change in area, calculated with respect to the average area in the 2 months.

ORIGINAL PAGE
COLOR PHOTOGRAPH

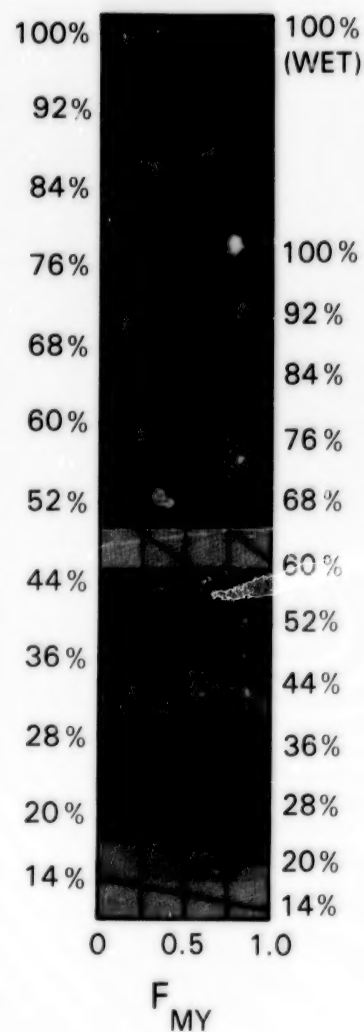
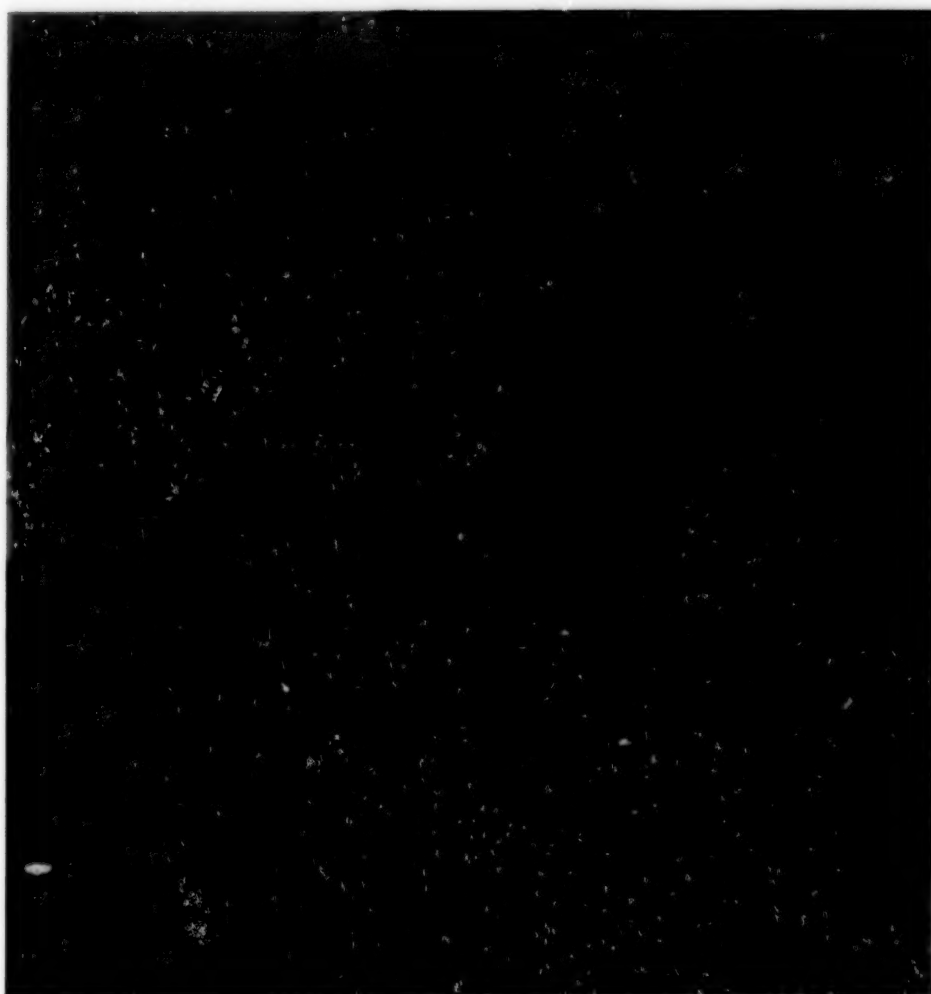


Figure 4-18a. Mean monthly sea ice concentrations for January 1973 and 1974.

**ORIGINAL PAGE
COLOR PHOTOGRAPH**

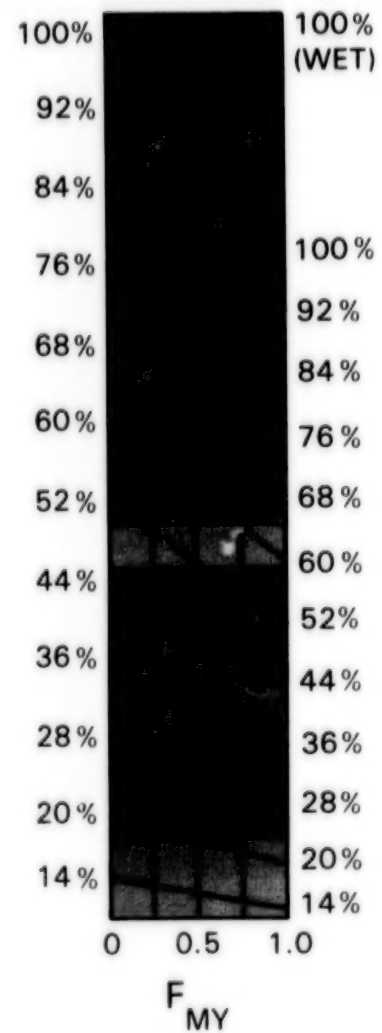
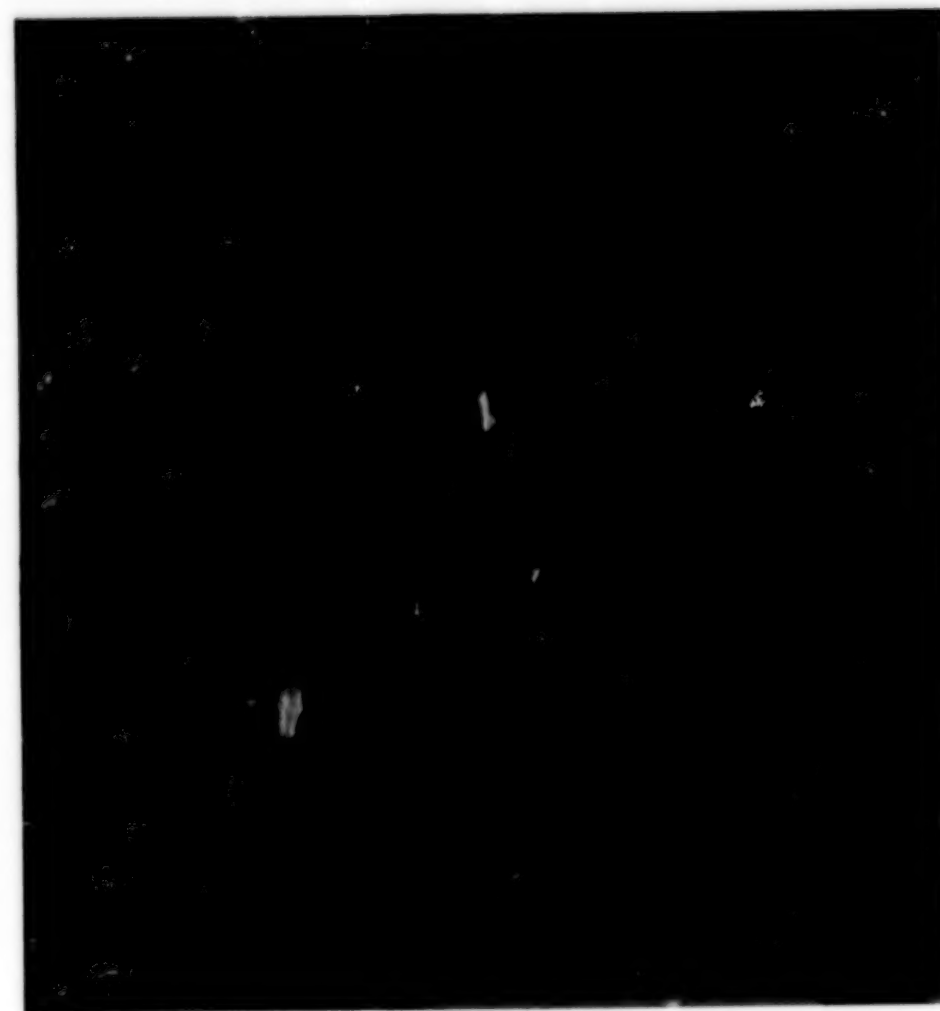
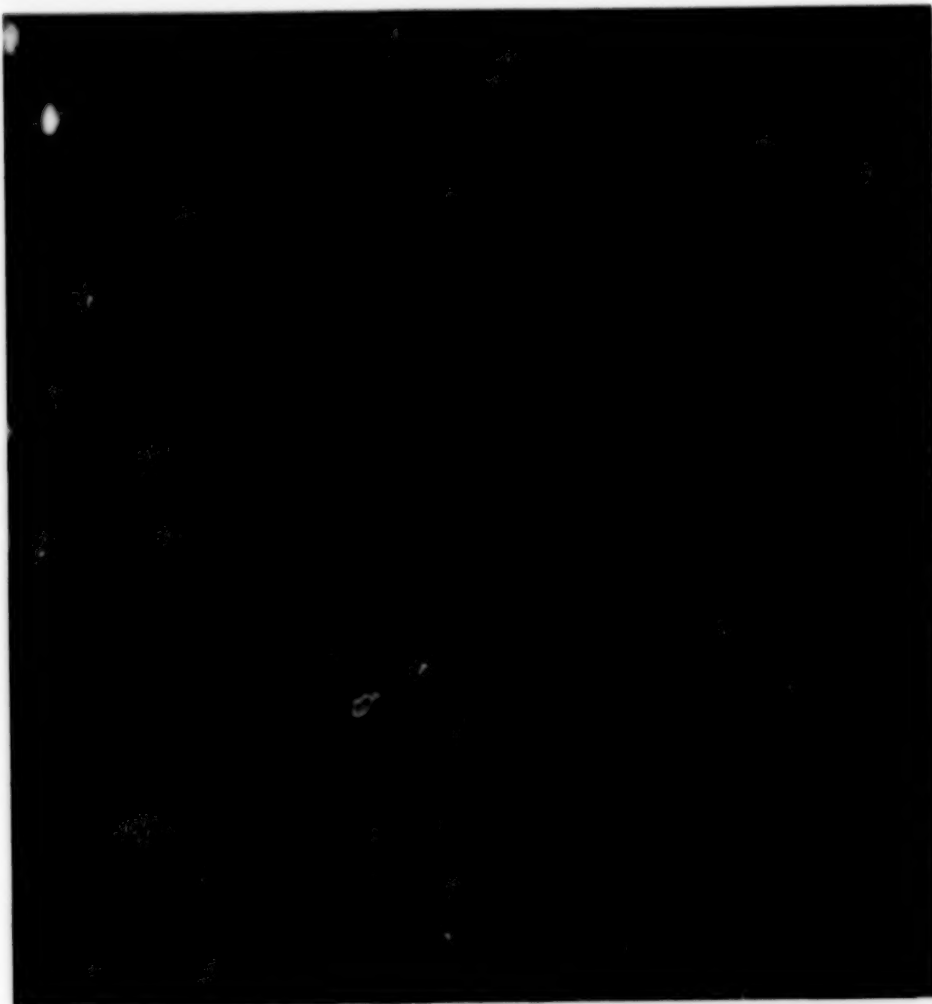


Figure 4-18b. Mean monthly sea ice concentrations for January 1975 and 1976.

ORIGINAL PAGE
COLOR PHOTOGRAPH

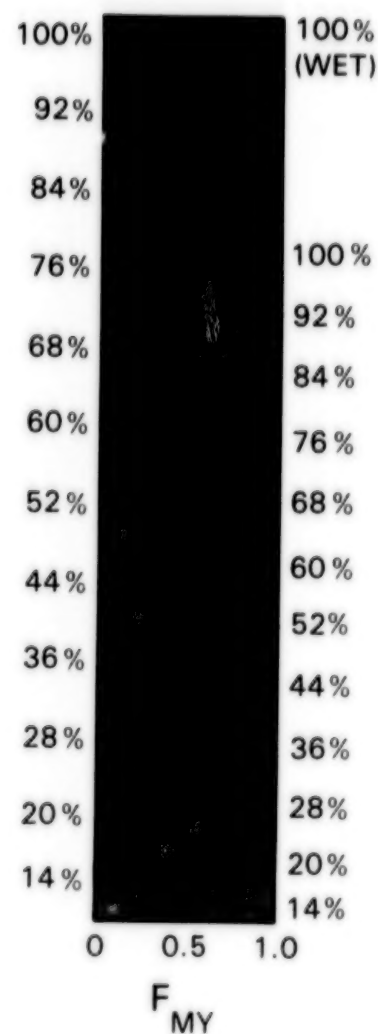


Figure 4-19a. Mean monthly sea ice concentrations for February 1973 and 1974.

ORIGINAL PAGE
COLOR PHOTOGRAPH

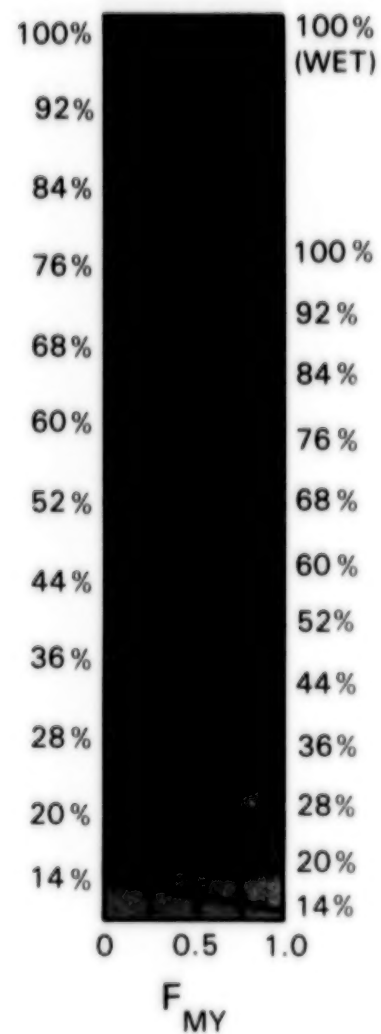
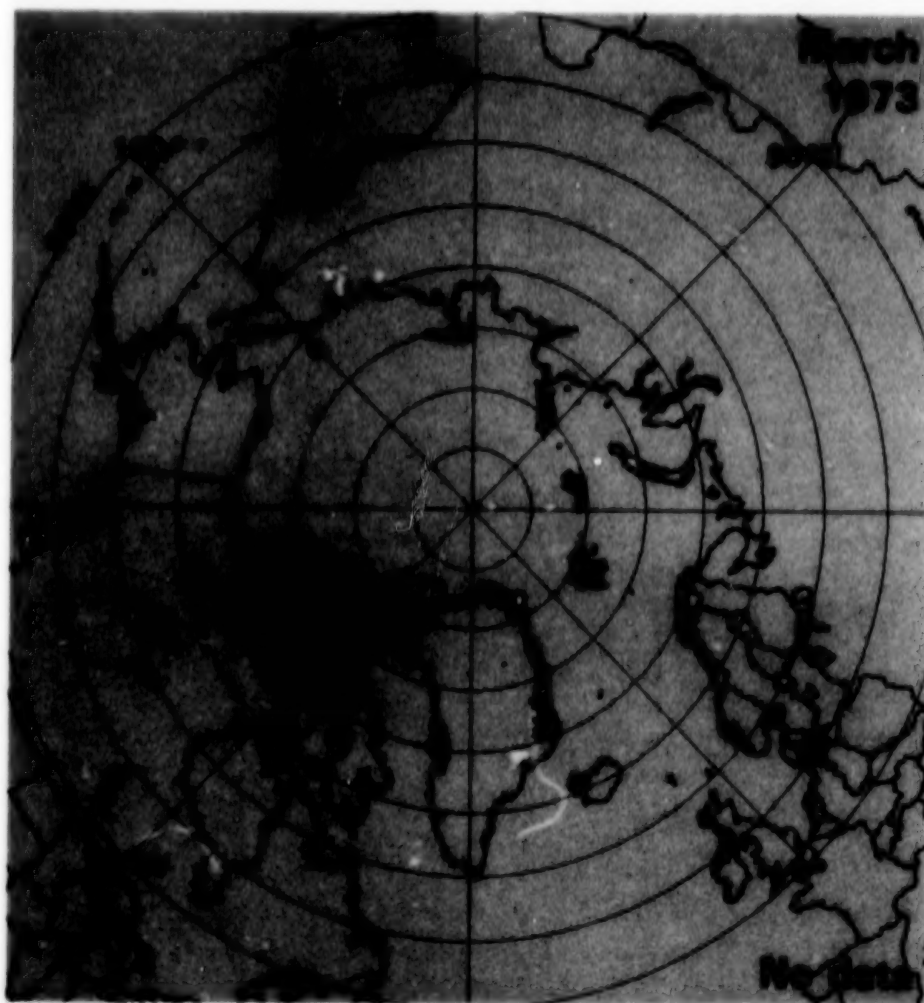


Figure 4-19b. Mean monthly sea ice concentrations for February 1975 and 1976.



ORIGINAL PAGE
COLOR PHOTOGRAPH

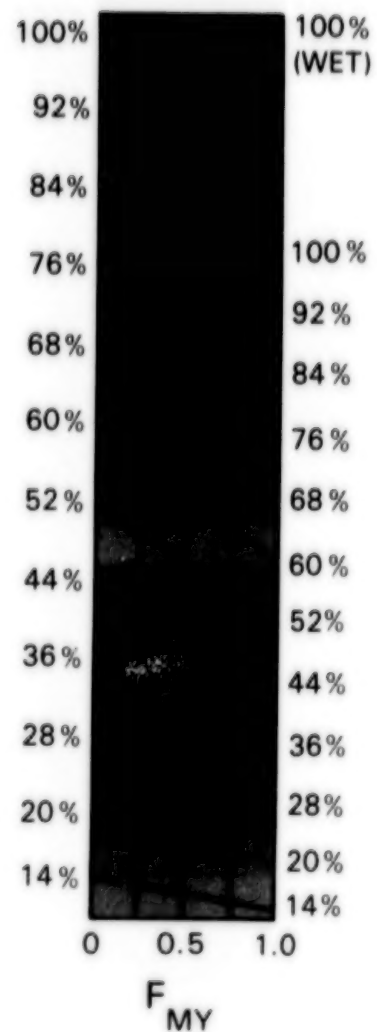
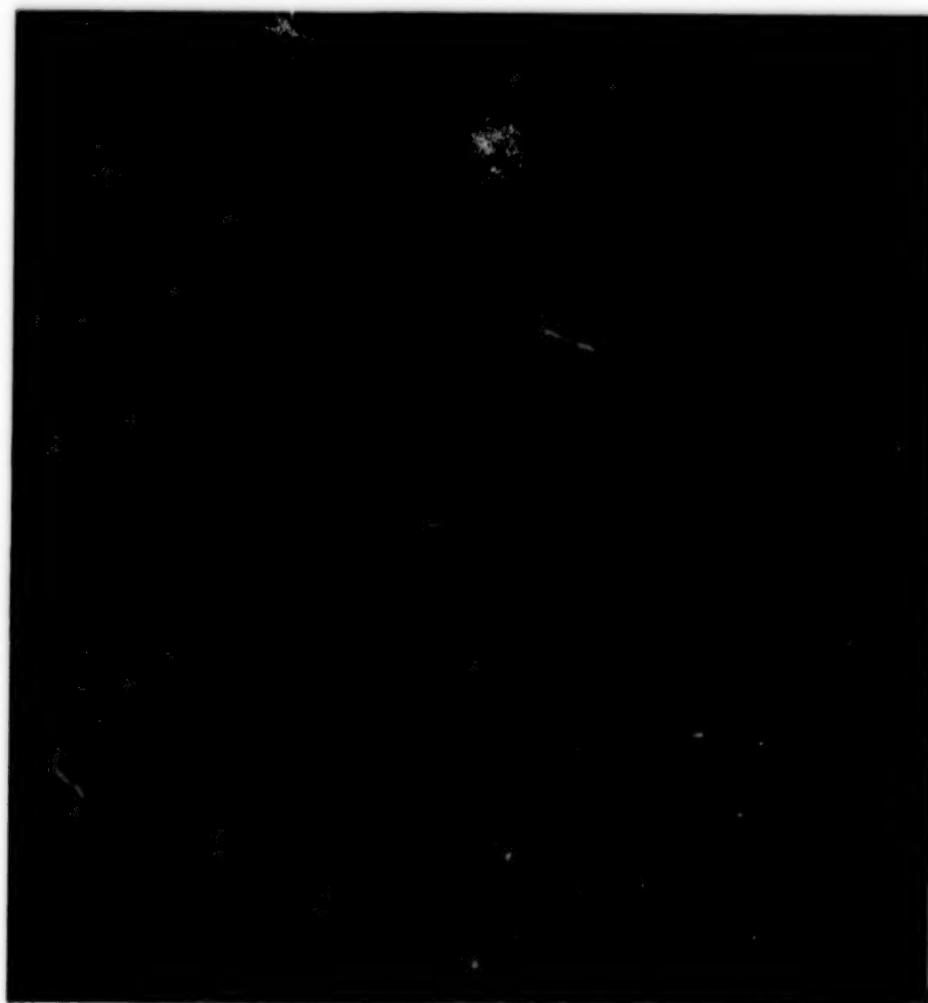


Figure 4-20a. Mean monthly sea ice concentrations for March 1973 and 1974.

ORIGINAL PAGE
COLOR PHOTOGRAPH

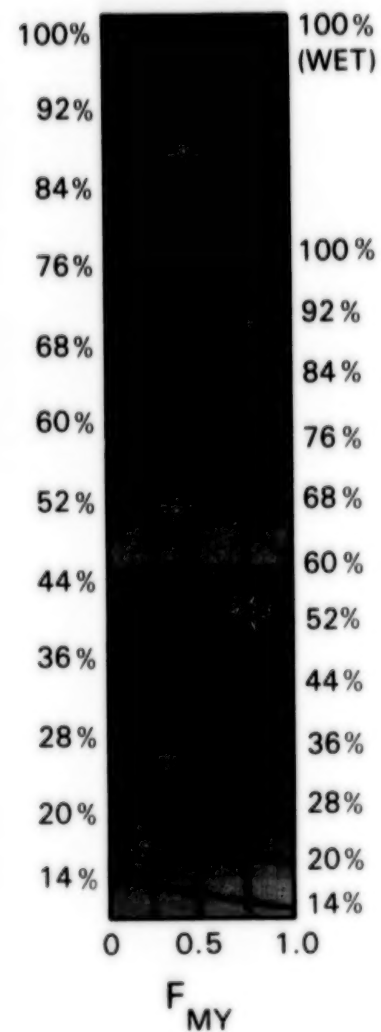
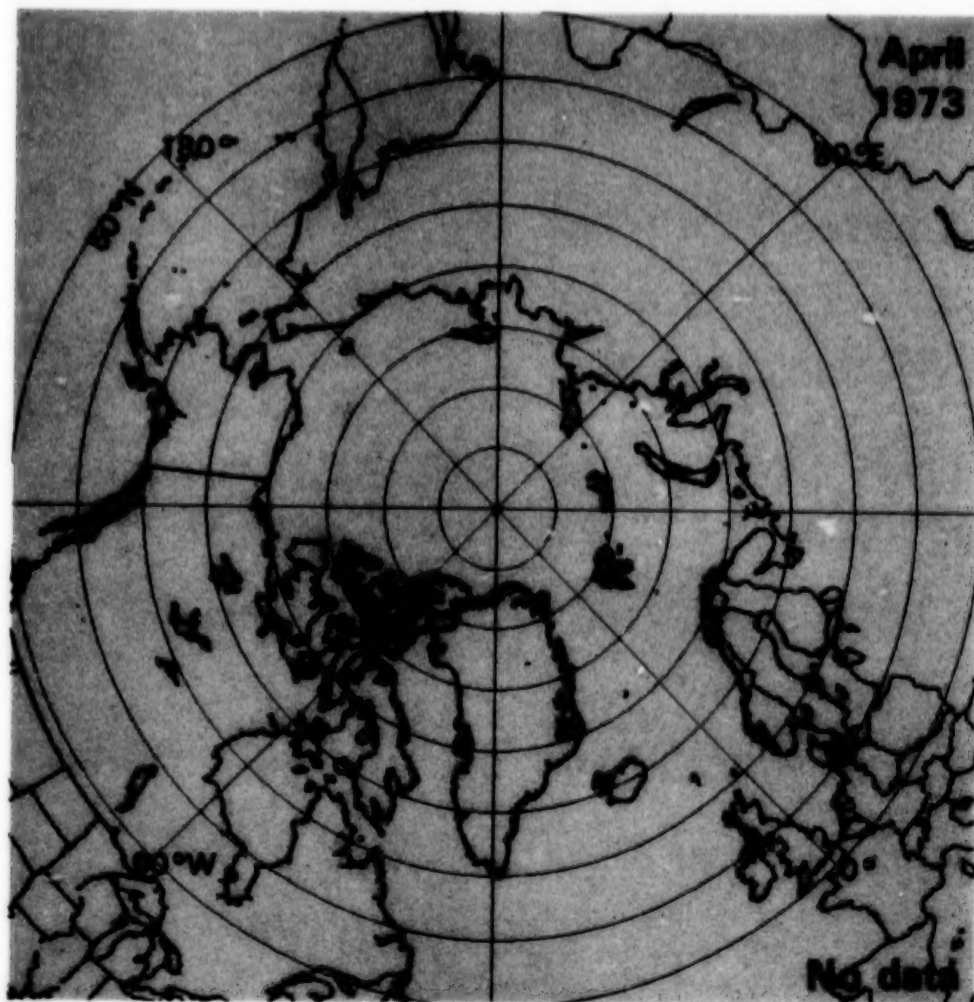


Figure 4-20b. Mean monthly sea ice concentrations for March 1975 and 1976.



ORIGINAL PAGE
COLOR PHOTOGRAPH

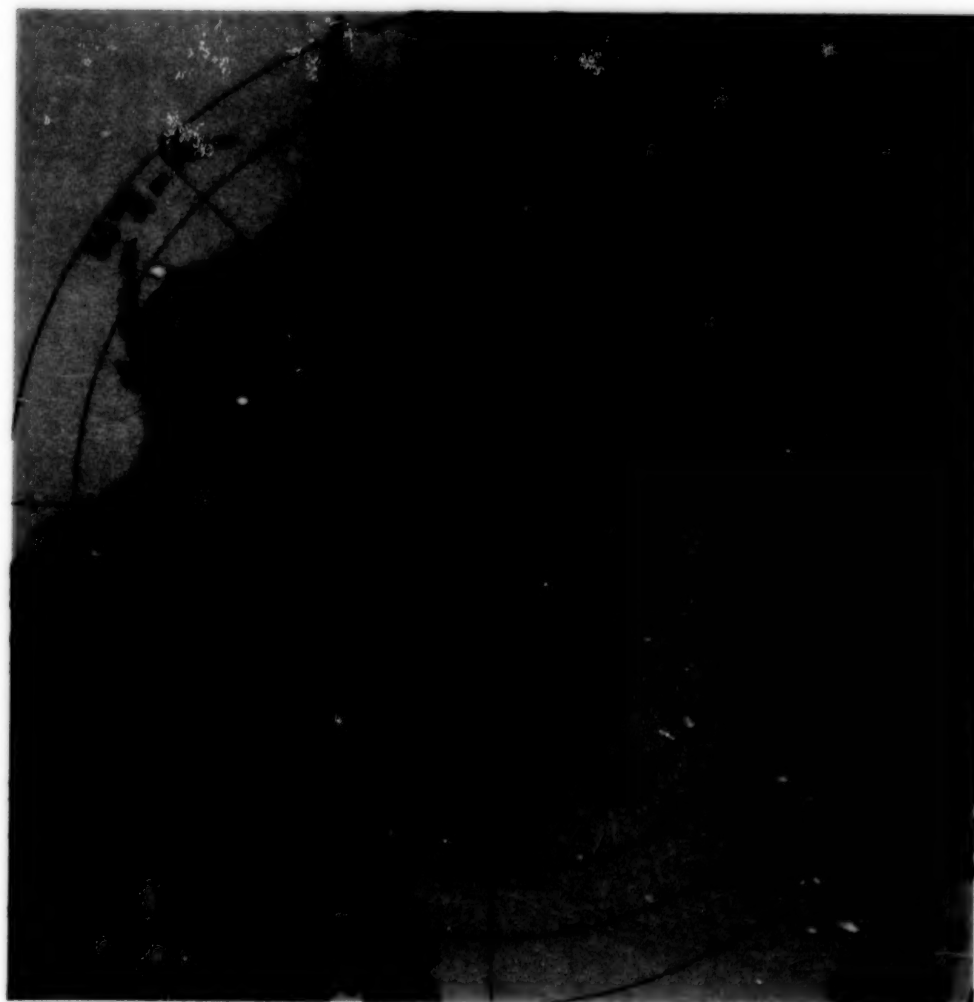
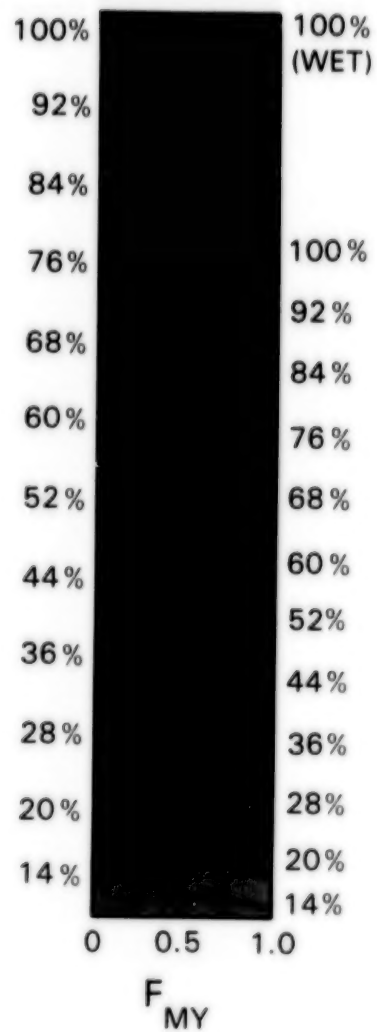


Figure 4-21a. Mean monthly sea ice concentrations for April 1973 and 1974.

ORIGINAL PAGE
COLOR PHOTOGRAPH

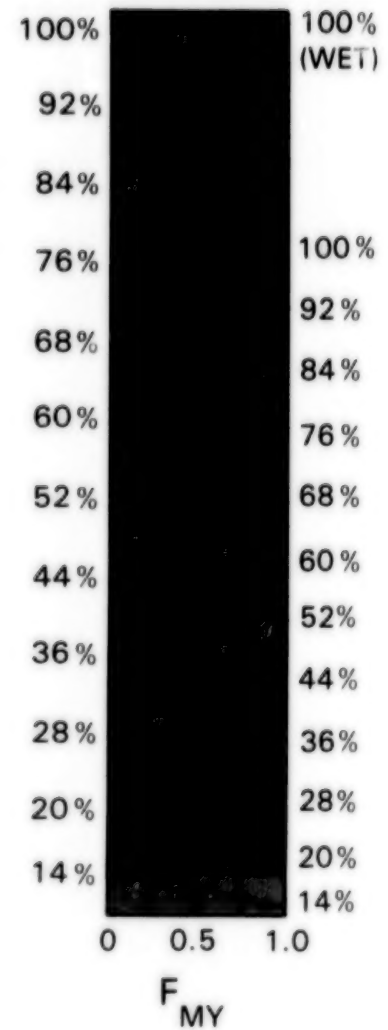


Figure 4-21b. Mean monthly sea ice concentrations for April 1975 and 1976.



ORIGINAL PAGE
COLOR PHOTOGRAPH

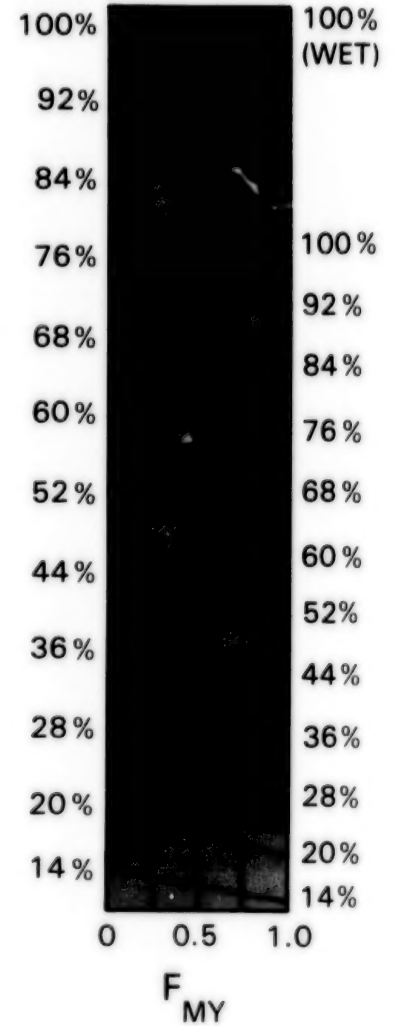


Figure 4-22a. Mean monthly sea ice concentrations for May 1973 and 1974.

ORIGINAL PAGE
COLOR PHOTOGRAPH

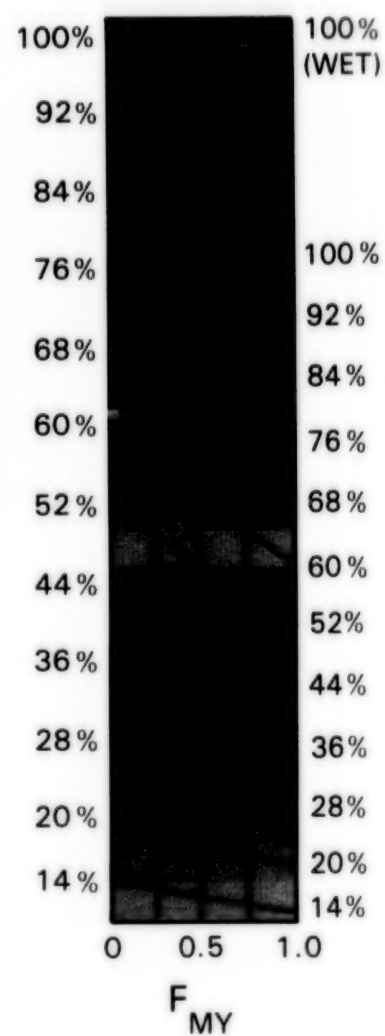


Figure 4-22b. Mean monthly sea ice concentrations for May 1975 and 1976.

ORIGINAL PAGE
COLOR PHOTOGRAPH

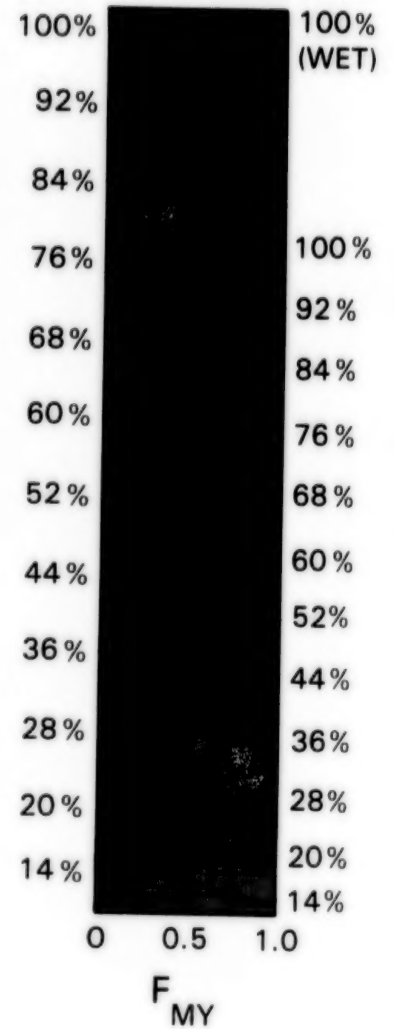
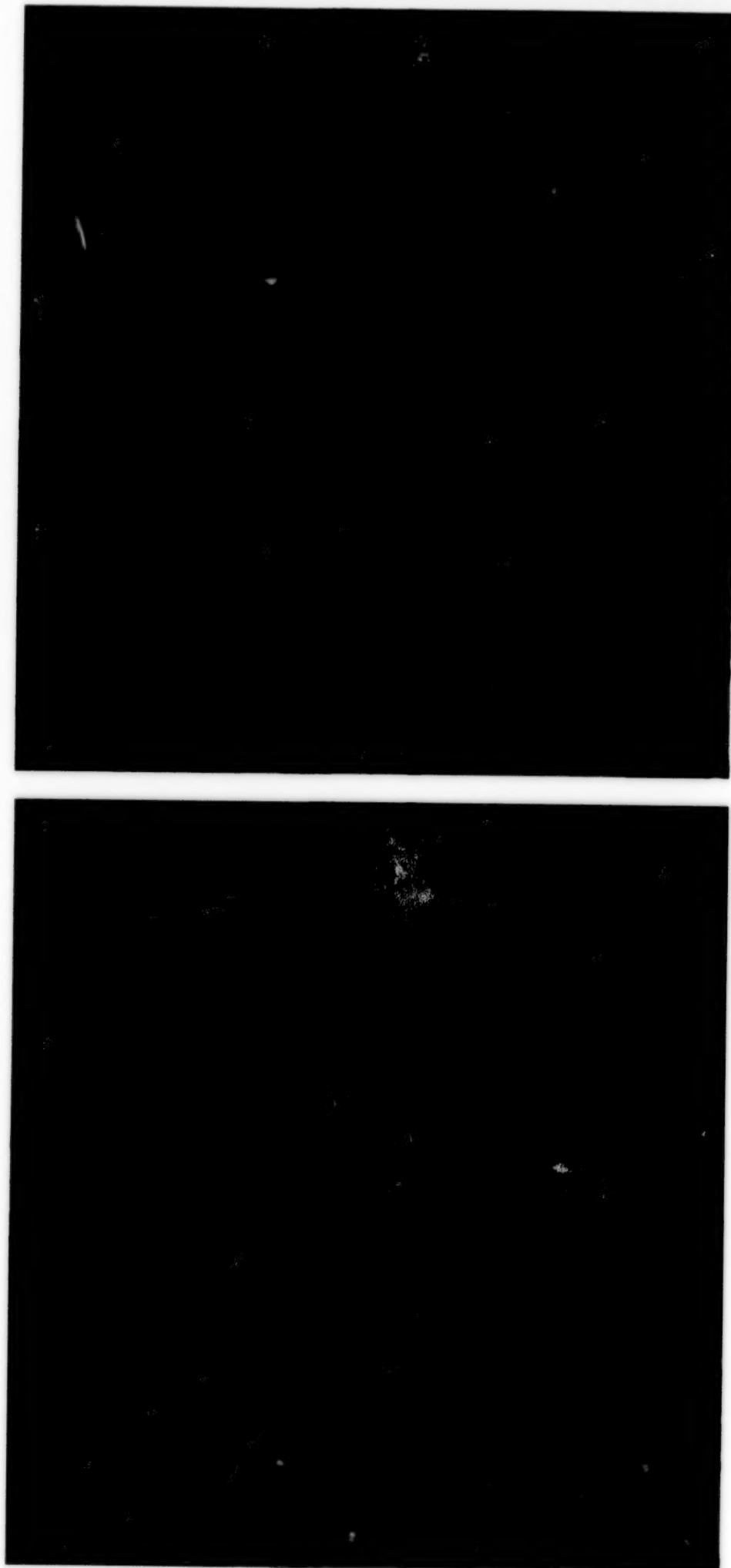


Figure 4-23a. Mean monthly sea ice concentrations for June 1973 and 1974.

ORIGINAL PAGE
COLOR PHOTOGRAPH

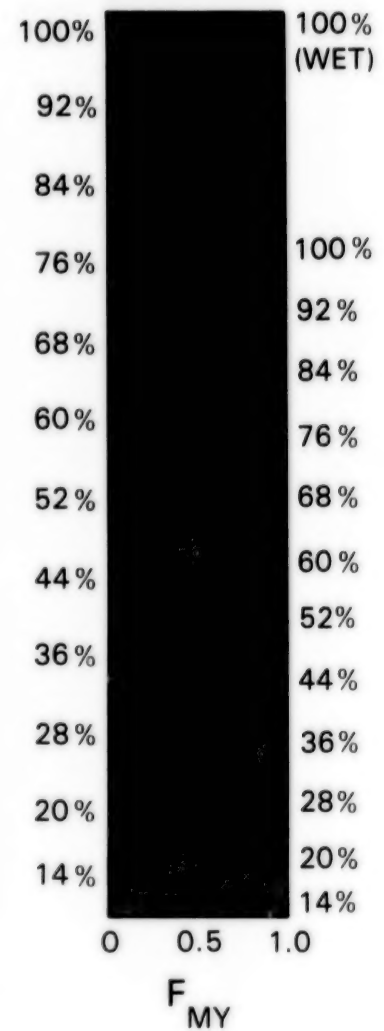
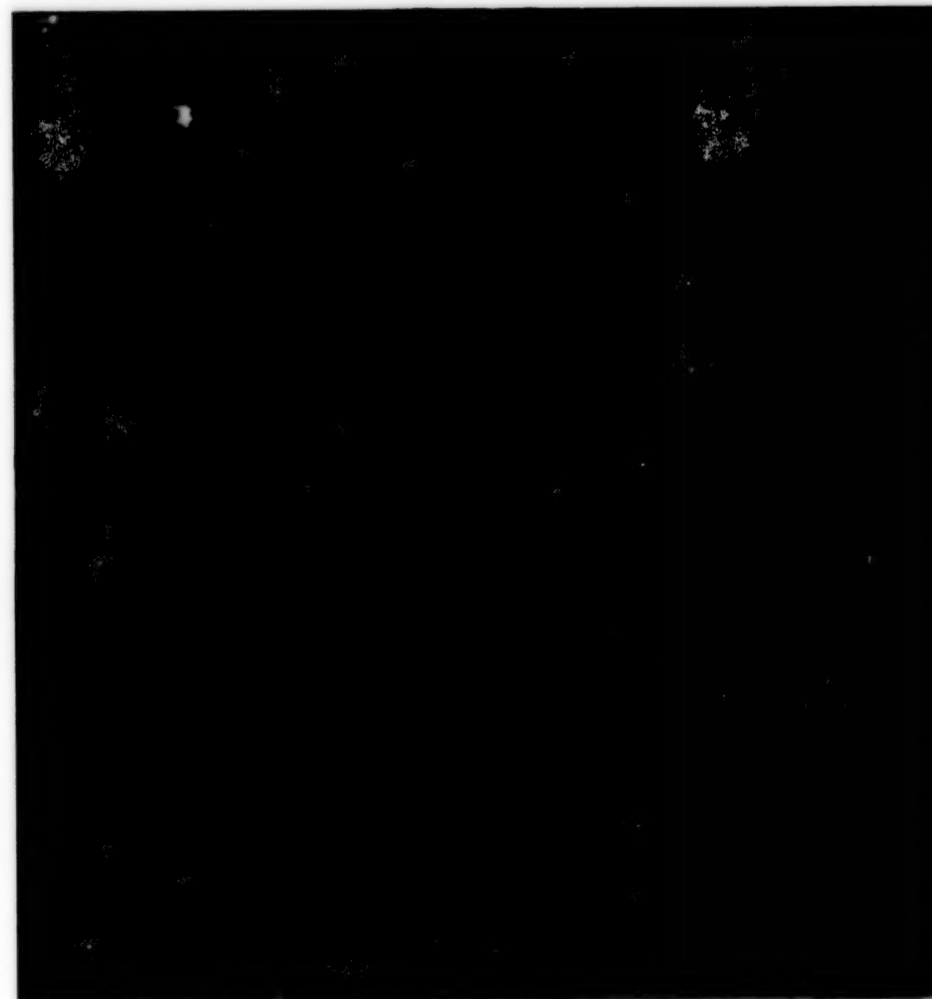
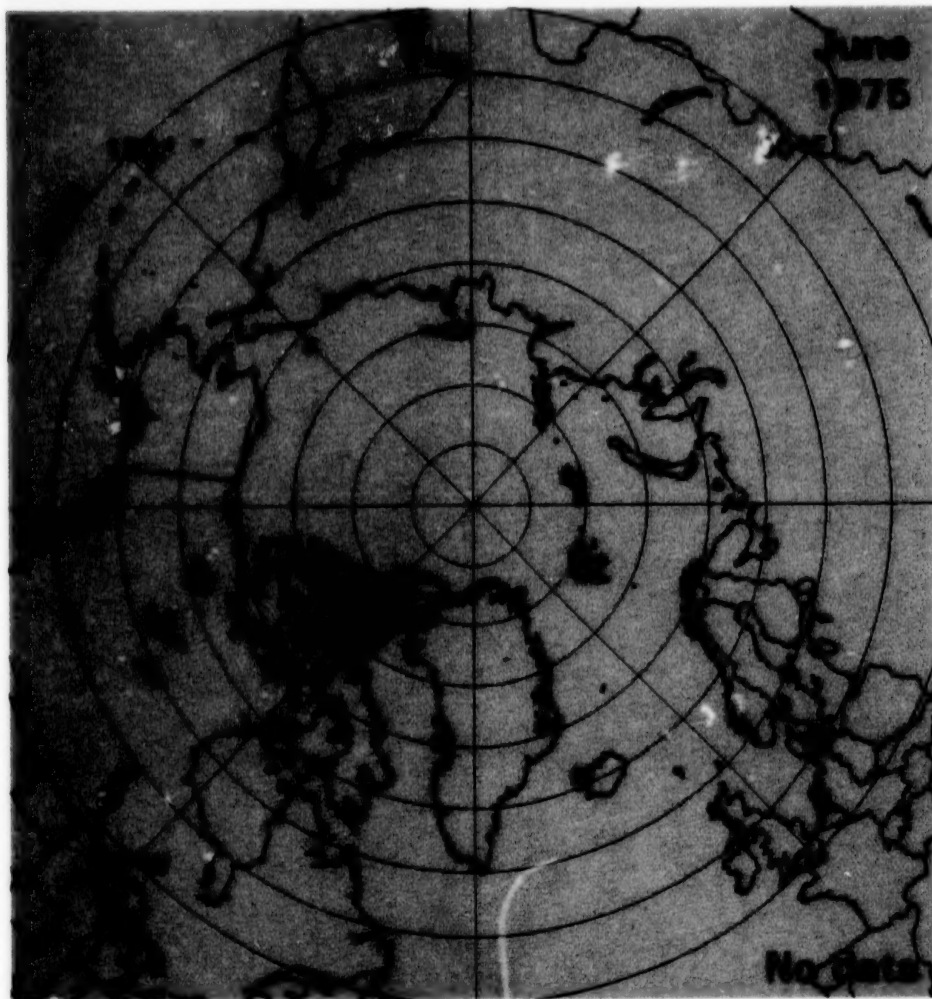


Figure 4-23b. Mean monthly sea ice concentrations for June 1975 and 1976.

ORIGINAL PAGE
COLOR PHOTOGRAPH

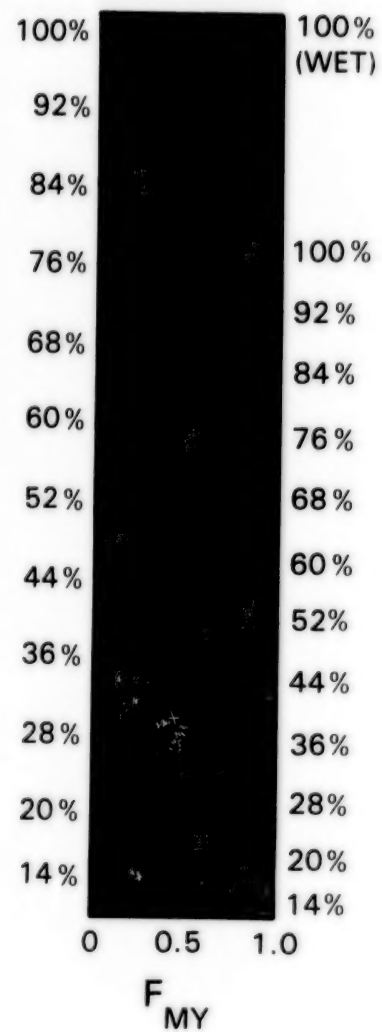
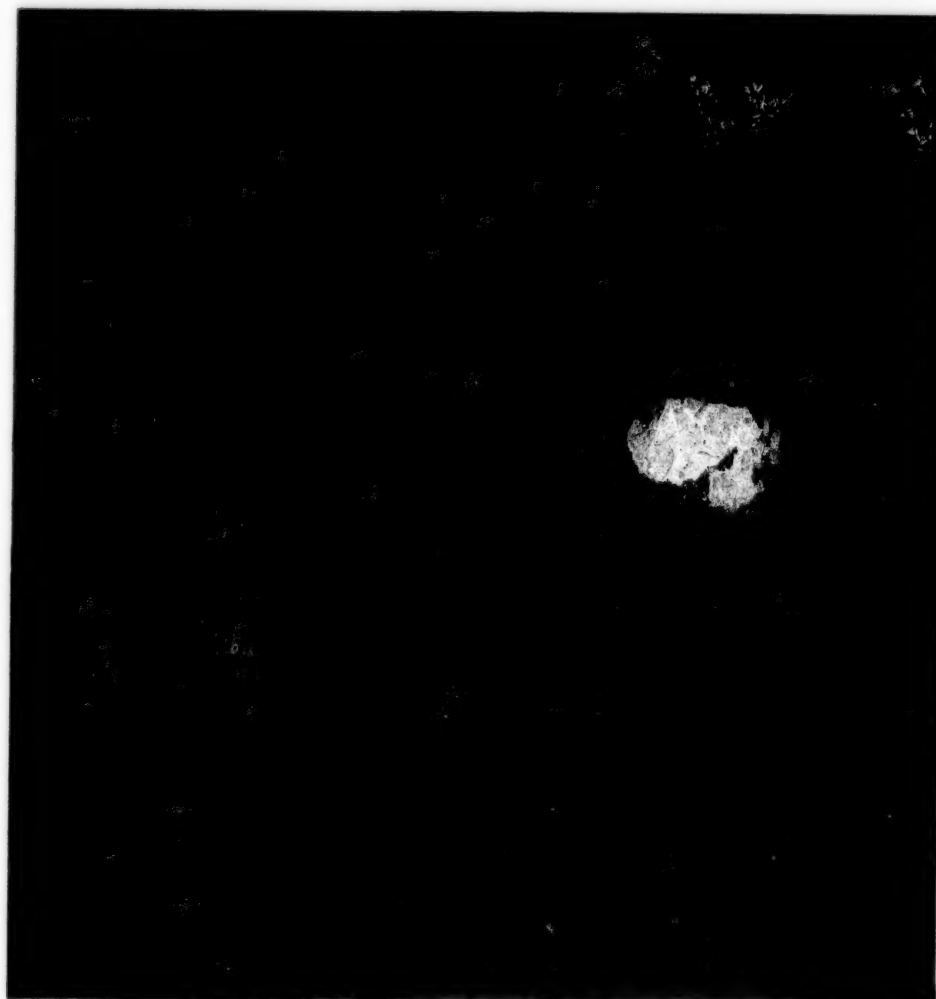
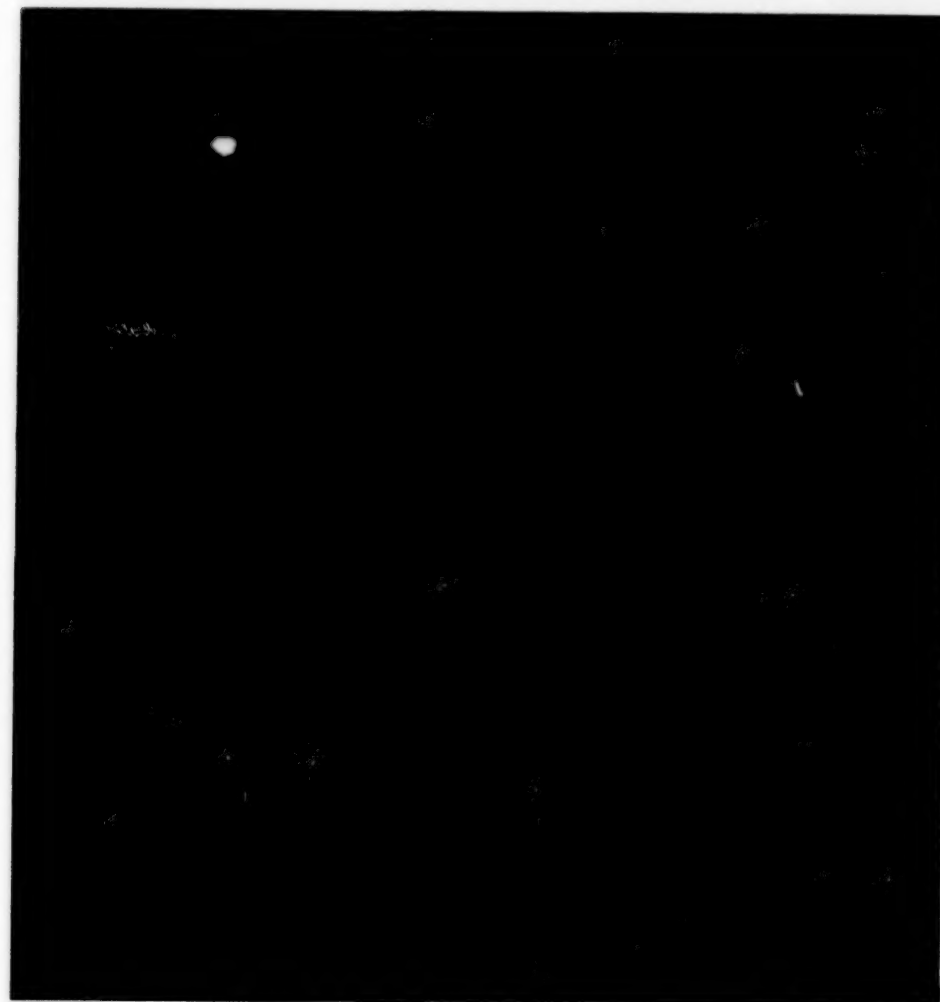
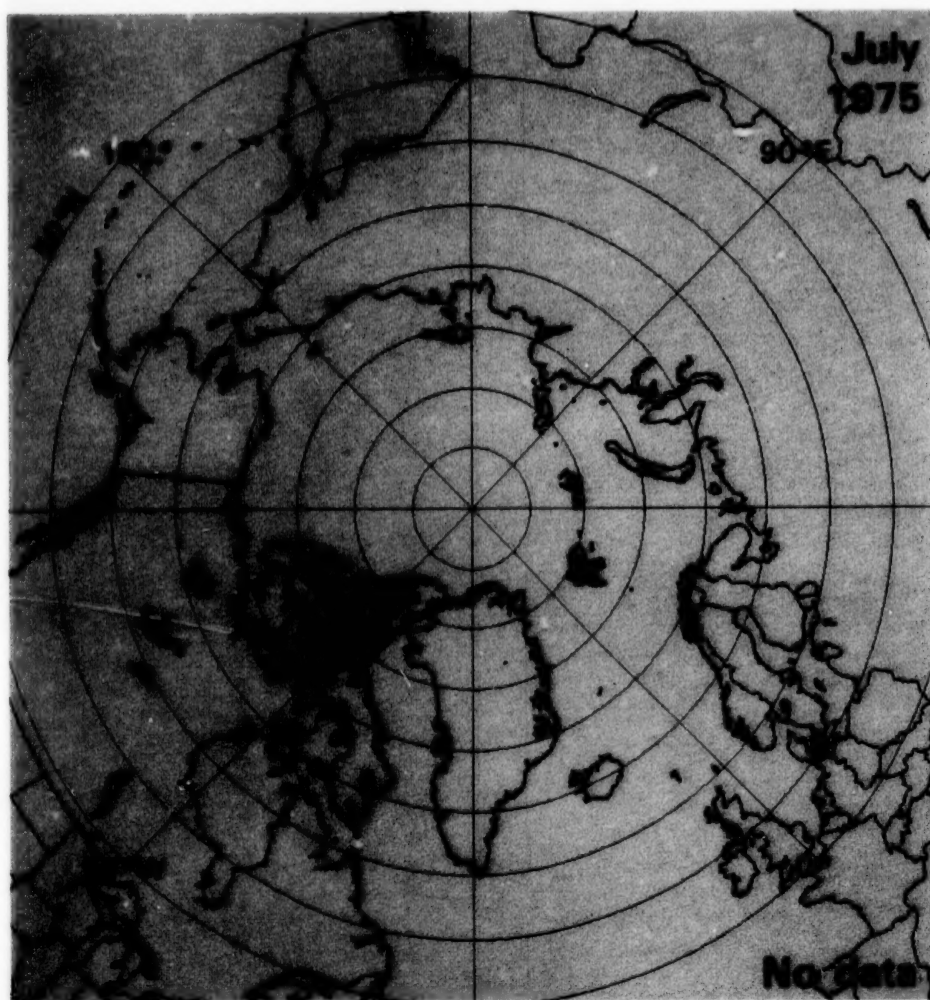


Figure 4-24a. Mean monthly sea ice concentrations for July 1973 and 1974.



ORIGINAL PAGE
COLOR PHOTOGRAPH

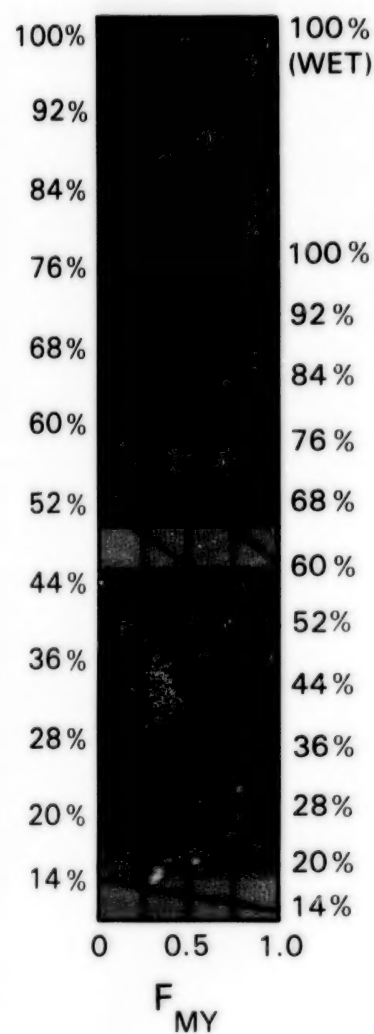
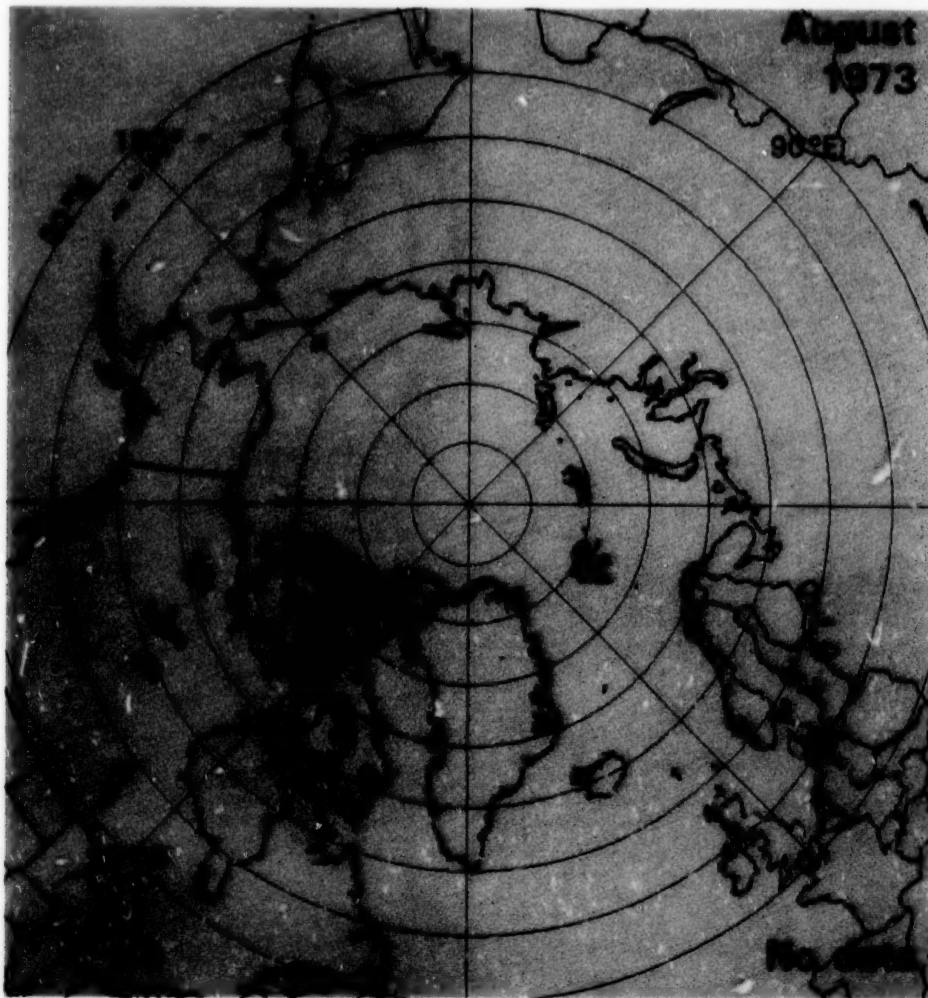


Figure 4-24b. Mean monthly sea ice concentrations for July 1975 and 1976.



ORIGINAL PAGE
COLOR PHOTOGRAPH

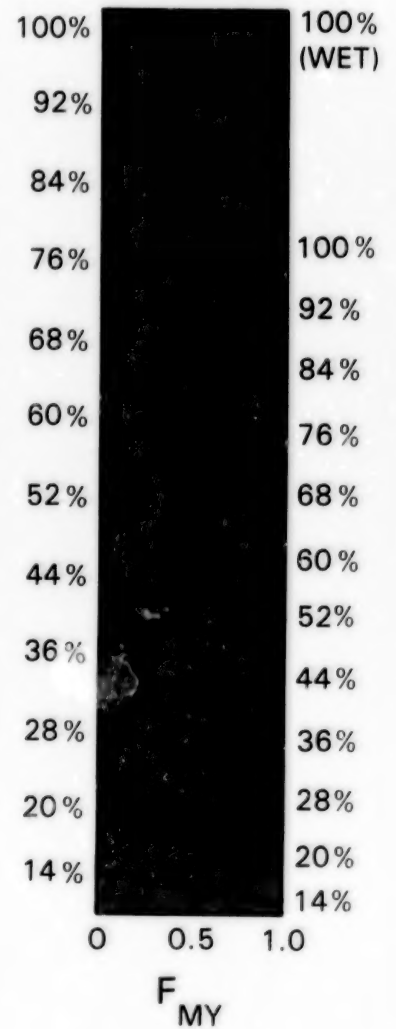
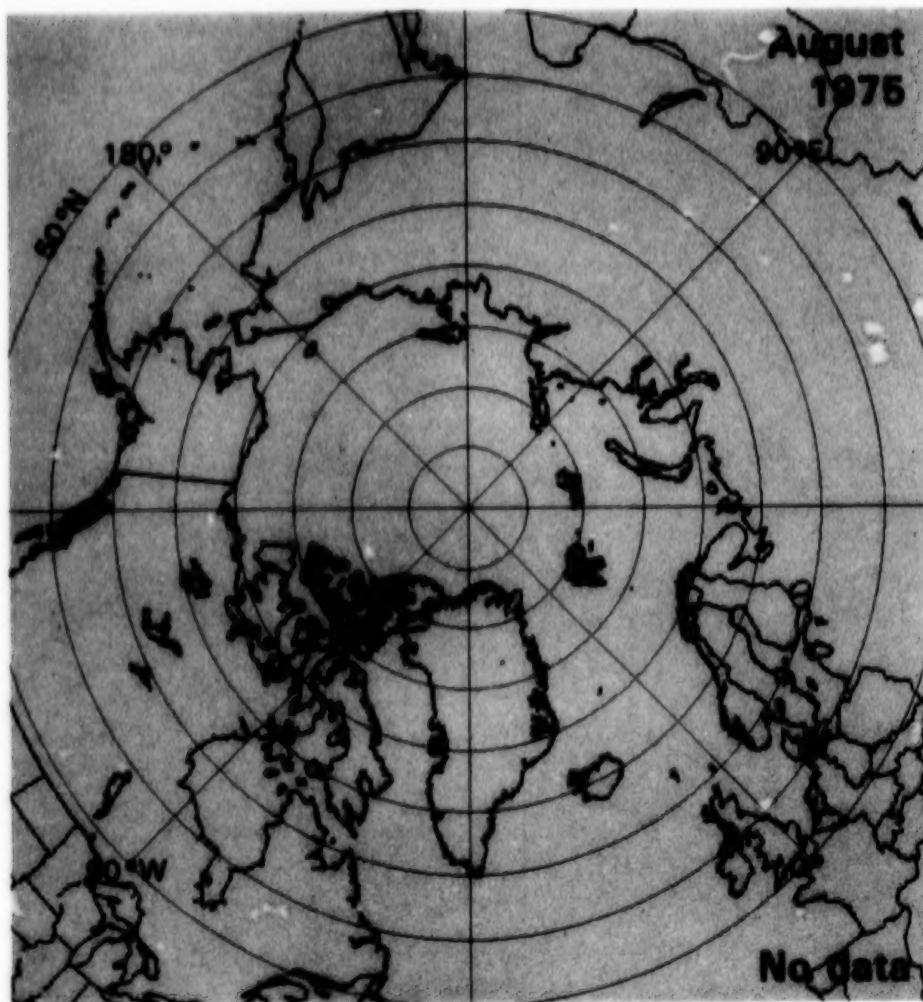


Figure 4-25a. Mean monthly sea ice concentrations for August 1973 and 1974.



ORIGINAL PAGE
COLOR PHOTOGRAPH

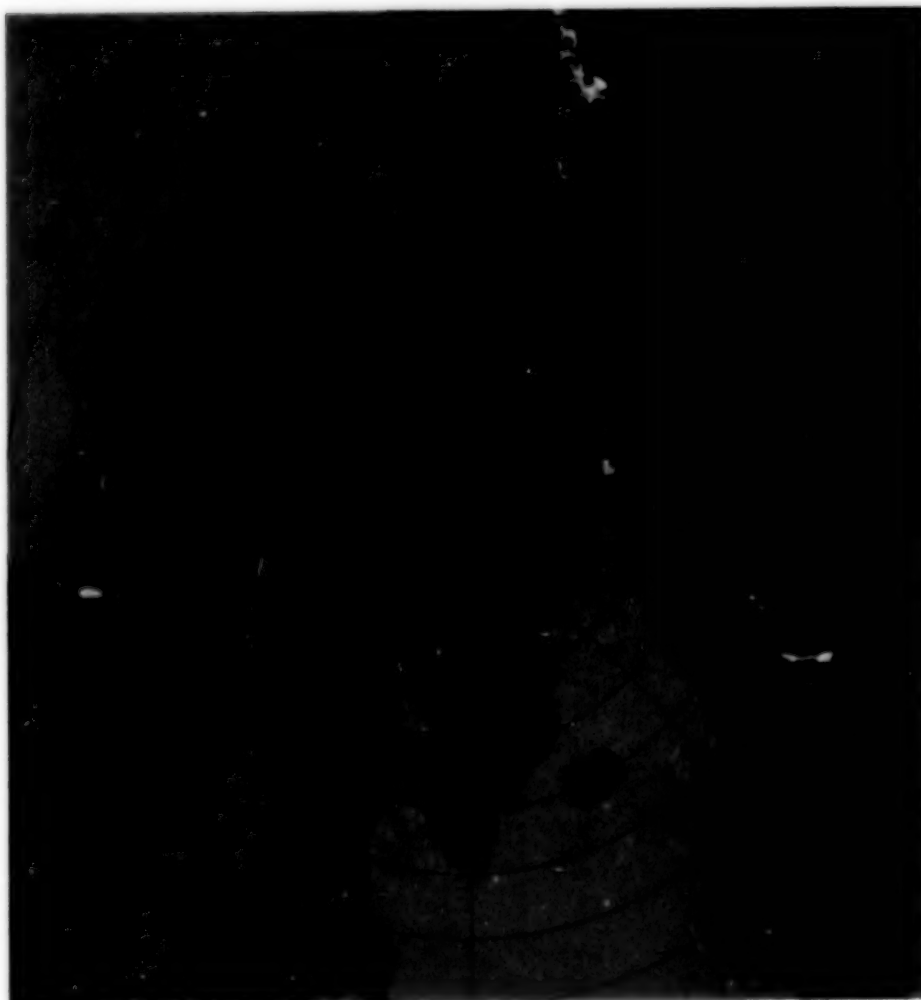
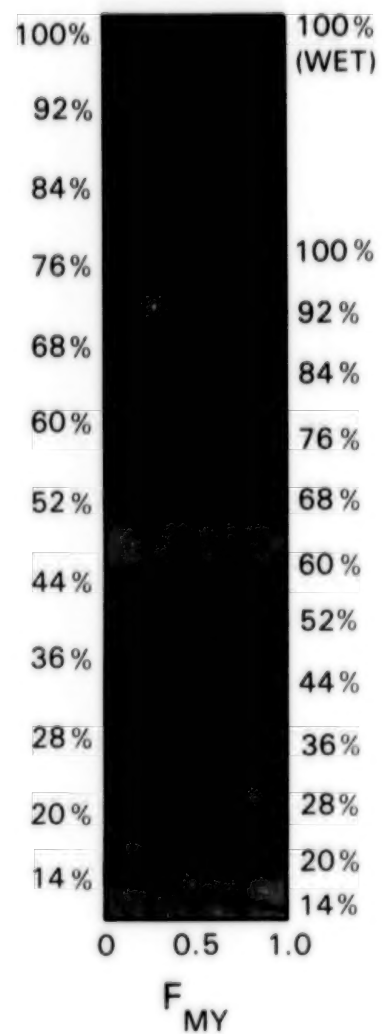
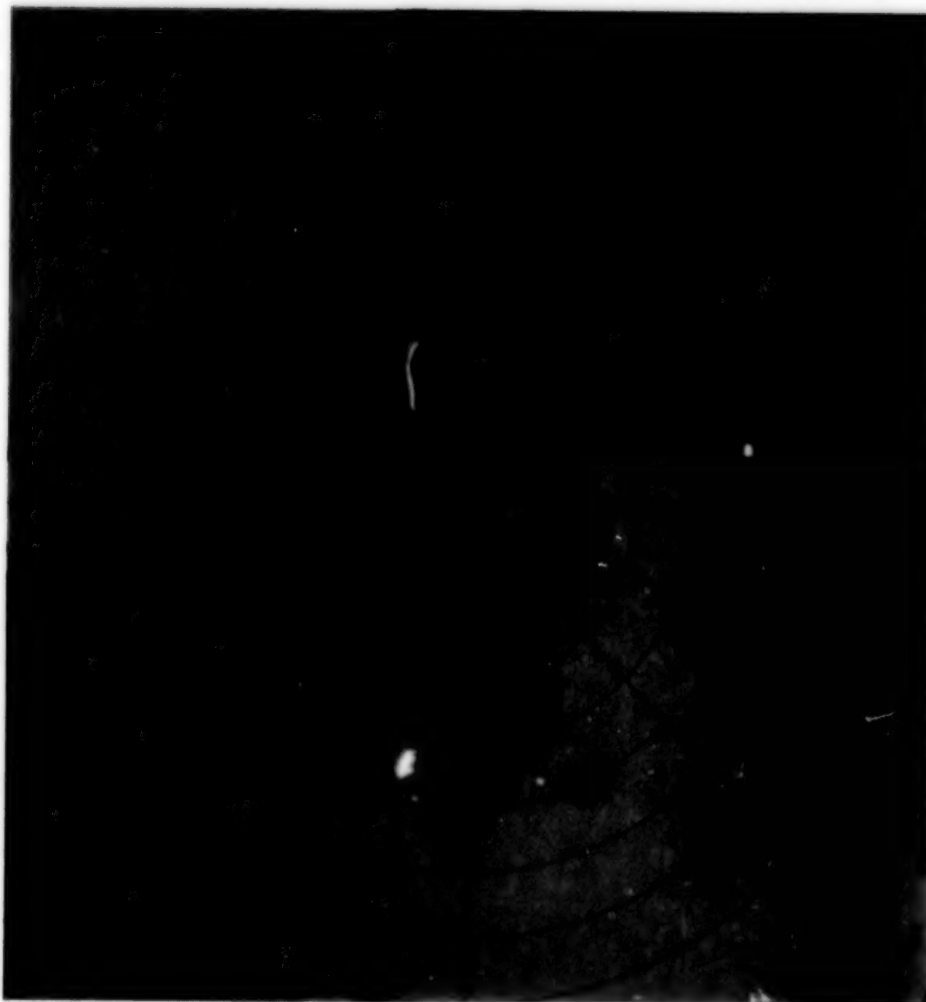
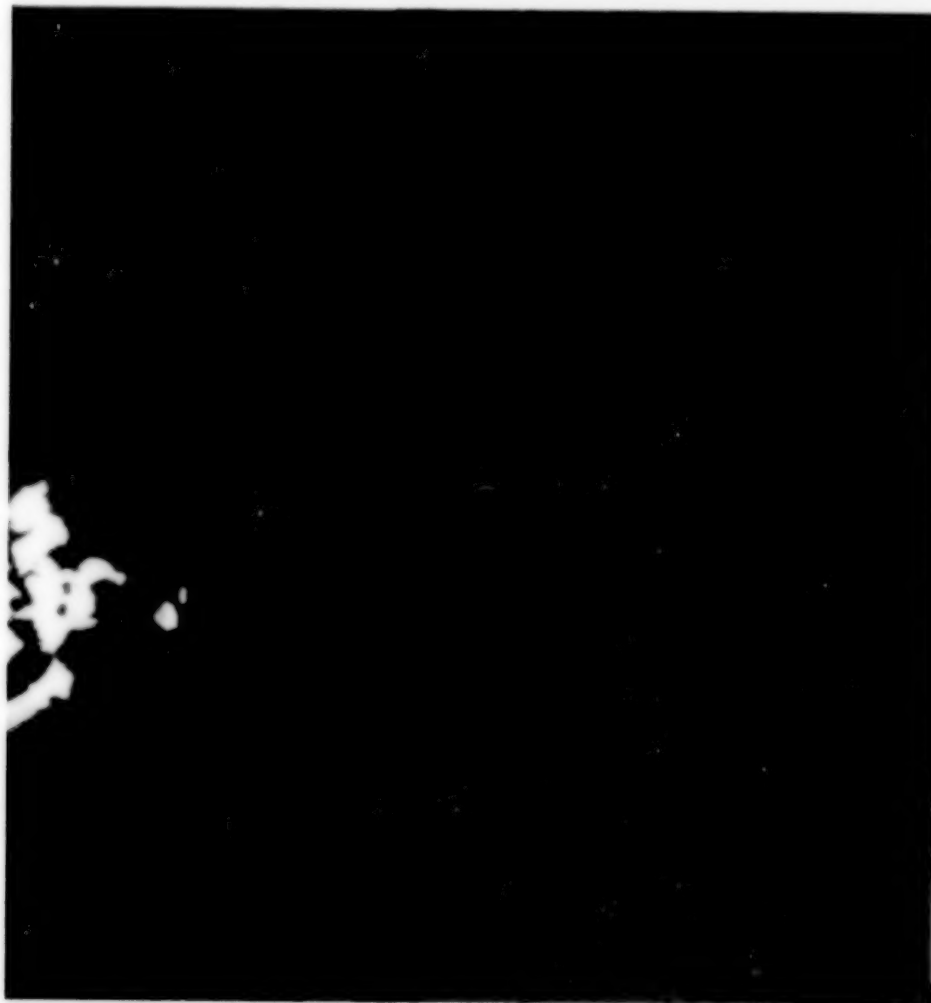


Figure 4-25b. Mean monthly sea ice concentrations for August 1975 and 1976.



ORIGINAL PAGE
COLOR PHOTOGRAPH

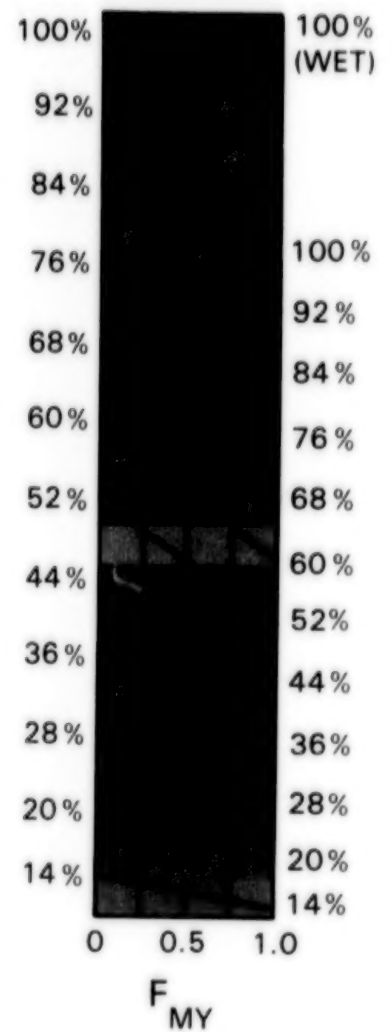


Figure 4-26a. Mean monthly sea ice concentrations for September 1973 and 1974.

ORIGINAL PAGE
COLOR PHOTOGRAPH

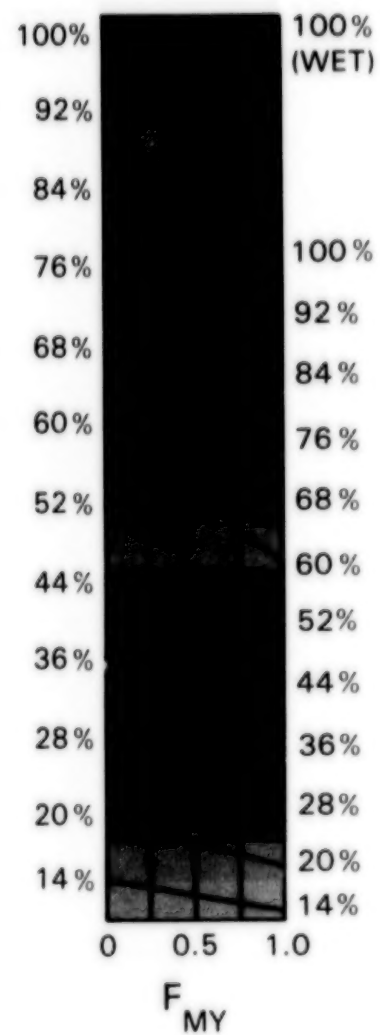
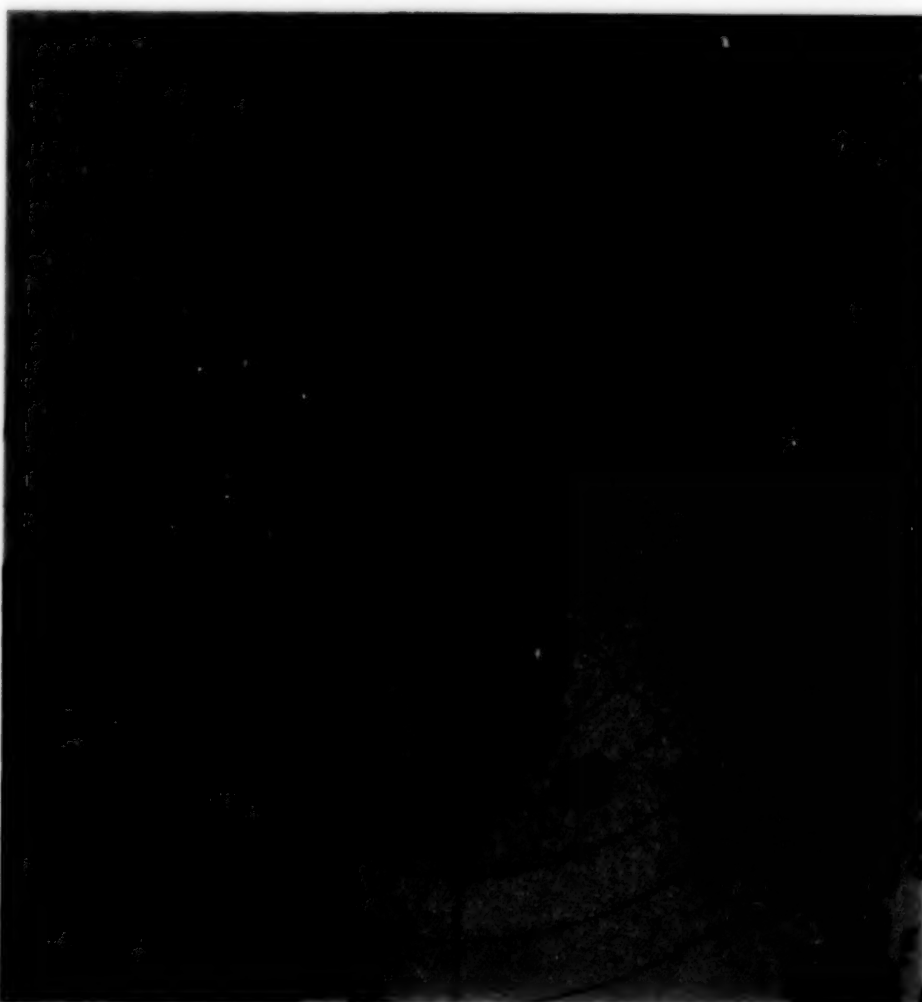
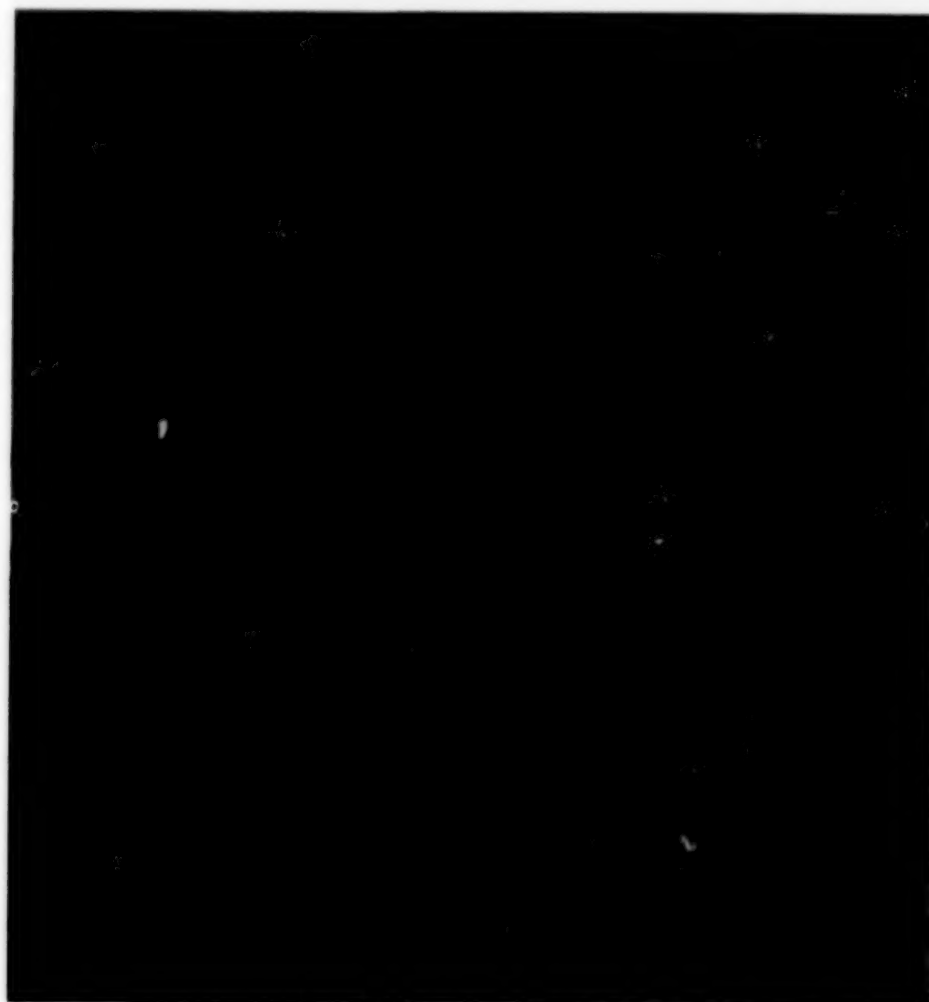


Figure 4-26b. Mean monthly sea ice concentrations for September 1975 and 1976.



ORIGINAL PACE
COLOR PHOTOGRAPH

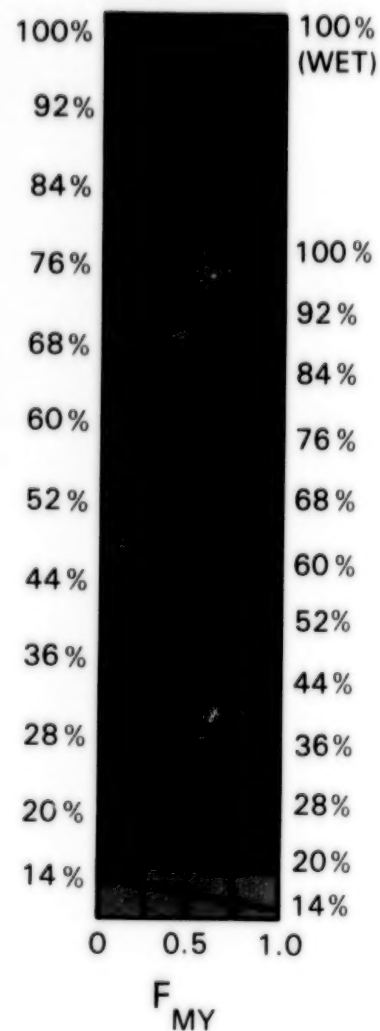


Figure 4-27a. Mean monthly sea ice concentrations for October 1973 and 1974.

**ORIGINAL PAGE
COLOR PHOTOGRAPH**

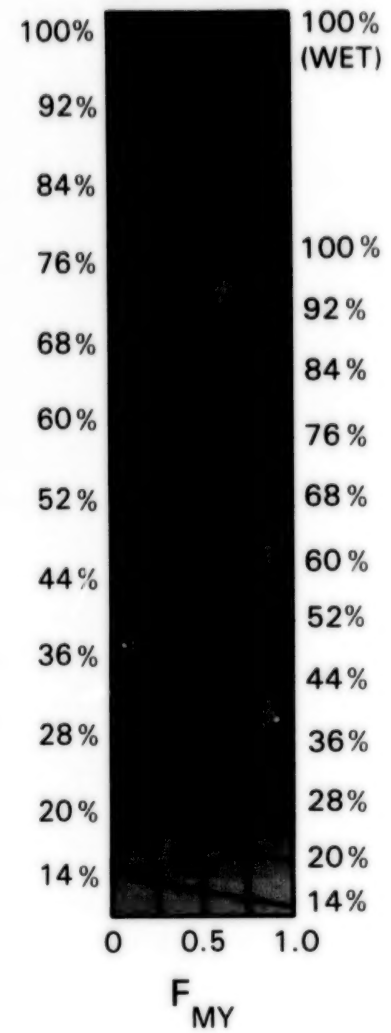
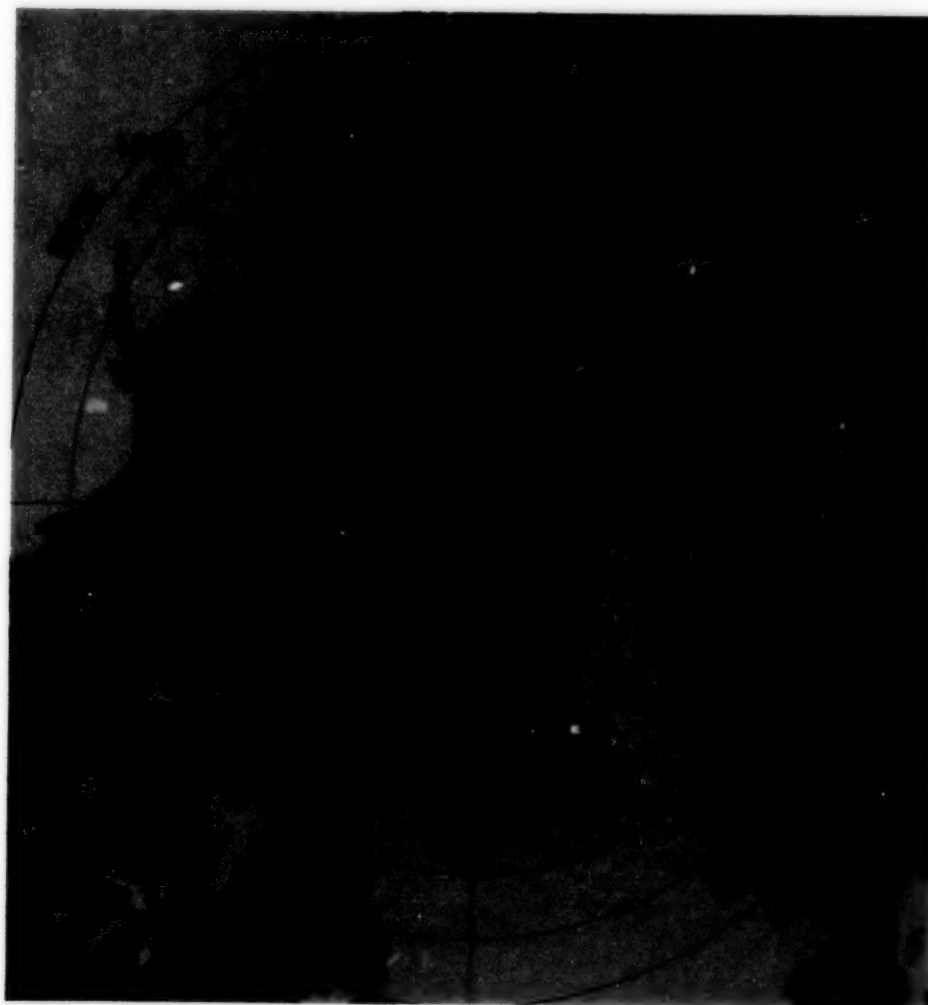
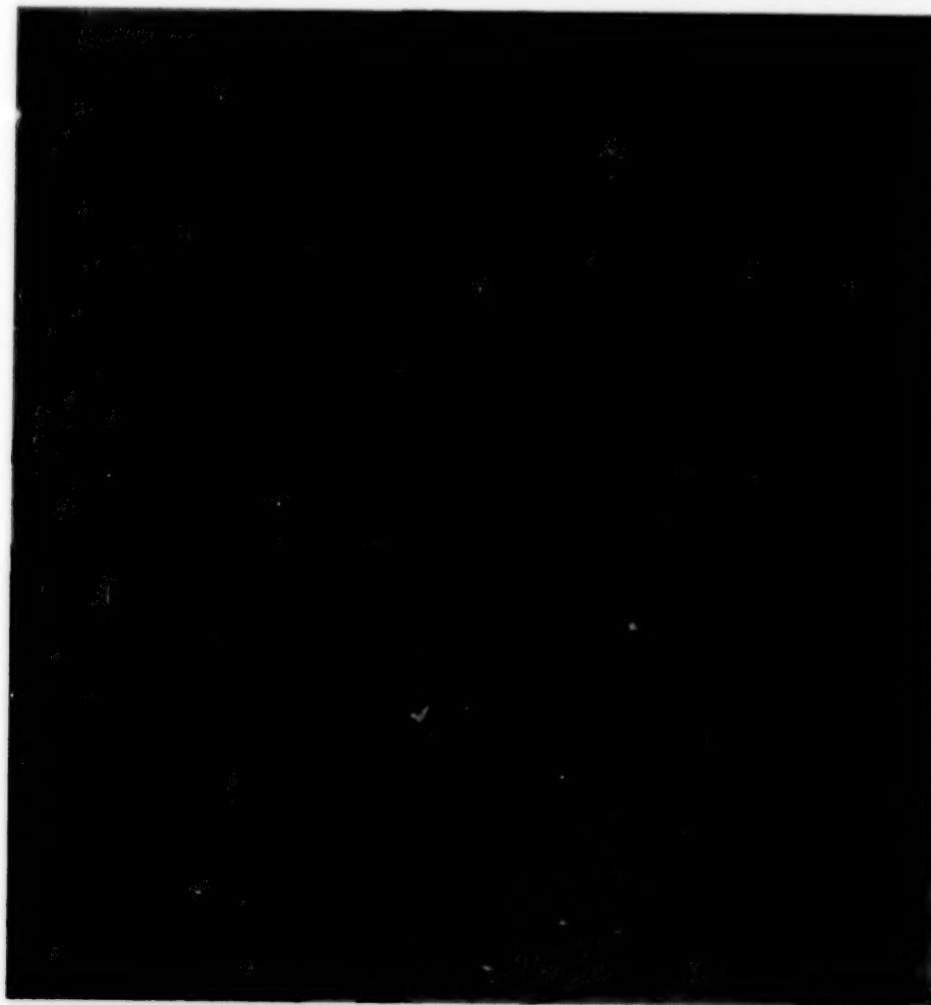


Figure 4-27b. Mean monthly sea ice concentrations for October 1975 and 1976.



ORIGINAL PAGE
COLOR PHOTOGRAPH

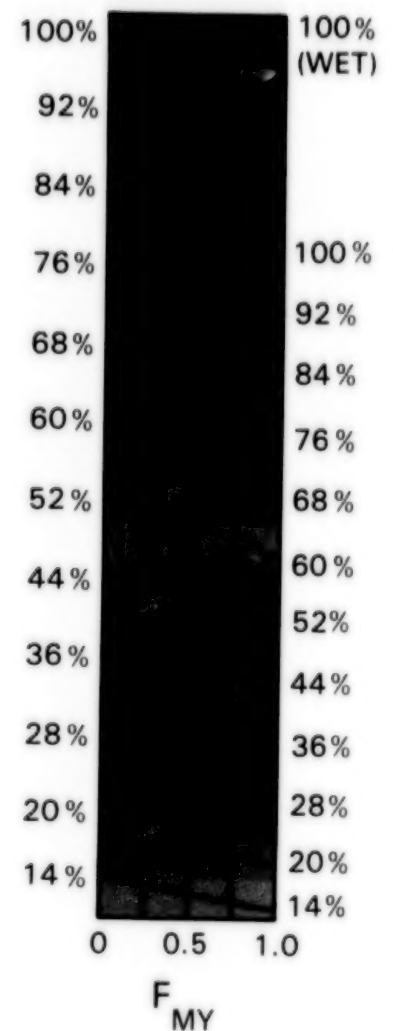


Figure 4-28a. Mean monthly sea ice concentrations for November 1973 and 1974.

ORIGINAL PAGE
COLOR PHOTOGRAPH

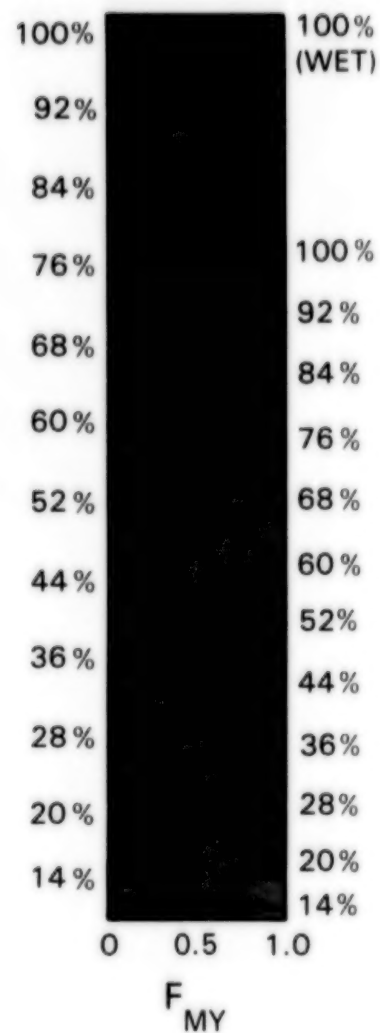
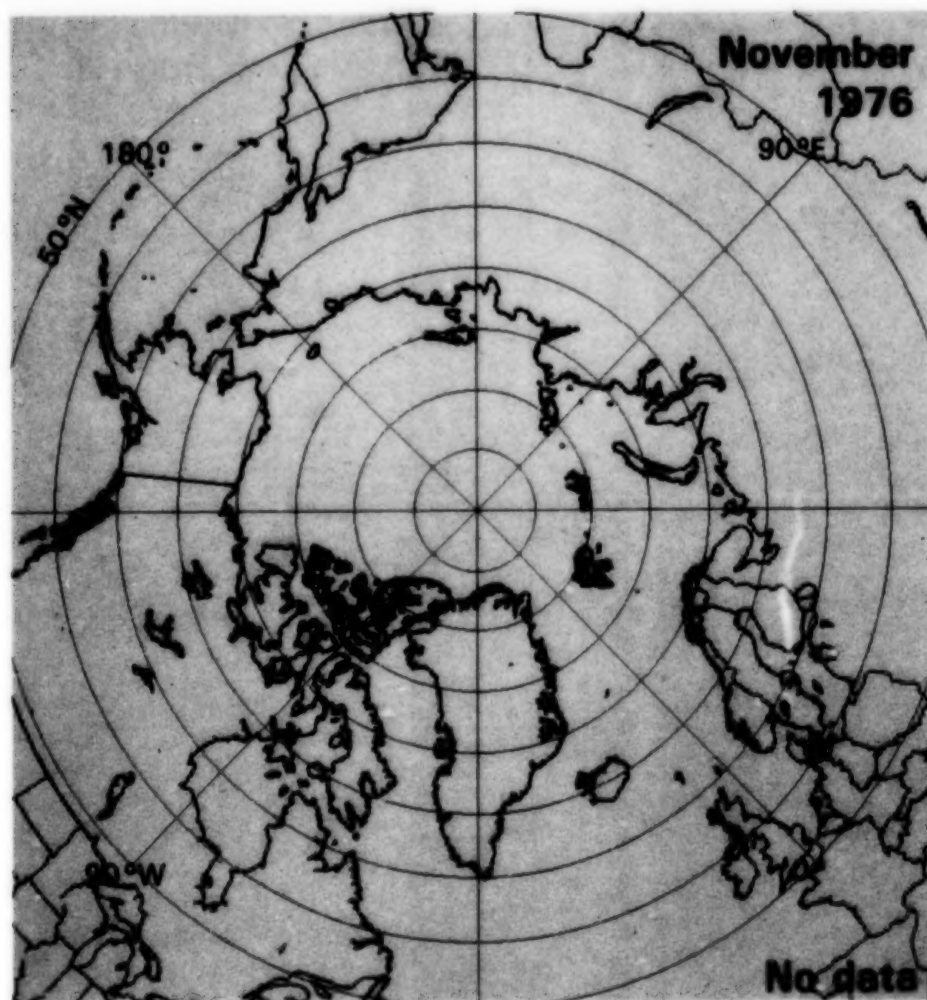
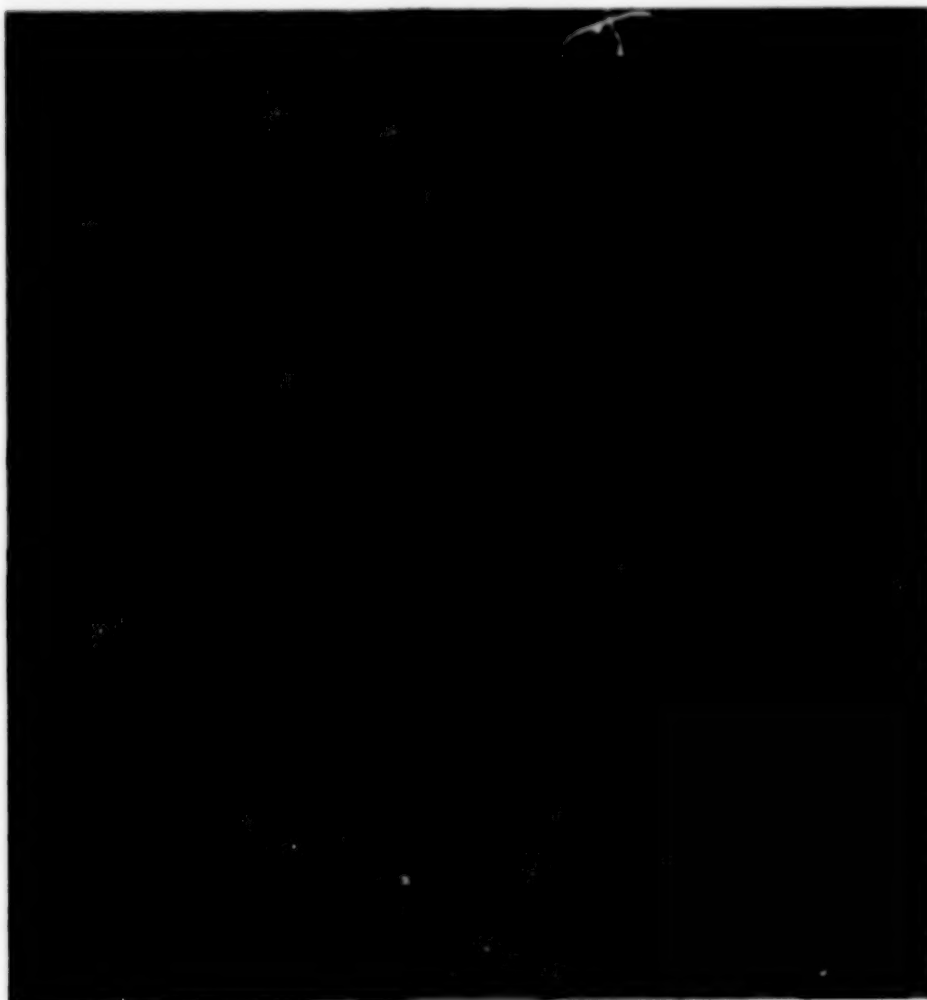


Figure 4-28b. Mean monthly sea ice concentrations for November 1975 and 1976.

ORIGINAL PAGE
COLOR PHOTOGRAPH

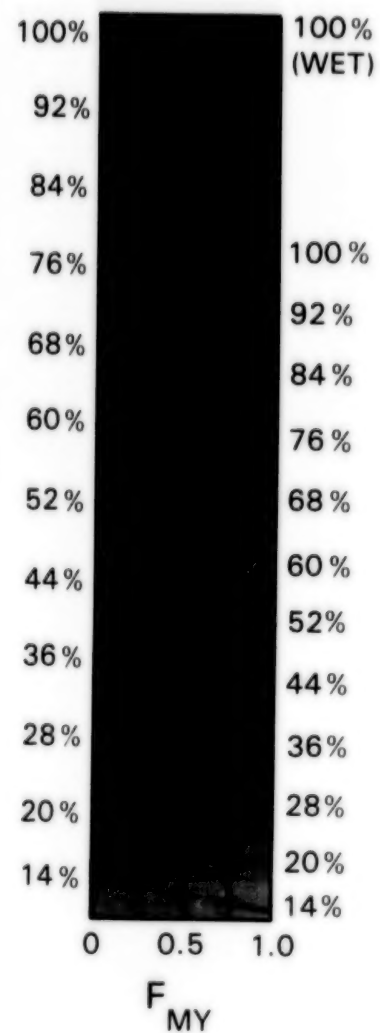


Figure 4-29a. Mean monthly sea ice concentrations for December 1973 and 1974.

ORIGINAL PAGE
COLOR PHOTOGRAPH

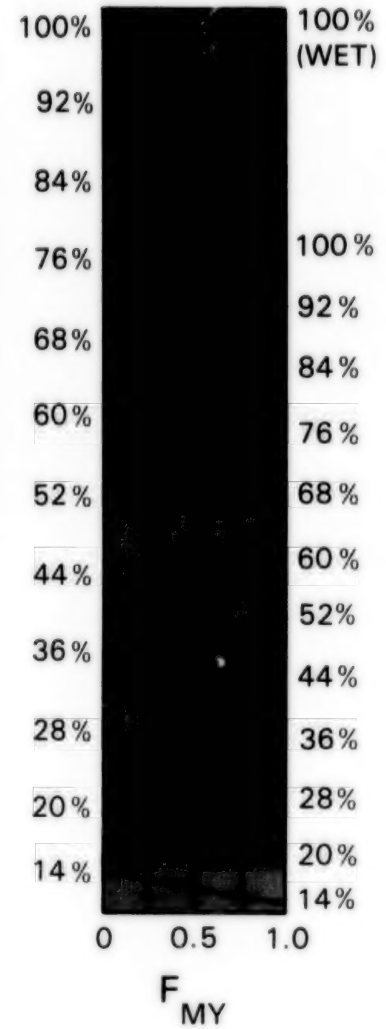
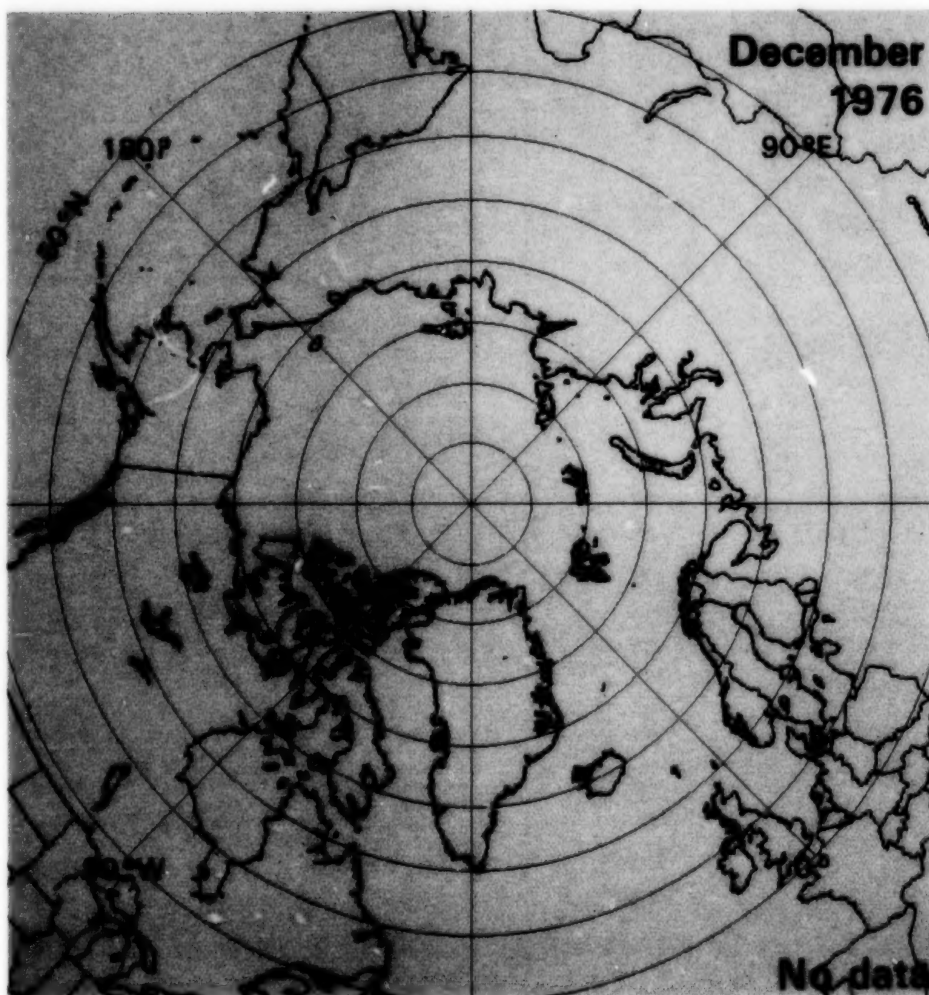
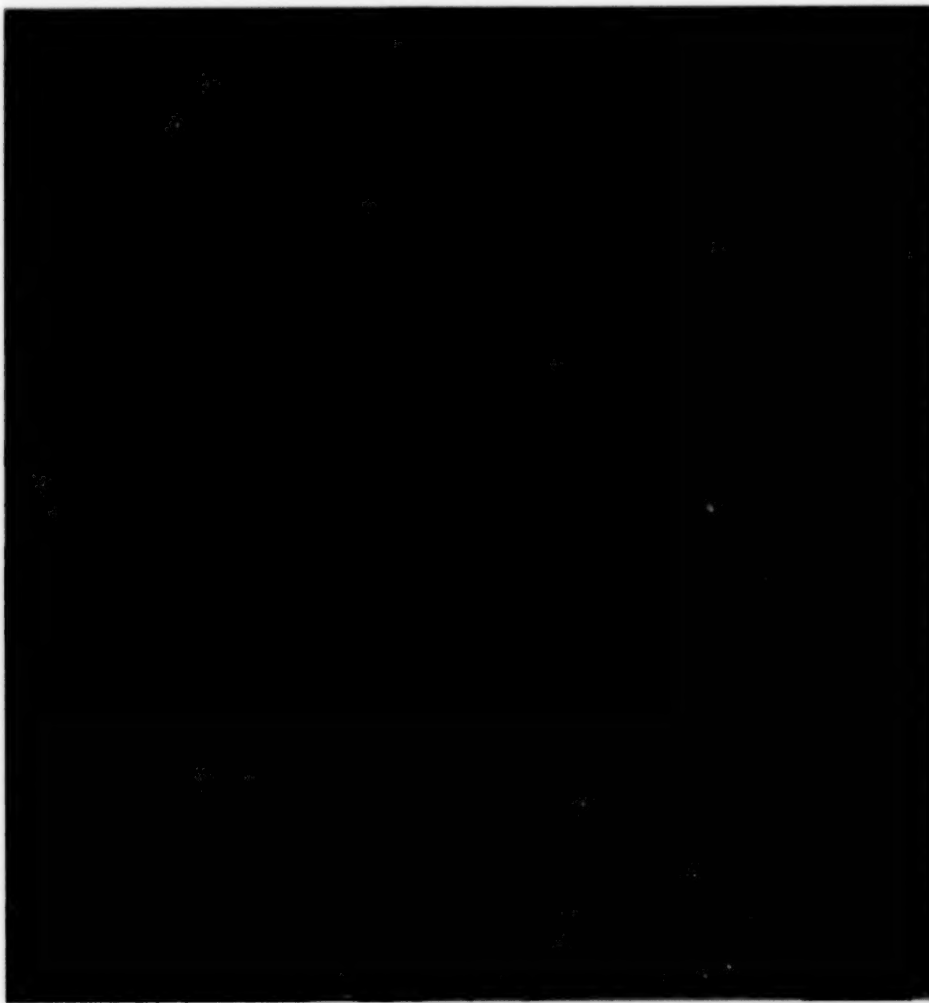


Figure 4-29b. Mean monthly sea ice concentrations for December 1975 and 1976.

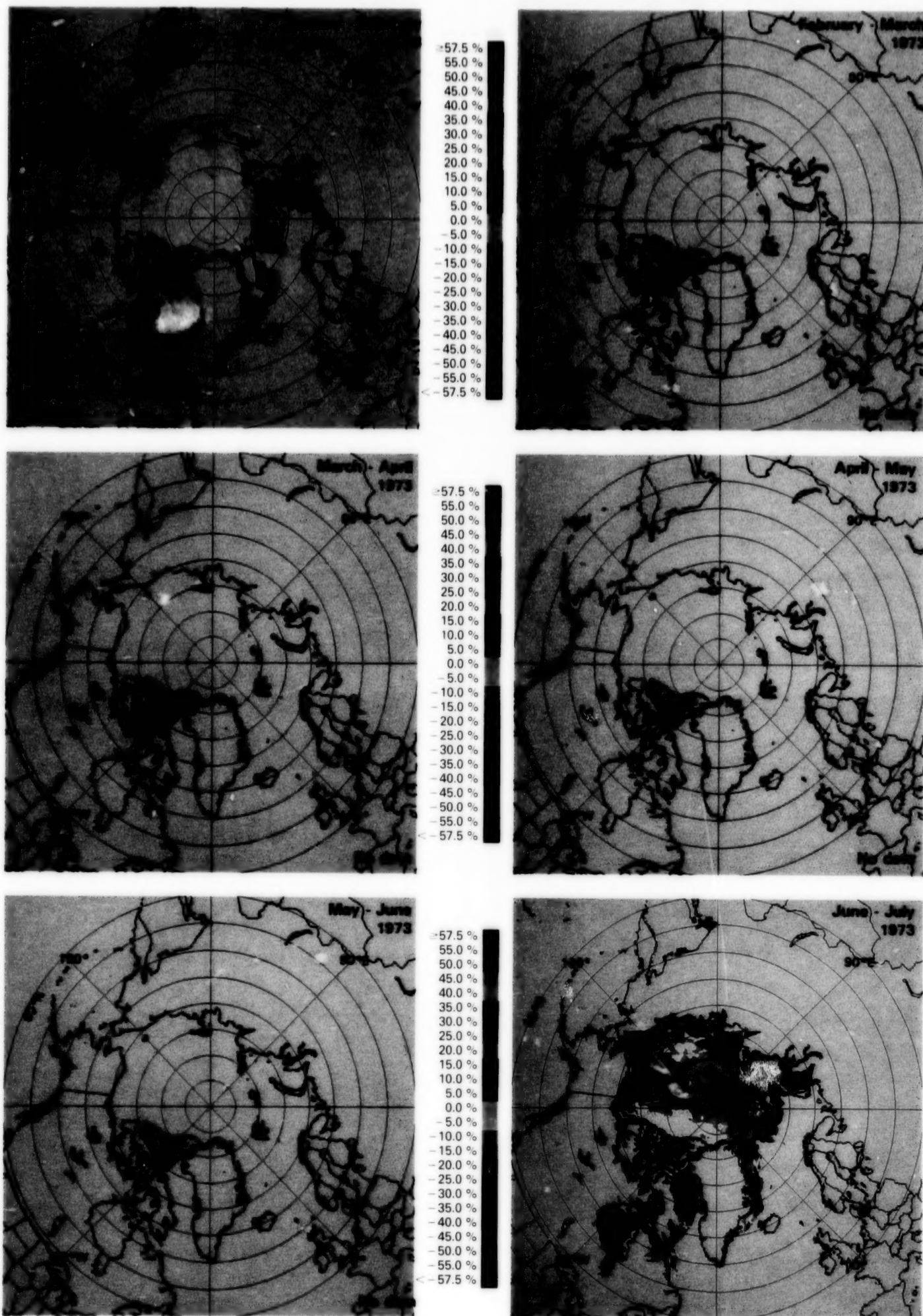
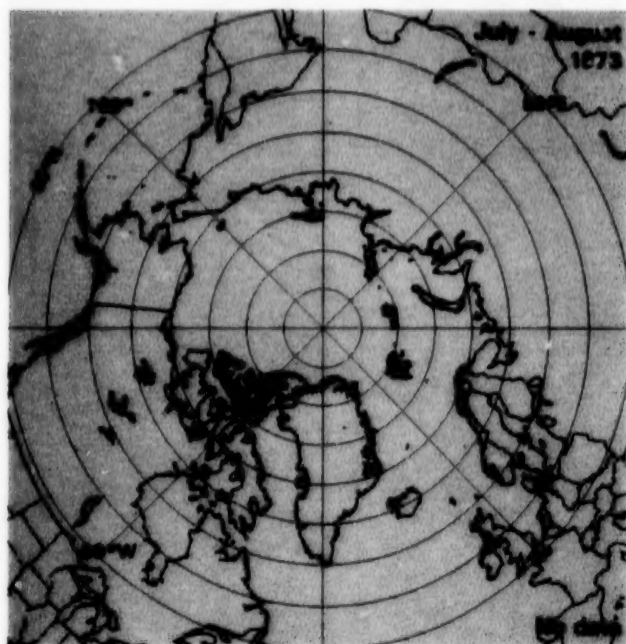
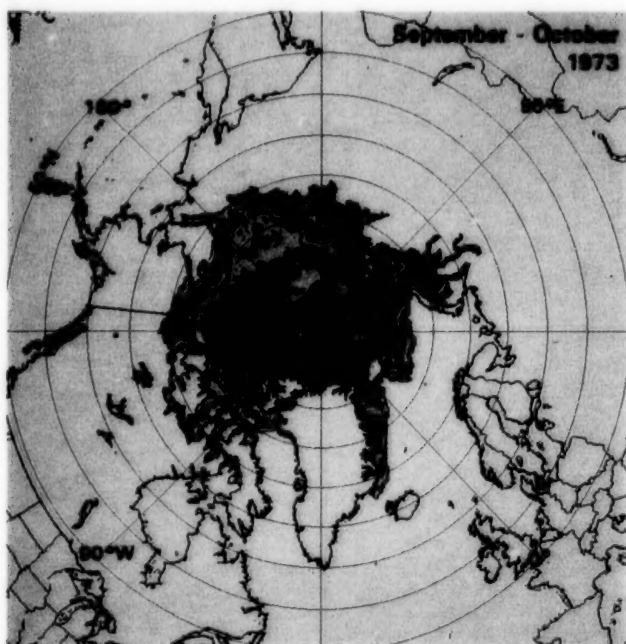
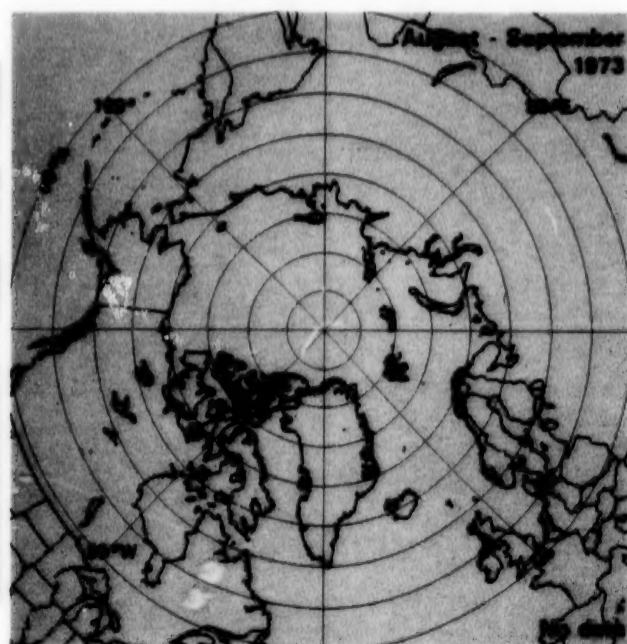


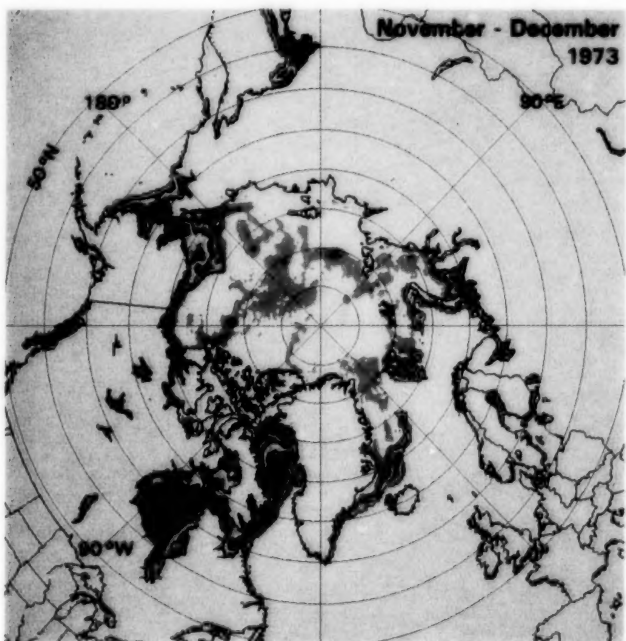
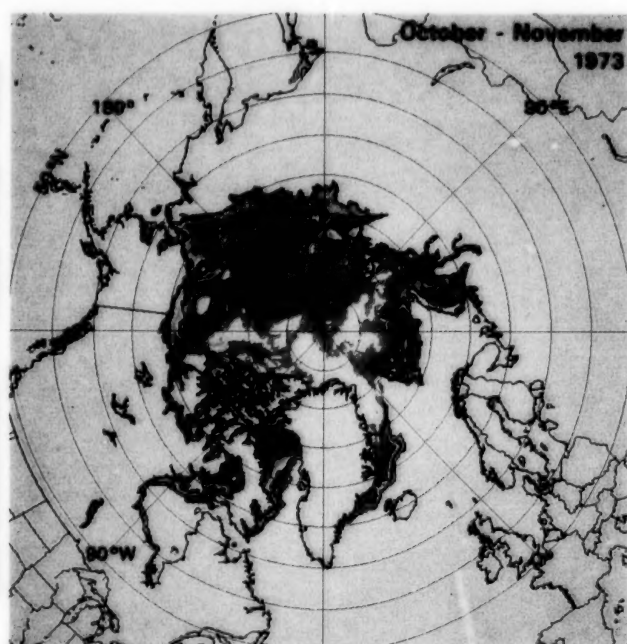
Figure 4-30. Sea ice concentration monthly change maps for January-February 1973 through June-July 1973.



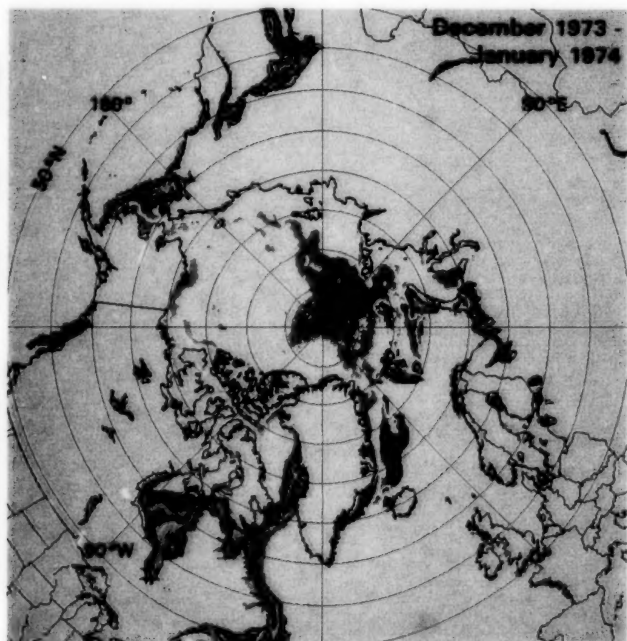
≥ 57.5 %
 55.0 %
 50.0 %
 45.0 %
 40.0 %
 35.0 %
 30.0 %
 25.0 %
 20.0 %
 15.0 %
 10.0 %
 5.0 %
 0.0 %
 -5.0 %
 -10.0 %
 -15.0 %
 -20.0 %
 -25.0 %
 -30.0 %
 -35.0 %
 -40.0 %
 -45.0 %
 -50.0 %
 -55.0 %
 < -57.5 %



≥ 57.5 %
 55.0 %
 50.0 %
 45.0 %
 40.0 %
 35.0 %
 30.0 %
 25.0 %
 20.0 %
 15.0 %
 10.0 %
 5.0 %
 0.0 %
 -5.0 %
 -10.0 %
 -15.0 %
 -20.0 %
 -25.0 %
 -30.0 %
 -35.0 %
 -40.0 %
 -45.0 %
 -50.0 %
 -55.0 %
 < -57.5 %



≥ 57.5 %
 55.0 %
 50.0 %
 45.0 %
 40.0 %
 35.0 %
 30.0 %
 25.0 %
 20.0 %
 15.0 %
 10.0 %
 5.0 %
 0.0 %
 -5.0 %
 -10.0 %
 -15.0 %
 -20.0 %
 -25.0 %
 -30.0 %
 -35.0 %
 -40.0 %
 -45.0 %
 -50.0 %
 -55.0 %
 < -57.5 %



ORIGINAL PAGE
 COLOR PHOTOGRAPH

Figure 4-31. Sea ice concentration monthly change maps for July-August 1973 through December 1973-January 1974.

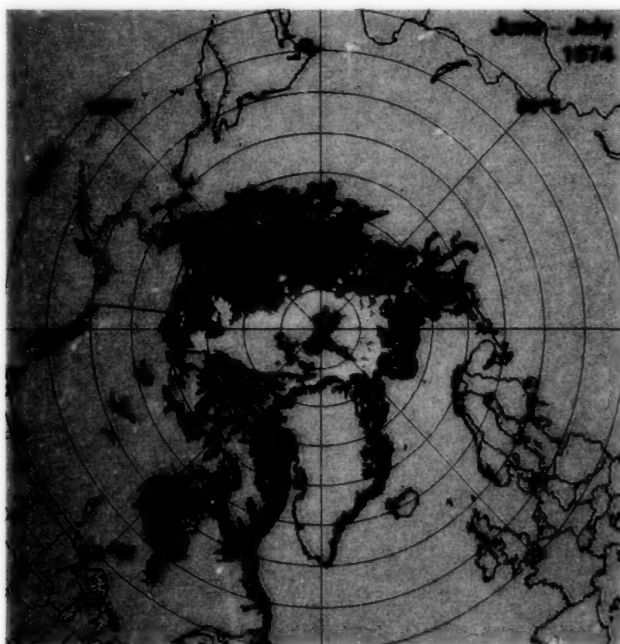
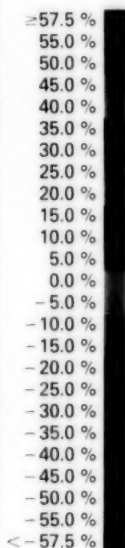
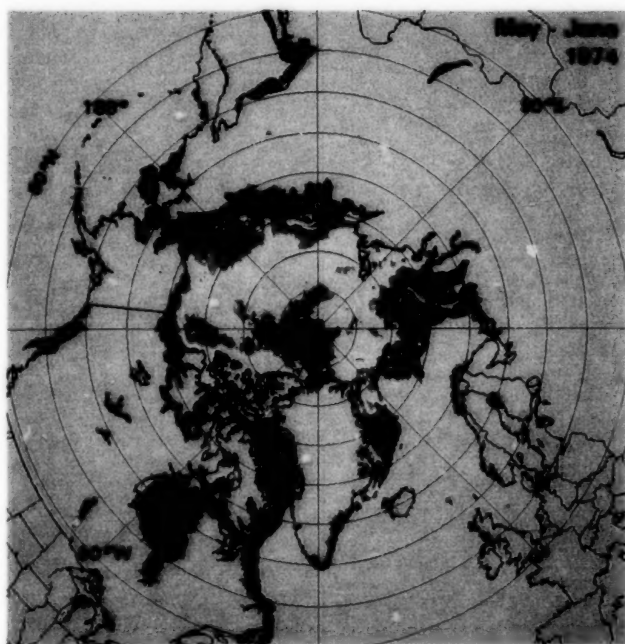
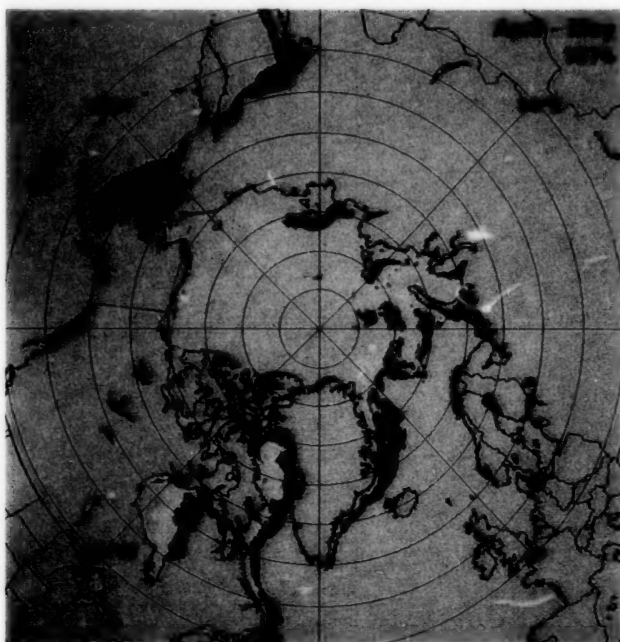
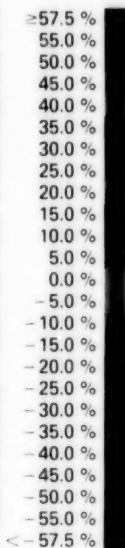
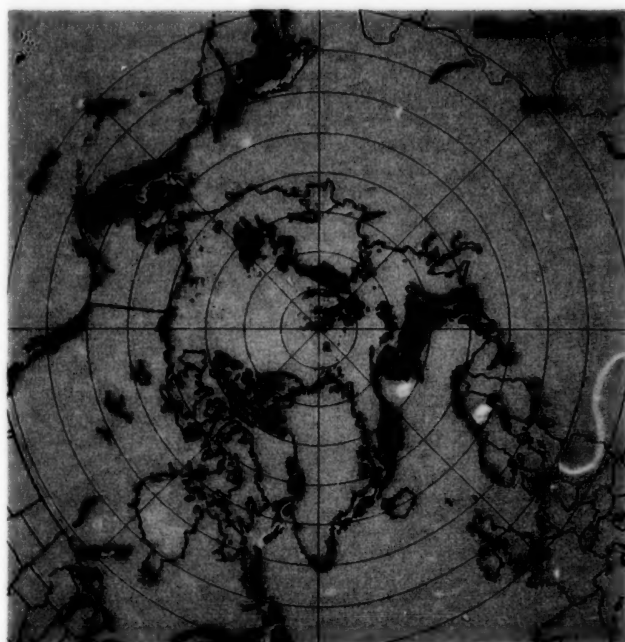
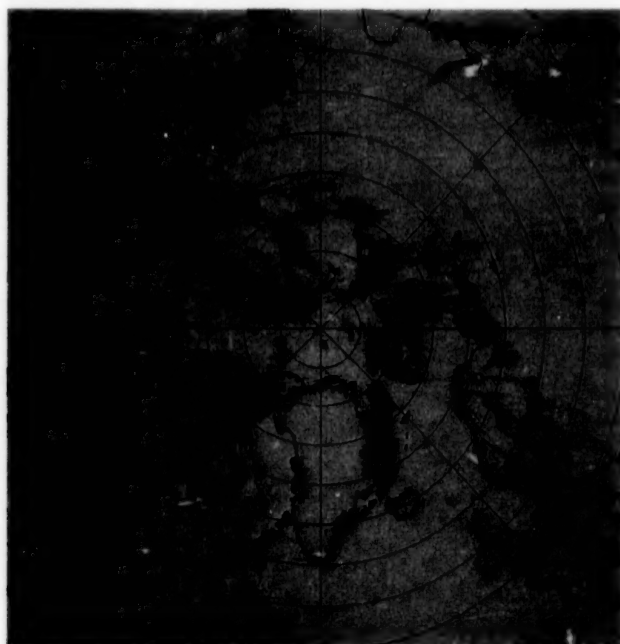
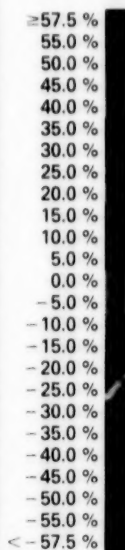


Figure 4-32. Sea ice concentration monthly change maps for January-February 1974 through June-July 1974.

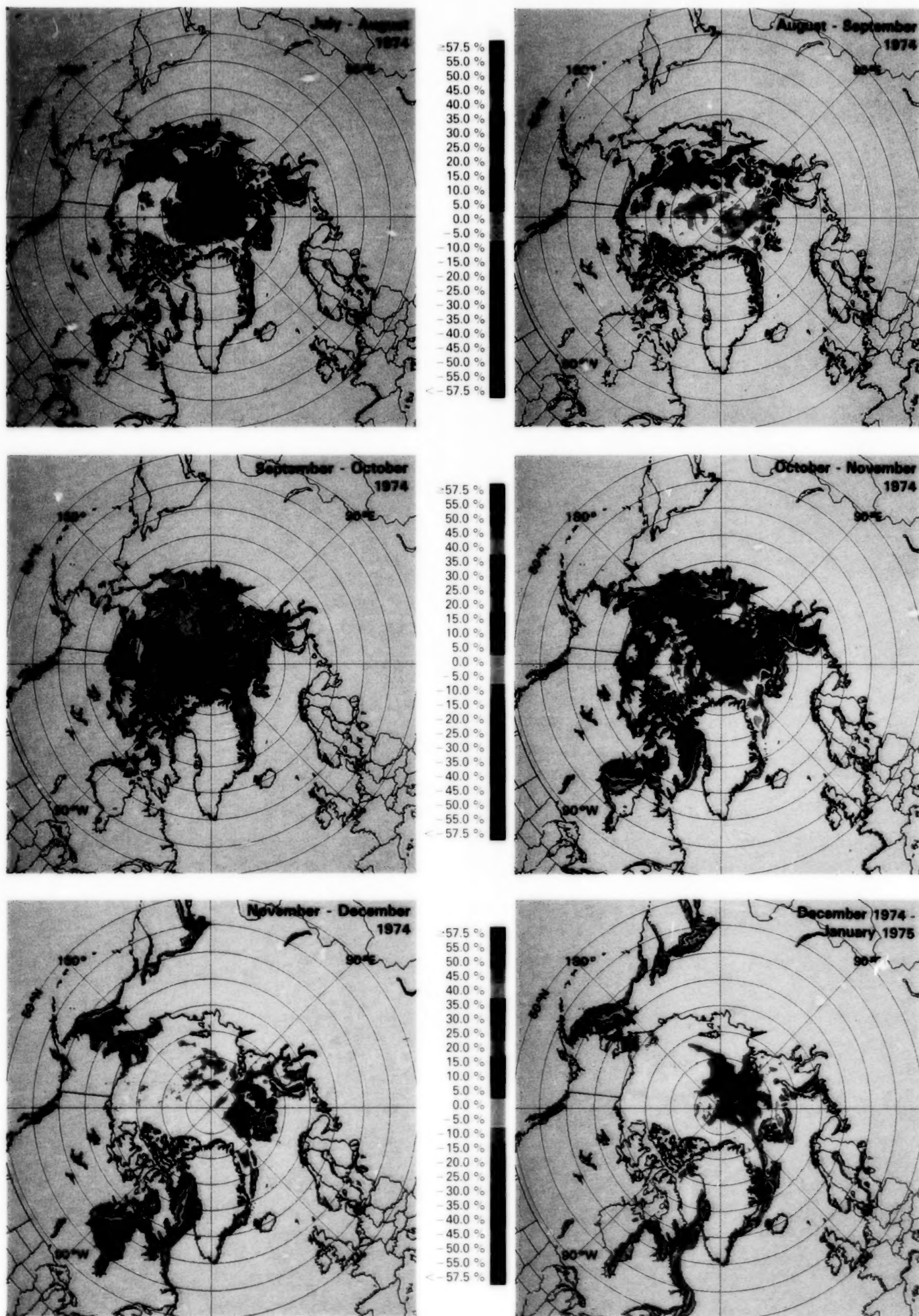


Figure 4-33. Sea ice concentration monthly change maps for July-August 1974 through December 1974-January 1975.

ORIGINAL PAGE
COLOR PHOTOGRAPH

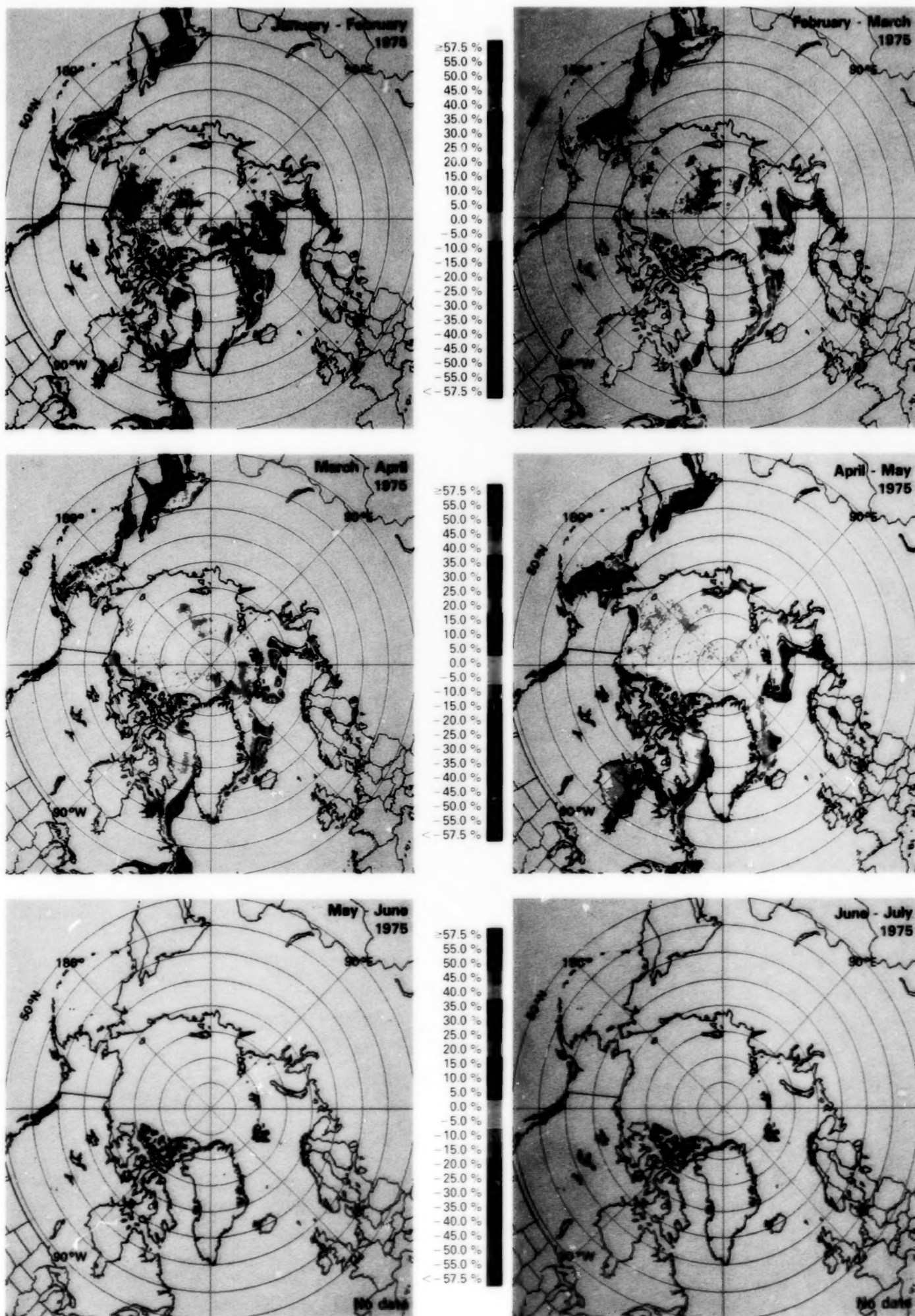
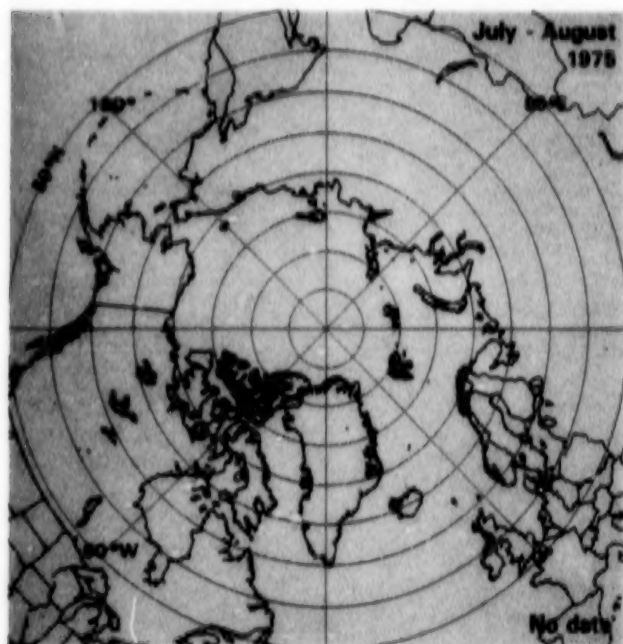
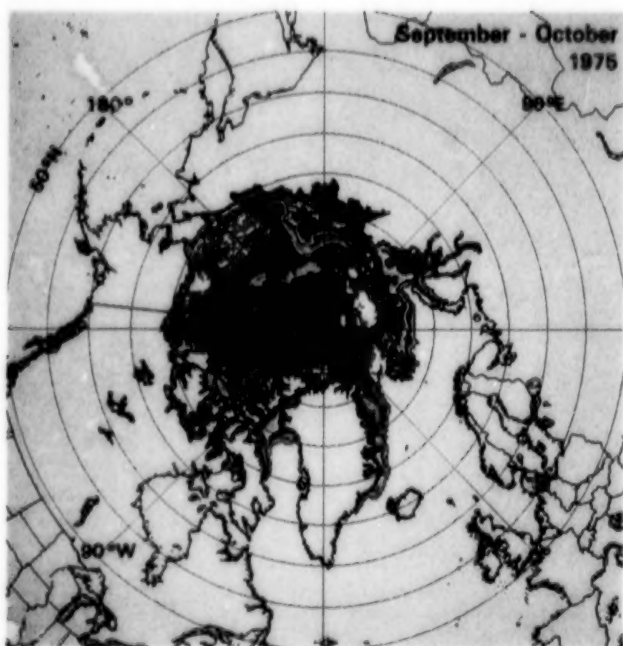
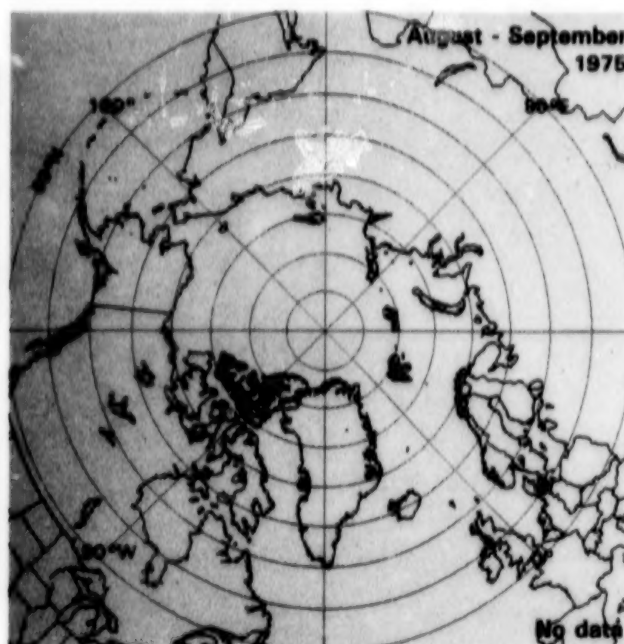


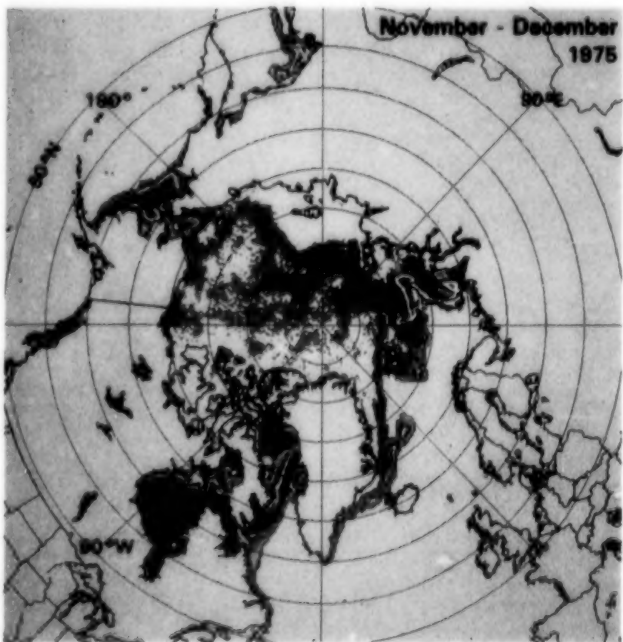
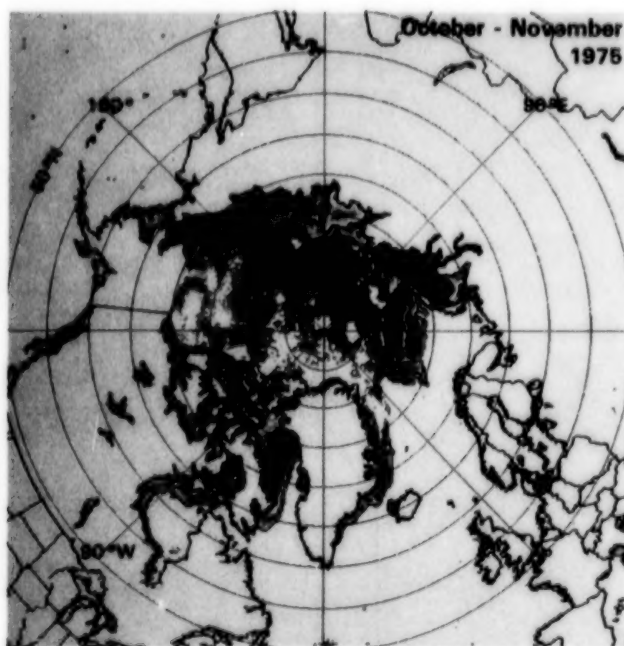
Figure 4-34. Sea ice concentration monthly change maps for January-February 1975 through June-July 1975.



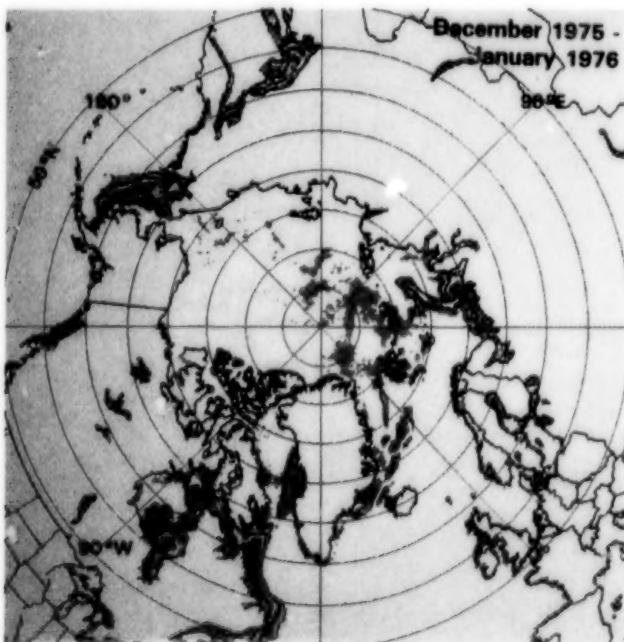
57.5 %
55.0 %
50.0 %
45.0 %
40.0 %
35.0 %
30.0 %
25.0 %
20.0 %
15.0 %
10.0 %
5.0 %
0.0 %
-5.0 %
-10.0 %
-15.0 %
-20.0 %
-25.0 %
-30.0 %
-35.0 %
-40.0 %
-45.0 %
-50.0 %
-55.0 %
-57.5 %



57.5 %
55.0 %
50.0 %
45.0 %
40.0 %
35.0 %
30.0 %
25.0 %
20.0 %
15.0 %
10.0 %
5.0 %
0.0 %
-5.0 %
-10.0 %
-15.0 %
-20.0 %
-25.0 %
-30.0 %
-35.0 %
-40.0 %
-45.0 %
-50.0 %
-55.0 %
-57.5 %



57.5 %
55.0 %
50.0 %
45.0 %
40.0 %
35.0 %
30.0 %
25.0 %
20.0 %
15.0 %
10.0 %
5.0 %
0.0 %
-5.0 %
-10.0 %
-15.0 %
-20.0 %
-25.0 %
-30.0 %
-35.0 %
-40.0 %
-45.0 %
-50.0 %
-55.0 %
-57.5 %



ORIGINAL PAGE
COLOR PHOTOGRAPH

Figure 4-35. Sea ice concentration monthly change maps for July-August 1975 through December 1975-January 1976.

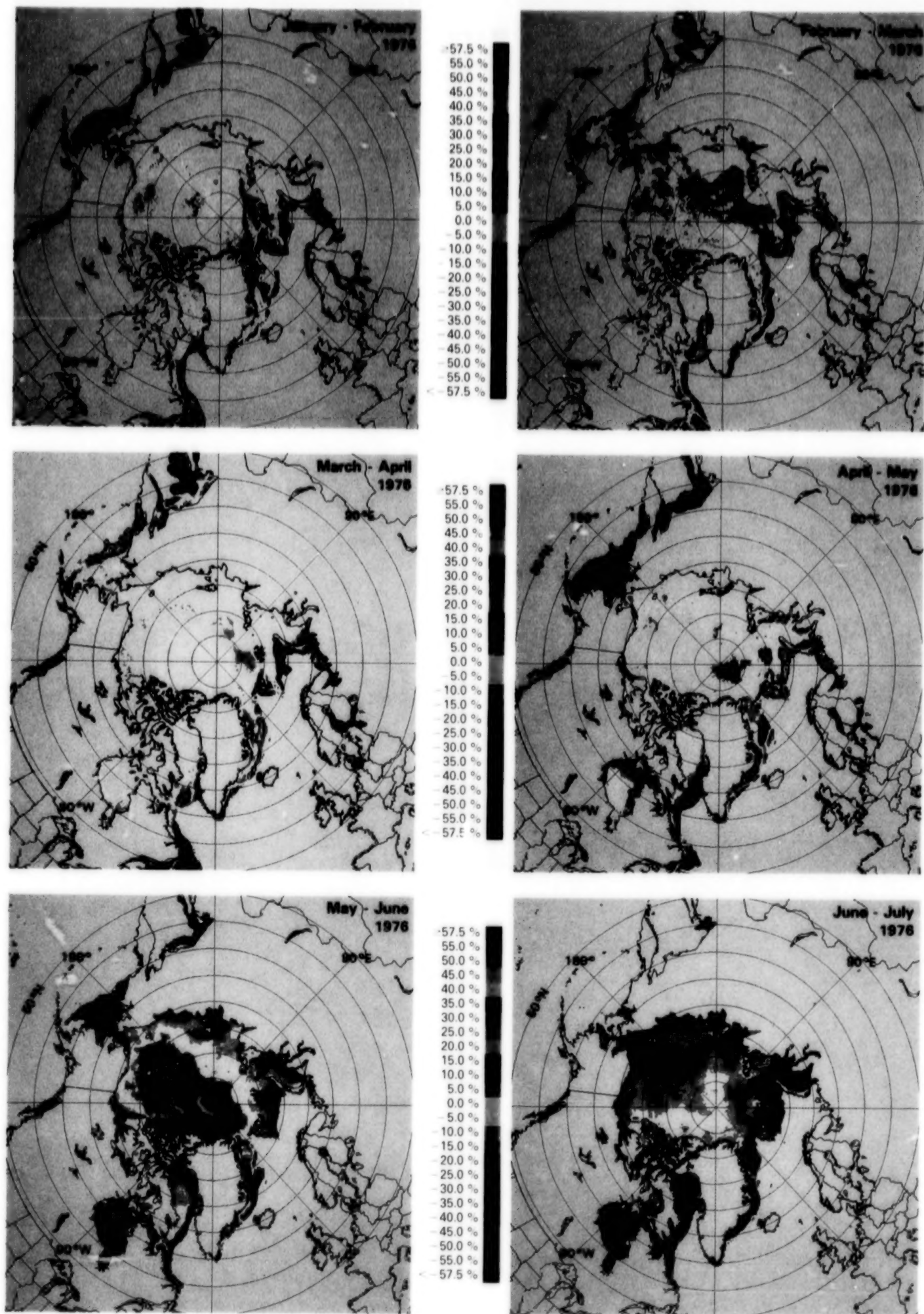
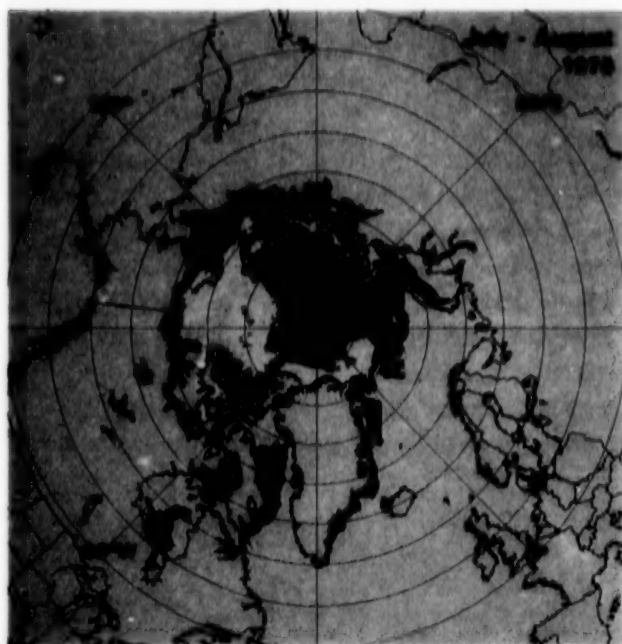
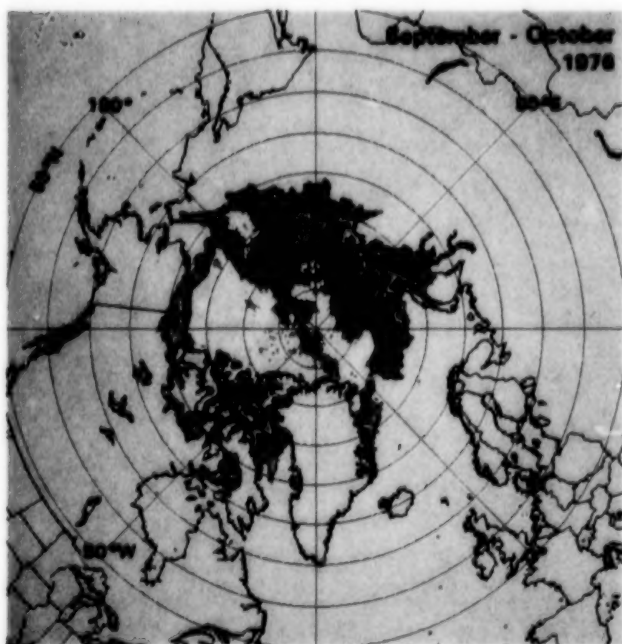
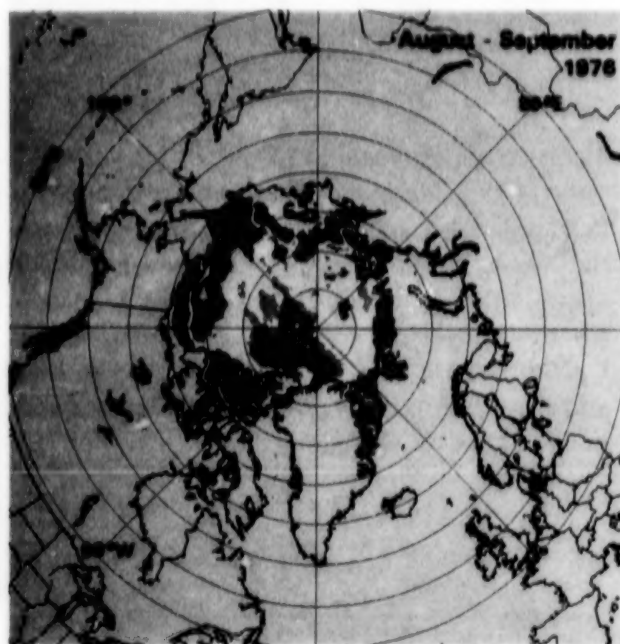


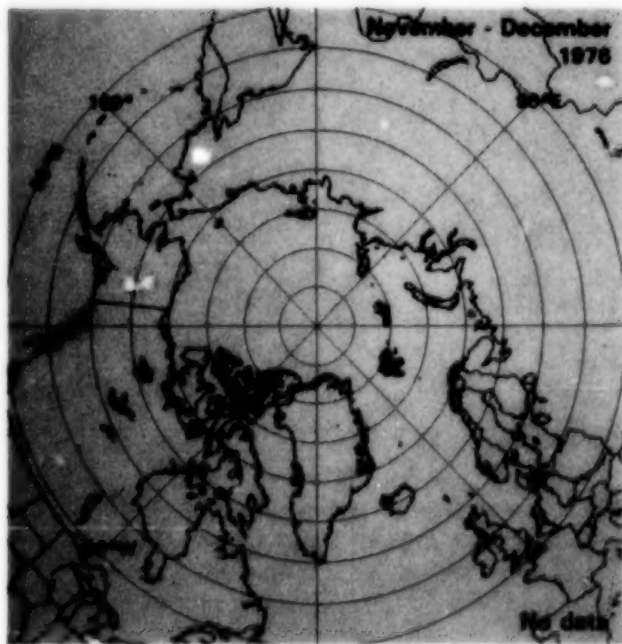
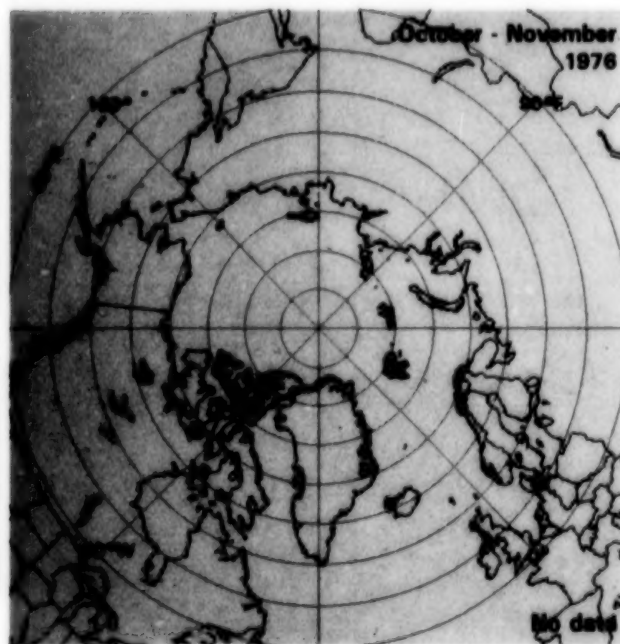
Figure 4-36. Sea ice concentration monthly change maps for January-February 1976 through June-July 1976.



57.5 %
55.0 %
50.0 %
45.0 %
40.0 %
35.0 %
30.0 %
25.0 %
20.0 %
15.0 %
10.0 %
5.0 %
0.0 %
-5.0 %
-10.0 %
-15.0 %
-20.0 %
-25.0 %
-30.0 %
-35.0 %
-40.0 %
-45.0 %
-50.0 %
-55.0 %
-57.5 %



57.5 %
55.0 %
50.0 %
45.0 %
40.0 %
35.0 %
30.0 %
25.0 %
20.0 %
15.0 %
10.0 %
5.0 %
0.0 %
-5.0 %
-10.0 %
-15.0 %
-20.0 %
-25.0 %
-30.0 %
-35.0 %
-40.0 %
-45.0 %
-50.0 %
-55.0 %
-57.5 %



57.5 %
55.0 %
50.0 %
45.0 %
40.0 %
35.0 %
30.0 %
25.0 %
20.0 %
15.0 %
10.0 %
5.0 %
0.0 %
-5.0 %
-10.0 %
-15.0 %
-20.0 %
-25.0 %
-30.0 %
-35.0 %
-40.0 %
-45.0 %
-50.0 %
-55.0 %
-57.5 %

ORIGINAL PAGE
COLOR PHOTOGRAPH

Figure 4-37. Sea ice concentration monthly change maps for July-August 1976 through November-December 1976.

Trans-Arctic Traverse in 1968. The drift arrows on the map show evidence of the two main features of average ice and upper-ocean circulation patterns in the Arctic: the Transpolar Drift Stream, extending northward from the East Siberian and Chukchi Seas toward the pole and continuing southward into and through the strait between Svalbard and Greenland; and the Beaufort Sea Gyre, a clockwise circulation in the Canadian Basin.

Since 1979, information on the ice pack motion has been greatly expanded by the operation of the Arctic Ocean Buoy Network of Argos-tracked, air-dropped drifting buoys. Data from this buoy network reveal that the ice circulation for 1979 (Figure 4-43) resembles the long-term drift by having the two main circulation features shown in Figure 4-42, whereas the 1983 circulation (Figure 4-44) does not. These two sets of buoy drifts illustrate the marked

ALL REGIONS

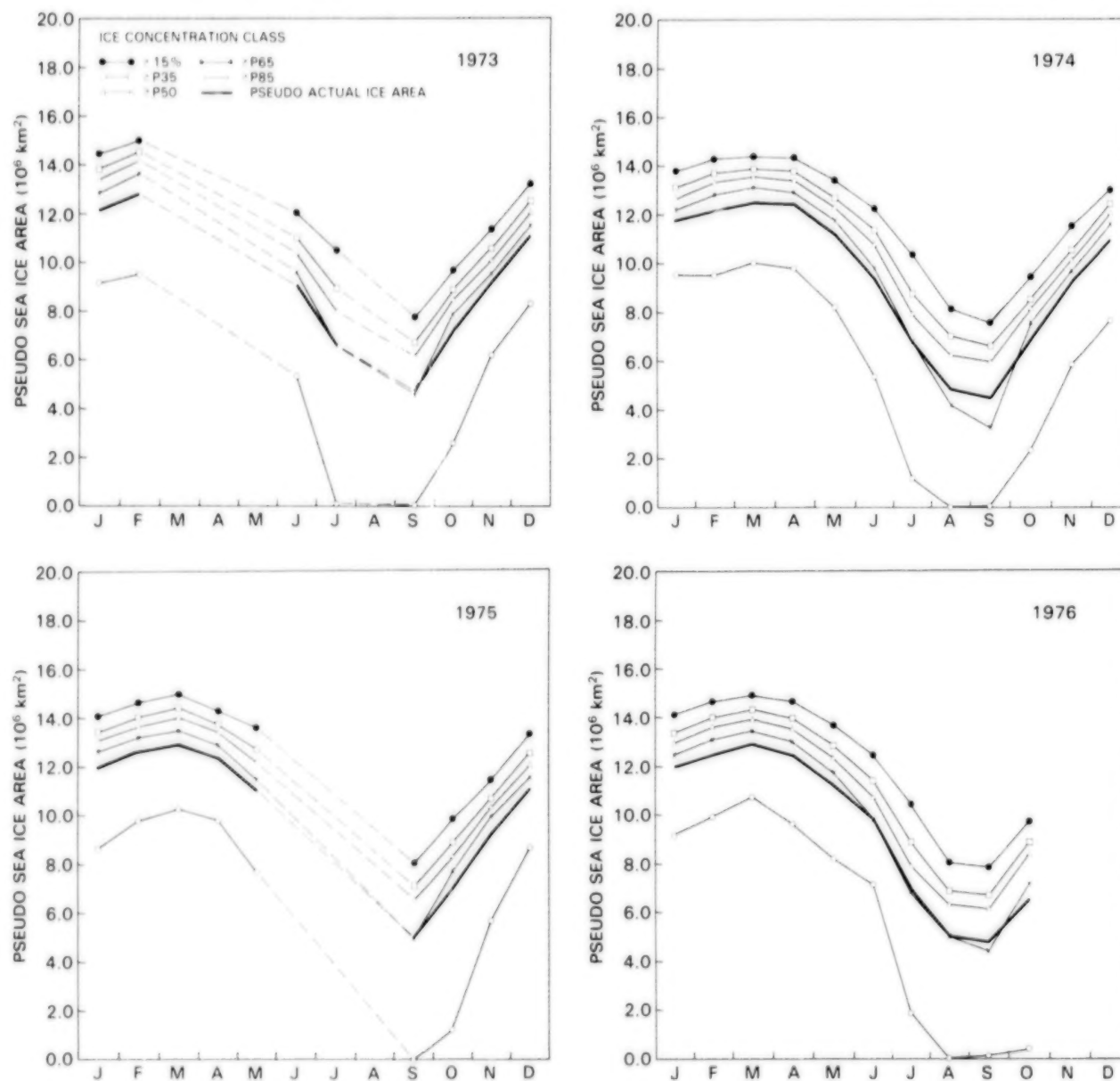


Figure 4-38. Yearly cycle of the ocean area covered by sea ice with concentration exceeding 15 percent, and yearly cycles of the P35, P50, P65, and P85 curves and the pseudo actual ice area, for the sum of the eight regions in Figure 4-2 in 1973, 1974, 1975, and 1976. The P35, P50, P65, P85, and pseudo actual ice area curves are defined in the caption for Figure 4-10.

interannual variations in the ice drift of the Arctic Ocean. The deviations from the mean velocity are important for all time scales, and Colony and Thorndike (1984), in an analysis of existing ice trajectory data, have discovered that for the time scale of 1 day the deviation from the mean greatly exceeds the mean, with the standard deviation being about 7 kilometers per day and the mean only about 2 kilometers per day.

Knowledge of the structure of the Arctic Ocean ice pack and its variations was greatly enhanced by the ESMR observations. The combination of complete spatial coverage and the temporal detail provided by sequential coverage at short time scales has led to an increased understanding of the Arctic ice cover (e.g., Campbell et al., 1984; Carleton, 1984; Carsey, 1982, 1985), even though the interpretation of the ESMR data for the Arctic Ocean is more

ALL REGIONS

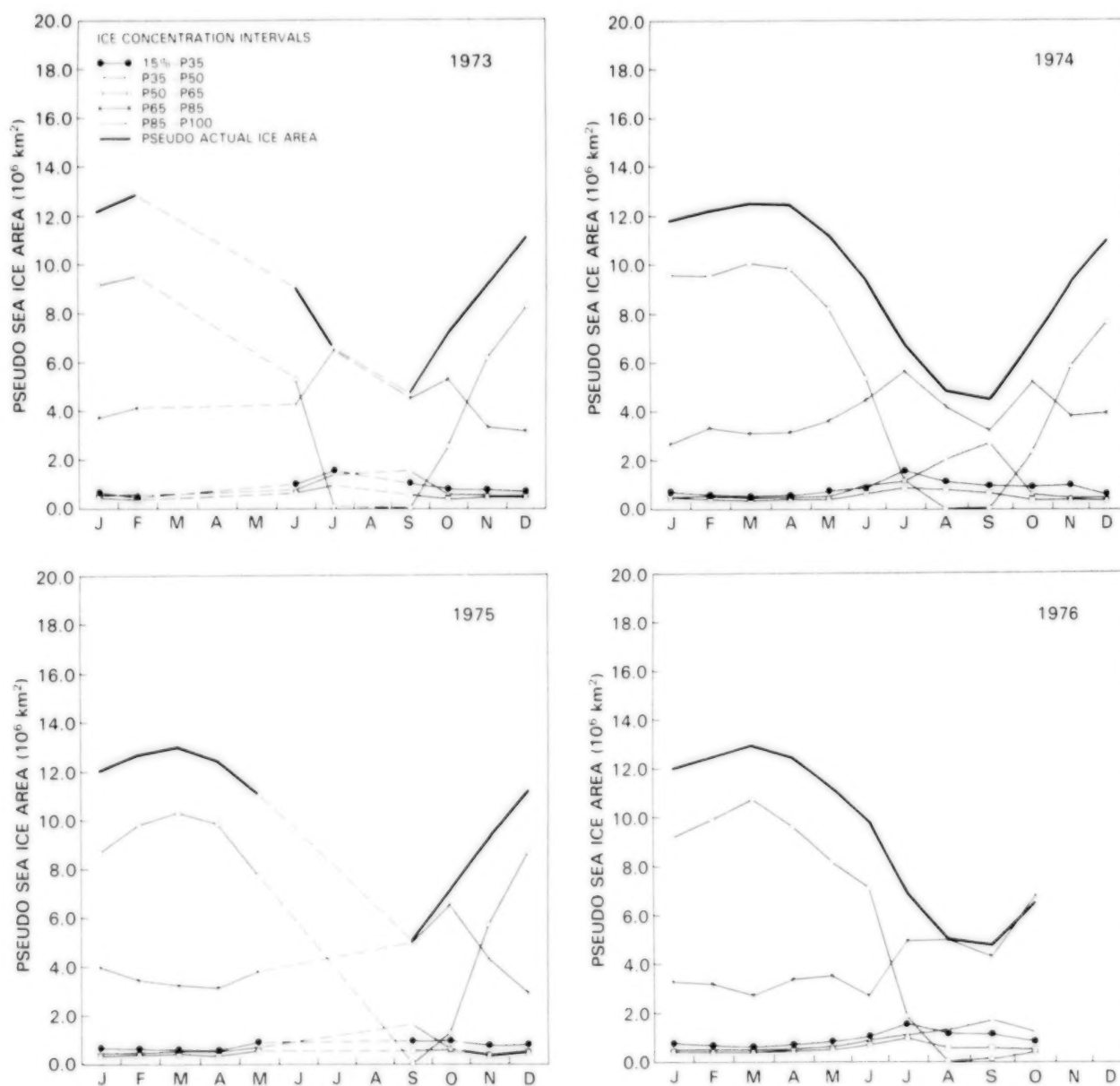


Figure 4-39. Yearly cycles of the ocean area covered by sea ice within the intervals 15 percent to P35, P35 to P50, P50 to P65, P65 to P85, and P85 to P100, and yearly cycle of the pseudo actual ice area, for the sum of the eight regions in Figure 4-2 in 1973, 1974, 1975, and 1976. The interval curves are calculated by subtracting the respective curves of Figure 4-38.

difficult than for many other Arctic areas. This difficulty arises because variations in ice type and concentration occur in the central Arctic during all seasons. The situation is further complicated during the seasons of ice/snow warming, melting, and re-freezing when free water occurs in the surface layer and melt ponds form that alternately refreeze and thaw. As discussed in Chapter 3, all of these phenomena cause the microwave emissions to vary. Thus, although during melt conditions the multiyear versus first-year ice distinction vanishes, the ESMR interpretation is more complex because (1) melt ponds and free water affect the microwave emissions and (2) *in-situ* observations of these phenomena are rare.

Although it is impossible to separate the variables of ice concentration and multiyear ice fraction on a single scene exclusively from the single frequency microwave data, the nomogram described in Chapter 3 and presented on the color-coded ice concentration images of this chapter can be used to determine ice concentration ranges, or, in localities where reasonable ice-type assumptions can be made, to infer ice concentration more narrowly. Because of the complexity introduced to the ice concentration interpretation by the existence of an indeterminate combination of first-year and multiyear ice amounts, both brightness temperature maps and ice concentration maps will be used for interpreting the ESMR data for the Arctic Ocean and the other three regions in

ALL REGIONS

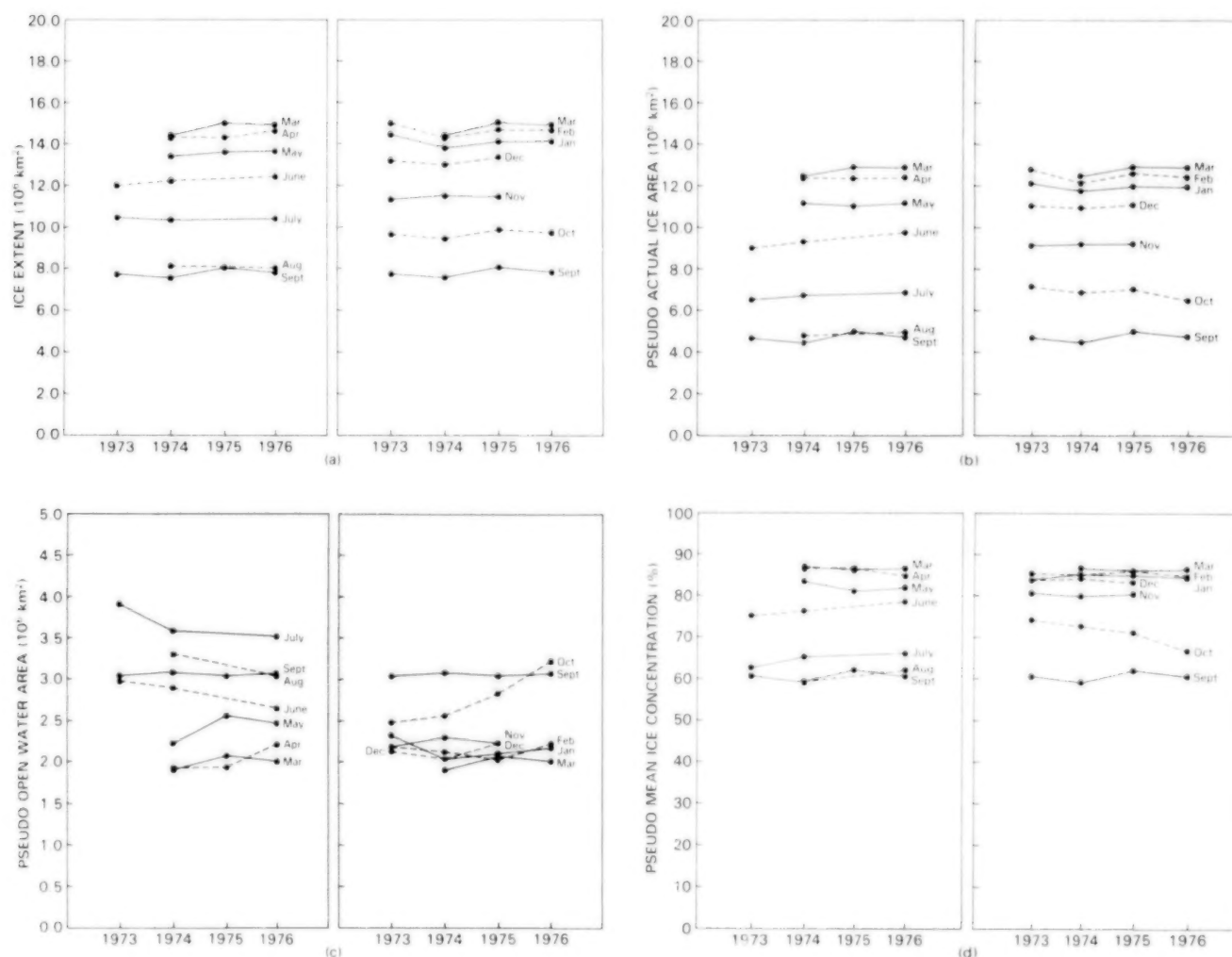


Figure 4-40. Month-by-month year-to-year changes in (a) sea ice extent, (b) pseudo actual ice area, (c) pseudo open water area within the ice pack, and (d) pseudo mean sea ice concentration, for the sum of the eight regions in Figure 4-2. The pseudo quantities are calculated with an ice emissivity of 0.92, appropriate for first-year ice.

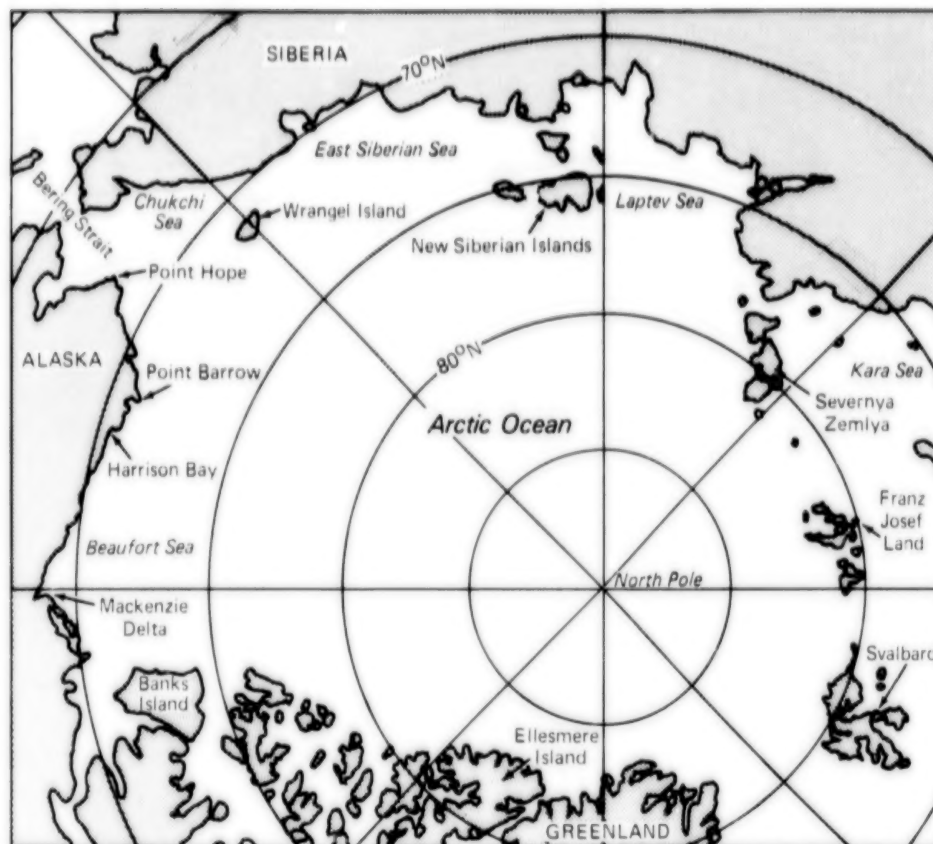


Figure 4-41. Location map for the Arctic Ocean region.

which significant amounts of both first-year and multiyear ice exist. These other regions are the Greenland Sea, the Kara and Barents Seas, and the Canadian Archipelago.

The Arctic Ocean ice pack experiences an 8-month "winter" season from November through June (Figure 4-11). Multiyear ice, with an average thickness of approximately 4 meters, covers most of the area between the North Pole and the north coasts of Canada and Greenland and has radiances ranging from 205 to 220 K. First-year ice, with an average thickness of approximately 1.5 meters, covers most of the East Siberian and Laptev Seas and has radiances between 235 and 245 K. In the other areas of the Arctic Ocean, various mixtures of these two ice types occur. In view of the significant temporal changes in the physical temperature distributions in the ice canopy, caution should be exercised in interpreting the details of the radiance distribution variations. The ice within the minimum ice boundary for any particular year becomes the multiyear ice for the following year. Carsey (1982) uses the ESMR data

to analyze the Arctic sea ice cover at the end of summer for the 1973 through 1976 period. The degree of mixing of first-year and multiyear ice depends on how much ice divergence and refreezing takes place in a given location, and how much compression of the newly formed ice into hummocks and ridges results from subsequent ice convergence.

Because the Arctic Ocean region (Figure 4-2) encompasses a wide variety of ocean depths and climatic contrasts, it is appropriate to describe the chronological evolution of various prominent features separately. Beginning with January, the least controversial feature in Figure 4-3 is the purple-colored area in the western Chukchi and Laptev Seas, labeled 100 percent total ice concentration on the $F_{MY} = 0$ side of the nomogram. Since the ice is not likely to be wet at this time of year, the data indicate that the ice is purely first-year ice and fully consolidated. This finding agrees with surface observations in this area (Gorshkov, 1983). Also, the area is usually ice free in late summer, consistent with the lack of multiyear ice in winter. On average, this

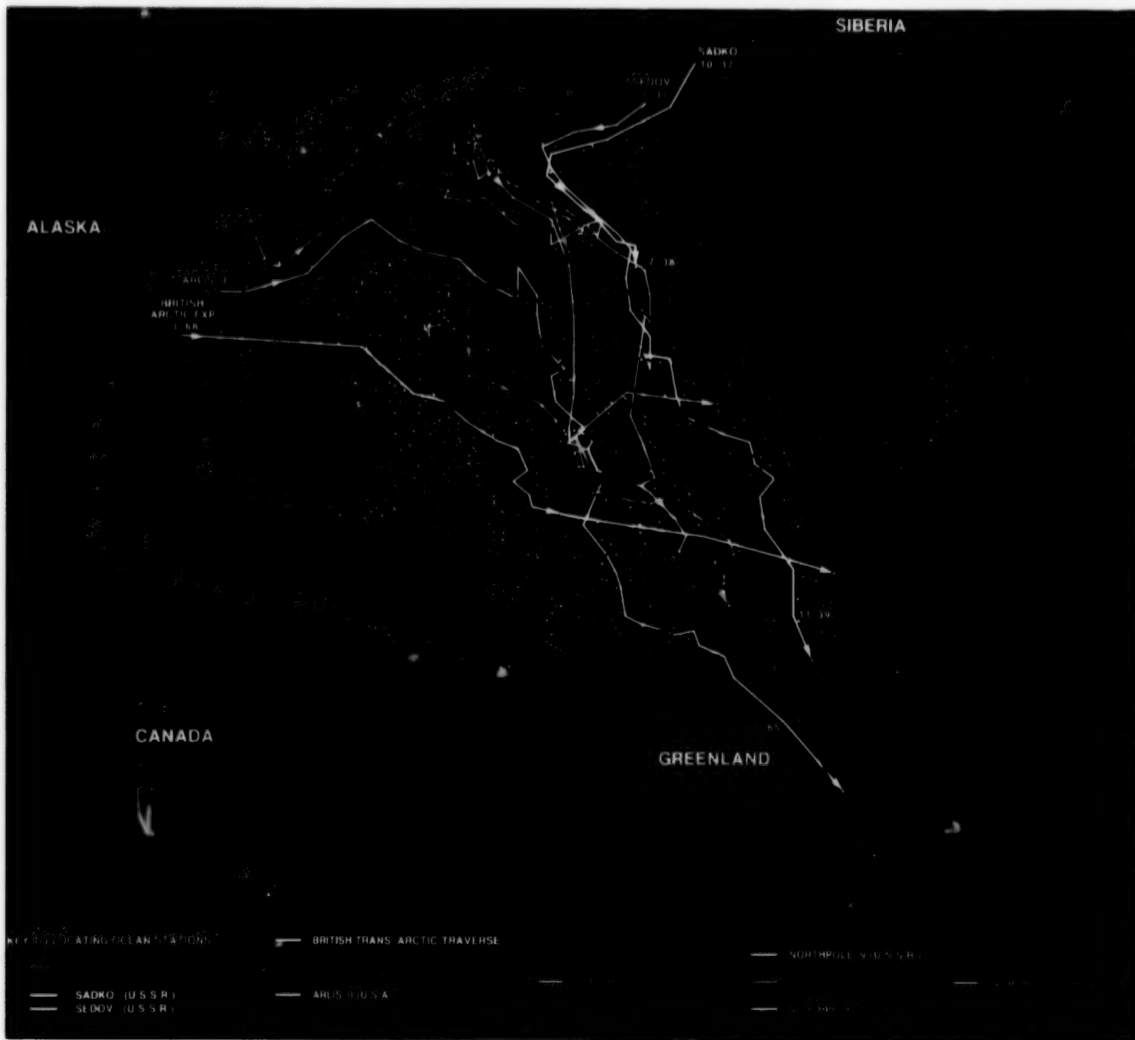


Figure 4-42. Drifts of ships and manned ice floe stations in the Arctic Ocean from the 1893-1896 voyage of the *Fram* through North Pole 20, plus the route of the 1968 British Trans-Arctic Traverse. [After Hastings (1971).]

area appears to retain very high ice concentrations through April (Figure 4-4). The area of fully consolidated first-year ice decreases in May, disappears in June, and reappears in November (Figures 4-5 through 4-8). Before the ice advance and during the ice retreat, it is not clear whether the adjacent areas in the various shades of red are lower concentrations of first-year ice or more-consolidated mixtures of first-year and multiyear ice, which can change on account of drifting ice. On the basis of these images, this ambiguity cannot be resolved with available knowledge of basic ice drift patterns such as the Beaufort Gyre and the Transpolar Drift Stream, because these drift patterns vary significantly from year to year (Colony and Thorndike, 1984). The ambigu-

ity is far less regarding the indication that the concentration decreases in the June through August period (Figures 4-5 and 4-6). On average, the open water area is at a maximum in the July through September period (Figures 4-6 and 4-7).

The year-to-year variations in the seasonal cycle are large (Figures 4-18 through 4-29). For instance, the maximum extent of the fully consolidated first-year ice area occurs in different months for different years, and the boundary of this area varies markedly from year to year in any given month, testifying to the marked variation in ice drift patterns. More locally, the interesting band of low concentration ice extending northwestward from Wrangel Island

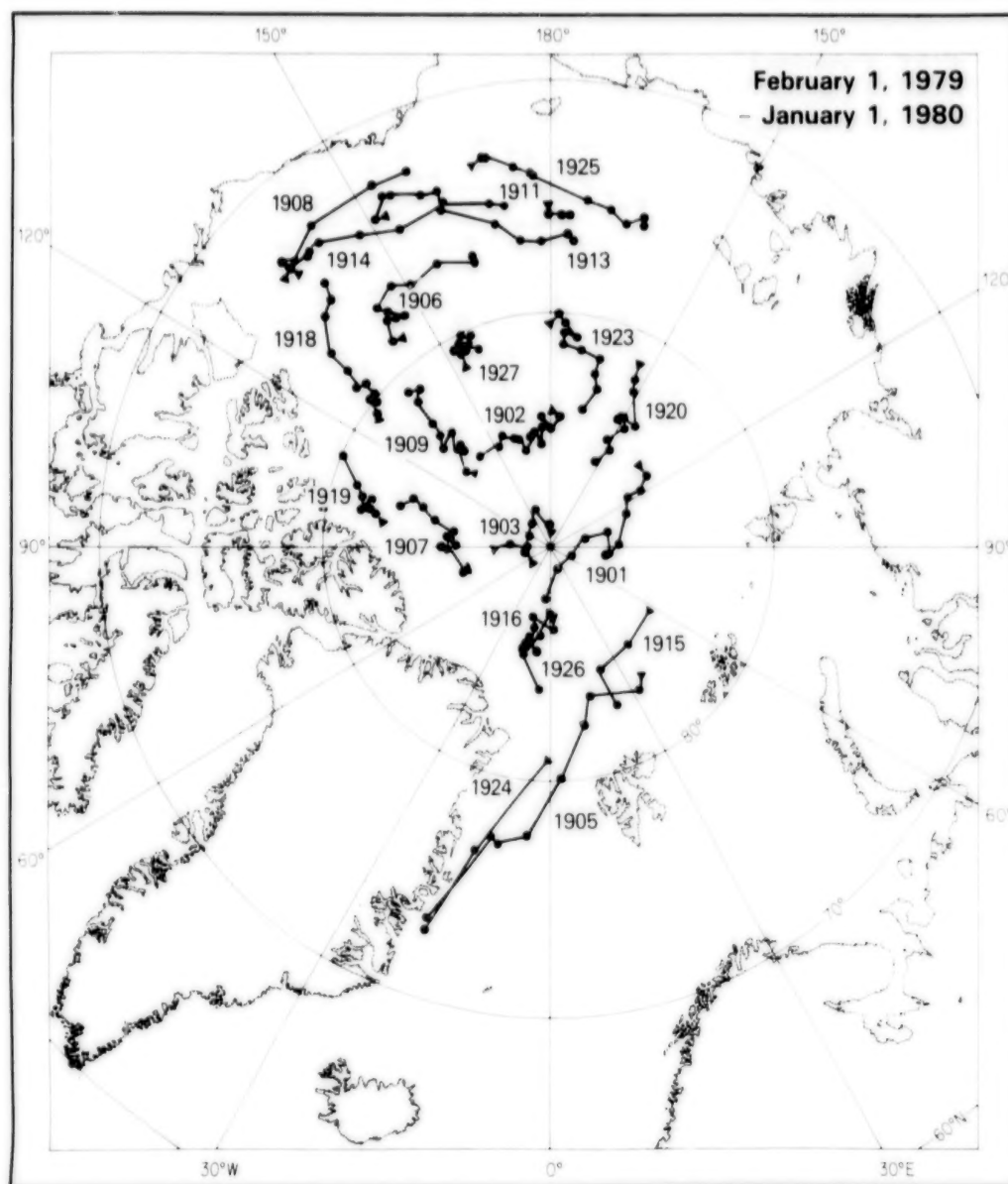


Figure 4-43. Drifts of the buoys in the Arctic Ocean Buoy Network for 1979. [After Thorndike and Colony (1980).]

in the 3-year-average May image (Figure 4-5) is most prominent in 1974 (Figure 4-22).

Another area where ice concentrations can be interpreted with relatively high confidence during the winter season is the sector between 45°W and 125°W (the northwestern tip of Banks Island). This region shows remarkably little change in the monthly ice concentration maps for November 1973 through June 1974 (Figures 4-28, 4-29, and 4-18 through 4-23). Analysis of the 3-day-averaged brightness temperature maps (not shown here) for this period reveals that brightness temperature changes within

each of these months are also small. Such small variations seem possible only in a highly consolidated ice pack, and so it is reasonable to conclude that the concentration in this sector is nearly 100 percent during this time period. Consequently, the nomograms included on the figures can be used to infer multiyear ice fractions in this area for the November through June period; for example, in January just north of Greenland at (45°W, 84°N), the multiyear ice fraction is approximately 100 percent in 1974 but approximately 70 percent in 1976. During the remainder of the annual cycle, the ice concentrations decrease, indicative of lead openings and meltpond

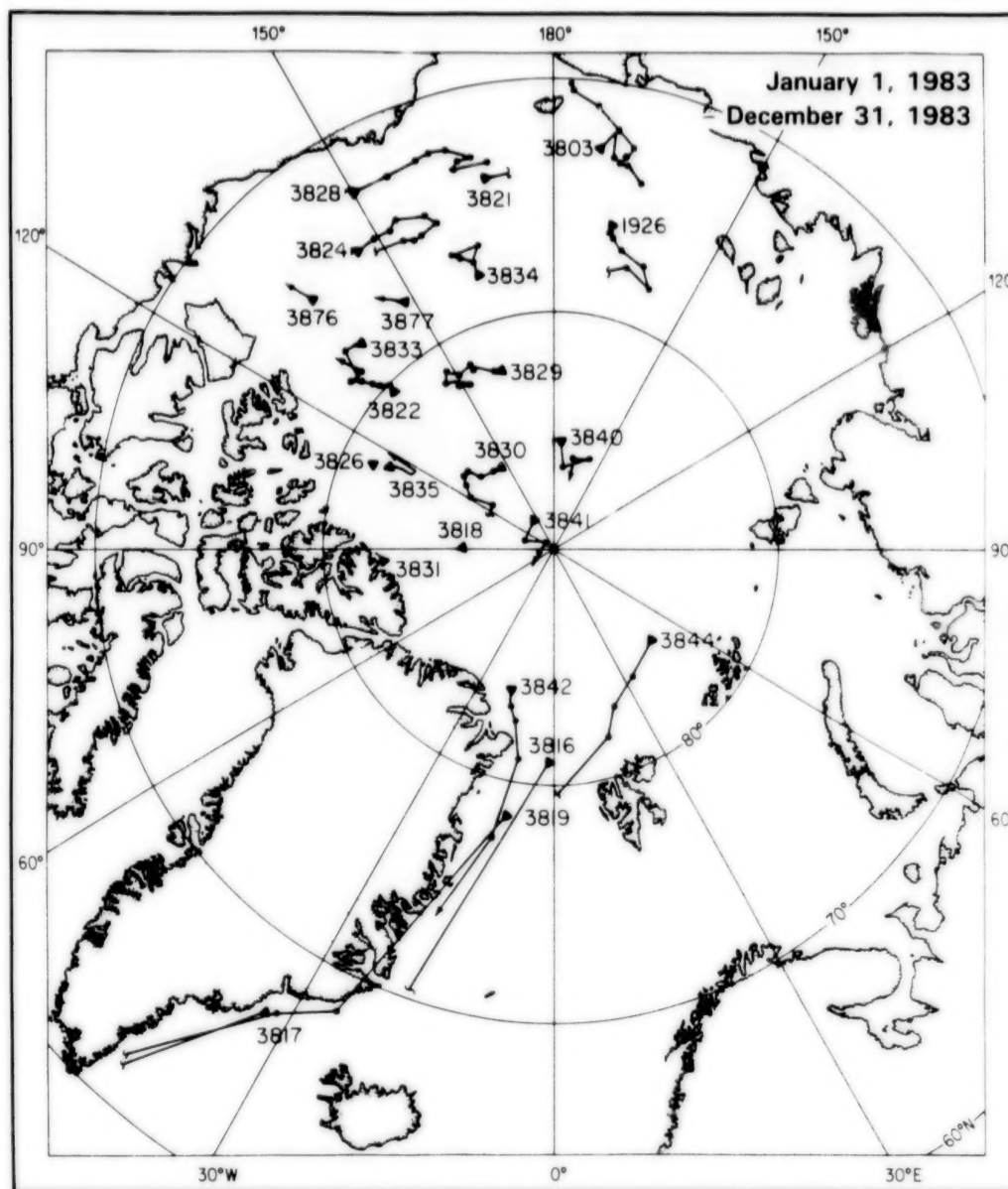


Figure 4-44. Drifts of the buoys in the Arctic Ocean Buoy Network for 1983. [From Colony and Muñoz (1985).]

formation. In the 4 years of data presented here, the ice concentrations indicated for this sector from 45°W to 125°W never fall below 64 percent.

The Beaufort Sea shows as great a variation in ice concentration and ice type mixtures as any area in the Arctic Ocean region. This sea, which is of particular interest to the United States and Canada because of its natural resources, has been the locale of numerous field measurement activities. The minimum ice concentrations in the Beaufort Sea for each of the 4 years appear to occur in September, when the area near the Mackenzie Delta appears as open

water in each of the four monthly ice concentration images (Figure 4-26). By contrast, the northern shore of Alaska from the Canadian border to Point Barrow shows a shore lead 300- to 600-kilometers long occurring in 1973, a lead 50-kilometers long in 1974, no lead in 1975, and ice reaching the shoreline in two places in 1976. [The 3-day-average brightness temperature images show the 1976 shore lead entirely open during the last part of September and early October.] These large variations in the summertime ice distributions coupled with the presence of the Beaufort Gyre and its variable amount of ice transport lead to wide variations in the multiyear ice fraction

from year to year. Using 2-day-averaged ESMR data, Carleton (1984) relates short term sea ice variations in the western Arctic in October 1976 to synoptic meteorological events, showing strong anticyclonic wind patterns associated with stable ice conditions and a quasi-stationary cyclonic system associated with rapidly changing ice conditions.

The basic yearly cycle for the Arctic Ocean region and many interannual differences are also apparent

in the time sequence plots of Figures 4-45 through 4-47. During the peak winter months of December through May, the entire region is covered with ice of a pseudo sea ice concentration of at least 65 percent, with most of the ice having pseudo ice concentrations exceeding 85 percent in each of the 4 years (Figures 4-45 and 4-46). The cumulative decay characteristics for the region are quite similar in the 2 years with full summer ESMR coverage, with decay

ARCTIC OCEAN

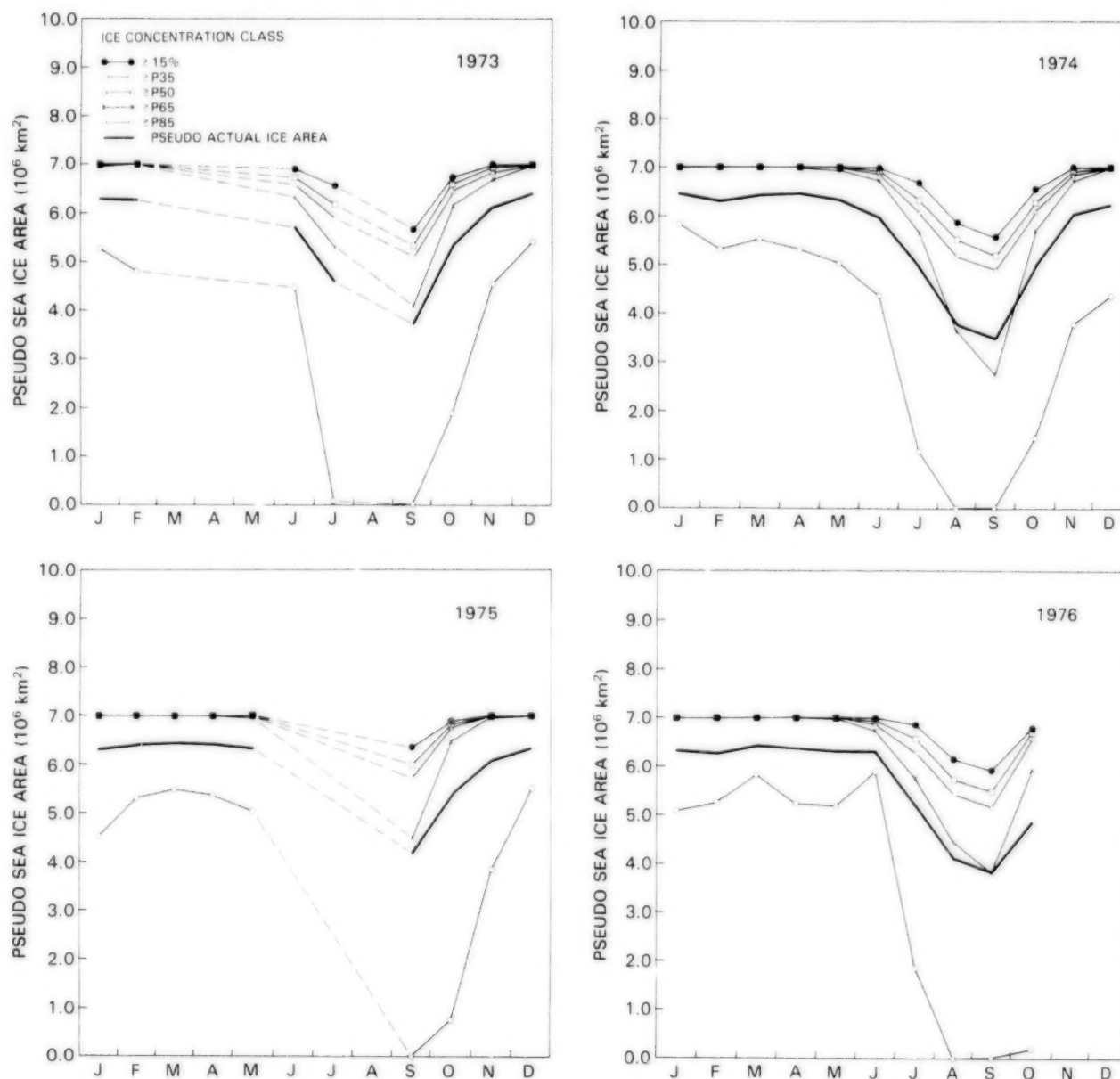


Figure 4-45. Yearly cycle of the ocean area covered by sea ice with concentration exceeding 15 percent, and yearly cycles of the P35, P50, P65, and P85 curves and the pseudo actual ice area, for the Arctic Ocean region in 1973, 1974, 1975, and 1976. The P35, P50, P65, P85, and pseudo actual ice area curves are defined in the caption for Figure 4-10.

occurring from June through September and showing maximum ice-extent decay rates from July to August, although the decay is somewhat greater in each of the pseudo ice concentration categories in 1974 than in 1976 (Figure 4-45). The pseudo mean ice concentration remains above 60 percent even in September (Figure 4-47d). Because the ice extent is so great throughout the year, covering almost the entire Arctic Ocean region, a strong inverse corre-

lation exists between the pseudo open water and the pseudo actual ice area (Figures 4-47b and 4-47c). Similar inverse correlations certainly do not exist in some of the regions with a much greater seasonal cycle in sea ice extent.

As an example of the wintertime variations in the multiyear/first-year ice distribution, microwave images of a localized region poleward from the shoreline of Harrison Bay obtained at much higher

ARCTIC OCEAN

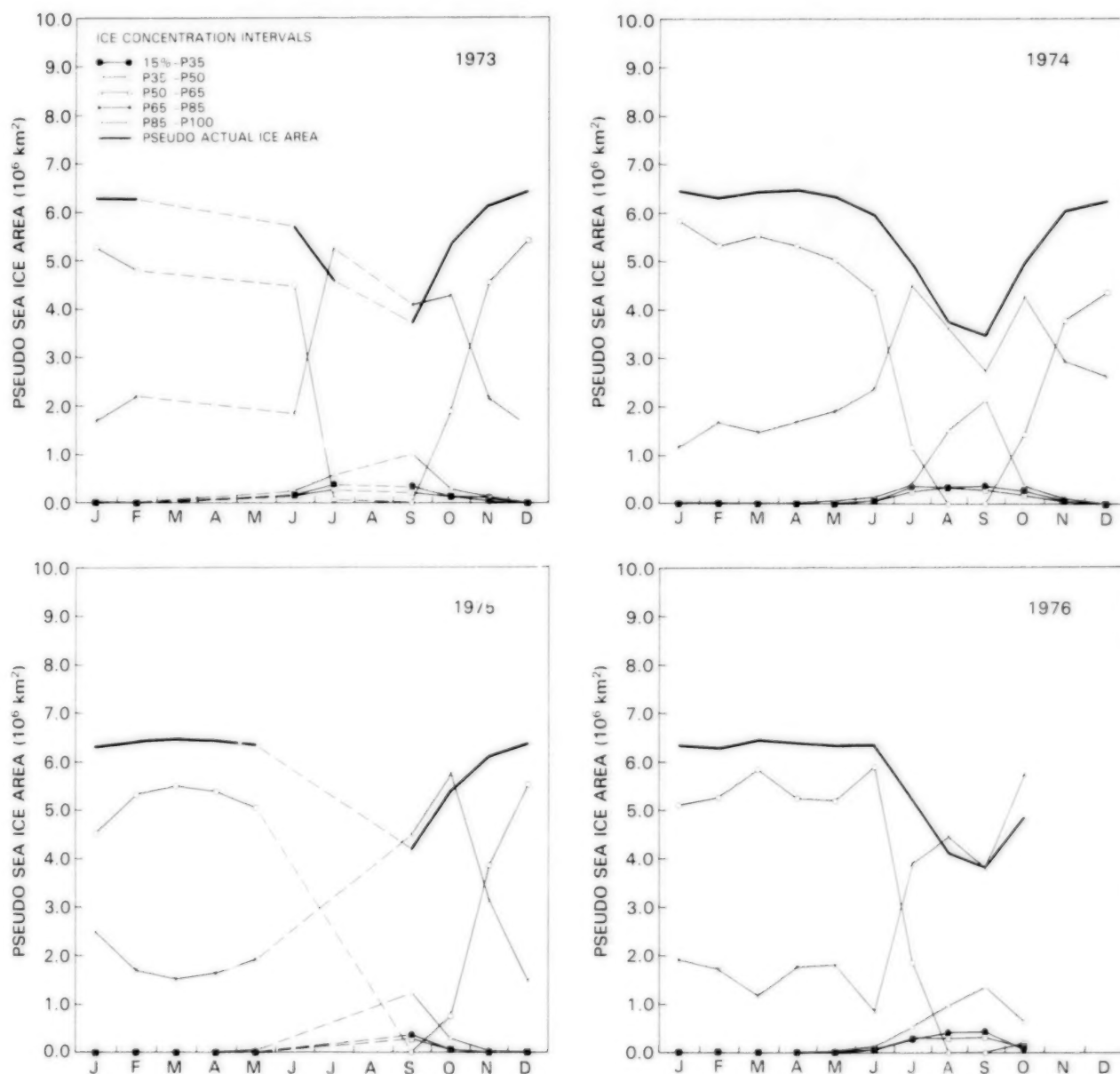


Figure 4-46. Yearly cycles of the ocean area covered by sea ice within the intervals 15 percent to P35, P35 to P50, P50 to P65, P65 to P85, and P85 to P100, and yearly cycle of the pseudo actual ice area, for the Arctic Ocean region in 1973, 1974, 1975, and 1976. The interval curves are calculated by subtracting the respective curves of Figure 4-45.

spatial resolution by the aircraft ESMR on the NASA Convair 990 airborne laboratory are shown in Figure 4-48. At these higher spatial and temporal resolutions, two distinct ice types are readily separable in the case of larger floes, first-year ice appearing red, with radiances near 248 K, and multiyear ice appearing blue and green, with radiances near 230 K. Surface observations during AIDJEX have indicated that intermediate radiances generally result from floes that consist of small chunks of multiyear ice cemented together by first-year ice. Note that the color scale on these images is not the same scale as that used on the monthly averaged images from the Nimbus 5 ESMR. The

100-kilometer band of ice (in red) along the shoreline is entirely first-year ice, although it contains evidence (in yellow and green lead patterns) of open leads that appear and disappear. Further north, another 100-kilometer band of medium-size multiyear floes (with radiances near 230 K) and refrozen polynyas (with radiances near 248 K) can be seen drifting generally from east to west and with variable rates during the 20-day time period shown. A third 100-kilometer band with less multiyear ice lies north of the second band. This third band of ice extends northward to 76.5°N, from which point the multiyear fraction gradually increases to near unity at 80°N (Figure 4-49).

ARCTIC OCEAN

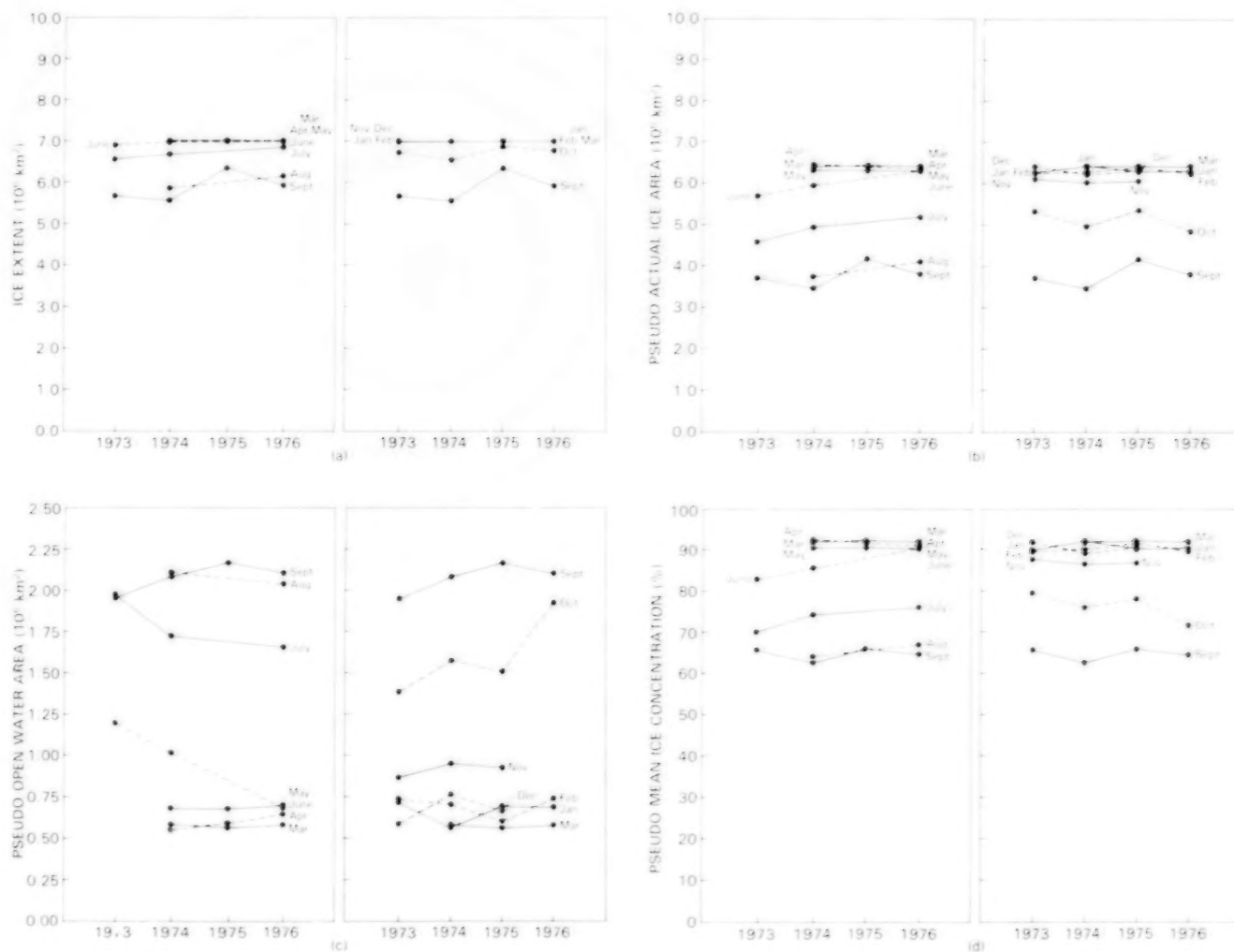


Figure 4-47. Month-by-month year-to-year changes in (a) sea ice extent, (b) pseudo actual ice area, (c) pseudo open water area within the ice pack, and (d) pseudo mean sea ice concentration, for the Arctic Ocean region. The pseudo quantities are calculated with an ice emissivity of 0.92, appropriate for first-year ice.

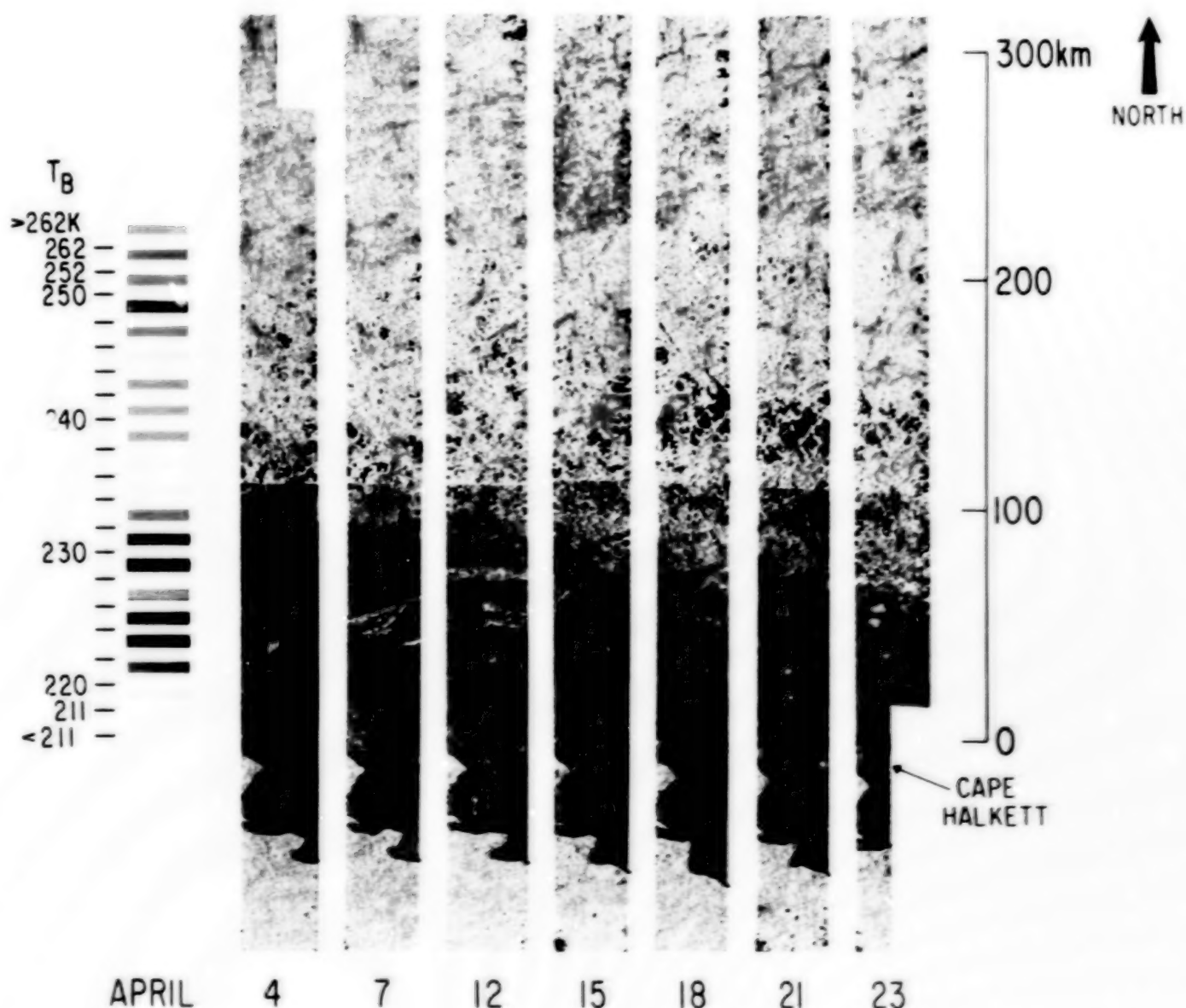


Figure 4-48. Successive microwave mosaic images of the sea ice of the western Beaufort Sea from Harrison Bay to 74°N in April 1972. The images show color-coded brightness temperatures at the 1.55-centimeter wavelength taken by an instrument on board the NASA Convair 990 aircraft. [From Campbell et al. (1976).]

In summer, when the pack ice in the central Arctic is no longer bounded by land on most of its perimeter, large areas of low ice concentrations within the ice pack have been observed in all 4 years, as discussed in Section 3.4. Despite the long-term averaging in producing the images in this chapter, this phenomenon is shown clearly in Figure 4-25, for August 1974. The four dark green areas extending poleward from the Chukchi Sea are also clearly identifiable in the brightness temperature image for

August 1974 (Figure 3-22). As revealed in 3-day-average brightness temperature images (not shown), rapid changes in brightness temperature occur in August 1974, but the evidence of the low ice concentrations in Figure 4-25 results from their general persistence throughout the monthly period. By contrast, similar large areas of low ice concentrations were observed also in 1976 on shorter time scales (see Section 3.4) but are obscured in the time-averaged images shown in Figure 4-25.

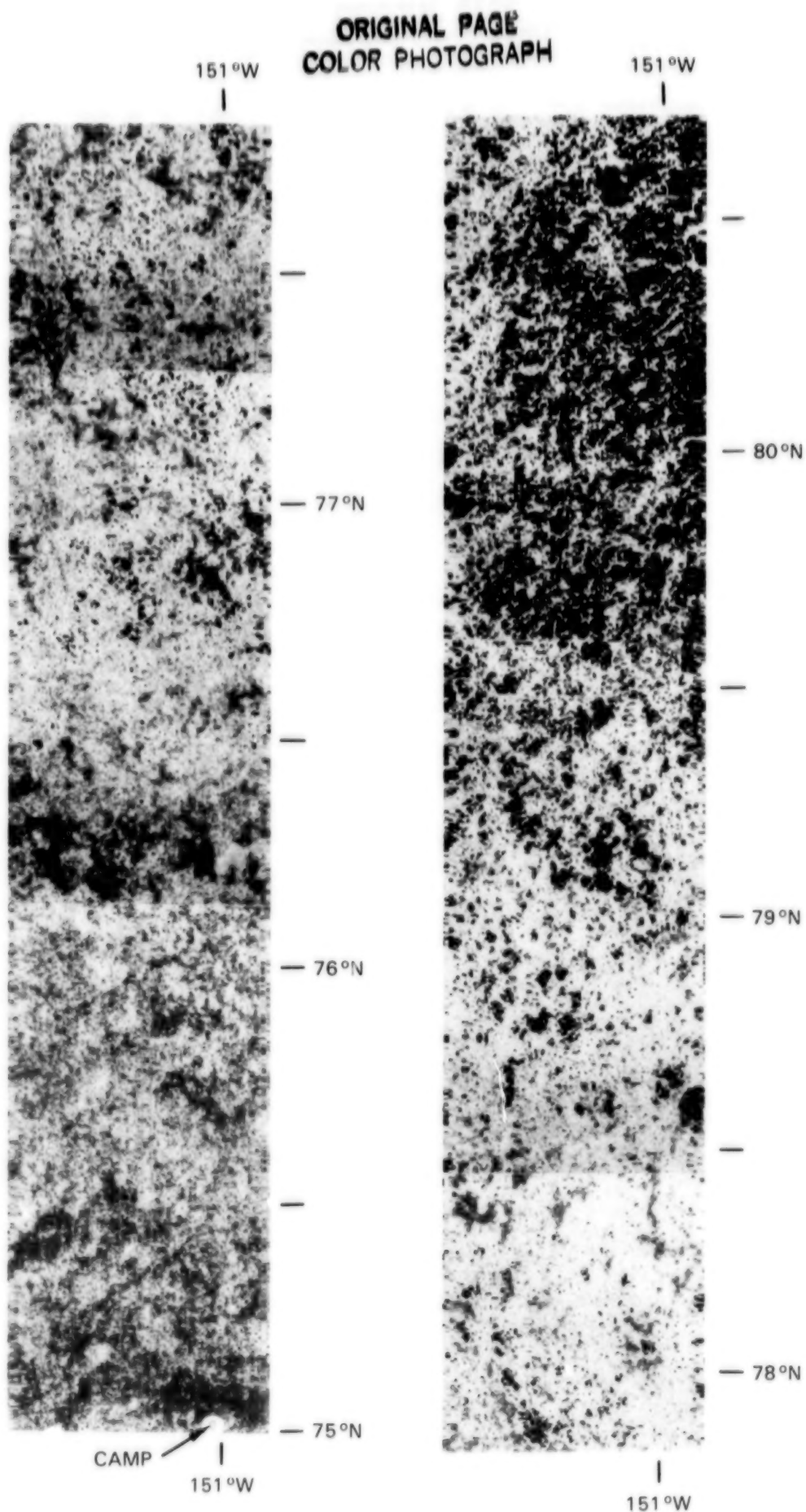


Figure 4-49. Aircraft microwave mosaic image of the sea ice along a NASA Convair 990 flight path from the AIDJEX camp at 151°W, 79°N northward to 80°45'N, on April 18, 1972. The image shows color-coded brightness temperatures at the 1.55-centimeter wavelength. The color code is identical to that presented in Figure 4-48. [From Campbell et al. (1976).]

4.3 SEA OF OKHOTSK

The Sea of Okhotsk is a fairly shallow body of water, with depths less than 400 meters over much of its 1,207,000 square kilometer area, and is bounded by the Kamchatka Peninsula, Siberia, Sakhalin Island, and the Pacific Ocean (Figure 4-50). The sea is separated from the Pacific by the Kuril Island chain and an accompanying sill, with its only remaining outlets being two narrow and very shallow straits to the west and south of Sakhalin Island, leading to the Sea of Japan. The protected nature of the sea facilitates the formation of sea ice, so that the Sea of Okhotsk tends to form ice earlier and retain it later than other regions of similar latitude. Not much is known about the early explorations of the sea, but likely the first non-natives to sail through the Sea of Okhotsk in modern times were those taking part in the early 18th century Russian expedition led by Vitus Bering, the principal goal of which was the exploration of the Bering Sea region to the east and the determination of whether Eurasia and North America are connected.

The Sea of Okhotsk is one of several regions for which the multiyear ice problem does not exist, because the ice cover disappears entirely during the summer. Free of ice for 4 months of the year, the sea begins to freeze over in a few coastal locations in November, attains its maximum ice coverage usu-

ally in March, and by June retains ice in only a few coastal locations (Figures 4-3 through 4-8 and 4-12). On a 4-year-average basis, the ice extent at the March maximum is about 900,000 square kilometers (Figure 4-12).

The ESMR data show that coastal ice generally forms first in the Penzhinskaya Guba in November, then in the Udskeya Guba in the northwest corner of the sea and along the Sakhalin Island coastline in December, then along the remainder of the northern and western boundaries in January, and finally along the Kamchatka Peninsula in February (Figures 4-3 through 4-8). The ice advances inward toward the center of the sea from all coastlines so that by mid-February most of the sea is covered with ice of at least 20-percent concentration (Figure 4-3). The retreat of the ice after the March maximum follows basically the reverse sequence from the ice growth, with the ice cover vanishing first in the center of the basin, then along the east coast, and then the north coast, with only small amounts of ice remaining in the Udskeya Guba by June. An exception to the temporal symmetry of the growth and retreat sequences finds the Penzhinskaya Guba largely free of ice well before some of the other coastal regions. Another asymmetry, not visible in the monthly averaged images but visible in the ESMR 3-day averages, is that while the ice retreat proceeds almost monotonically, the growth season is punctuated by temporary reversals, which gives a pulsation effect both for the ice edge and for the opening and closing of temporary polynyas. The reader is referred to Parkinson and Gratz (1983) and to Campbell et al. (1981) for further discussion of the 3-day images for the Sea of Okhotsk.

Significant interannual differences from the 4-year-average annual cycle of Figures 4-3 through 4-8 and 4-12 are apparent from the monthly averaged results for the individual years (Figures 4-18 through 4-29 plus 4-51 through 4-53). By far the heaviest ice cover of the 1973 through 1976 period occurred in February of 1973 (Figures 4-19, 4-51, and 4-53). Because of missing data in March through May of 1973, it is impossible to know from this data set whether the March 1973 ice coverage was even greater than the coverage in February 1973, or whether 1973 was also anomalous in not having March as the month of maximum ice coverage. In any event, the February 1973 ice coverage exceeds by 50 percent the average February ice coverage in

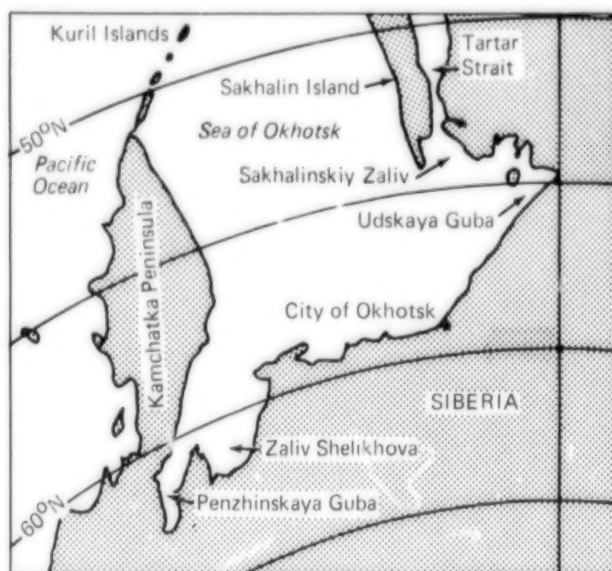


Figure 4-50. Location map for the Sea of Okhotsk region.

the other 3 years (Figure 4-53a), and even the January 1973 ice coverage exceeds the March maximum in both 1974 and 1976.

In each of the 3 years (1974 through 1976) with full winter satellite coverage by ESMR, March is the month of maximum ice coverage both in terms of ice extent and in terms of actual ice area (Figure 4-51). Of the 3 years, 1975 has the most ice and 1976

has slightly more ice than 1974 (Figures 4-53a and 4-53b). The fact of greater ice coverage in 1975 than in 1974 or 1976 is consistent throughout the period from January through May, and indeed is foreshadowed in the previous Decembers, for which the ice cover in 1974 exceeds the ice covers in 1973 and 1975. In all 4 years, the amount of ice is near zero in July through October (Figures 4-53a and 4-53b).

SEA OF OKHOTSK

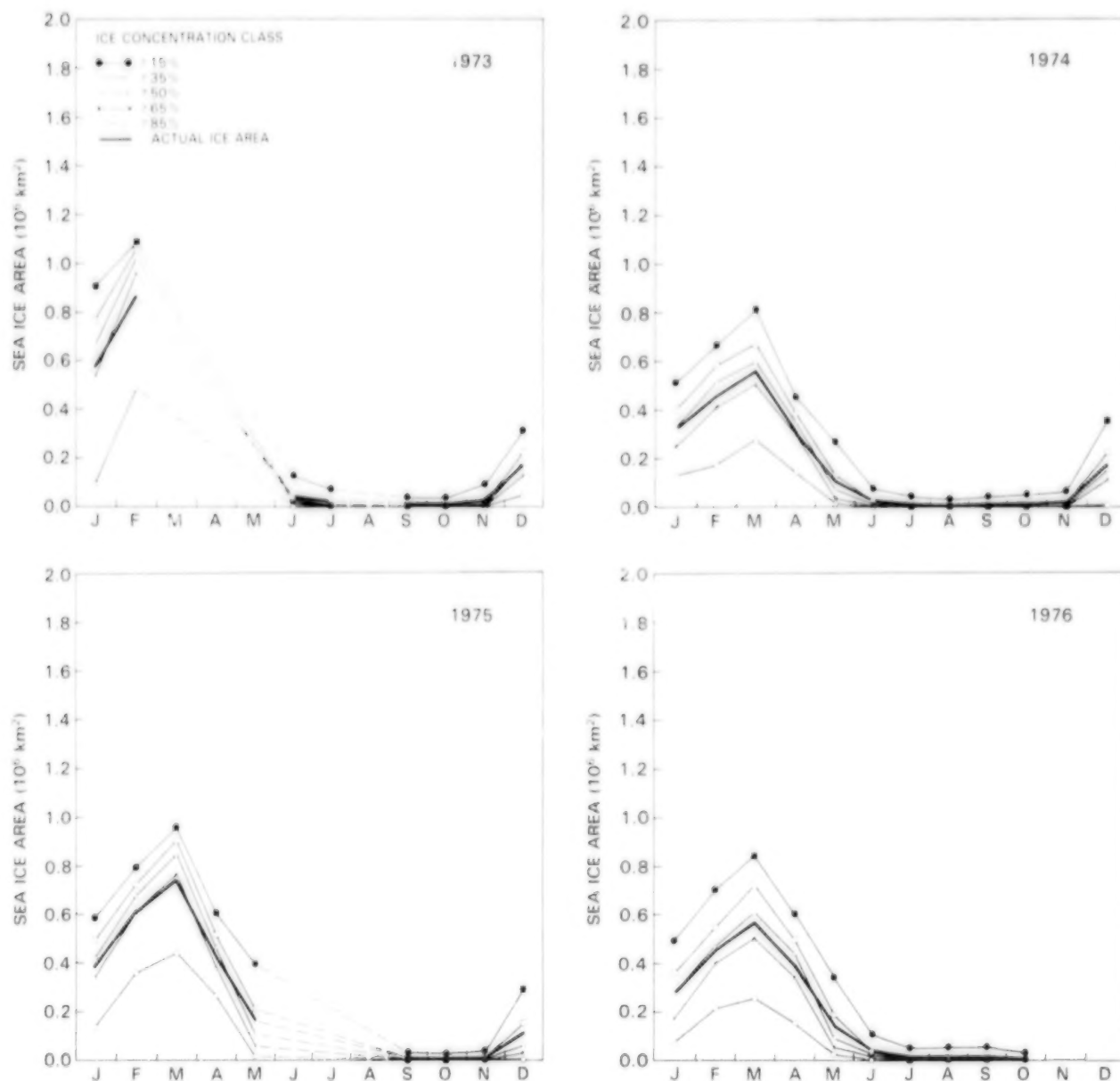


Figure 4-51. Yearly cycles of the ocean area covered by sea ice with concentration exceeding 15, 35, 50, 65, and 85 percent, and yearly cycle of the actual ice area, for the Sea of Okhotsk region in 1973, 1974, 1975, and 1976. The actual ice area is the integrated ocean surface area covered by sea ice, excluding leads and polynyas within the ice pack.

Mean ice concentrations in the Sea of Okhotsk are not as high as in several of the other regions, approaching 80 percent only in February 1973, the month of the heaviest sea ice cover in the Sea of Okhotsk region, and not exceeding 70 percent in any other month except February and March 1975 (Figure 4-53d). The relatively low wintertime mean ice concentrations are caused in part by the different geographies of the ice covers, with a far greater pro-

portion of the ice being near the ice edge in the Sea of Okhotsk than in many of the other regions.

By contrast, the high, nonzero values of mean ice concentration indicated for the Sea of Okhotsk in July through October (Figure 4-53d) result from the contamination of boundary ocean pixels by land values. The land mask, with a 30-kilometer resolution, cannot effect a complete separation of land

SEA OF OKHOTSK

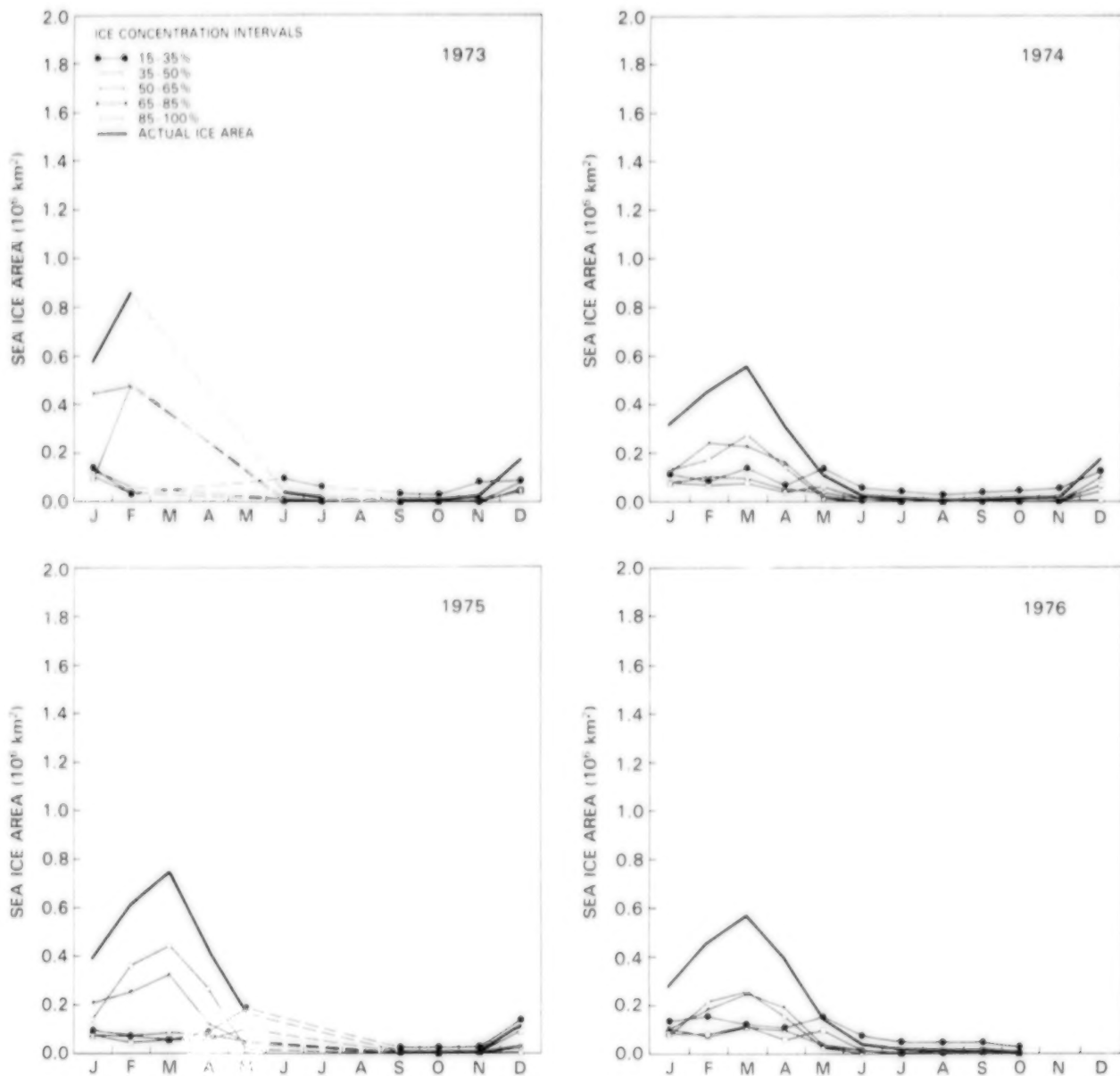


Figure 4-52. Yearly cycles of the ocean area covered by sea ice within ice concentration intervals 15 to 35, 35 to 50, 50 to 65, 65 to 85, and 85 to 100 percent, and yearly cycle of the actual ice area, for the Sea of Okhotsk region in 1973, 1974, 1975, and 1976.

from ocean, so that some ice is indicated for all months as a result of the much higher brightness temperatures of land than of open water. This is true also for each of the other regions.

On a spatial basis, the ice in the Sea of Okhotsk undergoes in each of the 4 years a growth/decay cycle similar to the one previously described for the 4-year average, although with a much more rapid growth period in 1973 (Figures 4-18 through 4-29). The ice concentration monthly difference maps show even more definitively the uniformity of the growth and decay when averaged on a monthly basis (Figures 4-9 and 4-30 through 4-37). With only small exceptions, the month-to-month changes show growth

or constancy throughout the sea from October through February and decay or constancy throughout the sea from March through July. The transition from growth to decay occurs from February to March, when the monthly difference images show a portion of the sea still undergoing growth and a portion undergoing decay.

Comparison of the general features of the cycle of sea ice distribution in the Sea of Okhotsk with the basic oceanographic features of water temperature, salinity, and bathymetry presented in Chapter 2 reveals that ice forms first in cold, shallow, low-salinity waters away from the warm Pacific inflow and sheltered from strong currents. The delay in ice

SEA OF OKHOTSK

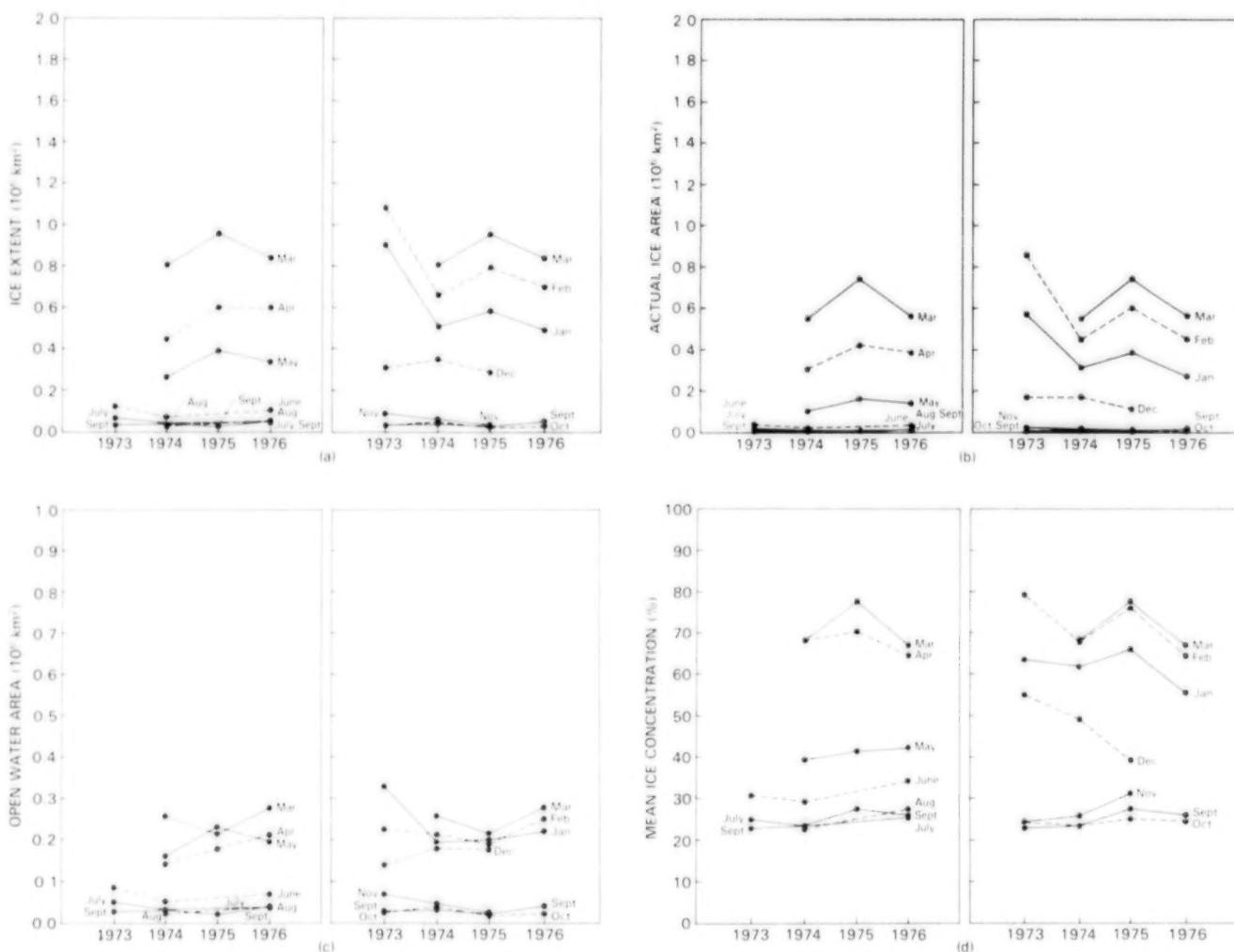


Figure 4-53. Month-by-month year-to-year changes in (a) sea ice extent, (b) actual ice area, (c) open water area within the ice pack, and (d) mean sea ice concentration for the Sea of Okhotsk region.

formation along the Kamchatka Peninsula and in the central portion of the sea is presumably caused by the warm, saline Pacific inflow in the West Kamchatka Current (see Figure 2-3). Parkinson and Gratz (1983) have identified two basic patterns of ice edge positioning that occur frequently in the ESMR data for the Sea of Okhotsk. These are a rectangular structure and a wedge structure, each of which is strongly correlated with the bathymetry of the region and with the known current system (Parkinson and Gratz, 1983). The correlations illustrate the important role played by convective depth and ocean currents in determining the regional and spatial growth and decay patterns observed in the seasonal sea ice cycle.

4.4 BERING SEA

Exceeded in area only by the Mediterranean and South China Seas, the Bering Sea is the third largest semi-enclosed sea in the world, with a surface area of 2.3×10^6 square kilometers. Its boundaries define a sector of approximately 1500 kilometers in radius with the Bering Strait at its vertex and bounded to the south by the Aleutian Island arc, to the east by the Alaskan coast, and to the west by Kamchatka Peninsula (Figure 4-54). The northeastern Bering Sea overlies a continental shelf of depths less than 200 meters, and the southwestern portion overlies an abyssal plain with depths exceeding 3500 meters (Figure 2-2). The continental shelf break, which runs in a northwest-southeast direction across the central portion of the sea, influences the regional oceanography and serves as a constraint on the maximum extent of sea ice during the winter months (Kinder, 1981; Overland and Pease, 1982; Muench and Schumacher, 1985).

The first known explorations of the Bering Sea and the Bering Strait were done during a Russian expedition to the region in 1648 under the leadership of Semyon Dezhnev. However, the sea and strait are named after the Dane Vitus Bering, who led another, more extensive Russian expedition in the early 18th century, encouraged by Peter the Great. Bering explored the coast of Kamchatka Peninsula and sailed into the strait, discovering the St. Lawrence and Diomed Islands in 1728, but he did not see the Alaskan coast at that time. Mikhail Gvozdev and Ivan Fyodorov first charted the strait in 1730, after which Bering led another expedition, in 1733, sailing along the northern coast of Siberia and reaching the

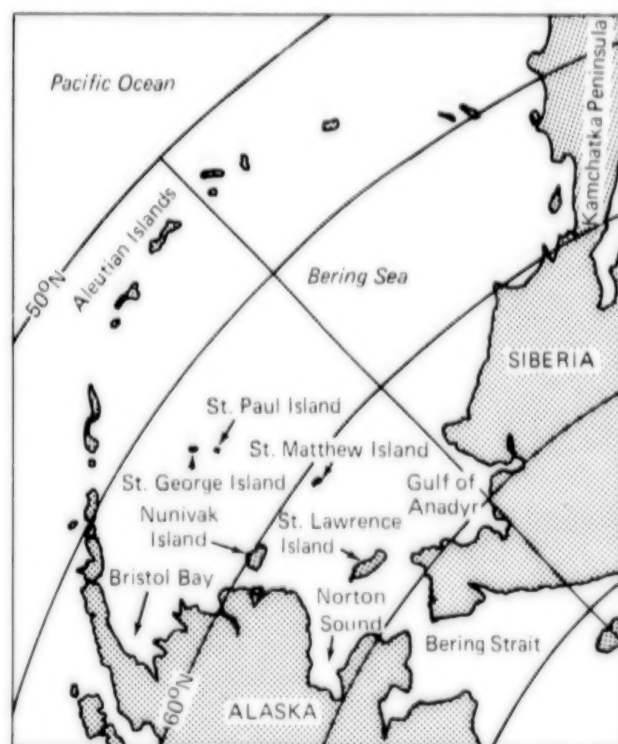


Figure 4-54. Location map for the Bering Sea region.

Gulf of Alaska in 1741. Suffering from scurvy, he landed on Bering Island in November of 1741, and died of hunger and cold on December 19, 1741. Later, in 1778, the Englishman James Cook passed through the Bering Sea and to the southern borders of the Arctic Ocean ice in an unsuccessful search for a Northwest Passage between the Orient and Europe.

As with many of the peripheral seas of the Arctic, the Bering Sea is a seasonal sea ice zone, with the ice cover disappearing during summer. Although ice free 4 months of the year, the Bering Sea is ice laden over approximately one third of its area during the winter months. *In-situ* ice formation begins in the northern coastal regions of the Bering Sea as early as November. The ice cover grows rapidly during December and January, reaching its maximum extent in March and April (Figures 4-3 through 4-8 and 4-12), then decreases rapidly after April. By June traces remain only in the northern coastal regions. The process of ice forming in the northern Bering Sea, being advected southward by atmospheric forcing, and dissipating at the ice edge has been described as a conveyor belt mechanism of ice production and has been studied extensively (Campbell et al., 1975;

Gloersen et al., 1975a, 1975b; Pease, 1980; Overland and Pease, 1982; Martin et al., 1983). Indeed, a major international experiment was conducted in this area during the lifetime of ESMR—the joint USSR/USA Bering Sea Experiment (BESEX) from February 15 to March 7, 1973, in which detailed studies of atmosphere/ice/ocean coupling were made. The results were reported in 20 papers of the Proceedings of the BESEX Symposium (Kondratyev et al., 1975).

The 4-year-averaged monthly ESMR data (Figures 4-3 through 4-8) show the onset of ice formation along the northern and eastern coastal regions of the Bering Sea in November. By December, an ice cover of at least 80 percent concentration extends from the Bering Strait to St. Lawrence Island, covers Norton Sound, and runs along the Alaskan coast. The ice edge extends from just south of Nunivak Island northwestward to Siberia with approximately 50 percent of the Gulf of Anadyr ice covered. The most rapid ice growth occurs from November to December (Figure 4-12) followed by more gradual growth until April. During this period, the ice cover extends farther southward in the eastern Bering, covering much of Bristol Bay and reaching the eastern Aleutian Islands. The ice cover does not extend as far south in the western portion of the sea; however, it is more consolidated there, with peak concentrations reaching 98 percent in March. Areas of persistent ice divergence are apparent in the mean monthly maps as areas of lower ice concentration. These areas are found typically south and southwestward of St. Lawrence, St. Matthew, and Nunivak Islands and along the Alaskan coast. Although the low ice concentrations in these areas are caused by northeasterly winds characteristic of the wintertime synoptic pattern, the area of low ice concentration between St. Lawrence Island and the Siberian coast may also result from weak currents moving the ice northward in this region.

Much of the variability in the Bering Sea ice cover during the winter months results from the influence of cyclones that generally track along the Aleutian chain, but frequently move into the Bering Sea bringing warm moist air from the Pacific Ocean and driving the ice cover northward. During spring, it is typically just this change in the cyclone tracks associated with a change in the large-scale atmospheric circulation that initiates the breakup of the ice cover (Overland and Pease, 1982). In contrast to the

growth of the ice cover, its breakup is rapid, taking place largely from April to June (Figure 4-12). The breakup, apparent in the monthly averaged ESMR data (Figures 4-4 through 4-6), begins as a retreat of the ice edge principally in the southeastern portion of the Bering Sea, but areas of low ice concentration and open water also appear early in the breakup season in the central Bering Sea south and west of St. Lawrence Island, a region of persistent ice divergence during winter. By June, the ice cover is almost totally gone, except for traces of ice in Norton Sound.

Significant year-to-year variability in the Bering Sea ice cover is evident from Figures 4-18 through 4-29 and Figures 4-55 through 4-57. Of the 4 years of data presented (noting, however, the missing data for March, April, and May of 1973), the month with the heaviest ice cover is April 1976, with the actual ice area exceeding 0.8×10^6 square kilometers. An increase in the total ice extent occurs from 1973 to 1976 for February and from 1974 to 1976 for March and May (data for 1973 is missing for these months). For both 1974 and 1976, the April ice extent exceeds that of March, while for 1975 the month of maximum ice cover is March (Figures 4-55 and 4-57a). The trend of the actual ice area for these months follows that of the ice extent, with the exception that the April 1974 actual ice area is below the actual ice areas for February and March (Figure 4-57b).

As with the 4-year averages, the seasonal decay of the Bering Sea ice cover in the individual years is consistently more rapid than its growth (Figure 4-55). There is, however, considerable interannual variability in the retreat of the ice extent. Interestingly, a more rapid retreat in the ice extent occurs from April to May in 1974 than in either 1975 or 1976 when the total ice extent is greater. In 1976, the retreat is greater from May to June, which is presumably also the case in 1975, although June data are missing for that year. By contrast, the decrease in actual ice area is greatest from April to May for both 1974 and 1976, although the April to May decrease in 1975 may have been exceeded by the May to June decrease.

Interannual differences in the spatial patterns of growth and decay are apparent in all seasons. The ice cover in November 1975 exceeds that in either of the preceding 2 years, covering the region north of St. Lawrence Island, covering Norton Sound, and

extending along the Alaskan coast to Nunivak Island (Figure 4-28). By December, the ice cover has increased rapidly in all 3 years, with 1973 having the least amount of ice and 1974 the most (Figures 4-29, 4-57a, and 4-57b). From January through April, there are considerable interannual differences in the spatial distribution of ice concentration (Figures 4-18 through 4-21), as well as differences in the cumula-

tive ice amounts (Figures 4-57a, 4-57b, and 4-57d). In January 1975 and 1976, the ice extent is noticeably greater in the eastern Bering region than it is in either 1973 or 1974 (Figure 4-18), and the mean ice concentration for the entire Bering Sea is greatest in 1975 (Figure 4-57d). From February through May, there is a clear interannual trend with both ice extent and actual ice area generally increasing from 1974 to

BERING SEA

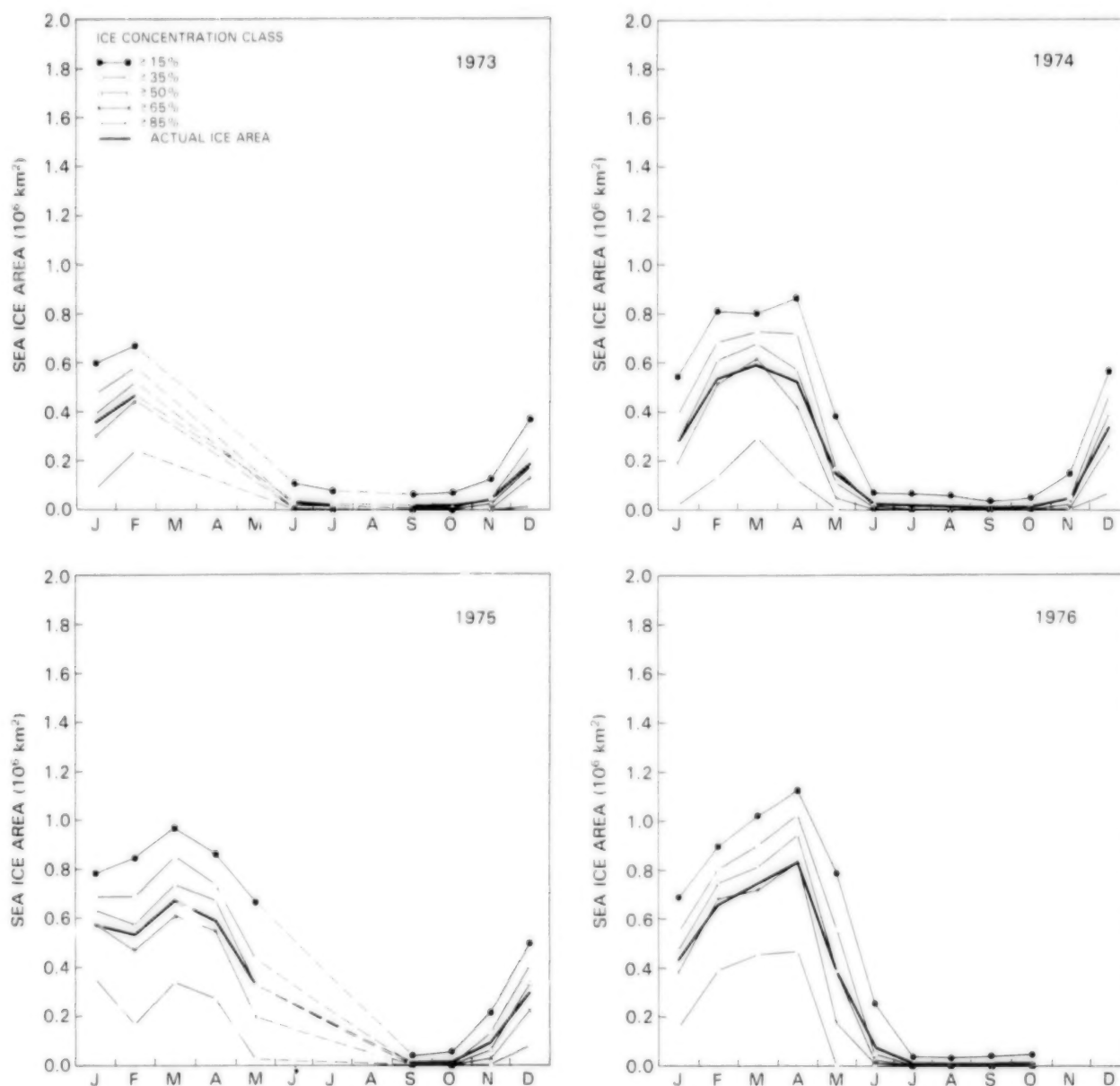


Figure 4-55. Yearly cycles of the ocean area covered by sea ice with concentration exceeding 15, 35, 50, 65, and 85 percent, and yearly cycle of the actual ice area, for the Bering Sea region in 1973, 1974, 1975, and 1976. The actual ice area is the integrated ocean surface area covered by sea ice, excluding leads and polynyas within the ice pack.

1976. It should be noted that the mean ice concentration, the ice extent, and the actual area of ice cover do not necessarily follow the same sequence (Figures 4-57a through 4-57d).

The spatial pattern of ice decay is approximately the reverse of the pattern of ice growth, with rapid retreat occurring first in the eastern Bering Sea. An

examination of Figure 4-32 shows the decay of the ice cover from March to April 1974 to be greatest in Bristol Bay. By May, the 1974 Bering Sea ice cover has retreated dramatically. Except for isolated regions of ice in the central Bering Sea and along the Siberian coast, the ice in May is confined to the area north of St. Lawrence Island (Figure 4-22). Ice decay in both 1975 and 1976 lags that in 1974, with the

BERING SEA

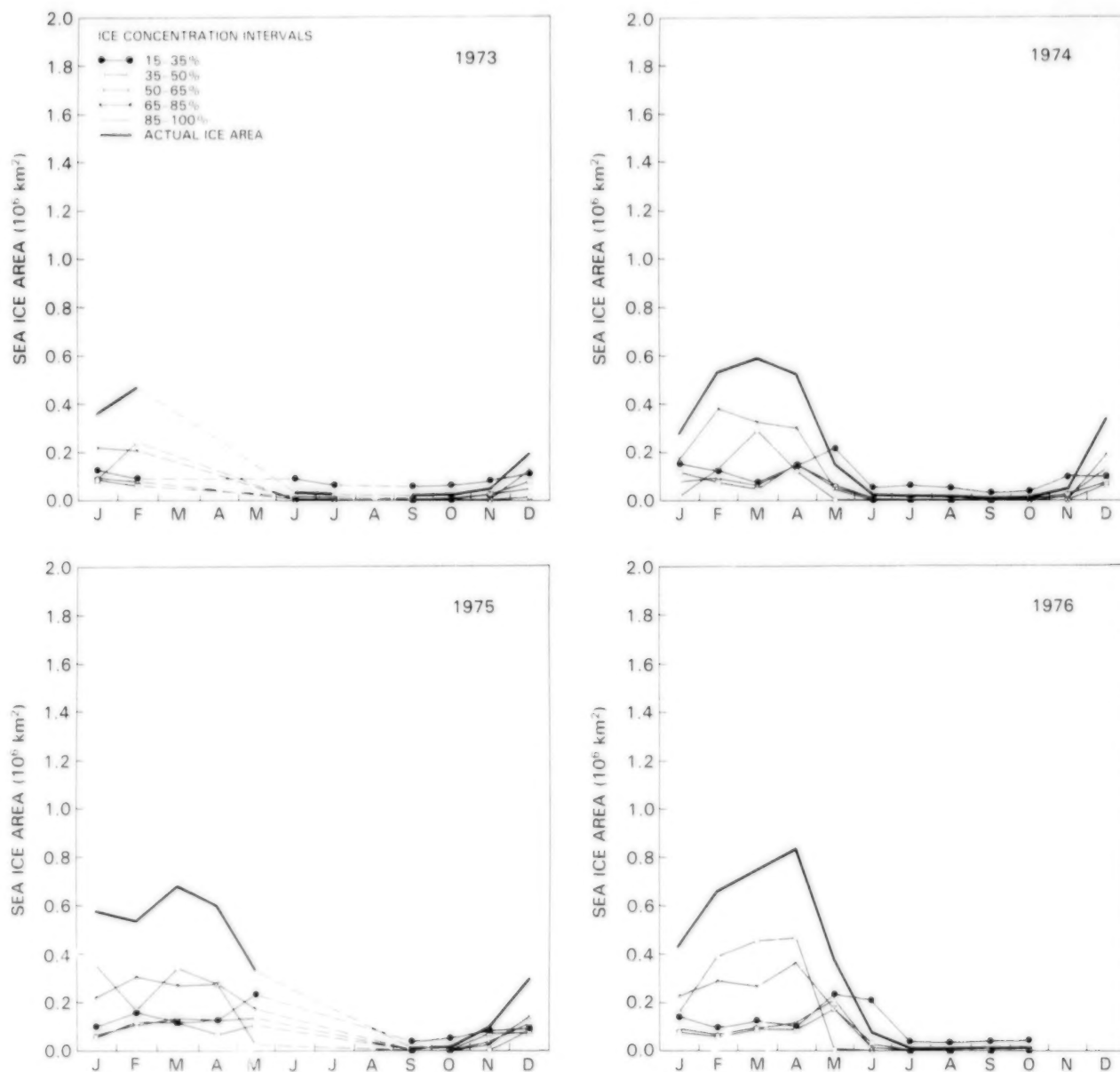


Figure 4-56. Yearly cycles of the ocean area covered by sea ice within ice concentration intervals 15 to 35, 35 to 50, 50 to 65, 65 to 85, and 85 to 100 percent, and yearly cycle of the actual ice area, for the Bering Sea region in 1973, 1974, 1975, and 1976.

April to May transition in 1975 showing a general retreat of the ice edge across the Bering Sea as well as a breakup south of St. Lawrence Island and along the Siberian coast (Figure 4-34). By contrast, in 1976 the April to May decay occurs throughout the entire ice-covered portion of the sea (Figure 4-36), with open water in May apparent in Bristol Bay and, to a lesser extent, in the vicinity of St. Lawrence Island (Figure 4-22). By June, the Bering Sea is essentially free of ice in the 3 years shown in Figure 4-23, except for trace amounts in Norton Sound and the Gulf of Anadyr in 1973 and 1976, the latter being a year of marked below normal air and sea surface temperatures (Niebauer, 1981).

4.5 HUDSON BAY

Located in northeastern Canada, Hudson Bay is a roughly oval-shaped area of about 819,000 square kilometers with very limited connections to the world's oceans (Figures 4-58 through 4-61). Hudson Strait provides a passage to the Atlantic, and Foxe Basin and the narrow straits of the Canadian Archipelago are the only links with the Arctic Basin to the north. The Hudson Bay region defined for the analysis in this volume (Figure 4-2) includes Foxe Basin and Hudson Strait. The bay is relatively shallow and flat, with an average depth of 100 meters and a greatest depth of only about 300 meters. The

BERING SEA

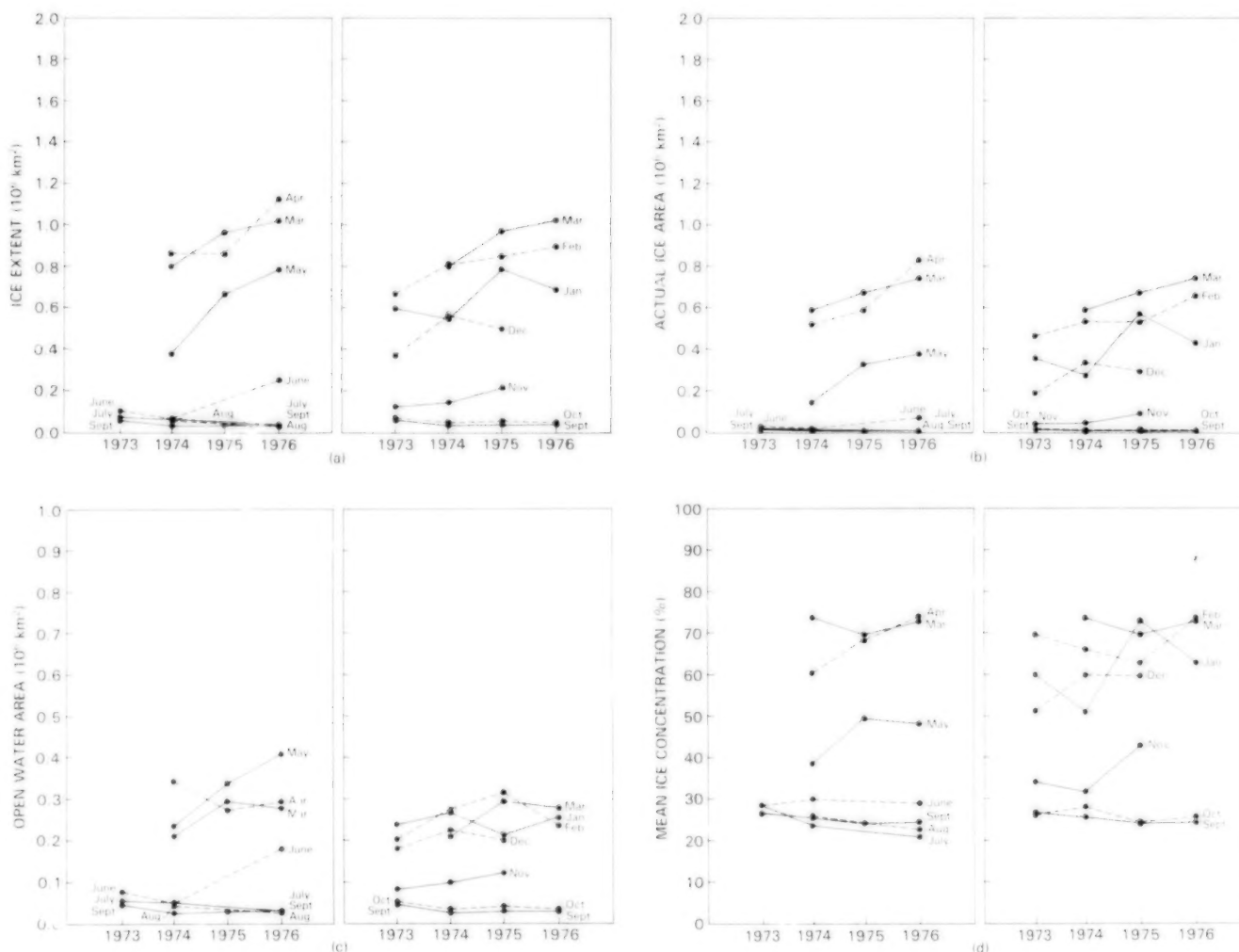


Figure 4-57. Month-by-month year-to-year changes in (a) sea ice extent, (b) actual ice area, (c) open water area within the ice pack, and (d) mean sea ice concentration for the Bering Sea region.

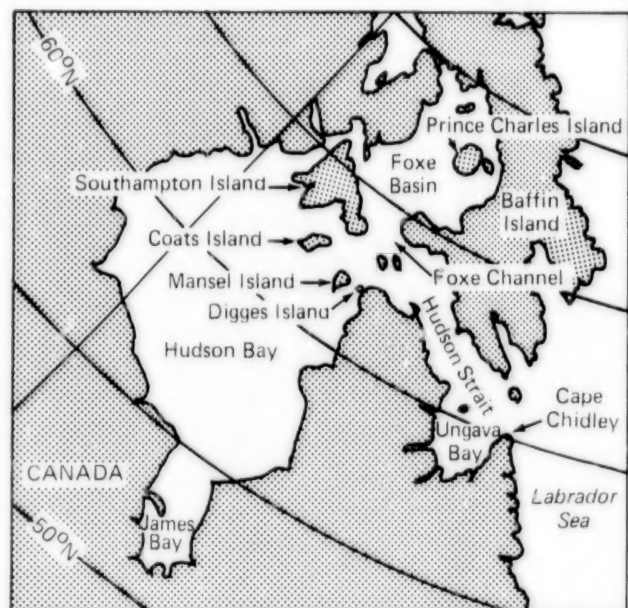


Figure 4-58. Location map for the Hudson Bay region.

salinity profile of the water column shows marked depth dependence, with the salinity averaging 31 parts per thousand below 25 meters and 23 parts per thousand above 25 meters. In the upper 1.8 meters, the salinity can be as low as 2 parts per thousand when the current is strong and ice is melting. Water temperature has a minimum of about -1.8°C in winter and may reach 11.5°C in September.

The bay is filled by inflow from numerous peripheral rivers and by currents from Foxe Basin to the north, contributing to a clockwise general circulation. Outflow occurs through Hudson Strait, rounding Cape Chidley, and passing into the Labrador Current. The magnitude of the outflow is highest in July. Tides are important considerations in the circulation because currents in the bay are sensitive to the tidal flows, especially those off the Labrador coast. The current movements associated with the tides also cause significant mixing of waters in the region.

Historically, Henry Hudson in 1610, seeking a Northwest Passage to the Orient, sailed through the ice-free strait later named for him and sighted the body of water later called Hudson Bay. He reached and named Digges Island at the entrance to the bay, but his explorations were cut short soon afterwards,

as he was seized by a mutinous crew and left with nine others to die. The 10 abandoned explorers were never heard from again. In 1612, Thomas Button became the first European to cross the bay to its western coast, which he and others explored in the next two decades while seeking a Northwest Passage. In 1631 Luke Foxe explored the waters west and east of Southampton Island and sailed part way up Foxe Channel. Further exploration of the channel awaited the efforts of Captain Middleton over a century later, in 1741 (Mirsky, 1948).

Hudson Bay is almost completely ice covered during the winter period and is completely ice free in summer (Figures 4-3 through 4-8). With the exception of some influx from Foxe Basin, the ice is local and essentially confined. Foxe Basin and Hudson Strait are also mostly covered by ice in winter, but there are slight differences in the freezeup time and the rate of growth in the two areas. Because Hudson Bay is ice free in summer, the ice cover during the rest of the year has a first-year ice signature, making the interpretation of the color scale, as in the cases of the Sea of Okhotsk and the Bering Sea, generally straightforward because of no contamination by multiyear ice. Ice begins forming in November at about the same place each year in the northwest portion of the bay and has almost completely covered the bay in December (Figures 4-28 and 4-29). The bay remains almost completely ice covered at least until May, when the first hints of ice breakup appear. Some of these early hints may be temporary events initiated by wind forcings. The patterns of ice decay show that basically the decay is from the north, with the ice retreating from the northeastern and northwestern coastlines in June (Figure 4-23) and remaining predominantly in the southwestern portion in July (Figure 4-24) before disappearing altogether by August (Figure 4-25).

The exact time of freezeup is impossible to infer directly from the monthly maps because of the averaging over monthly periods. Using 3-day-average maps from the same ESMR data set used to create the monthly maps, it is found that in 1975 the ice advance begins in mid-October in Foxe Basin, 2 weeks later in Hudson Bay, and 2 weeks after that in Hudson Strait. It takes about a month and a half until maximum ice cover is reached in Foxe Basin, about 2 months in Hudson Bay, and about a month and a half in Hudson Strait. By contrast, ice decay occurs almost simultaneously in the three areas,

starting at about the third week of April and ending at about the last week of July.

Monthly difference maps of the 4-year-average data show more distinctly the growth and decay patterns over a seasonal cycle (Figure 4-9). No significant growth or decay occurs for the period from January to April. The large-scale spring decay begins from April to May, including significant decreases

in ice concentration in each of Hudson Strait, Hudson Bay, and Foxe Basin. Monotonic decay continues until August, with the strongest activity occurring from June to July in all three areas. By August no ice remains except in Foxe Basin, where ice decay continues from August to September and ice growth begins in the September to October period. The growth expands to northwestern Hudson Bay and Hudson Strait from October to November

HUDSON BAY

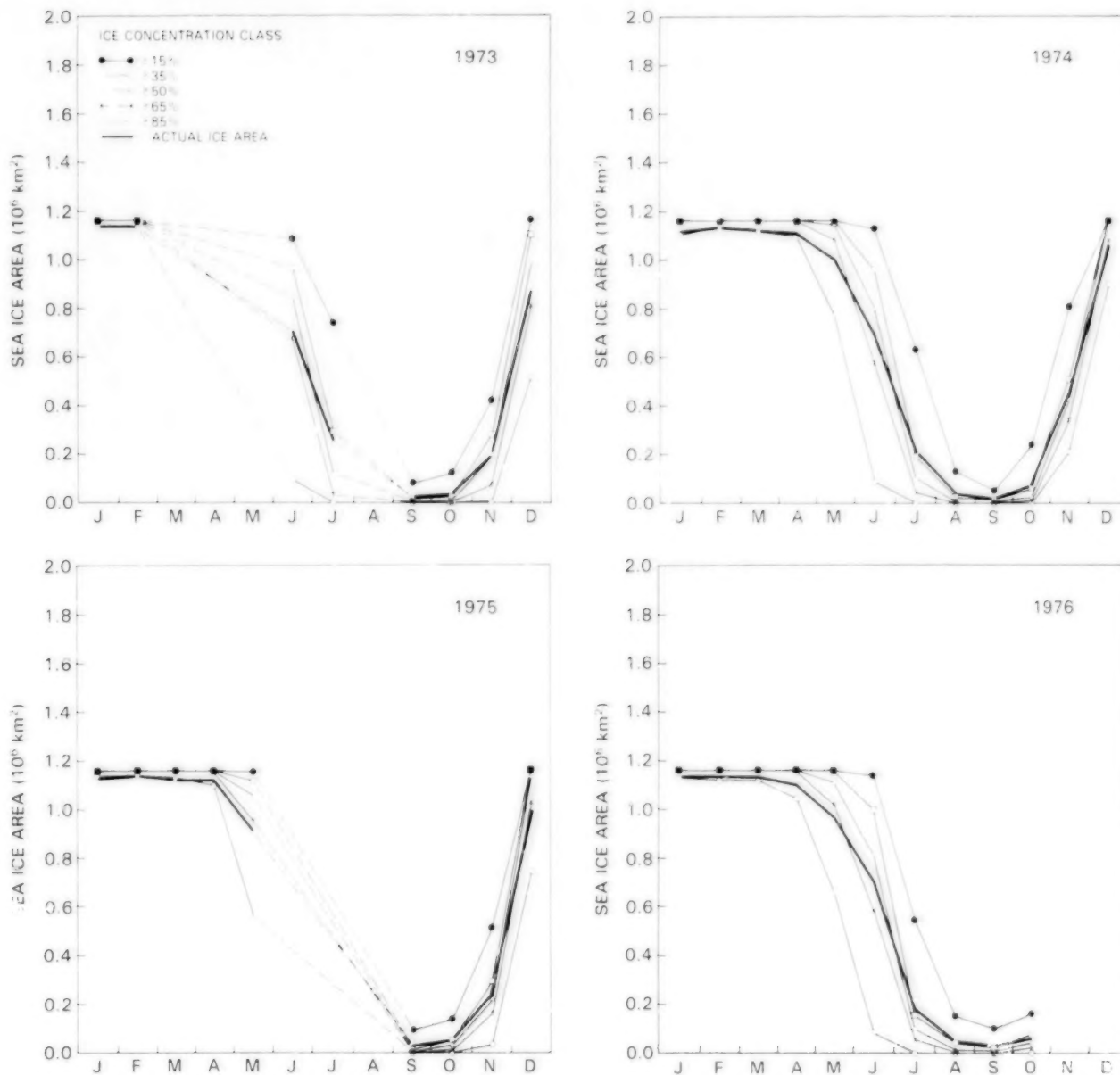


Figure 4-59. Yearly cycles of the ocean area covered by sea ice with concentration exceeding 15, 35, 50, 65, and 85 percent, and yearly cycle of the actual ice area, for the Hudson Bay region in 1973, 1974, 1975, and 1976. The actual ice area is the integrated ocean surface area covered by sea ice, excluding leads and polynyas within the ice pack.

and throughout the region by November to December. Significant growth continues from December to January, by which time the whole region is fully ice covered (Figure 4-9).

The monthly difference maps for the individual years (Figures 4-30 to 4-37) show that basically the interannual variation in the growth and decay pattern in the Hudson Bay region is not very large, al-

though year-to-year differences exist in the timing of freezeup and the length of the melt period.

The seasonal cycles of ice growth and decay in the Hudson Bay region are depicted quantitatively in Figures 4-59 through 4-61. For the 2 years with complete data coverage in winter and spring, 1974 and 1976, the decay characteristics are very similar (Figures 4-59 and 4-60). For each ice concentration class

HUDSON BAY

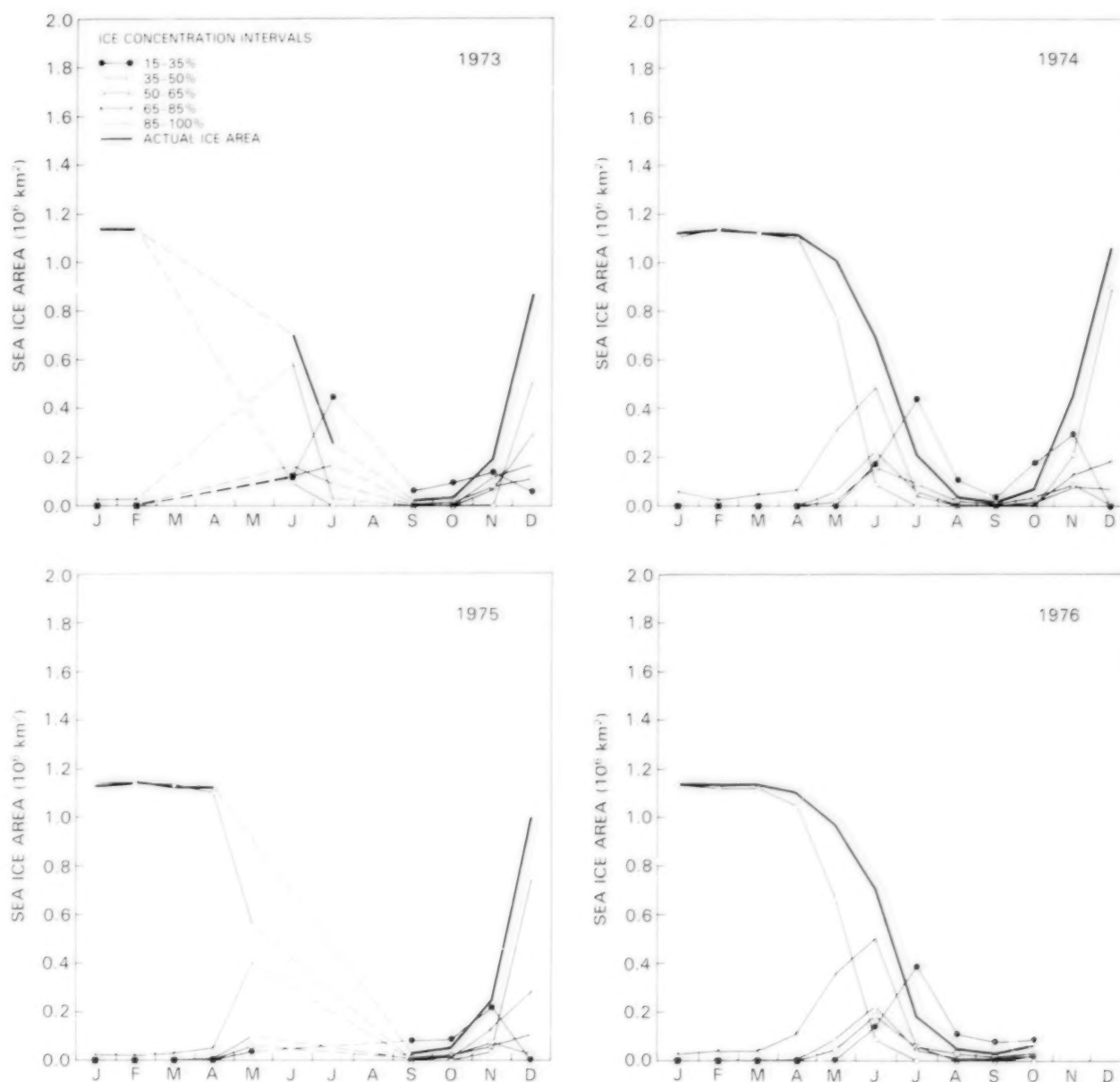


Figure 4-60. Yearly cycles of the ocean area covered by sea ice within ice concentration intervals 15 to 35, 35 to 50, 50 to 65, 65 to 85, and 85 to 100 percent, and yearly cycle of the actual ice area, for the Hudson Bay region in 1973, 1974, 1975, and 1976.

of Figure 4-59, the ice cover takes about 2 months to break up completely. The growth sequences are also similar for the 3 years with autumn data, except that freezeup probably occurred about a week earlier in 1974 than in 1973 or 1975, accounting for the high average October and November areal ice coverages in 1974.

For the growth period, the interannual variations previously mentioned for the ice concentration classes are naturally also apparent in the interval plots (Figure 4-60), with 1974 freezeup occurring earliest, and 1975 freezeup somewhat preceding that in 1973. Data are not available for the 1976 freezeup.

The interannual variability of the ice extent, the actual ice cover, and the amount of open water is greatest during the fall freezeup and least during winter (Figure 4-61). For the 7 months December through June, the bay, strait, and basin are almost entirely covered with ice, with the areal ice extent approximating the geographical area, at about 1.16×10^6 square kilometers (Figure 4-61), and the actual ice area being less than 0.3×10^6 square kilometers below that level for the middle 5 of those 7 months (Figure 4-61b). The closeness of the actual ice area to the ice extent reflects the very high sea ice concentrations, evident also in Figure 4-61d, which shows the mean ice concentrations to exceed 95 percent from January through April.

HUDSON BAY

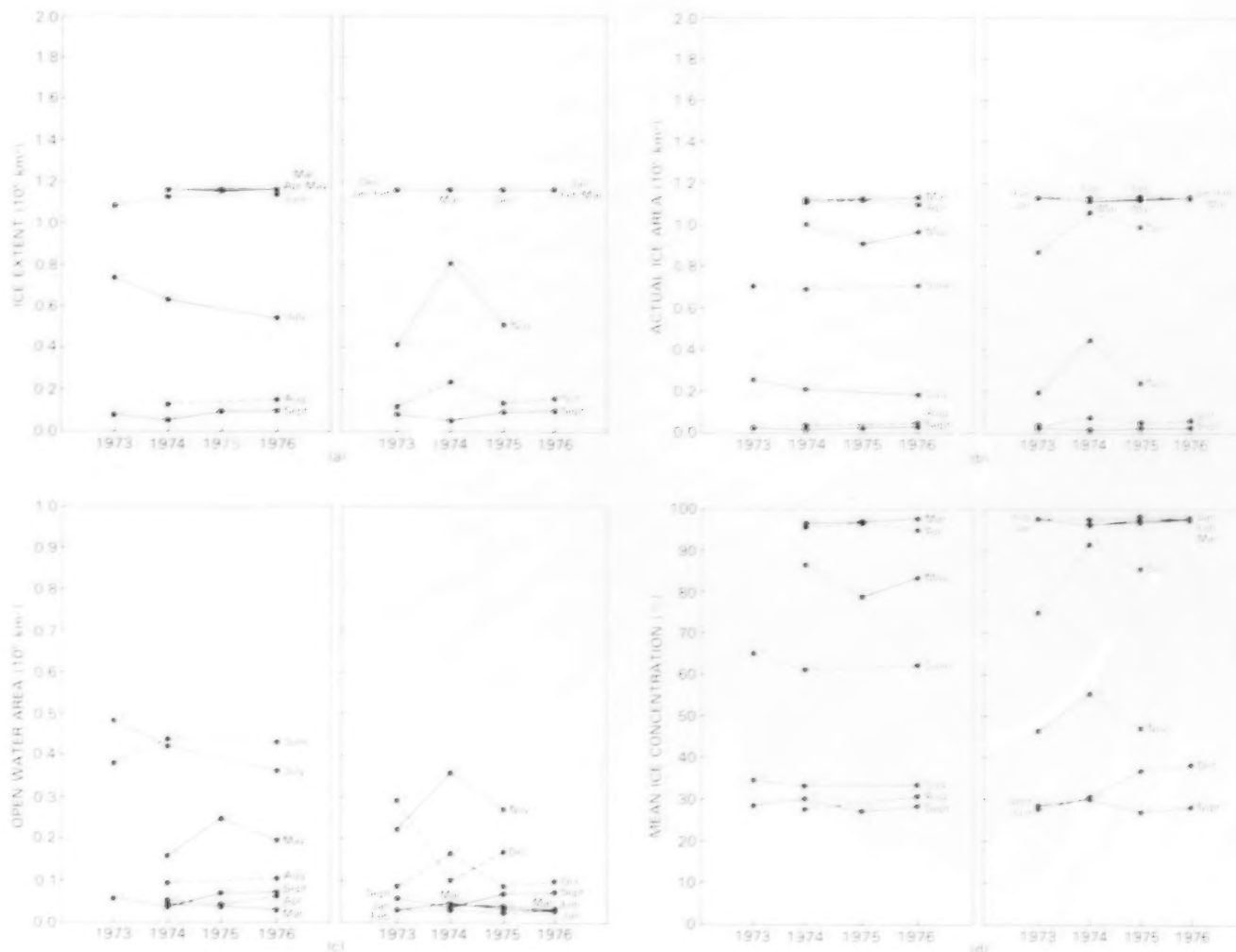


Figure 4-61. Month-by-month year-to-year changes in (a) sea ice extent, (b) actual ice area, (c) open water area within the ice pack, and (d) mean sea ice concentration for the Hudson Bay region.

In July, marked interannual variability in sea ice extent and lesser interannual variability in actual ice area are observed, with ice decay having proceeded furthest in 1976 and least in 1973. There are no data for July 1975. In the late summer, in August and September, the region is nearly ice free in each of the 4 years. Substantial interannual variability is again evident in fall, especially in November when the 1974 data clearly show earlier freezeup than in the other years, as previously indicated (Figures 4-61a and 4-61b). The open water distribution has two peaks, in late spring/early summer and in fall, surrounding the essentially zero values in summer. Slightly more open water occurs within the ice pack in spring than in fall (Figure 4-61c).

4.6 BAFFIN BAY/DAVIS STRAIT

Few parts of the Arctic figure as prominently in the history of polar exploration as do Baffin Bay and Davis Strait, two adjacent, relatively shallow bodies of polar waters located between Greenland and Baffin Island (Figures 4-62 through 4-65). Western man's efforts in this region are in part a long story of disappointment and tragedy. They started in 985 when Eric the Red and his fellow Norsemen explored and founded colonies in south-west Greenland, suggestively named "Greenland" by Eric to entice colonists to join him. Initially the colonies prospered, extending as far north as Davis Strait, but all of them mysteriously disappeared in the late Middle Ages. In the meantime, Eric's son Leif Ericsson reached Baffin Island at the beginning of the 11th century.

As with so much of the rest of the early exploration of the Arctic regions, the early more-extensive explorations of the Baffin Bay/Davis Strait region were guided in large part by the hope of finding a Northwest Passage to the Orient. Martin Frobisher set out in 1576 with that goal in mind, sailing as far as Frobisher Bay and making three voyages to Baffin Island between 1576 and 1578. John Davis led three expeditions between 1585 and 1587, rounding the southern tip of Greenland, arriving as far north as 72°N, and then heading westward across the widest part of Baffin Bay. His detailed descriptions of the Davis Strait area helped lead the way for the further explorations of Henry Hudson in Hudson Strait and William Baffin in Baffin Bay. In 1616 Baffin sailed north past Davis's furthest point of Sanderson's



Figure 4-62. Location map for the Baffin Bay/Davis Strait region.

Hope, still seeking a Northwest Passage. He reached and named Smith Sound, Jones Sound, and Lancaster Sound, but was then encouraged to head home by a heavy ice cover and a severe outbreak of scurvy debilitating the crew. The northernmost locations reached by Baffin were not reached again by those not native to the region for over two centuries (Mirsky, 1948).

The next major expeditions in the region were made after the Napoleonic Wars, when the British Admiralty, temporarily with a surplus of ships and sailors but no military encounters, renewed the search for a Northwest Passage. In 1818 an expedition under Captain John Ross and Lieutenant Edward Parry confirmed Baffin's earlier descriptions and penetrated about 50 miles into Lancaster Sound. In 1819 Parry returned through Baffin Bay into Lan-

caster Sound and beyond, exploring much of the Canadian Archipelago, and in 1845 an expedition led by Sir John Franklin also explored much of the same area, only to disappear entirely. (The Parry and Franklin expeditions are discussed further in Section 4.9.)

As in most parts of the Arctic, satellite observations of the Baffin Bay region have resulted in a

BAFFIN BAY/DAVIS STRAIT

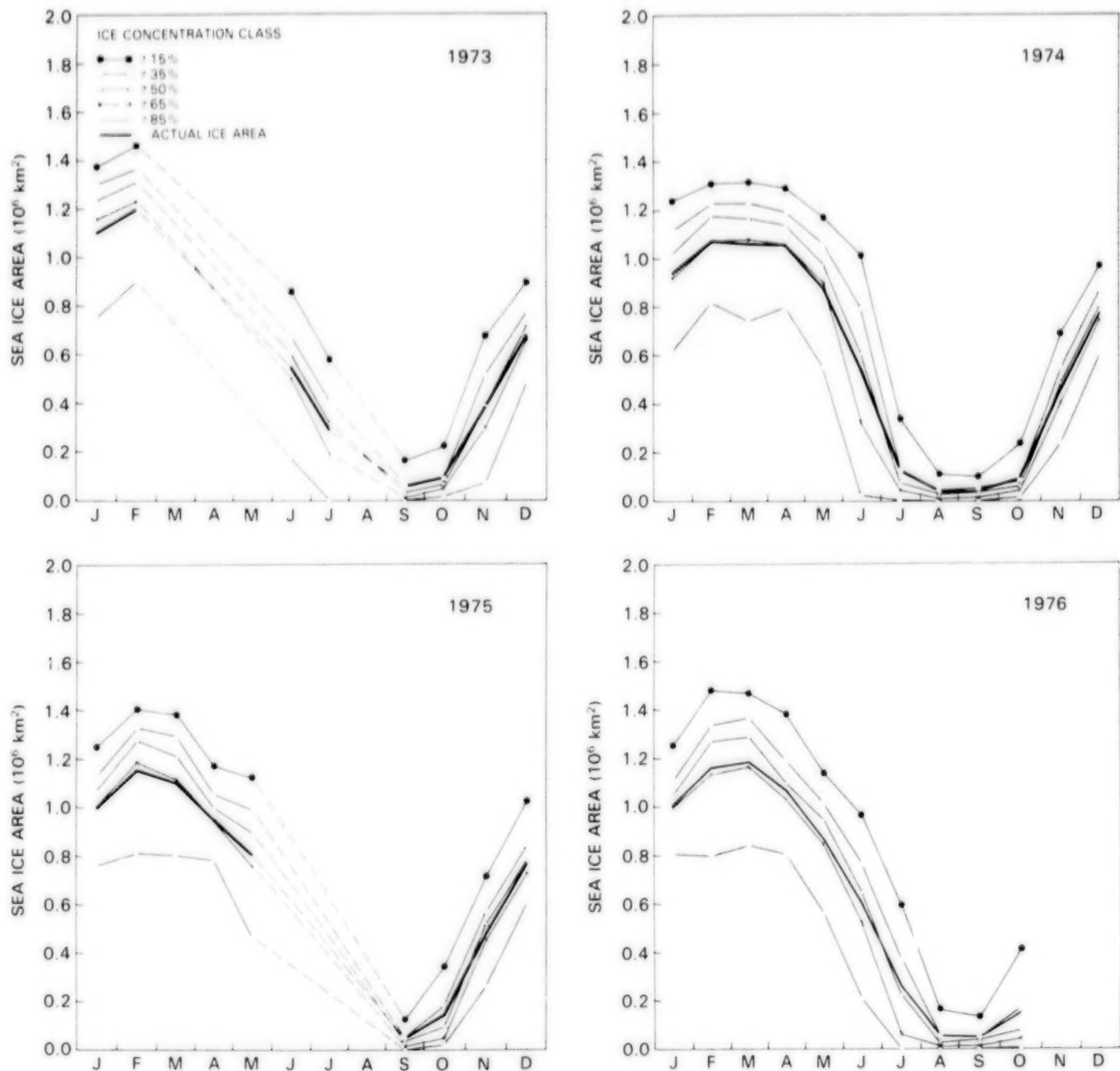


Figure 4-63. Yearly cycles of the ocean area covered by sea ice with concentration exceeding 15, 35, 50, 65, and 85 percent, and yearly cycle of the actual ice area, for the Baffin Bay/Davis Strait region in 1973, 1974, 1975, and 1976. The actual ice area is the integrated ocean surface area covered by sea ice, excluding leads and polynyas within the ice pack.

greatly enhanced knowledge of the complex behavior of its sea ice cover. Ramseier et al. (1975) analyzed Landsat imagery for the period March through November 1973 to obtain detailed ice dynamics information, such as the flux of ice eastward out of Lancaster Sound into Baffin Bay. Dey (1980b) used NASA imagery to study seasonal and annual variations of the ice cover during the period 1968 through

1979. Dey et al. (1979) used a combination of Landsat and NOAA imagery to study the breakup and freezing patterns in Baffin Bay, and Dey (1981a) used NOAA imagery to estimate ice fluxes into Baffin Bay during the period 1974 through 1978. Crawford and Parkinson (1981) used ESMR imagery to examine the wintertime North Water polynya between Greenland and Ellesmere Island, and Steffen

BAFFIN BAY/DAVIS STRAIT

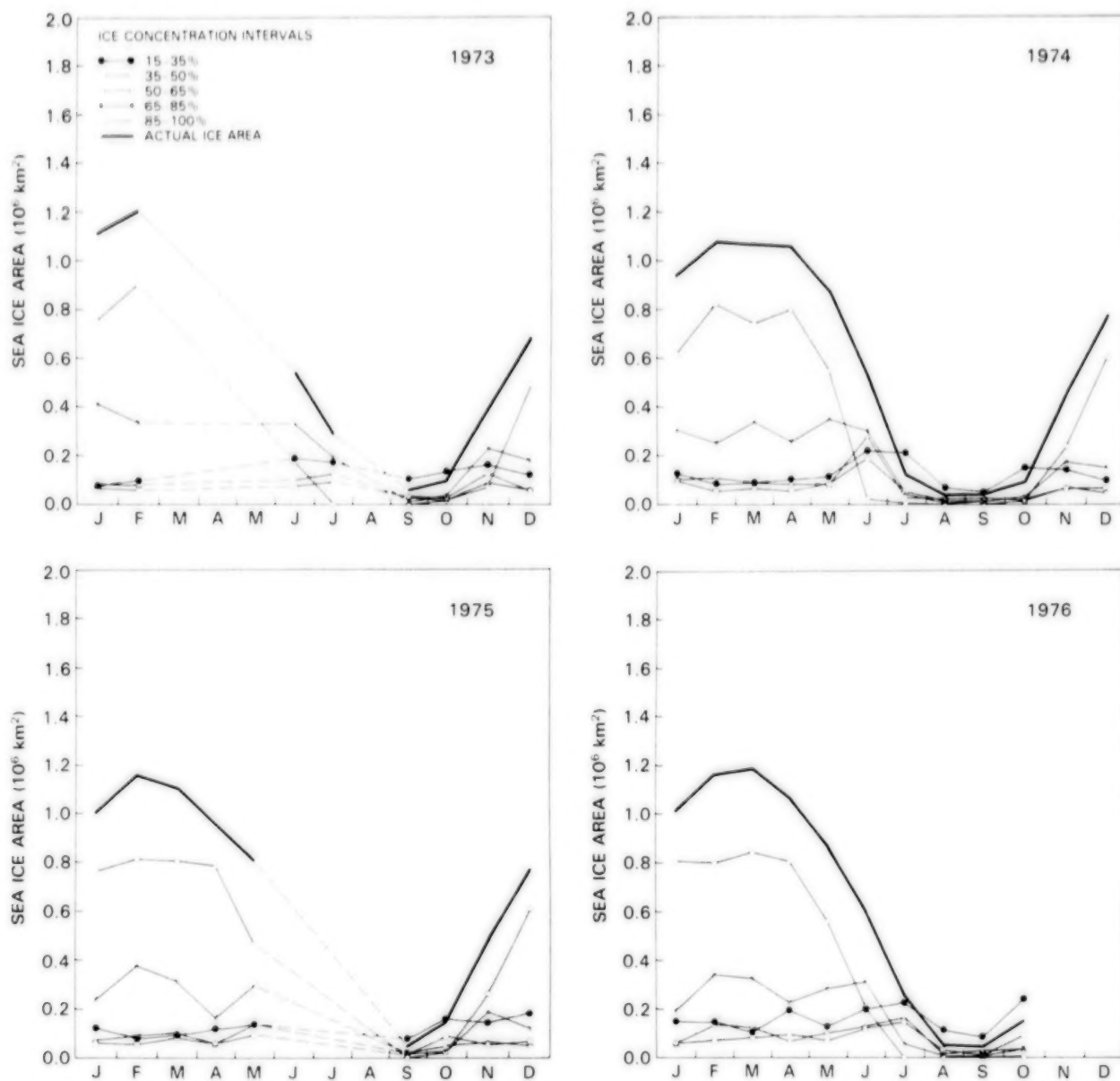


Figure 4-64. Yearly cycles of the ocean area covered by sea ice within ice concentration intervals 15 to 35, 35 to 50, 50 to 65, 65 to 85, and 85 to 100 percent, and yearly cycle of the actual ice area, for the Baffin Bay/Davis Strait region in 1973, 1974, 1975, and 1976.

(1985) did the same with a combination of Landsat, NOAA, and Nimbus satellite data plus measurements from aircraft. Ito (1982) created an atlas of sea ice conditions in northern Baffin Bay using visual observations from ground and aircraft as well as Landsat images. His atlas covers the period March through October for the years 1973 through 1976 and 1980 through 1981. Conveniently, much of the analysis of the high resolution visible and infrared satellite imagery provided in these studies concerned data from the ESMR time period.

The average behavior of the Baffin Bay/Davis Strait sea ice covers in the mid-1970s can be seen

from the 3- and 4-year mean monthly ice concentration maps of Figures 4-3 through 4-8 and from the monthly difference maps of Figure 4-9. Freezup begins in October in northern Baffin Bay (Figure 4-7) and proceeds rapidly southwards in November and December (Figure 4-8). By December all of Baffin Bay is ice covered, and the southern edge of the ice pack has reached its approximate winter limit, running from just south of the entrance to Hudson Strait northeastwards to the Greenland coast in the area of Holsteinsborg. This southwest-northeast orientation of the edge is maintained throughout winter and spring (Figures 4-3 through 4-5) by the combination of the warm West Greenland Current,

BAFFIN BAY/DAVIS STRAIT

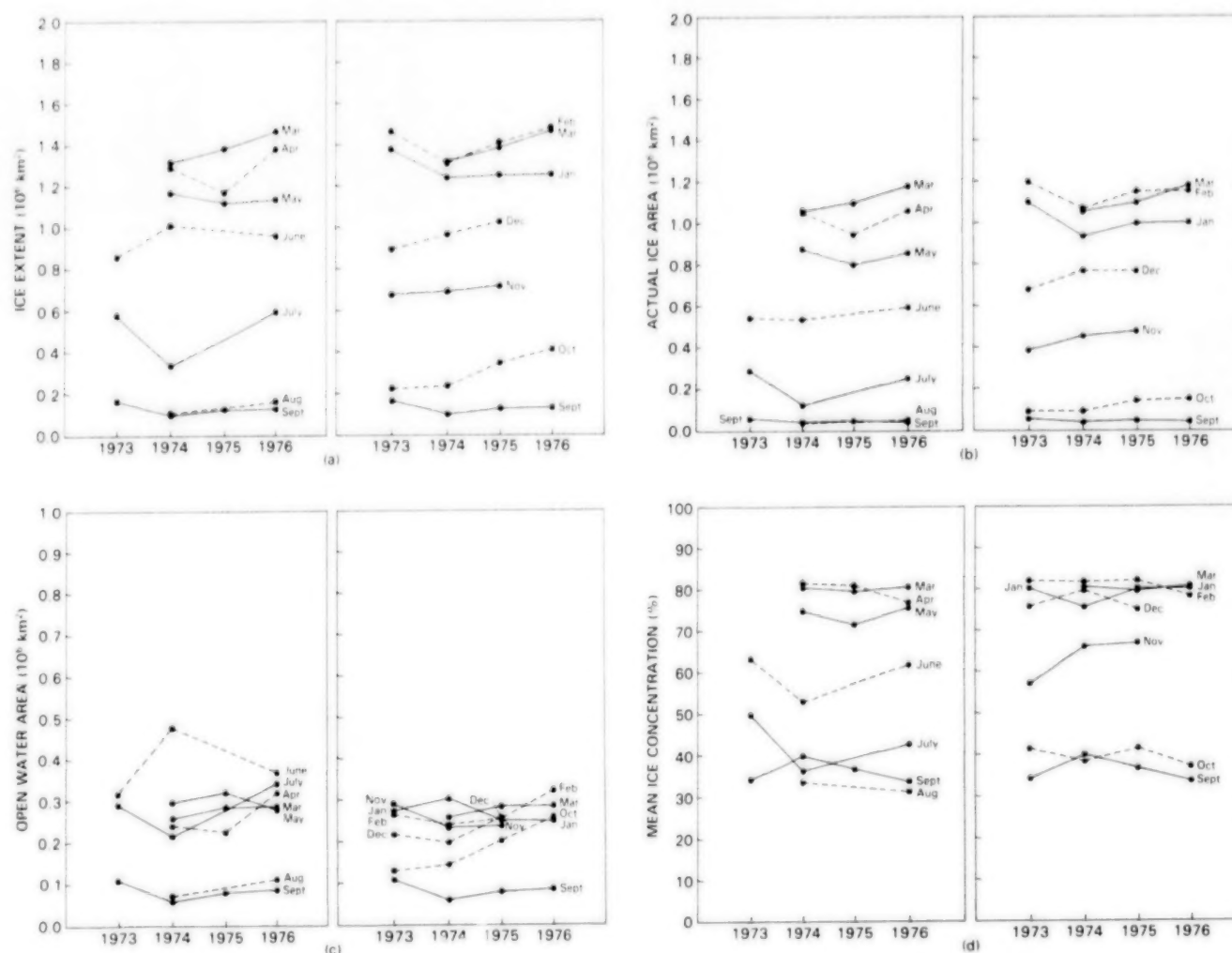


Figure 4-65. Month-by-month year-to-year changes in (a) sea ice extent, (b) actual ice area, (c) open water area within the ice pack, and (d) mean sea ice concentration for the Baffin Bay/Davis Strait region.

the counterclockwise water circulation in Baffin Bay, the cold Labrador Current, and the winter/spring cyclone passages.

Almost all of the ice formed in the Baffin Bay/Davis Strait region is first-year ice, although significant amounts of ice are advected into the bay through Lancaster Sound, Smith Sound, and, to a lesser extent, Jones Sound, and some of this advected ice has a multiyear ice signature. Dey (1981a) estimates the average flux into the bay through these three channels as 654 cubic kilometers per year, during the period 1974 through 1978. The greater part of this advected ice is first-year ice, and the winter ice cover of the entire bay is over 90 percent first-year ice, justifying the use of the first-year ice emissivity of 0.92 in the calculation of ice concentration. Fast ice forms along the coasts around much of the bay, in particular in the Melville Bay region in northeastern Baffin Bay, where it extends about 50 kilometers offshore, and at Home Bay along the Baffin Island coast, where it normally extends to about 70 kilometers offshore (Dey, 1980b).

The maximum ice extent in the Baffin Bay/Davis Strait region occurs in February (Figure 4-12), when the ice reaches southward along the Canadian coast beyond the 50°N limit of the maps presented here (Figure 4-3). Still, in spite of the southward extent of the ice to the west, most of the eastern portion of Davis Strait remains ice free, once again because of the powerful effect of the warm West Greenland Current.

From December through April, an area of reduced ice concentration exists in northern Baffin Bay and Smith Sound (Figures 4-8, 4-3, and 4-4). From the 3-day-average ESMR images, it is obvious that a recurring polynya opens and closes throughout the winter season (Crawford and Parkinson, 1981). This North Water polynya was first recorded by William Baffin in July 1616 and noticed by members of numerous expeditions over the next several centuries (Dunbar and Dunbar, 1972). In recent years, many studies of it have been made, such as those by Dunbar and Greenaway (1956), Dunbar (1969, 1972, 1973), Aber and Vowinkel (1972), Muller (1975), Ito and Muller (1977), Dey (1980a), Crawford and Parkinson (1981), and Steffen (1985). The North Water is produced by winds and oceanographic forces, and its behavior can vary significantly from year to year, as will be seen in the discussion of the

monthly ESMR maps for the individual years. The North Water was sufficiently persistent during the ESMR period to appear in the 3- and 4-year mean monthly ice concentration and brightness temperature maps.

The spring breakup in the Baffin Bay/Davis Strait region is complex. The marginal ice zone south of Davis Strait begins to migrate northward in April (Figure 4-4). By May this migration extends as far north as Disko Island in eastern Baffin Bay, and low ice concentrations appear in the region of the North Water (Figure 4-5). By June a large polynya covers the North Water area and rapidly opens to cover all of northern Baffin Bay in July (Figure 4-6). During the same period, the southern edge of the pack rapidly migrates northward, so that the ice breakup in the bay proceeds from the southeast and northwest simultaneously. The last part of the ice cover to remain in July is in the central western part of the bay, adjacent to Baffin Island. Linger ice can remain in this area on occasion throughout the summer (Markham, 1962; Dunbar, 1972), but during the ESMR time period the Baffin Bay/Davis Strait region is essentially free of ice during both August and September (Figures 4-6 and 4-7).

The previous discussion indicates the average behavior of the Baffin Bay/Davis Strait ice cover during the 4-year period 1973 through 1976. Observations made over the centuries since Baffin first traversed the bay have shown that large interannual variations occur, and the mean monthly ice concentration maps given in Figures 4-18 through 4-29 confirm these variations for the ESMR period. For instance, the October ice concentration maps (Figure 4-27) indicate that during the early freezeup the amount of ice in northern Baffin Bay is least in 1973, slightly more in 1974, more in 1975, and most in 1976. The ice edge in 1976 extends about 500 kilometers farther south than in 1973. ESMR data are missing in November and December of 1976, but the October trend toward greater ice extents from 1973 to 1974 and from 1974 to 1975 continues in both November and December (Figures 4-28 and 4-29). Thus, during the mid-1970 ESMR time period the fall freezeup in the Baffin Bay/Davis Strait region is more pronounced each successive year.

In each of the 3 years with ESMR coverage throughout the winter, the 2 months with the greatest ice coverage are February and March, with March

having a slightly greater ice extent than February in 1974 but February having a slightly greater ice extent in 1975 and 1976 (Figure 4-63). The monthly-difference maps (Figures 4-32, 4-34, and 4-36) clearly show that in 1975 the February to March transition has most of the ice edge retreating except for a small region at 60°N, in 1974 the February to March transition has a more elongated region of ice edge advance between 59°N and 63°N and an additional region of advance near 50°S, and, in sharp contrast, in 1976 the February to March transition has significant ice edge advance at both the southwesternmost and northeasternmost reaches of the ice edge and significant ice edge retreat in between. Of these 3 years, the year with the greatest amount of ice in each of these months, February and March, is 1976, and the year with the least amount of ice in these months is 1974, with a near-linear upward trend over the 3-year period 1974 through 1976 (Figure 4-65a). The February ice cover in 1973, for which year no monthly averaged data are available for March, April, or May, is very close to that in 1976.

The basic patterns of ice concentrations in February and March, at the time of maximum ice extent, are similar for each year. This includes fully compacted ice in northern Baffin Bay, concentrations of 90 to 96 percent in central Baffin Bay and in Smith Sound and Kane Basin to the north of the bay, and concentrations as high as 80 percent within 200 kilometers of the ice edge in southern Baffin Bay and Davis Strait. The area of near-total ice compaction is largest in 1976, the year with the greatest ice extent (Figures 4-19 and 4-20).

Notable interannual differences occur in the spring/summer progression of ice breakup and decay, especially in northern Baffin Bay. By May the southern edge of the ice cover has migrated rapidly northward along the west coast of Greenland in each year with ESMR data (1974, 1975, and 1976), with the most northerly limit occurring in 1974, when the ice edge extends into Melville Bay instead of stopping at Disko Island as in 1975 and 1976. However, at the northern reaches of the Baffin Bay/Davis Strait region, in the North Water area and Kane Basin, the decreased ice concentrations, which occur in each of the 3 years, are actually less in 1974 than in 1975 or 1976 (Figure 4-22), so that May 1974 seems to be colder in the northern reaches of the region and warmer in the southern reaches than May 1975 or May 1976.

The large polynyas in northern Baffin Bay in June also vary markedly from year to year (Figure 4-23). In 1973 a narrow open channel extends from Smith Sound through the western part of the North Water area, joining a large polynya in Lancaster Sound. In 1974 a small polynya exists in Smith Sound and a large polynya extends from Lancaster Sound eastward into northern Baffin Bay, but the North Water area remains ice covered. In 1976 the entire North Water area is open and low concentration ice fills eastern Lancaster Sound. These marked interannual contrasts reflect the highly variable nature of polynya dynamics in the North Water area at the time of ice breakup.

In July, with the exception of a small amount of ice along the coasts, northern and eastern Baffin Bay and the North Water area are ice free in each of the 3 years with available ESMR data, but significant interannual differences occur in southern and central Baffin Bay and Davis Strait (Figure 4-24). In 1973 a large pack covers most of the east coast of Baffin Island and extends eastward almost to the Greenland coast. In 1974 Baffin Bay and Davis Strait are almost entirely ice free, with a narrow band of ice hugging the east coast of Baffin Island. In 1976 an extensive pack covers most of the east coast of Baffin Island and extends eastward to fill about 70 percent of southern Baffin Bay. The 1976 pack is approximately equal in extent to that in 1973 (Figure 4-65a), but its mean ice concentration is decidedly less (Figures 4-65d and 4-24). In a study of interannual variations in the growth and decay patterns of the ice extent in the Davis Strait/Labrador Sea area from 1964 through 1974, Crane (1978) confirms the expected greater frequency of southerly air flow in years of early ice retreat, suggesting an atmospheric control over the rate of sea ice retreat in the region.

In August and September the Baffin Bay/Davis Strait region is essentially ice free in each year with ESMR data, although some ice remains in Kane Basin (Figures 4-25, 4-26, and 4-65a).

4.7 GREENLAND SEA

Located between Greenland on the west and the much smaller islands of Svalbard, Jan Mayen, and Iceland on the east (Figures 4-66 through 4-72), the Greenland Sea was traversed in 982 by Vikings under Eric the Red when they sailed west from Iceland and

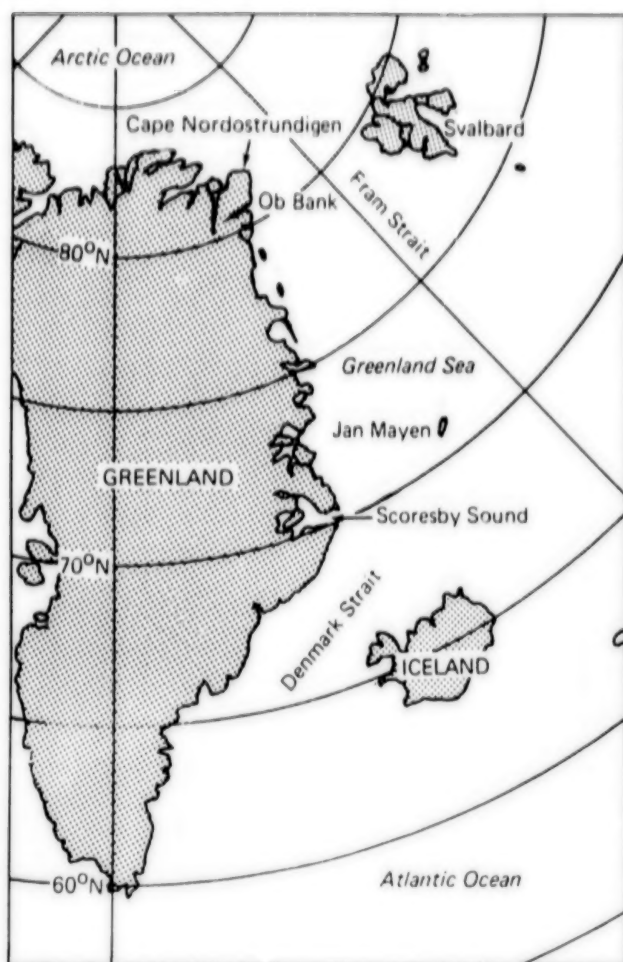


Figure 4-66. Location map for the Greenland Sea region.

discovered Greenland, and again in 986 when they repeated the journey, this time bringing approximately 450 immigrants to form the first Viking settlement on the island. During these voyages the Vikings also sailed considerable distances along the Greenland coast. Much more thorough explorations were carried out in the 19th century, particularly by the William Scoresbys in 1822, Captain Caving in 1823, Karl Koldewey between 1869 and 1871, and a sequence of Danish expeditions between 1879 and 1908. William Scoresby the father explored Scoresby Sound while his son mapped 800 miles of the coastline between 69°N and 72°N; Caving sailed north to 75°N; and Koldewey, although falling far short of the expedition's original goal of reaching the North Pole, traveled north to 77°N. The Danes succeeded in mapping the entire east coast of Greenland. Further explorations of much of the Greenland Sea

were made in the early 20th century by Fridtjof Nansen and B. Helland-Hansen (Mirsky, 1948).

The Greenland Sea is an extremely dynamic region for all three of its climatic components—atmosphere, sea ice, and ocean. The vast majority of the ice that exits the Arctic Ocean flows southward through the Fram Strait and into the Greenland Sea. Vinje (1976) has estimated that between 2 and 15 cubic kilometers of ice pass through the Strait each day. To illustrate the rapid drift of ice in the area, the drifts of the Papanin (1937-1938) and Arlis II (1965) manned drifting stations are shown in Figure 4-67, and we refer back to the drifts of several satellite-tracked buoys in the Greenland Sea plotted along with the Arctic Ocean buoys in Figures 4-43 and 4-44. By comparing these drifts to those of the Arctic Ocean (Figures 4-42 through 4-44), it can be seen that the monthly drift speeds in the Greenland Sea can be an order of magnitude greater than those in the Arctic Ocean. Not only does the ice move very rapidly in the Greenland Sea, but very large seasonal and interannual variations in the amount and extent of the ice cover occur, as illustrated in Figure 4-68 by summer and winter data from the period 1966 through 1975. The Greenland Sea region is one of intense meteorological activity during fall and winter and is one of the areas of strongest cyclogenesis in the Northern Hemisphere. A review of the ice cover characteristics in the region, based on extensive observations, can be found in Wadhams (1981).

The bathymetry of the Greenland Sea (Figure 2-2) helps to explain why it is the area of greatest water flux into and out of the Arctic Ocean. For many years it was believed that a submarine ridge, the so-called Nansen Sill, joined Svalbard and Greenland. In the late 1950s it was found not only that such a ridge does not exist but that instead a deep trough exists with depths of 3,000 to 4,000 meters. This trough, called the Lona Trough, is the only deep passage connecting the Arctic Ocean to the oceans to the south, helping to explain the fact that the Greenland Sea is one of the most dynamic ocean areas of the Arctic and surroundings. The surface currents in late summer illustrated in Figure 4-67 show the varied and dynamic nature of the circulation in the Greenland Sea: a northward-flowing current exists along the west coast of Svalbard while the rapid southward-flowing East Greenland Current flows through the Fram Strait, shedding many eddies. Not only is the East Greenland Current the strongest

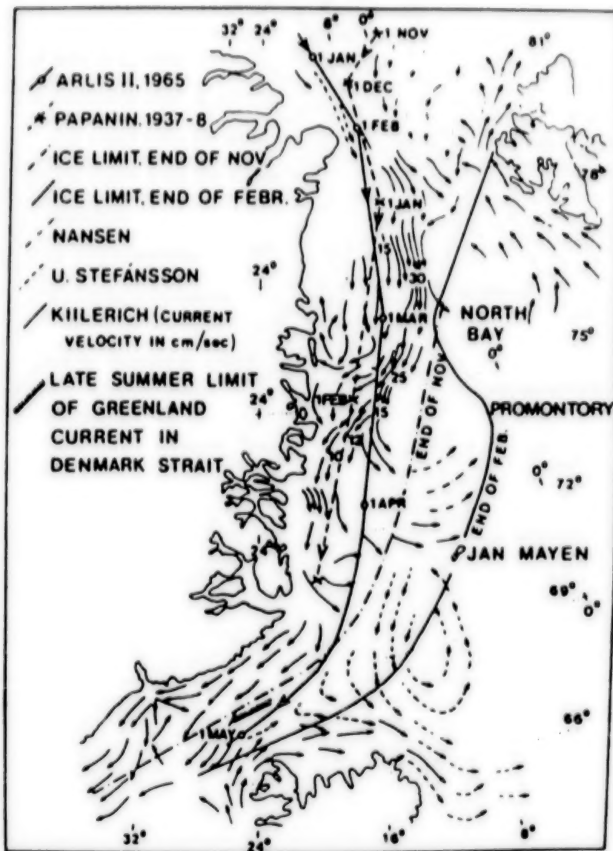


Figure 4-67. Drifts of the Papanin and Arlis II manned drifting stations in the Greenland Sea, along with average ice margins at the end of November and February, and the late summer currents in the area as determined by Nansen, Stefánsson, and Kiilerich. [From Einarsson (1972).]

ocean current in the Arctic and adjacent seas, but it also has the greatest current shears. This great shearing, coupled with swell penetration into the sea ice, causes the Greenland Sea ice cover to be made up primarily of small floes. These floes have dimensions ranging from several meters to several kilometers, with kilometer-size floes being relatively rare except for the floes of multiyear ice close to the Greenland coast. Thus, the gross structure of the Greenland Sea ice cover is quite different from that of the Arctic Ocean in terms of floe size and distribution, but its structure is quite similar in terms of ice type, because of containing large amounts of both multiyear ice and first-year ice. *In-situ* ice production in the Greenland Sea is exclusively first-year ice, as rapid ice transport prevents the growth of multiyear ice, but substantial amounts of multiyear ice are advected into the region from the Arctic Ocean.

Oceanographic conditions in the Greenland Sea, which is largely covered by a very active marginal ice zone, are dominated by the East Greenland Current, various frontal systems, eddies, and upwelling events along the ice edge. Another persistent feature of the area is the Jan Mayen Gyre, which provides an important mixing mechanism for the cold waters of the Greenland Sea and warmer Norwegian Sea waters. Fronts may be strong and persistent, such as the East Greenland Polar Front separating the cold, low-salinity, southward-flowing East Greenland Current from the more saline water in the Greenland Sea, or transient, such as ice edge meltwater fronts north of Svalbard. Meanders observed along the East Greenland Polar Front typically have wavelengths of 60 to 100 kilometers, while those of the meltwater fronts are usually smaller, with wavelengths on the order of 20 to 40 kilometers (Johannessen et al., 1983). The location of the East Greenland Polar Front correlates closely with the Greenland continental shelf, especially near the Ob Bank, suggesting that the front position is determined by bathymetric steering (Perdue, 1982).

Mesoscale eddies form along the fronts and the ice edge. In the marginal ice zone north of Svalbard, the scale of ice/ocean eddies observed during the Norwegian Remote Sensing Experiments (NORSEX) in 1978 and 1979 (NORSEX Group, 1983) were found to have horizontal dimensions on the order of 10 kilometers, which is approximately the Rossby internal radius of deformation for the area (Johannessen et al., 1983). Further downstream in the Fram Strait and the Greenland Sea, much larger eddies on the order of 50 to 80 kilometers are observed (Vinje, 1977; Wadhams and Squire, 1983). These large ice/ocean eddies appear to be generated through baroclinic instability of the East Greenland Polar Front. During the Marginal Ice Zone Experiment (MIZEX) in the Fram Strait region during June and July of 1984, a series of infrared images of the evolution and migration of a mesoscale eddy, reproduced in Figure 4-69, was obtained from the Advanced Very High Resolution Radiometer (AVHRR) on the NOAA 8 satellite.

Unlike the seasonal sea ice zones in the Sea of Okhotsk, Bering Sea, Hudson Bay, and Baffin Bay/Davis Strait regions, the Greenland Sea region retains a significant sea ice cover throughout the summer months in spite of the marginal ice zone nature of much of the region. The presence of summer ice

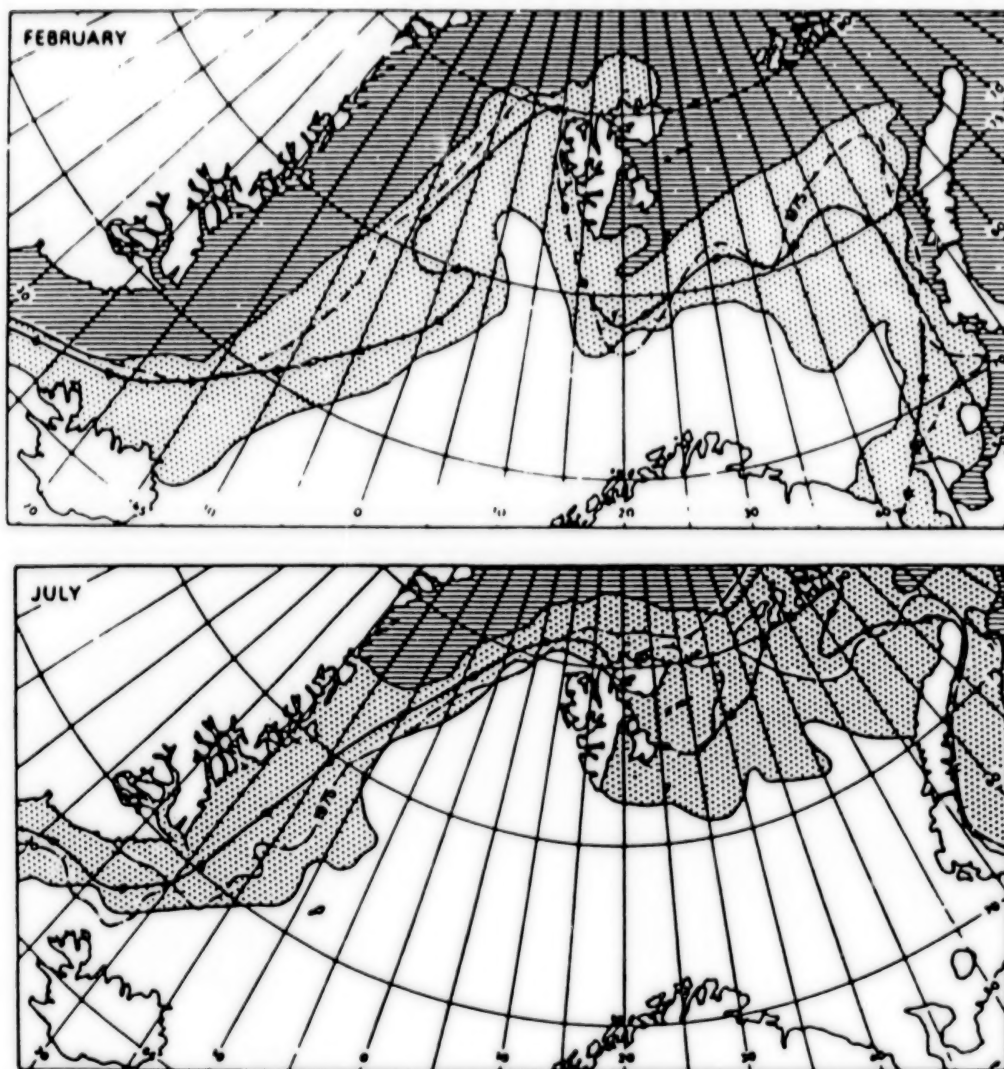


Figure 4-68. Mean and extreme limits of the sea ice edge in the Greenland and Barents Seas at the end of February and the end of July over the period 1966 through 1974. The mean limit of the ice edge as determined by the one-eighth ice cover contour is depicted by the thick black line, the 1975 limit is depicted by the dashed line, and the range of the ice edge over the 1966-1974 period is depicted by the dotted region. [From Vinje (1977).]

results largely from the advection of multiyear ice from the central Arctic through Fram Strait. Averaged over the 1973 through 1976 period, maximum ice cover in the Greenland Sea occurs during April, when the ice reaches just beyond the southern tip of Greenland (Figures 4-11 and 4-4). A sharp minimum in the ice cover occurs in August, when the ice reaches southward to a latitude of approximately 72°N (Figures 4-11 and 4-6). The ice cover experiences slow growth from August to October and more rapid growth from October to December, after which the total areal coverage of ice remains

approximately 1.05×10^6 square kilometers until the spring decay begins in May (Figure 4-11).

Among the major interannual differences in the edge position of the Greenland Sea ice cover are those occurring in the large projection of ice frequently extending from the coast of Greenland toward Svalbard (Figures 4-18 through 4-29). This projection has been observed frequently from as early as 1850, when Norwegian sealers began hunting in the area (Vinje, 1976). The sealers named the two major parts of the projection: the 'Odden' to the

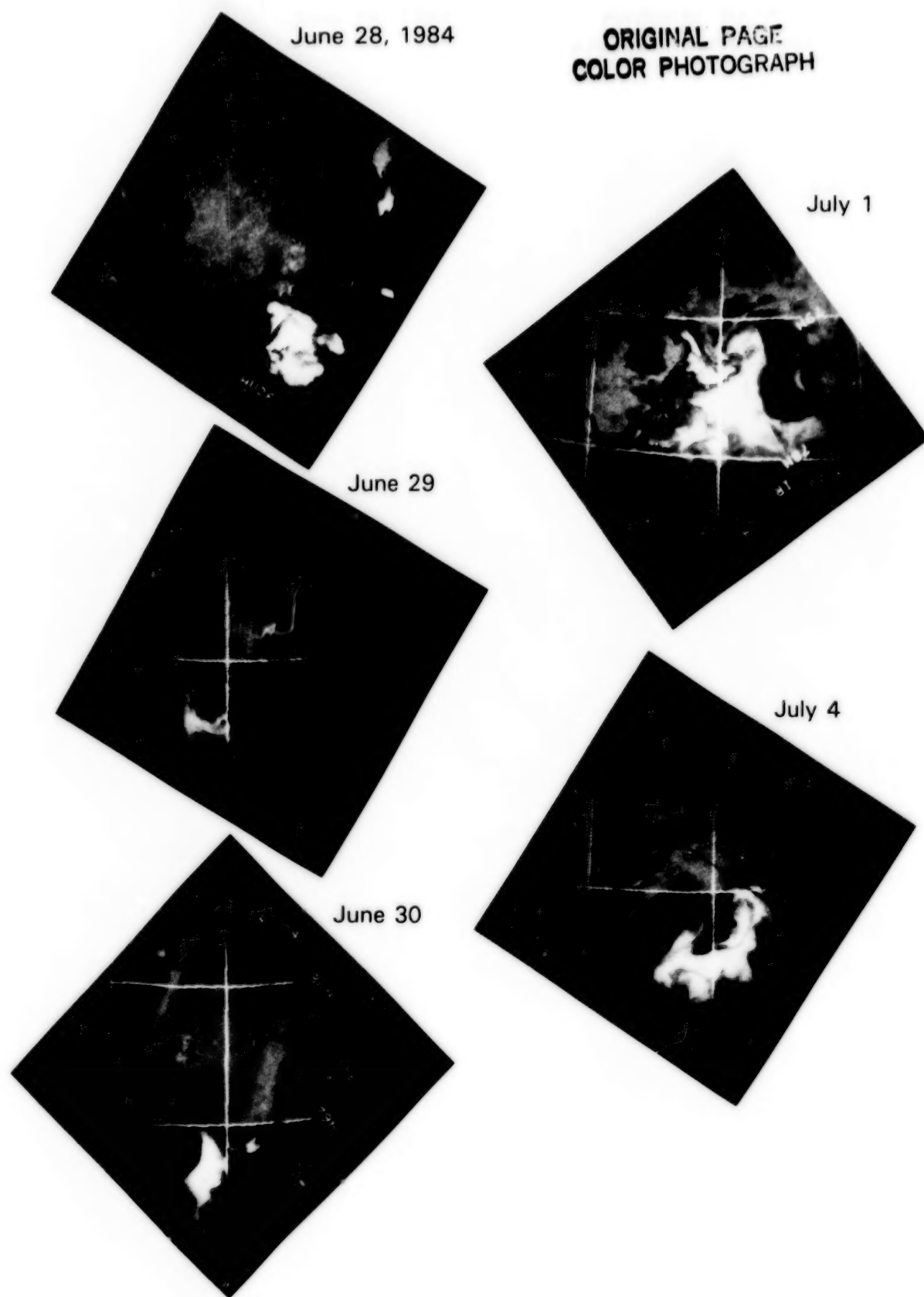


Figure 4-69. Infrared images of the marginal ice zone in the Fram Strait region during MIZEX East 1984 from the Advanced Very High Resolution Radiometer (AVHRR) on the NOAA 8 satellite. [From O. M. Johannessen, personal communication.]

south and the 'Nordbukta' to the north. Based on analysis of the 3-day imagery from the Nimbus 5 ESMR data set, the sea ice in the 'Odden' appears to be mostly new ice formed locally. Although sometimes blown away by strong winds, this ice generally follows the southern portion of the Jan Mayen Gyre. Warmer water is usually found in the 'Nordbukta,' presumably advected by the northern portion of the

gyre, and the ice in this area tends to be old ice. The large projection appears in the 3- and 4-year-average ice concentration images for December, January, and February (Figures 4-8 and 4-3), as well as in the 1973 and 1975 images. The 'Odden' appears in the map for January 1973 (Figure 4-18), with monthly average concentrations in the range of 60 to 70 percent, assuming predominantly first-year ice. The

GREENLAND SEA

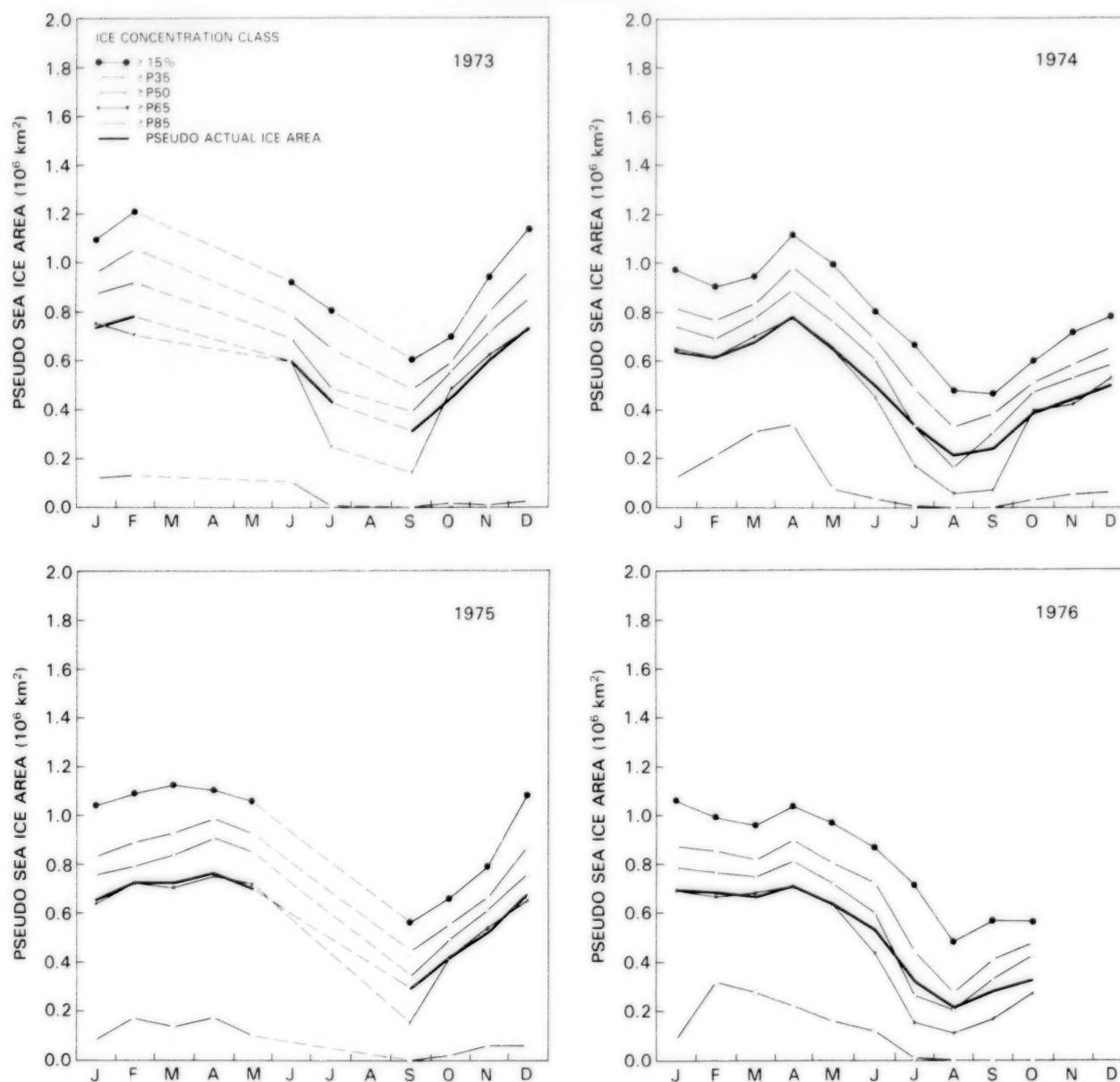


Figure 4-70. Yearly cycle of the ocean area covered by sea ice with concentration exceeding 15 percent, and yearly cycles of the P35, P50, P65, and P85 curves and the pseudo actual ice area, for the Greenland Sea region in 1973, 1974, 1975, and 1976. The P35, P50, P65, P85, and pseudo actual ice area curves are defined in the caption for Figure 4-10.

feature is more fully developed in the following month (February 1973 in Figure 4-19) as an ice prominence with average monthly concentrations of approximately 50 percent. Lack of data prevents the monitoring of the development of this feature by the ESMR from March through May 1973, and by June 1973 the feature is gone. The second occurrence visible in the ESMR data first appears in November 1973

and develops further in December 1973, when it appears as a thin projection extending away from the main pack and toward Svalbard (Figures 4-28 and 4-29). By January 1974, this second occurrence has disappeared.

A third occurrence of the Greenland Sea ice projection is visible in April and May of 1974, this time

GREENLAND SEA

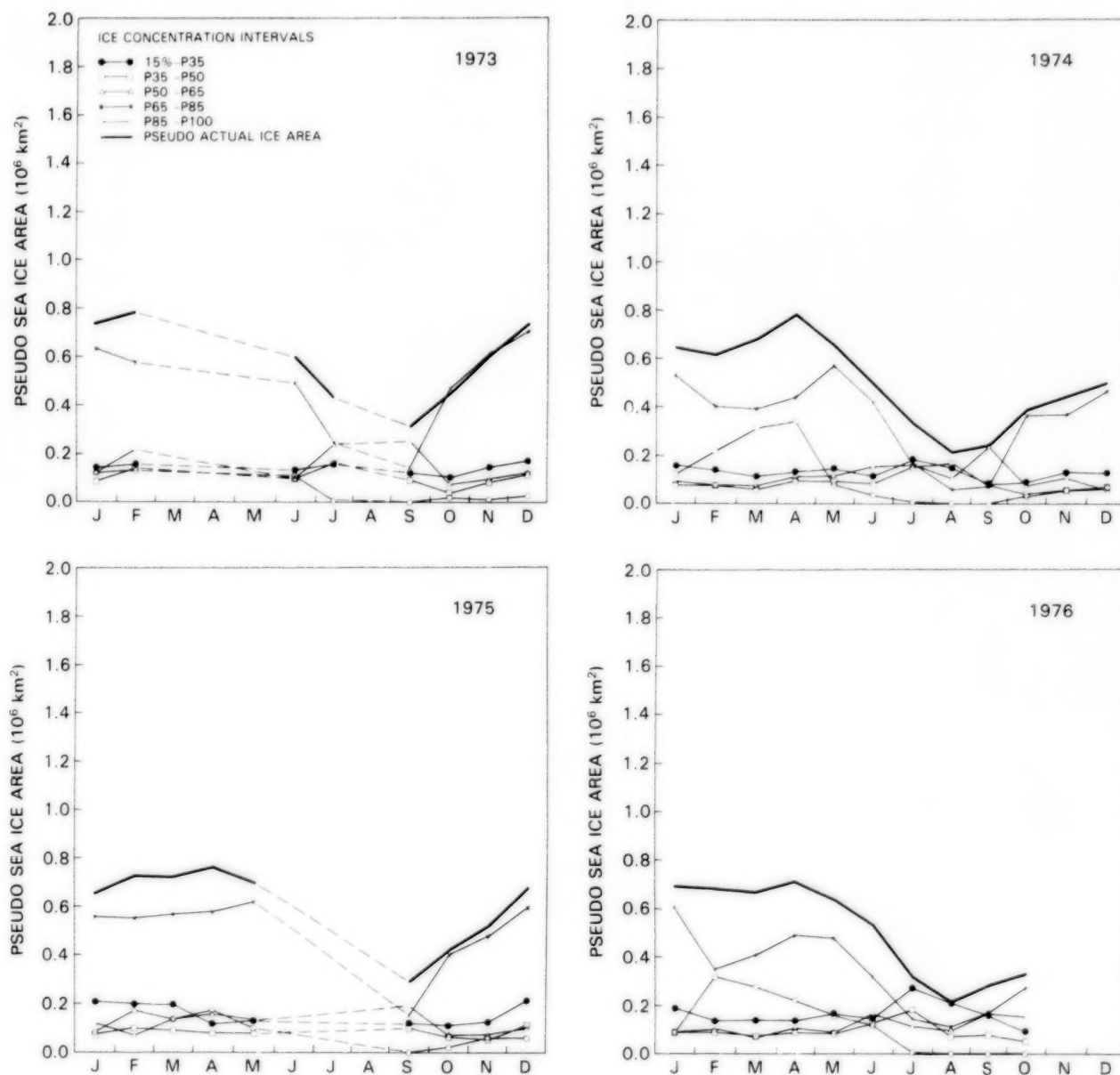


Figure 4-71. Yearly cycles of the ocean area covered by sea ice within the intervals 15 percent to P35, P35 to P50, P50 to P65, P65 to P85, and P85 to P100, and yearly cycle of the pseudo actual ice area, for the Greenland Sea region in 1973, 1974, 1975, and 1976. The interval curves are calculated by subtracting the respective curves of Figure 4-70.

with less prominence, and a fourth occurrence is visible in January 1975, when the feature appears as an ice pack largely separated from the main pack, with concentrations of approximately 30 percent. In February 1975, this feature has drifted to the east, further separating from the main pack with slightly increased concentrations. The projection persists through March and April with diminished concentrations and extent. A fifth occurrence appears during December 1975 and January 1976 (Figures 4-29 and 4-18). The growth and decay of this feature are particularly evident in the midwinter difference maps shown in Figures 4-30 through 4-37.

A time-lapse film of the ESMR images of the Greenland Sea (Campbell et al., 1980) reveals that these large ice projections from the ice pack to the east expand rapidly, with the edge moving on the order of 500 kilometers in about 10 days, and that they decay rapidly as well. During all 4 years of ESMR they arose at varying times between November and April, and the centroid of the projection originated at latitudes ranging from 70°N to 77°N.

Interannual variations in the ice cover of the Greenland Sea can also be seen in the plots of Figures 4-70 through 4-72. In 1974 April has the greatest ice

GREENLAND SEA

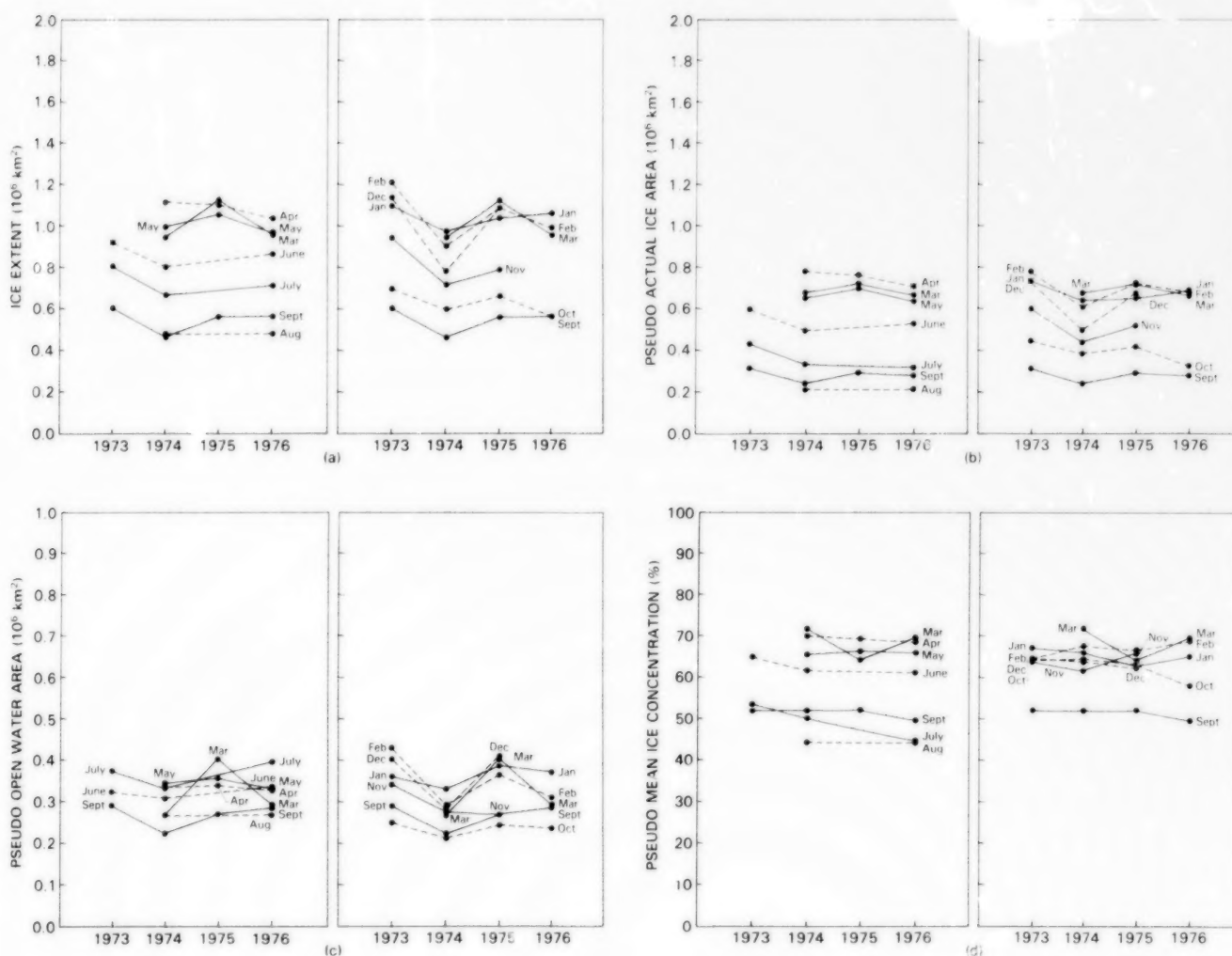


Figure 4-72. Month-by-month year-to-year changes in (a) sea ice extent, (b) pseudo actual ice area, (c) pseudo open water area within the ice pack, and (d) pseudo mean sea ice concentration, for the Greenland Sea region. The pseudo quantities are calculated with an ice emissivity of 0.92, appropriate for first-year ice.

extent, in 1975 March has the greatest ice extent, and in 1976 a double peak occurs with January and April both having ice extents of about 1.06×10^6 square kilometers. Data are insufficient in 1973 to establish which month has the greatest ice extent in that year, but February 1973 has a greater extent of ice, with over 1.2×10^6 square kilometers, than any of the months in the other 3 years (Figure 4-70). This situation is similar to that for the Sea of Okhotsk (Section 4.3).

From April until August the total ice area steadily and rapidly diminishes (Figure 4-70). At the peak of the summer season, in August and September, the pseudo actual ice area in each year is reduced to 0.2 to 0.4×10^6 square kilometers, which falls between 25 and 50 percent of its maximum winter value (Figure 4-72b).

Because the Greenland Sea ice pack, like that of the Arctic Ocean, is made up of mixtures of ice types, the same ambiguity between ice type and concentration exists when analyzing the ESMR data. During NORSEX, observations of ice type within the ice pack in Fram Strait and its surroundings during 1978 and 1979 show the pack to have been about 50 percent multiyear ice (NORSEX Group, 1983). The rapid divergence of the ice after passage through Fram Strait enhances the production of new ice to the south under freezing weather conditions, resulting in a relatively high fraction of first-year ice. No *in-situ* ice type measurements are available for the ESMR time frame; thus, an exact interpretation cannot be given. In the 4-year-average mean monthly ice concentration maps for January and February (Figure 4-3), the ice pack closest to the Greenland coast is seen to have concentrations somewhere in the 84- to 100-percent range, depending on the fraction of multiyear ice. Assuming that this part of the pack is actually compact ice, the ice concentration nomogram provides a maximum multiyear ice fraction, F_{MY} , of about 75 percent. The large monthly-average projections eastward in 1973 and 1975 have ice concentrations ranging from 30 to 60 percent, whereas in 1974 and 1976, when there are no such projections, the pack has higher average ice concentrations (Figures 4-18 and 4-19).

The association of reduced ice concentrations with the large ice projection eastward toward Svalbard is confirmed in the plots of Figures 4-72a and 4-72c. For instance, the amount of pseudo open water

within the Greenland Sea ice pack correlates positively with the total extent of the ice for February of each year, with 1973 having the greatest amount of open water, 1975 having the next greatest amount, then 1976, and finally 1974 with the least amount. This correlation results because the most extensive projection of ice has the most open water and the greatest area of reduced ice concentrations.

Another large zone of reduced ice concentrations, or a polynya, regularly occurs off the northeast coast of Greenland in June, July, and August (Figures 4-23 through 4-25). This polynya appears to be created by the combined action of oceanic upwelling and drainage winds flowing downslope from Greenland. Three-day-average data for all 4 years show its evolution, which progresses uniformly each year. During June and July 1984, aircraft flights over the region confirmed that the polynya existed throughout the summer.

4.8 KARA AND BARENTS SEAS

The Kara and Barents Seas, located north of Scandinavia and the western Soviet Union and separated by the elongated island Novaya Zemlya (Figures 4-73 through 4-76), provide an interesting contrast, as these two seas in such close proximity have markedly different ice covers. The Kara Sea is more typical for its high northern latitude, with a fairly solid ice cover for much of the year. The Barents Sea, by contrast, is significantly influenced by the warm waters of the Norwegian Current, resulting in predominantly open water for the majority of the sea even in the midst of winter.

Scandinavian and Russian sailors, fishermen, and sealers first crossed the Barents Sea and reached both Svalbard and Novaya Zemlya in the 13th century. The relatively open Barents Sea encouraged 16th century explorers to seek a Northeast Passage to the Orient by sailing eastward across the Barents Sea, but the ice cover and freezing gales encountered by the Englishman Steven Borough as he faced the Kara Sea after traversing the Barents Sea and the strait between Vaygach Island and Novaya Zemlya in 1556 discouraged further attempts until 1580, when unsuccessful attempts were made by Arthur Pet and Charles Jackman. In the 1590s, the Dutch explorer Willem Barents sailed the sea that was later named after him and reached Svalbard and northern

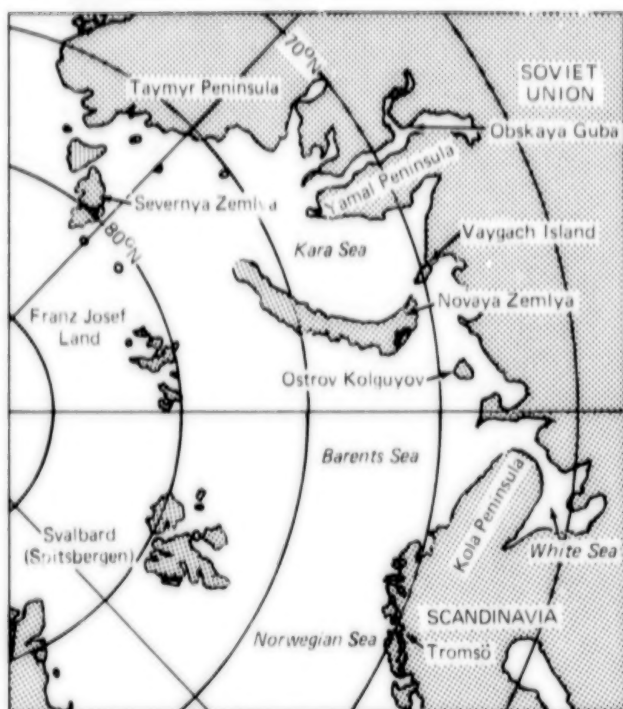


Figure 4-73. Location map for the Kara and Barents Seas region.

Novaya Zemlya. He was blocked by ice when trying to enter the Kara Sea, as were other Dutch explorers who were seeking a passage further to the south. Barents continued to explore north of Novaya Zemlya, but became stuck in the ice in August 1596 after rounding the northern tip of the island and died in June 1597 on the return trip (Mirsky, 1948). These several failed efforts in the 1590s essentially eliminated hopes for a Northeast Passage and led to intensified efforts at a Northwest Passage, contributing to the explorations mentioned in Sections 4.5 and 4.6 on Hudson Bay and Baffin Bay/Davis Strait and to the explorations mentioned in Section 4.9 on the Canadian Archipelago.

The Kara Sea was first penetrated by ship in 1869 by Johannessen and was mapped by Fridtjof Nansen in 1893 during the initial portion of the 3-year voyage and drift of the *Fram* across the Arctic Ocean (Fairbridge, 1966). Nils Adolf Erik, Baron Nordenskiöld, led the first successful accomplishment of a Northeast Passage in 1878 and 1879, leaving Tromsø, Norway, on July 18, 1878, and arriving in the Chukchi Sea to within 120 miles of the goal of the Pacific Ocean by September 28. At that time the expedition became ice bound until July 18, 1879. Two days

later, on July 20, they arrived in the Bering Strait and celebrated the completion of the Northeast Passage (Mirsky, 1948).

The typical yearly sea ice cycle in the mid-1970s as revealed in Figures 4-3 through 4-8 shows the Kara Sea to be largely ice free at the end of summer, ice remaining only in its northern portion, especially immediately to the south of Severnaya Zemlya. With the onset of fall growth, the ice edge moves southward to about 74°N in October and to about 71°N in November. The only small surviving area of ice-free waters in November is in the southwest portion of the sea. By December the sea is fully covered by ice of at least 60-percent concentration. The sea remains covered with ice from January through June, with the ice cover subsequently breaking up from the south in a fairly steady northward progression of the ice edge from June through September. The monthly difference maps (Figure 4-9) show that the Kara Sea experiences its heaviest ice growth from September to November, then lesser growth from November to January, after which the ice cover remains relatively constant until its major decay occurs in the 3 months from May to August.

The Barents Sea is largely blocked from receiving ice from the Kara Sea by Novaya Zemlya and from the central Arctic Ocean by the several islands along its northern boundary, and is kept relatively warm by the inflow of waters from the southwest. This combination of warm waters from the Norwegian Current and the geographical boundaries restricting ice transport from the east and north combine to keep the Barents Sea relatively free of ice for much of the year. In September, at the end of summer, the only ice remaining in the sea is a very small amount southeast of Franz Josef Land. The ice edge slowly moves south to about 78°N in October and to about 77°N in November and December. It remains at roughly this location—far north of the ice edge in other regions—through the winter and early spring, until ice edge retreat begins in June, with the northern edge reaching the northern boundary of the sea, at Franz Josef Land, in August (Figures 4-3 through 4-8). The failure of the northern ice edge to advance further south is again largely a result of the warm Norwegian Current, which derives from the Gulf Stream and the North Atlantic Current.

In winter and spring, ice also exists along the eastern and southern boundaries of the Barents Sea,

forming along the coasts of Novaya Zemlya and the Soviet Union. The ice along the southern boundary disappears almost entirely by May, and the ice along the eastern boundary disappears by July (Figures 4-3 through 4-8). The monthly difference maps show very clearly the growth of the coastal ice in the southeastern portion of the sea from November through February and its decay from February

through June (Figure 4-9). The February maximum ice coverage in the southeast considerably precedes the maximum coverage in the northern portion of the sea, where some growth is apparent even as late as from April to May. This northern portion, however, does have a retreat episode from January to February, interrupting its general growth season from September through April (Figure 4-9).

KARA AND BARENTS SEAS

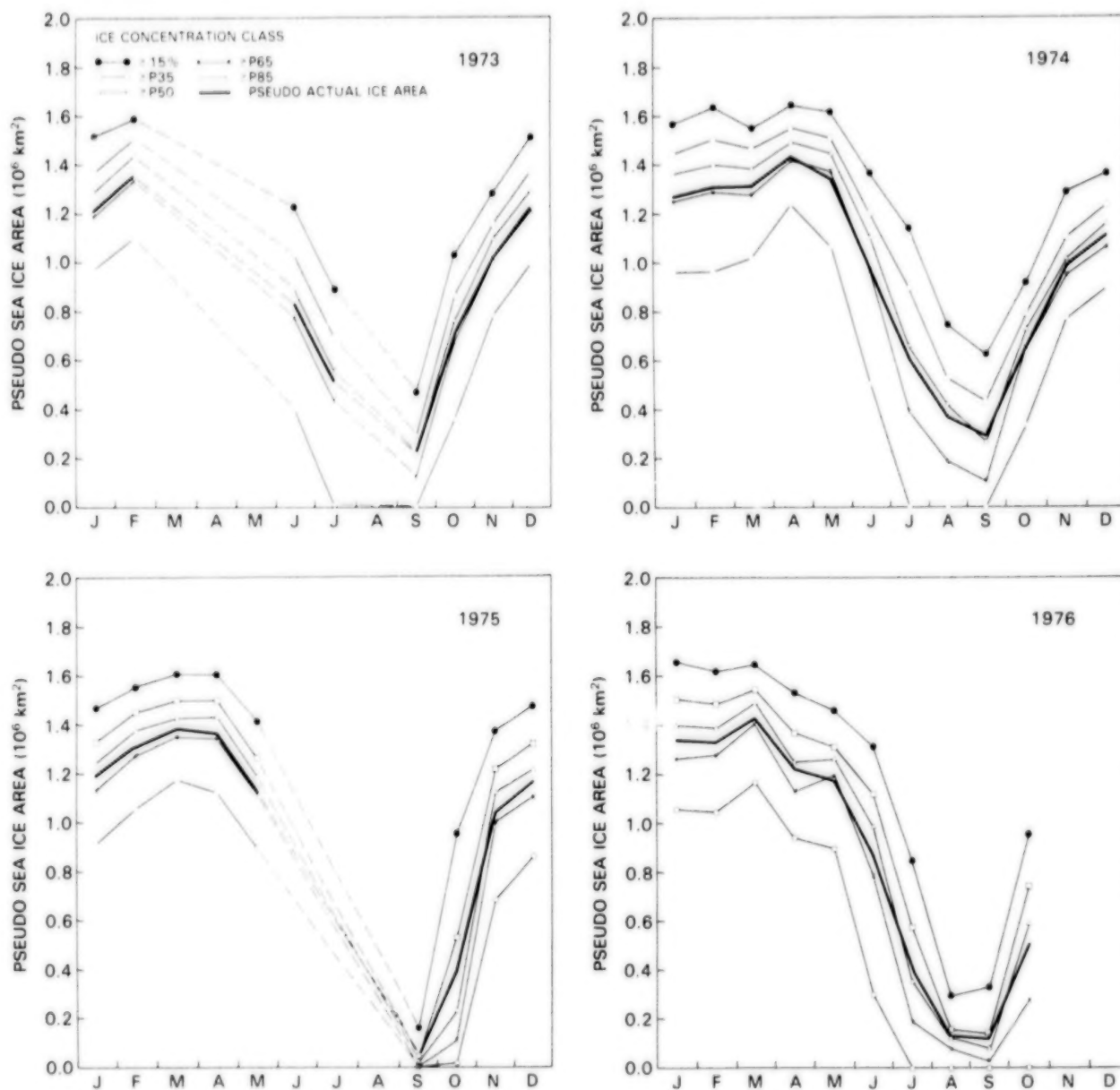


Figure 4-74. Yearly cycle of the ocean area covered by sea ice with concentration exceeding 15 percent, and yearly cycles of the P35, P50, P65, and P85 curves and the pseudo actual ice area, for the Kara and Barents Seas region in 1973, 1974, 1975, and 1976. The P35, P50, P65, P85, and pseudo actual ice area curves are defined in the caption for Figure 4-10.

Overall, the sea ice cover of the combined Kara and Barents Seas shows a growth from an ice extent of about 0.4×10^6 square kilometers in September to about 1.6×10^6 square kilometers in February, March, and April (Figure 4-11).

As with the other seven regions identified for regional analysis (Figure 4-2), the data for the Kara

and Barents Seas for the individual years reveal patterns similar to the patterns for the 4-year-average data but with many interannual differences apparent in the details (Figures 4-18 through 4-29). For instance, the January ice concentration in the Kara Sea is least in 1973, and the northern ice edge in the Barents Sea in February shows a prominent indentation into the ice cover in 1975 at about 55°E which

KARA AND BARENTS SEAS

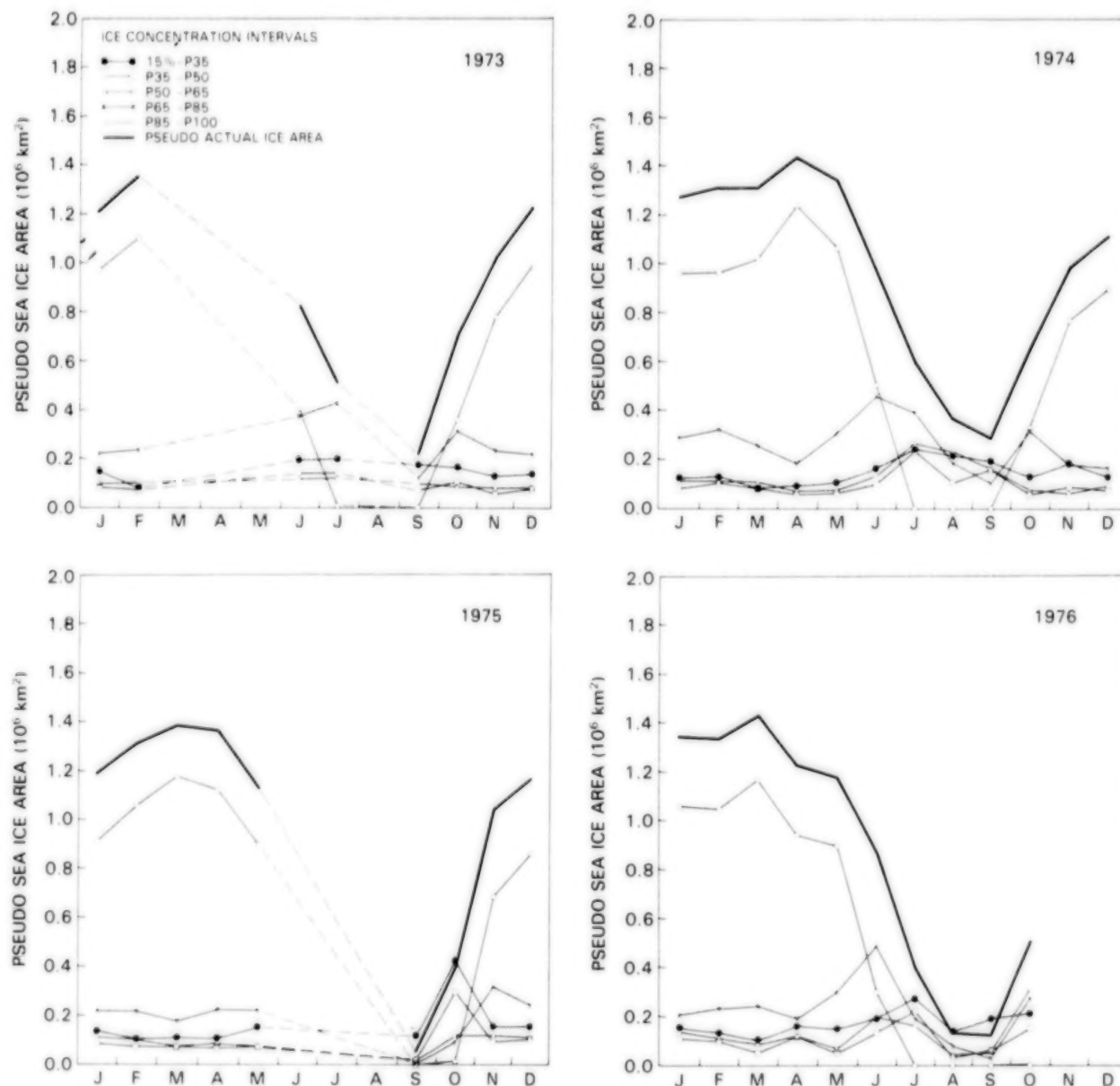


Figure 4-75. Yearly cycles of the ocean area covered by sea ice within the intervals 15 percent to P35, P35 to P50, P50 to P65, P65 to P85, and P85 to P100, and yearly cycle of the pseudo actual ice area, for the Kara and Barents Seas region in 1973, 1974, 1975, and 1976. The interval curves are calculated by subtracting the respective curves of Figure 4-74.

does not appear in the other 3 years. The April and May images show significantly more ice along the west coast of Novaya Zemlya in 1974 than in 1975 or 1976, and the two August images show far more ice remaining in the northeastern Barents Sea and northern Kara Sea in 1974 than in 1976. The full complement of four monthly averaged September images confirm that the earlier 2 years (1973 and 1974) had noticeably more ice in the Kara Sea than the later 2 years. However, the fall ice growth in October shows 1975 alone as the anomalous year, with the 1976 growth almost as great, although with lesser ice concentrations, as that in 1973 and 1974.

In 1974 an interesting shift occurs from a pattern of ice growth in the south and east of the Barents Sea and decay in the northern Barents Sea, occurring from January to February, to a pattern of growth in the north and decay along the south and east, occurring from February to May (Figure 4-32). The same shift occurs in 1976 (Figure 4-36), although the second phase lasts only from February to March. Perhaps the unseasonable ice edge retreats, in the north from January to February and in the south and east from February to March, were caused by a strong and shifting Norwegian Current, bringing unusually warm waters to the north in late

KARA AND BARENTS SEAS

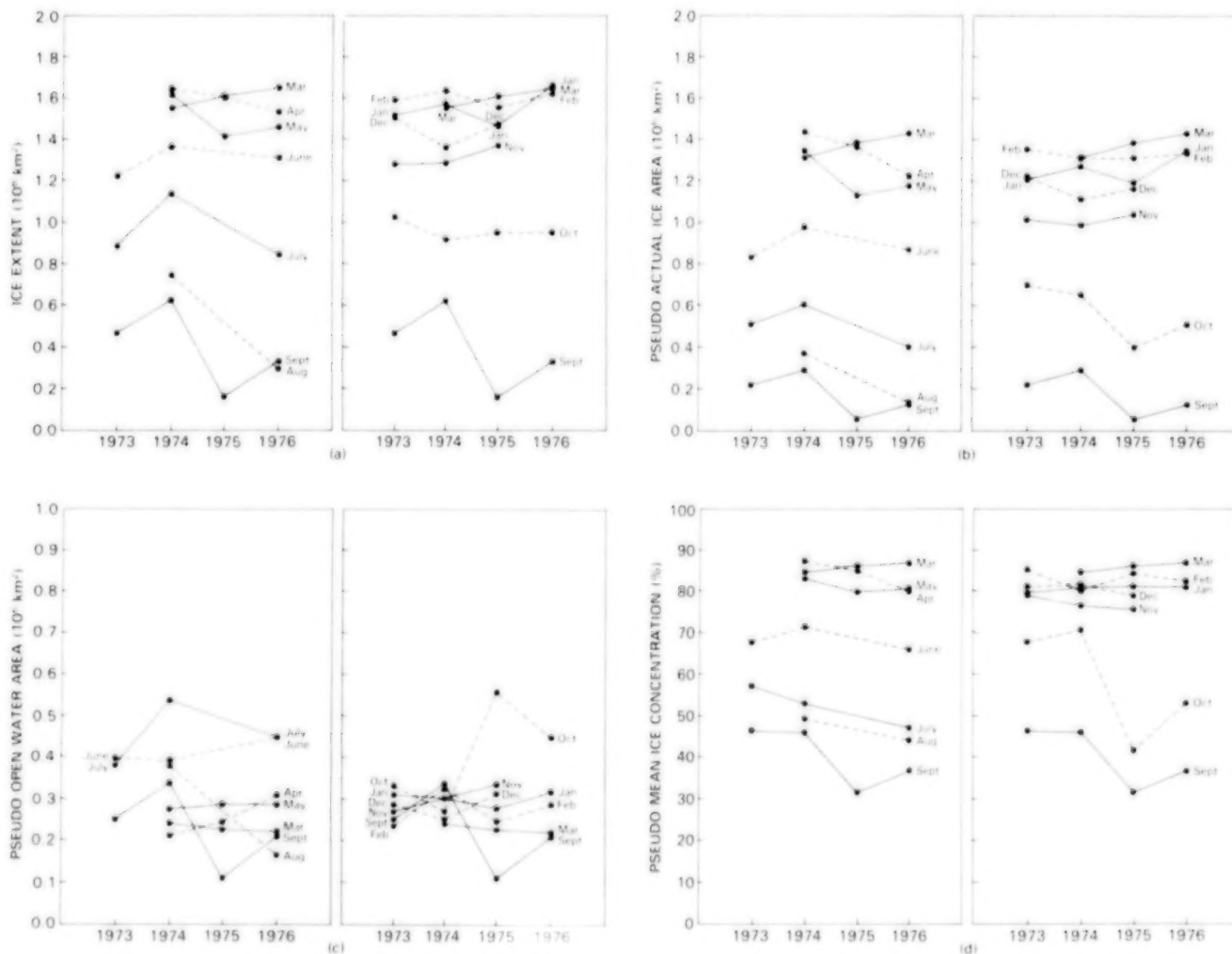


Figure 4-76. Month-by-month year-to-year changes in (a) sea ice extent, (b) pseudo actual ice area, (c) pseudo open water area within the ice pack, and (d) pseudo mean sea ice concentration, for the Kara and Barents Seas region. The pseudo quantities are calculated with an ice emissivity of 0.92, appropriate for first-year ice.

January or early February and then to the east and south.

For the combined Kara and Barents Seas, the data for the midwinter months are fairly consistent over the 4 years 1973 through 1976 in having a total ice extent of about 1.6×10^6 square kilometers and a pseudo actual ice coverage of about 1.3×10^6 square kilometers (Figure 4-74). However, the timing of maximum ice extent varies considerably, with an April maximum in 1975, but double maxima in 1974 and 1976, these occurring in February and April for 1974 and in January and March for 1976. As in the case of the Bering Sea, probably part of the reason for the inconstancy in the timing of maximum ice extent derives from interannual variations in the atmospheric fields, but in this case there is probably also considerable impact from the Arctic Ocean ice cover to the north and from the ocean currents advecting warm water from the southwest. From Figure 4-75 it is clear that in each year the majority of the ice-covered area in winter has pseudo sea ice areas exceeding 85 percent.

The summer months show a stronger interannual variation in the amount of ice in the Kara and Barents Seas than do the winter months over the 4 ESMR years, with the August and September ice extents varying significantly from 1 year to another (Figure 4-74). Over twice as much ice remains in August and September in 1974 than in 1976, and in September the remaining ice in 1975 is even less than that remaining in 1976 (Figures 4-74 and 4-76a). A similar situation occurs with the pseudo actual ice coverage (Figure 4-76b). The pseudo mean ice concentrations consequently also show much less year-to-year consistency in summer than in winter, when the pseudo mean concentrations range from 75 to 90 percent (Figure 4-76d).

4.9 CANADIAN ARCHIPELAGO

The Canadian Archipelago is a vast labyrinth of bays, straits, channels, sounds, islands, and peninsulas in northern Canada (Figure 4-77) throughout which sea ice undergoes great variations in morphology and dynamics. In the 19th century many explorers endeavored to find a passage through this complex region, and in the attempt discovered most of the islands and thoroughfares of the archipelago.

Many of the discoveries occurred during the expeditions led by Edward Parry in 1819-1820, 1821-1823, and 1824-1825, the expedition led by John Ross and James Clark Ross in 1829-1833, during which James Clark Ross located the magnetic North Pole, the expedition led by Sir John Franklin in 1845 to 1847, and the many expeditions sent over the subsequent 30 years to search for the Franklin expedition, which had disappeared in 1847 (Mirsky, 1948). Although failing to find the lost expedition or remains thereof, these latter expeditions succeeded in mapping much of the central archipelago not already mapped during the earlier expeditions, and thereby opened the way for future endeavors. It was not until the 20th century that Roald Amundsen made the first transit of the Northwest Passage in 1903-1906, a transit during which Amundsen learned the art of dogsledding from the Eskimos, making possible his successful dash to the South Pole 5 years later.

Satellite remote sensing using visible, infrared, and passive microwave sensors has greatly increased the knowledge of the complex sea ice dynamics and morphology of the archipelago. Ramseier et al. (1975) analyzed Landsat imagery for the period March to November 1973, and thereby obtained information on ice drift velocities, ice concentration, floe size distribution, fast ice and ice melt patterns, and dates of breakup and freezeup. Although they found the ice motion to be complex, they were able to delineate some general patterns, similar to those observed in previous years from aircraft and ships, such as the advection of ice southward through the passages between the northern islands of the archipelago into Viscount Melville Sound, eastward out of Lancaster Sound into Baffin Bay, and westward out of Amundsen Gulf into the Beaufort Sea. They observed ice velocities as great as 58 kilometers per day in Lady Ann Strait, while values of 20 to 30 kilometers per day were found common in Amundsen Gulf. Dey (1981a) analyzed NOAA infrared imagery for information on winter sea ice dynamics within the archipelago between 1974 and 1978 and included in his results calculated ice fluxes and velocities for two of the winters observed by ESMR, namely the winters of 1974-1975 and 1975-1976. Dey et al. (1979) used a combination of Landsat and NOAA imagery to map sea ice breakup and freezeup patterns in the archipelago for the July to November period in 1975 through 1977. McQuillan and Clough (1973) examined the economic aspects of the use of satellite

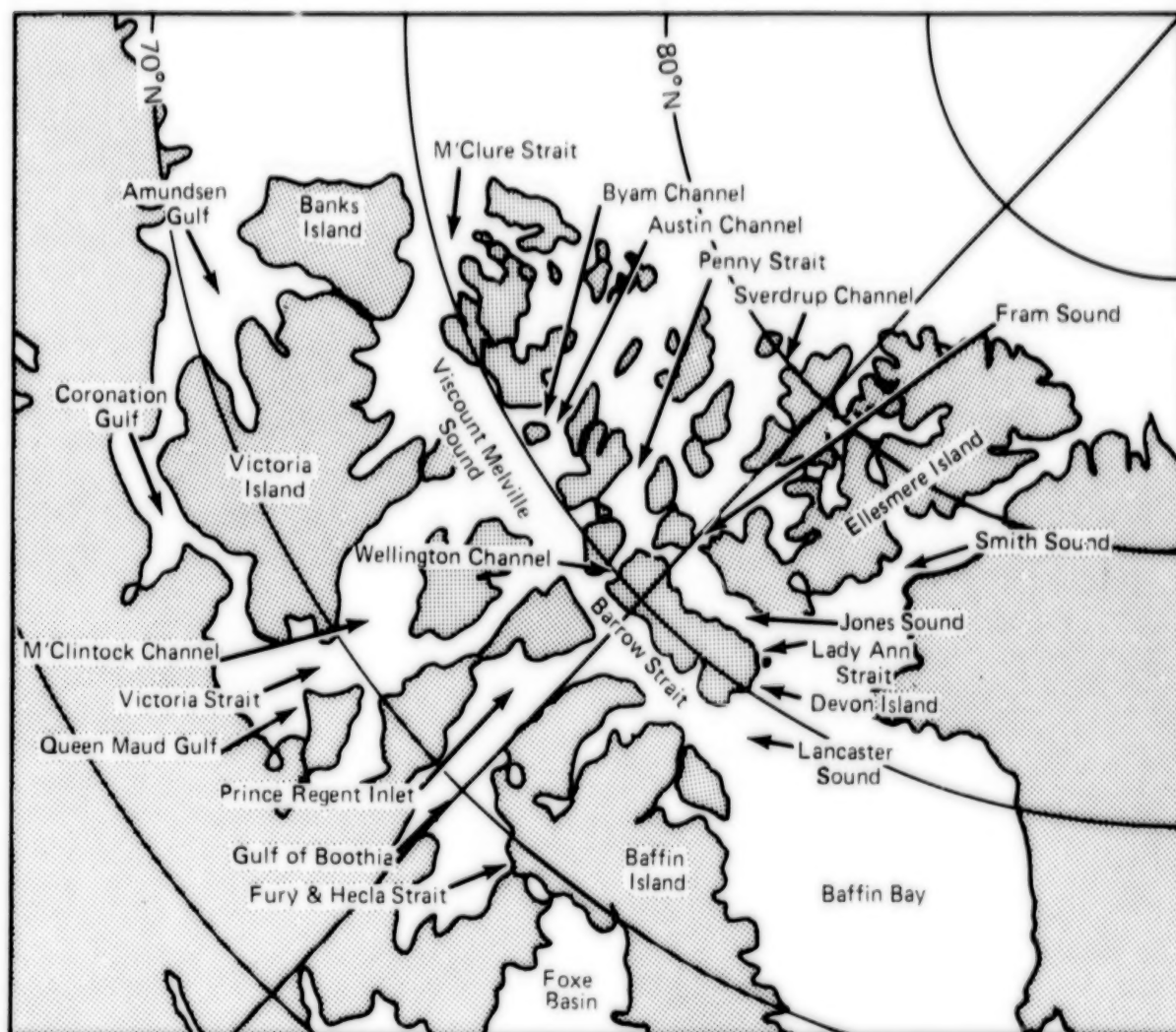


Figure 4-77. Location map for the Canadian Archipelago region.

sea ice observations for aiding ship routing through the Canadian Arctic, and they convincingly showed the possibility of substantial economic benefits. Studies by Dey (1981b, 1981c) and Marko (1977, 1978) further showed how satellite sea ice observations can be used as an aid for ship routing in the archipelago on a year-round basis.

Each of the studies mentioned in the previous paragraph used satellite visible and infrared imagery with resolutions in the 1- to 3-kilometer range. The ESMR imagery has a much coarser resolution (approximately 30 kilometers) but provides an additional contribution to our knowledge of the behavior of sea ice within the archipelago because of the completeness of the ESMR data set, with an image of

the entire region for most 3-day periods from 1973 through 1976, and because of the ESMR data being unaffected by poor weather or lighting conditions that can cause visible or infrared imagery to be unusable. Fortunately, several of the studies previously mentioned analyzed data acquired during the ESMR period, and those analyses have helped in the following interpretation of the ESMR data.

Averaged over the period 1973 through 1976, freezeup in the archipelago begins in October (Figure 4-11), when all the central and northern channels and sounds become fully ice covered but most of the southern ones have considerable amounts of open water—Amundsen Gulf has an ice concentration of 34 to 44 percent, depending on multiyear fraction,

Coronation Gulf has 16 to 20 percent, Queen Maud Gulf has 50 to 64 percent, and Foxe Basin to the southeast is mostly ice free. Of all the southern waterways only the Gulf of Boothia is fully ice covered at this time (Figure 4-7).

In November all the waterways of the archipelago are fully ice covered (Figure 4-8), although the ice cover morphology varies greatly from place to place. In some areas vast amounts of fast ice form, while in others, the ice moves throughout the winter. Both multiyear ice and first-year ice are abundant, and new ice forms within the archipelago during fall and, in areas where ice divergence occurs, also during winter. One such area of ice divergence, according to analyses by Dey (1981a), is Lancaster Sound. Barrow Strait normally dams up by December, and currents and winds advect ice eastward out of Lancaster Sound into northern Baffin Bay. The new ice that is formed is continually advected into northern Baffin Bay until Lancaster Sound becomes covered with landfast ice, usually in April. Multiyear ice is advected from the Arctic Ocean into and through the archipelago in significant amounts and some is formed there. First-year ice forms in all areas not occupied by multiyear ice. Dunbar (1973) and Dey (1981a) have made estimates of the amount of ice that is advected through the archipelago. Dunbar estimates the total annual export of ice through the archipelago into northern Baffin Bay as 225 cubic kilometers per year, and Dey estimates a 4-year average for 1974 through 1978 as 201 cubic kilometers per year.

In the midwinter months of January and February the ESMR images (Figure 4-3) suggest that on average all the waterways of the archipelago are covered with a mixture of multiyear and first-year ice. Assuming that these waterways are fully ice covered, the ESMR images and associated nomogram can be used to obtain the respective fractions of first-year ice and multiyear ice. The southern waterways of Amundsen Gulf, Coronation Gulf, and Queen Maud Gulf have the greatest amounts of first-year ice, with multiyear ice fractions ranging from 0 to 20 percent. The central archipelago waterway of Parry Channel, composed of M'Clure Strait, Viscount Melville Sound, Barrow Strait, and Lancaster Sound, has greater amounts of multiyear ice, with multiyear ice fractions ranging from 20 percent in the east to 50 percent in the west. The northern waterways, such as Sverdrup Channel, have the greatest amounts of

multiyear ice, with multiyear ice fractions ranging predominantly from 60 to 90 percent.

By April the ESMR images reflect the onset of the warming of the surface layer of the ice, with brightness temperatures ranging from 240 to 250 K appearing in all the southern waterways (Figure 3-28). As discussed in Chapter 3, this warming causes the surface layer to become the dominant determinant of the brightness temperature, and the multiyear ice/first-year ice distinction vanishes until freezeup occurs in the fall. By May the surface warming zone has progressed northward to Parry Channel, and by June essentially all of the ice in the archipelago has undergone surface warming. As melt ponds form and open water appears, the brightness temperatures and ice concentrations decrease (Figures 3-29 and 4-5).

The time of ice breakup averaged over the ESMR timespan varies greatly within the archipelago. By July the breakup is apparent in the southern waterways of Amundsen Gulf, Coronation Gulf, and Queen Maud Gulf, and in the eastern sector of Parry Channel, namely in Barrow Strait and Lancaster Sound (Figure 4-6). By August the breakup has proceeded into the Gulf of Boothia, Prince Regent Inlet, Viscount Melville Sound, Jones Sound, Fram Sound, and Wellington Channel (Figure 4-6), and by September the breakup has reached its maximum extent (Figure 4-7). Dey et al. (1979) mapped the breakup patterns for 1975 and 1976 using NOAA and Landsat imagery, and their breakup patterns for these years closely match the corresponding ESMR patterns.

The previous discussion indicates the average behavior of sea ice within the archipelago during the ESMR period. Observations over the last 80 years have shown that great interannual variations occur, and the ice concentration maps of Figures 4-18 through 4-29 and the plots of Figures 4-78 through 4-80 identify many of these interannual differences for the ESMR time period.

The ice concentration maps for October (Figure 4-27) reveal dramatic differences in freezeup patterns. In 1973 all of the southern waterways are essentially ice free, including Coronation Gulf, Amundsen Gulf, Queen Maud Gulf, Victoria Strait, and the southern end of M'Clintock Channel. The northern end of M'Clintock Channel, the Gulf of

Boothia, Prince Regent Inlet, Lancaster Sound, Jones Sound, Barrow Strait, and the eastern end of Viscount Melville Sound have ice in low concentrations. In 1974, with the exception of Lancaster Sound, all of these waterways are ice covered. In October 1975, Amundsen Gulf, Coronation Gulf, and Queen Maud Gulf are ice free, while Lancaster Sound and Jones Sound are mostly ice covered. In

1976, Amundsen Gulf and Coronation Gulf are ice free, but Queen Maud Gulf as well as Lancaster Sound and Jones Sound are mostly ice covered. Thus, 1973 is an exceptional freezeup year, having a late freezeup with abnormal amounts of open water occurring throughout the archipelago. This finding is corroborated in Ramseier et al. (1974), who find from analysis of Landsat images that 1973

CANADIAN ARCHIPELAGO

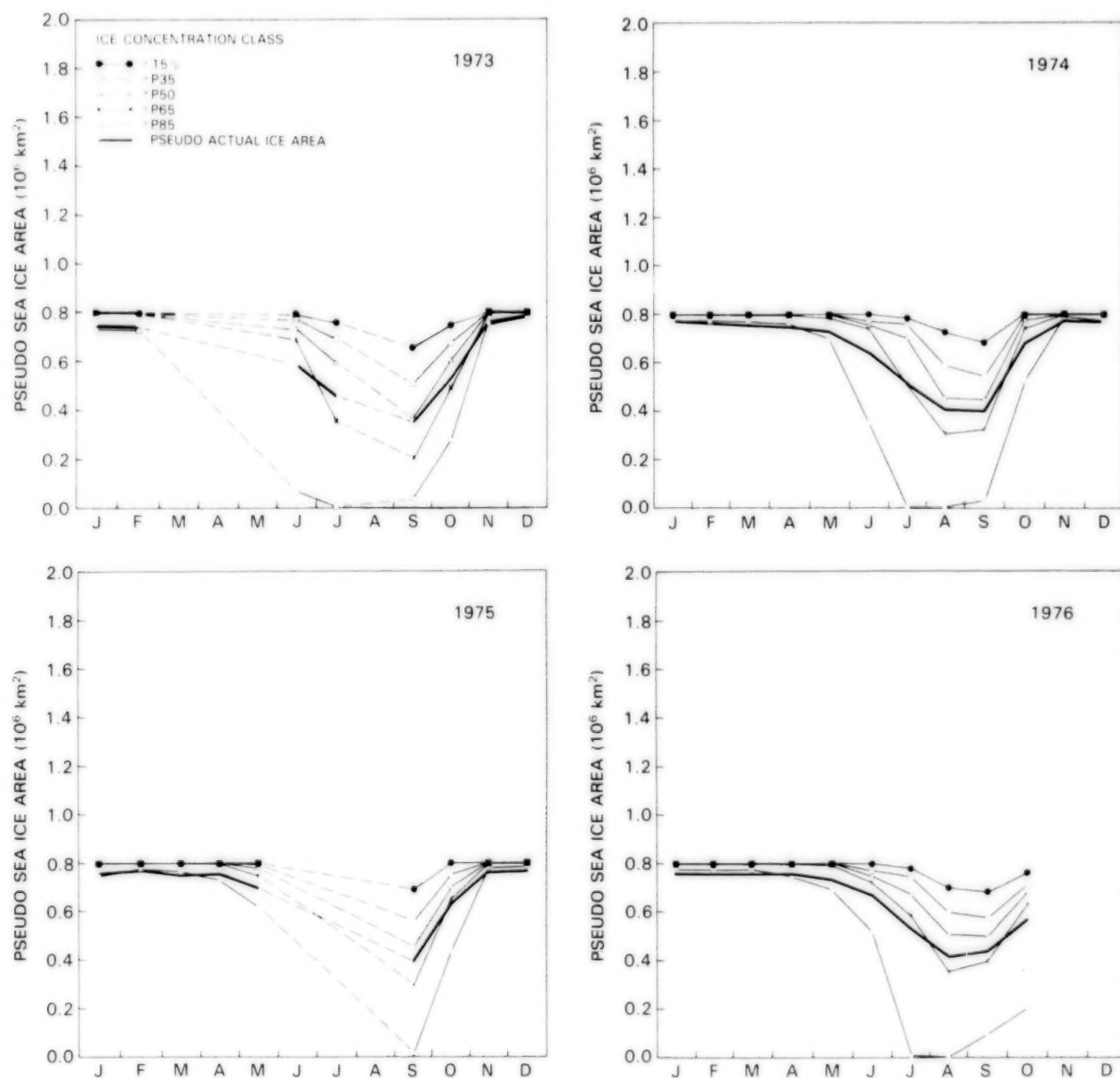


Figure 4-78. Yearly cycle of the ocean area covered by sea ice with concentration exceeding 15 percent, and yearly cycles of the P35, P50, P65, and P85 curves and the pseudo actual ice area, for the Canadian Archipelago region in 1973, 1974, 1975, and 1976. The P35, P50, P65, P85, and pseudo actual ice area curves are defined in the caption for Figure 4-10.

had an extremely ice-free fall season. Indeed, they note that in some areas it was almost unprecedented and was comparable to the most ice-free year (1962) that has been documented since AES (Atmospheric Environment Service) Ice Central has maintained records on this phenomenon. The ESMR data show 1974 as an exceptional year in the opposite direction, with a very early freezeup. The situation in 1975 and 1976 more closely approximates the normal freezeup

year. The low ice concentrations in Lancaster Sound, Jones Sound, Smith Sound, and the Gulf of Boothia in October 1976 were also found by Dey (1981a), using imagery from the NOAA Thermal Infrared Radiometer (NOAA-TIR).

By November, the archipelago has become almost completely ice covered, a situation which remains through April, as shown in the seasonal cycles of

CANADIAN ARCHIPELAGO

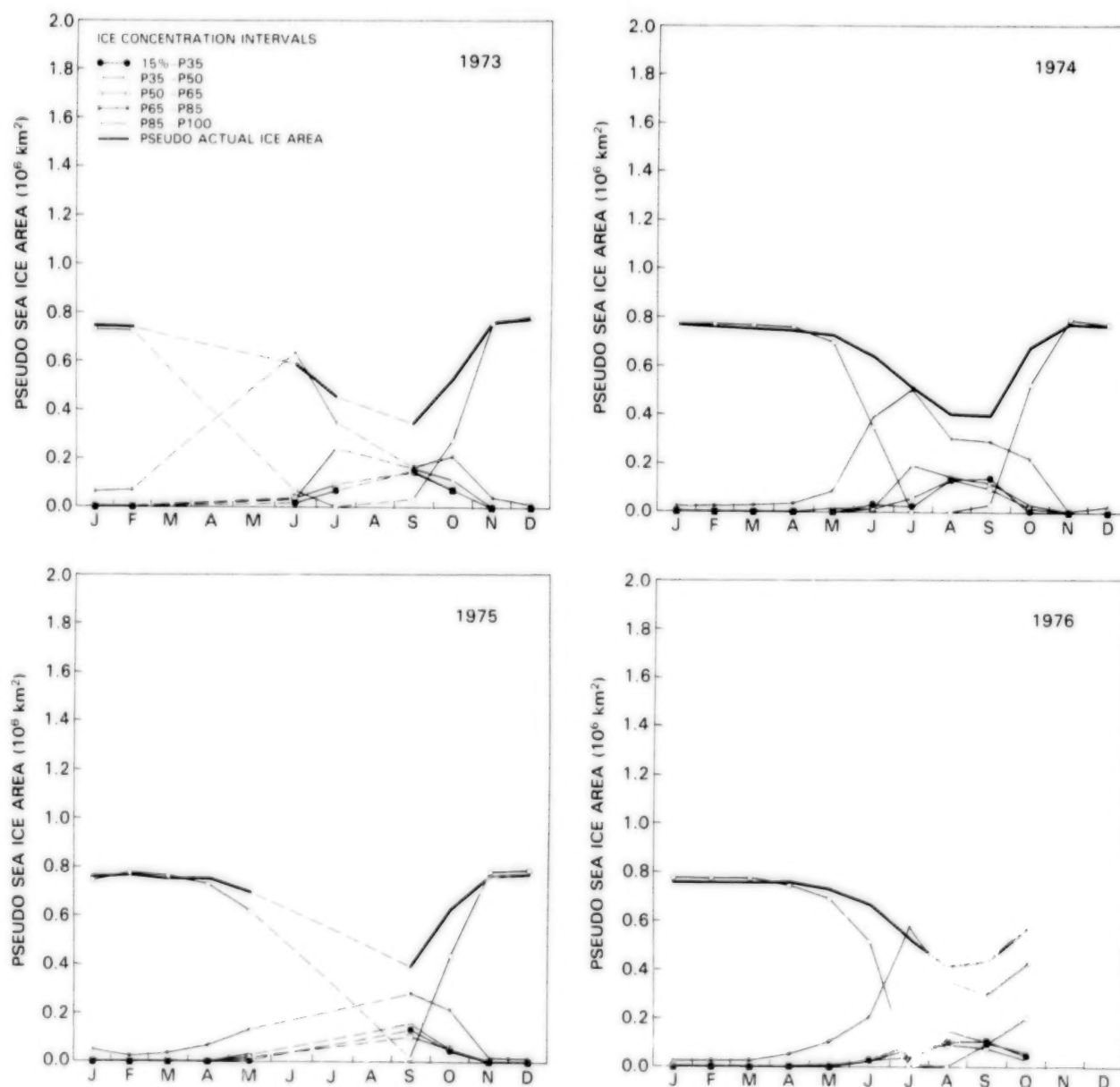


Figure 4-79. Yearly cycles of the ocean area covered by sea ice within the intervals 15 percent to P35, P35 to P50, P50 to P65, P65 to P85, and P85 to P100, and yearly cycle of the pseudo actual ice area, for the Canadian Archipelago region in 1973, 1974, 1975, and 1976. The interval curves are calculated by subtracting the respective curves of Figure 4-78.

ice extents (Figure 4-78). Spatially, all the waterways are ice covered in each year during the midwinter period (Figures 4-18 and 4-19). These contain mixtures of multiyear and first-year ice, with none of the waterways being covered exclusively with one ice type. New ice is produced in some locations, such as Lancaster Sound, until April, but because the brightness temperature of new ice is approximately that of first-year ice, and because the waterways in this region at this time of year are essentially fully ice covered, the ice concentration images in conjunction with the nomogram can be used to determine the first-year and multiyear ice fractions. In each of the 4 ESMR years, the ice covers of the southern

waterways of Amundsen Gulf, Coronation Gulf, Queen Maud Gulf, and Victoria Strait are predominantly first-year ice, with multiyear ice fractions largely under 20 percent.

The central archipelago waterway of Parry Channel has a varying winter ice cover from year to year (Figures 4-18 and 4-19). In 1973 western Parry Channel, namely M'Clure Strait and Viscount Melville Sound, has approximately equal amounts of multiyear and first-year ice, as does Lancaster Sound and M'Clintock Channel. In 1974 the entire Parry Channel is covered with predominantly first-year ice, with multiyear ice fractions ranging from 0 to 30 percent.

CANADIAN ARCHIPELAGO

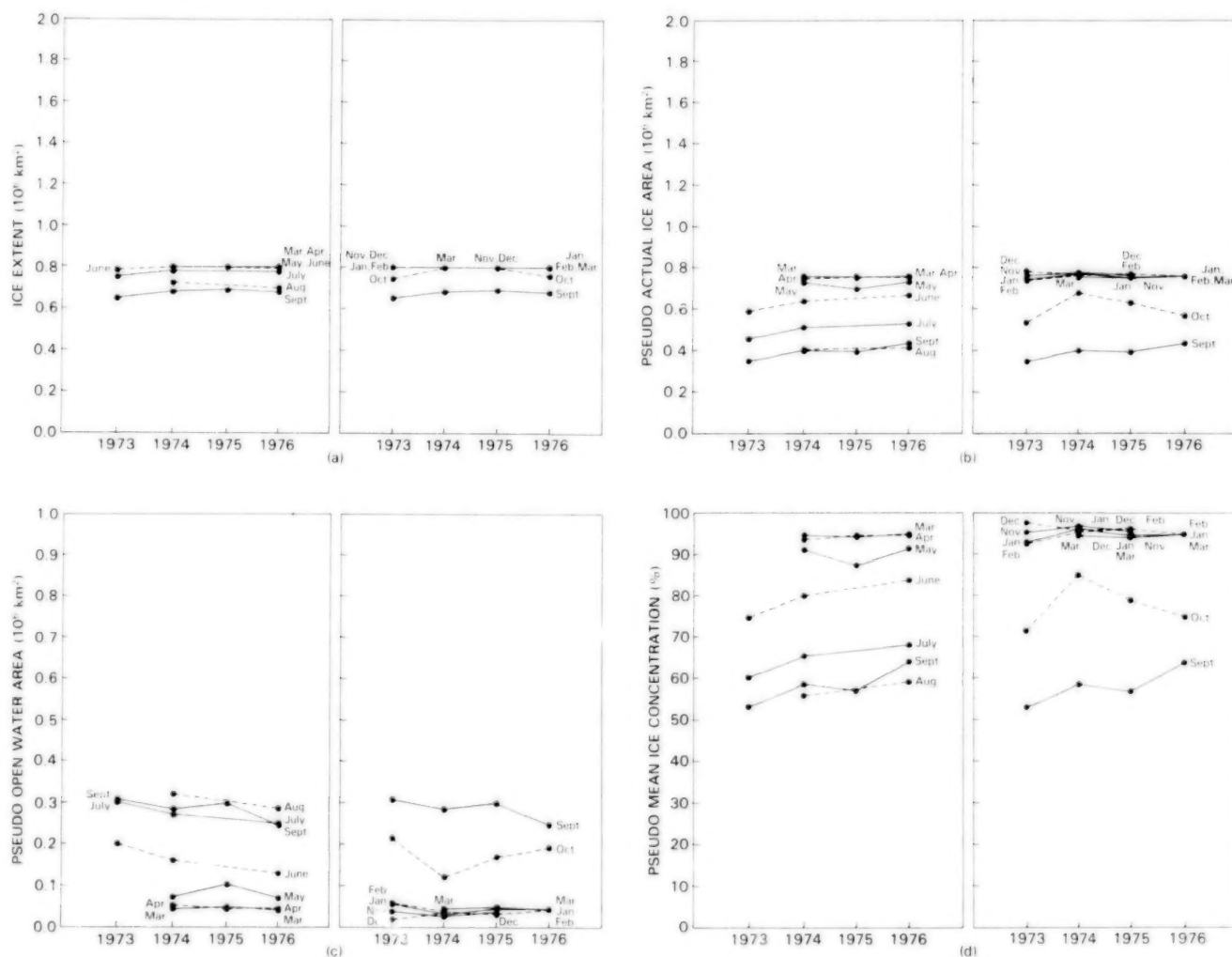


Figure 4-80. Month-by-month year-to-year changes in (a) sea ice extent, (b) pseudo actual ice area, (c) pseudo open water area within the ice pack, and (d) pseudo mean sea ice concentration, for the Canadian Archipelago region. The pseudo quantities are calculated with an ice emissivity of 0.92, appropriate for first-year ice.

In 1975 M'Clure Strait has about 80 percent multi-year ice, while eastern Parry Channel has more first-year ice. In 1976 Parry Channel has an ice-type distribution similar to the 4-year-average one, with multiyear ice fractions varying from about 20 percent in the east to about 50 percent in the west. It is instructive to note that the winter with the greatest amount of first-year ice in Parry Channel, 1974, follows the fall, 1973, with the most open water going into freezeup, lending support to the ice concentration algorithm and the interpretation of the nomogram, as the lower than normal amounts of multi-year ice at freezeup in 1973 are reflected in the winter ice coverage of 1974. In the northern archipelago also, the winter multiyear ice fractions are lower in 1974 than in the other 3 years (Figures 4-18 and 4-19).

By April the brightness temperatures (Figure 3-18) clearly show the onset of surface warming. In each of the 3 years with available ESMR data (April 1973 is missing), the surface warming begins in the southern archipelago waterways. In 1975 the warming has progressed farther north than in 1974 and 1976, with M'Clintock Channel and the Gulf of Boothia covered. By May (Figure 3-19) the warming front has progressed to the north in each of the 3 years to include Parry Channel. By June (Figure 3-20) the surface warming has covered the entire archipelago in 1974 and 1976. The ESMR data show a strong similarity in the pattern of surface warming for the 4 years, always beginning in April in the southern waterways and proceeding northward in a roughly linear progression. These results are visible in part in the ice concentration maps as well (Figures 4-21 through 4-23).

The July maps (Figure 4-24) show that the breakup in 1973, 1974, and 1976 has commenced in each

year in the southern waterways of Amundsen Gulf, Coronation Gulf, and Queen Maud Gulf and in the eastern waterways of Lancaster Sound and Jones Sound. The Amundsen Gulf shows the sharpest contrast among the 3 years, with a large region of open water in 1973, a much lesser region of open water in 1976, and very little open water in 1974. Of the two August maps (Figure 4-25), 1974 shows a more advanced melting and breakup than 1976 in M'Clintock Channel but a less advanced breakup in Amundsen Gulf. The progression of the breakup in both years proceeds basically northward from the southern waterways and westward from the eastern waterways.

The September maps (Figure 4-26) show the maximum breakup in terms of total sea ice extent (Figure 4-78). The year which has the largest breakup in the archipelago (i.e., the most open water and ice of reduced concentration) is 1973 (Figure 4-80). Not only is this year the most open of the 4 ESMR years, but, as mentioned earlier for the October conditions, it has the most extensive breakup since the most ice-free year ever recorded, 1962 (Ramseier et al., 1974). All the major waterways of the southern and eastern archipelago are open. Viscount Melville Sound is almost ice free, and the ice present has low concentrations. Indeed, in September 1973 the Parry Channel could easily have been traversed by an icebreaker or ice-strengthened ship, providing a Northwest Passage. The northern archipelago also has many small ice-free areas in 1973.

The ESMR September data also show additional interannual differences, such as the significantly lower ice concentrations in M'Clure Strait and Viscount Melville Sound in 1975 than in 1974 and 1976.

THE ARCTIC SEA ICE COVER AS A WHOLE AND INTERREGIONAL COMPARISONS

5.1 INTRODUCTION

The monthly averaged sea ice concentrations mapped in Chapter 4 and described there on a region-by-region basis are further examined in this chapter from the perspective of the sea ice cover as a whole, including various interregional connections. As detailed in Section 4.1, over the 4-year period of the Nimbus 5 ESMR data set, 1973 through 1976, the Northern Hemisphere sea ice cover represented by the eight regions of Figure 4-2 experienced an average yearly cycle ranging from a minimum sea ice extent of 7.8×10^6 square kilometers in September to a maximum sea ice extent of 14.8×10^6 square kilometers in March. Many interannual differences in the regional ice covers are noted, and some explained, in Sections 4.2 through 4.9. In this chapter, several of the common features that are mentioned in Chapter 4 for individual regions, both regarding the ice cover itself and regarding the apparent oceanographic and atmospheric influences, will be tied together more closely.

5.2 OCEANOGRAPHIC INFLUENCES

For several of the regions discussed in Chapter 4, oceanographic influences were seen to be primary determinants of the ice edge position. Warm currents from the south either prevent or delay ice formation at relatively high latitudes, and cold currents from the north at times transport ice and cold water far southward of the location of the original ice formation. Figure 5-1 summarizes some of these influences by identifying major currents from Figure 2-3 along with the monthly average ice distributions from the maps of 4-year-averaged monthly ice concentrations in Figures 4-3 through 4-8.

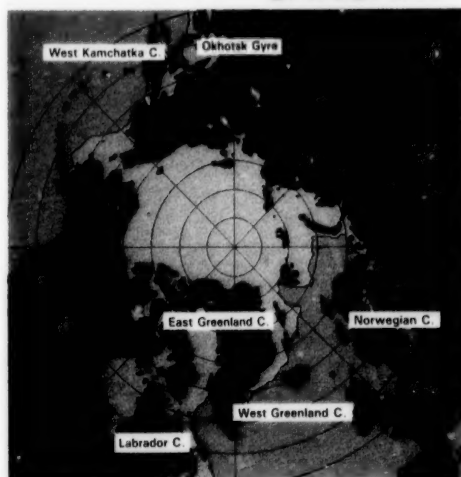
Among the important oceanographic influences suggested by Figure 5-1, the warm West Greenland Current maintains an asymmetric ice pattern in the Baffin Bay/Davis Strait region throughout the win-

ter, with ice extending considerably farther south in the west than in the east of the bay and strait, and prevents ice formation along the southwestern coast of Greenland throughout the year. The warm West Kamchatka Current and associated Okhotsk Gyre have a similar impact on the ice cover of the Sea of Okhotsk, resulting in a highly asymmetric pattern, with most of the winter ice predominantly along the west and north coasts of the sea. The Norwegian Current, the other major warm current influencing the Northern Hemisphere sea ice cover, is the strongest of these three north-flowing currents and the one with the most pronounced effects. This current extends along the coast of Norway from the Gulf Stream and North Atlantic Current to the southwest (Figure 2-3), and the heat it transports northward maintains the region north of Scandinavia free of ice throughout the year in spite of the very high latitudes involved (70° to 75°N).

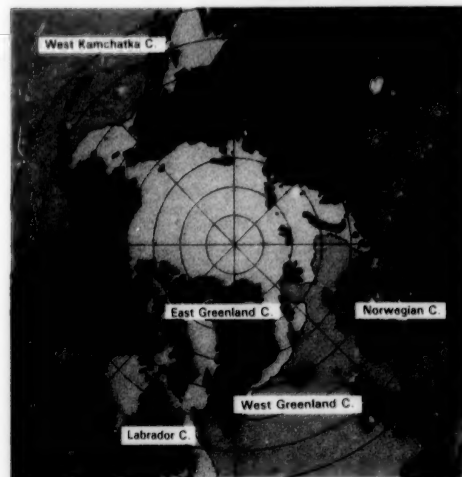
By contrast, the cold Transpolar Drift Stream and East Greenland Current together transport ice far to the south along the east coast of Greenland, so that in winter the ice reaches the southern tip of Greenland, at 60°N , and even at the minimum summer extent the ice reaches southward to 72°N . Similarly, the cold Labrador Current contributes to maintaining a wintertime sea ice cover along the east coast of Canada far south of the latitude of the ice edge in the rest of the North Atlantic (Figure 5-1a). Results from several numerical models help confirm the impact of these various ocean currents on the ice edge position. For example, Parkinson and Washington (1979) and Hibler (1979) show that omission of the currents in the model formulations leads to a much more latitudinally uniform ice edge positioning in the North Atlantic than occurs in reality, and Hibler and Bryan (1984) obtain a much improved simulated ice edge positioning after including fairly realistic ocean currents.

ORIGINAL PAGE
COLOR PHOTOGRAPH

JANUARY



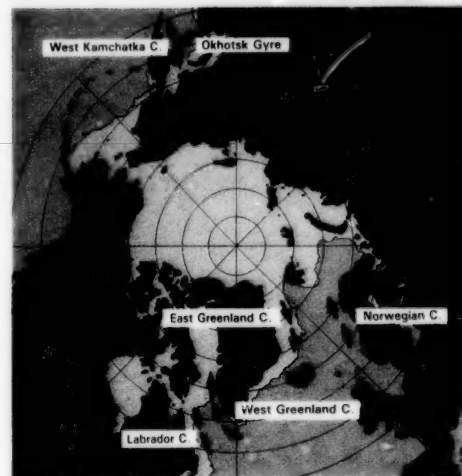
FEBRUARY



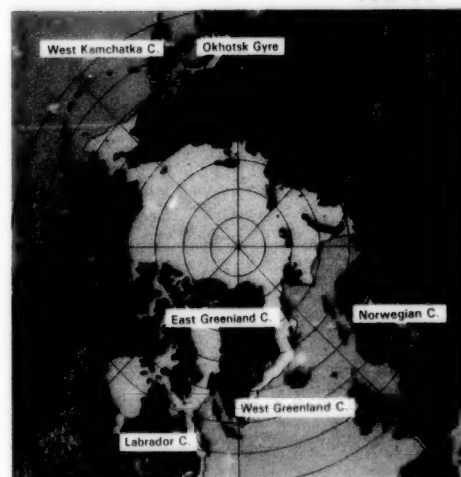
MARCH



APRIL



MAY



JUNE

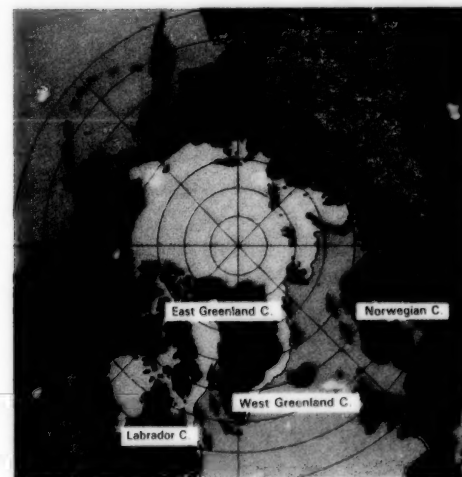
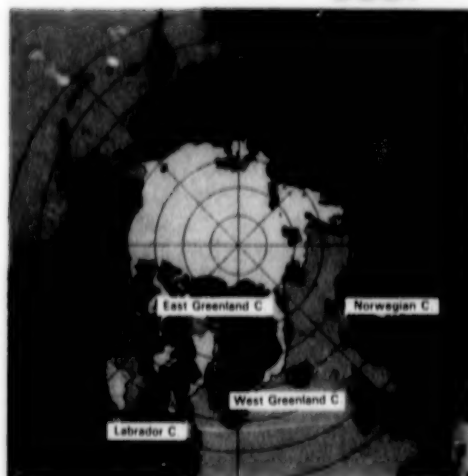


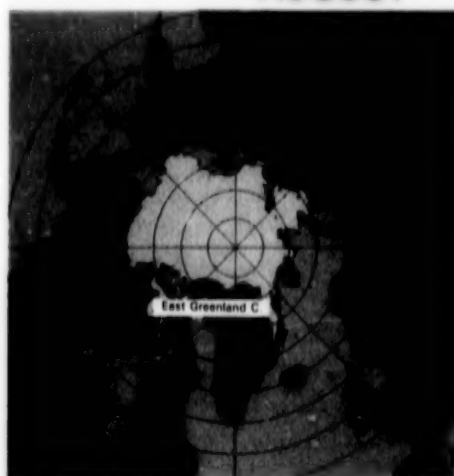
Figure 5-1a. Monthly sea ice distributions, indicated in white for ice concentrations equal to or greater than 15 percent, and major ocean currents influencing the ice edge position, January through June. The sea ice distributions are determined from the 4-year-average monthly maps of Figures 4-3 through 4-8.

ORIGINAL PAGE
COLOR PHOTOGRAPH

JULY



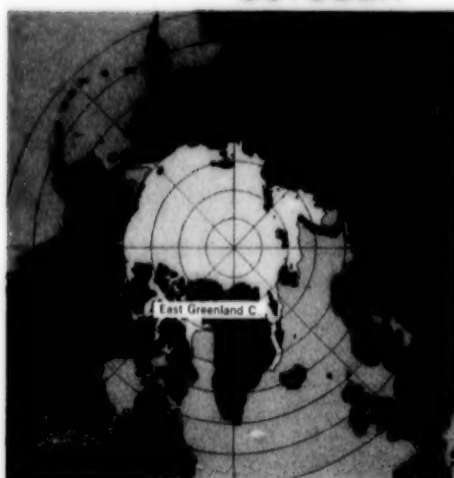
AUGUST



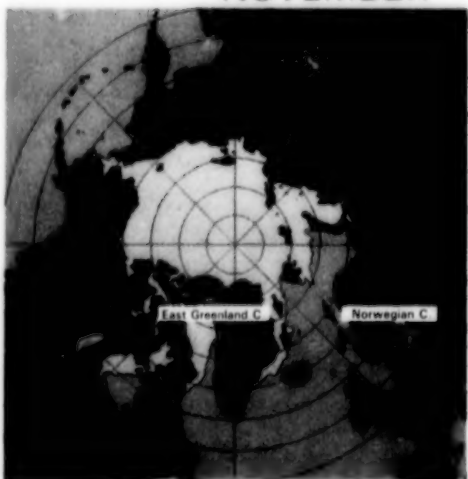
SEPTEMBER



OCTOBER



NOVEMBER



DECEMBER

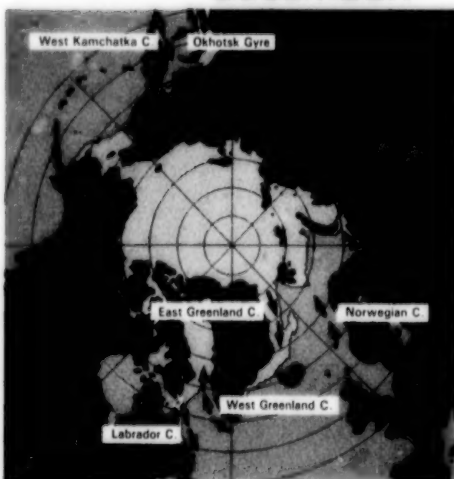


Figure 5-1b. Monthly sea ice distributions, indicated in white for ice concentrations equal to or greater than 15 percent, and major ocean currents influencing the ice edge position, July through December. The sea ice distributions are determined from the 4-year-average monthly maps of Figures 4-3 through 4-8.

Another oceanographic impact mentioned in Chapter 4 for the ice covers in several of the individual regions is that of the ocean bathymetry (Figure 2-2). In the Sea of Okhotsk, as the winter ice grows, the Tinro and Derugin Basins are not covered by ice until late in the season, and in the Bering Sea the outer edge of the continental shelf appears to serve as a boundary beyond which the ice does not advance. In these two seas the relatively warm Pacific Ocean water is the major input to the deep-water basins, whereas the continental shelf regions are influenced to a greater extent by cold river inflows and, in the case of the Bering Sea, by flow from the Arctic Ocean through the Bering Strait. As a result, in the Sea of Okhotsk and the Bering Sea, the ice is preferentially located over the continental shelves.

Bathymetric controls also appear significant in the Greenland Sea and the central Arctic Ocean. Along the coast of Greenland, as in the Sea of Okhotsk and the Bering Sea, ice is preferentially found in the continental shelf region, whereas in the Arctic Ocean the situation is the reverse. In the Arctic Ocean, as the ice melts in summer its coastal retreat is largest along the coasts with wide continental shelves (compare Figures 2-2 and 4-26), in part because of water runoff from the south.

Although, as just indicated, such oceanographic factors as currents and ocean bathymetry exert major controls on the basic seasonal cycle of sea ice distributions, the factors having the greatest impact on interannual variations in sea ice distributions are probably atmospheric factors rather than oceanographic factors. Interannual variations in ocean currents influence the ice distributions, but the interannual variations in the atmospheric pressure, wind, and temperature fields seem to be much more pronounced than those in the oceans and hence tend to have the greater impact in creating interannual contrasts in the ice.

5.3 ATMOSPHERIC INFLUENCES AND OUT-OF-PHASE RELATIONSHIPS IN THE SEA ICE COVER

Interannual fluctuations of the ice extent about its mean position, for any given month, are probably determined largely by interannual differences in the regional and hemispheric atmospheric circulation patterns. Associations between the extent of the Arc-

tic sea ice cover and atmospheric variables have been the subject of numerous investigations which have identified major interactions and provided many illustrative examples (e.g., Crane, 1978; van Loon and Rogers, 1978; Rogers and van Loon, 1979; Walsh and Johnson, 1979a, 1979b; Campbell et al., 1981; Walsh and Sater, 1981; Crane et al., 1982).

The ESMR monthly mean sea ice distributions from Figure 5-1 are repeated in Figure 5-2 together with the surface air temperature freezing contour obtained from the monthly climatological data set used for Figure 2-6. From shortly after the time of minimum sea ice extent in September to the time of maximum sea ice extent in March, the growth of the ice cover lags the southward movement of the freezing line. Then as the ice decay season begins, the ice retreats more slowly than the poleward movement of the temperature contours, with the result that by May, the freezing line has overtaken the retreating ice cover in its northward movement everywhere except in the northern Greenland and Barents Seas (Figure 5-2a). The lag in the sea ice response to the freezing line, during both the growth season and the decay season, results from the greater thermal inertia of the oceans and ice over that of the atmosphere.

A well-known phenomenon influenced by air/sea/ice interactions is the so-called "seesaw" effect between the air temperatures of Greenland and northern Europe, whereby colder than normal winters in Greenland are associated with warmer than normal winters in northern Europe and vice versa. This effect was noted as early as 1765 by Crantz, and more recently has been the subject of extensive investigations by van Loon and Rogers (1978), Rogers and van Loon (1979), and Meehl and van Loon (1979). Within their broader-based study, Rogers and van Loon (1979) show that following an anomalously cold winter in the Greenland region, the Greenland ice conditions remain severe through the following August, while the Baltic Sea has lighter than normal ice conditions during winter and spring. Seesaw variations observed in the strength of the Aleutian and Icelandic Lows during the winter months extend this type of relationship across the Northern Hemisphere.

The 4 years of ESMR data are insufficient to establish whether similar seesaw relationships exist on a long-term basis for the sea ice covers in the various regions, but several out-of-phase relationships are

apparent. For example, the sea ice extents and actual ice areas of the Sea of Okhotsk and the Kara and Barents Seas show an out-of-phase behavior, particularly for January and February (Figures 4-53a and 4-53b versus Figures 4-76a and 4-76b). Comparison with the corresponding data for the Greenland Sea (Figures 4-72a and 4-72b) shows the Greenland Sea to be in phase with the Sea of Okhotsk and out of phase with the Kara and Barents Seas. Interestingly, both the Sea of Okhotsk and the Greenland Sea have their most extensive ice covers of the ESMR period in February 1973 (there are no March 1973 ESMR data), even though in general February is not the month of maximum ice coverage in either of the two seas.

Other interesting out-of-phase relationships between regional sea ice covers are occasionally observed in the Bering and Okhotsk Seas. For example, in 1976 from March to April, the Bering Sea experienced an increase in sea ice extent, actual ice area, and mean ice concentration, whereas the Sea of Okhotsk experienced a decrease in each of these variables (Figures 4-53a, 4-53b, and 4-53d versus Figures 4-57a, 4-57b, and 4-57d). This out-of-phase behavior of the two seas, separated from each other by the narrow but influential Kamchatka Peninsula, is also observable in the color images of monthly mean ice concentrations (Figures 4-20, 4-21, and especially 4-36). The out-of-phase variations have been noted in an analysis of selected daily ESMR ice concentration maps for the two regions (Campbell et al., 1981) and have been studied more thoroughly by Cavalieri and Parkinson (1986). The latter have shown an association between the out-of-phase fluctuations in sea ice extent and large-scale atmospheric circulation patterns.

The observed sea ice decrease from March to April in the Sea of Okhotsk in 1976 marks the beginning of the seasonal sea ice decay period, as it also does in 1974 and 1975. By contrast, the Bering Sea shows more variability, with the ice growth period extending to April in 1974 and 1976, but only to March in 1975 (Figure 4-55). The greater variability in the Bering Sea, and also in Baffin Bay/Davis Strait, the Greenland Sea, and the Kara and Barents Seas (Figures 4-64, 4-70, and 4-74), reflects the greater susceptibility to the passage of atmospheric high and low pressure systems. In a study of 25 years of sea ice data, Walsh and Johnson (1979a) also find a high interannual variability in these same seas and much

lower variability at intervening longitudes, suggesting that in this regard the 4 years of ESMR data are not anomalous.

5.4 OVERALL SEA ICE TRENDS AND INTERREGIONAL COMPARISONS

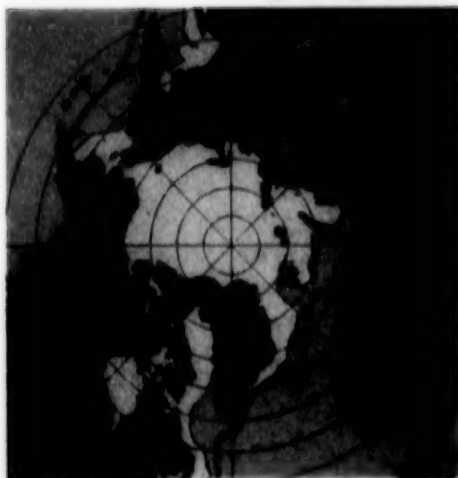
The ice extent and pseudo actual ice area for the Northern Hemisphere show an approximately symmetrical growth and decay cycle, with maximum values in March and minimum values in September, the two equinox months (Figure 5-3). Most of the ice growth occurs over the 4 months September through January, and most of the ice decay occurs over the 4 months April through August, so that the duration of near maximum ice cover is about twice as long as near minimum ice cover, the former lasting from January through April and the latter only during August and September. Thus, much of the seasonal sea ice region has an ice cover for most of the year.

As with the sum of the eight regions (Figure 5-3), in each of the individual regions the time series of pseudo actual ice cover are similar to those of ice extent (Figures 5-4 and 5-5), although with more interannual variability in the individual regions than in the total. The Arctic Ocean and Canadian Archipelago both experience very long winters, lasting 8 months with maximum possible ice extent. Hudson Bay has maximum ice coverage for 6 months, whereas in the other five regions the ice never fully covers the region, leading to more variability in the winter ice distributions. Still, in both the Greenland Sea and the Kara and Barents Seas, as in Hudson Bay, the heavy winter ice cover lasts for 6 months. In the Sea of Okhotsk, the Bering Sea, and Baffin Bay/Davis Strait, the winter is shorter and has more pronounced ice extent peaks. The Sea of Okhotsk is basically free of ice for about 6 months each year and the Bering Sea for about 5 months (Figures 5-4 and 5-5).

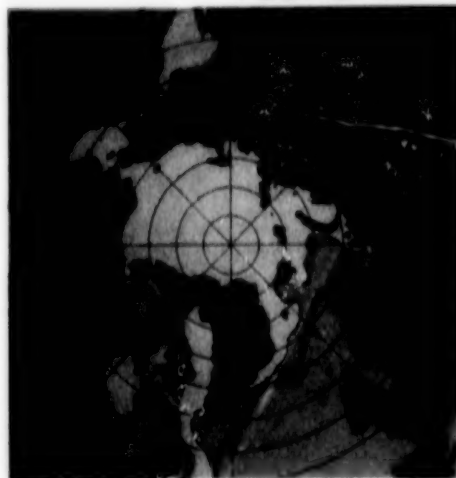
The onset of significant seasonal ice growth occurs in early October in the Arctic Ocean, the Kara and Barents Seas, and the Canadian Archipelago, slightly later in the Greenland Sea, Hudson Bay, and Baffin Bay/Davis Strait, later still in the Bering Sea, and even later in the Sea of Okhotsk, where very little ice growth occurs before December. In most cases, the onset of ice growth in a region with little or no late-summer ice depends on the proximity to the summer ice edge to the north and on the general

ORIGINAL PAGE
COLOR PHOTOGRAPH

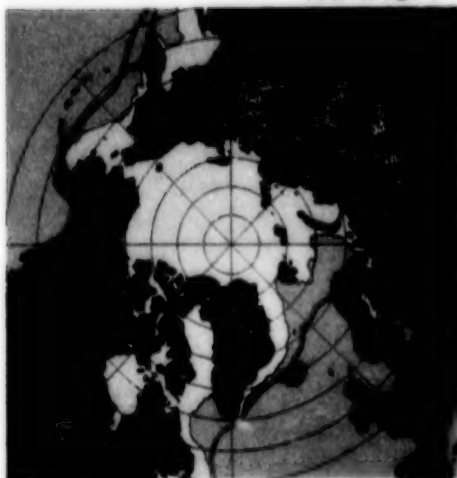
JANUARY



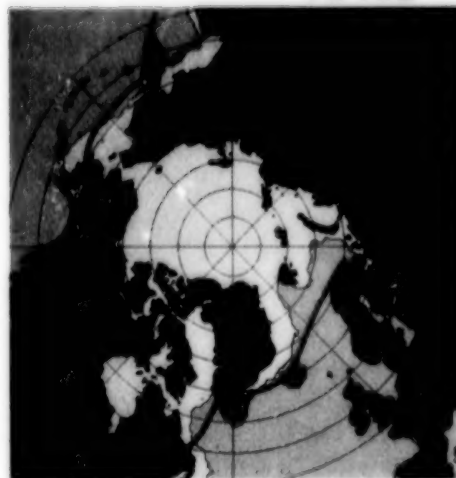
FEBRUARY



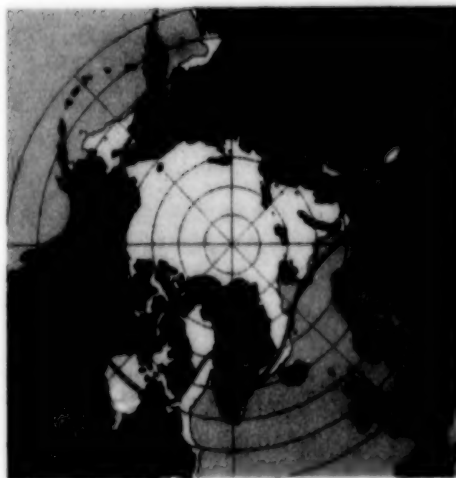
MARCH



APRIL



MAY



JUNE

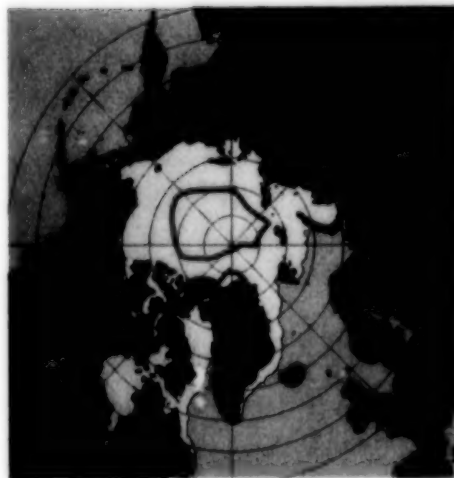
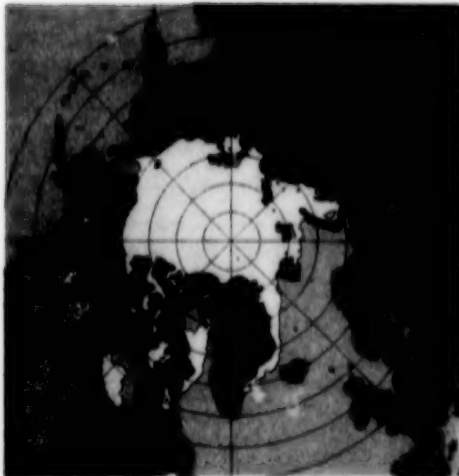


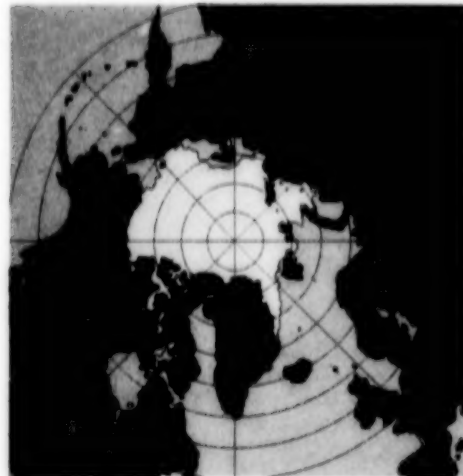
Figure 5-2a. Monthly sea ice distributions, as in Figure 5-1a, and the 271.2 K freezing isotherm from climatological surface air temperatures, January through June.

ORIGINAL PAGE
COLOR PHOTOGRAPH

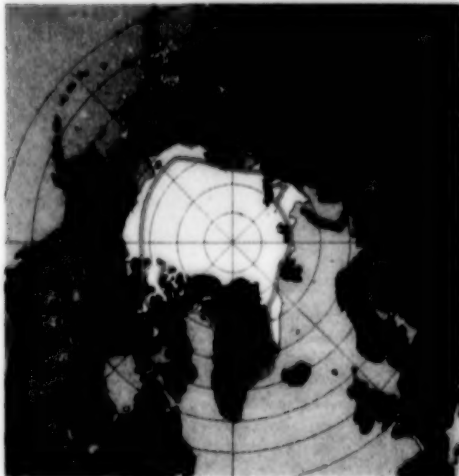
JULY



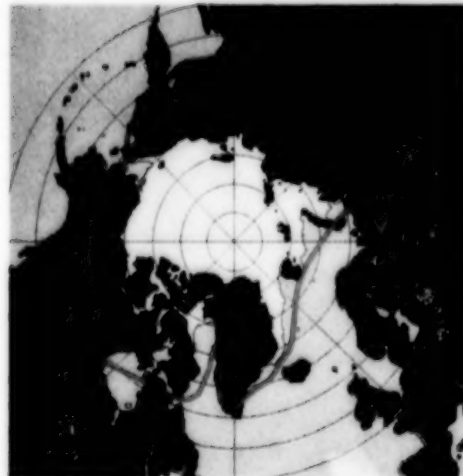
AUGUST



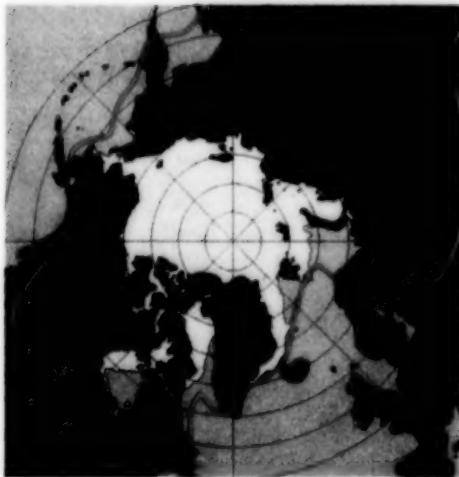
SEPTEMBER



OCTOBER



NOVEMBER



DECEMBER

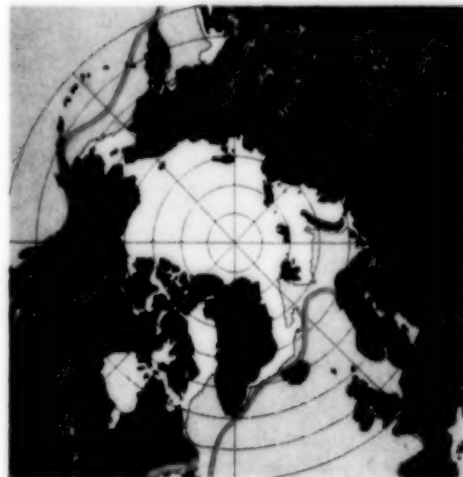


Figure 5-2b. Monthly sea ice distributions, as in Figure 5-1b, and the 271.2 K freezing isotherm from climatological surface air temperatures, July through December.

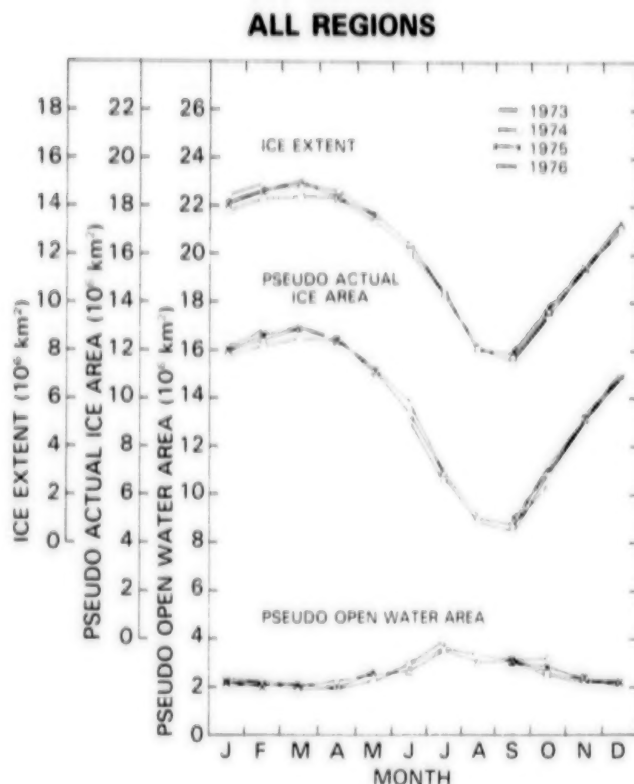


Figure 5-3. Interannual variations of the yearly cycles of sea ice extent (ice concentrations equal to or greater than 15 percent), pseudo actual ice area, and pseudo open water area within the ice pack for the sum of the eight regions in Figure 4-2.

cooling patterns in the Northern Hemisphere. Thus, for example, ice growth occurs earlier in the Barents Sea than in the Bering Sea, because the former is adjacent to the summer Arctic ice edge where ice advance occurs very early in fall. The decay progression is approximately reversed from the growth progression, with significant ice breakup and melt initiated in early April in the Sea of Okhotsk and as late as July in the Arctic Ocean basin. Despite the differences in the duration of the ice cover from one region to another, a near symmetry in the overall growth and decay cycle exists for the Northern Hemisphere ice cover as a whole, as mentioned earlier (Figure 5-3). This contrasts with the situation observed in the Antarctic, where the growth period is considerably longer than the decay period (Cavalieri and Parkinson, 1981; Zwally et al., 1983a; Comiso and Zwally, 1984).

The overall seasonal cycle of pseudo open water area within the ice pack shows an approximately Gaussian distribution peaking in midsummer (Figure

5-3). However, for the individual regions, an approximate Gaussian distribution for the open water or pseudo open water area occurs only in the Arctic Ocean and the Canadian Archipelago, in both of which substantial amounts of ice survive the summer. In Hudson Bay, Baffin Bay/Davis Strait, and the Kara and Barents Seas, the open water curves contain two peaks, one during spring and the other during fall (Figures 5-4 and 5-5). This reflects the near total ice cover in winter in these regions and, in the former two cases, the near total disappearance of the ice during summer. By contrast, the Sea of Okhotsk and the Bering Sea have as much open water within the ice pack in winter as in spring and fall and hence do not exhibit double peaks. The open water distributions in these two seas also partly reflect rapid ice retreat in spring, rapid advance in fall, and the near total disappearance of the ice in summer. The open water distribution in the Greenland Sea is fairly level throughout the year, with a slight decrease in late summer/early fall.

The open water amounts derive from leads and polynyas within the ice pack. On a monthly average basis, during the winter the leads and polynyas in the Arctic are all smaller than the 30-kilometer ESMR resolution, in contrast to the occasional Weddell polynya in the Antarctic, which can cover 200,000 square kilometers (*Antarctic Sea Ice, 1973-1976*). Furthermore, in the Antarctic, numerous coastal polynyas are observed during winter, and many of these are at least partially driven by katabatic winds from the ice sheet (Zwally et al., 1983a; Bromwich and Kurtz, 1984; Zwally et al., 1985; Cavalieri and Martin, 1985). In the Arctic, the most intensely studied analogous feature is the North Water polynya in northern Baffin Bay (Dunbar, 1969; Dunbar and Dunbar, 1972; Crawford and Parkinson, 1981; Steffen, 1985). Located at (77°N , 73°W), this polynya exhibits, on a monthly average basis, ice concentrations of about 90 percent in January through April (Figures 4-18 through 4-21). ESMR 3-day-averaged data reveal recurrent openings of the polynya during winter (Crawford and Parkinson, 1981). Smaller scale polynyas such as the occasional polynya south of St. Lawrence Island in the Bering Sea (Martin and Kauffman, 1981) are generally not visible in the wintertime monthly average maps, but resolvable polynyas are visible in the Bering Sea and numerous other locations during the spring breakup. Of interest is the channel-like opening in the Laptev Sea, which becomes apparent

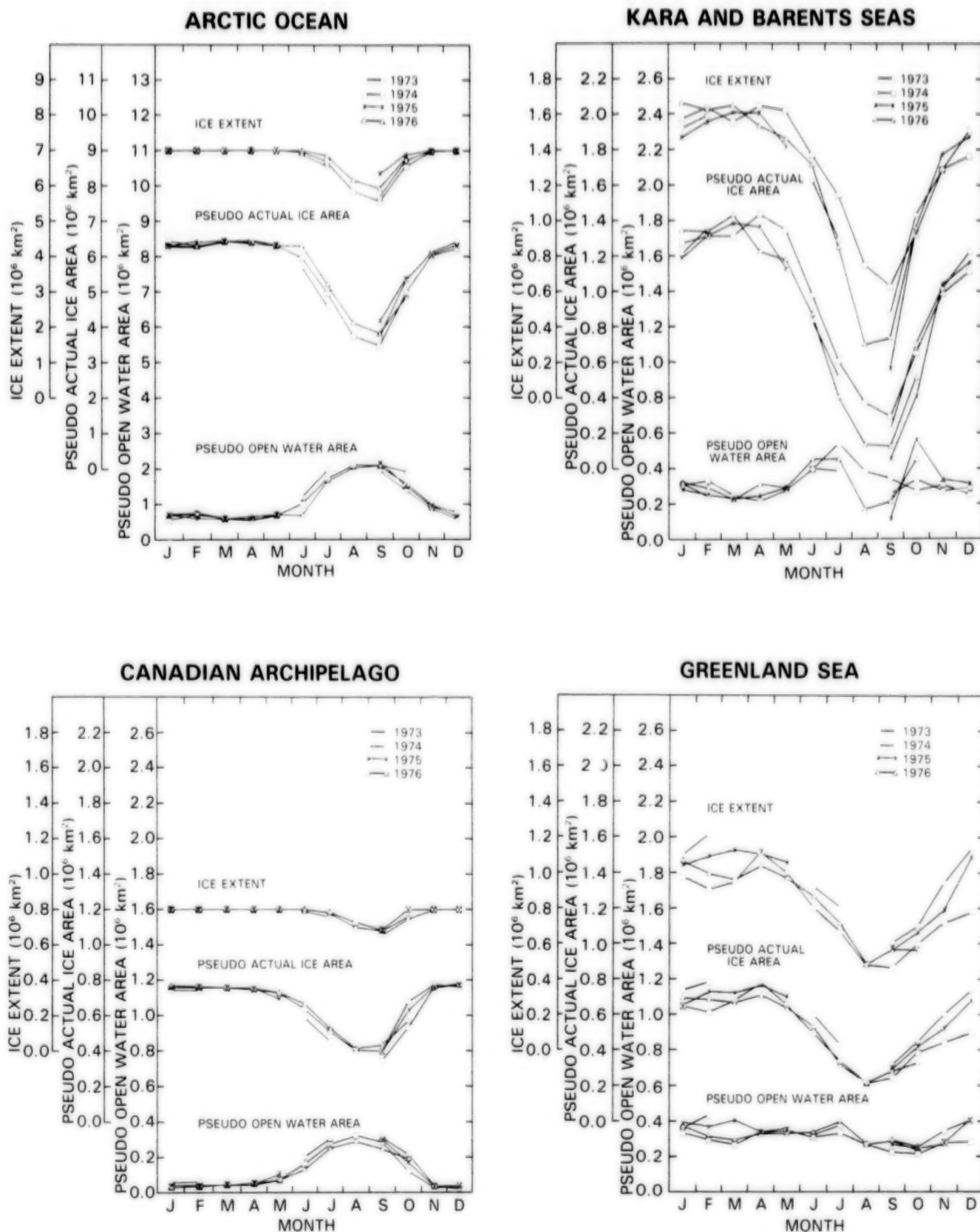


Figure 5-4. Interannual variations of the yearly cycles of sea ice extent (ice concentrations equal to or greater than 15 percent), pseudo actual ice area, and pseudo open water area within the ice pack for the following regions: Arctic Ocean, Kara and Barents Seas, Canadian Archipelago, and Greenland Sea.

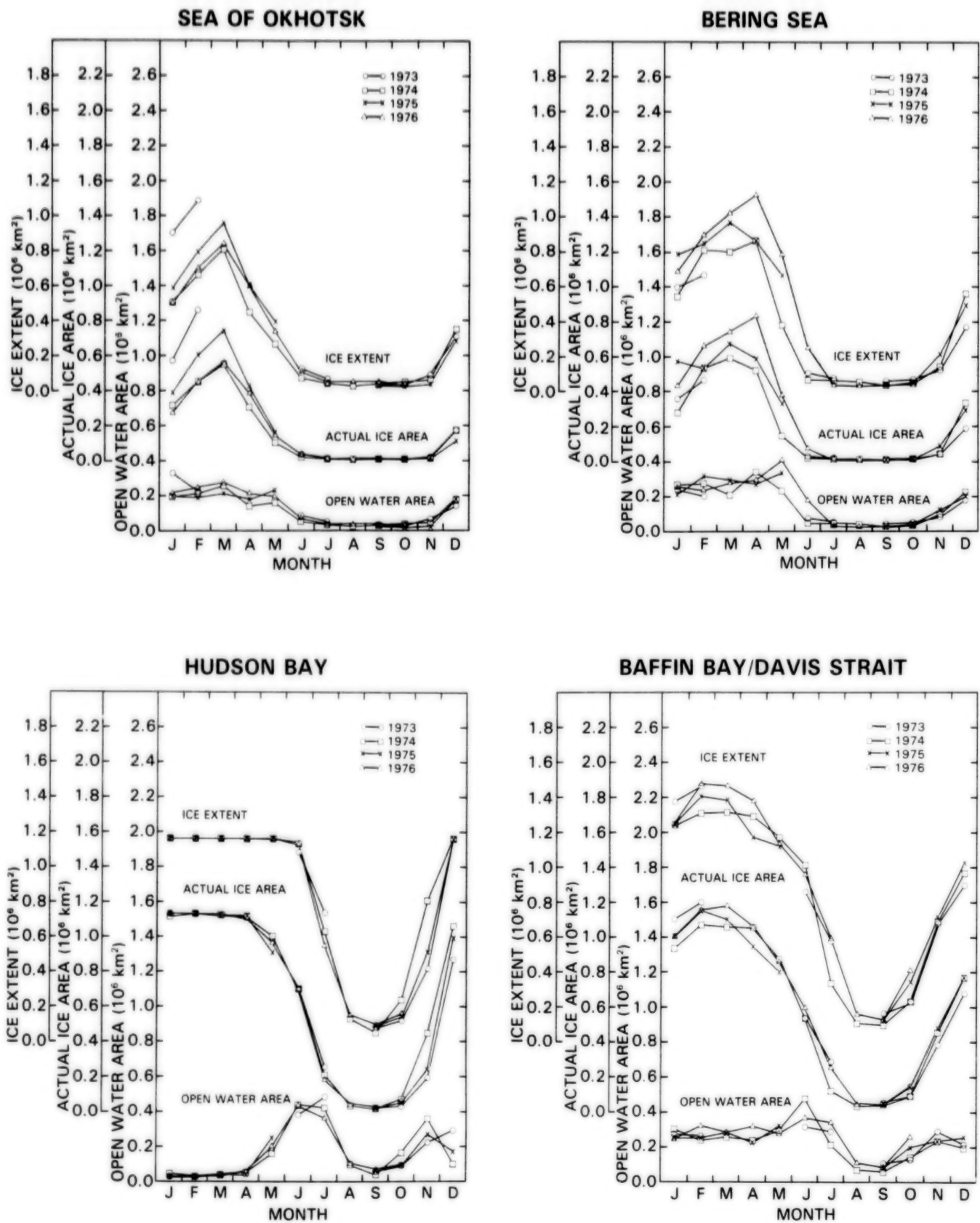


Figure 5-5. Interannual variations of the yearly cycles of sea ice extent (ice concentrations equal to or greater than 15 percent), actual ice area, and open water area within the ice pack for the following regions: Sea of Okhotsk, Bering Sea, Hudson Bay, and Baffin Bay/Davis Strait.

usually in May and has considerable interannual variability in its size and shape by June and July (Figures 4-22 through 4-24). Within the central Arctic Ocean, numerous small polynyas are a well-known occurrence in summer and contribute to the reduced concentrations derived from the ESMR. The low-brightness-temperature regions discussed in Section 3.4 may be indications of concentrated areas of open polynyas or melt ponds, both of which strongly influence the summer heat balance of the Arctic (Fletcher, 1969; Maykut, 1978).

Based on and further summarizing the ice concentration data of Chapter 4, Figure 5-6 presents maps of the yearly average ice concentrations for each of the 4 years 1973 through 1976, and Figure 5-7 presents a map of the average ice concentrations over the entire 4 years. Although eliminating the important seasonal cycle shown in the monthly averages of Chapter 4, the images of Figures 5-6 and 5-7 have value in showing the statistically averaged conditions over the year, incorporating both the length of the sea ice season and the mean ice concentration during that season. For instance, Hudson Bay, which remains covered with very highly concentrated first-year ice for 7 months of the year and is nearly ice free for 3 of the remaining 5 months, is shown in Figures 5-6 and 5-7 to have, on average, an ice concentration between 48 and 64 percent. The lower average concentrations (20 to 48 percent) in the Sea of Okhotsk and the Bering Sea reflect the shorter sea ice seasons in those two seas. The ice covers in the Greenland Sea, the Kara Sea, the Canadian Archipelago, and the central Arctic are more difficult to interpret because of the presence of multiyear ice.

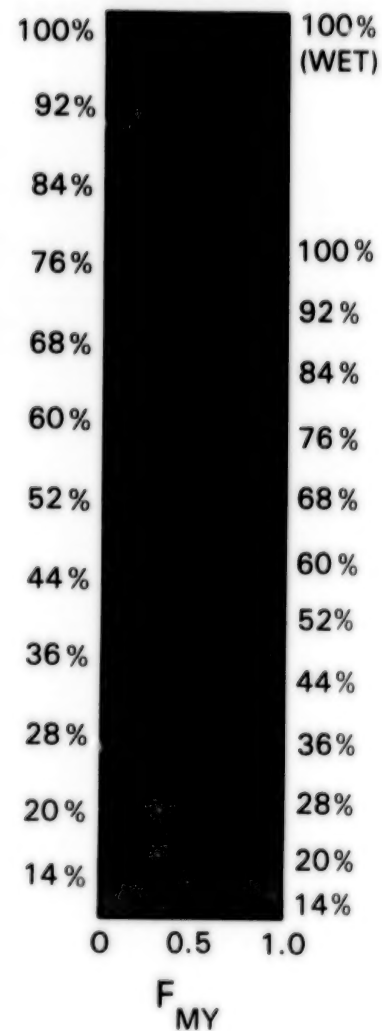
Year-to-year variations in ice cover in the different regions are also apparent in Figure 5-6, both in regard to individual features and in regard to overall ice concentration levels. For instance, the prominent ice tongue protruding from the Greenland Sea toward the Norwegian Sea in 1973 between 71° and 76°N is not visible in the yearly averaged maps for the other 3 years. Such year-to-year variations are highlighted in yearly difference maps (Figure 5-8), indicating the overall growth and decay of the ice cover from 1 year to the next, and in maps of the differences between the ice concentrations in the individual years and the 4-year-averaged ice concentrations (Figure 5-9). The data of Figure 5-6 have also been integrated regionally and in total to portray

the year-to-year differences in overall sea ice extents (Figure 5-10).

From 1973 to 1974 the yearly average ice cover decreases in the Sea of Okhotsk and the Greenland Sea, while increasing somewhat in the Bering Sea, Hudson Bay, and the Canadian Archipelago, and exhibiting both areas of increase and areas of decrease in the Arctic Ocean, the Kara and Barents Seas, and Baffin Bay/Davis Strait. In the Arctic Ocean region, decreases in the ice cover are apparent in the East Siberian Sea and the northern Chukchi Sea, and increases are apparent in the Laptev and Beaufort Seas (Figure 5-8). Overall there is a slight decrease in the ice cover from 1973 to 1974 (Figure 5-10).

From 1974 to 1975, the ice covers of the Sea of Okhotsk, the Bering Sea, and the Greenland Sea have significant increases, the ice cover of the Kara Sea has a significant decrease, and the ice cover of the Barents Sea has a significant increase in the north and a significant decrease in the east (Figure 5-8). Lesser increases are apparent in Baffin Bay, as are decreases in the Canadian Archipelago. The Arctic Ocean changes are mixed, although the largest changes from 1974 to 1975 are the increases in the Chukchi and East Siberian Seas, where decreases had occurred from 1973 to 1974. Overall, the total ice cover for the eight regions increases from 1974 to 1975 by a factor several times the slight decrease from 1973 to 1974 (Figure 5-10). This increase, however, is followed by a lesser decrease from 1975 to 1976, when slight decreases occur in most areas except at the Bering Sea ice edge, where the ice cover extends farther equatorward in 1976 than in 1975, and at scattered locations elsewhere within the pack. The largest ice concentration decrease from 1975 to 1976 occurs in the Greenland Sea (Figure 5-8).

Specific features already mentioned, such as the unusually heavy ice cover in the Sea of Okhotsk in 1973 and the light ice cover in the Bering Sea in 1973, are also apparent on the maps of the deviations of the individual years from the 4-year average (Figure 5-9). Other facts that are not apparent on earlier maps become apparent with the difference maps. For instance, at least on an annually averaged basis, 1974 was a more "average" year than 1973, in terms of having lesser areas of large deviations from the mean. Of course the standard of comparison here is only the 4-year period 1973 through 1976.



**ORIGINAL PAGE
COLOR PHOTOGRAPH**

Figure 5-6a. Annual mean sea ice concentrations for 1973 and 1974. Months without data are accounted for by interpolation.

ORIGINAL PAGE
COLOR PHOTOGRAPH

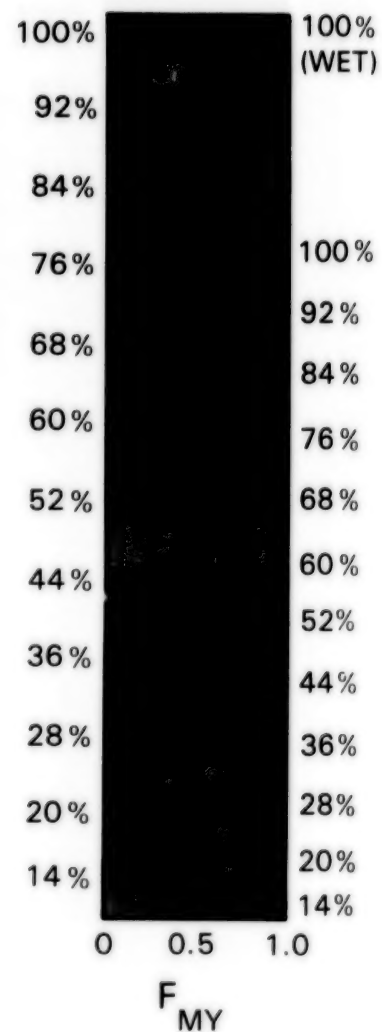
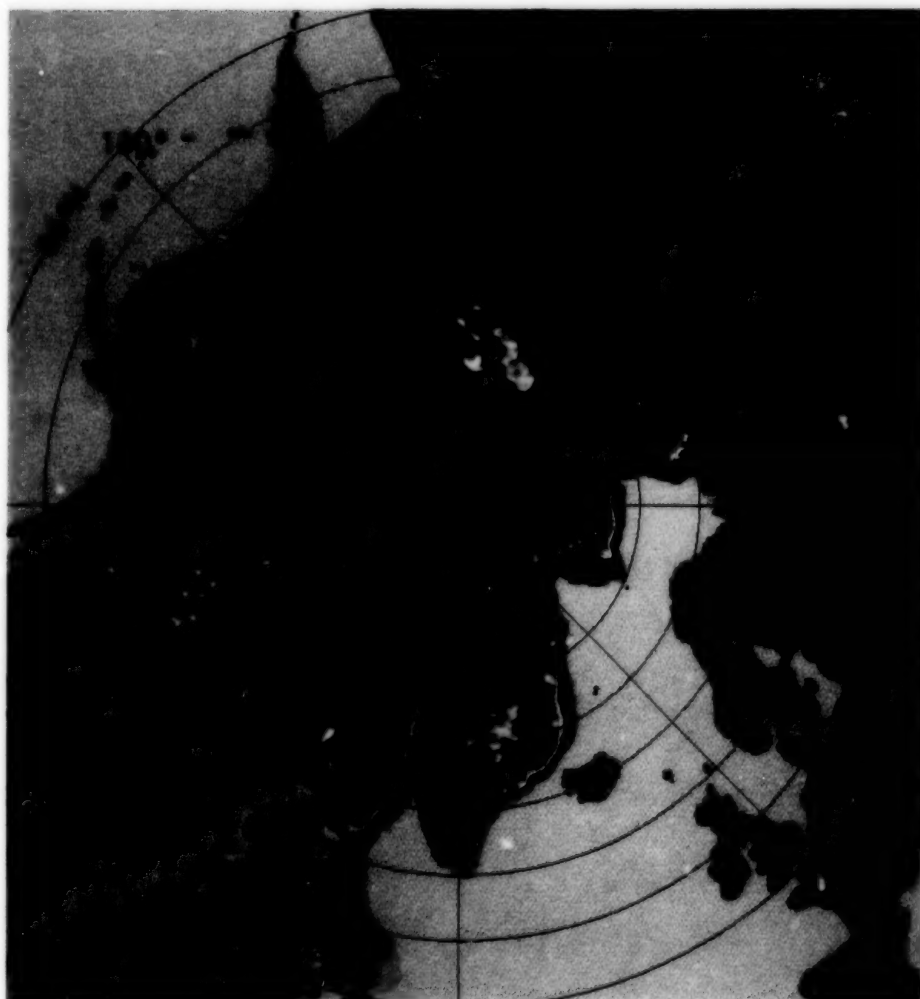


Figure 5-6b. Annual mean sea ice concentrations for 1975 and 1976. Months without data are accounted for by interpolation.

ORIGINAL PAGE
COLOR PHOTOGRAPH

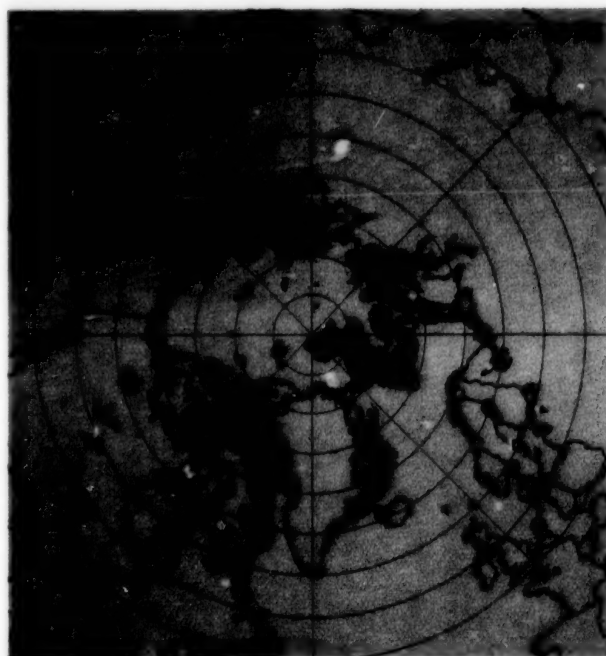


Figure 5-7. Four-year average of annual mean sea ice concentrations.

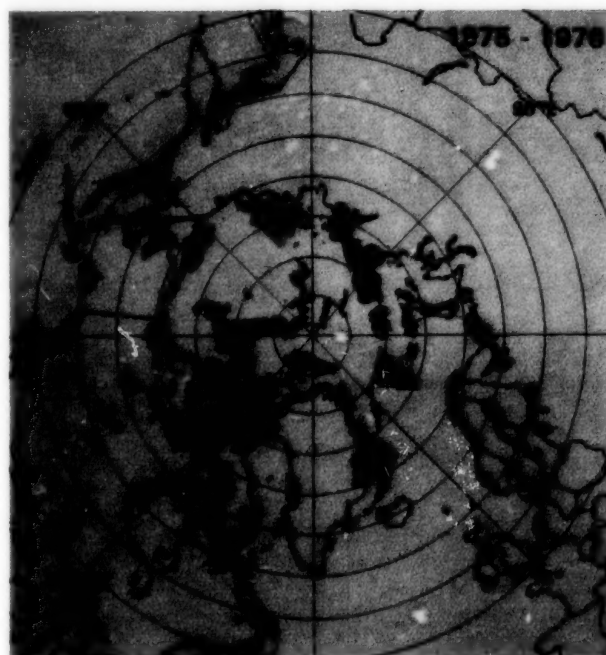
ORIGINAL PAGE
COLOR PHOTOGRAPH



-57.5 %
-55.0 %
-50.0 %
-45.0 %
-40.0 %
-35.0 %
-30.0 %
-25.0 %
-20.0 %
-15.0 %
-10.0 %
-5.0 %
0.0 %
5.0 %
10.0 %
15.0 %
20.0 %
25.0 %
30.0 %
35.0 %
40.0 %
45.0 %
50.0 %
55.0 %
57.5 %



-57.5 %
-55.0 %
-50.0 %
-45.0 %
-40.0 %
-35.0 %
-30.0 %
-25.0 %
-20.0 %
-15.0 %
-10.0 %
-5.0 %
0.0 %
5.0 %
10.0 %
15.0 %
20.0 %
25.0 %
30.0 %
35.0 %
40.0 %
45.0 %
50.0 %
55.0 %
57.5 %



-57.5 %
-55.0 %
-50.0 %
-45.0 %
-40.0 %
-35.0 %
-30.0 %
-25.0 %
-20.0 %
-15.0 %
-10.0 %
-5.0 %
0.0 %
5.0 %
10.0 %
15.0 %
20.0 %
25.0 %
30.0 %
35.0 %
40.0 %
45.0 %
50.0 %
55.0 %
57.5 %

Figure 5-8. Change in annual mean sea ice concentrations from 1973 to 1974, from 1974 to 1975, and from 1975 to 1976. In each case the data for the earlier year are subtracted from the data for the later year.

ORIGINAL PAGE
COLOR PHOTOGRAPH

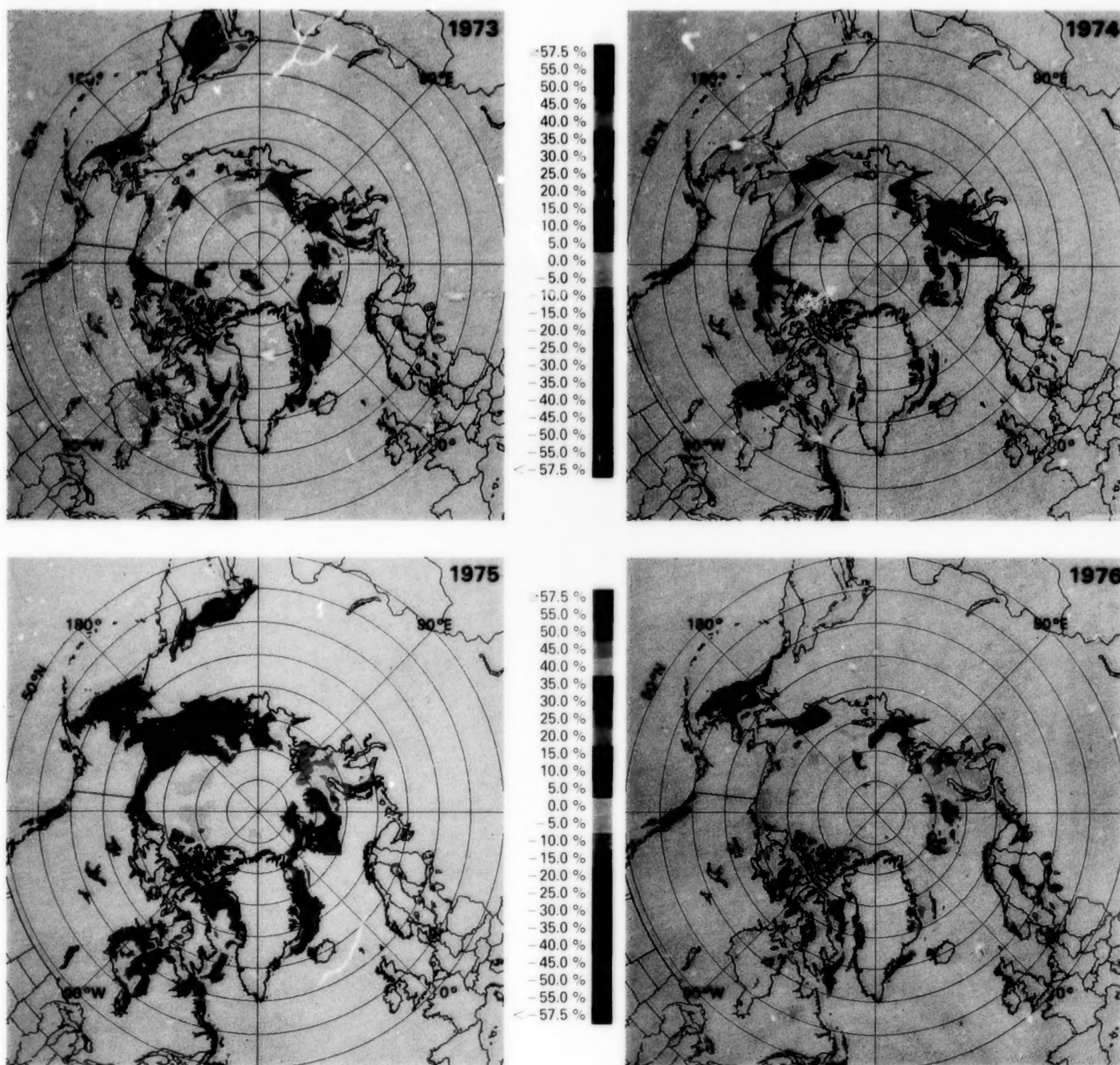


Figure 5-9. Differences between the annual mean sea ice concentrations and the 4-year average of the annual means. In each case the data for the 4-year average are subtracted from the data for the individual year.

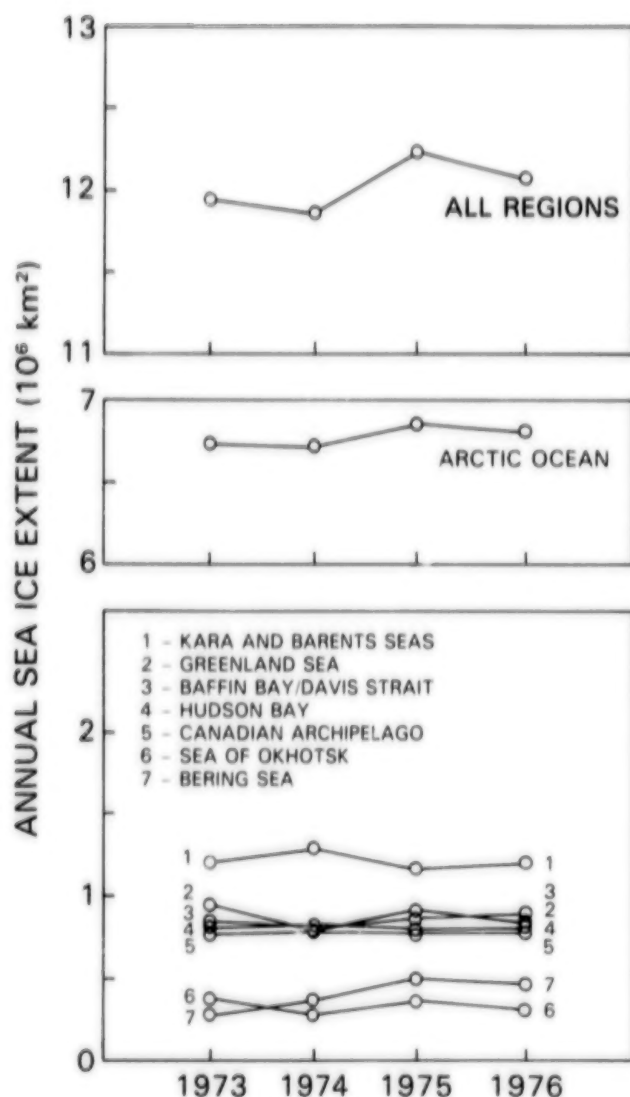


Figure 5-10. Year-to-year changes in annual mean sea ice extent for each region of Figure 4-2 and for the sum of the regions.

There is no overall trend of either increasing Arctic sea ice amounts or decreasing Arctic sea ice amounts over the 4-year ESMR period (Figure 5-10). In fact, not one of the eight regions exhibits a consistent 4-year trend of either an increasing or a decreasing nature. This lack of a trend contrasts markedly with the Antarctic situation for the same period, in which both the Weddell Sea and the southern ocean as a whole exhibit a consistent decrease in the annual mean sea ice extents (*Antarctic Sea Ice, 1973-1976*). Notably, however, the 4-year decrease in the Antarctic was not maintained in the late 1970s or early 1980s (Chiu, 1983; Zwally et al., 1983b).

Figures 5-11 through 5-13 present the annual cycles of the pseudo mean sea ice concentrations for each region for each of the 4 years and for the sum of the eight regions for each of the 4 years. These are the same pseudo mean concentrations that are arranged to show the interannual differences by month in Chapter 4, and hence, as there, they represent the mean concentrations within the sea ice region. Specifically, the concentrations are averaged over all pixels with concentrations of at least 15 percent, so that the area over which the averaging is performed is smaller in the summer than in the winter. For the sum of the eight regions, the pseudo mean ice concentrations are 82 to 86 percent throughout the winter and decrease only to 59 to 62 percent in summer (Figure 5-11). In winter, Hudson Bay shows the highest mean ice concentrations, at approximately 97 percent, followed by the Canadian Archipelago and the Arctic Ocean. However, the latter two regions have their values artificially depressed by the multiyear ice complication discussed in Chapters 3 and 4. The regions with the lowest mean concentrations during winter are the Greenland Sea, with values consistently between 61 and 73 percent, and the Bering Sea and Sea of Okhotsk, both of which show stronger contrasts from month to month within the winter and also from year to year. Each of the eight regions has a pronounced yearly cycle, with the highest mean concentrations in winter and the lowest in summer. This situation contrasts with the corresponding results in *Antarctic Sea Ice*,

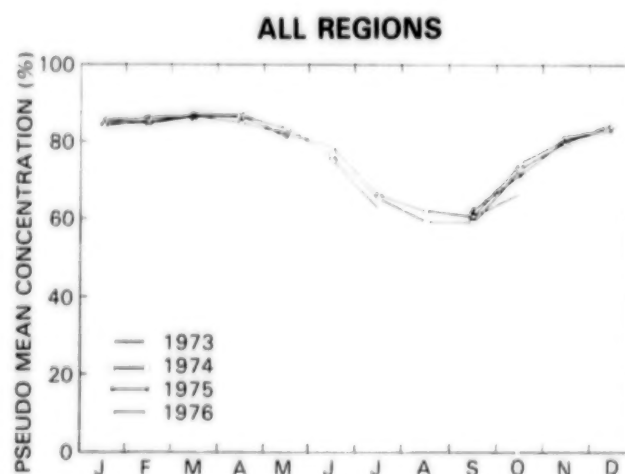


Figure 5-11. Pseudo mean sea ice concentrations, showing the yearly cycle and interannual variations, for the sum of the eight regions in Figure 4-2.

1973-1976, where the mean sea ice concentrations do not have as clearly defined an annual cycle in either the Bellingshausen-Amundsen Seas sector or the Pacific Ocean sector.

The pseudo mean ice concentrations (Figures 5-11 through 5-13) are an indication of the compactness of the ice and the amount of open water in leads and polynyas. The mean concentrations of 75 to 80 percent in the wintertime Antarctic ice pack, which is largely unconstrained by land boundaries, are approximately the same as the values found in the similarly unconstrained marginal seas of the Arctic (the Barents Sea, Greenland Sea, Sea of Okhotsk, Bering Sea, and Baffin Bay/Davis Strait). In Arctic regions that are largely constrained by land (the Arctic Ocean, Hudson Bay, and the Canadian Archipelago), the average open water in winter is only a few

percent, which is smaller than the estimated measurement error of the ESMR. In the Arctic Ocean the pseudo mean concentration value of about 91 percent translates to an open water percentage between 0 percent (if the multiyear ice fraction exceeds 0.5) and 9 percent (if the ice is exclusively first-year ice). The fraction of multiyear ice in the Arctic Ocean can be roughly estimated by assuming that the observed pseudo actual ice area at the summer minimum, 3.8×10^6 square kilometers (Figure 5-4), is the area of ice that becomes multiyear ice in winter. Dividing by the ice area in winter, $6.3-7.0 \times 10^6$ square kilometers, gives an average multiyear ice fraction of 54-60 percent. This in conjunction with the calculated 91 percent pseudo mean ice concentration in winter implies a near total sea ice coverage, with almost no open water, in winter in the Arctic Ocean (cf., Figure 3-39). It is important to recall,

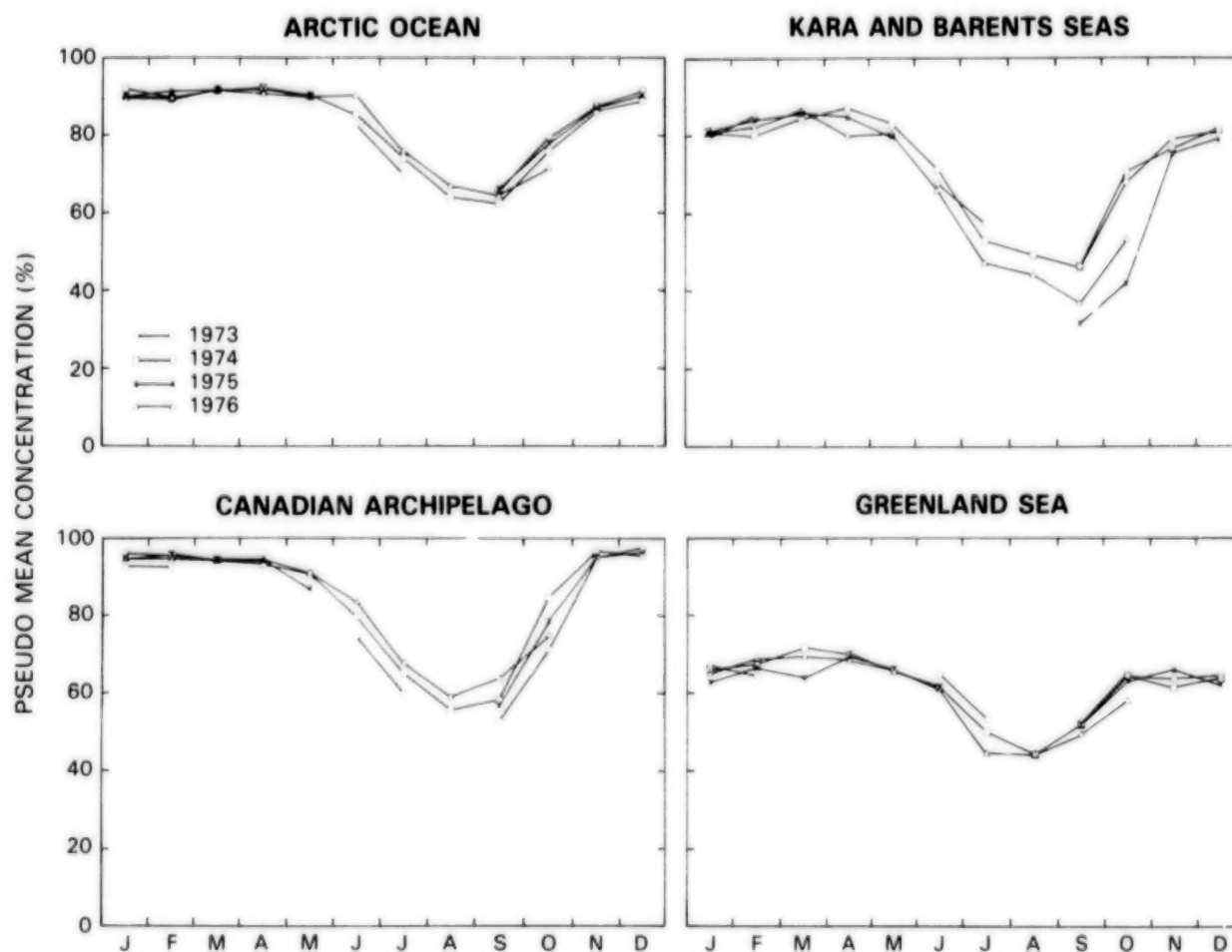


Figure 5-12. Pseudo mean sea ice concentrations, showing the yearly cycle and interannual variations, for the following regions: Arctic Ocean, Kara and Barents Seas, Canadian Archipelago, and Greenland Sea.

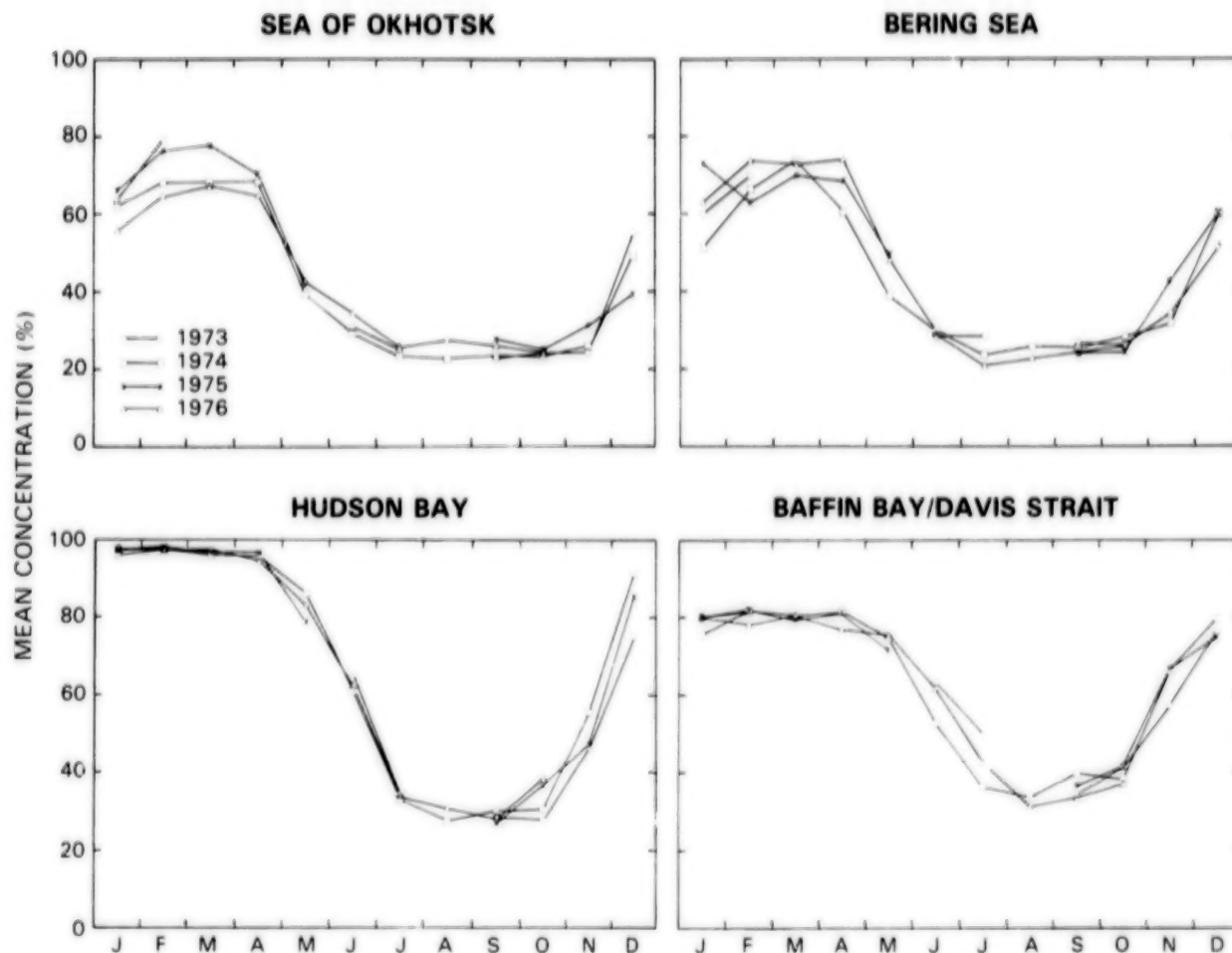


Figure 5-13. Mean sea ice concentrations, showing the yearly cycle and interannual variations, for the following regions: Sea of Okhotsk, Bering Sea, Hudson Bay, and Baffin Bay/Davis Strait.

however, that the error bars are large (Figure 3-40), so that the open water percentage could be anywhere within the range of 0 to about 10 percent.

In summary, in this volume the Arctic sea ice cover for the years 1973 through 1976 is described with a variety of mapped and plotted results derived from the microwave data of the Nimbus 5 ESMR. This 4-year period exhibited significant seasonal and interannual variations in each of the eight regions chosen for analysis (the Arctic Ocean, Sea of Okhotsk, Bering Sea, Hudson Bay, Baffin Bay/Davis Strait, Greenland Sea, Kara and Barents Seas, and Canadian Archipelago), but no consistent trend

toward either increasing or decreasing sea ice cover. In as much as polar sea ice can be a sensitive indicator of climate change, even though no climate change is indicated by the data presented in this volume, still the detailed description of global sea ice conditions in the mid-1970s here and in the companion volume *Antarctic Sea Ice, 1973-1976* should be valuable in analyzing the existence and extent of climate change in the future. When future sea ice data sets are compared with the ice conditions of the 1970s and analyzed in conjunction with changes in other climate variables and with the results of numerical simulations, a better understanding of climate change should result (Parkinson and Kellogg, 1979; Parkinson and Bindshadler, 1984).

REFERENCES

- Aagaard, K., Arctic Ocean, in *McGraw-Hill Encyclopedia of Ocean and Atmospheric Sciences*, S. Parker, ed., McGraw-Hill, New York, 21-27, 1980.
- Aber, P., and E. Vowinckel, Evaluation of North Water spring ice cover from satellite photographs, *Arctic*, **25**, 263-271, 1972.
- Alexander, V., Interrelationships between the seasonal sea ice and biological regimes, *Cold Regions Science and Technology*, **2**, 158-178, 1980.
- Andreas, E. L., and S. F. Ackley, On the differences in ablation seasons of Arctic and Antarctic sea ice, *J. Atmos. Sci.*, **39**, 440-447, 1982.
- Armstrong, T., B. Roberts, and C. Swithinbank, *Illustrated Glossary of Snow and Ice*, Scott Polar Research Institute, Cambridge, Great Britain, 60 pp., 1973.
- Barry, R. G., Arctic Ocean ice and climate: perspectives on a century of polar research, *Ann. Assoc. Amer. Geographers*, **73**, 485-501, 1983.
- Botkin, D. B., L. Hobbs, J. Kelly, and E. Pecan, Marine mammals and the biosphere, in *Report of the Conference on the Use of Remote Sensing of Marine Mammals*, Santa Barbara Institute for Environmental Studies, Santa Barbara, California, 1981.
- Bromwich, D. H., and D. D. Kurtz, Katabatic wind forcing of the Terra Nova Bay polynya, *J. Geophys. Res.*, **89**, 3561-3572, 1984.
- Campbell, W. J., The wind driven circulation of ice and water in a polar ocean, *J. Geophys. Res.*, **70**, 3279-3301, 1965.
- Campbell, W. J., Analysis of Arctic ice features, in *Earth Resources Technology Satellite-1 Symposium Proceedings, September 29, 1972*, W. A. Finch, Jr., comp., NASA TM X-66193, Greenbelt, Maryland, 129-130, 1973.
- Campbell, W. J., P. Gloersen, and R. O. Ramseier, Synoptic ice dynamics and atmospheric circulation during the Bering Sea Experiment, in *Proceedings of the Final Symposium on the Results of the Joint Soviet-American Expedition, Leningrad, May 12-17, 1974*, K. Ya. Kondratyev, Yu. I. Rabinovich, and W. Nordberg, ed., Gidrometeoizdat, Leningrad, 164-185, 1975.
- Campbell, W. J., P. Gloersen, W. J. Webster, T. T. Wilheit, and R. O. Ramseier, Beaufort Sea ice zones as delineated by microwave imagery, *J. Geophys. Res.*, **81**, 1103-1110, 1976.
- Campbell, W. J., R. O. Ramseier, W. F. Weeks, and J. A. Wayenberg, Visual observations of floating ice from Skylab, in *Skylab Explores the Earth*, NASA SP-380, National Aeronautics and Space Administration, Washington, D.C., 353-379, 1977.
- Campbell, W. J., J. Wayenberg, J. B. Ramseyer, R. O. Ramseier, M. R. Vant, R. Weaver, A. Redmond, L. Arsenault, P. Gloersen, H. J. Zwally, T. T. Wilheit, T. C. Chang, D. Hall, L. Gray, D. C. Meeks, M. L. Bryan, F. T. Barath, C. Elachi, F. Leberl, and T. Farr, Microwave remote sensing of sea ice in the AIDJEX main experiment, *Boundary-Layer Meteorol.*, **13**, 309-337, 1978.
- Campbell, W. J., R. O. Ramseier, H. J. Zwally, and P. Gloersen, Arctic sea-ice variations from time-lapse passive microwave imagery, *Boundary-Layer Meteorol.*, **18**, 99-106, 1980.

PRECEDING PAGE BLANK NOT FILMED

PRECEDING PAGE BLANK NOT FILMED

- Campbell, W. J., R. O. Ramseier, H. J. Zwally, and P. Gloersen, Structure and variability of Bering and Okhotsk sea-ice cover by satellite microwave imagery, in *Energy Resources of the Pacific*, M. T. Halbouty, ed., American Association of Petroleum Geologists, Tulsa, Oklahoma, 343-354, 1981.
- Campbell, W. J., P. Gloersen, and H. J. Zwally, Aspects of Arctic sea ice observable by sequential passive microwave observations from the Nimbus-5 satellite, in *Arctic Technology and Policy*, I. Dyer and C. Chrystostomidis, ed., Hemisphere Publishing, New York, 197-222, 1984.
- Carleton, A. M., Synoptic sea ice-atmosphere interactions in the Chukchi and Beaufort Seas from Nimbus 5 ESMR data, *J. Geophys. Res.*, **89**, 7245-7258, 1984.
- Carsey, F. D., Arctic sea ice distribution at end of summer 1973-1976 from satellite microwave data, *J. Geophys. Res.*, **87**, 5809-5835, 1982.
- Carsey, F. D., Summer Arctic sea ice character from satellite microwave data, *J. Geophys. Res.*, **90**, 5015-5034, 1985.
- Cavalieri, D. J., and S. Martin, A passive microwave study of polynyas along the Antarctic Wilkes Land coast, in *Oceanology of the Antarctic Continental Shelf*, S. S. Jacobs, ed., American Geophysical Union, Washington, D.C., 227-252, 1985.
- Cavalieri, D. J., and C. L. Parkinson, Large-scale variations in observed Antarctic sea ice extent and associated atmospheric circulation, *Mon. Weather Rev.*, **109**, 2323-2336, 1981.
- Cavalieri, D. J., and C. L. Parkinson, On the relationship between atmospheric circulation and the fluctuations in the sea ice extents of the Bering and Okhotsk Seas, *J. Geophys. Res.*, submitted, 1986.
- Cavalieri, D. J., P. Gloersen, and W. J. Campbell, Determination of sea ice parameters with the Nimbus 7 SMMR, *J. Geophys. Res.*, **89**, 5355-5369, 1984.
- Chang, T. C., and P. Gloersen, Microwave emission from dry and wet snow, in *Operational Applications of Satellite Snow Cover Observations*, A. Rango, ed., NASA SP-391, National Aeronautics and Space Administration, Washington, D.C., 399-407, 1975.
- Chiu, L. S., Variation of Antarctic sea ice: an update, *Mon. Weather Rev.*, **111**, 578-580, 1983.
- CLIMAP Project Members, The surface of ice age Earth, *Science*, **191**, 1131-1137, 1976.
- Coachman, L. K., Bering Sea, in *McGraw-Hill Encyclopedia of Ocean and Atmospheric Sciences*, S. Parker, ed., McGraw-Hill, New York, 70-71, 1980.
- Colony, R., and E. A. Muñoz, *Arctic Ocean Buoy Program Data Report January 1983 - December 1983*, Polar Science Center, Applied Physics Laboratory, University of Washington, Seattle, 115 pp., 1985.
- Colony, R., and A. S. Thorndike, An estimate of the mean field of Arctic sea ice motion, *J. Geophys. Res.*, **89**, 10,623-10,629, 1984.
- Comiso, J. C., Sea ice effective microwave emissivities from satellite passive microwave and infrared observations, *J. Geophys. Res.*, **88**, 7686-7704, 1983.
- Comiso, J. C., Characteristics of winter Arctic sea ice using multispectral microwave observations, *J. Geophys. Res.*, in press, 1986.
- Comiso, J. C., and H. J. Zwally, Concentration gradients and growth/decay characteristics of the seasonal sea ice cover, *J. Geophys. Res.*, **89**, 8081-8103, 1984.
- Cox, G. F. N., and W. F. Weeks, Salinity variations in sea ice, *J. Glaciol.*, **13**, 109-120, 1974.
- Crane, R. G., Seasonal variations of sea ice extent in the Davis Strait-Labrador Sea area and relationships with synoptic-scale atmospheric circulation, *Arctic*, **31**, 434-447, 1978.
- Crane, R. G., Atmosphere-sea ice interactions in the Beaufort/Chukchi Sea and in the European sector of the Arctic, *J. Geophys. Res.*, **88**, 4505-4523, 1983.

- Crane, R. G., R. G. Barry, and H. J. Zwally, Analysis of atmosphere-sea ice interactions in the Arctic Basin using ESMR microwave data, *Internat. J. Remote Sensing*, **3**, 259-276, 1982.
- Crawford, J. P., and C. L. Parkinson, Wintertime microwave observations of the North Water polynya, in *Oceanography from Space*, J. F. R. Gower, ed., Plenum Press, New York, 839-844, 1981.
- Crutcher, H. L., and J. M. Meserve, *Selected Level Heights, Temperatures, and Dew Points for the Northern Hemisphere*, NAVAIR 50-1C-52 (revised), Chief of Naval Operations, Naval Weather Service Command, Washington, D.C., 420 pp., 1970.
- Dey, B., Applications of satellite thermal infrared images for monitoring north water during the periods of polar darkness, *J. Glaciol.*, **25**, 425-438, 1980a.
- Dey, B., Seasonal and annual variations in ice cover in Baffin Bay and northern Davis Strait, *Canadian Geographer*, **24**, 368-384, 1980b.
- Dey, B., Monitoring winter sea ice dynamics in the Canadian Arctic with NOAA-TIR images, *J. Geophys. Res.*, **86**, 3223-3235, 1981a.
- Dey, B., Sea ice cover and related atmospheric conditions in Arctic Canada during the summer of 1978, *Mon. Weather Rev.*, **108**, 2092-2097, 1981b.
- Dey, B., Shipping routes, ice cover and year-round navigation in the Canadian Arctic, *Polar Rec.*, **20**, 549-559, 1981c.
- Dey, B., H. Moore, and A. F. Gregory, Monitoring and mapping sea-ice breakup and freezeup of Arctic Canada from satellite imagery, *Arctic and Alpine Res.*, **11**, 229-242, 1979.
- Dunbar, M., The geographical position of the North Water, *Arctic*, **22**, 438-441, 1969.
- Dunbar, M., Increasing severity of ice conditions in Baffin Bay and Davis Strait and its effect on the extreme limits of ice, in *Sea Ice: Proceedings of an International Conference, 10-13 May 1971, Reykjavik, Iceland*, T. Karlsson, ed., National Research Council of Iceland, Reykjavik, 87-93, 1972.
- Dunbar, M., Ice regime and ice transport in Nares Strait, *Arctic*, **26**, 282-291, 1973.
- Dunbar, M., and M. J. Dunbar, The history of the North Water, *Proceedings of the Royal Society of Edinburgh, Ser. B*, **72**, 231-241, 1972.
- Dunbar, M., and K. R. Greenaway, *Arctic Canada from the Air*, Defense Research Board, Ottawa, 1956.
- Edgerton, A. T., A. Stogryn, and G. Poe, *Microwave Radiometric Investigations of Snowpacks*, Final Report 1285 R-4 for U.S. Geological Survey contract 14-08-001-11828, Aerojet-General Corp., Microwave Division, El Monte, California, 1971.
- Einarsson, T., Sea currents, ice drift, and ice composition in the East Greenland Current, in *Sea Ice: Proceedings of an International Conference, 10-13 May 1971, Reykjavik, Iceland*, T. Karlsson, ed., National Research Council of Iceland, Reykjavik, 23-32, 1972.
- Fairbridge, R. W., ed., *The Encyclopedia of Oceanography*, Reinhold Publishing, New York, 1021 pp., 1966.
- Fletcher, J. O., The influence of the Arctic pack ice on climate, in *Meteorological Monographs*, Vol. 8, J. M. Mitchell, Jr., ed., American Meteorological Society, Boston, 93-99, 1969.
- Gloersen, P., and F. T. Barath, A scanning multi-channel microwave radiometer for Nimbus-G and SeaSat-A, *IEEE J. of Oceanic Engr.*, **OE-2**, 172-178, 1977.
- Gloersen, P., and J. K. Larabee, An optical model for the microwave properties of sea ice, NASA TM-83865, Greenbelt, Maryland, 25 pp., 1981.
- Gloersen, P., W. Nordberg, T. J. Schmugge, T. T. Wilheit, and W. J. Campbell, Microwave signatures of first-year and multiyear sea ice, *J. Geophys. Res.*, **78**, 3564-3572, 1973.

- Gloersen, P., T. T. Wilheit, T. C. Chang, W. Nordberg, and W. J. Campbell, Microwave maps of the polar ice of the Earth, *Bull. Amer. Meteorol. Soc.*, **55**, 1442-1448, 1974.
- Gloersen, P., R. O. Ramseier, W. J. Campbell, T. C. Chang, and T. T. Wilheit, Variation of ice morphology of selected mesoscale test areas during the Bering Sea Experiment, in *Proceedings of the Final Symposium on the Results of the Joint Soviet-American Expedition, Leningrad, May 12-17, 1974*, K. Ya. Kondratyev, Yu. I. Rabinovich, and W. Nordberg, ed., Gidrometeoizdat, Leningrad, 196-218, 1975a.
- Gloersen, P., R. O. Ramseier, W. J. Campbell, P. M. Kuhn, and W. J. Webster, Ice thickness distribution as inferred from infrared and microwave remote sensing during the Bering Sea Experiment, in *Proceedings of the Final Symposium on the Results of the Joint Soviet-American Expedition, Leningrad, May 12-17, 1974*, K. Ya. Kondratyev, Yu. I. Rabinovich, and W. Nordberg, ed., Gidrometeoizdat, Leningrad, 282-293, 1975b.
- Gloersen, P., H. J. Zwally, A. T. C. Chang, D. K. Hall, W. J. Campbell, and R. O. Ramseier, Time dependence of sea-ice concentration and multiyear ice fraction in the Arctic Basin, *Boundary-Layer Meteorol.*, **13**, 339-359, 1978.
- Gordon, A. L., Deep Antarctic convection west of Maud Rise, *J. Phys. Oceanogr.*, **8**, 600-612, 1978.
- Gorshkov, S. G., ed., *Arctic Ocean*, Vol. 3 of *World Ocean Atlas*, Pergamon Press, Oxford, 189 pp., 1983.
- Gray, A. L., R. K. Hawkins, C. E. Livingstone, L. Drapier Arsenault, and W. M. Johnstone, Simultaneous scatterometer and radiometer measurements of sea-ice microwave signatures, *IEEE J. of Oceanic Engr.*, **OE-7**, 20-32, 1982.
- Grenfell, T. C., A theoretical model of the optical properties of sea ice in the visible and near infrared, *J. Geophys. Res.*, **88**, 9723-9735, 1983.
- Grenfell, T. C., and J. C. Comiso, Multifrequency passive microwave observations of first-year sea ice grown in a tank, *IEEE Trans. Geoscience and Remote Sensing*, in press, 1986.
- Grenfell, T. C., and A. W. Lohanick, Temporal variations of the microwave signatures of sea ice during the late spring and early summer near Mould Bay NWT, *J. Geophys. Res.*, **90**, 5063-5074, 1985.
- Grenfell, T. C., and G. A. Maykut, The optical properties of ice and snow in the Arctic Basin, *J. Glaciol.*, **18**, 445-463, 1977.
- Hanson, A. M., The snow cover of sea ice during the Arctic Ice Dynamics Joint Experiment, 1975 to 1976, *Arctic and Alpine Research*, **12**, 215-226, 1980.
- Hastings, A. D., Jr., Surface climate of the Arctic Basin: Report ETL TR-71-3, Earth Sciences Division, Geographic Sciences Laboratory, U.S. Army Topographic Laboratories, Fort Belvoir, Virginia, 1971.
- Henderson-Sellers, A., and M. F. Wilson, Surface albedo data for climatic modeling, *Rev. Geophys. and Space Phys.*, **21**, 1743-1778, 1983.
- Herman, Y., Topography of the Arctic Ocean, in *Marine Geology and Oceanography of the Arctic Seas*, Y. Herman, ed., Springer-Verlag, New York, 73-79, 1974.
- Hibler, W. D., A dynamic thermodynamic sea ice model, *J. Phys. Oceanogr.*, **9**, 815-846, 1979.
- Hibler, W. D., and K. Bryan, Ocean circulation: its effects on seasonal sea-ice simulations, *Science*, **224**, 489-492, 1984.
- Hibler, W. D., and J. E. Walsh, On modeling seasonal and interannual fluctuations of Arctic sea ice, *J. Phys. Oceanogr.*, **12**, 1514-1523, 1982.
- Hibler, W. D., S. Ackley, W. F. Weeks, and A. Kovacs, Top and bottom roughness of a multiyear ice floe, *AIDJEX Bull.*, **13**, 77-91, 1972.
- Holcombe, R. M., Similarities and contrasts between the Arctic and Antarctic marine climates, in *Polar Atmosphere Symposium*, Part I (Meteorology Section), R. C. Sutcliffe and P. M. Breistein, ed., Pergamon Press, London, 9-17, 1958.

- Hollinger, J. P., B. E. Troy, R. O. Ramseier, K. W. Asmus, M. F. Hartman, and C. A. Luther, Microwave emission from high Arctic sea ice during freeze-up, *J. Geophys. Res.*, **89**, 8104-8122, 1984.
- Holt, B., and S. A. Digby, Processes and imagery of first-year fast sea ice during the melt season, *J. Geophys. Res.*, **90**, 5045-5062, 1985.
- Imbrie, J., and K. P. Imbrie, *Ice Ages, Solving the Mystery*, Enslow, Short Hills, New Jersey, 224 pp., 1977.
- Ito, H., *Sea Ice Atlas of Northern Baffin Bay*, Department of Geography, Swiss Federal Institute of Technology, Zurich, 142 pp., 1982.
- Ito, H., and F. Muller, Horizontal movement of fast ice in the North Water area, *J. Glaciol.*, **19**, 547-554, 1977.
- Jackson, J. D., *Classical Electrodynamics*, John Wiley & Sons, New York, 641 pp., 1962.
- Johannessen, O. M., W. D. Hibler, P. Wadhams, W. J. Campbell, K. Hasselmann, I. Dyer, and M. Dunbar, *MIZEX, A Program for Mesoscale Air-Ice-Ocean Interaction Experiments in Arctic Marginal Ice Zones: II. A Science Plan for a Summer Marginal Ice Zone Experiment in the Fram Strait/Greenland Sea: 1984*, Cold Regions Research and Engineering Laboratory Special Report 83-12, Hanover, New Hampshire, 47 pp., 1983.
- Ketchum, R. D., and A. W. Lohanick, Passive microwave imagery at 33 GHz, *Remote Sensing Environ.*, **2**, 211-233, 1980.
- Killworth, P. D., Deep convection in the world ocean, *Rev. Geophys. and Space Phys.*, **21**, 1-26, 1983.
- Kinder, T. H., A perspective of physical oceanography in the Bering Sea, 1979, in *The Eastern Bering Sea Shelf: Oceanography and Resources*, Vol. 1, D. W. Hood and J. A. Calder, ed., University of Washington Press, Seattle, 5-13, 1981.
- Kondratyev, K. Ya., Yu. I. Rabinovich, and W. Nordberg, ed., *Proceedings of the Final Symposium on the Results of the Joint Soviet-American Expedition, Leningrad, May 12-17, 1974*, Gidrometeoizdat, Leningrad, 316 pp., 1975. (Republished as *USSR/USA Bering Sea Experiment* by A. A. Balkema, Rotterdam, 307 pp., 1982.)
- Kunzi, K. F., S. Patil, and H. Rott, Snow-cover parameters retrieved from Nimbus-7 Scanning Multichannel Microwave Radiometer (SMMR) data, *IEEE Trans. Geoscience and Remote Sensing*, **GE-20**, 452-467, 1982.
- Lake, R. A., and E. L. Lewis, Salt rejection by sea ice during growth, *J. Geophys. Res.*, **75**, 583-597, 1970.
- Lamb, H. H., *Climate: Present, Past, and Future*, Methuen and Co., London, 613 pp., 1972.
- Lamb, H. H., The climate environment of the Arctic Ocean, in *The Arctic Ocean*, L. Rey, ed., John Wiley & Sons, New York, 135-161, 1982.
- Lemke, P., Stochastic description of air-sea ice interaction, in *Geophysics of Sea Ice*, N. Untersteiner, ed., Plenum Press, New York, in press, 1986.
- Leonov, A. K., *The Sea of Okhotsk*, National Technical Information Service, Springfield, Virginia, 1960.
- Lohanick, A. W., and T. C. Grenfell, Variations in brightness temperature over cold first-year sea ice near Tuktoyaktuk, Northwest Territories, *J. Geophys. Res.*, **91**, 5133-5144, 1986.
- Loshchilov, V. S., Snow cover on the ice of the central Arctic (in Russian), *Problemy Arktiki i Antarktiki*, **17**, 36-45, 1964.
- Markham, W. E., *Summer Breakup Pattern in the Canadian Arctic*, Circ. Ser. TEC-421, CIR-3586, Canadian Department of Transportation, Meteorological Branch, 7 pp., 1962.
- Marko, J. R., *A Satellite-Based Study of Sea Ice Dynamics in the Central Canadian Arctic Archipelago*, Contractor Report Series 77-4, Institute of Ocean Sciences, Sidney, British Columbia, 1977.
- Marko, J. R., *A Satellite Imagery Study of Eastern Parry Channel*, Contractor Report Series 78-05, Institute of Ocean Sciences, Sidney, British Columbia, 1978.

- Martin, S., A field study of brine drainage and oil entrainment in first-year sea ice, *J. Glaciol.*, **22**, 473-502, 1979.
- Martin, S., and P. Kauffman, A field and laboratory study of wave damping by grease ice, *J. Glaciol.*, **27**, 283-313, 1981.
- Martin, S., P. Kauffman, and C. Parkinson, The movement and decay of ice edge bands in the winter Bering Sea, *J. Geophys. Res.*, **88**, 2803-2812, 1983.
- Maykut, G. A., Energy exchange over young sea ice in the central Arctic, *J. Geophys. Res.*, **83**, 3646-3658, 1978.
- Maykut, G. A., Large-scale heat exchange and ice production in the central Arctic, *J. Geophys. Res.*, **87**, 7971-7984, 1982.
- Maykut, G. A., and N. Untersteiner, Some results from a time-dependent thermodynamic model of sea ice, *J. Geophys. Res.*, **76**, 1550-1575, 1971.
- McQuillan, A. K., and D. J. Clough, *Benefits of Remote Sensing of Sea Ice*, Resource Report 73-3, Canadian Center Remote Sensing, Department of Energy, Mines and Resources, 33 pp., 1973.
- Meehl, G. A., and H. van Loon, The seesaw in winter temperatures between Greenland and northern Europe. Part III: Teleconnections with lower latitudes, *Mon. Weather Rev.*, **107**, 1095-1106, 1979.
- Meeks, D. C., R. O. Ramseier, and W. J. Campbell, A study of microwave emission properties of sea ice — AIDJEX 1972, in *Proceedings of the 9th International Symposium on Remote Sensing of the Environment*, Ann Arbor, University of Michigan, Ann Arbor, 307-322, 1974.
- Mirsky, J., *To the Arctic: The Story of Northern Exploration from Earliest Times to the Present*, Alfred A. Knopf, Inc., New York, 334 pp., 1948.
- Muench, R. D., and J. D. Schumacher, On the Bering Sea ice edge front, *J. Geophys. Res.*, **90**, 3185-3197, 1985.
- Muller, F., *North Water Project, Progress Report: 1 October, 1974 to 30 September, 1975*, Geographisches Institut ETH, Zurich, Switzerland, 1975.
- Nakawo, M., and N. K. Sinha, Growth rate and salinity profile of first-year sea ice in the high Arctic, *J. Glaciol.*, **27**, 315-330, 1981.
- Niebauer, H. J., Recent fluctuations in sea ice distributions in the eastern Bering Sea, in *The Eastern Bering Sea Shelf: Oceanography and Resources*, Vol. 1, D. W. Hood and J. A. Calder, ed., University of Washington Press, Seattle, 133-140, 1981.
- Niebauer, H. J., Multi-year sea ice variability in the Eastern Bering Sea — an update, *J. Geophys. Res.*, **88**, 2733-2742, 1983.
- NORSEX Group (B. Farrelly, J. A. Johannessen, O. M. Johannessen, E. Svendsen, K. Kloster, I. Horjen, C. Mätzler, W. J. Campbell, J. Crawford, R. Harrington, L. Jones, C. Swift, V. E. Delnore, D. Cavalieri, P. Gloersen, S. V. Hsiao, O. H. Shemdin, T. W. Thompson, R. O. Ramseier), Norwegian remote sensing experiment in a marginal ice zone, *Science*, **220**, 781-787, 1983.
- Overland, J. O., and C. H. Pease, Cyclone climatology of the Bering Sea and its relation to sea ice extent, *Mon. Weather Rev.*, **110**, 5-13, 1982.
- Palmen, E., and C. W. Newton, *Atmospheric Circulation Systems: Their Structure and Physical Interpretation*, J. Van Mieghem, ed., International Geophysics Series, Vol. 13, Academic Press, New York, 603 pp., 1969.
- Parkinson, C. L., and R. A. Bindshadler, Response of Antarctic sea ice to uniform atmospheric temperature increases, in *Climate Processes and Climate Sensitivity*, J. E. Hansen and T. Takahashi, ed., Maurice Ewing Series, Vol. 5, American Geophysical Union, Washington, D.C., 254-264, 1984.
- Parkinson, C. L., and A. J. Gratz, On the seasonal sea ice cover of the Sea of Okhotsk, *J. Geophys. Res.*, **88**, 2793-2802, 1983.
- Parkinson, C. L., and W. W. Kellogg, Arctic sea ice decay simulated for a CO₂-induced temperature rise, *Climatic Change*, **2**, 149-162, 1979.

- Parkinson, C. L., and W. M. Washington, A large-scale numerical model of sea ice, *J. Geophys. Res.*, **84**, 311-337, 1979.
- Pease, C. H., Eastern Bering Sea ice processes, *Mon. Weather Rev.*, **108**, 2015-2023, 1980.
- Perdue, W. F., *Oceanographic Investigation of the East Greenland Polar Front in Autumn*, masters thesis, Naval Postgraduate School, Monterey, California, 1982.
- Polar Research Board, Committee on the Role of the Polar Regions in Climatic Change (chaired by J. M. Mitchell, Jr., and W. W. Kellogg), *The Polar Regions and Climatic Change*, National Academy Press, Washington, D.C., 59 pp., 1984.
- Ramseier, R. O., P. Gloersen, and W. J. Campbell, Variation in the microwave emissivity of sea ice in the Beaufort and Bering Seas, in *Proceedings of the URSI Commission II—Specialist Meeting on Microwave Scattering and Emission from the Earth*, E. Schanda, ed., Institute of Applied Physics University, Berne, Switzerland, 87-93, 1974.
- Ramseier, R. O., P. Gloersen, W. J. Campbell, and T. C. Chang, Mesoscale description for the principal Bering Sea ice experiment, in *Proceedings of the Final Symposium on the Results of the Joint Soviet-American Expedition, Leningrad, May 12-17, 1974*, K. Ya. Kondratyev, Yu. I. Rabonovich, and W. Nordberg, ed., Gidrometeoizdat, Leningrad, 234-270, 1975.
- Reed, R. J., Principal frontal zones of the Northern Hemisphere in winter and summer, *Bull. Amer. Meteorol. Soc.*, **41**, 591-598, 1960.
- Robock, A., The seasonal cycle of snow cover, sea ice and surface albedo, *Mon. Weather Rev.*, **108**, 267-285, 1980.
- Rogers, J. C., Meteorological factors affecting interannual variability of summertime ice extent in the Beaufort Sea, *Mon. Weather Rev.*, **106**, 890-897, 1978.
- Rogers, J. C., and H. van Loon, The seesaw in winter temperatures between Greenland and Northern Europe. Part II: Some oceanic and atmospheric effects in middle and high latitudes, *Mon. Weather Rev.*, **107**, 509-519, 1979.
- Ruddiman, W. F., and A. McIntyre, Late Quaternary surface ocean kinematics and climatic change in the high-latitude North Atlantic, *J. Geophys. Res.*, **82**, 3877-3887, 1977.
- Ruddiman, W. F., and A. McIntyre, Warmth of the subpolar North Atlantic Ocean during Northern Hemisphere ice-sheet growth, *Science*, **204**, 173-175, 1979.
- Ruddiman, W. F., and A. McIntyre, Oceanic mechanisms for amplification of the 23,000-year ice-volume cycle, *Science*, **212**, 617-627, 1981.
- SMHI, *Climatological Ice Atlas for the Baltic Sea, Kattegat, Skagerrak and Lake Vänern (1963-1979)*, Swedish Meteorological and Hydrological Institute, Norrköping, Sweden, and Institute of Marine Research, Helsinki, Finland, 220 pp., 1982.
- Steffen, K., *Surface Temperature and Sea Ice of an Arctic Polynya: North Water in Winter*, Geographisches Institut der Eidgenössische Technische Hochschule, Zurich, 193 pp., 1985.
- Stiles, W. H., and F. T. Ulaby, The active and passive microwave response to snow parameters I, Wetness, *J. Geophys. Res.*, **85**, 1037-1044, 1980.
- Stommel, H., On the smallness of sinking regions in the ocean, *Proc. Nat. Acad. Sci., USA*, **48**, 766-772, 1962.
- Svendsen, E., K. Kloster, B. Farrelly, O. M. Johannessen, J. A. Johannessen, W. J. Campbell, P. Gloersen, D. Cavalieri, and C. Mätzler, Norwegian remote sensing experiment: evaluation of the Nimbus 7 Scanning Multichannel Microwave Radiometer for sea ice research, *J. Geophys. Res.*, **88**, 2781-2791, 1983.
- Swift, C. T., Passive microwave remote sensing of the ocean—a review, *Boundary-Layer Meteorol.*, **18**, 25-54, 1980.
- Swift, C. T., L. S. Fedor, and R. O. Ramseier, An algorithm to measure sea ice concentration with microwave radiometers, *J. Geophys. Res.*, **90**, 1087-1099, 1985.

- Swithinbank, C., Arctic pack ice from below, in *Sea Ice: Proceedings of an International Conference, 10-13 May 1971, Reykjavik, Iceland*, T. Karlsson, ed., National Research Council of Iceland, Reykjavik, 246-254, 1972.
- Thorndike, A. S., and R. Colony, *Arctic Ocean Buoy Program Data Report 19 January 1979-31 December 1979*, Polar Science Center, University of Washington, Seattle, 131 pp., 1980.
- Thorndike, A. S., D. A. Rothrock, G. A. Maykut, and R. Colony, The thickness distribution of sea ice, *J. Geophys. Res.*, **80**, 4501-4513, 1975.
- Tooma, S. G., R. A. Menella, J. P. Hollinger, and R. D. Ketchum, Comparison of sea-ice type identification between airborne dual-frequency passive microwave radiometry and standard laser/infrared techniques, *J. Glaciol.*, **15**, 225-239, 1975.
- Troy, B. E., J. P. Hollinger, R. M. Lerner, and M. M. Wisler, Measurement of the microwave properties of sea ice at 90 GHz and lower frequencies, *J. Geophys. Res.*, **86**, 4283-4289, 1981.
- Untersteiner, N., Natural desalination and equilibrium salinity profile of perennial sea ice, *J. Geophys. Res.*, **73**, 1251-1257, 1968.
- Untersteiner, N., AIDJEX review, in *Sea Ice Processes and Models*, R. S. Pritchard, ed., University of Washington Press, Seattle, 3-11, 1980.
- van Loon, H., and J. C. Rogers, The seesaw in winter temperatures between Greenland and northern Europe. Part I: General description, *Mon. Weather Rev.*, **106**, 296-310, 1978.
- Vant, M. R., R. B. Gray, R. O. Ramseier, and V. Makios, Dielectric properties of fresh and sea ice at 10 and 35 GHz, *J. Appl. Phys.*, **45**, 4712-4717, 1974.
- Vant, M. R., R. O. Ramseier, and V. Makios, The complex-dielectric constant of sea ice at frequencies in the range 0.1-40 GHz, *J. Appl. Phys.*, **49**, 1234-1280, 1978.
- Vinje, T. E., Sea ice conditions in the European sector of the marginal seas of the Arctic, 1966-1975, in *Norsk Polarinstitute Arbok 1975*, Norsk Polarinstitute, Oslo, 163-174, 1976.
- Vinje, T. E., Some observations from Nimbus-6 data collecting platform in polar areas, in *Proceedings of the Joint IAGA/IAMAP Assembly, Seattle, August 22-September 3, 1977*, S. Ruttenberg, ed., National Center for Atmospheric Research, Boulder, Colorado, 124-132, 1977.
- Vowinckel, E., and S. Orvig, The climate in the north polar basin, in *Climate of the Polar Regions*, Vol. 14 of *World Survey of Climatology*, Elsevier Publishing, Amsterdam, 129-252, 1970.
- Wadhams, P., The ice cover in the Greenland and Norwegian Seas, *Rev. Geophys. and Space Phys.*, **19**, 345-393, 1981.
- Wadhams, P., and R. J. Horne, An analysis of ice profiles obtained by submarine sonar in the Beaufort Sea, *J. Glaciol.*, **25**, 401-424, 1980.
- Wadhams, P., and V. A. Squire, An ice-water vortex at the edge of the East Greenland Current, *J. Geophys. Res.*, **88**, 2770-2780, 1983.
- Walker, E. R., and P. Wadhams, Thick sea-ice floes, *Arctic*, **32**, 140-147, 1979.
- Walsh, J. E., and C. M. Johnson, An analysis of Arctic sea ice fluctuations, 1953-1977, *J. Phys. Oceanogr.*, **9**, 580-591, 1979a.
- Walsh, J. E., and C. M. Johnson, Interannual atmospheric variability and associated fluctuations in Arctic sea ice extent, *J. Geophys. Res.*, **84**, 6915-6928, 1979b.
- Walsh, J. E., and J. E. Sater, Monthly and seasonal variability in the ocean-ice-atmosphere systems of the North Pacific and the North Atlantic, *J. Geophys. Res.*, **86**, 7425-7445, 1981.
- Warren, B. A., Deep circulation of the world ocean, in *Evolution of Physical Oceanography*, B. A. Warren and C. Wunsch, ed., Massachusetts Institute of Technology Press, Cambridge, 6-41, 1981.
- Warren, S. G., and W. J. Wiscombe, A model for the spectral albedo of snow, II, Snow containing

- atmospheric aerosols, *J. Atmos. Sci.*, **37**, 2734-2745, 1980.
- Weeks, W. F., Sea ice conditions in the Arctic, *AIDJEX Bull.*, **34**, 173-205, 1976.
- Weeks, W. F., and S. F. Ackley, *The growth, structure, and properties of sea ice*, CRREL Monograph 82-1, Cold Regions Research and Engineering Laboratory, Hanover, New Hampshire, 130 pp., 1982.
- Wentz, F. J., A model function for ocean microwave brightness temperatures, *J. Geophys. Res.*, **88**, 1892-1908, 1983.
- Wilheit, T. T., W. Nordberg, J. Blinn, W. Campbell, and A. Edgerton, Aircraft measurements of microwave emission from Arctic sea ice, *Remote Sensing Environ.*, **2**, 129-139, 1972.
- WMO (World Meteorological Organization), *WMO Sea-Ice Nomenclature, Terminology, Codes, and Illustrated Glossary*, WMO/OMM/BMO No. 259, TP 145, Secretariat of the World Meteorological Organization, 1970.
- WMO/ICSU (World Meteorological Organization/International Council of Scientific Unions), *Report of the WMO/CAS-JSC-CCCO Meeting of Experts on the Role of Sea Ice in Climatic Variations*, WCP-26, World Meteorological Organization, Geneva, 63 pp., 1982.
- Yakovlev, G. N., *Ice Routes of the Arctic*, translated from Russian by the Canadian Department of National Defense, Ottawa, 342 pp., 1977.
- Zwally, H. J., Microwave emissivity and accumulation rate of polar firn, *J. Glaciol.*, **18**, 195-215, 1977.
- Zwally, H. J., and P. Gloersen, Passive microwave images of the polar regions and research applications, *Polar Rec.*, **18**, 431-450, 1977.
- Zwally, H. J., J. C. Comiso, C. L. Parkinson, W. J. Campbell, F. D. Carsey, and P. Gloersen, *Antarctic Sea Ice, 1973-1976: Satellite Passive-Microwave Observations*, NASA SP-459, National Aeronautics and Space Administration, Washington, D.C., 206 pp., 1983a.
- Zwally, H. J., C. L. Parkinson, and J. C. Comiso, Variability of Antarctic sea ice and changes in carbon dioxide, *Science*, **220**, 1005-1012, 1983b.
- Zwally, H. J., J. C. Comiso, and A. L. Gordon, Antarctic offshore leads and polynyas and oceanographic effects, in *Oceanology of the Antarctic Continental Shelf*, S. S. Jacobs, ed., American Geophysical Union, Washington, D.C., 203-226, 1985.

APPENDIX A

DATA PROCESSING, COMPILATION, AND STORAGE

A.1 INTRODUCTION

This appendix provides the details of the data processing used for converting the Nimbus 5 ESMR data to the form presented in this volume. The microwave brightness temperatures are from the same data set used for *Antarctic Sea Ice, 1973-1976*, and the handling of the data was identical for the Northern and Southern Hemispheres through the compilation of 3-day-averaged gridded values. This appendix reflects that fact, with much of the basic material on the data handling through that stage being repeated, with clarifications, from the earlier volume. Where the data handling differed from that used for the Antarctic, as in the interpolations for monthly averaging, these differences are elaborated.

A.2 DATA STREAM

The telemetry data from the Nimbus 5 satellite, launched in December 1972, were transmitted to two spaceflight tracking and data network stations located near Fairbanks, Alaska, and Rosman, North Carolina. The data received in Alaska were recorded as the satellite passed overhead and were then transmitted over a microwave link to the Meteorological Data Handling System (MDHS) at the Goddard Space Flight Center (GSFC). The data received in North Carolina were relayed directly to GSFC over a wideband data link. At GSFC, the telemetry data were unpacked, decommutated, supplemented with flags and end of files, and stored on magnetic tapes called experimental tapes (ET's). For data processing convenience, the data from the ESMR instrument were combined from several ET's to form stacked experimental tapes (SET's). The 10-bit telemetry data on the ET's were converted to 32-bit format on the SET's for use on the GSFC computers.

The SET's were then used with ephemeris tapes to generate Earth-located calibrated brightness temperature (CBT) tapes, which are the primary source of calibrated radiometer data used for the sea ice analysis in this volume and the earlier *Antarctic Sea Ice, 1973-1976*. The CBT tapes contain the time, the calibration parameters, the measured brightness temperatures (T_B 's), and the corresponding geographical coordinates (Table A-1). Each CBT tape was written at 6250 bits per inch and has approximately 180 files, each of which contains one orbit of data.

In order to provide a synoptic representation of the data in the polar regions, a polar stereographic mapping, described later, was employed. The grid size is 293 by 293, with each map cell representing an area varying from about 32 by 32 kilometers near the poles to about 28 by 28 kilometers near 50-degrees latitude (Figure A-1).

The Nimbus 5 ESMR recorded radiation from 78 scan positions varying from 50 degrees to the left to 50 degrees to the right of the satellite track (Wilheit, 1972). Full coverage of the entire polar area could be obtained from a sequence of six satellite orbits, or one-half day of good data, if all 78 beam positions were utilized. However, because of the large disparity in the radiometer field of view from the outer beam position to the middle beam position (70 by 140 kilometers compared with 25 by 25 kilometers), generally only the middle 52 beam positions were used, for a swath-angle coverage of ± 30.5 degrees and a minimum resolution of 29 by 42 kilometers. This swath angle corresponds to a spatial coverage of about 1280 kilometers on the Earth's surface. Because ESMR data from poleward of 85-degrees latitude are obtainable only through use

Table A-1
CBT Data Record Format for ESMR*

Word No.	Quantity	Units	Scale	Description
1	Year	Year		Year associated with data
2	Day	Days		
3	Hour	Hours		
4	Minute	Minutes		
5	Second	Seconds		
6	Program ID			Unique program identification
7	Pitch error	Degrees	× 10	Pitch fine error
8	Roll error	Degrees	× 10	Roll fine error
9	RMP indicated rate high		× 10	
10	Latitude	Degrees	× 10	Latitude of subsatellite point
11	Longitude	Degrees	× 10	Longitude of subsatellite point
12	Height	Kilometers		Height of spacecraft
13	Hot-load mean		× 10	
14	Hot load		× 100	
15	Cold-load mean		× 10	
16	Cold load		× 100	
17	MUX 1			Average antenna temperature
18	MUX 2			Phase-shift temperature
19	MUX 3			Ferrite-switch temperature
20	MUX 4			Ambient-load temperature
21	MUX 5			Hot-load temperature
22	MUX 6			Automatic gain control (AGC)
23-41	Engineering data			
42	Beam position 79			
43-46	MUX 1-MUX 4			
47-124	Latitude	Degrees	× 10	Latitudes of the 78 scan positions
125-202	Longitude	Degrees	× 10	Longitudes of the 78 scan positions
203-280	Brightness temperature	Kelvins	× 10	Brightness temperatures of the 78 scan positions

*Source: Wilheit, 1972.

of the outer beam positions, these outer positions, which were otherwise discarded, were used to cover the region between 85 degrees and the poles. Furthermore, because the ESMR senses horizontally polarized radiation, a scan-angle dependent correction was applied to the data, as discussed at the end of Section A.3.2, to make each observation approximately equivalent to a nadir observation, which is nonpolarized.

With the above restrictions on beam positions and with additional rejection of data because of occasional instrumental problems, about 3 days of data were generally required to provide near-complete spatial coverage of the polar regions. Three-day-average maps were therefore generated for all periods that contained valid data from launch until May 1977. From these secondary products, monthly mean T_B maps were created and used with interpolated monthly surface temperature maps to calculate monthly ice concentrations. The monthly T_B maps appear in Chapter 3, and the monthly ice concentration maps appear in Chapter 4. Yearly and multi-yearly average maps were also created and appear in Chapters 3 and 5. Interpolation and weighting procedures to account for missing data while creating the monthly and yearly T_B maps are described in Section A.4.2.

A.3 CALIBRATION AND QUALITY CONTROL

A.3.1 Determination of Latitude and Longitude

Initially, ephemeris data based on several weeks of predictive calculations were used to compute the latitude and longitude of the field of view of the Earth's surface corresponding to each scan angle of the radiometer as the satellite orbits the Earth. However, use of these data often caused serious Earth-location errors up to several hundred kilometers. These errors were substantially reduced by using definitive ephemeris data calculated from satellite tracking parameters. The new procedure was implemented in 1975 for newly acquired data, and all prior CBT tapes were revised at that time. Results were checked by comparing Earth locations generated from these data with continental boundaries. The calculated positionings appear to be accurate to well within 30 kilometers, which is the approximate resolution used for mapping the data.

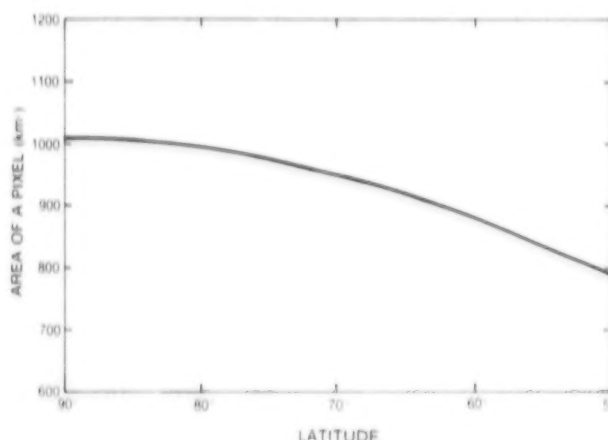


Figure A-1. Area of a map element (pixel) as a function of latitude.

A.3.2 Initial Calibration Algorithm

Initial calibration of the radiometer was based on a cold-load reference temperature (T_C) provided by a sky horn measuring the 3 K cosmic background and a hot-load reference temperature (T_H) determined by a floating ambient termination in the spacecraft. Eight scans of data were required to produce a complete set of calibration parameters (Table A-2). The calibration temperatures, T_C and T_H , were calculated from the various temperatures and automatic gain control of the multiplex data (MUX 1 through MUX 6 in Table A-1), and the values of four ambient and four cold calibration voltages (V_H and V_C , respectively) were averaged through the eight scans. For each beam position, the brightness temperature, T_{IN} , corresponding to voltage V was then calculated by:

$$T_{IN} = T_H + \frac{T_C - T_H}{V_C - V_H} (V - V_H) \quad , \quad (A-1)$$

which provided the basis for calibrating the ESMR instrument.

Additional corrections to the calibration of the instrument had to be applied to account for antenna ohmic loss, which is a function of beam position and the temperature of the phase shifters. Further corrections were required for the effects of side lobes and different viewing angles. In particular, a scan-angle-dependent correction was applied to convert each observation to make it approximately equivalent to a nadir observation. The procedure relied on available ground-truth data, statistical analysis, and

Table A-2
Framing Format of the ESMR Data in SET Tapes

Word Number	Scan Number	Number of Bits/Word	Description
1-78	1	10	V_{1-78} for beam positions 1-78
79	1		Hot reference
80	1		Average antenna temperature
81-128	2		V_{1-78} for beam positions 1-78
129	2		Cold reference
130	2		Average phase-shifter temperature
131-208	3		V_{1-78} for beam positions 1-78
209	3		Hot reference
210	3		Ferrite-switch temperature
211-288	4		V_{1-78} for beam positions 1-78
289	4		Cold reference
290	4		Ambient-load temperature
291-368	5		V_{1-78} for beam positions 1-78
369	5		Hot reference
370	5		Dicke-load temperature
371-448	6		V_{1-78} for beam positions 1-78
449	6		Cold reference
450	6		AGC count
451-528	7		V_{1-78} for beam positions 1-78
529	7		Hot reference
530	7		Multiplex calibration
531-608	8		V_{1-78} for beam positions 1-78
609	8		Cold reference
610	8		Frame identification number

modeling, with a set of correction parameters A_0 and A_1 , for each beam position, I , empirically determined from ocean data and then used to obtain the final calibrated brightness temperature:

$$T_B(I) = A_0(I) + A_1(I) \times T_{IN}(I) \quad (A-2)$$

Further details can be found in Wilheit (1973).

To check the correction for conversion to nadir observations, selected 293 by 293 images were generated using only the nadir beam positions and these were compared with images for the same period using the middle 52 positions. The comparison showed consistency over the oceans, over sea ice, and over ice sheets.

A.3.3 Calibration Adjustments and Data Gaps

When all available calibrated data were initially processed and mapped to 3-day-average images, many of the maps were found to be contaminated by abnormal brightness temperatures. It was determined that unforeseen problems with the input data had led to improper calibration of selected orbits and portions of orbits. For example, parity read errors in the middle of certain input SET's caused the improper unpacking of some of the calibration parameters.

The initial procedure used for removing the badly calibrated data was crude but effective. A polaroid color image of each map was produced and checked for abnormal features, features that were usually easy to detect because at least eight scans would be affected. Problem orbits and portions of orbits were then determined by using a graphical overlay on the images, and problem time intervals were determined by examining a printout of the data for the entire orbit. Time intervals containing clearly inaccurate data were excluded in the final processing of the maps. In a later version of the mapping software, most of these inaccurate data were automatically eliminated by requiring the values of the calibration parameters to fall within certain acceptable limits.

Both the hot-load and cold-load reference temperatures are needed to calibrate the radiometer adequately. Sometimes the hot-load reference was not recoverable because of hardware or processing problems. When this occurred, the instrument was said to be in "glitch mode." The ESMR was in glitch mode occasionally during the 1973 through 1976 period, most seriously in March, April, May, and August of 1973 and in November and December of 1976. Because of the glitch-mode problems, the usable data obtained during these months were insufficient for generating monthly averages. Although the radiometer was in glitch mode for as long as a few days at other times, there were generally enough well-calibrated data to form reasonable monthly averages. The only other months during the 1973 through 1976 period without monthly averaged data obtainable from the Nimbus 5 ESMR are June, July, and August of 1975. During these 3 months, the data acquisition instruments for Nimbus 5 were turned off because the power for the instruments was needed for the newly launched Nimbus 6 satellite. In September 1975, data acquisition for the Nimbus

5 ESMR was restored but only on an every-other-day basis.

Another instrumental problem led to additional calibration adjustments. This problem was identified through studies of the temporal variation of T_B in the ice-free areas of the southern ocean. These studies revealed some unexpected time-dependent shifts, which were later confirmed as global rather than hemispheric through studies of T_B variations in the Northern Hemisphere oceans. At the 1.55-centimeter wavelength of the ESMR, sea water is expected to have minimal or no seasonal variation in T_B because the emissivity is inversely proportional to the surface physical temperature (Wilheit, 1972). Although T_B is affected by roughness, foam, water vapor, and rainfall, none of these has seasonal characteristics consistent with the observed shifts. Therefore the shifts were assumed to be caused by calibration or instrumental problems. Consequently, a normalization procedure was applied to the monthly average T_B data. Much of this procedure is described in Comiso and Zwally (1980) for the Antarctic. A summary of the earlier description and a discussion of the adjustments added for the Arctic data are provided in the following paragraphs.

To investigate the time dependence of T_B , various subsets of the data in the monthly maps were binned in intervals of 1 K. An example of a winter distribution for the latitude zone of 55°S to 65°S is presented in Figure A-2. In the Southern Hemisphere, the contribution from the ocean typically appears as a narrow peak at approximately 135 K with a width of about ± 4 K. The brightness temperature at which the ocean peak occurs varies from month to month, as indicated in Figure A-3. In the 1973 data, a decrease of approximately 8 K occurs from January to July. In the 1976 data, a much larger decrease is evident from April to June and is followed by a recovery in July with a general decrease for the remainder of the year. During 1974 and 1975, T_B is much less variable.

A similar time series analysis of the brightness temperatures of the ocean peaks in the T_B distributions was done for the Northern Hemisphere, and the results for the North Atlantic are shown in Figure A-4. The Northern Hemisphere data show overall consistency with the Southern Hemisphere data, although with some discrepancies, such as the greatly reduced magnitude of the January-to-July decrease

in the 1973 data. The major discrepancies are perhaps caused by differences in atmospheric and surface conditions in the two regions. The April-to-June decrease in the 1976 data is more uniform over the

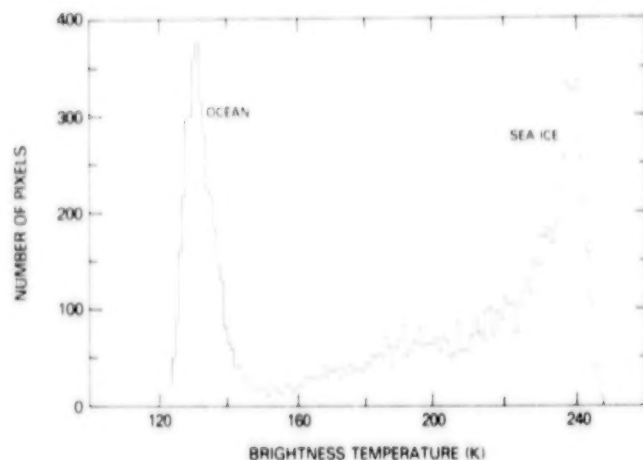


Figure A-2. Typical winter distribution of brightness temperatures in map elements (pixels) between 55°S and 65°S. [From Zwally et al. (1983).]

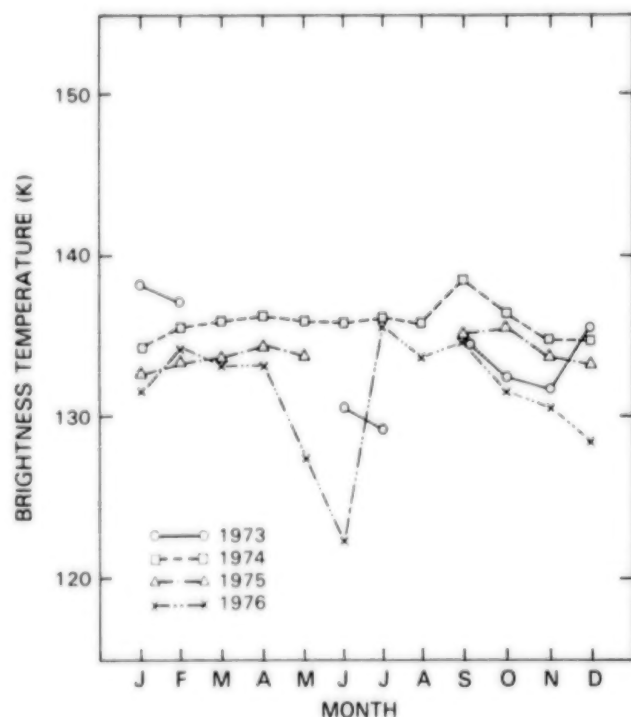


Figure A-3. Brightness temperatures with the highest frequency of occurrence in the ice-free ocean area (histogram ocean peak) in the Weddell Sea between 55°S and 65°S for each month of available data from 1973 through 1976, prior to correction for calibration shifts. [From Zwally et al. (1983).]

two hemispheres and is apparently caused by fluctuations in instrumental characteristics not accounted for in the calibration of the sensor (Paul Hwang, personal communication, 1982).

Further analysis of the apparently anomalous shifts in T_B from April to July of 1976 was made by examining both ocean and highly concentrated sea ice areas on the 3-day-average maps. Shifts in brightness temperature in both ocean and ice areas occurred at about the same time. In the Southern Hemisphere, the initial downward shift is about 10 K for the ocean and 8 K for the sea ice, and the recovery shift is about 13 K for the ocean and 25 K for the sea ice. Such recovery shifts, if noninstrumental, would require changes in physical temperature of about 27 K on the ice and 30 K in the water, assuming ice and water emissivities to be constant during the period. Temperature changes that large are considered so unlikely that the abrupt T_B shifts are concluded to be instrumental in nature. Examination of the time variations of T_B over the Antarctic and Greenland ice sheets revealed similar anomalous

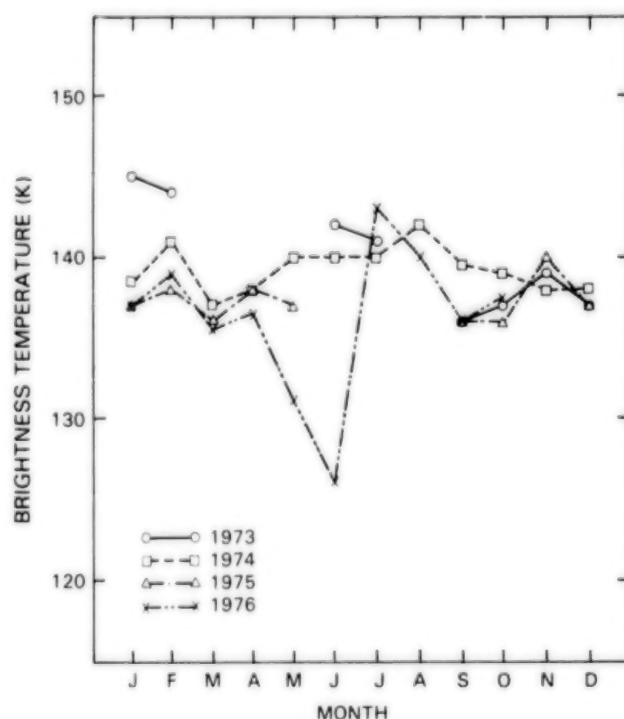


Figure A-4. Brightness temperatures with the highest frequency of occurrence in the ice-free ocean area (histogram ocean peak) in the North Atlantic between 55°N and 65°N for each month of available data from 1973 through 1976, prior to correction for calibration shifts.

time-dependent shifts, supporting the conclusion of an instrumental problem.

The normalization procedure used to adjust for anomalous shifts assumed that the ocean T_B , including atmospheric contributions, was constant over time for each hemisphere. The constant assumed was the average value of the T_B 's at the monthly ocean peaks, this value being 135 K in the Antarctic and 138.3 K in the Arctic. The standard deviation of the ocean T_B 's in the Arctic is slightly larger than the standard deviation in the Antarctic, with the result that in both hemispheres the T_B value five standard deviations below the peak is about 120 K, which is the estimated brightness temperature of calm ice-free ocean. In all months throughout the 4-year period, each monthly averaged map was normalized by a constant offset to force the ocean peak to occur at 135 K in the Antarctic and at 138.3 K in the Arctic. The offsets in the Arctic, determined from data in the North Atlantic and Bering and Okhotsk Seas, are listed in Table A-3.

Table A-3
Adjustments to Monthly Averaged
Brightness Temperatures

Month	Year			
	1973	1974	1975	1976
January	-3.7	-1.8	1.9	1.6
February	-2.6	-1.5	2.3	1.5
March	--	0.5	2.2	3.6
April	--	1.0	3.3	3.6
May	--	0.1	2.4	1.9
June	-3.7	-1.6	--	-1.1
July	-4.6	-4.6	--	-2.4
August	--	-4.7	--	-1.4
September	-1.8	-1.5	2.1	2.6
October	-0.9	0.7	2.6	0.6
November	-1.9	1.0	2.2	--
December	-1.5	0.6	2.9	--

Because the anomalous shifts were more pronounced from May 18, 1976 through the remainder of 1976 than in earlier months, more-extensive data adjustments were done on all 3-day images following May 15, 1976. These adjustments were of the form

$$T_B = a + b T_B' , \quad (A-3)$$

where T_B' is the uncorrected brightness temperature, and T_B is the corrected brightness temperature. The coefficients a and b were determined from the distribution of T_B' in selected ocean and high concentration ice areas. Because the variations were short-term, a separate a and b pair was determined for each 3-day map.

Partial confirmation of the validity of this normalization is provided by the consistency of the corrected brightness temperatures over the Antarctic and Greenland ice sheets, which undergo a seasonal variation but little interannual variation. The effect of the normalization on the Greenland ice sheet is shown in Figure A-5. Clearly the normalization procedure reduces the interannual variations. The absolute calibration of the brightness temperature is unimportant in this procedure, because the method sets a value of 0-percent ice concentration in known areas of open water and 100-percent ice concentration in sea ice regions where T_B has its highest values.

A.4 DATA MAPPING AND AVERAGING

The 3-day-average brightness temperature data are mapped from the orbital format given on the CBT tapes to a 293 by 293 grid of cells uniformly subdividing a polar stereographic map. The data are placed into cells according to the geographic coordinates of the center of the radiometer field of view. Overlapping data in a cell from separate orbits in the same 3-day period are averaged to give a single brightness temperature assumed to be located at the center of the cell.

A.4.1 Polar Stereographic Map

The mapping of the ESMR data is consistently done onto polar stereographic maps. Such maps are constructed by projecting points on the Earth's surface onto a plane tangent to the surface at either the

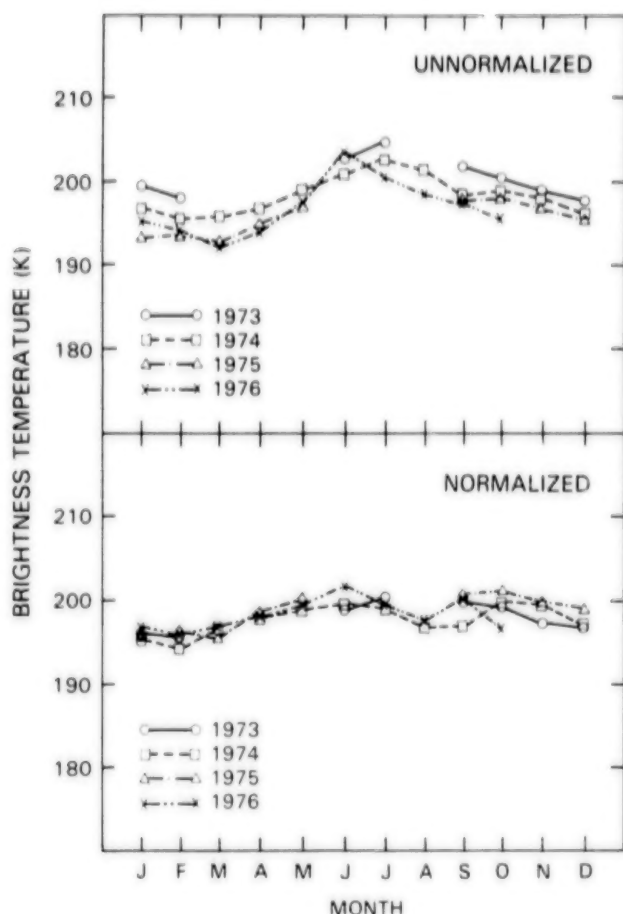


Figure A-5. Brightness temperatures with the highest frequency of occurrence in the central region of the Greenland ice sheet for each month of available data from 1973 through 1976, prior to and subsequent to normalization to correct for calibration shifts.

North or the South Pole, with the vertex of the projection being the opposite pole. This concept is illustrated in Figure A-6a, where a point B on the Earth's surface is projected to the polar plane at C.

The coordinates of each element on the projected map are determined as follows: The distance r from the pole to the projected point is calculated as

$$r = d \tan \alpha, \quad (\text{A-4})$$

where d is the diameter of the Earth, and α is the angular projection at the opposite pole expressed in terms of latitude, ϕ , as

$$\alpha = \frac{\gamma}{2} = \frac{90 - \phi}{2}. \quad (\text{A-5})$$

Using the axes and orientation of Figure A-6b for the Northern Hemisphere maps in this volume, the x and y components of the data element with latitude ϕ and east longitude λ are given by:

$$x = d \tan \left(\frac{90^\circ - \phi}{2} \right) \cos (\lambda - 45^\circ), \quad (\text{A-6})$$

$$y = d \tan \left(\frac{90^\circ - \phi}{2} \right) \sin (\lambda - 45^\circ). \quad (\text{A-7})$$

The standard map used for the images in this volume is a 293- by 293-square grid enclosing the 50°N latitude circle. For the coordinate system selected and a scaled value of d equal to 401.78, each point on the map can be expressed by a set of integer coordinates (J, I) defined by:

$$J = 147 + x + 0.5, \quad (\text{A-8})$$

$$I = 147 - y + 0.5. \quad (\text{A-9})$$

The standard format used on the computer tapes for the 293- by 293-gridded data is shown in Table A-4. On the tapes, each map is followed by an end-of-file mark, and data are preceded by a header record containing information about the data and the recording format (Table A-5).

A.4.2 Interpolation Procedures and Determination of Monthly Averages

Because of processing and calibration problems mentioned previously, some 3-day-average maps had as many as 20 percent of the data cells empty. The 20-percent data loss occurred much more frequently after the Nimbus 6 satellite launch in June 1975, when data became available only every other day. Fortunately, most of the empty cells are located outside the sea ice region. Nonetheless, for proper weighting of data in the monthly averaged maps, various interpolations were made to fill some of the empty cells in the 3-day-averaged maps. Because the Arctic data have considerably more data gaps than the Antarctic data, a more complete interpolation procedure was necessary than was used for *Antarctic Sea Ice, 1973-1976*.

To create the monthly averaged brightness temperature maps in the Arctic case, an initial spatial interpolation was carried out on all 3-day images. In

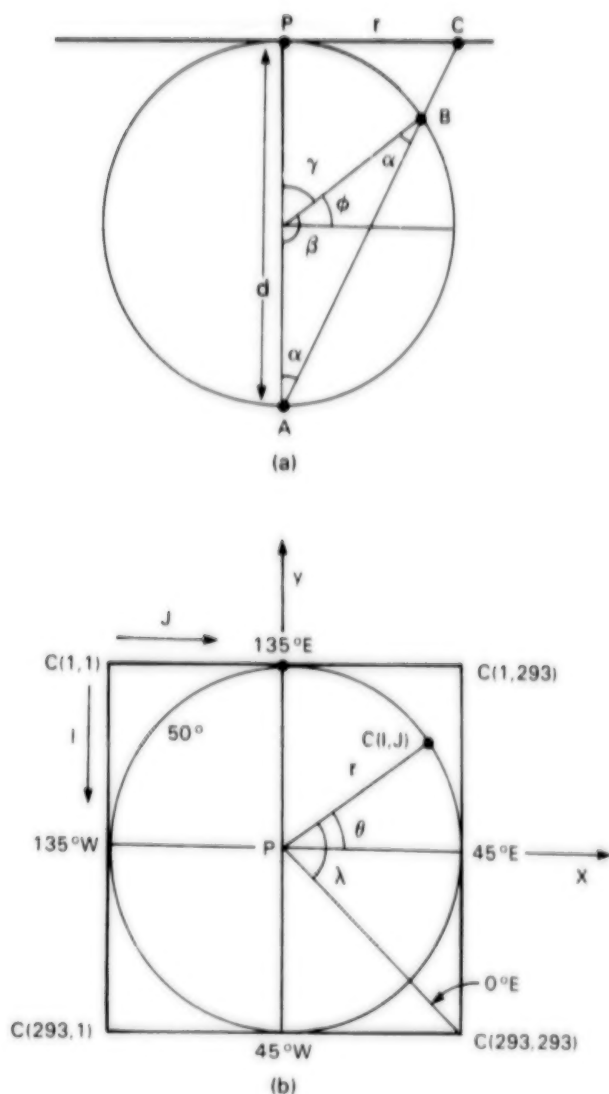


Figure A-6. Schematic diagram for polar stereographic mapping in the Northern Hemisphere.

this initial interpolation, all missing data points that were within two pixels of good data on two opposite sides (in the x direction, y direction, or diagonally) were filled in with interpolated values. Next, temporal interpolation was performed, with missing data filled in by time interpolation whenever there were good data both in either of the two previous 3-day periods and in either of the two subsequent 3-day periods. Following these two sets of interpolations, the 1976 calibration shift described in Section A.3.3 was made for each 3-day period from May 18 through October 30 of 1976. It was at this point that the initial weighted monthly averaging was performed, followed by the normalization to force ocean temperatures to peak at 138.3 K, described in Section A.3.3. The resulting monthly average

brightness temperature data were color coded and mapped into the images presented in Chapter 3. The brightness temperature data were then used in conjunction with climatological atmospheric temperatures to obtain monthly average sea ice concentrations by the method described in Section 3.6. The ice concentration maps are presented in Chapter 4.

A.4.3 Time Averaging and Spatial Summations of Ice Areas

The data shown in the monthly average ice concentration maps of Chapter 4 were further combined into 4-year-average monthly maps by averaging the data for individual years element by element:

$$\bar{C}_{ij}^M = \frac{1}{4} \sum_{N=3}^6 C_{ij}^{MN}, \quad (\text{A-10})$$

where C_{ij}^{MN} is the monthly average ice concentration in element ij for month M of year $1970 + N$, and \bar{C}_{ij}^M is the 4-year-average ice concentration for month M . In cases with missing months due to data gaps, the 4-year-average monthly maps become 3-year or 2-year averages instead, with the appropriate changes in equation A-10.

Chapter 4 also includes time series plots of sea ice extents and pseudo actual ice areas. The monthly average ice extent, E^{MN} , for month M of year $1970 + N$ is determined from the 293 by 293 grid of monthly average ice concentrations, C_{ij}^{MN} , as

$$E^{MN} = \sum_{i,j} a_{ij}, \quad (\text{A-11})$$

$$C_{ij}^{MN} \geq 15\%$$

where a_{ij} is the geographic area of element ij (calculated as a function of latitude and longitude), and the summation is taken over all map elements with monthly average pseudo ice concentration (calculated with $\epsilon_1 = 0.92$) of at least 15 percent. Similar summations are performed for determining the areal ice coverage in the other ice concentration categories of the form $C_{ij}^{MN} \geq c$, simply by replacing 15 percent in equation A-11 by the appropriate value of c .

Table A-4
Standard Format* for Polar Stereographic Maps

Record Number	Length (bytes)	Format	Number of Words	Description
1	1465	(See below) [†]	293	Heading (only the first 20 words are meaningful)
2	1465	293I5	293	Row 1 data (× 50)
3	1465	293I5	293	Observation population of row 1
4	1465	293I5	293	Row 2 data (× 50)
5	1465	293I5	293	Observation population of row 2
•	•	•	•	•
•	•	•	•	•
•	•	•	•	•
586	1465	293I5	293	Row 293 data (× 50)
587	1465	293I5	293	Observation population of row 293

*Data format 2 indicates standard format. (See Table A-5.)

[†] (9I5, 2A5, 8I5, A5, 255I5, 18I5)

The monthly average pseudo actual ice area is

$$A^{MN} = \sum_{i,j} C_{ij}^{MN} a_{ij} \quad (A-12)$$

$$C_{ij}^{MN} \geq 15\%$$

The error introduced in equation A-12 by the truncation of pseudo concentrations less than 15 percent is small because of the general sharpness of the ice boundary and the weighting by concentration in the summation. In most months this error is significantly less than the opposing error, generally leading to calculated ice areas which are too high, that would be introduced in the absence of any truncation. This opposing error would result from the variability of the brightness temperature over ice-free ocean, falsely indicating small ice concentrations far from the ice edge. The sea ice extents and pseudo actual ice

areas for the sea ice covers in the individual analysis regions of Figure 4-2 are also calculated by equations A-11 and A-12, although with i,j pairs ranging only over points in the individual region.

The equations to calculate average ice extents \bar{E}^M and average pseudo actual ice areas \bar{A}^M from the maps for the 4-year-average monthly conditions are similar to equations A-11 and A-12:

$$\bar{E}^M = \sum_{i,j} a_{ij} \quad (A-13)$$

$$\bar{C}_{ij}^M \geq 15\%$$

and

$$\bar{A}^M = \sum_{i,j} \bar{C}_{ij}^M a_{ij} \quad (A-14)$$

$$\bar{C}_{ij}^M \geq 15\%$$

Table A-5
Header Record for Polar Stereographic Maps

Word	Type	Number of Bytes/Word	Description
1	15	4	Projection type (1 for polar stereographic)
2	15	4	Number of columns (293)
3	15	4	Number of rows (293)
4	15	4	Scale (2.5×10^6)
5	15	4	Latitude enclosed (50.0°)
6	15	4	Greenwich orientation (45°)
7	15	4	Radius of the Earth
8	15	4	J-coordinate of the pole (147)
9	15	4	I-coordinate of the pole (147)
10-11	A5	4	Data type* (TB, ICE CON, SURF TEMP, or CLIM PRES)
12	15	4	Start time (day)
13	15	4	Start time (hour)
14	15	4	Start time (minutes)
15	15	4	Stop time (day)
16	15	4	Stop time (hour)
17	15	4	Stop time (minutes)
18	15	4	Year data was collected
19	15	4	Data format (2 for standard format)
20	A5	4	Data identification
21-293	15	4	Meaningless

*The abbreviations used in words 10 and 11 for the data variables are as follows: TB is brightness temperature, ICE CON is ice concentration, SURF TEMP is mean monthly climatological surface air temperature, and CLIM PRES is mean monthly climatological sea-level pressure.

In Chapter 4, the difference is noted between the 4-year-average extent (equation A-13) and the average of the extents for the 4 individual years, which is

$$\begin{aligned}
 \langle E^M \rangle &= \frac{1}{4} \sum_{N=3}^6 E^{MN} \\
 &= \frac{1}{4} \sum_{N=3}^6 \sum_{i,j} a_{ij} \quad (A-15) \\
 &\quad C_{ij}^{MN} \geq 15\%
 \end{aligned}$$

A similar difference occurs for the pseudo actual ice areas, for which the average for 4 years is

$$\langle A^M \rangle = \frac{1}{4} \sum_{N=3}^6 \sum_{i,j} C_{ij}^{MN} a_{ij} \quad (A-16)$$

$C_{ij}^{MN} \geq 15\%$

The differences derive from the truncation to exclude data elements with calculated pseudo ice concentrations below 15 percent. Near the ice edge, \bar{C}_{ij}^M may be less than 15 percent even though some years have ice concentrations exceeding 15 percent. This would contribute toward making $\langle E^M \rangle$ greater than \bar{E}^M and $\langle A^M \rangle$ greater than \bar{A}^M . By contrast, at other locations near the ice edge, \bar{C}_{ij}^M may be equal to or greater than 15 percent although some years have C_{ij}^{MN} less than 15 percent, contributing toward making $\langle E^M \rangle$ less than \bar{E}^M and $\langle A^M \rangle$ less than \bar{A}^M . Because of these differences, averages of the areas for the individual years (e.g., $\langle E^M \rangle$ and $\langle A^M \rangle$) have better absolute accuracy than the areas from the 4-year-average maps (e.g., \bar{E}^M and \bar{A}^M).

A.5 REFERENCES

Comiso, J. C., and H. J. Zwally, Corrections for anomalous time dependent shifts in the brightness temperature from the Nimbus 5 ESMR, NASA TM-82055, Greenbelt, Maryland, 18 pp., 1980.

Wilheit, T. T., The Electrically Scanning Microwave Radiometer (ESMR) experiment, in *Nimbus 5 User's Guide*, NASA/Goddard Space Flight Center, Greenbelt, Maryland, 59-105, 1972.

Wilheit, T. T., ESMR corrections to the user's guide, in *Nimbus 5 Data Catalog*, 3, NASA/Goddard Space Flight Center, Greenbelt, Maryland, 5-2 through 5-6, 1973.

Zwally, H. J., J. C. Comiso, C. L. Parkinson, W. J. Campbell, F. D. Carsey, and P. Gloersen *Antarctic Sea Ice, 1973-1976: Satellite Passive-Microwave Observations*, NASA SP-459, National Aeronautics and Space Administration, Washington, D.C., 206 pp., 1983.

APPENDIX B

ICE EDGE CONTOUR MAPS

This appendix presents contour maps of the ice edge on a monthly averaged basis for each month with available ESMR data over the 4-year period 1973 through 1976 (Figures B-1 through B-4). The ice edge is defined as the 14-percent ice concentration contour, visible on the color-coded monthly averaged ice concentration images of Chapter 4 as the color break between the two lightest shades of blue on the color scale. The ice edges not only are among the most important variables for climate studies but are believed to be depicted very well by the ESMR data, having much smaller error bars than the error bars for contours of higher ice concentration

amounts. The ice edges are contoured here in black-and-white format for easy reproducibility.

In addition to the ice edges for the individual months, the monthly ice edges for the 4-year-averaged data are also presented (Figure B-5). As with the corresponding color-coded images in Figures 4-3 through 4-8, these monthly multiyear averages are generally 4-year averages, but sometimes 3- or even 2-year averages, depending on data availability. In each case, the years involved in the averaging are indicated on the ice-edge map.

PRECEDING PAGE BLANK NOT FILMED

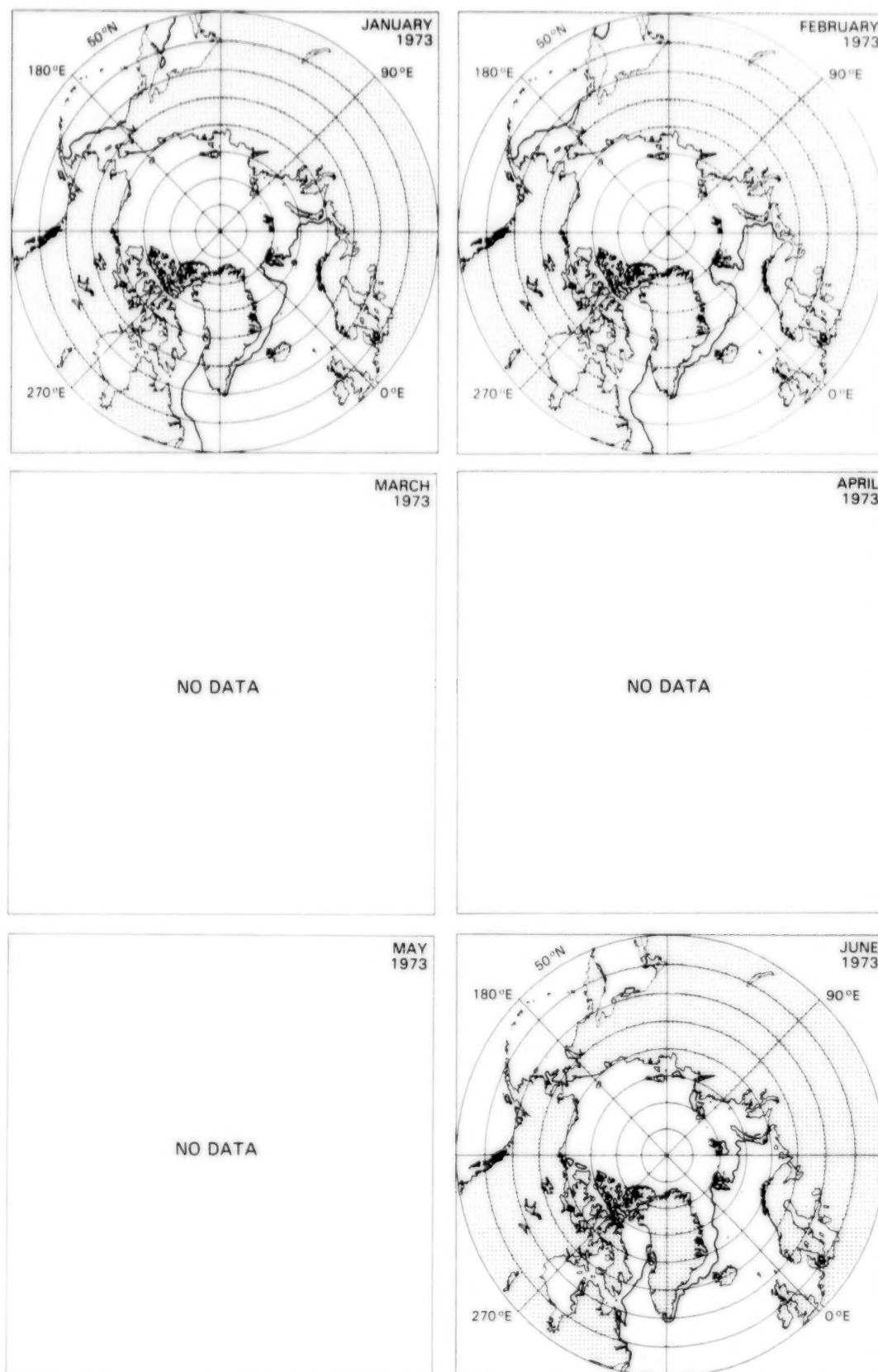


Figure B-1a. Mean monthly ice extents for January through June 1973.

ORIGINAL PAGE IS
OF POOR QUALITY

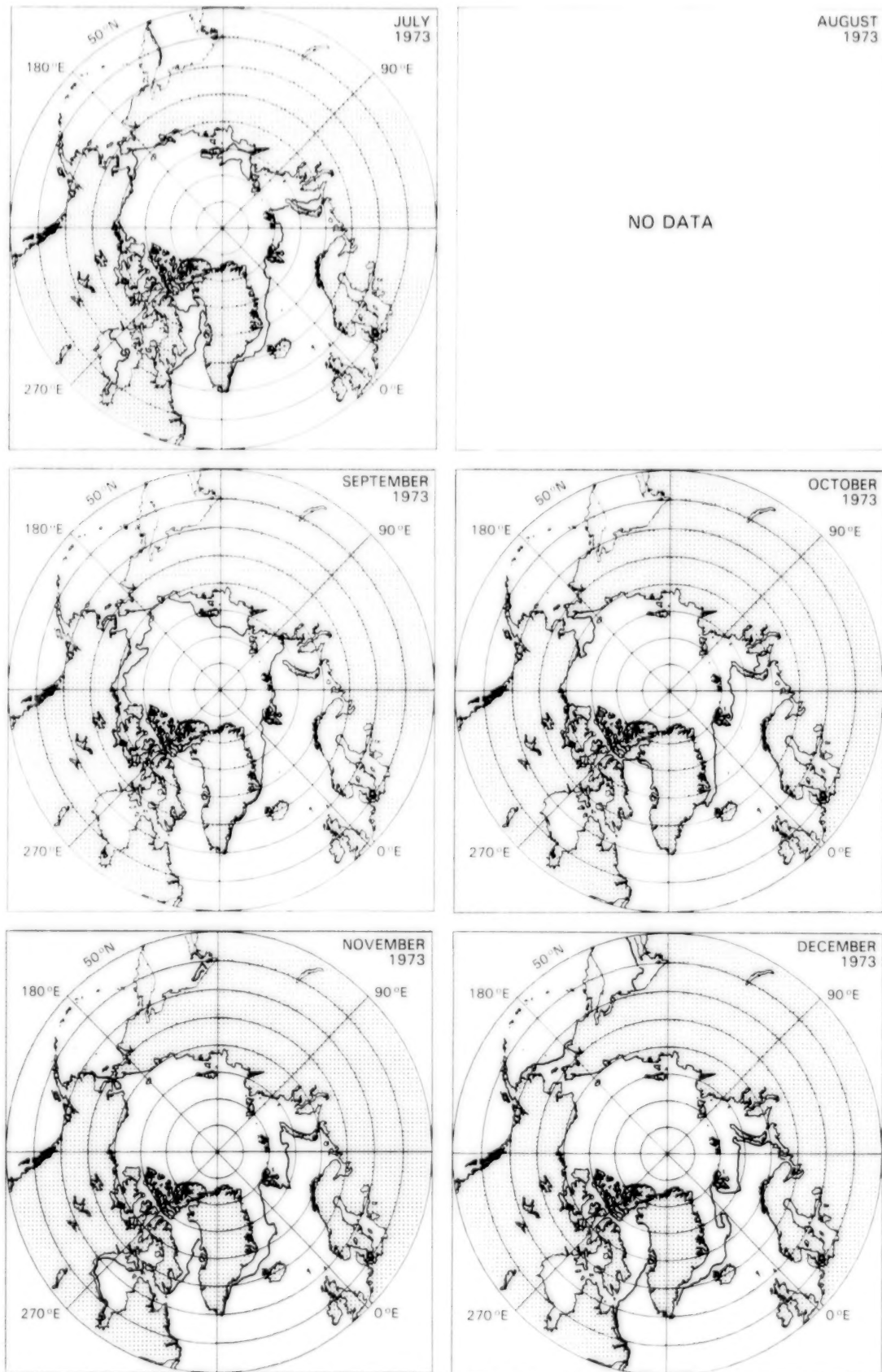


Figure B-1b. Mean monthly ice extents for July through December 1973.

ORIGINAL PAGE IS
OF POOR QUALITY

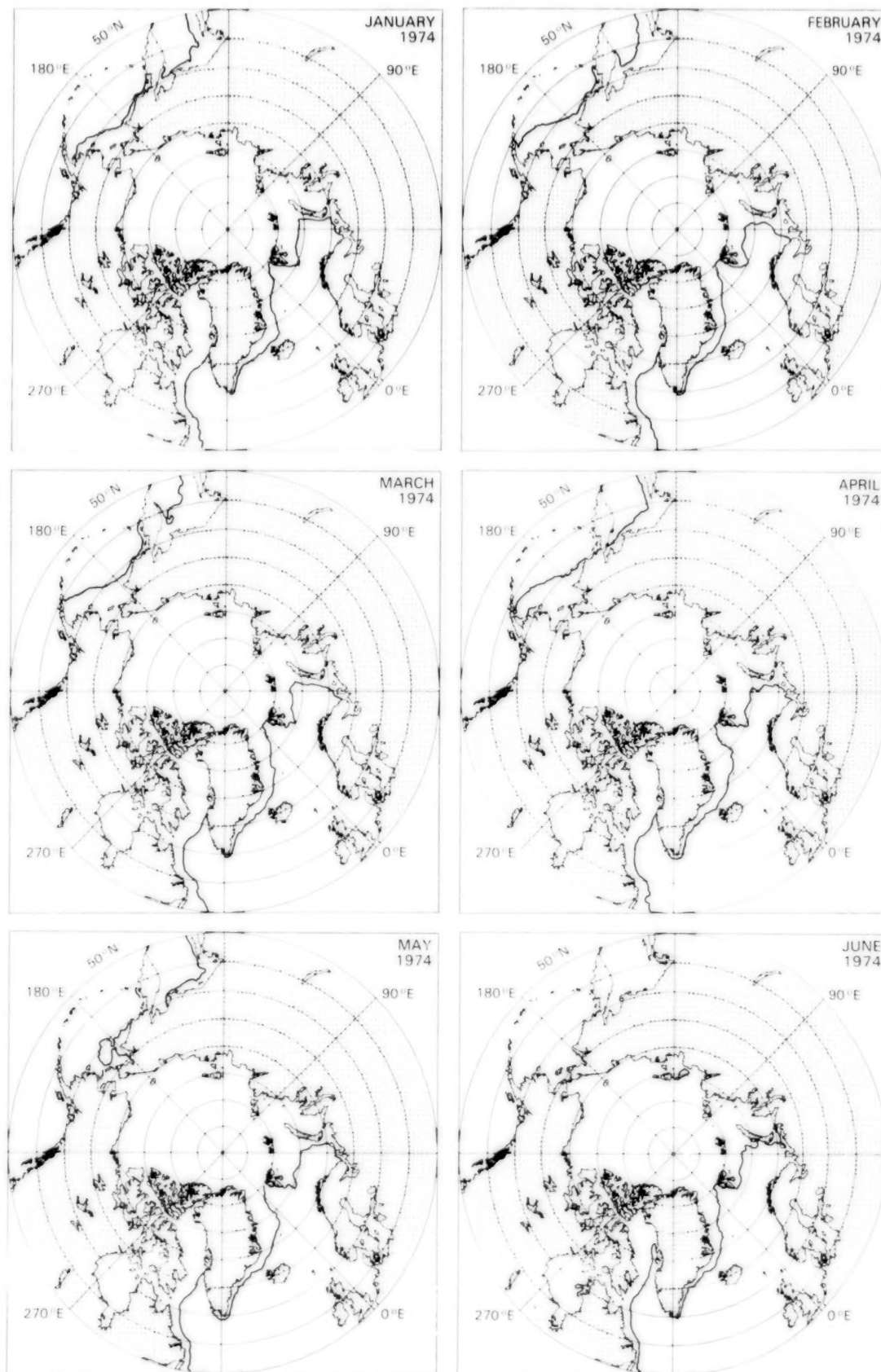


Figure B-2a. Mean monthly ice extents for January through June 1974.

ORIGINAL PAGE IS
OF POOR QUALITY

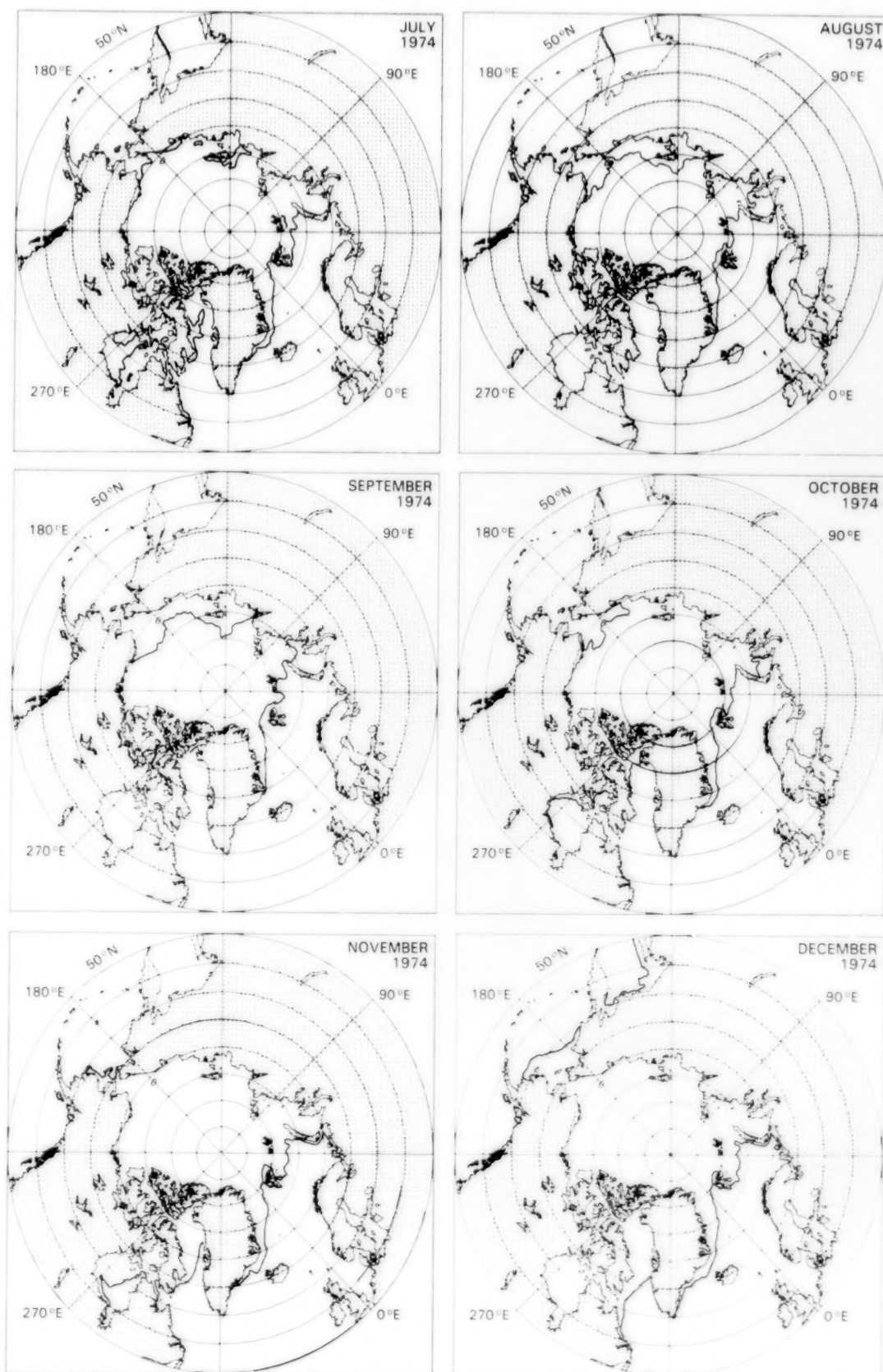


Figure B-2b. Mean monthly ice extents for July through December 1974.

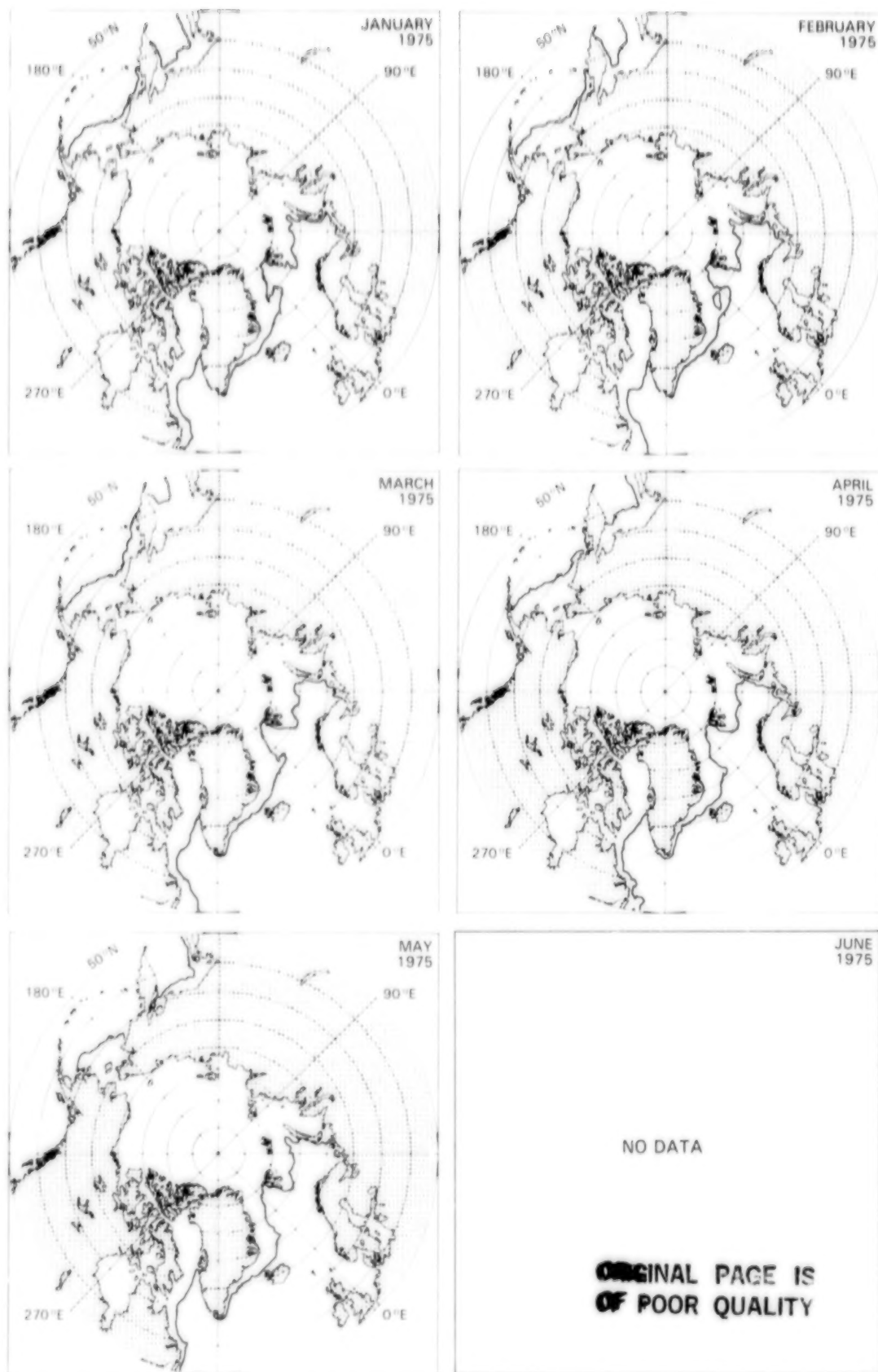


Figure B-3a. Mean monthly ice extents for January through June 1975.

ORIGINAL PAGE IS
OF POOR QUALITY

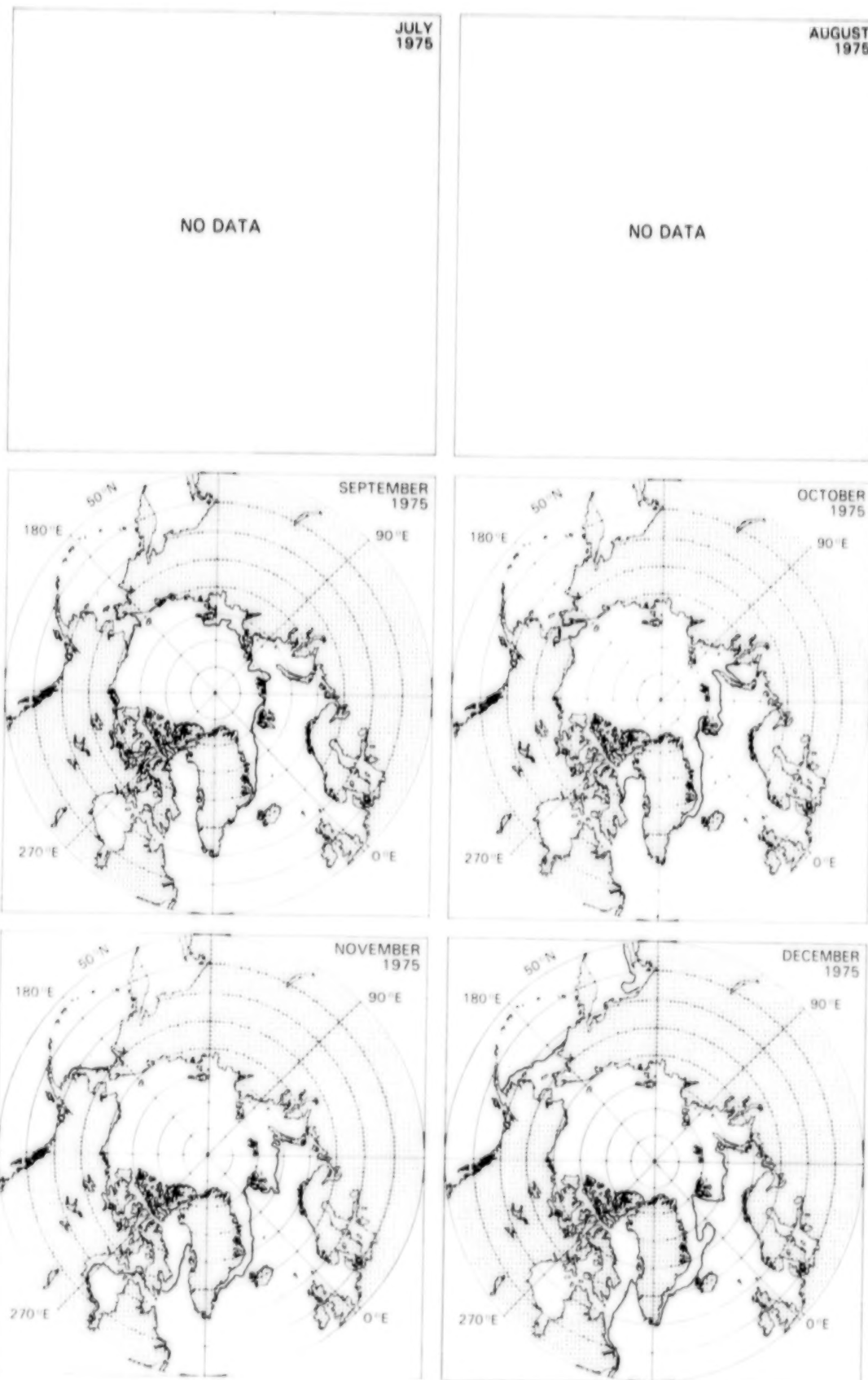


Figure B-3b. Mean monthly ice extents for July through December 1975.

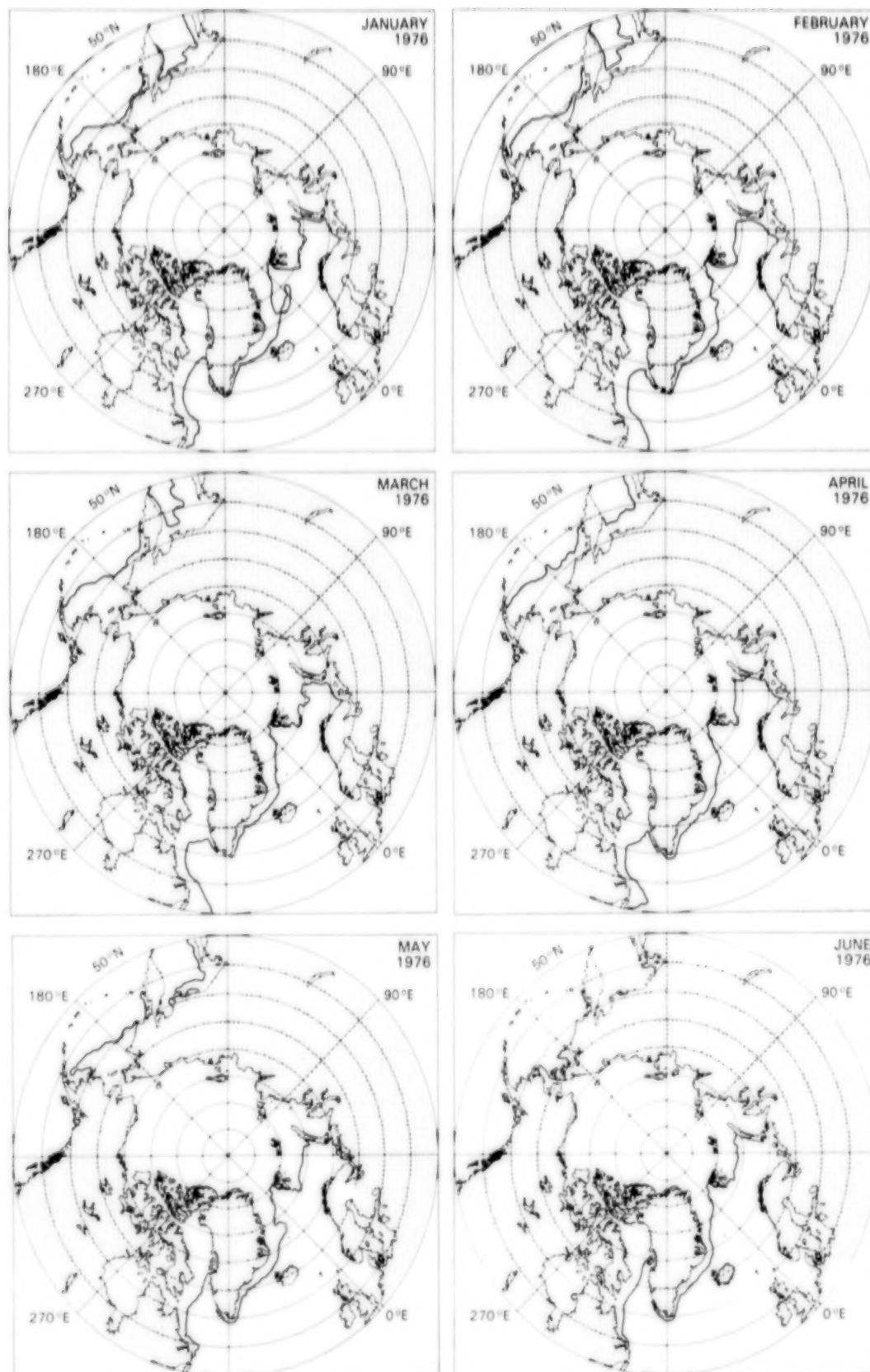


Figure B-4a. Mean monthly ice extents for January through June 1976.

ORIGINAL PAGE IS
OF POOR QUALITY

ORIGINAL PAGE IS
OF POOR QUALITY

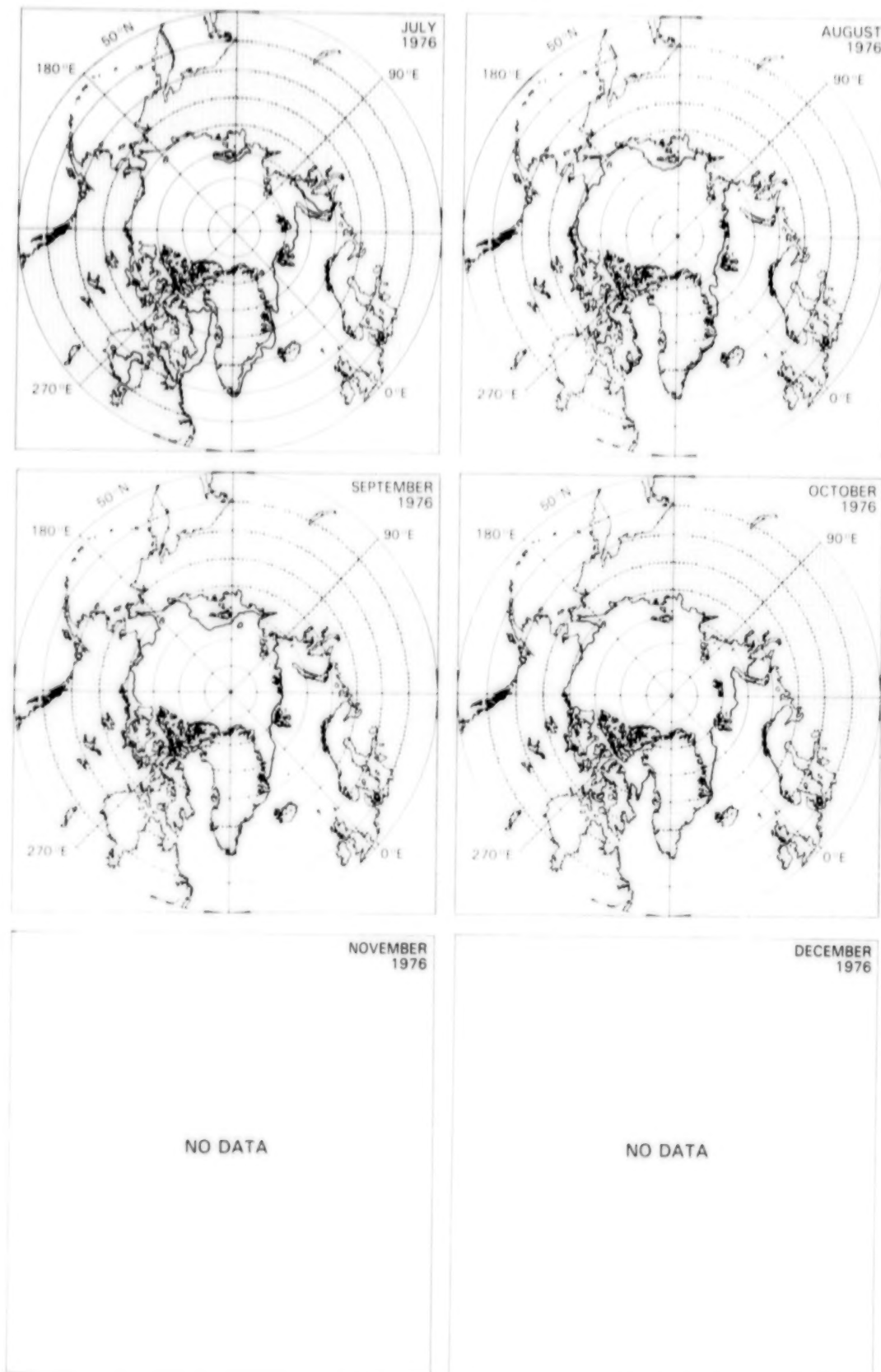


Figure B-4b. Mean monthly ice extents for July through December 1976.

ORIGINAL PAGE IS
OF POOR QUALITY

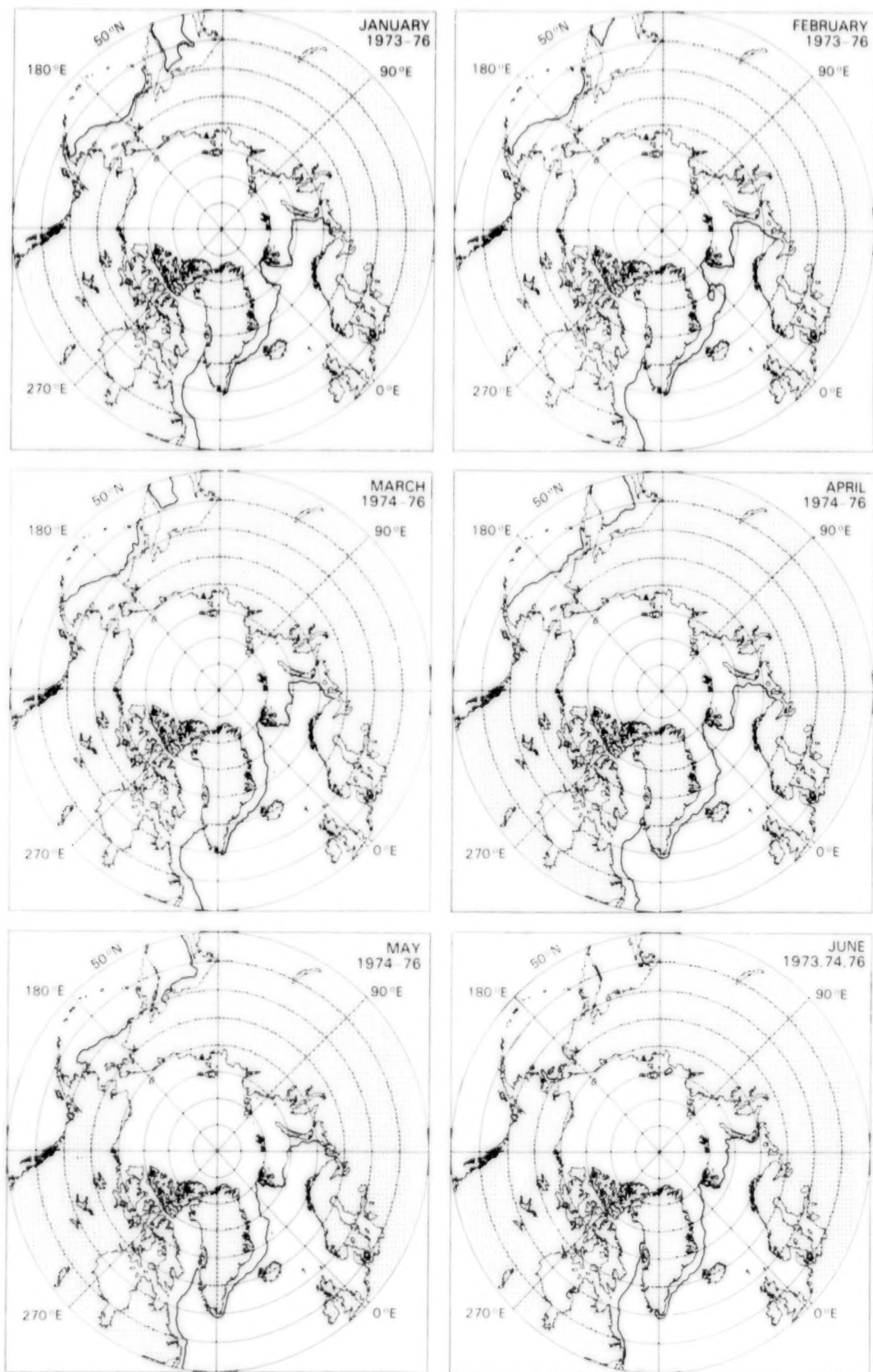


Figure B-5a. Mean monthly ice extents for January through June, averaged for the years indicated.

ORIGINAL PAGE IS
OF POOR QUALITY

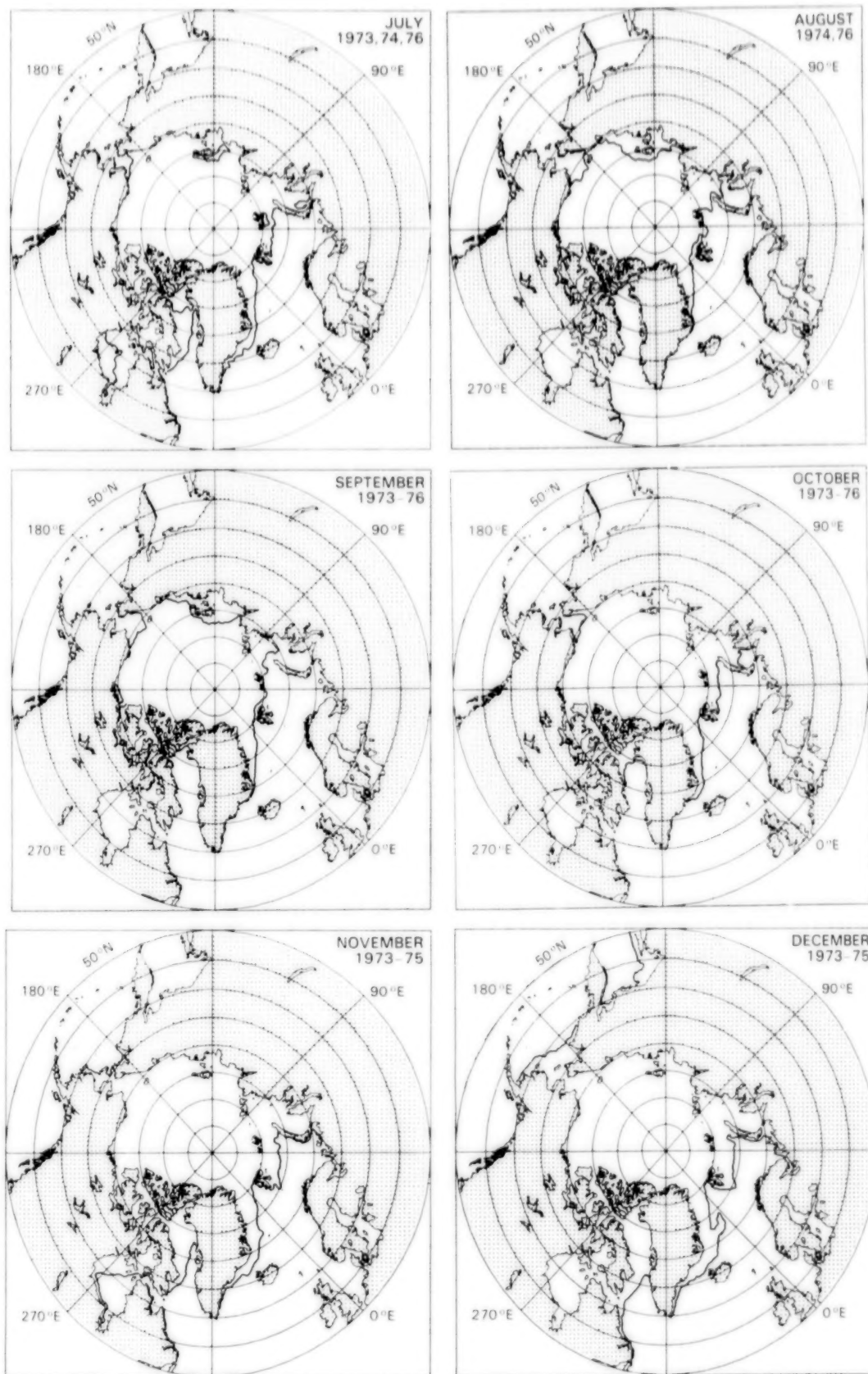


Figure B-5b. Mean monthly ice extents for July through December, averaged for the years indicated.

APPENDIX C

AREAL DISTRIBUTIONS OF ICE CONCENTRATIONS

This appendix presents 156 selected areal distributions of the calculated pseudo sea ice concentrations of Chapter 4. In addition to showing seasonal, regional, and interannual variations in these distributions, the plots help to confirm the overall effectiveness of the ice concentration calculations and the consistency in the normalization of the data as described in Appendix A.

Figures C-1a and C-1b show the areal distributions over the sum of the eight regions of Figure 4-2 for the complete yearly cycle obtained from the 4-year-average monthly maps. The large ocean area not covered by ice is reflected in the peak occurring near 0-percent pseudo ice concentration in every month. In each month, the distributions are approximately level from 20- to 60-percent pseudo ice concentration and are substantially higher within the 60- to 100-percent concentration range. In this latter range, the seasonal variation of the ice is clearly evident, with minimum ice cover in August and September and maximum ice cover in February and March. The occurrence of double ice peaks in December, January, and February reflects the existence of two distinct ice types: multiyear ice with a lower emissivity and first-year ice with a higher emissivity. In most months the distributions also show maximum pseudo ice concentrations somewhat greater than 100 percent. These unrealistically high values reflect in part the uncertainties associated with spatial and temporal fluctuations in ice emissivity and physical temperature. Only from July through September are the maximum pseudo ice concentrations less than 100 percent, which is consistent with reductions in both ice concentration and emissivity during the summer period.

Figures C-2a and C-2b show the March, June, September, and December distributions for each year

for the sum of the eight analysis regions of Chapter 4 (Figure 4-2), and Figures C-3 through C-10 show the corresponding sets of plots for each individual region. Significant year-to-year and seasonal variations are clearly evident in the distributions, especially above 60-percent ice concentration. These variations depict in a different form some of the seasonal and interannual variations described in detail in Chapter 4.

In the Arctic Ocean, open water areas are expected to be minimal in winter and have been estimated to cover no more than 11 percent of the region during winter. The March and December plots in Figures C-3a and C-3b indeed show that all the Arctic Ocean data in these months have high pseudo ice concentrations. Furthermore, the plots generally have double peaks, believed to correspond to the first-year and multiyear ice types. The data representing 70- to 85-percent pseudo ice concentrations are generally observations from the central Arctic, where multiyear ice is prevalent, with emissivities of approximately 0.84 rather than the 0.92 value used in the pseudo ice concentration calculations. Thus, as discussed in Chapters 3 and 4, the real ice concentrations are considerably higher than the 70- to 85-percent pseudo ice concentrations shown in the plots. In June, the width of the consolidated ice peak is narrower than the widths in March and December because of surface melt, which tends to reduce the contrast in emissivity between multiyear ice and first-year ice (Chapter 3). In September, most of the ice has pseudo ice concentrations between 60 and 80 percent. Although this is consistent with the expected lower ice concentrations during the summer breakup, the lower pseudo ice concentrations are also in part due to meltponded surfaces.

As expected, for the four seasonal sea ice regions with essentially no multiyear ice (the Sea of Okhotsk,

ALL REGIONS

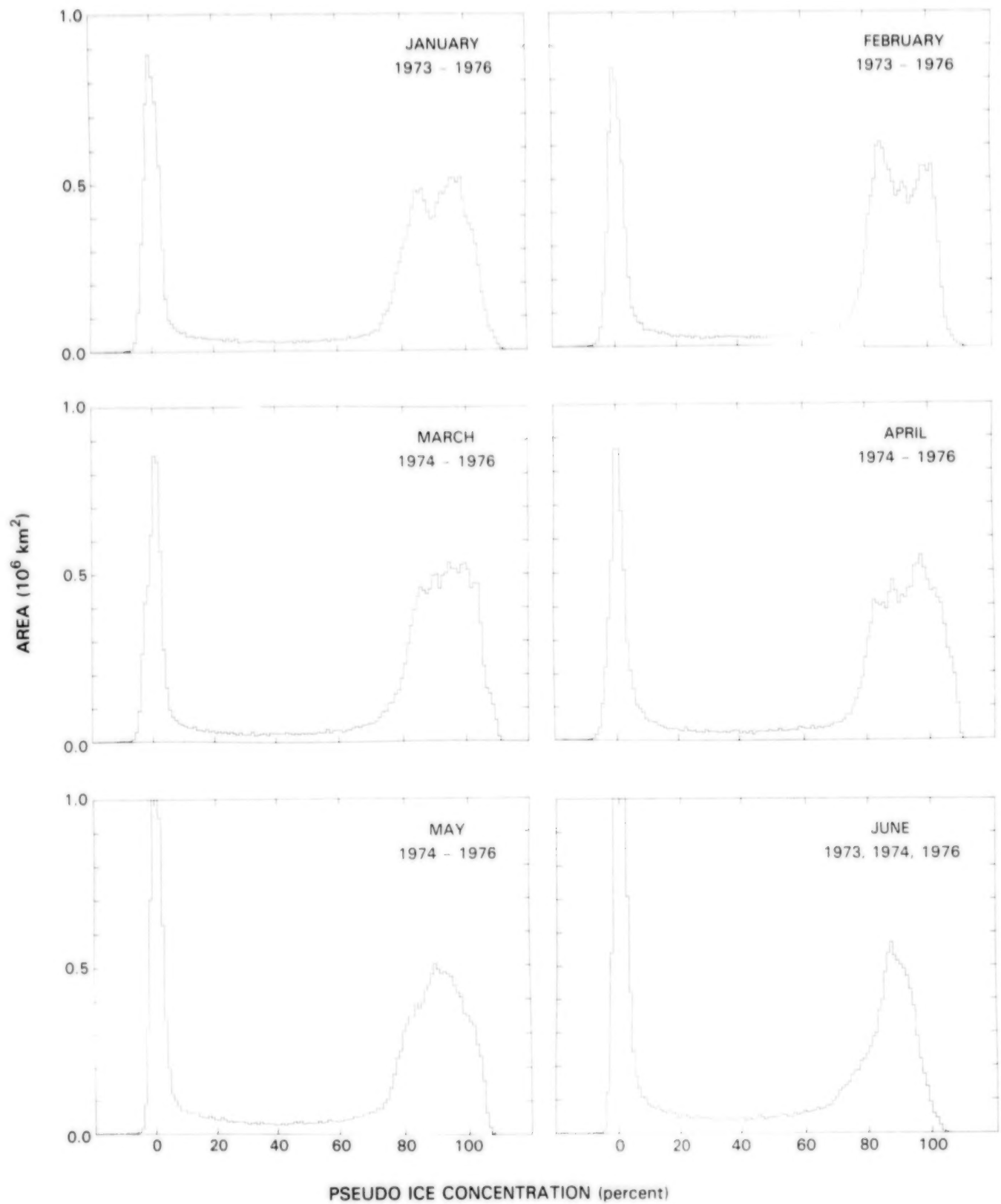


Figure C-1a. Areal distributions of pseudo ice concentrations for the Northern Hemisphere for the 4-year-average (1973-1976) monthly values from January to June. The Northern Hemisphere is represented by the sum of the eight regions of Figure 4-2.

ALL REGIONS

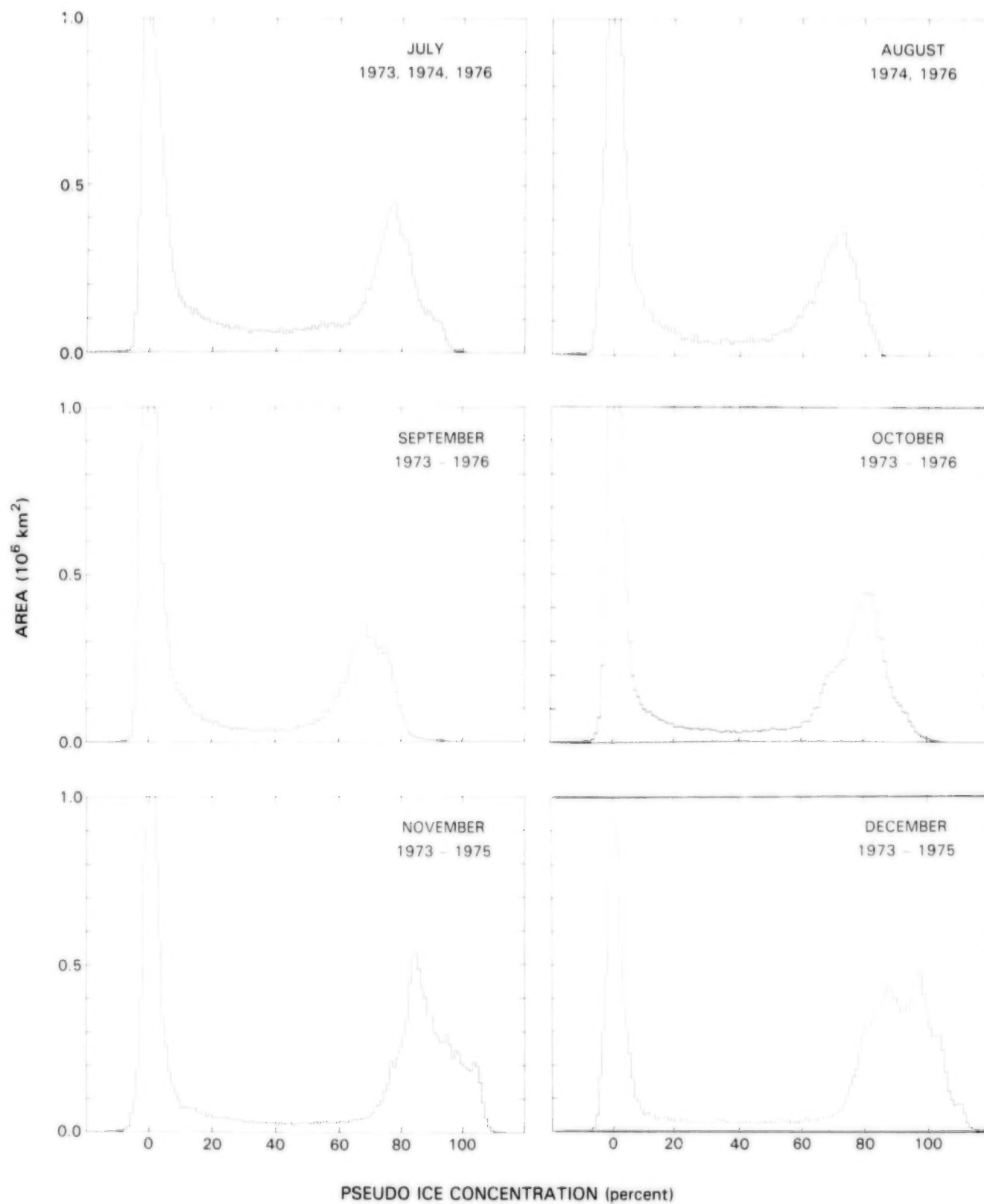


Figure C-1b. Areal distributions of pseudo ice concentrations for the Northern Hemisphere for the 4-year-average (1973-1976) monthly values from July to December. The Northern Hemisphere is represented by the sum of the eight regions of Figure 4-2.

ALL REGIONS

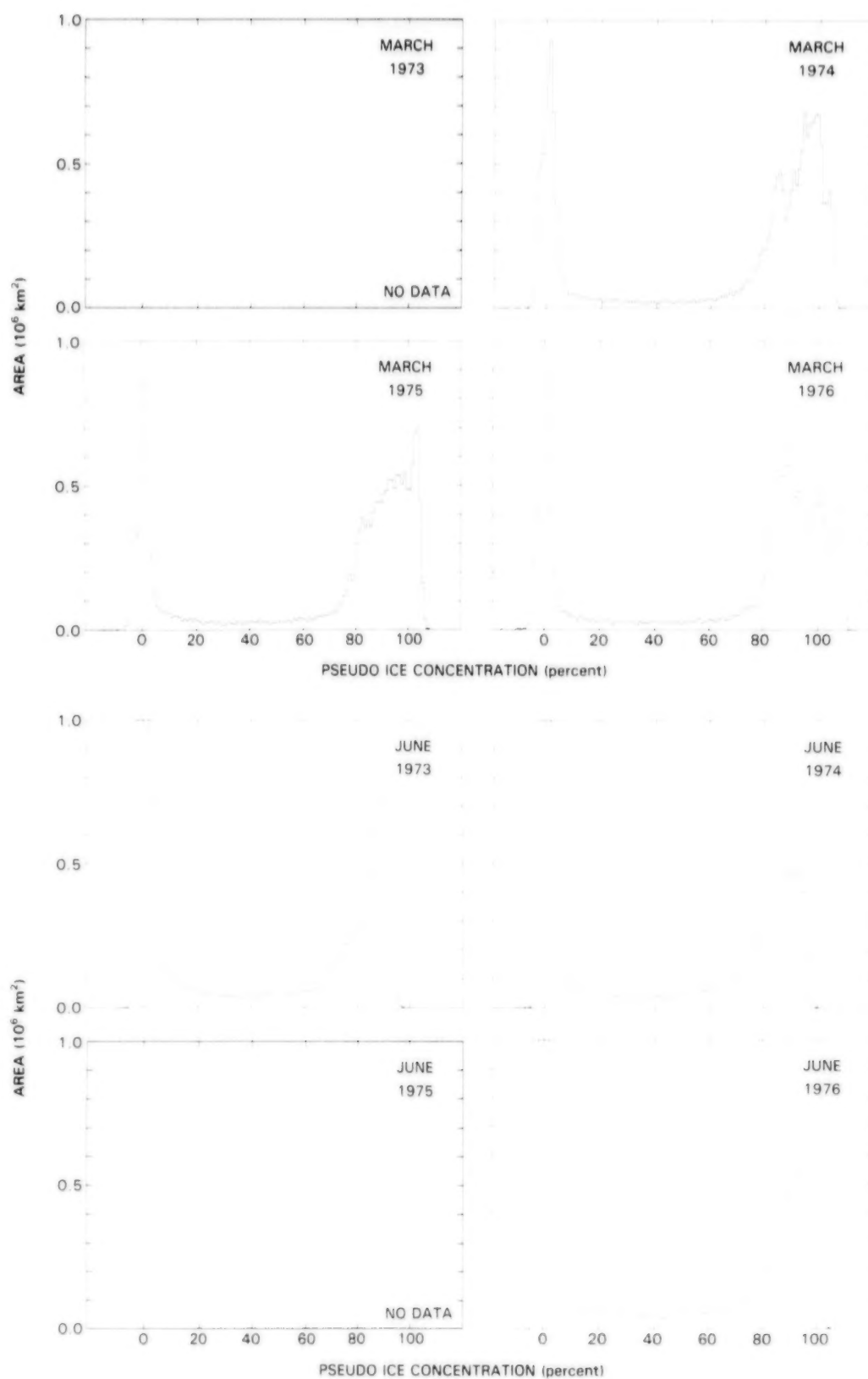


Figure C-2a. Year-to-year comparison of areal distributions of pseudo ice concentrations for the sum of the eight regions of Figure 4-2 for March and June.

ALL REGIONS

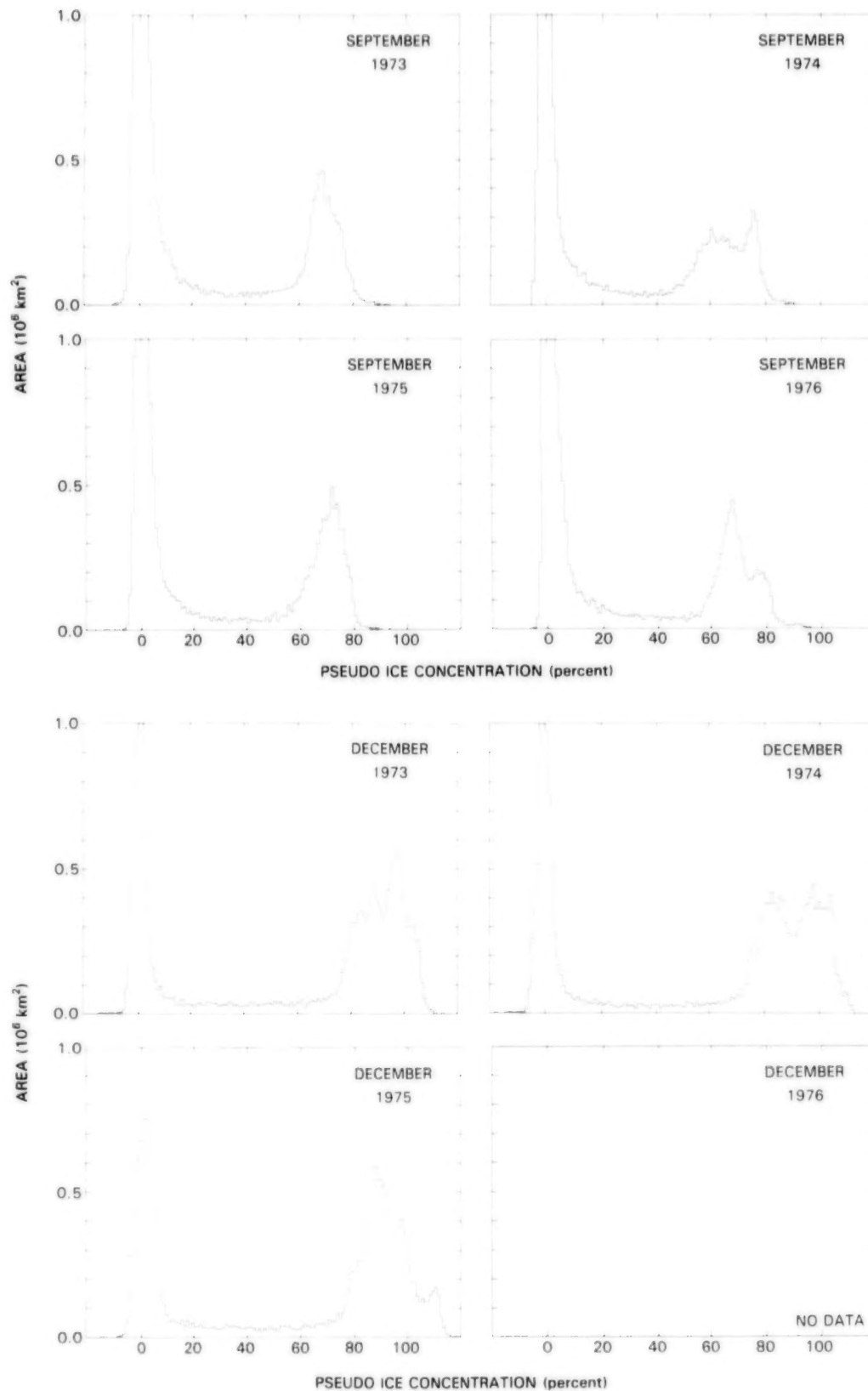


Figure C-2b. Year-to-year comparison of areal distributions of pseudo ice concentrations for the sum of the eight regions of Figure 4-2 for September and December.

ARCTIC OCEAN

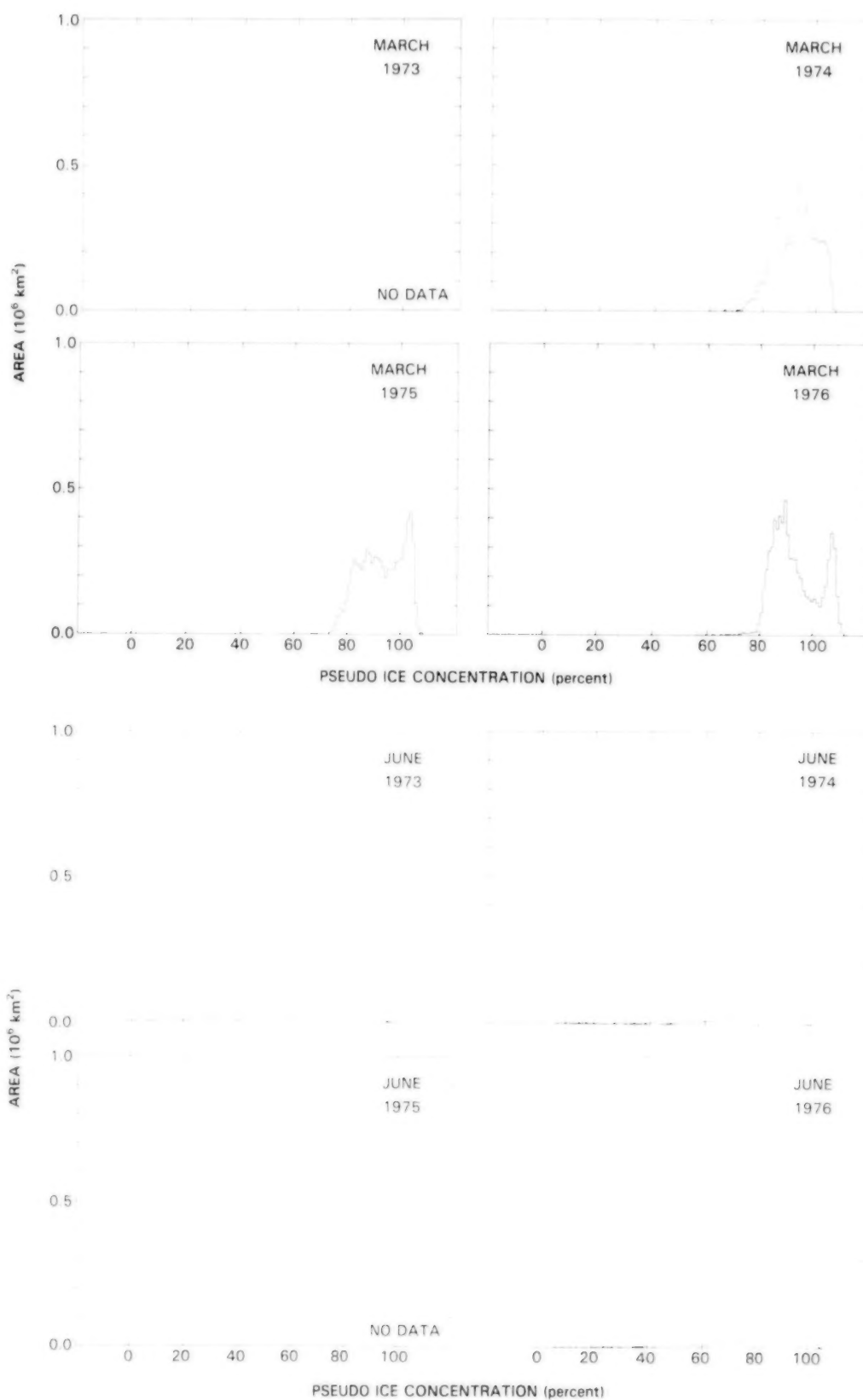


Figure C-3a. Year-to-year comparison of areal distributions of pseudo ice concentrations for the Arctic Ocean for March and June.

ARCTIC OCEAN

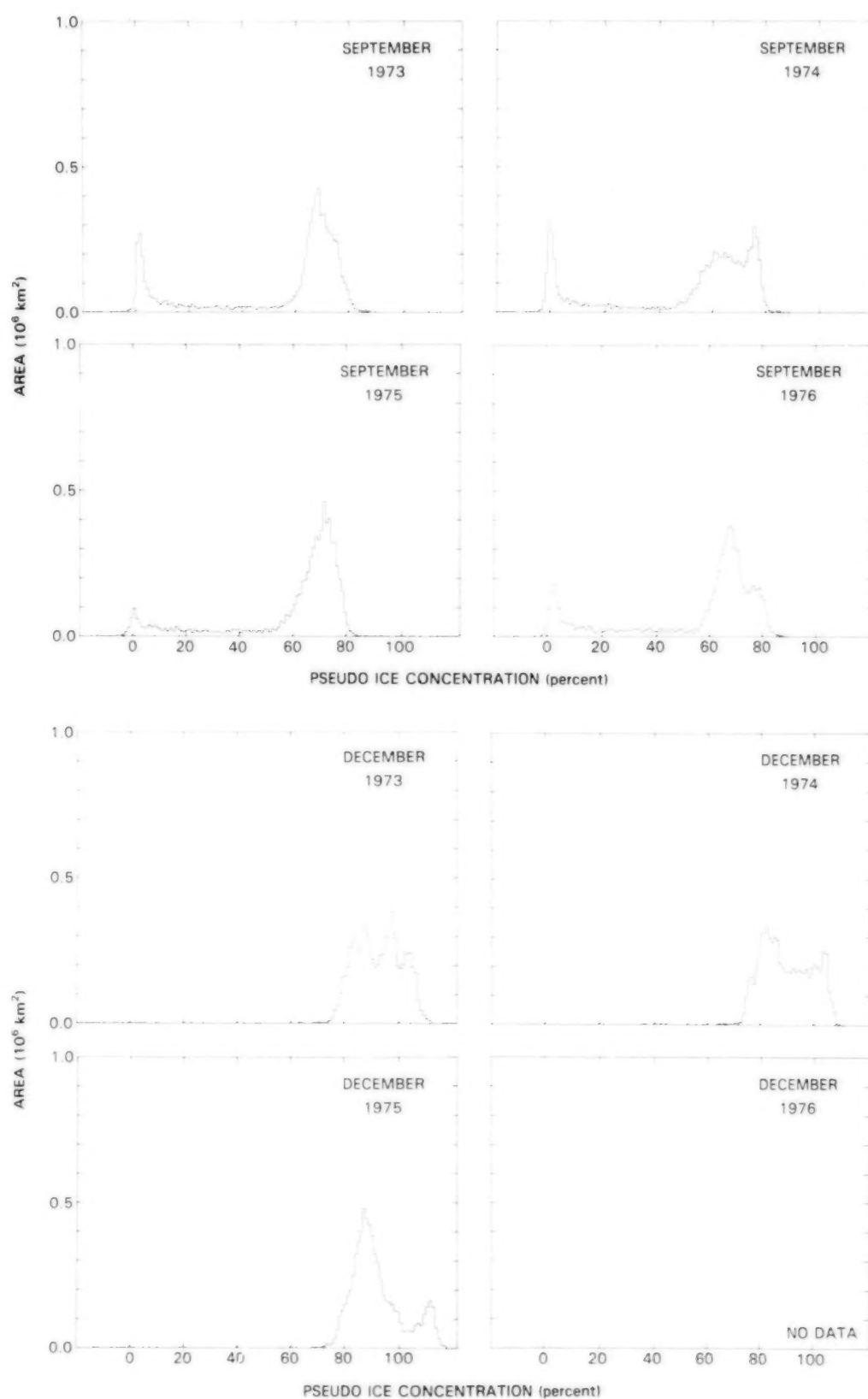


Figure C-3b. Year-to-year comparison of areal distributions of pseudo ice concentrations for the Arctic Ocean for September and December.

SEA OF OKHOTSK

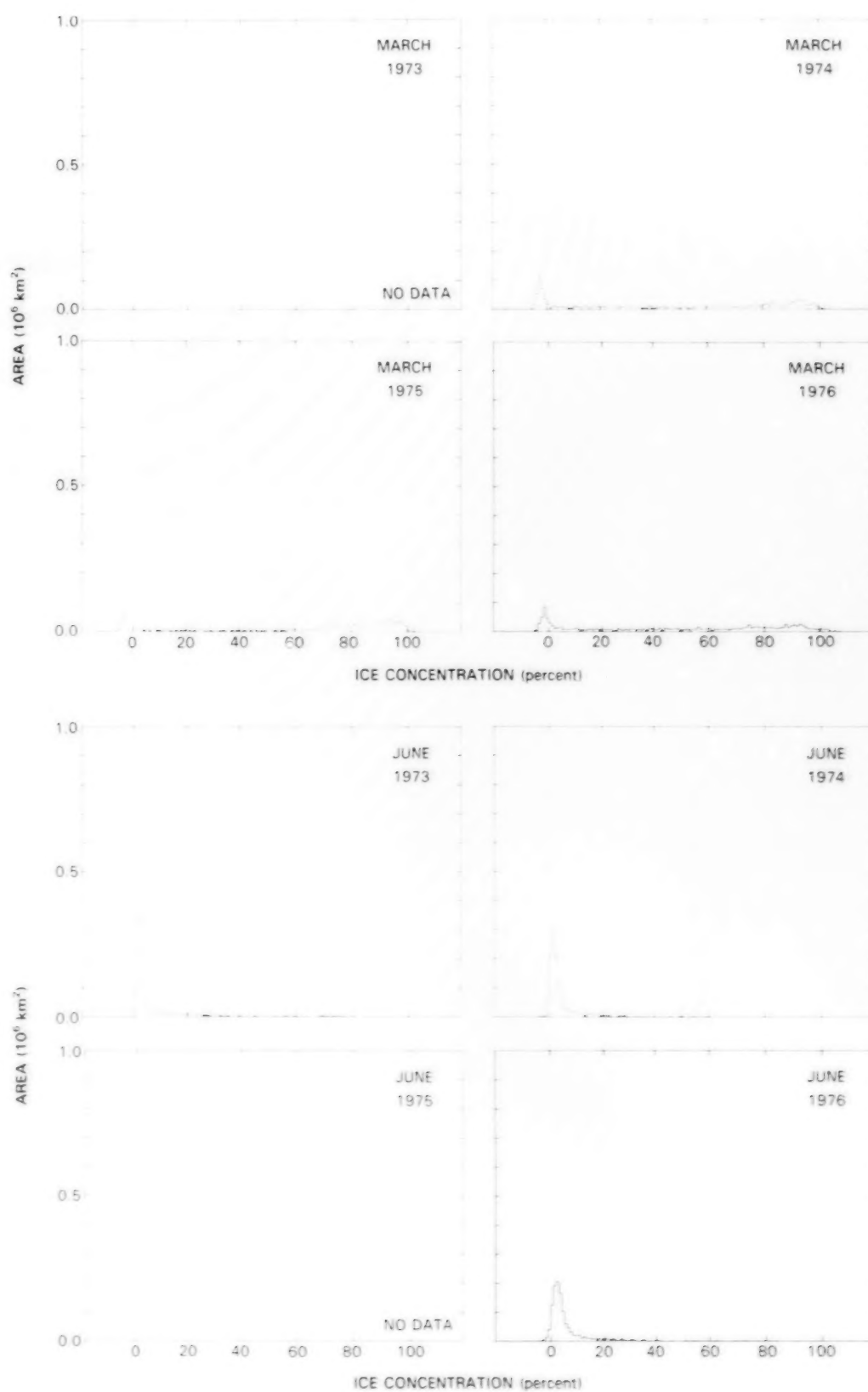


Figure C-4a. Year-to-year comparison of areal distributions of ice concentrations for the Sea of Okhotsk for March and June.

SEA OF OKHOTSK

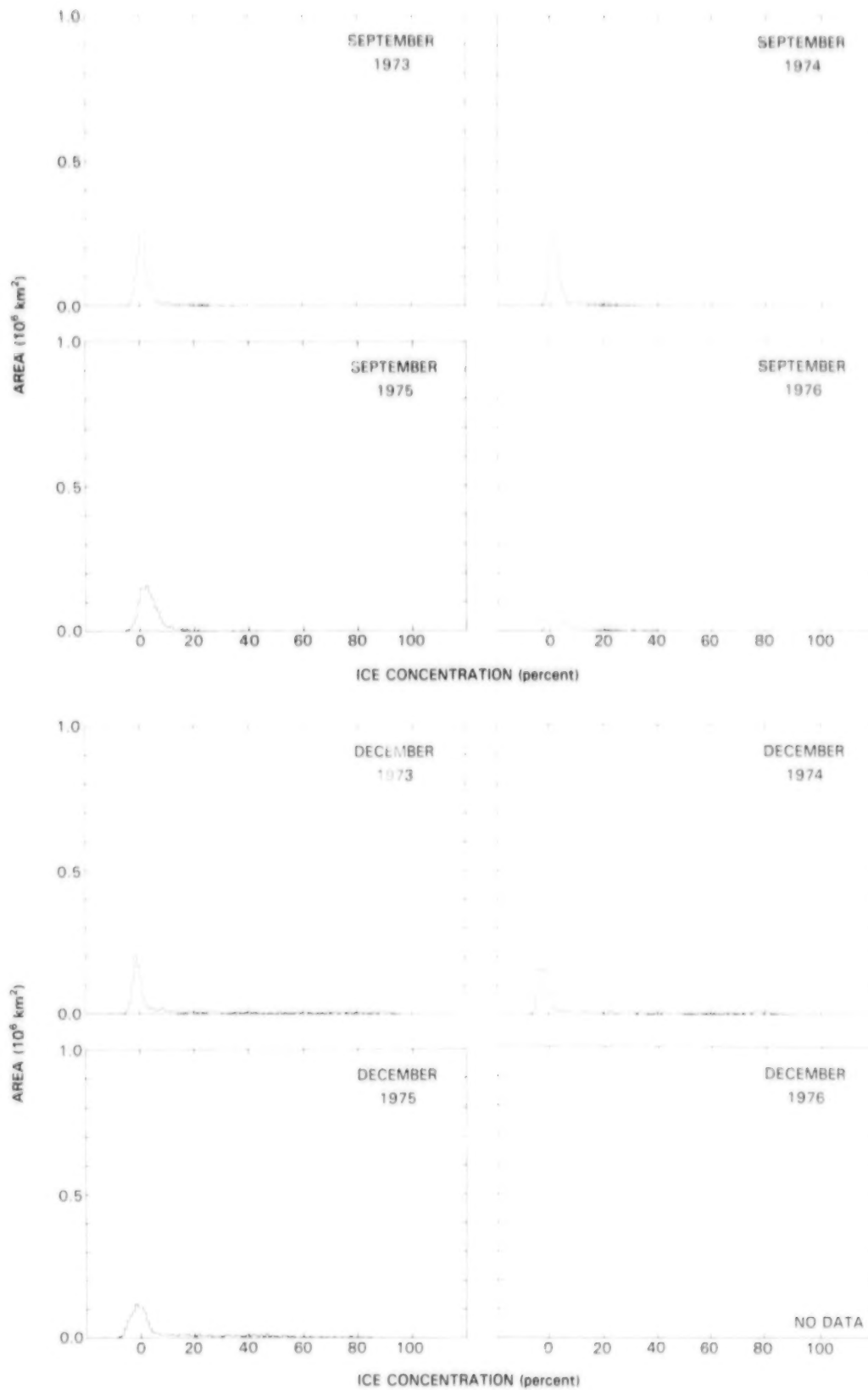


Figure C-4b. Year-to-year comparison of areal distributions of ice concentrations for the Sea of Okhotsk for September and December.

BERING SEA

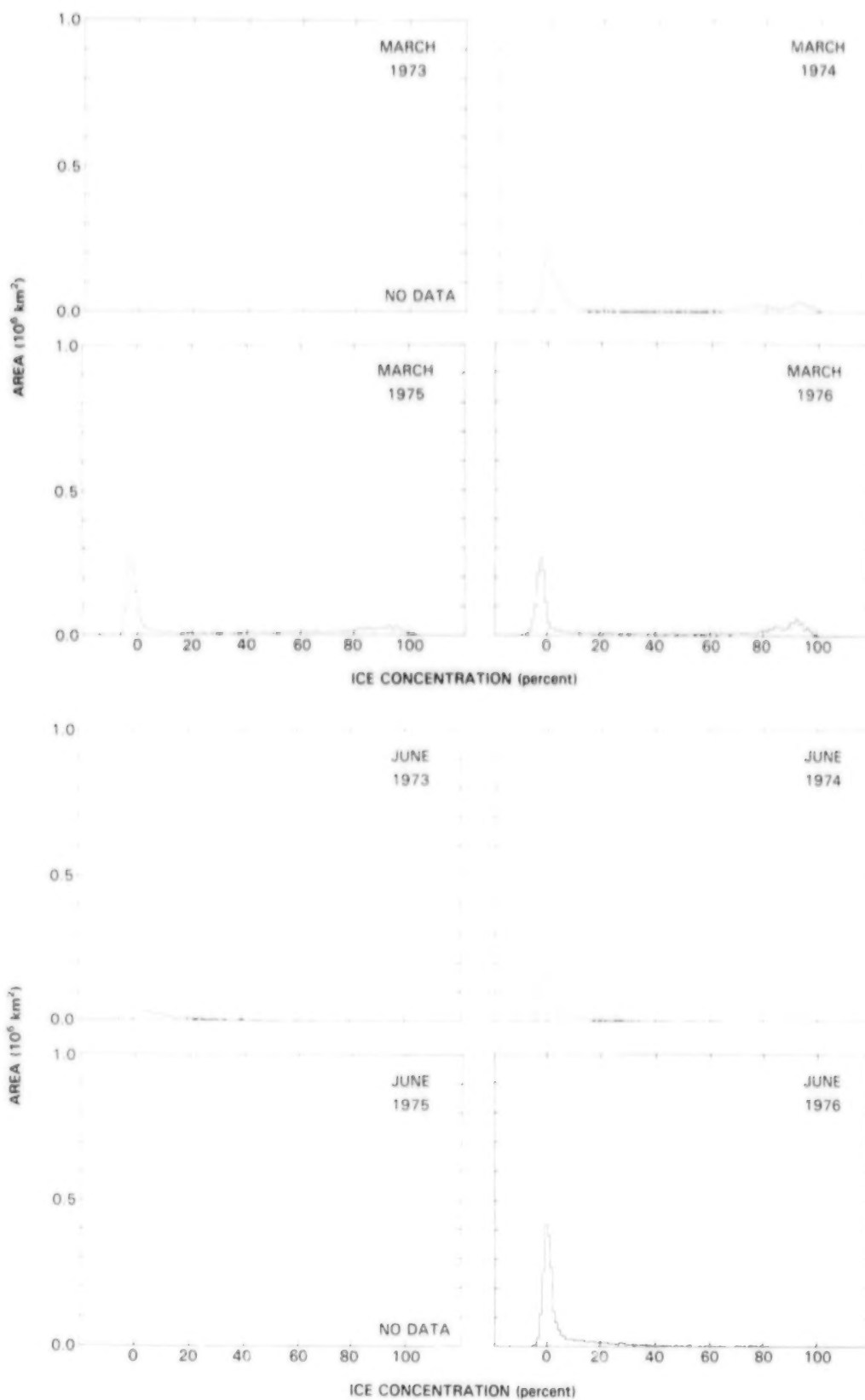


Figure C-5a. Year-to-year comparison of areal distributions of ice concentrations for the Bering Sea for March and June.

BERING SEA

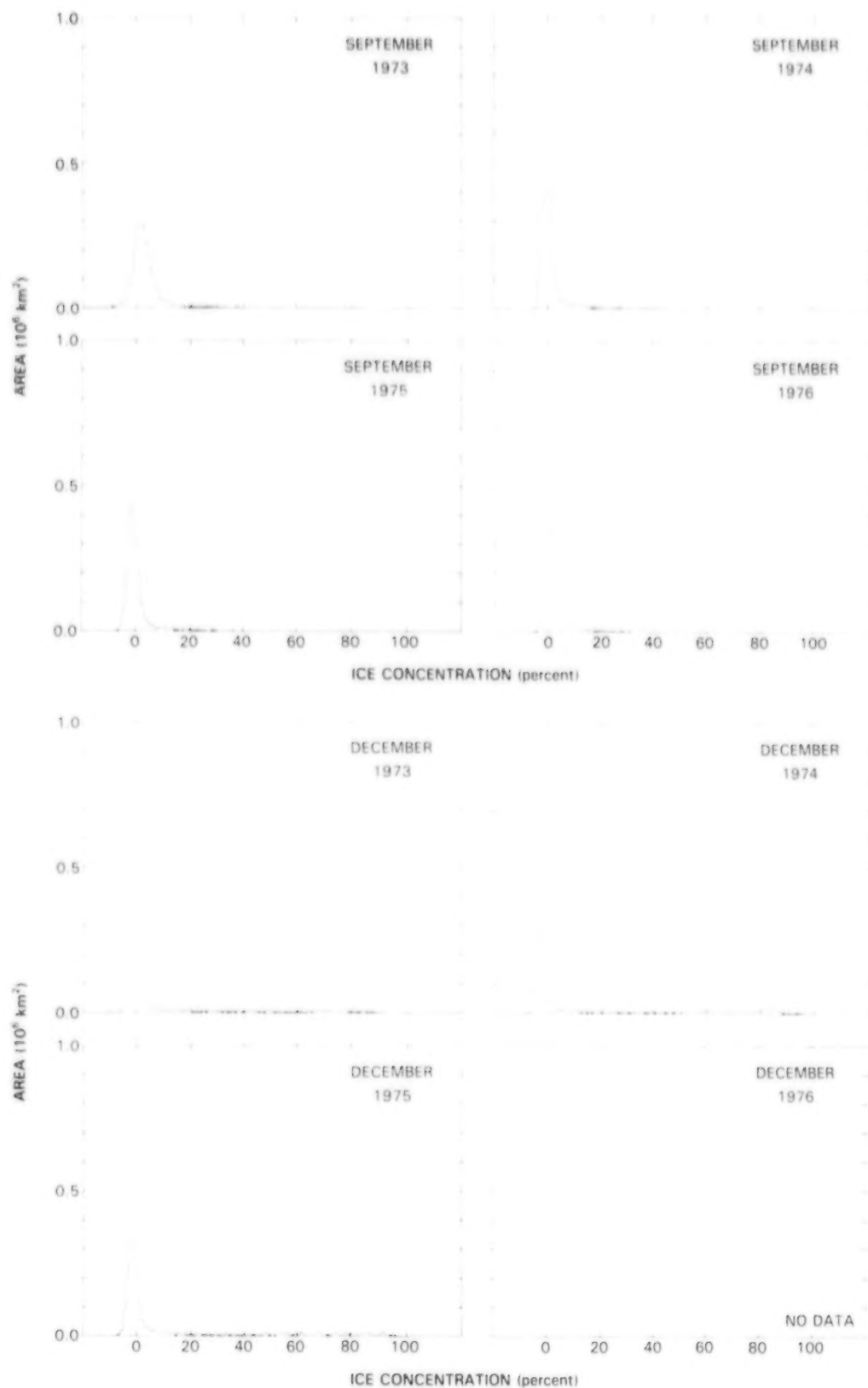


Figure C-5b. Year-to-year comparison of areal distributions of ice concentrations for the Bering Sea for September and December.

HUDSON BAY

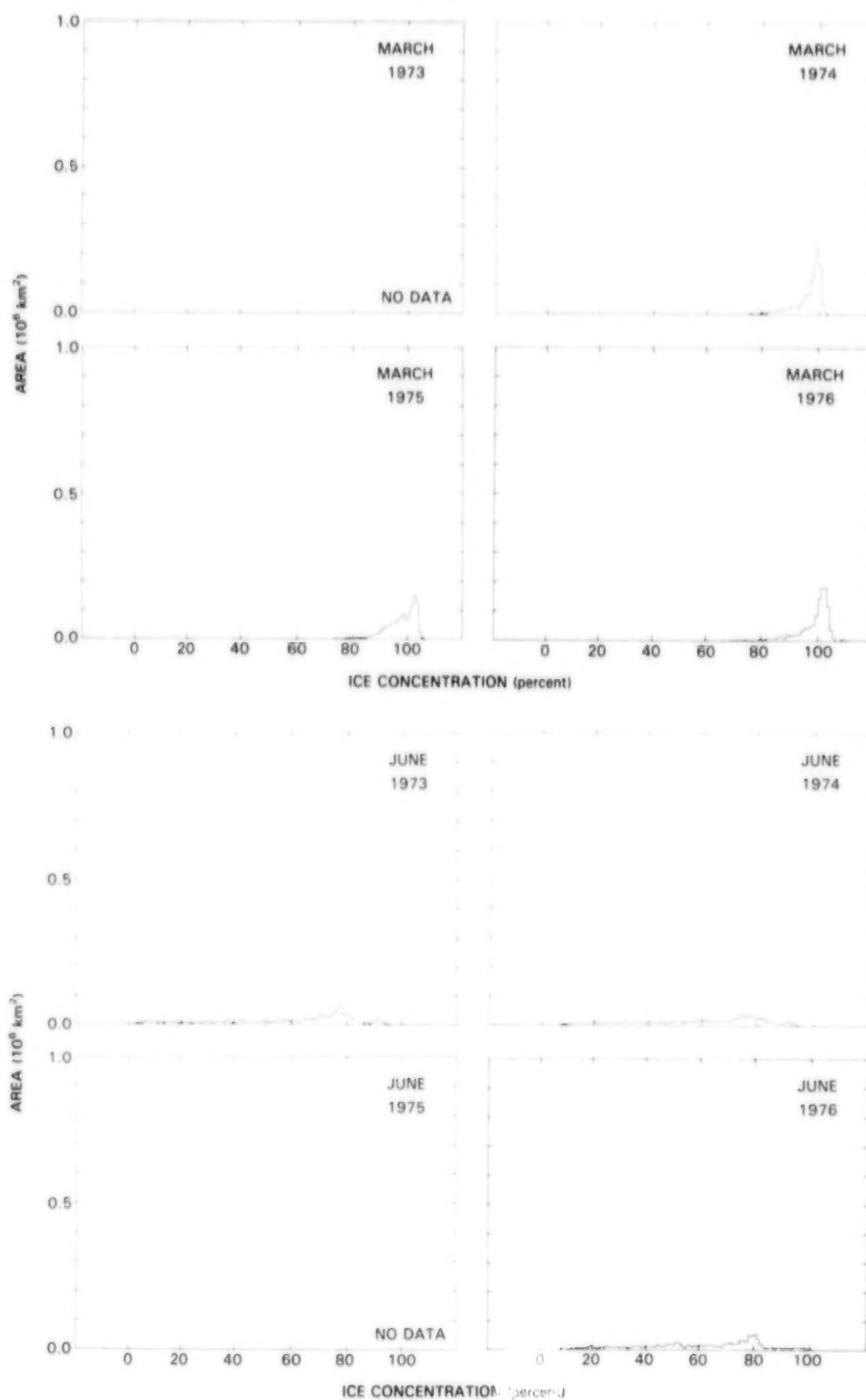


Figure C-6a. Year-to-year comparison of areal distributions of ice concentrations for Hudson Bay for March and June.

HUDSON BAY

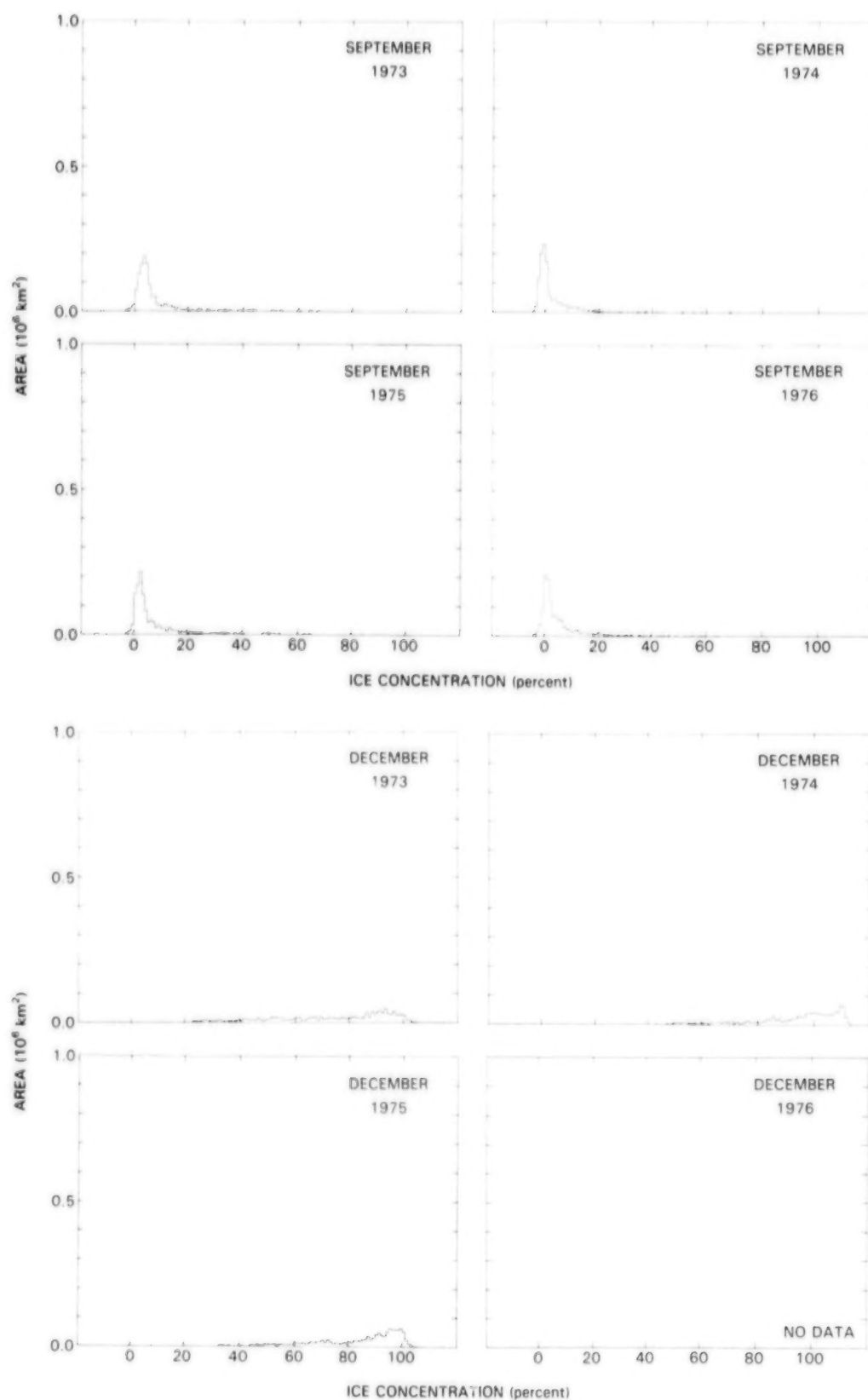


Figure C-6b. Year-to-year comparison of areal distributions of ice concentrations for Hudson Bay for September and December.

BAFFIN BAY/DAVIS STRAIT

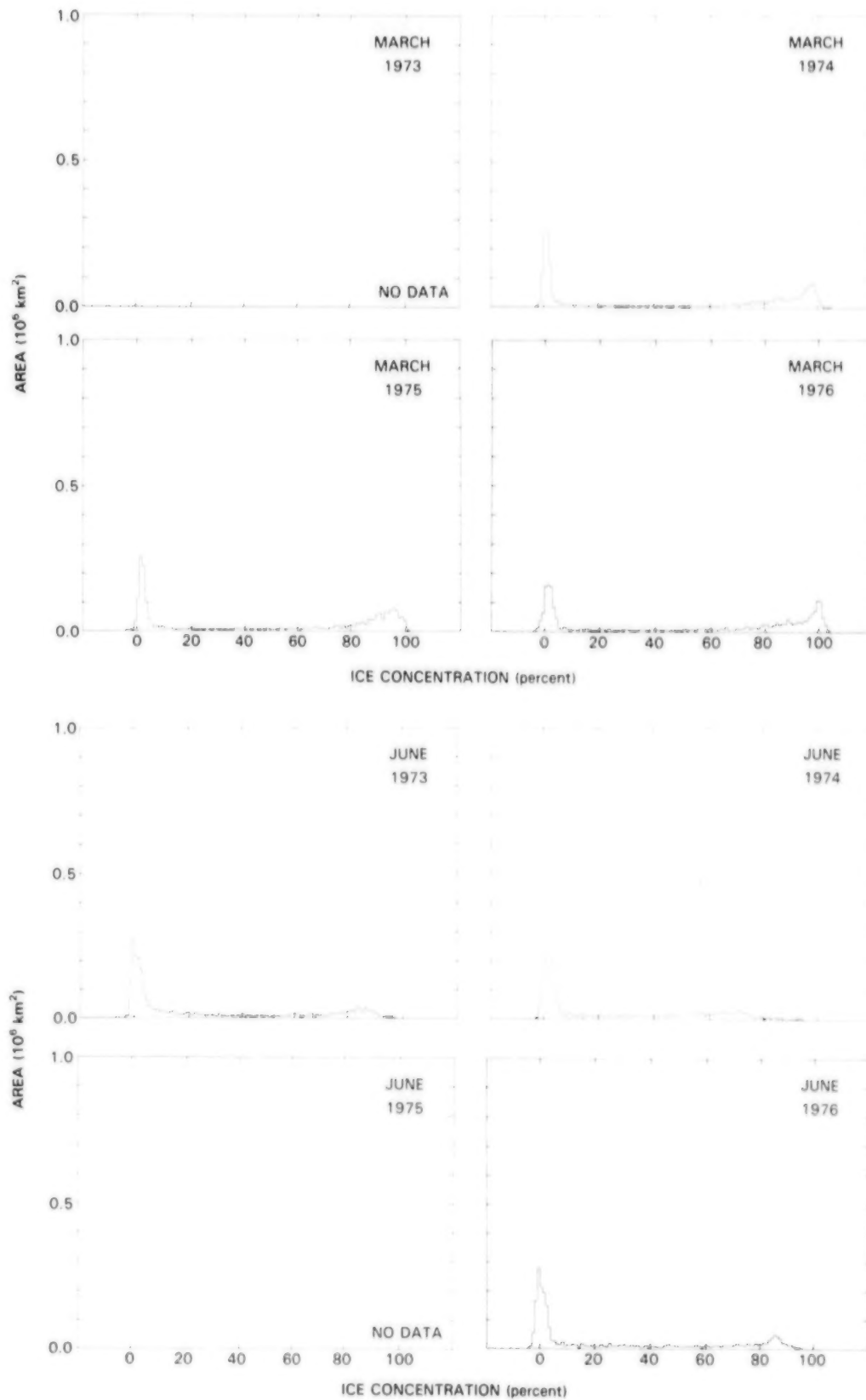


Figure C-7a. Year-to-year comparison of areal distributions of ice concentrations for Baffin Bay/Davis Strait for March and June.

BAFFIN BAY/DAVIS STRAIT

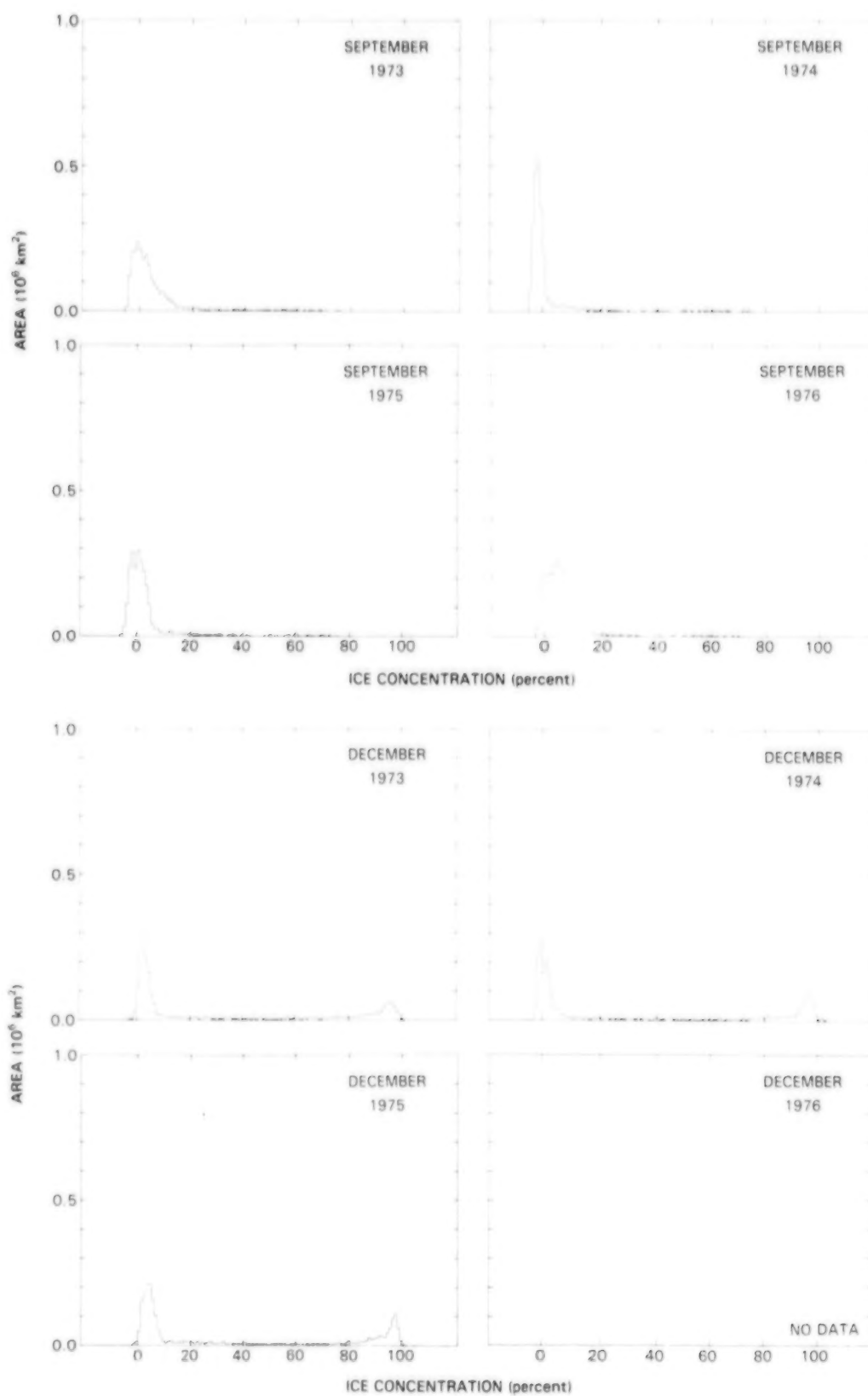


Figure C-7b. Year-to-year comparison of areal distributions of ice concentrations for Baffin Bay/Davis Strait for September and December.

GREENLAND SEA

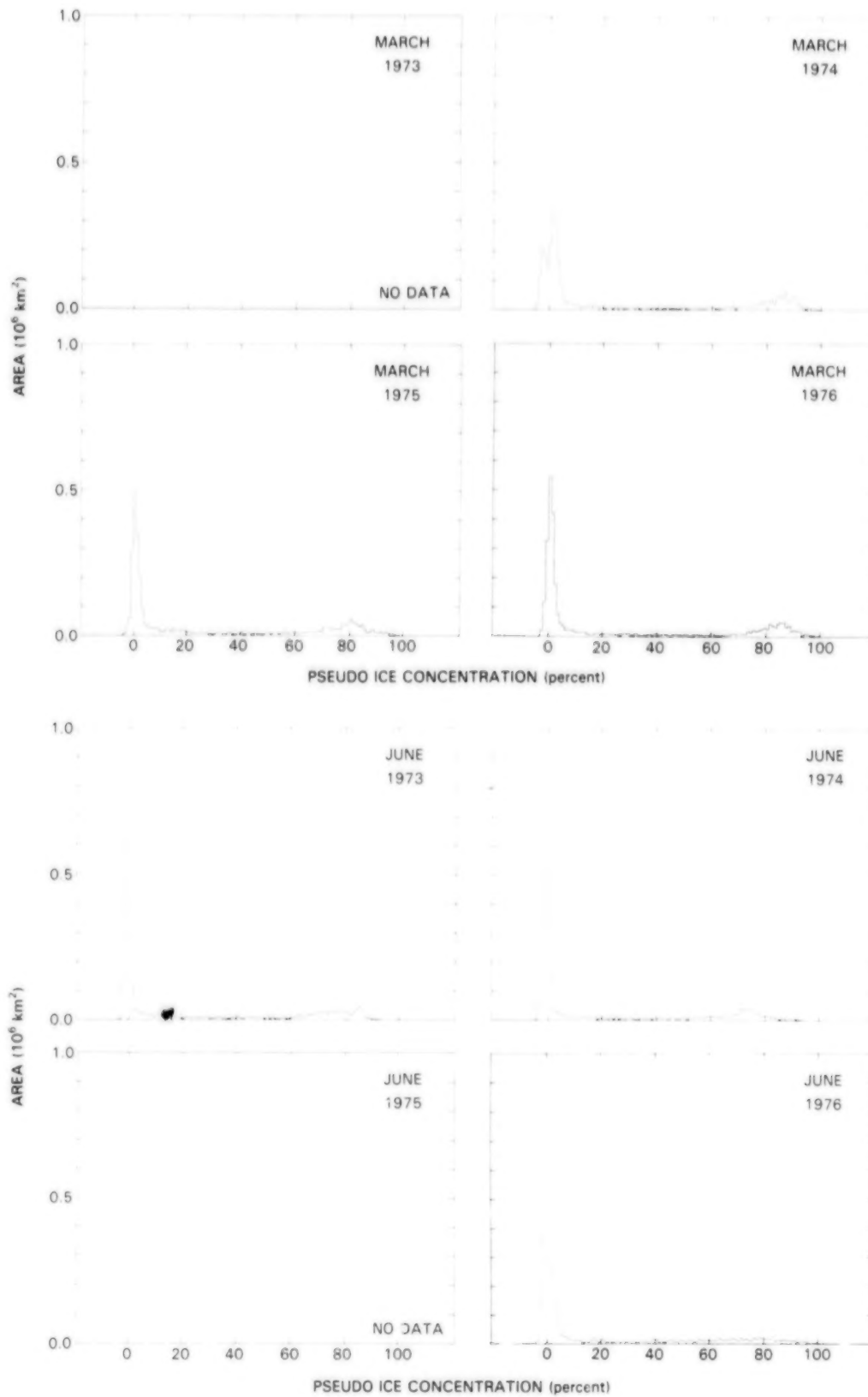


Figure C-8a. Year-to-year comparison of areal distributions of pseudo ice concentrations for the Greenland Sea for March and June.

GREENLAND SEA

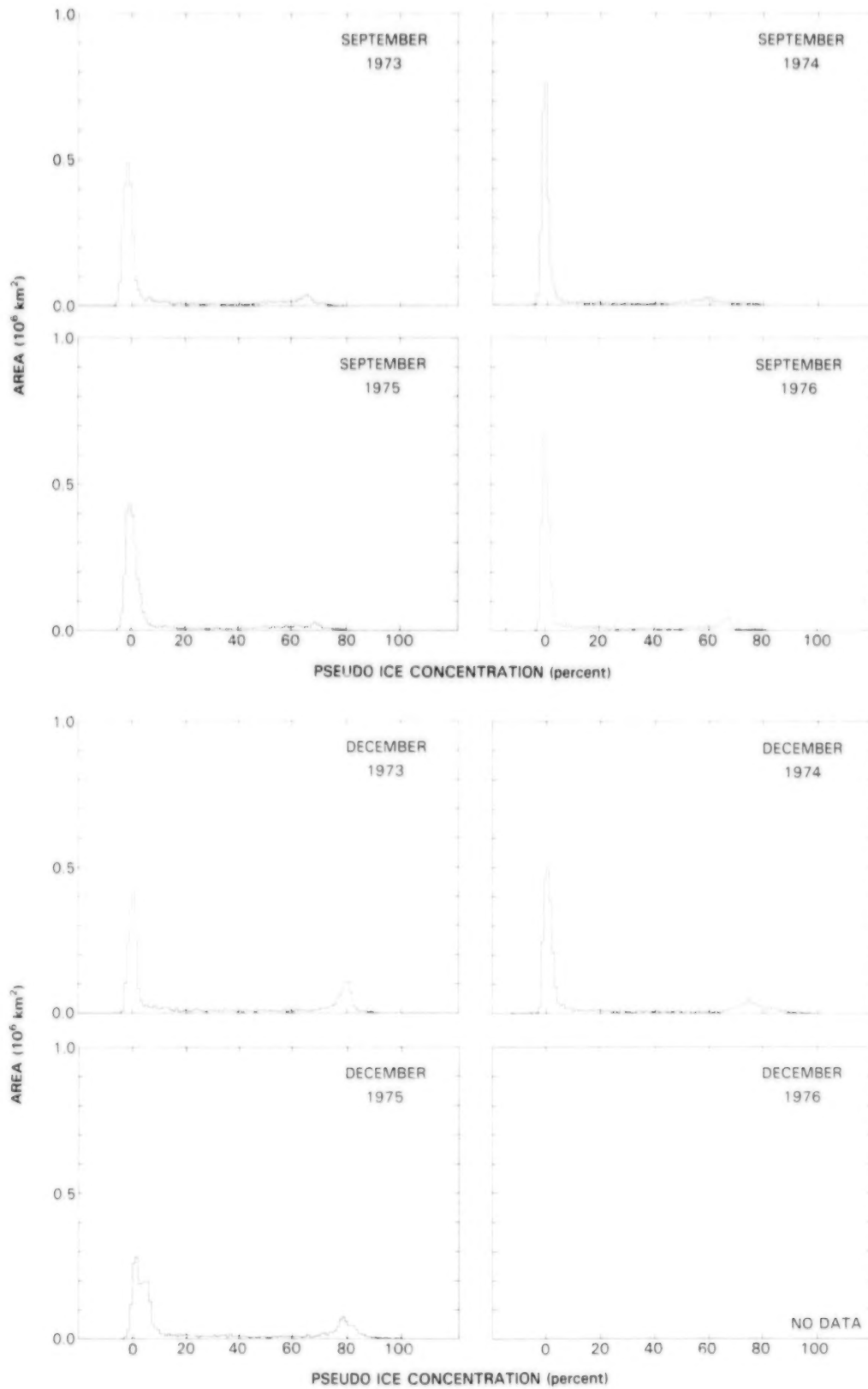


Figure C-8b. Year-to-year comparison of areal distributions of pseudo ice concentrations for the Greenland Sea for September and December.

KARA AND BARENTS SEAS

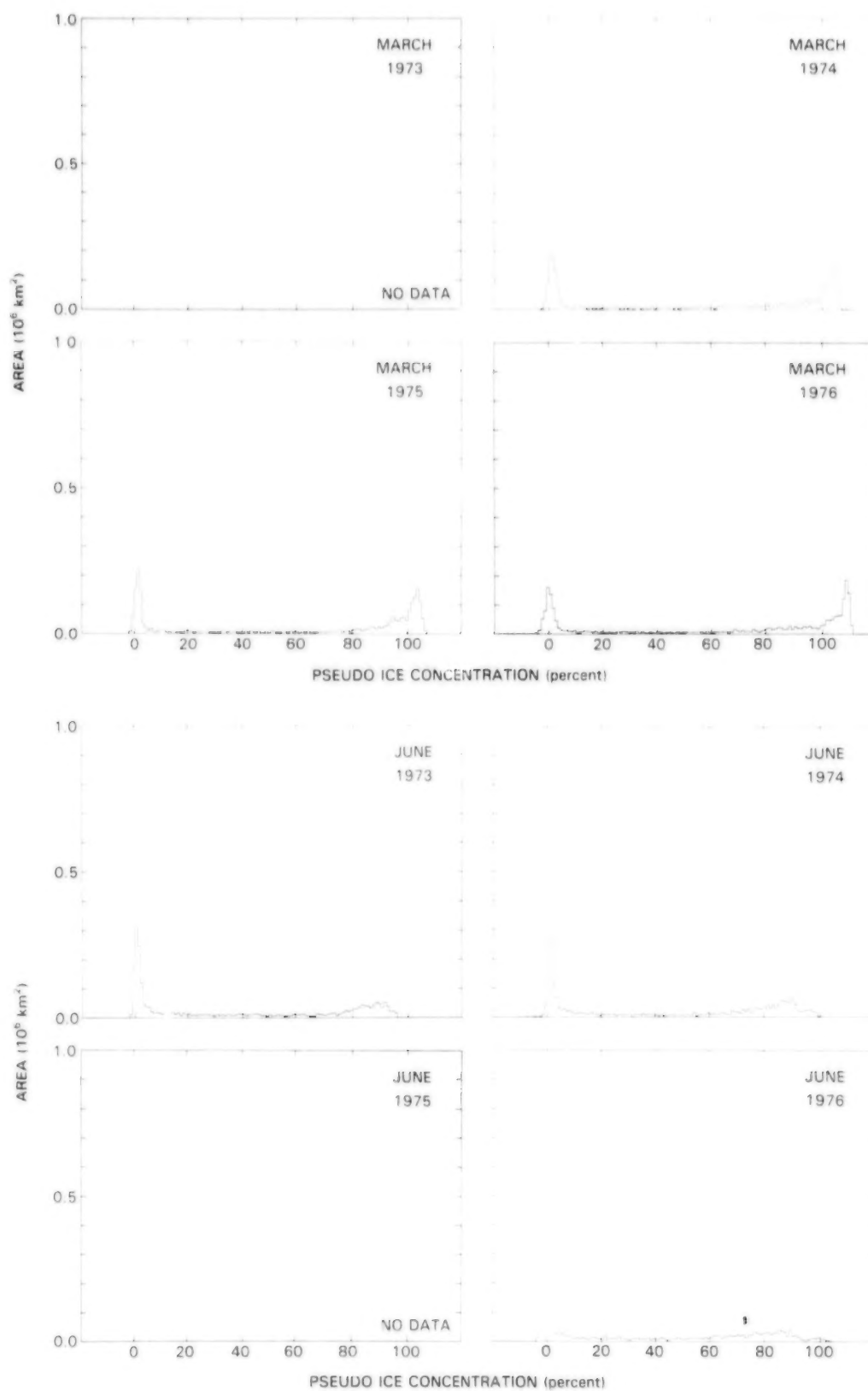


Figure C-9a. Year-to-year comparison of areal distributions of pseudo ice concentrations for the Kara and Barents Seas for March and June.

KARA AND BARENTS SEAS

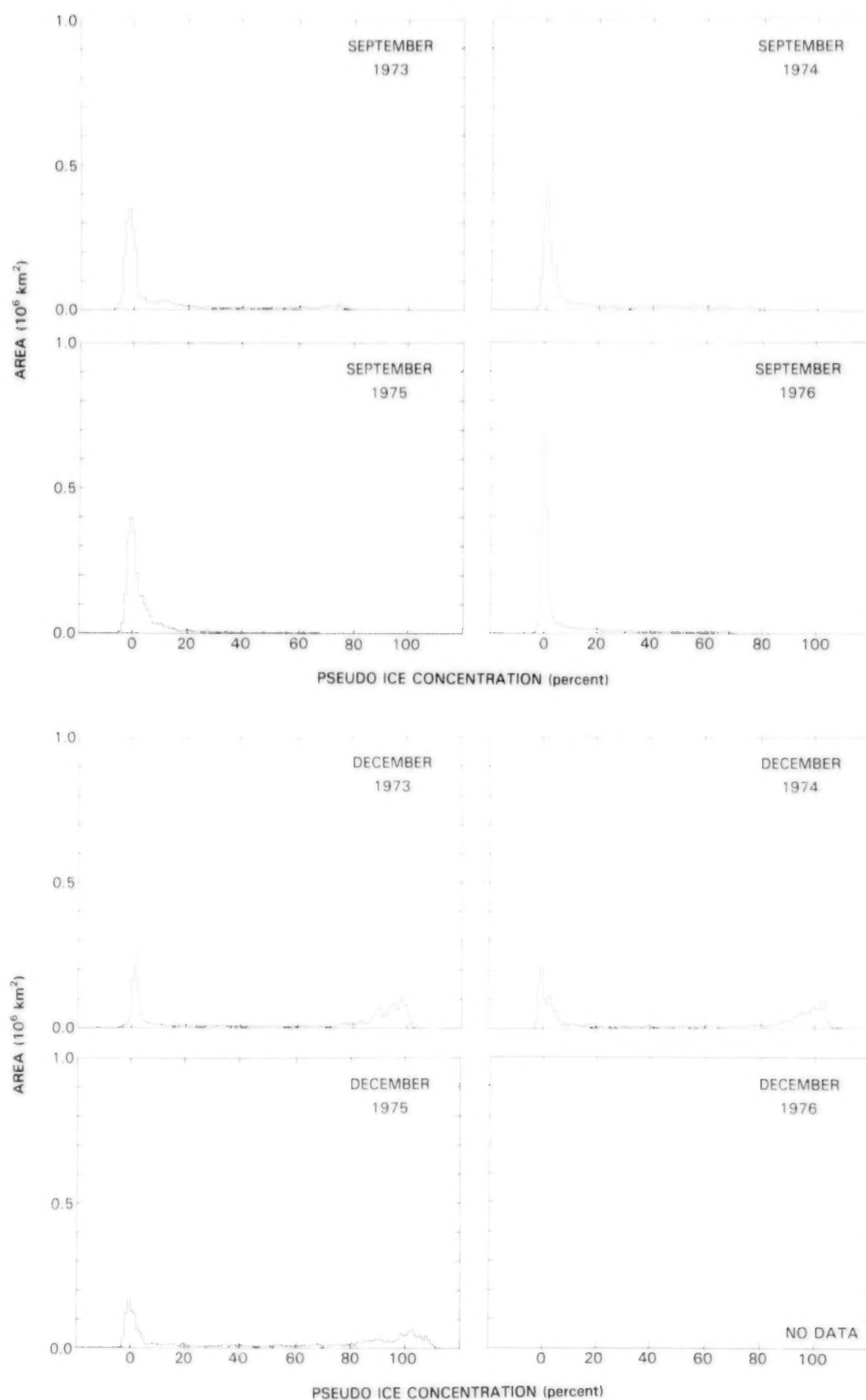


Figure C-9b. Year-to-year comparison of areal distributions of pseudo ice concentrations for the Kara and Barents Seas for September and December.

CANADIAN ARCHIPELAGO

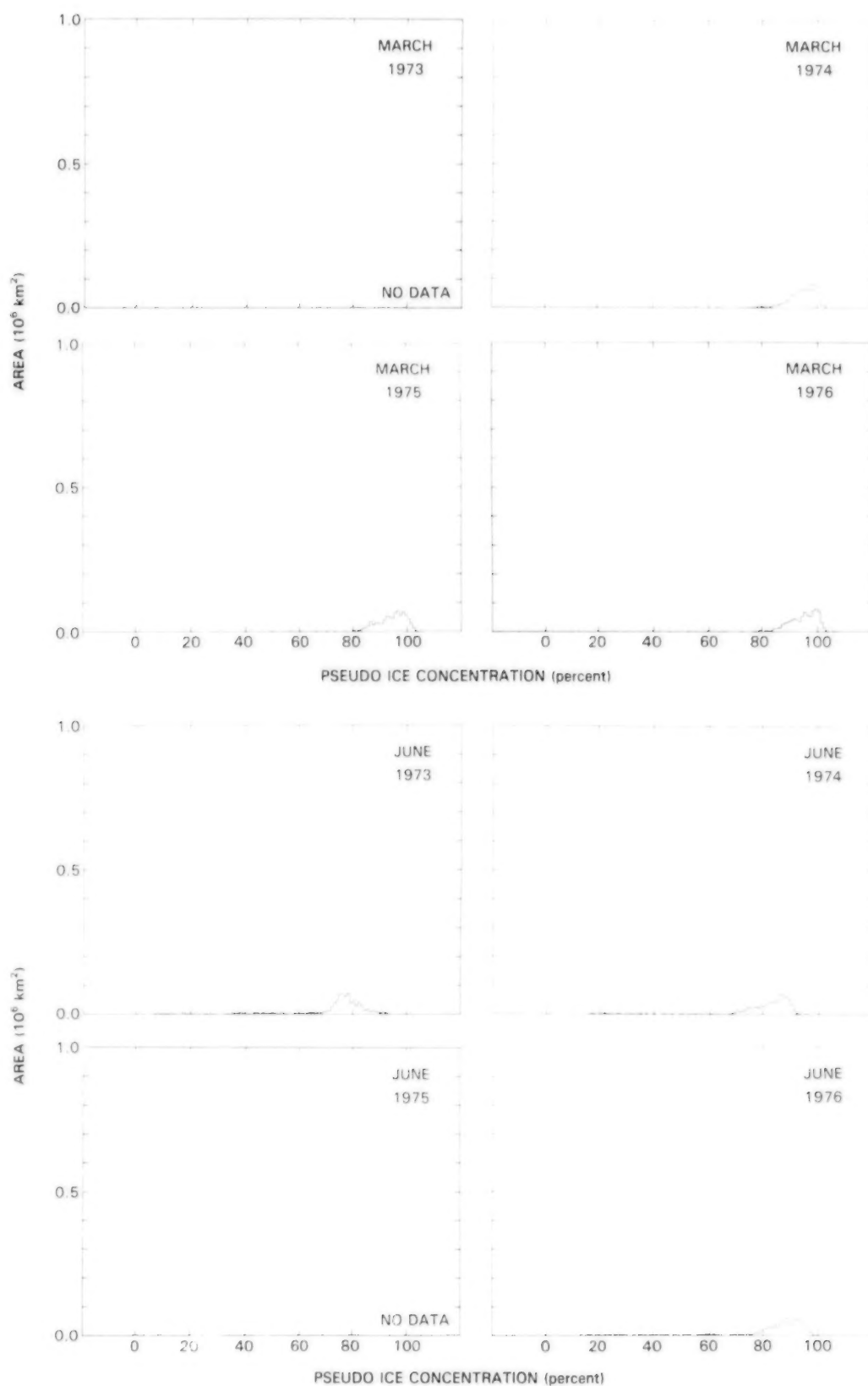


Figure C-10a. Year-to-year comparison of areal distributions of pseudo ice concentrations for the Canadian Archipelago for March and June.

CANADIAN ARCHIPELAGO

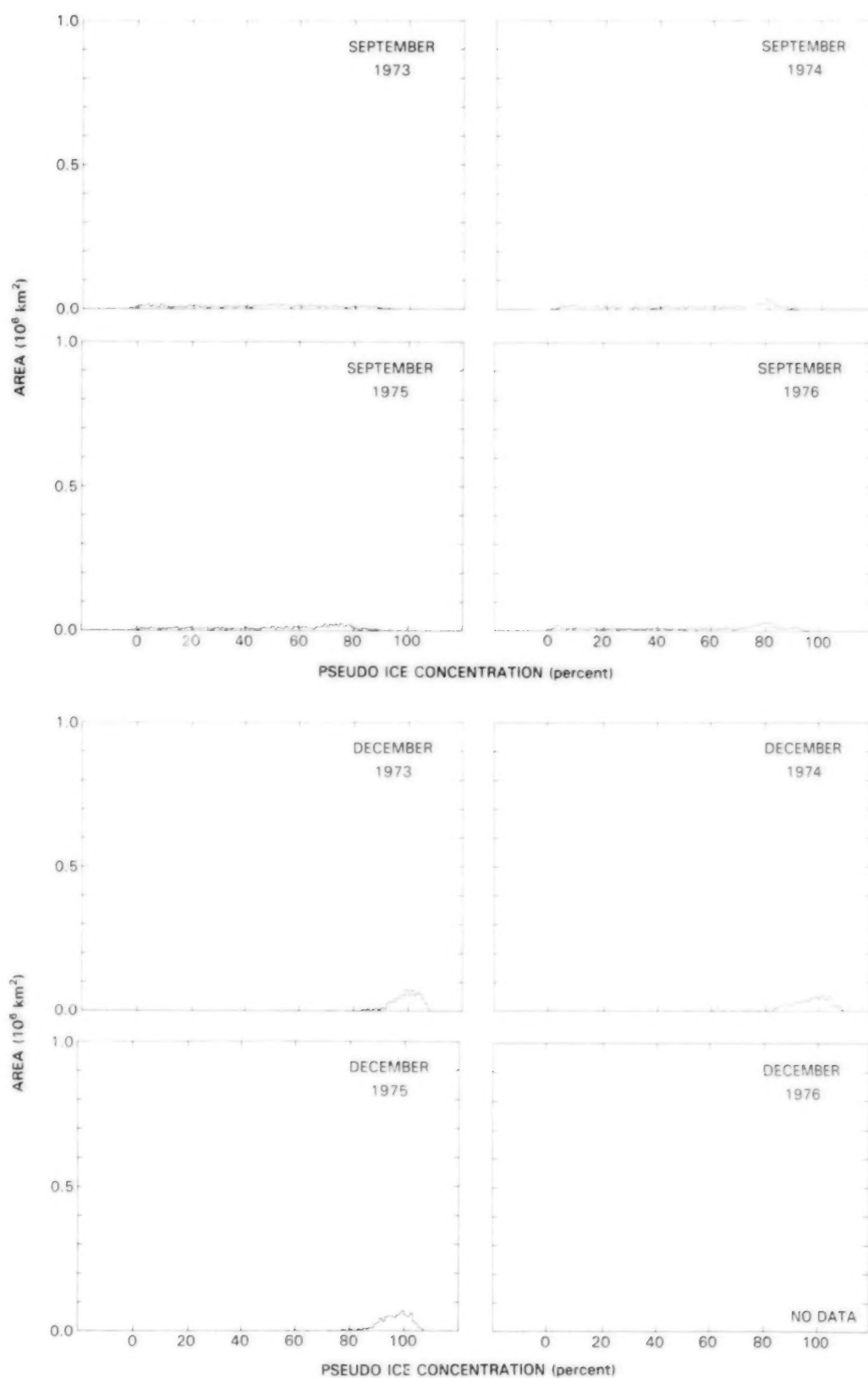


Figure C-10b. Year-to-year comparison of areal distributions of pseudo ice concentrations for the Canadian Archipelago for September and December.

Bering Sea, Hudson Bay, and Baffin Bay/Davis Strait), the areal distributions for September are practically level at 0 for all ice concentrations exceeding 15 percent. The slight rightward shifting of the ocean peak from March to June in both the Sea of Okhotsk and the Bering Sea (Figures C-4a and C-5a) reflects a slight seasonal dependence of the brightness temperature of the ice-free ocean. The uniform and near solid ice cover of Hudson Bay in winter, as well as its exclusively first-year ice character, are reflected in the March distributions by the total absence of an ice-free ocean peak and the fairly narrow ice peak near 100-percent ice concentration (Figure C-6a).

The Greenland Sea curves differ from the curves of the other regions in that they reveal almost no ice with pseudo concentrations exceeding 90 percent (Figures C-8a and C-8b). This suggests, for the Greenland Sea, that where first-year ice exists, it is not heavily concentrated. The extremely high pseudo ice concentrations in the Kara and Barents Seas in March 1976 (Figure C-9a) confirm the almost total absence of multiyear ice there in that year, a point also mentioned in Chapter 4 and further confirmed in the areal distribution plots by the absence of any ice during the previous September (Figure C-9b).

As discussed in Chapters 3 and 4, key approximations used in determining pseudo ice concentrations from the microwave data are the assumptions of constant values of 0.92 and 138.3 K for the sea ice emissivity and the ocean brightness temperature, respectively, and the calculation of ice temperatures from mean monthly climatological air temperatures. The areal distribution curves in this appendix help to confirm the legitimacy of these approximations. In particular, the narrowness of the ice-free ocean peaks in most of the curves and the approximate consistency in their horizontal placement help to justify the use of a constant value for the ocean brightness temperature; and the fact that in winter the ice peaks in the first-year ice regions occur near 95 to 100 percent shows the appropriateness of the 0.92 value for the emissivity of first-year ice. At the same time, the distributions do naturally reflect the various errors introduced by these approximations, as discussed in Chapter 3 and Appendix A. Nonetheless, the areal distributions show overall consistency with our interpretations of the multiyear and first-year ice differences, and the variations at the high ice concentration levels are within the estimated error.

APPENDIX D

ACRONYMS

AES	Atmospheric Environment Service	NESDIS	National Environmental Satellite, Data and Information Service
AGC	Automatic Gain Control		
AIDJEX	Arctic Ice Dynamics Joint Experiment	NOAA	National Oceanic and Atmospheric Administration
AVHRR	Advanced Very High Resolution Radiometer	NORSEX	Norwegian Remote Sensing Experiment
BESEX	Bering Sea Experiment	NSF	National Science Foundation
CBT	Calibrated Brightness Temperature	SET	Stacked Experimental Tape
DOD	Department of Defense	SMMR	Scanning Multichannel Microwave Radiometer
ESMR	Electrically Scanning Microwave Radiometer	SSMI	Special Sensor Microwave Instrument
ET	Experimental Tape	THIR	Temperature-Humidity Infrared Radiometer
GSFC	Goddard Space Flight Center		
MDHS	Meteorological Data Handling System	TIR	Thermal Infrared Radiometer
MIZEX	Marginal Ice Zone Experiment	USGS	United States Geological Survey
NASA	National Aeronautics and Space Administration	WMO	World Meteorological Organization

c . 4

INDEX

- acronyms, 287
- actual ice area, definition, 118
 - time sequences
 - Baffin Bay/Davis Strait, 188, 220
 - Bering Sea, 180, 220
 - Hudson Bay, 184, 220
 - Okhotsk, Sea of, 175, 220
 - (see also pseudo areas)
- aircraft ESMR data, 48-54, 169-171
- air pockets within the ice, 14
- air pressures, climatological sea level, 30-31, 34-35
 - maps of, 34-35
- air temperatures, climatological surface, 30-33, 98
 - maps of, 32-33
- albedo, 30
- Aleutian Islands, 22-23
- Aleutian Low, 30-31, 39
- Amundsen, Roald, 203
- Antarctic sea ice, 1, 18, 95, 121, 218, 227-228
- anticyclones, 31, 38
- Arctic Ice Dynamics Joint Experiment (AIDJEX),
 - viii, 17, 48-54, 169
- Arctic Ocean, 1, 2, 21, 23, 26, 124, 214
- Arctic Ocean Buoy Network, 160, 165-166
- Arctic Ocean region, 109, 111, 124-126, 160-171, 215, 218, 265,
 - map of, 163
- atmospheric features, 26, 30-39
- atmospheric influences on the sea ice cover, 2,
 - 21, 30, 109, 167, 176-177, 190, 198, 214-218
- Baffin, William, 185, 189
- Baffin Bay, 1, 22, 24, 26, 185-188
- Baffin Bay/Davis Strait region, 109, 111, 185-190, 211, 215, 218
 - map of, 185
- Barents, Willem, 198
- Barents Sea, 22-23, 198-202, 218
 - (see also Kara and Barents Seas region)
- bathymetry, 21, 23-24, 214
 - map of, 23
- Beaufort Gyre, 19, 24-25, 160, 166
- Beaufort Sea, 22-23, 166
- Bering, Vitus, 172, 176
- Bering Gyre, 24-25
- Bering Sea, 1, 22-24, 26, 176
- Bering Sea Experiment (BESEX), 17, 177
- Bering Sea region, 109, 111, 176-180, 214-215, 218, 221, 227
 - map of, 176
- Bering Strait, 22-24
- Borough, Steven, 198

- bottom water formation, xv, 2
- brightness temperature histograms, 97, 246
- brightness temperature maps, satellite ESMR, 59
 - annual means, 92-93
 - four-year monthly averages, 86-91
 - monthly averages, 62-85
 - three-day averages, 49, 57, 59, 60
- brightness temperatures, 42, 94
 - equation for, 94
 - ice, 61
 - time variability of, 45-48
 - uncertainty in, 102
 - water, 58, 96, 247
 - uncertainty in, 102
- brightness temperatures, aircraft ESMR, 50-56
 - maps of, 52, 55, 56
- brine, 10, 14
- brine drainage, 10, 14
- British Trans-Arctic Traverse, 164
- Button, Thomas, 181
- calibrated brightness temperature (CBT) tapes, 241-242
- calibration procedure, 59-60, 243-247
- Canadian Archipelago region, 109, 111, 203-209, 215, 218
 - map of, 204
- Canadian Basin, 23, 124
- Chukchi Rise, 23
- Chukchi Sea, 22-23
- climatic impacts of sea ice, 1-2, 31
- columnar ice, 3
- concentration, sea ice (see sea ice concentration)
- conical-scan instruments, 41
- continental shelf, 21, 23-24
- continental slope, 23
- contour maps (see sea ice edge contour maps)
- Convair 990, 16, 49, 51
- convective depth, 21, 26
- conveyor belt mechanism, 176
- Cook, James, 176
- cross-scan instruments, 41
- cyclones, 31, 38
- data manipulations, 58, 241-251
 - calibration adjustments, 59-60, 243-247
 - interpolations, 58, 248-249
 - normalizations, 58-59, 245-247
- data processing, 241-251
- Davis, John, 185
- Davis Strait, 1, 22, 24, 26, 185
 - (see also Baffin Bay/Davis Strait region)
- density, sea ice, 14-15
- Derugin Basin, 23-24
- Dezhnev, Semyon, 176
- dielectric properties of sea ice, 44
- Digges Island, 181
- Diomedede Island, 176
- Dutch East India Company, 124
- Earth location of data elements, 243
- East Greenland Current, xvi, 24-26, 191-192, 211
- East Greenland Polar Front, 192
- East Kamchatka Current, 24-25

- Electrically Scanning Microwave Radiometer (ESMR)
 - aircraft, 48-54
 - limitations of, 95, 162
 - satellite, vii-viii, xv, 1, 16, 18, 41, 204, 241, 243
 - validation of, 48-54
- Emissivity, 42-43
 - (see also microwave emissivity)
- Ericsson, Leif, 185
- Eric the Red, 185, 190
- Erik, Nils Adolf, 199
- error analysis, 101-107
- Eurasian Basin, 23, 26, 124
- experimental tapes (ET's), 241
- fast ice, 189, 205
- field of view of sensor, 41-42
- finger rafting, 3-4, 9
- firn, microwave properties of, 61
- first-year ice, 3, 6-8, 10-11, 13-15, 18, 41-48, 265
 - definition, 43
 - emissivity of, 44, 103
 - microwave radiation from, 45-48
 - optical depth of, 43
- floes, sea ice, 3, 6-11, 17
- Foxe, Luke, 181
- Foxe Basin, 180-182
- Fram*, 124, 126, 164, 199
- Fram Strait, 21, 24, 191-192, 194
- Franklin, Sir John, 186, 203
- frazil ice, 3, 8
- freeboard layer, 14, 16, 44
- freezing point, 21
- Fresnel's law, 42
- Frobisher, Martin, 185
- Fyodorov, Ivan, 176
- Ginungagap, 124
- glitch mode, 245
- gray ice, 3-5, 7
- gray-white ice, 3-4
- grease ice, 3, 8, 10
- Greenland, 59, 61, 185, 191, 246-248
- Greenland Sea, 1, 22-23
- Greenland Sea region, 109, 111, 190-198, 214-215, 218, 221, 227, 286
 - map of, 191
- gridding of images, 59
- Gulf Stream, 24, 26, 30
- Gvozdev, Mikhail, 176
- heat transport, negative, 2
- Hudson, Henry, 181, 185
- Hudson Bay, 1, 22, 24, 26, 180-181
- Hudson Bay region, 109, 111, 180-185, 215, 218, 221, 227, 286
 - map of, 181
- Hudson Strait, 180-182
- hummocks, 3, 10, 12
- ice edge, 61
 - (see also sea ice edge contour maps)

- ice-edge sharpness, 122
- Iceland ice records, 2
- Icelandic Low, 30-31
- ice sheets and ice shelves, 61
(see also Greenland)
- index of refraction, 42
- interpolation procedures, 58, 248-249
- inversion, temperature, 30
- inversion techniques, 43
- Jackman, Charles, 198
- Jan Mayen Gyre, 192, 195
- Kamchatka Peninsula, 22, 24, 215
- Kara and Barents Seas region, 109, 111, 198-203, 215, 218
map of, 199
- Kara Sea, 1, 22-24, 198-199
- keels, 3
- Koldewey, Karl, 191
- Kuril Basin, 24
- Labrador Current, xvi, 25-26, 189, 211
- Labrador Sea, 22-24
- Lady Ann Strait, 24
- Lancaster Sound, 24
- Laptev Sea, 22-23
- leads, 3-5, 17, 218
microwave effects of, 48, 53
- Lena River, 24-25
- Little Ice Age, 2
- location map, 22
- Lomonosov, Mikhail, 125
- Lomonosov Ridge, 23, 124
- Lona Trough, 191
- low-radiance envelopes, 53-54, 58
- Mackenzie River, 24-25
- marginal ice zone, 192, 194
(see also Baffin Bay/Davis Strait region, Bering Sea region, Hudson Bay region, Okhotsk region)
- Marginal Ice Zone Experiment (MIZEX), 192
- mean sea ice concentration, time sequences of
Baffin Bay/Davis Strait, 188, 229
Bering Sea, 180, 229
Hudson Bay, 184, 229
Okhotsk, Sea of, 175, 229
- melt, ice sheet surface, 61
- melt ponds, 3, 5, 12, 16, 30
microwave effects of, 16, 43, 48, 51-53, 103
- meltwater, 10
- Mercator, Gerardus, 124
- microwave brightness temperatures (see brightness temperatures)
- microwave emissivity, 42-48, 103
effects on brightness temperature, 94
uncertainty in, 102
- microwave radiometry, vii, 41-48
- multiyear ice, 3, 5, 10, 12-15, 18, 41-48, 265
definition, 43
emissivity of, 44, 103
microwave radiation from, 45-48, 61
optical depth of, 43
- multiyear ice fraction, 42, 101, 228-229
calculation of, 49, 94-95

- nadir observations, equivalent, 41, 243-244
- Nansen, Fridtjof, 124, 191, 199
- Nansen Sill, 191
- new ice, 3-4, 43-45
- nilas, 3
- Nimbus 5, 1, 16, 245
- Nimbus 6, 245
- nomograms, 18, 42, 49, 95, 98, 101, 162
 pictured, 101
- Nordbukta, 195
- Nordenskiold, Baron, 199
- normalization procedure, 58-59, 245-247
- North Atlantic Current, 24-26, 30
- Northeast Passage, 198
- North Water polynya, 187, 189-190, 218
- Northwest Passage, 1, 176, 181, 185, 199, 203, 209
- Norwegian Current, xvi, 24-25, 109, 198-199, 202, 211
- Norwegian Remote Sensing Experiment (NORSEX), 192, 198
- Norwegian Sea, 22-24
- Novaya Zemlya, 198-200, 202
- numerical modeling of sea ice, 109, 211
- Ob Bank, 192
- Ob River, 24-25
- ocean circulation, 24-26
- ocean mixed layer, 26
- oceanographic features, 21, 23-26
- oceanographic influences on the sea ice cover, 2, 21, 23-29, 176, 192, 198, 211-214
 (see also East Greenland Current, Norwegian Current, West Greenland Current, West Kamchatka Current)
- ocean salinities, 21, 26
 maps of, 27
- ocean temperatures, 21, 26
 maps of, 28-29
- Odden, 193, 195
- Okhotsk, Sea of, 1, 22, 24, 26, 172
- Okhotsk Gyre, 25-26, 211
- Okhotsk region, Sea of, 109, 111, 172-176, 214-215, 218, 221, 227
 map of, 172
- open water area, time sequences of
 Baffin Bay/Davis Strait, 188, 220
 Bering Sea, 180, 220
 Hudson Bay, 184, 220
 Okhotsk, Sea of, 175, 220
 (see also pseudo areas)
- open water within the ice pack, 17, 228
 (see also leads, polynyas)
- optical depth, 42-44
- out-of-phase relationships, 214-215
- Pacific Gyre (see Beaufort Gyre)
- pancake ice, 3, 6, 10
- Parry, Edward, 186, 203
- Parry Channel, 205, 208
- Pet, Arthur, 198
- Peter the Great, 176
- Planck's law, 42

- polar easterlies, 31
- polarization, 243
- polar stereographic maps, 241, 247-249
- polynyas, 3, 9, 17, 53, 169, 190, 198, 218, 221
 - microwave effects of, 48, 53
 - (see also North Water polynya)
- pressures, climatological sea level, 30-31, 34-35, 38
 - maps of, 34-35
- pseudo actual ice area, definition, 118, 250
- pseudo areas (actual ice, open water, mean sea ice concentration), time sequences of
 - all regions, 162, 218, 227
 - Arctic Ocean, 169, 219, 228
 - Canadian Archipelago, 208, 219, 228
 - Greenland Sea, 197, 219, 228
 - Kara and Barents Seas, 202, 219, 228
- pseudo ice concentration histograms
 - all regions, 266-269
 - Arctic Ocean, 270-271
 - Canadian Archipelago, 284-285
 - Greenland Sea, 280-281
 - Kara and Barents Seas, 282-283
 - (see also sea ice concentration histograms)
- pseudo sea ice area, definition, 104, 118
- radiative transfer, 43
 - equation for, 95
- rafting, 3, 6-7
 - finger rafting, 3-4, 9
- Rayleigh-Jeans approximation, 42
- reflectance, 42
- refractive index, 42
- regions used for analysis, 109, 111
- remote sensing, 1, 16-18
- resolution, ESMR, 16-17, 41, 241
- ridging, 3, 5, 7-8, 10, 15-16
- Ross, James Clark, 203
- Ross, John, 186, 203
- Saint Lawrence Island, 176
- salinity, sea ice, 10, 13-14, 16, 42, 44
 - effects on brightness temperature, 42
 - salinity profiles, 13-14
- salt ejection during freezing, 1-2
- salt transport, negative, 2
- Scanning Multichannel Microwave Radiometer (SMMR), 18, 41, 43
- Scoresby, William, 191
- sea ice/atmosphere interactions, 1-2, 21, 30, 109, 167, 214
 - (see also atmospheric influences on the sea ice cover)
- sea ice concentration, definition, 42, 94
- sea ice concentration calculation, 16-18, 41-42, 94-101
 - accuracy of, 18, 102-103
- sea ice concentration color-coded maps
 - annual means, 222-223
 - four-year-average annual means, 224
 - four-year monthly averages, 112-117
 - monthly averages, 128-151
 - month-to-month changes, 152-159
 - month-to-month changes averaged over 4 years, 119-120
 - year-to-year changes in annual means, 225
- sea ice concentration histograms
 - Baffin Bay/Davis Strait, 278-279
 - Bering Sea, 274-275
 - Hudson Bay, 276-277
 - Okhotsk, Sea of, 272-273
 - (see also pseudo ice concentration histograms)
- sea ice drift patterns, 160-161, 164-166, 187, 189, 191-192, 203, 205

- sea ice edge contour maps
 - four-year monthly averages, 110, 262-263
 - monthly averages, 254-261
- sea ice extent, definition, 104, 118, 249
 - annual means, 227
 - time sequences
 - all regions, 162, 218
 - Arctic Ocean, 169, 219
 - Baffin Bay/Davis Strait, 188, 220
 - Bering Sea, 180, 220
 - Canadian Archipelago, 208, 219
 - Greenland Sea, 197, 219
 - Hudson Bay, 184, 220
 - Kara and Barents Seas, 202, 219
 - Okhotsk, Sea of, 175, 220
- sea ice impacts on ocean and atmosphere, v, xv, 1-2
- sea ice properties
 - density, 14-15
 - emissivity, 42-48, 94, 102-103
 - index of refraction, 42
 - optical depth, 42-44
 - salinity, 10, 13-14, 16, 42, 44
 - snow cover, 14, 16, 30, 43, 45, 48, 51
 - temperature, 10, 14, 96, 98, 102-103
 - thickness, 3, 14-15, 45, 125, 163
- sea ice seasonal growth/decay cycle, xv-xvi, 1, 109-209, 215, 218
 - growth/decay rates, 127
 - time sequences of ice concentration classes and ice concentration intervals
 - four-year averages, 121-126
 - individual years
 - all regions, 160-161
 - Arctic Ocean, 167-168
 - Baffin Bay/Davis Strait, 186-187
 - Bering Sea, 178-179
 - Canadian Archipelago, 206-207
 - Greenland Sea, 195-196
 - Hudson Bay, 182-183
 - Kara and Barents Seas, 200-201
 - Okhotsk, Sea of, 173-174
 - uncertainties in, 103-107
- sea ice types, 2-3
 - columnar ice, 3
 - first-year ice, 3, 6-8, 10-11, 13-15, 18, 41-48, 103, 265
 - frazil ice, 3, 8
 - gray ice, 3-5, 7
 - gray-white ice, 3-4
 - grease ice, 3, 8, 10
 - multiyear ice, 3, 5, 10, 12-15, 18, 41-48, 61, 103, 265
 - new ice, 3-4, 43-45
 - nilas, 3
 - pancake ice, 3, 6, 10
 - second-year ice, 3, 46
 - shorefast ice, 10
 - shuga, 3
 - slush ice, 3, 9
 - summer ice, 43-44
 - white ice, 7, 9
 - young ice, 3, 5
- second-year ice, 3, 46
- seesaw relationships, 214
- shear zone, 10
- shorefast ice, 10
- shuga, 3
- Siberian-Canadian Arctic Front, 31, 39
- Siberian High, 31
- Skylab Snow and Ice Experiment, 17
- slush ice, 3, 9
- Smith Sound, 24
- snow cover, 14, 16, 30
 - emissivity of, 51
 - microwave effects of, 43, 45, 48
 - optical depth of, 43
- snow-ice layer, 10
- Special Sensor Microwave Instrument (SSM/I), 41
- stacked experimental tapes (SET's), 241, 244
- summer ice, 43-44
- Temperature-Humidity Infrared Radiometer (THIR) data, 98-100

- temperature, sea ice, 10, 14
 - calculation of, 96, 98
 - uncertainty in, 102–103
 - temperature profiles, 14
- temperatures, climatological surface air, 30–33, 98
 - maps of, 32–33
- temperatures from THIR, 98–100
- thermal inertia, 214
- thickness, sea ice, 3, 14–15, 125, 163
 - effects on emissivity, 45
- Tinro Basin, 23–24
- Transpolar Drift Stream, 19, 24–25, 160, 211
- trends, 227
- Vikings, 190–191
- water densities, 21, 26
- water salinities, 21, 26
 - maps of, 27
- water temperatures, 21, 26
 - maps of, 28–29
- Weddell polynya, 218
- West Greenland Current, xvi, 24–26, 188–189, 211
- West Kamchatka Current, xvi, 25, 176, 211
- white ice, 7, 9
- winds, geostrophic, 31, 36–37
 - maps of, 36–37
- Yenisei River, 24–25
- young ice, 3, 5

END

DATE

FILMED

AUG 31 1987